Environmental Thermal Mechanical Testing Systems

Phoenix is proud to introduce the latest generation of Phoenix Environmental Thermal Mechanical Testing Systems.

Sectors such as aerospace and nuclear endeavour to replicate accurate service conditions for material and component testing, to de-couple and quantify the effects of different thermal and environmental effects on failure.

To support our ongoing work with leading UK universities and research centres, Phoenix has developed a high quality, versatile and compact system, equipped with a full range of control and measurement sensors.

The scope and versatility of the Phoenix ETMTS, which can be used to test materials including metals, ceramics and composites, allows for the widest possible range of accurate and flexible testing.

For more information come and see us on our stand or visit: www.phoenix-mt.co.uk

5th International Small Sample Test Techniques Conference

SSTT 2018

Determination of Mechanical Properties of Materials by Small Punch and Other Miniature Testing Techniques

Edited by:

Robert Lancaster (UK) & Spencer Jeffs (UK)

Papers reviewed by the International Scientific Committee:

Eberhard Altstadt (DE)
Gavin Baxter (UK)
Karel Matocha (CZ)
Martin Abdendroth (DE)
Matthias Bruchhausen (NL)
Raghu Prakash (IN)
Roberto Lacalle (ES)
Robert Lancaster (UK)
Roger Hurst (UK)
Shin-ichi Komazaki (JP)
Spencer Jeffs (UK)
Stefan Holmström (NL)
Steve Brett (UK)
Wei Sun (UK)

July 10-12 2018, Swansea University Bay Campus, Wales, UK

Contents

Plenary Session

Small Scale Testing for Tensile and Fracture Behaviour of Steel

Alternative Miniaturised Test Methods

Impression Creep

Miniaturised Tensile Testing

Small Scale Testing of Advanced Materials

Small Scale Creep Testing

Small Scale Testing Methodologies and Standardisation

Posters

European standard on small punch testing of metallic materials

M. Bruchhausen [1],*, E. Altstadt [2], T. Austin [3], P. Dymacek [4], S. Holmström [5], S. Jeffs [6], R. Lacalle [7], R. Lancaster [8], K. Matocha [9], and J. Petzova [10]

[1] European Commission, JRC, 1755 LE Petten, The Netherlands; matthias.bruchhausen@ec.europa.eu

[2] Helmholtz-Zentrum Dresden-Rossendorf, 01328 Dresden, Germany; e.altstadt@hzdr.de

[3] European Commission, JRC, 1755 LE Petten, The Netherlands; simon.austin@ec.europa.eu

[4] Institute of Physics of Materials AS CR, 61662 Brno, Czech Republic; pdymacek@ipm.cz

[5] European Commission, JRC, 1755 LE Petten, The Netherlands; stefan.holmstrom@ec.europa.eu

[6] Institute of Structural Materials, Swansea University, SA1 8EN Swansea, United Kingdom; s.p.jeffs@swansea.ac.uk

[7] Inesco Ingenieros, Santander, 39005 Spain; lacaller@inescoingenieros.com

[8] Institute of Structural Materials, Swansea University, SA1 8EN Swansea, United Kingdom; r.j.lancaster@swansea.ac.uk

[9] Faculty of Metallurgy and Materials Engineering, VŠB-Technical University of Ostrava, 70833 Ostrava, Czech Rep; matocha.karel@email.cz

[10] VUJE, 91864 Trnava, Slovak Republic; jana.petzova@vuje.sk

* Correspondence: matthias.bruchhausen@ec.europa.eu; Tel.: +31-224-565218

Abstract: In the 1980s, studying the effect of neutron irradiation and temper embrittlement on structural materials for the fusion and fission programmes was a major challenge. In this context the development of small specimen test techniques began, allowing the characterization of structural materials for nuclear applications with small amounts of material. The small punch technique is of one these small specimen test approaches. It is widely used for the development and monitoring of structural materials, however there is currently no comprehensive international standard for small punch testing. An EN standard on small punch testing is currently being developed under the auspices of ECISS/TC101/WG1. Besides describing the apparatus, procedures, and specimens, it will include recommendations for the estimation of tensile, fracture and creep properties from small punch testing as well as machine readable formats for representing and transferring test data.

This paper describes the current status of the standard and highlights some of the changes with regard to the current CWA 15672 (2007).

Keywords: small punch test, standard

1. Introduction

The need for the characterization of irradiated materials for the fission and fusion programs has led to much research into small specimen test techniques [1]. These test techniques have received much interest especially for nuclear applications because they reduce the exposure of staff to radiation, the cost of irradiation experiments and the amount radioactive waste.

The small punch (SP) technique is a small specimen test technique which has received much interest since its introduction in the 1980s in the fusion and fission programs for structural alloys mainly in the U.S. and Japan [2-7].

Nowadays, the SP technique is used for the characterization of structural materials for nuclear power plants [8,9]. It is more and more also being used in other industries like aerospace [10,11], automotive [12] or off-shore [13] and for non-metallic materials like polymers [14] or bones [15].

Despite this increasing use of the SP test there is currently no international standard covering the most relevant aspects of small punch testing. National standards or other guidance documents exist in some countries [16-18] or are under preparation [19]. The most recent European guidance is the CEN Workshop Agreement (CWA) 15627, a pre-normative document [20]. An EN standard "Metallic materials - Small punch test method" is currently being formulated under the auspices of ECISS/TC101/WG1[1]. This standard will cover the estimation of tensile and fracture mechanics properties from cryogenic to high temperatures from SP testing as well as address the estimation of uniaxial creep properties from small punch creep (SPC) data.

---

[1]Working Group (WG) 1 of the Technical Committee (TC) 101 "Test methods for steel (other than chemical analysis)" within the European Committee for Iron and Steel Standards (ECISS)

This article gives an overview of the most important points of the new standard and highlights some of the differences to the current CWA 15627. Note however that at the time of writing the public enquiry phase of the standardization process has not yet started. It may well be that the public enquiry will lead to changes in the standard.

2. Principle of SP testing

In an SP or SPC test, a punch with a hemispherical tip or a ball is pushed through a disc specimen along its axis (Figure 1). The SP test is displacement-controlled, i.e. the punch is pushed with constant velocity of the cross head w through the specimen and the force F required to keep the punch moving is measured as a function of punch displacement v (at the punch tip) or specimen deflection u (measured on the lower side of the specimen, opposite to the contact point between punch and specimen).

In contrast the SPC test is force-controlled, i.e. the punch is pressed with constant force on the specimen and the displacement v or deflection u are measured as a function of time t.

Typical examples of an SP and an SPC curve are shown in Figure 2 (a) and (b).
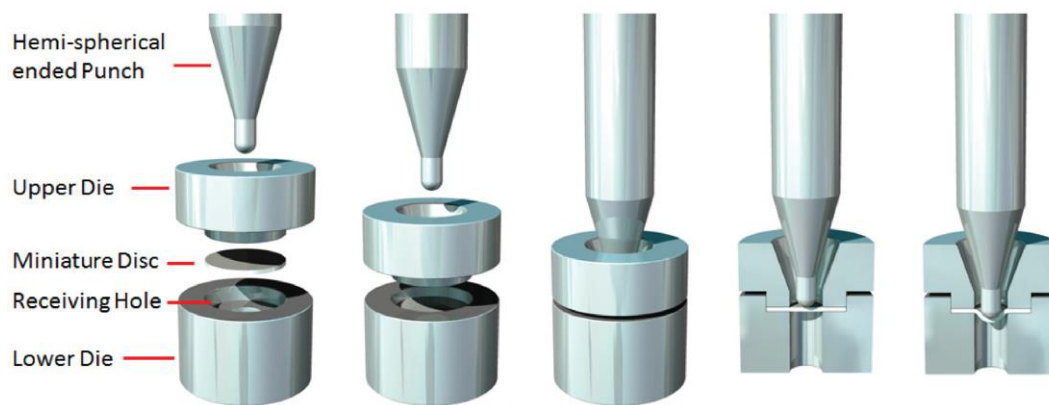
Figure 1. Schematic of a SP test [21].

(a)   (b)
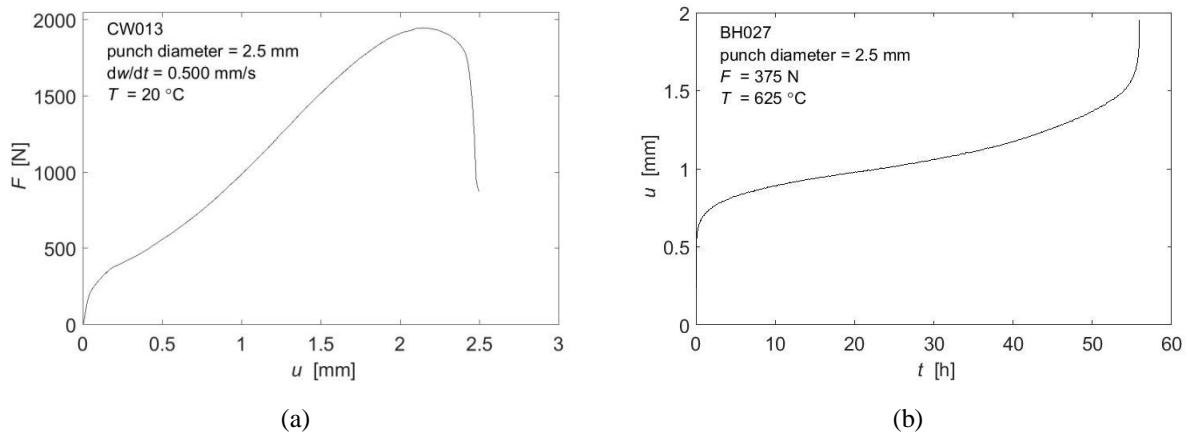
Figure 2. (a) Force-deflection curve from an SP test [22] and **(b)** creep-deflection curve from a SPC test [23].

3. Scope and structure of the new EN standard

The new EN standard specifies the equipment and procedures for carrying out SP and SPC tests of metallic materials. Its informative annexes give guidance for estimating tensile, fracture mechanical and creep material properties.

The standard has the following clauses:
1. Introduction
2. Scope

4. Test piece and test rig

The new standard allows two types of specimen: besides the most frequently used "standard" specimen with a diameter D_S of 8 mm and an initial thickness h_0 of 0.5 mm also "miniature" TEM sample sized specimens may be used where D_S=3 mm, h_0=0.25 mm. However, since there is less experience with the miniature SP specimen, in some cases the more detailed recommendations are given for the larger specimen only.

The preparation of the test pieces follows the same lines as the CWA 15627.

For the test rig, CWA 15627 specifies a punch tip radius r = 1.25 mm for SP tests and a range of r = 1.00-1.25 mm for SPC tests. The new standard stipulates a common r for each specimen size for SP and SPC testing (Table 1).

During the test, the specimen is clamped between an upper and a lower die. The lower die has a receiving hole with diameter D and a chamfer of length L. Both, D and L depend on the type of specimen used (Figure 3, Table 1).
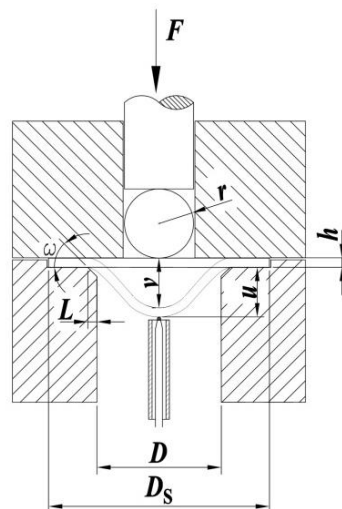
Figure 3. Sketch indicating the main geometrical denominations.

Table 1. Main geometric characteristics of the SP/SPC rig for standard (D_S=8 mm) and miniature specimens (D_S=3 mm).

Test piece	D [mm]	r [mm]	L [mm]
Standard	4	1.25	0.2
Miniature	1.75	0.5	0.2

5. Estimation of material properties

While the provisions with regard to the test piece, the rig, and the test itself remain largely the same as in the CWA 15627, the recommendations in the informative annexes with regard to data evaluation have in some cases been changed and extended quite significantly.

5.1. Estimation of proof stress

Estimates of proof strength $R_{p0.2}$ are obtained from SP data by correlating them to characteristic points on the force deflection curve [24,25]:

$$R_{p0.2} = \beta_{Rp0.2} \frac{F_3}{h_0^2},$$ (1)

where F_e is the elastic-plastic transition force and $\beta_{Rp0,2}$ is an empirical correlation coefficient which depends on the geometry of the test rig.

The new standard maintains equation (1) for relating $R_{p0,2}$ to F_e. Several approaches for determining F_e are discussed in the literature [24,25]. If displacement data is used, the new standard uses the same bilinear fit included in the CWA 15627:

$$f(u) = \begin{cases} \frac{f_A}{u_A} u & \text{for} \quad 0 \leq u < u_A \\ \frac{f_B - f_A}{u_B - u_A}(u - u_A) + f_A & \text{for} \quad u_A \leq u \leq u_B \end{cases}$$ (2)

The fitting parameters f_A, f_B and u_A are determined by minimizing the error:

$$err = \int_0^{u_B} [F(u) - f(u)]^2 \, du.$$ (3)

The standard defines F_e directly as the intersection point f_A (i.e. $F_e = f_A$, Figure 4 (a)) whereas the CWA 15627 used the projection of f_A on the curve $F(u)$ (i.e. $F_e = F(u_A)$). The changes were made because data from a round robin exercise showed less scatter for f_A than for $F(u_A)$. If punch displacement v is used rather than specimen deflection u, a very similar trilinear fit (Figure 4 (b)) is used which is defined as:

$$f(v) = \begin{cases} 0 & \text{for} \quad 0 \leq v < v_0 \\ \frac{f_A}{v_A - v_0}(v - v_0) & \text{for} \quad v_0 \leq v < v_A \\ \frac{f_B - f_A}{v_B - v_A}(v - v_A) + f_A & \text{for} \quad v_A \leq v \leq v_B \end{cases}$$ (4)

(a)

(b)
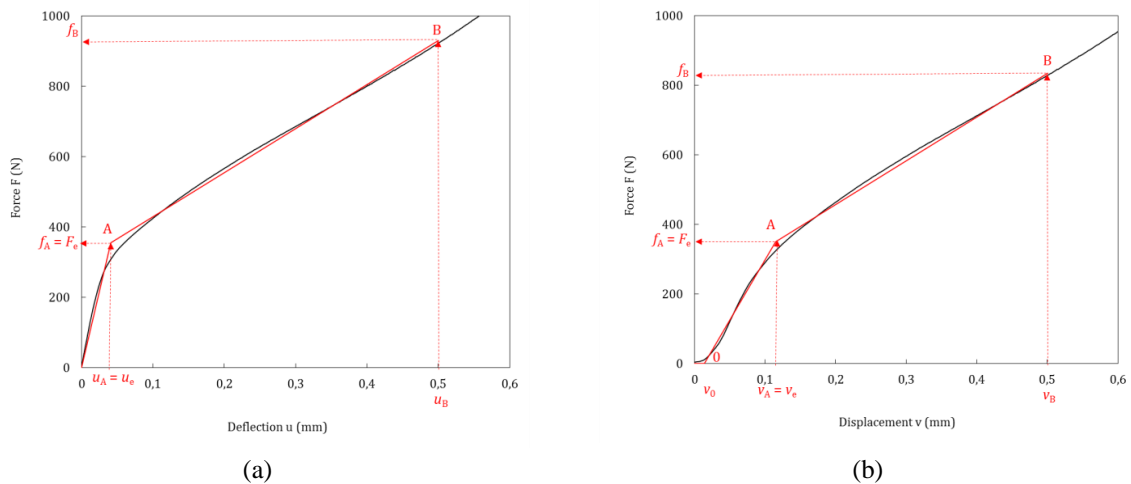
Figure 4. Determination of F_e by **(a)** bilinear method from a force-deflection curve and **(b)** by trilinear method from a force-displacement curve.

The recommended values for $\beta_{Rp0.2}$ for the standard 8 mm specimen are given in Table 2.

Table 2. Proposed $\beta_{Rp0.2}$ values for standard test piece and standard device configuration (steels with $R_{p0.2}$ between 200 and 1000 MPa).

Test piece	Curve type	$\beta_{Rp0.2}$
Standard (8 mm)	$F(u)$	0.510
Standard (8 mm)	$F(v)$	0.479

5.2 Estimation of utlimate tensile strength

For estimating the ultimate tensile strength R_m most authors use correlations between R_m and F_m very similar to that for $R_{p0.2}$ (Equation 1) The best results are obtained by [25]:

$$R_m = \beta_{Rm}\frac{F_m}{h_0 u_{m,}} \qquad (5)$$

where F_m is the maximum force reached during the test and β_{Rm} is a geometry dependent correlation coefficient which needs to be determined experimentally.

Besides this established method, the standard includes a different approach where R_m is directly calculated from the force F_i at a specific deflection u_i or displacement v_i on the SP curve:

$$R_m = \beta_{Rm}\frac{F_i}{h_0^2}, \qquad (6)$$

The location u_i has been determined numerically and is largely independent from the tensile material properties [26]. It is associated with the onset of plastic instability. The correlation factor β_{Rm} has also been determined numerically and verified experimentally for a number of F/M steels [26]. Its values for the geometry and the two types of specimen in the standard are reproduced in Table 3.

Table 3. Parameters for Equation (3) as function of the SP test geometry and the curve type.

Geometry	r (mm)	D (mm)	Lower die edge type	h_0 (mm)	Curve type	$u_i \mid v_i$ (mm)	β_{Rm}
Standard	1.25	4.0	Chamfer 0.2 x 45°	0.5	$F(u)$	0.552 (u_i)	0.192
Standard	1.25	4.0	Chamfer 0.2 x 45°	0.5	$F(v)$	0.645 (v_i)	0.179
Miniature	0.5	1.75	Chamfer 0.2 x 45°	0.25	$F(u)$	0.282 (u_i)	0.205
Miniature	0.5	1.75	Chamfer 0.2 x 45°	0.25	$F(v)$	0.320 (v_i)	0.197

5.3. Estimation of DBTT

The estimation of the ductile to brittle transition temperature (DBTT) was one of the main drivers for the development of the SP test method. The DBTT is the threshold temperature where the material behavior changes from brittle to ductile failure with rising temperature. The temperature at which the transition from brittle to ductile failure occurs is reflected in a rise of the fracture energy. The transition temperature T_{CVN} derived from the change of the absorbed energy in Charpy impact tests is often used as DBTT.

Similarly, an SP transition temperature T_{SP} can be determined from the force-deflection or the force-displacement curve. Many studies have shown that the transition temperatures from SP (T_{SP}) testing are much lower than from Charpy (T_{CVN}). The following relation is often used:

$$T_{SP} = \alpha T_{CVN}. \qquad (7)$$

T_{SP} and T_{CVN} have to be expressed in absolute temperature. $\alpha \approx 0.4$ in many cases [3,7,27,28], although other values have been reported in some cases [27-29].

For determining T_{SP} the small punch energy E_{SP} needs to be calculated as a function of temperature. E_{SP} is the integral of the SP force-deflection curve:

$$E_{SP} = \int_0^{u_m} F(u)du. \qquad (8)$$

Note that the upper integration limit is u_m, the deflection at maximum force as proposed in [30,31] (in contrast to the provisions in CWA 15627 according to which the integration is carried out up to a point where the force has dropped to 80% of its maximum). For the determination of T_{SP} it does not matter whether the integration is carried out over deflection u or displacement v. While the calculated energy values will change, this will not have a significant impact on T_{SP} itself.

In the case of brittle failure the SP curve can have some discontinuities where the force drops quasi-instantaneously because of cracking [5]. Such an event is referred to as pop-in (Figure 5). If an SP curve features pop-ins, the integration should be carried out up to the first significant pop-in, where a significant pop-in is defined as a force drop ΔF corresponding to 10% of the maximum force during the test [32]. The threshold of 10% was selected to be well above any noise level so it can be easily detected on the SP curve:

$$\Delta F = 0.1 F_m. \tag{9}$$
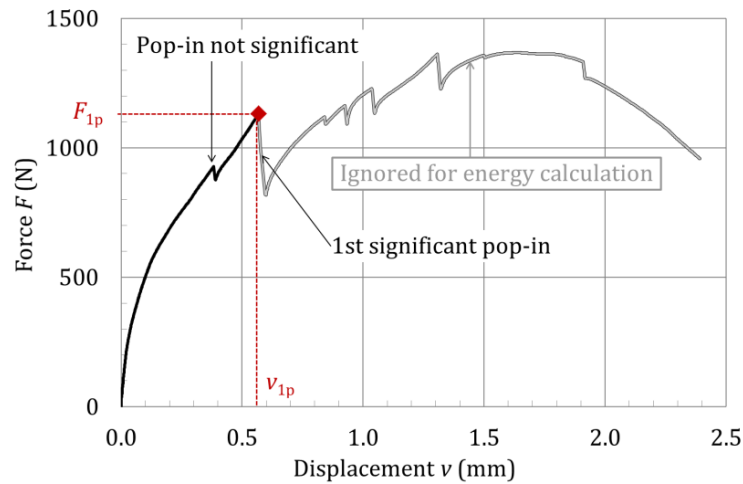
Figure 5. Force-displacement curve of a 13Cr-ODS-steel; energy calculation by integration up to the first significant pop-in.

Before determining T_{SP} from the $E_{SP}(T)$ data it is useful to normalize E_{SP} by F_m as this leads to a constant level in the upper shelf [31]:

$$E_n = \frac{E_{SP}}{F_m}. \tag{10}$$

Then T_{SP} can be determined by performing a least square fit of the following equation to the data [31]:

$$E_n(T) = \frac{E_{US} + E_{LS}}{2} + \frac{E_{US} - E_{LS}}{2} tanh\left[\frac{T - T_{SP}}{C}\right], \tag{11}$$

where E_{US}, E_{LS}, C and T_{SP} are the fitting parameters. In this parametrization E_{US} and E_{LS} are the upper and lower shelf energies (normalized by F_m) i.e. the asymptotes of $E_n(T)$ for very high and low temperatures. Figure 6 shows an example of the T_{SP} determination.
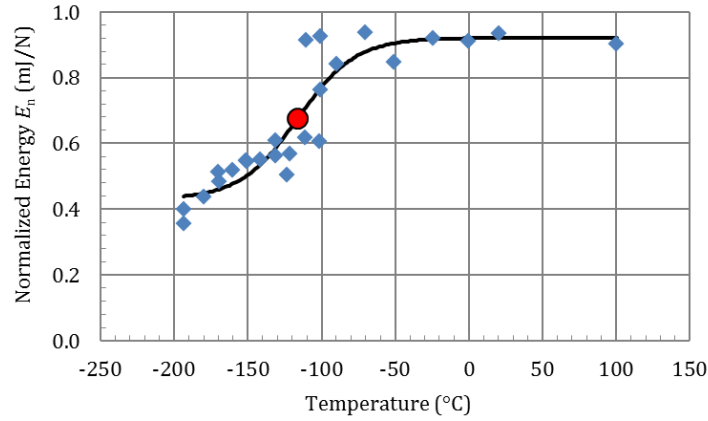
Figure 6. Determination of T_{SP} using the normalised energy E_n for steel P92; T_{SP} = -116 °C (circled symbol).

Alternatively, the DBTT can be estimated based on $T_{SP,\varepsilon}$, the SP transition temperature determined from the effective fracture strain ε_f. The effective fracture strain is defined as:

$$\varepsilon_f = ln\left[\frac{h_0}{h_f}\right],\tag{12}$$

where h_0 is the initial specimen thickness and h_f is the specimen thickness measured adjacent to the area of failure. h_f can be measured by cutting the specimen or non-destructively by techniques like 3D optical microscopy or X-ray computed tomography [31,32].

Once ε_f has been determined for a number of temperatures, $T_{SP,\varepsilon}$ can be calculated just as T_{SP} by fitting the function:

$$\varepsilon_f(T) = \frac{\varepsilon_{US}+\varepsilon_{LS}}{2} + \frac{\varepsilon_{US}-\varepsilon_{LS}}{2} \, tanh\left[\frac{T-T_{SP,\varepsilon}}{C'}\right].\tag{13}$$

5.3. Estimation of fracture toughness

The significant differences in terms of specimen thickness, triaxiality or loading mode between conventional fracture toughness tests [34] and SP tests make the task of developing a methodology for estimating fracture properties complex. In this sense, the proposals included in the standard should be understood more as semi-quantitative approaches which, in any case can be used as a tool for screening criteria or as a valuable alternative to conventional tests in situations where it is impossible to machine standard fracture samples. On the other hand, it should be noted that the reliability of fracture toughness estimations by SP tests is on the order of magnitude of that achieved by correlations based on Charpy tests, which are widely accepted by in-use structural integrity codes [35].

Three options for the estimation of fracture toughness will be incorporated in the EN standard. The first one proposes to correlate the SP and Charpy transition temperatures (section 5.2) and then to use one of the existing correlations in literature [36] between the ductile-brittle Charpy transition temperature and K_{Ic} fracture toughness.

The second proposal estimates the fracture toughness in terms of J_{Ic}, by using the effective fracture strain, see equation (14).

$$J_{Ic} = k\varepsilon_f - J_0\tag{14}$$

where k and J_0 are material-dependent fitting parameters.

The last of the methodologies included in the standard uses test pieces with a lateral notch (Figure 7). This notch allows any orientation of the material to be characterized, and, at the same time, allows the application of the principles of fracture mechanics, which require a pre-existing defect. The procedure for the estimation of the fracture resistance with this type of test specimen is based on the determination of the notch opening at the moment of cracking initiation. This value can be identified with the critical value of δ or CTOD of the material [37].
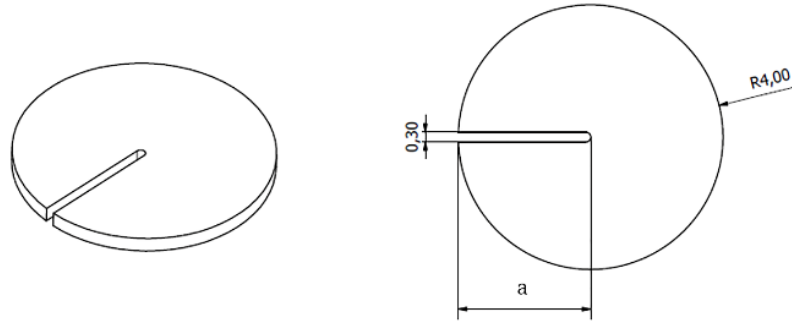
Figure 7. Notched test piece for fracture toughness estimation.

5.4. Estimation of creep properties

The main issue when using SPC data to estimate uniaxial creep properties is the conversion of the SPC force F to the uniaxial creep stress σ. The current CWA 15627 provides the following semi-empirical relation [20]:

$$\frac{F}{\sigma} = 3.33 k_{\text{SP}} \frac{r^{1.2} h_0}{(0.5D)^{0.2}} \tag{15}$$

where r is the punch radius and D the diameter of the receiving hole. k_{SP} is a ductility related empirical correlation factor. However, k_{SP} does not only depend on the material but also on temperature [20,38] which limits its usefulness.

The soon to be published EN standard therefore includes a dedicated annex (annex G) which details a different approach in which the conversion from force to creep stress can be estimated through the "empirical force to stress conversion model" (EFS). The EFS (see Equation 16) was optimized by means of a large database from low alloy and 9Cr steels, such as 14MoV63, X20CrMoV121, P91, P92 and Eurofer-97, but also on a small data set of 316L stainless steel. The EFS force to stress ratio Ψ_{EFS} is given by:

$$\Psi_{\text{EFS}} = \frac{F}{\sigma} = 1.916\, u_{\text{min}}^{0.6579} \text{ [N/MPa]}, \tag{16}$$

where u_{min} is the deflection at which the SPC deflection rate $\dot{u}$ reaches its minimum. The Ψ for the data set used for optimization is shown in Figure 8. It can be seen that the scatter in u_{min} can be substantial. The uniaxial test stresses corresponding to the SPC force at equal time to rupture have been log-linearly interpolated from uniaxial isothermal stress-time data [39, 40].
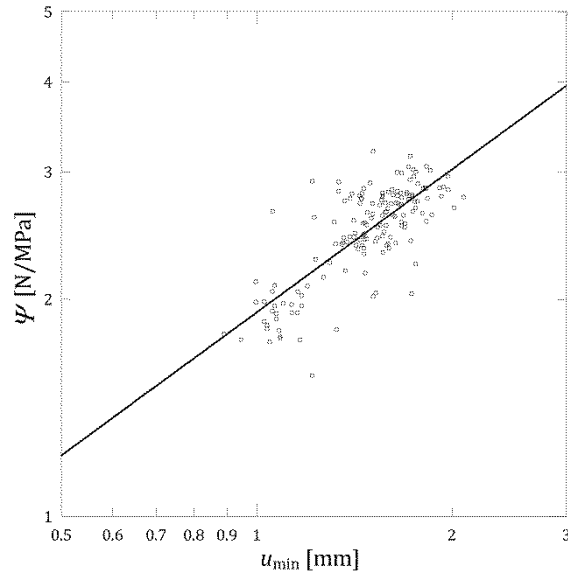
Figure 8. Relationship between Ψ_{EFS} (PSI) and the deflection u_{min} for a variety of steels tested at different organizations. Using the approach in eq. 15, Ψ would be constant and appear as a horizontal line.

In Figure 9 an SPC test curve for 316L stainless steel is shown together with a 3D profilometer scan of the ruptured specimen. The assessment of the SPC curve gives the following test specific values for equivalent stress and creep strain rate determination: t_r=14.3 h, $\dot{u}$ = 0.000231 mm/h, u_{min} =1.53 mm.

(a)   (b)
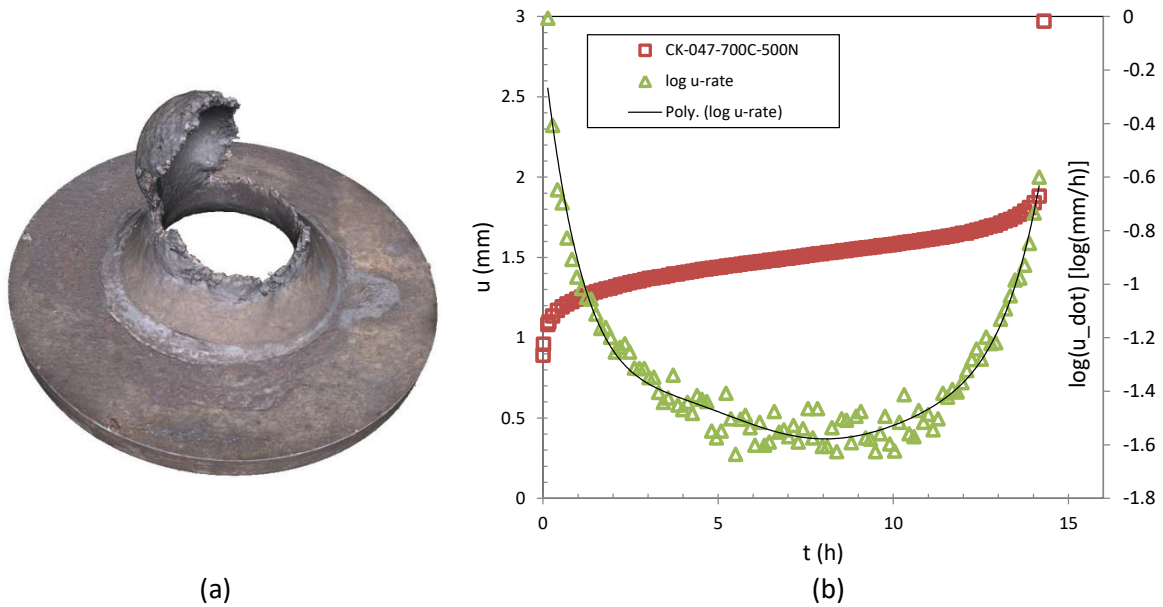
Figure 9. (a) 3D profilometer image of 316L SPC fracture (test CK-047 at 700°C / 500 N, t_r=14.3 h) [41]. Note ductile "hat" type fracture and **(b)** the corresponding time-deflection and deflection rate curves.

In Figure 10 uniaxial creep strength for a thick section forging steel (F92) is plotted against SPC equivalent stress at equal rupture times for equations 15 and 16. The "default value" k_{SP}=1 [20] used in equation 15 is appropriate for steels like P91 but not well suited for the softer F92 forging steel.
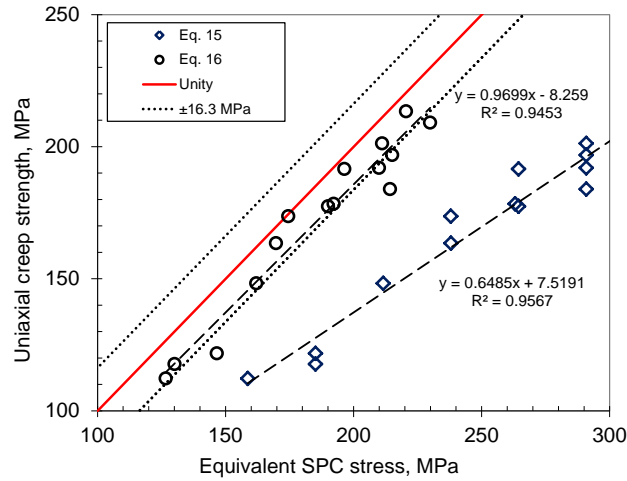
Figure 10. Equivalent SPC stress for F92 estimated by equations 15 and 16. Note that in equation 15 the default k_{SP} value 1 was used which works well for P91 and P92 steels but not for the softer F92.

Annex G also includes a formula for converting the measured minimum deflection rate to an equivalent minimum creep strain rate (equation 17). The equivalent minimum strain rate $\dot{\varepsilon}_{min}$ (1/h) can be calculated from the minimum deflection rate $\dot{u}$ [mm/h] of an SPC test as:

$$\dot{\varepsilon}_{min} = 0.3922 \dot{u}_{min}^{1.191} \text{ [1/h]}. \tag{17}$$

The correlation between minimum deflection rate and minimum uniaxial strain rate is shown Figure 11.
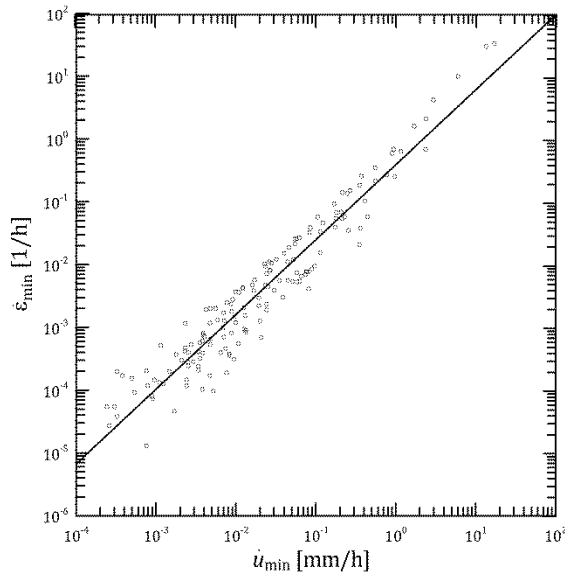
Figure 11. Relation between the minimum deflection rate $\dot{u}_{min}$ and the minimum strain rate $\dot{\varepsilon}$.

6. Data Formats

With mechanical testing having the potential to produce large volumes of data of high inherent intellectual and commercial value, standardized formats offer the opportunity to transfer data efficiently and reliably between digital systems e.g. from test facility to database, database to data processing package, etc. In this context, data formats derived from mechanical testing standards for tensile, creep and fatigue testing have been developed in the scope of a series CEN Workshops on engineering materials data. The methodology relies on treating mechanical testing

standards as specifications from which a data model can be derived. This data model can then be implemented as a data format using the implementation technology of choice.

6.1. Examination of the documentary testing standard

In accordance with the methodology developed during the CEN Workshops on engineering materials data, examination of the EN 15627 small punch testing standard has yielded the structure and content of a corresponding data model, where structure refers to the hierarchical organization of categories of information and is derived primarily from an examination of the table of contents, while content means the fields that can be assigned values and is derived from a close examination of individual clauses. For both the structure and the content, the examination of the testing standard yields tables that map entries in the standard to features in the model. The structural features of the EN 15627 data model are listed in Table 4.

Table 4. Structural features of the EN 15627 data model.

Source	URI
[EN 15627] EN Standard title.	sp
[EN 15627, 8.4 and 9.5] Clause title.	sp:test_report
[EN 15627, 6] First paragraph.	sp:test_report:test_piece
[EN 15627, 6] Table 6.1.	sp:test_report:test_piece:dimensions
[EN 15627, 8.2 and 9.3] Clause title.	sp:test_report:procedure
[EN 15627, 4] Term 4.1.	sp:test_report:procedure:punch
[EN 15627, European Forward] Paragraph 2.	sp:test_report:results
[EN 15627, 2] First paragraph.	sp:test_report:results:properties
[EN 15627, 8.4 and 9.5] Sixth list item.	sp:test_report:results:curve

In turn and as shown in Figure 10, the information in the mapping tables can be presented graphically.
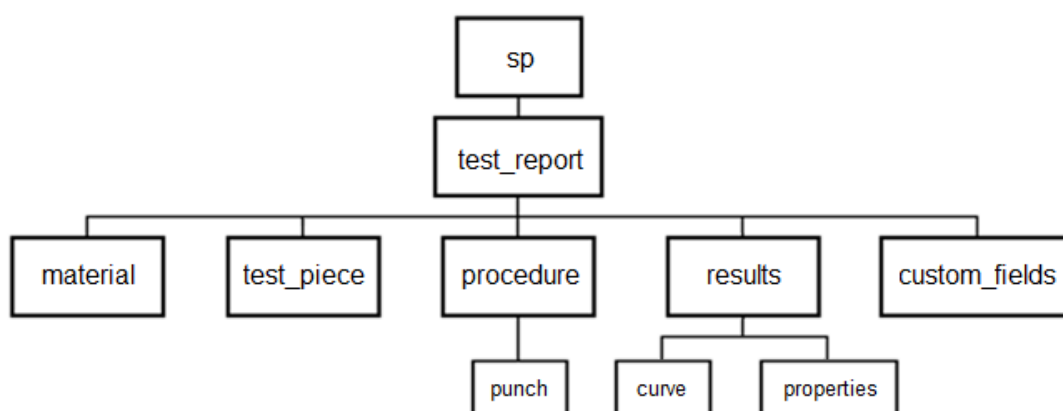
Figure 12. Structural features of the EN 15627 data model.

Having established the structure, the preliminary content is determined from an examination of the vocabulary and symbols clauses, with subsequent examination of the remaining clauses allowing the content to be fully elaborated. Again, this procedure results in tables and figures similar to those of Figure 12 and Table 4, respectively.

This methodology has been applied to EN 15627, yielding an XSD (XML Schema Definition) data format that is intended to be made available from http://uri.cen.eu and referenced from the standard.

7. Conclusions

The new EN standard on SP testing of metallic materials defines the test rig and the procedures for carrying out SP and SPC tests from cryogenic to high temperatures. These provisions are largely consistent with the current CWA 15627. Notable modifications in the new standard are the alignment of the punch diameter between SP and SPC tests and the harmonization of the used symbols. Besides the most frequently used specimen, the new standard will allow using a miniaturized TEM sample sized specimen.

In its informative annexes the new standard provides guidance for the estimation of tensile, fracture mechanical and creep material properties. In particular for the estimation of ultimate tensile strength R_{m} and the creep properties the recommendations differ from the provisions in CWA 15627. While the recommended methods for estimating $R_{\mathrm{p0.2}}$, DBTT and fracture toughness mostly follow those in CWA 15627, they are described in more detail and differ in some points.

The new standard includes the definition of a standard data format to make the test results machine readable and will simplify the exchange of test data between different electronic systems and organizations.

At the time of writing the comments from ECISS/TC101 on the draft standard have been received and implemented. The public enquiry period is expected to start early this summer. Depending on the outcome of the public enquiry, the publication of the final standard can be expected in the course of 2019.

Acknowledgments

References

1. Lucas G., The development of small specimen mechanical test techniques, *Journal of Nuclear Materials*, **1983**, *117*, 327–339, https://doi.org/10.1016/0022-3115(83)90041-7

2. Manahan M.P.; Argon A.S.; Harling O.K., The development of a miniaturized disk bend test for the determination of postirradiation mechanical properties. *Journal of Nuclear Materials*, **1981**, *103 & 104*,1545-1550, https://doi.org/10.1016/0022-3115(82)90820-0

3. Baik J.-M.; Kameda J.; Buck O., Small punch test evaluation of intergranular embrittlement of an alloy steel. *Scripta Metallurgica*, **1983**, *17*,1443-1447, https://doi.org/10.1016/0036-9748(83)90373-3

4. Misawa T.; Sugawara H.; Miura R.; Hamaguchi Y., Small specimen fracture toughness tests of HT-9 steel irradiated with protons, *Journal of Nuclear Materials*, **1985**, *133-134*, 313-316, https://doi.org/10.1016/0022-3115(85)90158-8

5. Kameda J.; Buck O., Evaluation of the ductile-to-brittle transition temperature shift due to temper embrittlement and neutron irradiation by means of a small-punch test, *Materials Science and Engineering*, **1986**, *83(1)*, 29-38, https://doi.org/10.1016/0025-5416(86)90171-0

6. Mao X.; Takahashi H., Development of a further-miniaturized specimen of 3 mm diameter for tem disk (ø 3 mm) small punch tests, *Journal of Nuclear Materials*, **1987**, *150(1)*, 42-52, https://doi.org/10.1016/0022-3115(87)90092-4

7. Misawa T.; Adachi T.; Saito M.; Hamaguchi Y, Small punch tests for evaluating ductile-brittle transition behavior of irradiated ferritic steels, *Journal of Nuclear Materials*, **1987**, *150(2)*, 194-202, https://doi.org/10.1016/0022-3115(87)90075-4

8. Kopriva R., Eliasova I., Kytka M., Implementation of Small Punch Testing and Automated Ball Indentation in the Process of Irradiated NPP Materials Degradation Evaluation. ASME. International Conference on Nuclear Engineering, **2016**, *Volume 5: Student Paper Competition* ():V005T15A043, https://doi.org/10.1115/ICONE24-60620

9. Petzová J.; Březina M.; Kapusňák M.; Kupča L., Application of small punch testing methods for thermal ageing monitoring at primary circuit components in nuclear power plant. *Proceedings of ASME Pressure Vessels and Piping Division Conference*, **2015**, *Vol. 1A*, https://doi.org/10.1115/PVP2015-45539

10. Hurst R.; Lancaster R.J.; Jeffs S.P.; Bache M.R., The contribution of small punch testing towards the development of materials for aero-engine applications, *Theoretical and Applied Fracture Mechanics*, **2016**, *86, Part A*,

11. Lancaster R.J.; Illsley H.W.; Davies G.R.; Jeffs S.P.; Baxter G.J., Modelling the small punch tensile behaviour of an aerospace alloy, *Materials Science and Technology (United Kingdom)*, **2017**, *33(9)*, 1065-1073, https://doi.org/10.1080/02670836.2016.1230168

12. Fernández M.; Rodríguez C; Belzunce F.J; García T.E., Use of small punch test to estimate the mechanical properties of sintered products and application to synchronizer hubs, *Metal Powder Report*, **2017**, 72(5), https://doi.org/10.1016/j.mprp.2016.02.056

13. Walters C.L.; Bruchhausen M.; Lapetite J.-M.; Duvalois W., Fracture Testing of Existing Structures Without the Need for Repairs. *ASME. International Conference on Offshore Mechanics and Arctic Engineering*, **2017**, *Volume 4: Materials Technology* ():V004T03A027. https://doi:10.1115/OMAE2017-61420

14. Rodríguez C.; Cuesta I.I.; Maspoch M.L.L.; Belzunce F.J, Application of the miniature small punch test for the mechanical characterization of polymer materials, *Theoretical and Applied Fracture Mechanics*, **2016**, *86*, 78-83, https://doi.org/10.1016/j.tafmec.2016.10.001

15. Singh J., Sharma N.K., Sehgal S.S.; Small Punch Testing: an alternative testing technique to evaluate tensile behavior of cortical bone, *Journal of Mechanics in Medicine and Biology*, **2017**, 17(6), https://doi.org/10.1142/S0219519417501020

16. Standards Press of China (SPC), *Small punch test methods of metallic materials for in-service pressure equipments – part 1: General requirements*, 2012, GB/T 29459.1– 012.

17. Standards Press of China (SPC), *Small punch test methods of metallic materials for in-service pressure equipments – part 2: Method of test for tensile properties at room temperature*, 2012, GB/T 29459.2–2012.

18. The Society of Materials Science, *Standard for small punch creep test – estimation of residual life for high temperature component*. Japan, 2012, ISBN 978-4-901381-38-3.

19. ASTM WK 61832, New practice for Small Punch test method for metallic materials on https://www.astm.org/DATABASE.CART/WORKITEMS/WK61832.htm (accessed on 27 March 2018)

20. European Committee for Standardization, *Small punch test method for metallic materials*, 2007, CEN Workshop Agreement, CWA 15627:2007 E.

21. Lancaster R.; Davies G.; Illsley H.; Jeffs S.; Baxter G., Structural integrity of an electron beam melted titanium alloy, *Materials*, **2016**, *9(6)*, p. 470, https://doi:10.3390/ma9060470

22. de Weerd W.; Bruchhausen M., Small punch tensile/fracture test data for AISI 316L ar material at 20 °C and a displacement rate of .00833 mm/s (fifth repeat test), version 1.0, European Commission JRC, [Dataset], http://dx.doi.org/10.5290/2700156

23. Lapetite J.-M.; Holmström S.; Bruchhausen M., Small punch creep test data for P92 ar material at 625 °C and a load of 375 N, **2016**, version 1.3, European Commission JRC, [Dataset], http://dx.doi.org/10.5290/2700101

24. Bruchhausen M.; Holmström S.; Simonovski I.; Austin T.; Lapetite J.-M.; Ripplinger S.; de Haan, F., Recent developments in small punch testing: Tensile properties and DBTT, *Theoretical and Applied Fracture Mechanics*, **2016**, *86*, 2–10, https://doi.org/10.1016/j.tafmec.2016.09.012

25. García T.E.; Rodríguez C.; Belzunce F.J.; Suárez C., Estimation of the mechanical properties of metallic materials by means of the small punch test, *Journal of Alloys and Compounds*, **2014**, *582*, 708-717, https://doi.org/10.1016/j.jallcom.2013.08.009

26. Altstadt E.; Houska M.; Simonovski I.; Bruchhausen M.; Holmström S.; Lacalle R., On the estimation of ultimate tensile stress from small punch testing, *International Journal of Mechanical Sciences*, **2018**, *136*, 85-93, https://doi.org/10.1016/j.ijmecsci.2017.12.016

27. Kameda J., A kinetic model for ductile-brittle fracture mode transition behavior, *Acta metallurgica*, **1986**, *34(12)*, 2391-2398, https://doi.org/10.1016/0001-6160(86)90142-2

28. Turba K.; Hurst R; Hähner P.; Evaluation of the ductile–brittle transition temperature in the NESC-I material using small punch testing, *International Journal of Pressure Vessels and Piping*, **2013**, *111-112*, 155-161, https://doi.org/10.1016/j.ijpvp.2013.07.001

29. Contreras M.A.; Rodríguez C.; Belzunce F.J.; Betegón C. Use of the small punch test to determine the ductile-to-brittle transition temperature of structural steels. *Fatigue & Fracture of Engineering Materials & Structures*, **2008**, *31,*727-737, https://doi.org/10.1111/j.1460-2695.2008.01259.x

30. Altstadt E., Ge H.E., Kuksenko V., Serrano M., Houska M., Lasan M., Bruchhausen M., Lapetite J.-M., Dai Y., 2016. Critical evaluation of the small punch test as a screening procedure for mechanical properties. *Journal of Nuclear Materials*, **2016**, 472, 186–195, https://doi.org/10.1016/j.jnucmat.2015.07.029

31. Bruchhausen M.; Holmström S., Lapetite J.-M.; Ripplinger S., On the determination of the ductile to brittle transition temperature from small punch tests on Grade 91 ferritic-martensitic steel, *International Journal of Pressure Vessels and Piping*, **2017**, *155*, 27-34, https://doi.org/10.1016/j.ijpvp.2017.06.008

32. Altstadt E., Serrano M., Houska M., García-Junceda A., 2016. Effect of anisotropic microstructure of a 12Cr-ODS steel on the fracture behaviour in the small punch test. *Materials Science and Engineering: A*, **2016**, 654, 309–316, https://doi.org/10.1016/j.msea.2015.12.055

33. Bruchhausen M.; Lapetite J.-M.; Ripplinger S.; Austin, T., Small punch tensile/fracture test data and 3D specimen surface data on Grade 91 ferritic/martensitic steel from cryogenic to room temperature, *Data in Brief*, **2016,** *9*, 245-251, https://doi.org/10.1016/j.dib.2016.08.061

34. ASTM E 1820-17, Standard Test Method for Measurement of Fracture Toughness, *Annual Book of ASTM Standards*, 2017.

35. BS7910:2013, Guide to methods for assessing the acceptability of flaws in metallic structures, BSI, 2013.

36. Shekhter A.; Croker A.B.L.; Hellier A.K.; Moss C.J.; Ringer S.P., Towards the Correlation of Fracture Toughness in an Ex-Service Power Generation Rotor, *International Journal of Pressure Vessels and Piping*, **2000**, *77*, 113-116, https://doi.org/10.1016/S0308-0161(99)00091-5

37. Lacalle R.; Álvarez J.A.; Arroyo B.; Gutiérrez-Solana F., Methodology for fracture toughness estimation based on the use of Small punch notched specimens and the CTOD concept, In: The 2nd International Conference SSTT 2012, Conference Proceedings, October 2012.

38. Holmström S.; Hähner P.; Hurst R.; Bruchhausen M.; Fischer B.; Lapetite J.-M.; Gupta M., 2014. Small punch creep testing for material characterization and life time prediction". In 10th Liege Conference: Materials for Advanced Power Engineering 2014, Lecomte-Beckers J.; Dedry O.; Oakey J.; Kuhn. B, (eds.), 627–635.

39. Holmström S.; Li Y.; Dymacek P.; Vacchieri E.; Jeffs S.; Lancaster R.; Omacht D.; Zdenek K.; Anelli E.; Rantala J.; Tonti A.; Komazaki S.; Narveena; Bruchhausen M.; Hurst R.; Hähner P.; Richardson M.; Andres D., Creep strength and minimum strain rate estimation from Small Punch Creep tests, *Materials Science & Engineering A* (under review)

40. Dymáček P., Li Y., Dobeš F., Stevens P., New approach to determination of uniaxial creep properties from small punch creep curves, Materials at High Temperatures (under review)

41. Lapetite J-M; Holmström S; Bruchhausen M, Small punch creep test data for AISI 316L ar material at 700 °C and a load of 500 N, **2018**, version 1.0, European Commission JRC, [Dataset], http://dx.doi.org/10.5290/2700158

Numerical investigation of the influence of friction in SPT experiments

M. Abendroth [1,*], H. Zielke [2]

[1] TU Bergakademie Freiberg; martin.abendroth@imfd.tu-freiberg.de
[2] TU Bergakademie Freiberg; henry.zielke@imfd.tu-freiberg.de
* Correspondence: martin.abendroth@imfd.tu-freiberg.de; Tel.: +49-3731-39-4132

Abstract: Virtually all SPT test stands, which are operated in different laboratories, cause contact between different parts of the SPT due to the technical design. These frictional influences can lead to erroneous test results since the force transmitted from the punch to the sample is reduced. This influence can be considerable, particularly in the case of creep tests at high temperatures. The present work analyses various typical experimental setups and the influence of inaccuracies in the setup on the test results. Finally, some requirements and suggestions for an optimized experimental setup are derived.

Keywords: small punch test; friction; finite elements

1. Introduction

The small punch test (SPT) has been used now for more than thirty years to determine mechanical properties from miniaturized samples. The use of small samples becomes necessary if a sufficient amount of material for the production of standard sized samples is not available.

The SPT is used in different sizes and different types. The smallest specimens are standard TEM sized specimen [1,2]. Other authors use specimens cut from remnants of CHARPY specimens, which are square shaped [3–5]. There has been a lot of effort to standardize the SPT and its usage [6], but this is still a running process. At least, there is a common understanding about the important features of the test.
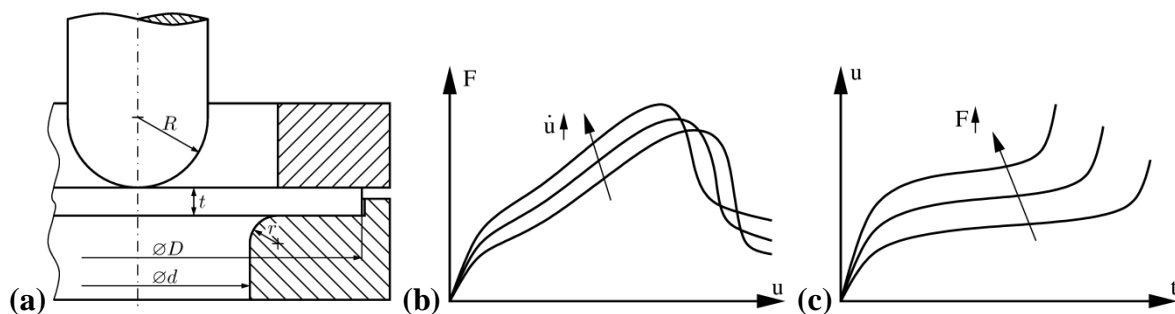
Figure 1. (a) Scheme of a SPT loading device and typical results for the different types of the SPT. (b) CDR-SPT and (c) CF-SPT for a visco-plastic metallic material with a strain induced damage evolution.

A disk or square shaped specimen with a diameter or length D and a thickness t is placed on a circular die with a receiving hole of diameter d. This receiving die can have a rounded or straight chamfer edge of size r. The specimen can be clamped between the receiving die and a down-holder. There are also cases where the specimen is not clamped, usually for testing very brittle materials to avoid initial deformations during clamping. The specimen is loaded centrically using a punch with a spherical tip of radius R. The loading can be a constant displacement rate (CDR) of the punch or a constant force (CF) applied to the punch followed by a holding (creep) time. The experimental results of the test are usually the punch displacement and/or the specimen deflection u and the punch force F. In case of time dependent material behaviour these values are stored together with the time t after starting the test. Figure 1(a) shows the typical test set-up and results for the different types of the SPT considering elastic, visco-plastic material with strain induced damage evolution.

The CDR-SPT can be performed at different punch velocities or specimen deflection rates. The result as shown in Figure 1(b) is a load deflection curve (LDC), which starts with a short linear section related to the elastic response of the specimen, followed by a typical knee whose height is related to the initial yield strength of the tested material. The next part of the curve corresponds to the ductile and strain rate related hardening. The decreasing slope just

ahead of the force maximum indicates a localization of deformation and the onset of material damage. The increasing damage leads finally to a decreasing load bearing capacity of the material due to the failure of the specimen. There is a remaining force at the end of the test, which is due to the frictional force between the penetrating punch and the specimen. If the punch speed is increased the curve is shifted to higher forces due to the strain rate sensitivity and the onset of damage happens at smaller deflections [7].

The CF-SPT is used to determine the material creep behaviour at different loads (stresses). As in uniaxial tensile creep tests we distinguish three parts of the curve, which are related to primary, secondary and tertiary creep, see Figure 1(c) middle. The primary part of the curve is also influenced by some initial plastic deformation at rather high strain rates. The tertiary part is of course also influenced by a localization of deformation and increasing creep damage. For increasing test forces a higher mean specimen deflection will be observed together with decreasing failure times [8]. In contrast to tensile creep tests there is an initial plastic deformation within the specimen, which might have an influence on the subsequent creep behaviour.

The SPT has been applied to a lot of different materials. Numerous evaluation approaches have been developed to correlate SPT-results to those obtained by conventional (standard) specimens. But one important fact just recently came into focus, which is the friction between the different parts of the setup. There is a contact between specimen and receiving die, between specimen and downholder and most important between specimen and punch. The punch itself is somehow guided (not shown in Figure 1) to deform the specimen at its exact centre.

Now, the question is how the contact properties influence the test results. Only a few studies have been found in literature, which explicitly focus on this problem [9–13]. The aim of this paper is to fill some of the gaps and to give suggestions about optimal test setups and evaluation strategies.

2. Models

First, the models for this numerical study are introduced. The material model is composed additively using an elastic, a plastic and a visco-plastic part and could be extended considering material damage [7]. The geometrical models are based on a "perfect" setup and are then changed using imperfections, which might appear in "real" test setups.

2.1 Material model

For the numerical experiments two different material behaviours are considered. For the CDR-SPT an elastic-plastic material model is chosen, which is further extended to an elastic visco-plastic model to simulate CF-SPT experiments. Both models are used in a finite-element framework, where small elastic deformations but finite plastic deformations are considered.

2.1.1 Elastic plastic model

Since an incremental plasticity approach is used, the strain rate $\dot{\varepsilon}_{ij}$ is split into an elastic $\dot{\varepsilon}_{ij}^{\mathrm{el}}$ and a plastic part $\dot{\varepsilon}_{ij}^{\mathrm{pl}}$.

$$\dot{\varepsilon}_{ij} = \dot{\varepsilon}_{ij}^{\mathrm{el}} + \dot{\varepsilon}_{ij}^{\mathrm{pl}} \tag{1}$$

The stresses are computed using HOOKE's law

$$\dot{\sigma}_{ij} = C_{ijkl} \dot{\varepsilon}_{kl}^{\mathrm{el}} . \tag{2}$$

For isotropic elastic material the elastic stiffness tensor is defined as

$$C_{ijkl} = \frac{E}{3(1-2\nu)} \delta_{ij} \delta_{kl} + \frac{E}{2(1+\nu)} (\delta_{ik}\delta_{jl} + \delta_{il}\delta_{jk} - \frac{2}{3}\delta_{ij}\delta_{kl}) , \tag{3}$$

where E denotes the elastic modulus and ν Poisson's ratio. The plastic strain rate is

$$\dot{\varepsilon}_{ij}^{\mathrm{pl}} = \dot{\lambda} \frac{\partial f}{\partial \sigma_{ij}} , \tag{4}$$

The yield condition is

$$f = q - \sigma_{eq}(\varepsilon_{eq}^{pl}) = 0 \tag{5}$$

with q denoting the plastic potential (von Mises stress)

$$q = \sqrt{s_{ij}s_{ij}} \qquad \text{with} \qquad s_{ij} = \sigma_{ij} - \frac{1}{3}\delta_{ij}\sigma_{ij}. \tag{6}$$

To model strain hardening the Voce hardening law is used

$$\sigma_{eq}(\varepsilon_{eq}^{pl}) = \sigma_0 + \sigma_1\varepsilon_{eq}^{pl} + \sigma_2\left[1 - \exp\left(-n\varepsilon_{eq}^{pl}\right)\right] \tag{7}$$

with the initial yield stress σ_0, linear hardening modulus σ_1, non-linear hardening modulus σ_2 and the non-linear hardening exponent n.

2.1.2 Elastic visco-plastic material

For CF-SPT simulations the elastic-plastic material law is extended by a creep strain rate $\dot{\varepsilon}_{ij}^{cr}$.

$$\dot{\varepsilon}_{ij} = \dot{\varepsilon}_{ij}^{el} + \dot{\varepsilon}_{ij}^{pl} + \dot{\varepsilon}_{ij}^{cr} \tag{8}$$

The creep strain rate is modelled using a simple Norton power law

$$\dot{\varepsilon}_{ij}^{cr} = Aq^m N_{ij} \tag{9}$$

with the parameters A and m and the direction of creep strain

$$N_{ij} = \frac{\partial q}{\partial \sigma_{ij}}. \tag{10}$$

2.1.3 Contact modelling and properties

The normal behaviour is simulated using "hard" contact enforced by the ABAQUS penalty method. The tangential behaviour follows COULOMB's friction law

$$F_t = \mu F_n, \tag{11}$$

where F_n denotes the normal force and μ the friction coefficient.

2.1.4 Material properties

A fictitious material is assumed having the material parameters listed in table 1. The parameters are chosen such that they are near to those of a high-strength steel.

Table 1. Material parameters.

E [MPa]	v [-]	σ_0 [MPa]	σ_1 [MPa]	σ_2 [MPa]	n [-]	A [s^{-1}MPa^{-1}]	m [-]
210000	0.3	500	250	250	15	$1\cdot10^{-32}$	12

2.2 SPT setup

Figure 2(a) shows a cross section view of the reference model of a typical SPT set-up. The specimen (1) D=8mm, t=0.5mm is supported concentrically by the receiving die (2) with a bore diameter of d=4mm and a straight chamfer edge r=0.5mm x 45°. The punch (3) has a spherical tip with radius R=1.25mm and a thicker cylindrical part d=6mm, which is rounded at the top, where it comes in contact with the push plate (6). The punch is guided by a lower (4) and upper (5) guiding socket, both having a slightly larger inner diameter than the outer diameter of the punch. The diameter difference is 0.1mm in both cases. Receiving die and the two guidance sockets are rigidly fixed

in space. The contact pairs specimen – die , specimen – punch are modelled using COULOMB's friction model with a friction coefficient μ_2. The other two contact pairs punch – lower guidance and punch – upper guidance become relevant only if the punch is tilted, which will happen in real world conditions. This tilting of the punch results in one ore two additional active contact pairs, which will reduce the force effectively acting on the specimen. The friction coefficient here is μ_1.

Therefore, two imperfect models are used to simulate "real world" conditions. In model B receiving die, specimen and punch tip are aligned exactly concentric, but the punch is tilted such that it just touches the upper guiding socket. Model C accounts for a situation, where the punch tip is shifted horizontally until one side of the punch touches the wall of the lower guiding socket. Additionally, lower die and specimen are non-concentric to the punch tip. Here, the deformation of the specimen causes an additional horizontal force, acting at the punch, causing increasing contact forces between punch and lower guidance socket. The amount of non-concentricity is denoted by Δx .

a) Model A   **b)** Model B   **c)** Model C
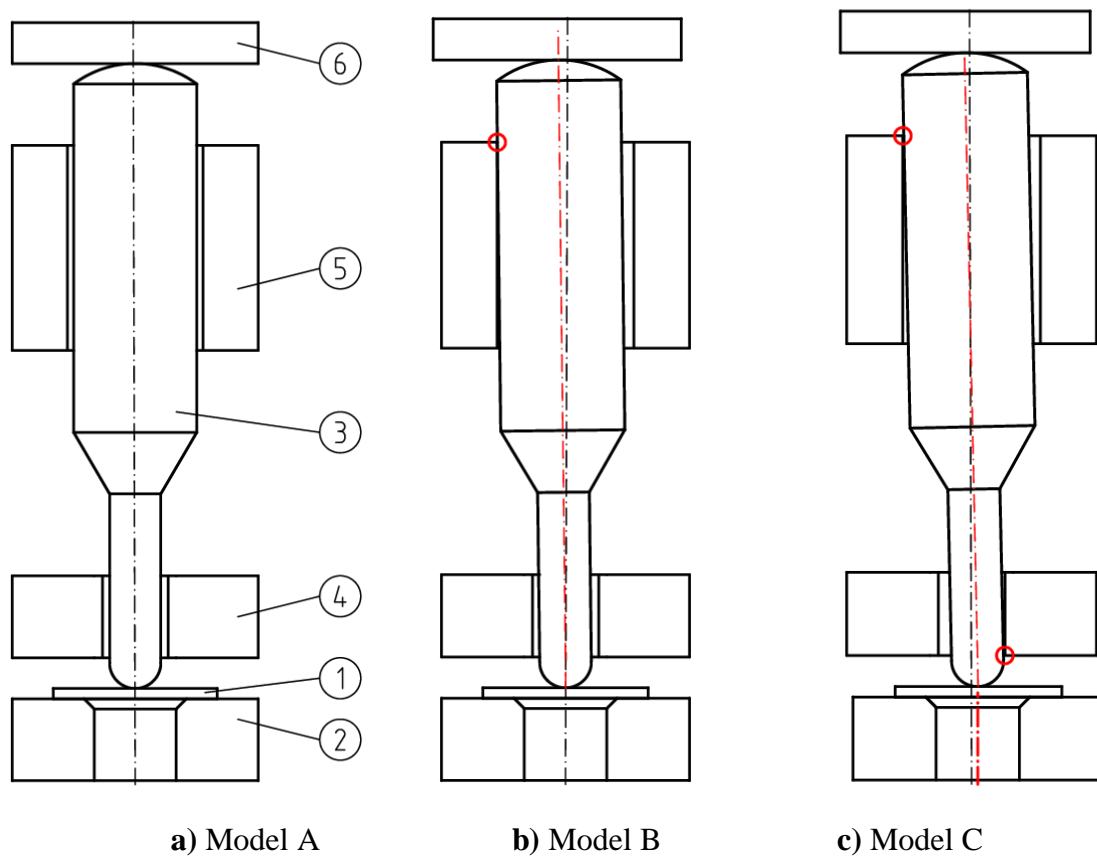
Figure 2. Model of the SPT, 1-specimen, 2-receiving die, 3-punch, 4-lower guidance, 5-upper guidance, 6-punching plate. **a)** Perfect Model; **b)** Friction between punch and upper guiding; **c)** Friction between punch and guiding and non-concentric receiving die. The red circles indicate contact locations.

3. Results

Tables 2 – 4 give an overview about the different cases that have been simulated. The first column denotes the number of the simulation, the second column corresponds to the model according to Figure 2, next three columns define the friction coefficients and shift Δx of the lower die and specimen, and the last column defines the test type (CDR: constant deflection rate, CF: constant force). For CDR-SPT simulations the maximum punch displacement is $u = 3.0$ mm and the load deflection curves are plotted. For CF-SPT simulations a punch force of $F = 350$ N is applied and the punch displacement is plotted over time.

3.1. Model A

Table 2. Simulated cases with model A.

Case	Model	μ_1	μ_2	Δx	Type
1	A	-	0.0	0.0	CDR
2	A	-	0.1	0.0	CDR
3	A	-	0.2	0.0	CDR
4	A	-	0.3	0.0	CDR
5	A	-	0.4	0.0	CDR
6	A	-	0.5	0.0	CDR
7	A	-	0.0	0.0	CF
8	A	-	0.1	0.0	CF
9	A	-	0.2	0.0	CF
10	A	-	0.3	0.0	CF
11	A	-	0.4	0.0	CF
12	A	-	0.5	0.0	CF

Model A considers only the contact between punch and specimen, which has the major influence on the results. Since this arrangement is axisymmetric, 2D-axisymmetric simulations are performed. Figure 3 shows on the left the load-deflection curves for the CDR-SPT. As long as the specimen deflection $u < 0.6$ mm, no friction effects are visible, because there is no sliding between punch and specimen. For specimen deflections $u > 0.6$ mm the influence of friction increases. The maximum load for a CDR-SPT with $\mu_2 = 0.5$ is about 30% higher with respect to test with $\mu_2 = 0.0$. For larger friction coefficients the maximum load occurs at larger specimen deflection. For CF-SPTs shown on the right side of Figure 3 the influence of the friction coefficient is even more severe with respect to the time of failure. No friction means a time of failure of 10000s whereas for a friction coefficient of 0.5 the time of failure reaches 370000s, which means an increase of 3700%.
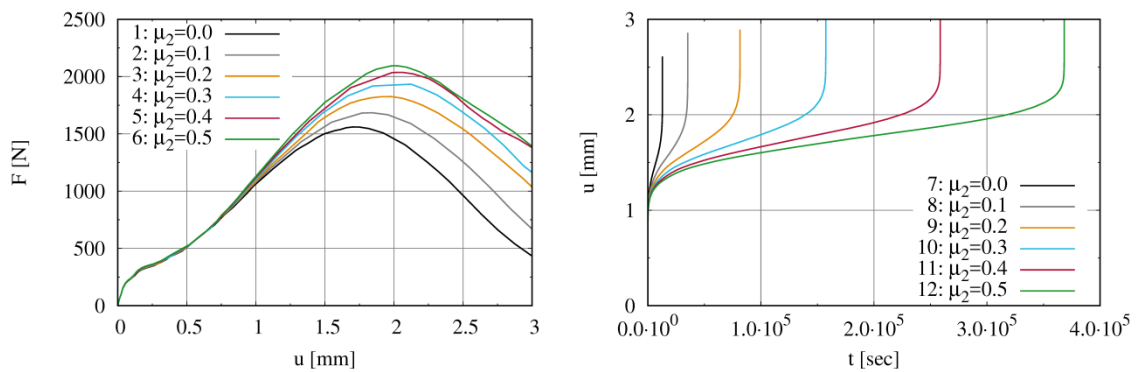
Figure 3. a) CDR-SPT, cases 1 – 6 ; **b)** CF-SPT, cases 7 – 12. Variation of friction coefficient μ_2 for the contact between punch and specimen. There is no contact between punch and guidance.

3.2 Model B

Table 3. Simulated cases with model B.

Case	Model	μ_1	μ_2	Δx	Type
13	B	0.0	0.2	0.0	CDR
14	B	0.1	0.2	0.0	CDR
15	B	0.2	0.2	0.0	CDR
16	B	0.3	0.2	0.0	CDR
17	B	0.4	0.2	0.0	CDR
18	B	0.5	0.2	0.0	CDR
19	B	0.0	0.2	0.0	CF
20	B	0.1	0.2	0.0	CF

21	B	0.2	0.2	0.0	CF
22	B	0.3	0.2	0.0	CF
23	B	0.4	0.2	0.0	CF
24	B	0.5	0.2	0.0	CF
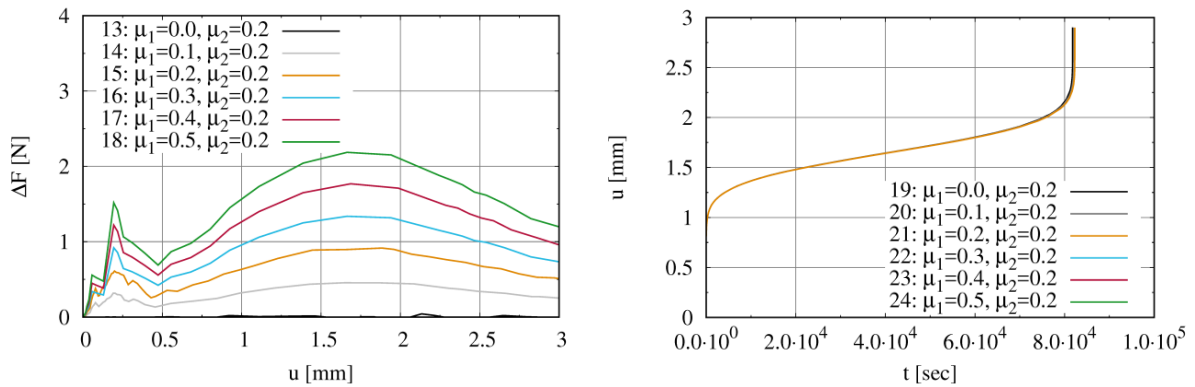
Figure 4. a) CDR-SPT, cases 13 – 18; **b)** CF-SPT, cases 19 – 24. Variation of the friction coefficient μ_1 for the contact between punch and guidance, friction coefficient $\mu_2 = 0.2 = \text{const.}$ for the contact between punch and specimen.

Model B considers in contrast to model A an additional contact between punch and the upper guiding assuming that the punch is slightly tilted, as depicted in Figure 2(b). These second contact generates an upward pointing frictional force, which effectively reduces the punch force acting on the specimen. This reduction ΔF is shown on the left hand side in Figure 4. It is around 1% of the current punch force. The CF-SPT results of these simulations are shown on the right in Figure 4. Such a small reductions of the punch force reduce the time of failure not significantly.

3.3 Model C
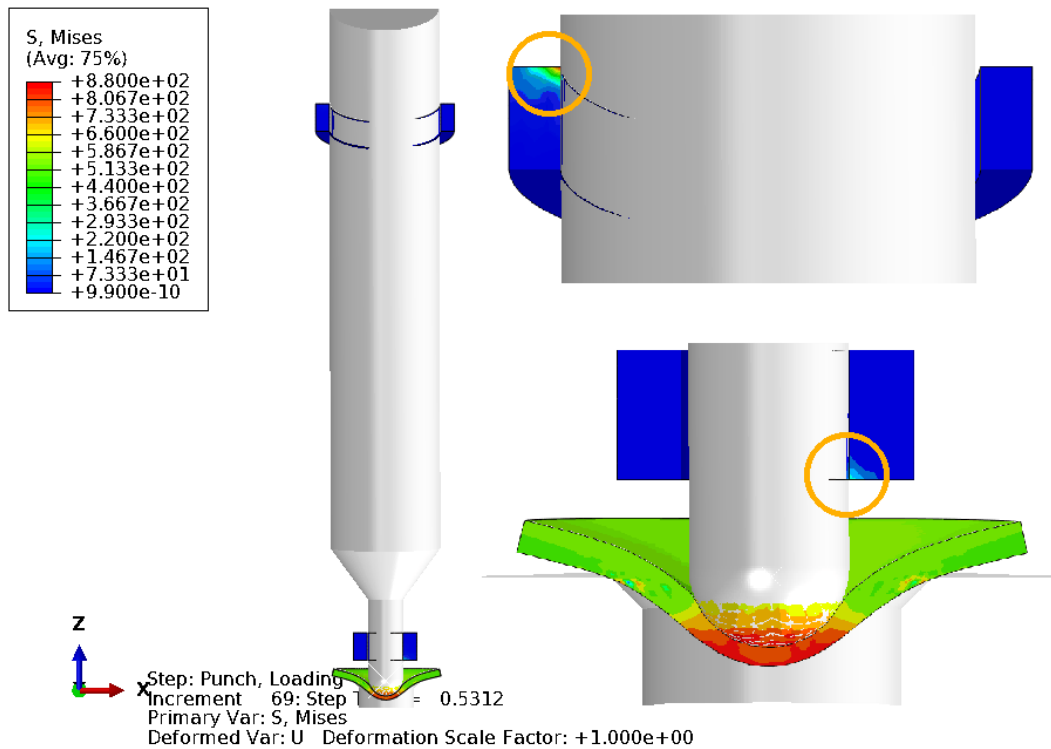
Figure 5. ABAQUS Model C. The orange circles show the two locations where the punch touches the guidance.

Table 4. Simulated cases using model C.

Case	Model	μ_1	μ_2	Δx	Type
25	C	0.1	0.2	0.0	CDR
26	C	0.1	0.2	0.1	CDR
27	C	0.1	0.2	0.2	CDR
28	C	0.2	0.2	0.0	CDR
29	C	0.2	0.2	0.1	CDR
30	C	0.2	0.2	0.2	CDR
31	C	0.3	0.2	0.0	CDR
32	C	0.3	0.2	0.1	CDR
33	C	0.3	0.2	0.2	CDR
34	C	0.4	0.2	0.0	CDR
35	C	0.4	0.2	0.1	CDR
36	C	0.4	0.2	0.2	CDR
37	C	0.5	0.2	0.0	CDR
38	C	0.5	0.2	0.1	CDR
39	C	0.5	0.2	0.2	CDR
40	C	0.0	0.2	0.1	CF
41	C	0.1	0.2	0.1	CF
42	C	0.2	0.2	0.1	CF
43	C	0.0	0.2	0.2	CF
44	C	0.1	0.2	0.2	CF
45	C	0.2	0.2	0.2	CF

In model C the punch is tilted such that it touches the upper guidance at the left and the lower guidance at the right side. Additionally the specimen and receiving die can be shifted to the right by Δx. Then, the specimen is loaded non-concentric, which results in an additional horizontal force acting on the punch and increasing the contact pressure and therewith the friction forces. Figure 5 shows the model in detail. The friction coefficient between specimen and punch is kept constant $\mu_2 = 0.2$, whereas the friction coefficient for the contact between punch and guidance μ_1 is varied. Figure 6 – 10 show on the left side the load-displacement curve of the punch and on the right side the force reduction due to the friction between punch and its guidance.
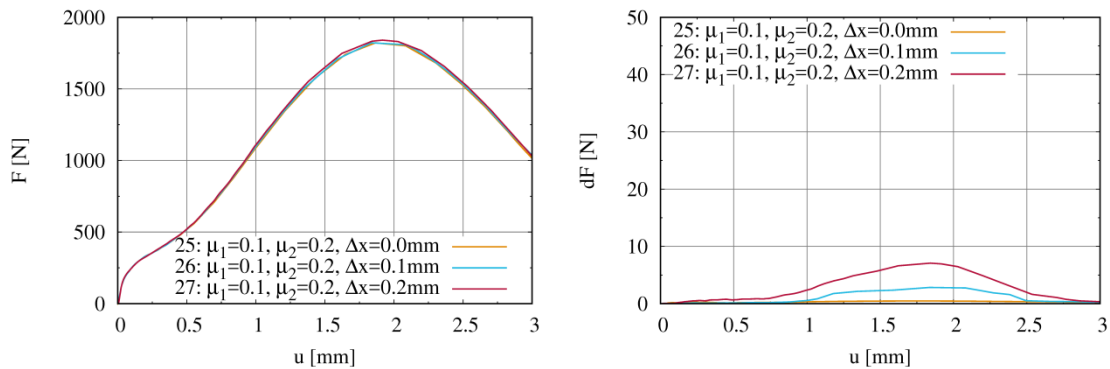
Figure 6. CDR-SPT cases 25 – 27. Variation of non-concentricity of die and specimen Δx, $\mu_1 = 0.1$, $\mu_2 = 0.2$.
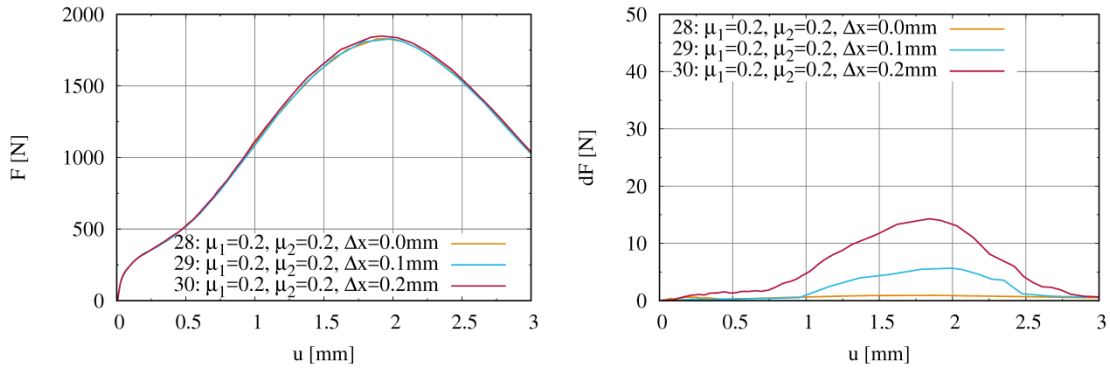
Figure 7. CDR-SPT cases 28 – 30. Variation of non-concentricity of die and specimen Δx, $\mu_1 = 0.2$, $\mu_2 = 0.2$.
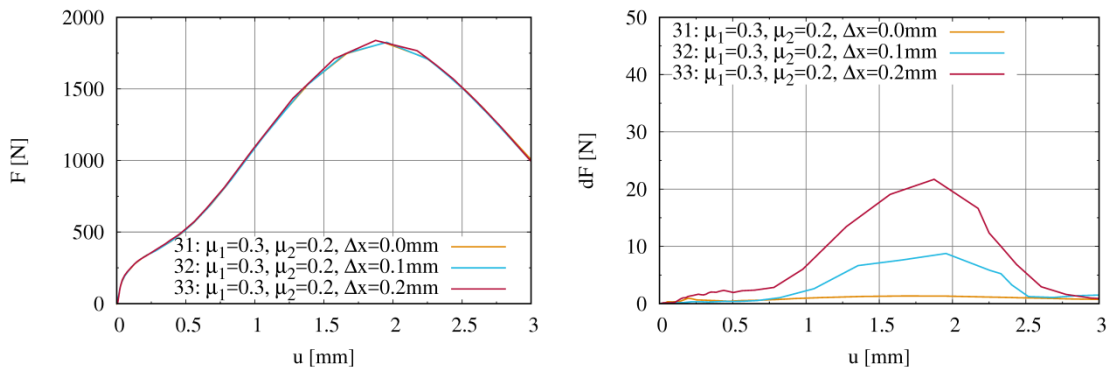
Figure 8. CDR-SPT cases 31 – 33. Variation of non-concentricity of die and specimen Δx, $\mu_1 = 0.3$, $\mu_2 = 0.2$.
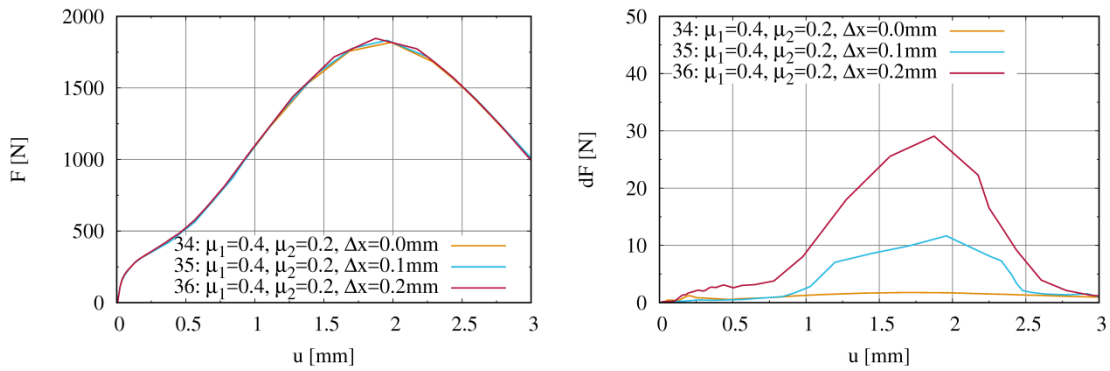
Figure 9. CDR-SPT cases 34 – 36. Variation of non-concentricity of die and specimen Δx, $\mu_1 = 0.4$, $\mu_2 = 0.2$.
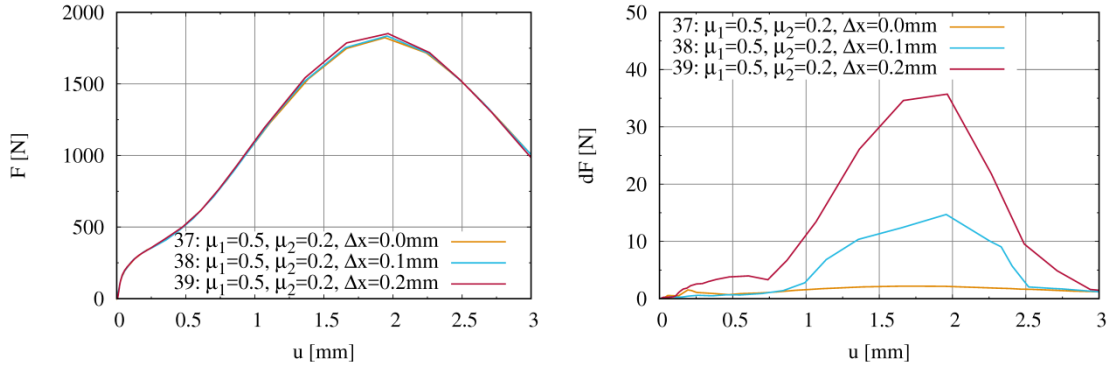
Figure 10. CDR-SPT cases 37 – 39. Variation of non-concentricity of die and specimen Δx, $\mu_1 = 0.5$, $\mu_2 = 0.2$.
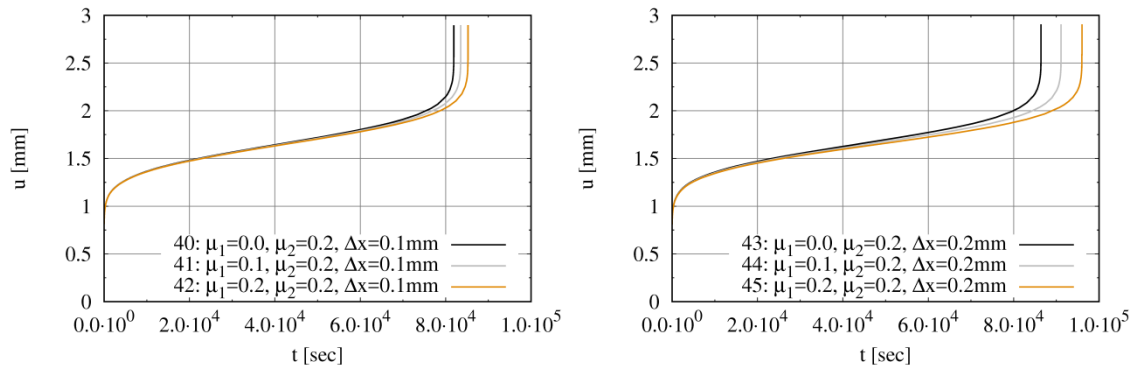
Figure 11. a) CF-SPT, cases 40 – 42, $\Delta x = 0.1$ mm; **b)** CF-SPT, cases 43 – 45, $\Delta x = 0.2$ mm. Variation of the friction coefficient μ_1 for the contact between punch and guidance, friction coefficient $\mu_2 = 0.2 = \text{const.}$ for the contact between punch and specimen.

For the CF-SPT the force reduction in model C has a visible effect and can increase the time of failure by 10%.

3.4 Specimen thickness reduction

As seen in section 3.1, the friction between specimen and punch has a significant effect in both test types CDR- and CF-SPT. Therefore, the friction coefficient becomes an important parameter within the model. To be able to identify material parameters using curve fitting algorithms the friction coefficient should be known, which raises the question how to identify this parameter. Figure 12 shows results from 2D-axisymmetric CDR-SPT simulations (model A) where the friction coefficient is varied between 0.0 and 0.5. For increasing friction coefficients the remaining central specimen thickness also increases. Figure 13 shows the reduction of the central specimen thickness Δt for both CDR- and CF-SPT as function of the punch displacement. Until $u = 2$ mm only small deviations between the two test types are observed. If the thickness reduction can be measured exactly the important friction coefficient μ_2 can be estimated, as shown at the right hand side in Figure 14, where experiment and simulation are compared for a single 9Cr specimen with an identified friction coefficient $\mu_2 = 0.26$. u_{top} denotes the punch deflection and u_{bot} the central specimen deflection. The left diagram in Figure 14 shows experiments on 9Cr specimen in comparison with simulations with varying friction coefficient. These results suggest that the friction coefficient may vary between 0.2 and 0.4 for this particular test setup. The punch material in this setup is a polished fully hardened stainless steel.

(a) $\mu = 0.0$ **(b)** $\mu = 0.1$ **(c)** $\mu = 0.2$

(d) $\mu = 0.3$ **(e)** $\mu = 0.4$ **(f)** $\mu = 0.5$
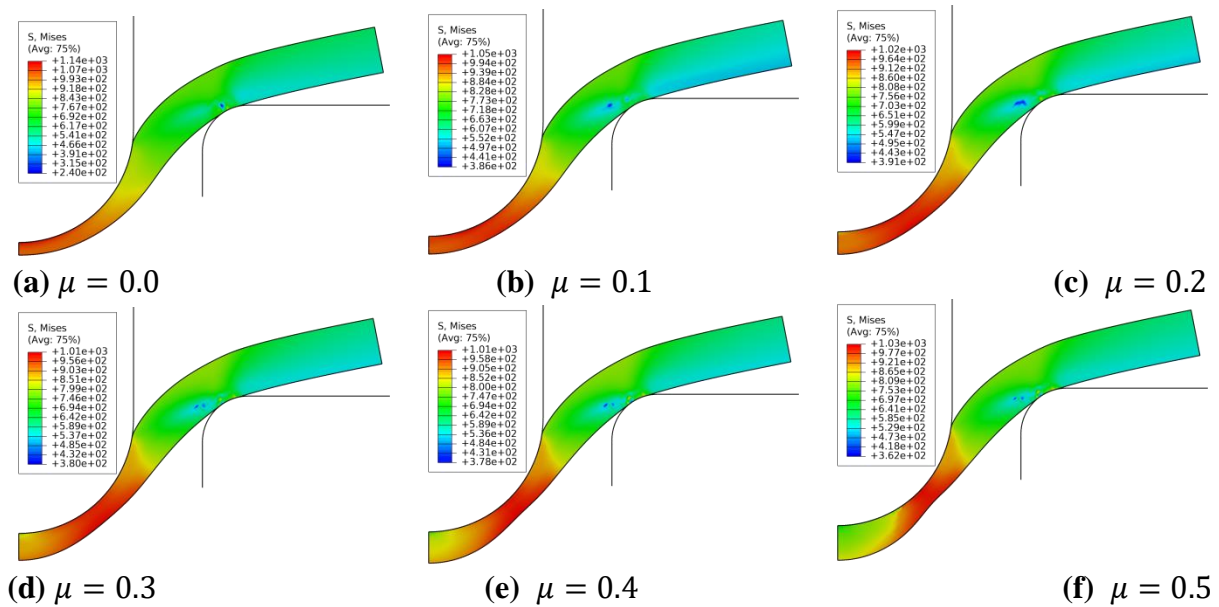
Figure 12. CDR-SPT, cases 1 – 6. Reduction of the central specimen thickness for model A for a constant deflection $u = 2$ mm. Variation of the friction coefficient $\mu_2 = 0.0 \ldots 0.5$ for the contact between punch and specimen.
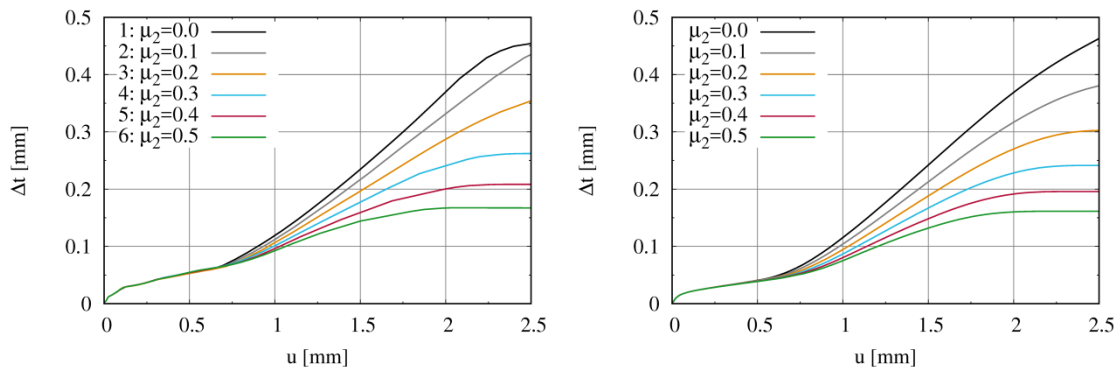
Figure 13. a) CDR-SPT; **b)** CF-SPT. Reduction of central specimen thickness for model A. Variation of the friction coefficient μ_2 for the contact between punch and specimen.

Figure 14. a) Comparison between experiments and simulations on 9Cr-Steel. **b)** Comparison of experiment and simulation for a single specimen with identified friction coefficient.
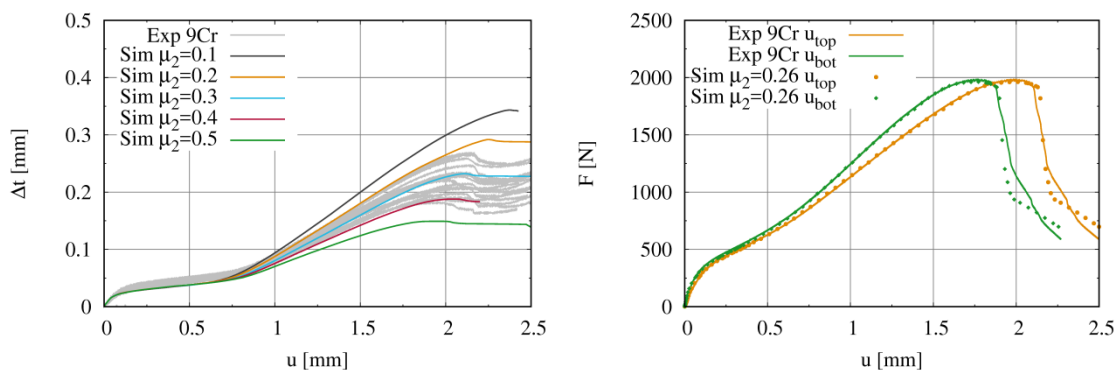
4. Conclusions

This numerical study shows the importance of friction effects in CDR- and CF-SPTs. The friction between punch and its guidance could be controlled by an exact alignment of the setup and a proper lubrication of the punch. Then these effects might be neglectable. But the friction between specimen and punch can't be avoided and must be therefore taken into account during test evaluation. One method to determine the friction coefficient is the continuous measurement of the central specimen thickness during testing. The thickness reduction is mainly controlled by friction, but not totally independent from the material behaviour, why a precise simulation using a proper material law is necessary to identify friction coefficients. Especially in CF-SPTs at elevated temperatures, the friction coefficient might depend on temperature, punch force, testing time and punch and specimen material, which makes the identification of the friction coefficient a challenging task.

References

1. Manahan, M.P.; Argon, A.S.; Harling, O.K. The development of a miniaturized disk bend test for the determination of postirradiation mechanical properties. *Journal of Nuclear Materials*, 103:1545-1550, 1981.
2. Kameda, J. and Mao, X. Small-punch and TEM-disc testing techniques and their application to characterization of radiation damage. *Journal of Materials Science*, 27(4):983-989, 1992.
3. Baik, J.M.; Kameda, J; Buck, O. Small Punch Test evaluation of intergranular embrittlement of an alloy steel. *Script Metallurgica*, 17:1443-1447, 1983.
4. Baik, J.M.; Kameda, J.; Buck. O. Development of small punch tests for ductile-brittle transition temperature measurement of temper embrittled Ni-Cr steels. In *The use of small-scale specimens for testing irradiated material*, W.R. Corwin, G.E. Lucas, editors, pp. 92-111. ASTM STP 888, Philadelphia, PA, 1986.
5. Linse, T.; Kuna, M..; Schuhknecht, J.; Viehrig. H.-W. Application of the Small-Punch Test to Irradiated Reactor Vessel Steels in the Brittle-Ductile Transition Region. *Journal of ASTM International*, 5(4):1-14, 2008.
6. CEN. Workshop Agreement CWA 15627:2006, *Small Punch Test method for Metallic Materials*. Technical report, Brussels, Belgium, 2006.
7. Abendroth, M.; Kuna. M. Identification of ductile damage and fracture parameters from the small punch test using neural networks. *Engineering Fracture Mechanics*, 73(6):710-725, 2006.
8. Dymacek, P.; Milicka. K. Creep small-punch testing and its numerical simulations. *Materials Science and Engineering A*, 510-511:444-449, 2009.
9. Andres, D.; Dymacek. P. Study of the upper die clamping conditions in the small punch test. *Theoretical and Applied Fracture Mechanics*, 86:117-123, 2016.
10. Cacciapuoti, B.; Sun, W.; McCartney. D.G. A study on the evolution of the contact angle of small punch creep test of ductile materials. *International Journal of Pressure Vessels and Piping*, 145:60-74, 2016.
11. Fa-Kun, Z.; Guo-Yan, Z.; Shan-Tung. T. Numerical investigation of frictional effect on measuring accuracy of different small specimen creep tests. *International Journal of Pressure Vessels and Piping*, 110:42{49, 2013.
12. Zhang, L.; Min, J.; Carsley, J.; Stoughton, T.B.; Lin. J. Experimental and theoretical investigation on the role of friction in Nakazima testing. *International Journal of Mechanical Sciences*, 133:217-226, 2017.
13. Selent, M.; Abendroth, M.; Kuna. M. Experimental and Numerical Investigations on the Creep Behaviour of Heat-Resisting Chromium Steel X10CrMoVNb9-1 by Means of Small Punch Test. *Transactions of the Indian Institute of Metals*, 69:629-633, 2016.

Current status of the small punch test standardization within the ASTM

R. Kopriva [1,*], M. Brumovsky [1] and P. Petelova [1]

[1] ÚJV Řež, a. s., Hlavní 130, Řež, 250 68 Husinec, Czech Republic
* Correspondence: radim.kopriva@ujv.cz; Tel.: +420-725-628-839

Abstract: Since 2014, considerable attention has been paid to the standardization of small punch test technique within the American Society of Testing and Materials (ASTM). In 2016 large inter-laboratory study has been launched within the ASTM subcommittee E10.2 - Behavior and Use of Nuclear Structural Materials, involving 12 laboratories and 6 evaluated structural materials from the nuclear power plant components. Paper describes the current status of ASTM standardization, results of the inter-laboratory study, lessons learned and open questions remaining to be solved for the successful completion of the standardization process.

Keywords: small punch test; standardization; ASTM

1. Introduction

In the terms of industrial components operational life management, the current trend of lifetime extension requires precise information of structural materials degradation. Conventional methods of mechanical testing are usually based on the use of large specimens and higher consumption of structural materials, whose availability and volume is often limited. For the determination of material properties, sampling of the necessary volume of material is in most cases connected with affecting the integrity or even destruction of the assessed component. Moreover, in the field of nuclear power energy sector, several components are not usually covered by programs of surveillance testing samples, e.g. reactor pressure vessel internals.

Innovative testing method of Small Punch Testing (SPT) is based on the determination of material properties from miniaturized testing specimens and its semi-destructive approach is very promising for the possibility of present data base of materials testing results enlargement. Even though the SPT has been introduced already in 1981 [1], currently the method is unfortunately not supported by the fully-fledged and globally accepted normative document. In 2007, the first initiative towards the preparation of the full standard was established, when the pre-normative document CWA15627 was created as a result of the cooperation within the European community of testing laboratories [2]. At present, the development of European standard continues within the European Committee for Standardization (European Committee for Iron and Steel Standardization - ECISS, subcommittee TC101) with the expected publication of the standard in 2019 [3].

Since 2014, after the 6th International Symposium on Small Specimen Test Techniques (January 2014, Houston, USA), considerable attention has been paid to the standardization of small punch test technique within the American Society of Testing and Materials (ASTM). In 2017, large inter-laboratory study (ILS) was launched to establish the precision statement for the proposal of a new ASTM test. This activity is performed within the Committee E10 on Nuclear Technology and Applications, Subcommittee E10.02 on Behavior and Use of Nuclear Structural Materials. Twelve laboratories around the world participated in this ILS where six different structural materials were tested. Together, more than 460 test specimens were included in this program and more than 3,200 test results were obtained and analyzed.

2. Laboratories

For the purpose of inter-laboratory study, group of testing laboratories was created to fulfil the ASTM requirements on the sufficient volume of obtained results. To assure the validity of the round robin testing 12 testing laboratories were involved. In the inter-laboratory study, ÚJV Řež, a. s. is the administrator and supplier of testing materials. Detailed overview on the participants is available in Table 1.

Table 1. Testing laboratories involved in the inter-laboratory study.

Laboratory	Country
Helmholtz-Zentrum Dresden-Rossendorf (HZDR)	Germany
VÚJE a.s.	Slovakia
ÚJV Řež, a. s.	Czech Republic
COMTES FHT	
EC JRC Petten	Netherlands
CIEMAT	Spain
Swansea University	Great Britain
National Nuclear Laboratory (NNL)	
Central Research Institute of Electric Power Industry (CRIEPI)	Japan
Korea Atomic Energy Research Institute (KAERI)	Korea
Indira Gandhi Centre for Atomic Research (IGCAR)	India
East China University for Science and Technology (ECUST)	China

3. Materials and Methods

For the inter-laboratory study 6 different materials from the nuclear industry were selected (see Table 2). Chosen materials cover wide range of mechanical properties – from basic carbon steels (e.g. 22K) up to highly-alloyed stainless steels (e.g. 10Ch11N20T3R). Also material A533B (JRQ), the IAEA correlation monitoring material [4], was included for its wide use in the programs dedicated to the nuclear materials degradation research. All materials were supplied by the ÚJV Řež, a. s. to the participants in the form of grinded cylinders with the diameter of 8 mm and length approximately of 50 mm to ensure the sufficient volume of material for specimens preparation. From the material A533B (JRQ), ÚJV Řež, a. s. also prepared complete testing samples that were also shipped to participants to determine the influence of the machining and finishing procedures on the test results.

Table 2. Chemical composition of materials included in the inter-laboratory study (mass %).

Material	C	Si	Mn	P	S	Cr	Ni	Ti	Mo	Cu	V
A533B (JRQ)	0.18	0.20	1.42	0.020	0.017	0.12	0.84	-	0.51	0.14	0.002
15Kh2MFA [1]	0.16	0.20	0.50	0.020	0.020	2.84	0.11	-	0.70	0.06	0.300
08Kh18N10T [2]	0.06	0.62	1.32	0.022	0.003	17.55	10.80	0.31	0.25	0.08	0.046
22K [1]	0.20	0.23	0.76	0.005	0.001	0.22	0.32	0.01	0.10	0.13	0.020
10Kh11N20T3R [1]	0.03	0.29	0.65	0.007	0.002	10.48	18.40	2.05	0.04	0.04	0.038
COST F	0.12	0.07	0.57	0.010	0.007	10.58	0.37	-	1.51	-	0.190

All participants were given instructions and recommendations how to perform the preparation of testing samples and how to conduct the testing and data acquisition to ensure the comparability of testing outputs. For the testing specimen, geometry of 8 mm diameter and 0.5 mm thickness was selected. Specimens were recommended to be prepared by the electric discharge cutting and subsequent grinding and finishing. Other methods of initial cutting were also allowed, however the removal of material thickness affected by the cutting procedure was necessary to achieve, e.g. EDM cutting of intermediate product with thickness 0.65 mm, grinding on abrasive paper

---

[2] *Equivalent materials - 15Kh2MFA (15CrMoVA), 08Kh18N10T (AISI 321), 22K (ASME SA 515 Grade 70), 10Ch11N20T3R (11Cr-20Ni)*

with a recommended abrasive grit size designation P320 followed by fine grinding (P1200) to the final thickness with an accuracy of ± 1 % h_0.

Table 3. Requested testing data to be recorded for each specimen.

F_m [N]	Maximum force recorded during the SP test
F_e [N]	Force characterizing the transition from linearity to the stage associated with the spread of the yield zone through the specimen thickness (plastic bending stage)
u_m [mm]	Punch displacement corresponding to the maximum force F_m
u_f [mm]	Punch displacement corresponding to fracture at 20 % force drop, i.e. $F_f = 0.8 \, F_m$
E_{SP} (E_{TO}, E_{PL}) [J]	SP fracture energy obtained from the area under the force punch displacement curve up to fracture at 20 % force drop ($F_f = 0.8 \, F_m$)
ε_f [-]	Effective fracture strain

4. Evaluation

During the 2017, participants of the ILS submitted testing data to the ÚJV Řež, a. s. for further statistical evaluation. The data collection phase of the inter-laboratory study was completed in October 2017. Subsequently, extensive evaluation of the inter-laboratory study was carried out in accordance with ASTM E691-15 for inter-laboratory testing requirements [5], where in addition to a standard statistical evaluation of results the data consistency within a laboratory and between laboratories should also be assessed. Together the total evaluation consisted of 56 excel files and 112 separate charts. Typical example of data evaluation is given on Figure 1 – Figure 3.
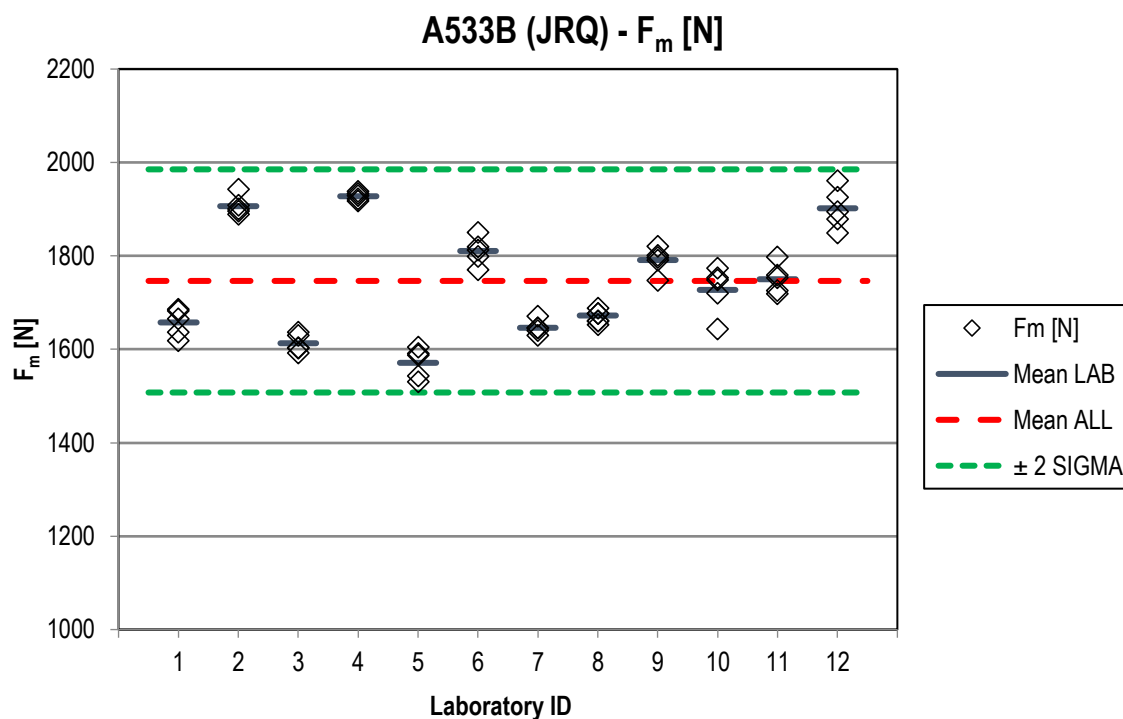
Figure 1. Comparison of SP maximum force results between participating laboratories (A533B JRQ).

Also participating laboratories have sent supplementary information related specimen preparation technique, testing procedures and used equipment to enable more detailed comparison and determine possible open issues to be address during the preparation of the final standard. Key areas of the testing procedure with existing open issues to be addressed include – type of used indenter (ball / punch), geometry of the lower die receiving hole edge (radius / chamfer) and the way of the specimen final thickness measurement for the fracture strain determination.

Based on the evaluated inter-laboratory comparison, changes to the draft WK61832 were proposed so that they can be incorporated into the final version of the standard during the balloting process in the period from May 2018.
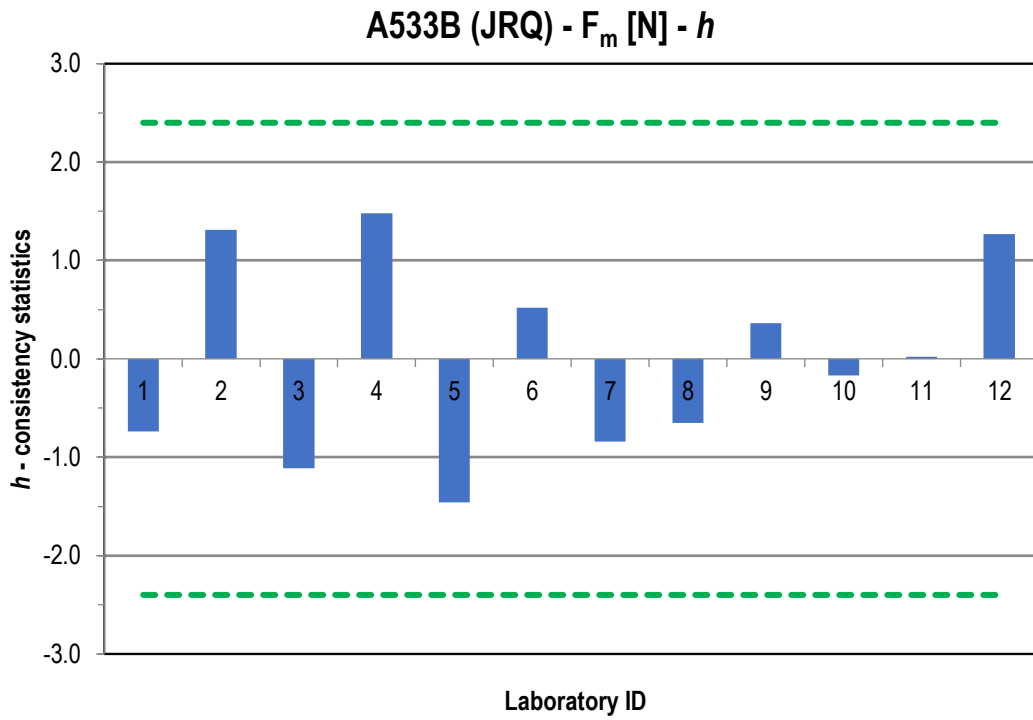
Figure 2. Inter-laboratory consistency statistic *h* for maximum force F_m and A533B JRQ material.
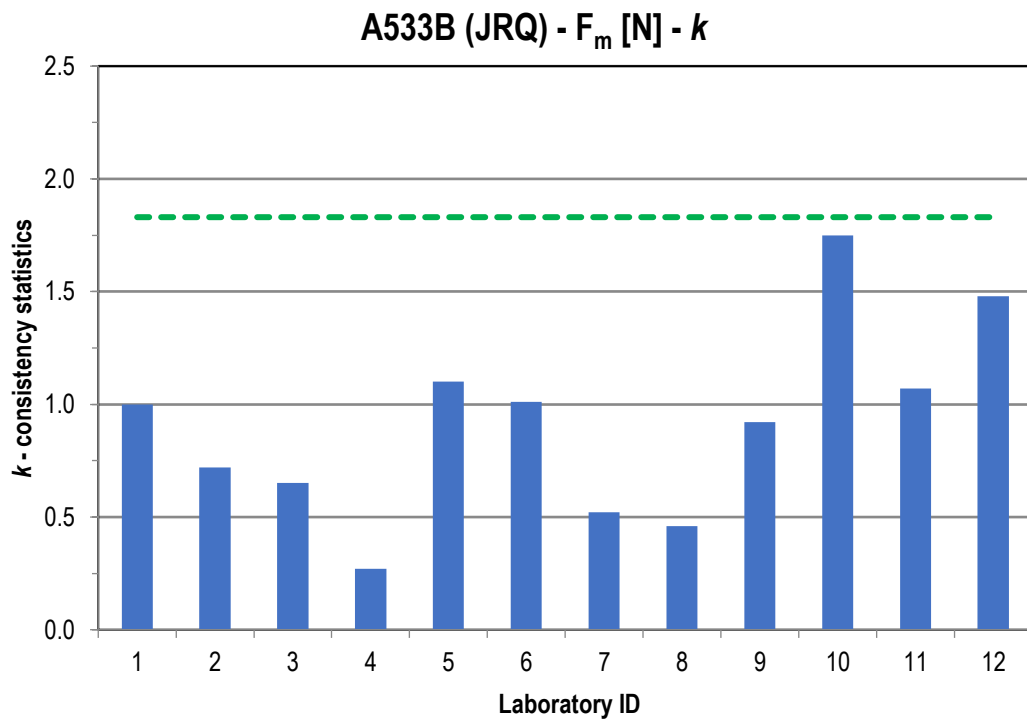
Figure 3. Intra-laboratory consistency statistics *k* for maximum force F_m and A533B JRQ material.

5. Discussion

The paper summarizes the current status of inter-laboratory study ILS1408 ongoing within the ASTM, committee E10 on Nuclear Technology and Applications. Based on the evaluation participating testing laboratories results the research report was created with the accordance with the ASTM procedures. The precision statement was determined through the statistical examination of 3241 test results from 463 tests from 12 laboratories, on 7 groups of materials. The report was after completion submitted in the January 2018 to the ASTM approval and subsequently subcommittee ballot of the draft standard was prepared. Successful balloting process will address current uncertainties in the testing procedure and will be a basis for the preparation of fully-fledged ASTM standard.

References

1. Manahan, M.P.; Argon, A.S.; Harling, O.K. The development of a miniaturized disk bend test for the determination of postirradiation mechanical properties. *J. of Nucl. Mat.*, 1981, vol. 104, p. 1545-1550. *doi: 10.1016/0022-3115(82)90820-0*
2. CWA 15627, CEN Workshop Agreement. Small Punch Test Method for Metallic Materials, CWA 15627:2007 D/E/F, European Committee for Standardization, Brussels, Belgium, 2007.
3. Bruchhausen, M. et al. European Standard on Small Punch Testing of Metallic Materials, ASME Pressure Vessels and Piping Conference, 2017, *ISBN: 978-0-7918-5790-8, doi: 10.1115/PVP2017-65396*
4. IAEA TECDOC 1230. Reference Manual on the IAEA JRQ Correlation Monitor Steel for Irradiation Damage Studies, IAEA, Vienna, Austria, 2001
5. ASTM E643-15. Standard Test Method for Ball Punch Deformation of Metallic Sheet Material, ASTM International, West Conshohocken, PA, USA, 2015, *doi: 10.1520/E0643-15*

Successfully estimating tensile strength by small punch testing

S. Holmström [1*], I. Simonovski [1], D. Baraldi [1], M. Bruchhausen [1], E. Altstadt [2], R. Delville [3]

[1] European Commission, Joint Research Centre, Petten, The Netherlands
[2] Helmholtz-Zentrum Dresden-Rossendorf (HZDR), Dresden, Germany
[3] SCK·CEN Belgian Nuclear Research Centre, Mol, Belgium
* Correspondence: stefan.holmstrom@ec.europa.eu

Abstract: The Small Punch (SP) test is a relatively simple test well suited for material ranking and material property estimation in situations where standard testing is not possible or considered too material consuming. The material tensile properties, e.g. the ultimate tensile strength (UTS) and the proof strength are usually linearly correlated to the force-deflection behaviour of a SP test. However, if the test samples and test set-up dimensions are not according to standardized dimensions or the material ductility does not allow the SP sample to deform to the pre-defined displacements used in these correlations, the standard formulations can naturally not be used. Also, in cases where no supporting UTS data is available the applied correlation factors cannot be verified. In this paper a formulation is proposed that enables the estimation of UTS without supporting uniaxial tensile strength data for a range of materials, both for standard type and for curved (tube section) samples. The proposed equation was originally developed for estimating the equivalent stress in small punch creep but is also found to robustly estimate the UTS of several ductile ferritic, ferritic/martensitic and austenitic steels. It is also shown that the methodology can be further applied on non-standard test samples and test set-ups and to estimate the properties of less ductile materials such as 46% cold worked 15-15Ti cladding steel tubes. In the case of curved samples the UTS estimates have to be corrected for curvature to match the corresponding flat specimen behaviour. The geometrical correction factors are dependent on tube diameters and wall thicknesses and were determined by finite element simulations. The outcome of the testing and simulation work shows that the UTS can be robustly estimated both for flat samples as well as for thin walled tube samples. The usability of the SP testing and assessment method for estimating tensile strength of engineering steels in general and for nuclear claddings in specific has been verified.

Keywords: small punch testing, tensile strength, fuel claddings

1. Introduction

In a small punch (SP) test the local stresses and strains are biaxial in nature [1]. It has been shown to be a challenging task to estimate uniaxial (equivalent) stress from the force displacement curve of the SP test [2,3]. A new standard [4] is currently under preparation within the European Committee for Iron and Steel Standardization (ECISS), Technical Committee 101 (TC101), working group 1 (WG1) to replace the current CEN Workshop Agreement [5]. The new standard covers the classical Small Punch (SP) test for tensile property estimation and the Small Punch Creep (SPC) test for creep property evaluation. In this paper some new insight, gained from the SPC equivalent stress determination [6], is used for estimating the tensile strength.

In the SP test a hemispherical punch or a ball is forced at a constant displacement rate through a disc specimen (Figure 1) that is clamped between an upper and a lower die. The main result of a SP test is the measured force F as a function of displacement v (at the punch tip) or deflection u (below the sample). The measured displacement v has to be corrected for compliance. The difference between displacement and deflection is the change of the specimen thickness at the punch tip.

Example SP force-displacement curves for the two standardized SP test set-ups and specimen sizes are shown in Figure 2a and in normalized form in Figure 2b.
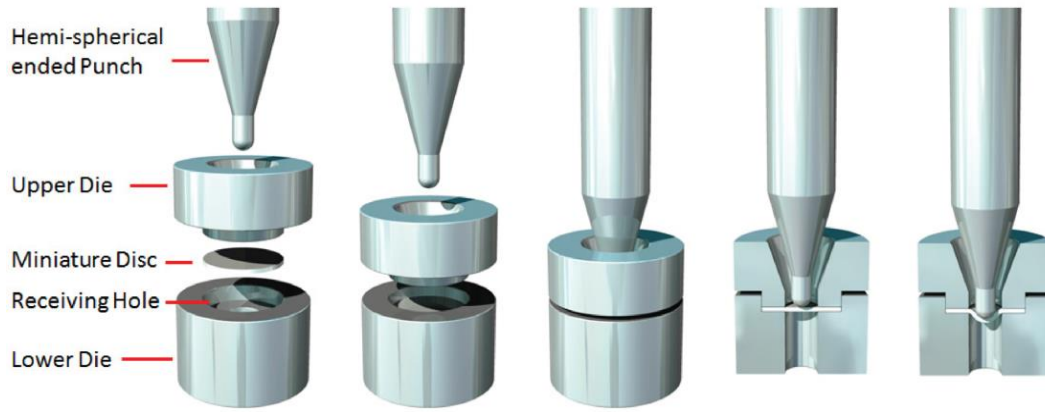
Figure 1. Schematic of a SP test set-up [7].

(a)   (b)
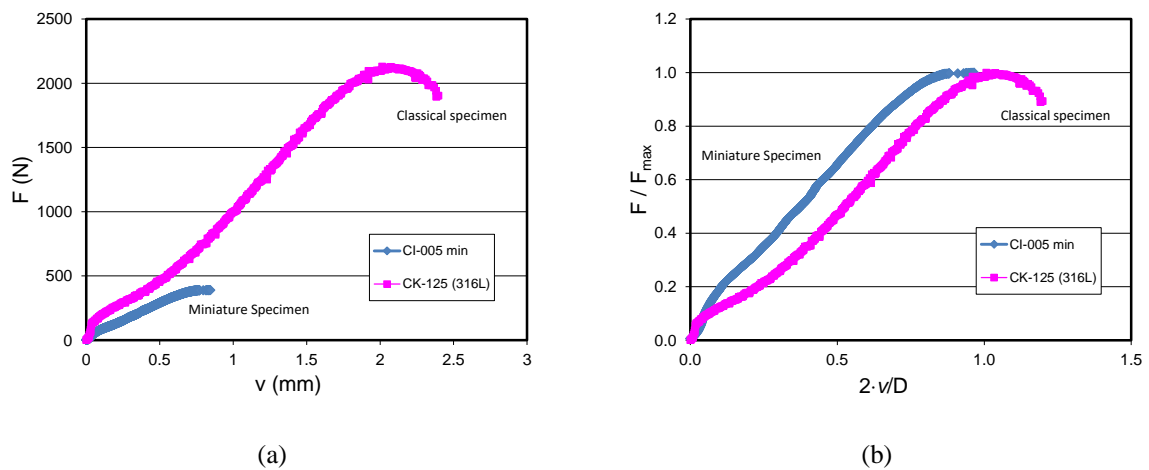
Figure 2. (a) Force-displacement curves for a standard 0.5 thick and a miniature 0.25 mm thick 316L steel sample [8] and **(b)** the corresponding normalized curves with force normalized with the maximum force F_{max} and the displacement normalized by $2 \cdot v/D$, where D is the receiving hole diameter.

1.1 Test rig set-ups

The new standard (presented in [4]) includes two types of SP or SPC specimen, i.e. a specimen with a diameter $D_S = 8$ mm and an initial thickness $h_0 = 0.5$ mm and a specimen with $D_S = 3$ mm and $h_0 = 0.25$ mm. The standard test rig specifics for these two types are given in Table 1 together with other set-ups found in literature [2,5,11]. The lower die has a receiving hole with diameter D and a chamfer of length L. Both, D and L depend on the type of specimen used (Table 1).

Table 1. Main geometric characteristics of different SP test set-ups and specimen. Note that also a radius (instead of a chamfer (L)) can be used. The specimen and test set-ups given in bold are used in this paper.

Specification number S_{NR}#	Test piece dimensions (D_s / h_0) [mm]	D [mm]	r [mm]	L [mm]	*Note*
#1	**8/0.5**	**4**	**1.25**	**0.2**	**Standard set-up [2]**
#2	8/0.5	4	1-1.25	0.2	CWA 15627 [2, 5]
#3	8/0.5	4	1-1.25 (1.19)[1]	0.2	Japanese SPC [9]
#4	**3/0.25**	**1.75**	**0.5**	**0.2**	**Standard set-up [2]**
#5	3/0.25	2	0.5	0.2	MATTER [10]
#6	3/0.25	1.5	0.5	0.2	MATTER [10]
#7	**Curved samples**[2]	**4**	**1.25**	**#N/A**	**Tube sections [11]**

1) Kagoshima University uses ⌀2.38 mm balls

2) Curved tube samples: with outer diameters and wall thicknesses as in Table 1.

2. Materials

The materials assessed here are from various projects and test campaigns as given under the sub-headings below. The test materials and their room temperature (RT) ultimate tensile strengths are given in Tables 2-4. These values are estimated by SP tests later in this paper.

2.1 ECISS/TC101 round robin materials

The main materials used by ECISS/TC101/WG1 for the estimation of tensile properties were different heat treatments of P92 pipe. To study the impact of differing yield to tensile strength ratios the 316L was also tested. The TC101 test materials are given in Table 2. All the ECISS/TC101/WG1 materials, except 316L-miniature, are tested at room temperature with test specification number S_{NR}#1 (Table 1) and the miniature test sample with S_{NR}#4 .

Table 2. TC101 materials and their ultimate tensile strength at room temperature.

Material and designation	Uniaxial Rm (MPa) at RT
P92– as received	808[1],
P92– Heat treatment 1	675[1]
P92– Heat treatment 2	707[1]
P92– Heat treatment 3	726[1]
P92– Heat treatment 4	733[1]
316L – miniature	569[2]
316L	569[2]

1) As given by material supplier (MMV).

2) As measured by JRC [8].

2.2 TASTE project materials

In the EERA JPNM pilot project TASTE [11-13] the main material of interest was the nuclear grade titanium stabilized 15-15Ti (DIN 1.4970) stainless steel cladding [14]. The 15-15Ti is the primary choice for fuel cladding of several current fast spectrum research reactor projects. The main test material was the 24% cold worked (24%CW) 15-15Ti cladding tube material, manufactured by Sandvik on behalf of SCK•CEN. The material batch has passed tight quality control, i.e. stringent composition, grain sizes and mechanical properties (yield strength, tensile strength and elongation at rupture) control and tight product tolerances (diameters, straightness and ovality), roughness and defect controls. A smaller batch with a cold-work level of 46% (46%CW) was also produced and tested. For the 46%CW the deformation level is intended to simulate irradiation damaged material in the sense of work-hardening saturation demonstrated by the small difference between the proof stress and the ultimate tensile strength. The 46%CW also has markedly decreased total elongation [15,16].

The 15-15Ti material properties (axial) at RT performed on full tubes (no waist) and on sections cut from the wall (with waist) are given in 3 together with the properties of the reference material P91. All the JRC curved specimens analyzed for this paper were tested with a test-set-up with D=4 mm, r=1.25 mm and no chamfer (S_{NR}#7 in Table 1). The chamfer cannot be manufactured on a curved surface. The flat reference P91 specimens were tested with the standard test set-up (S_{NR}#1 in Table 1), with the standard thickness (h_0=0.5 mm), and with a reduced thickness to comply with the tube specimen, i.e. h_0=0.45 mm. The flat test set-up always has a chamfer (Table 3).

Table 3. TASTE project materials, sample types (inner diameter ID or flat) and their ultimate tensile strengths at RT.

Material and designation	Tube ID / h_0 D / h_0 (mm)	Uniaxial R_m (MPa) at RT
15-15Ti CW24% CURVED	6.55 / 0.45	810[1] 857[2]
15-15Ti CW46% CURVED	6.55 / 0.45	925[1] 929[2]
P91 CURVED	6.55 / 0.45[4]	680[3]
P91 FLAT	Flat/0.45 Flat/0.50	680[3]

1) As given by the material supplier [11], tested on full tube.

2) As measured from axial tube samples [15, 16], tested on tube section.

3) As measured from standard size uniaxial samples [17].

4) Inner surface as from EDM cut.

2.3 ASTM round robin materials

In the US the American Society for Testing and Materials (ASTM) has an ongoing work item [18] for the development of a SP standard. The scope of the work is to enable estimates of yield and tensile strength up to a temperature of 450°C for metallic materials. JRC has taken part in this effort as a member of an inter-laboratory round-robin testing. The tested steels are given in Table 4. The measured UTS and proof stresses were not provided until after the delivery of the test data and the tensile property estimates.

Table 4. All materials tested at RT with specimen $\varnothing 8$ mm; h_0=0.500 mm and a test-set-up with D=4 mm, r=1.25 mm and L=0.2 mm (S_{NR}#1).

Material and designation	Uniaxial R_m (MPa) at RT
A533B	625
A533B (batch 2)	635
COST F	852
22K	498
10Kh11N20T3R	958
08Kh18N10T	560
15Kh2MFA	986

3. Classical and recently developed estimation procedures for force to stress conversion

The simplest force to stress conversion can be found in the CEN Work Shop Agreement (CWA, Code of Practice) [5]. The conversion is meant for small punch creep (SPC) test giving a constant force to stress ratio $\Psi=F/\sigma$, allowing for different test set-up dimensions and specimen thicknesses. The CWA equivalent creep stress σ_{SPC} can be calculated as:

$$\sigma_{SPC} = \frac{F_{SPC}}{3.33 \cdot k_{SP} \cdot R^{-0.2} \cdot r^{1.2} \cdot h_0} \quad \text{MPa} \tag{1}$$

where F_{SPC} (in N) is the SPC test force (load), h_0 the initial specimen thickness, k_{SP} a "ductility" parameter and r, R are the puncher radius and receiving hole radius (in mm) as given in Table 1. For the standard test set-up (S_{NR}#1) the Ψ_{CWA}=1.895 when k_{SP}=1. This conversion factor works well for steels like P91, where the minimum deflection rate is reached at a deflection of around 1 mm. The draw-back of this method is that k_{SP} is not a constant and it can be both temperature and force dependent [18].

The CWA model is based on the Chakrabarty [1] membrane stretch equations. The Chakrabarty (CHA) model gives the Ψ_{CHA} as a function of displacement v. Full CHA curves can be defined for each test set-up using the equations given in [1]. The maximum $\Psi_{CHA\text{-}max}$ at $v_{CHA\text{-}max}$ can be calculated with Eq. (1). The $\Psi_{CHA}=\Psi_{CWA}$ at a displacement v_{max}=1.58 mm for the standard test set-up and specimen size (s_{NR}#1).

The corresponding classical equation (CLA) in [5] for estimating the (uniaxial) ultimate tensile strength R_m with small punch "tensile" tests (SP) is:

$$R_{m-CLA} = \beta_{Rm-CLA} \cdot \frac{F_m}{h_0 \cdot u_m} \quad \text{MPa} \tag{2}$$

where F_m (in N) is the maximum force reached during the test and $\beta_{Rm\text{-}CLA}$ is a geometry dependent correlation coefficient which needs to be determined. The main draw-back of this method is that the $\beta_{Rm\text{-}CLA}$ has to be established by correlation to actual uniaxial tensile tests or by Finite Element Analysis (FEA) simulation with the right constitutive equations in place. It has been found that the correlation factor seems to be somewhat material dependent but mainly test-setup and specimen thickness dependent. In this paper the classical model (CLA) is used for estimating tensile strength as in Eq. (2), with a constant value for $\beta_{Rm\text{-}CLA} = 0.276$, optimized in the MATTER project [19] for P91 steel for the standard test set-up and a specimen thickness of 0.5 mm.

The above method seemingly works well for ductile materials but does not give adequate results for less ductile materials failing at deflections well below $v_{CHA\text{-}max}$. For less ductile materials other methods have to be applied.

A new promising method for both ductile and less ductile materials has been proposed by Altstadt et al. [3] and it has been included in the new standard as an Annex. The Altstadt method (ALT), optimized on finite element simulated materials, correlates the force F_i to the ultimate tensile strength at a much lower displacement v_i in the force-displacement curve. The ALT model correlation to the tensile strength is:

$$R_{m-ALT} = \beta_{Rm-ALT} \cdot \frac{F_i}{h_0^2} \quad \text{MPa} \tag{3}$$

The F_i (in N) of the ALT method is extracted from the test data at the displacement v_i=0.645 mm or a deflection of u_i=0.55 mm. The model parameters are to date only defined for the S_{NR}#1 and S_{NR}#4 test set-ups (see Table 1). The correlation coefficient $\beta_{Rm\text{-}ALT}$ is 0.179 for S_{NR}#1. This is an average value for a range of simulated materials with different tensile strengths and ductilities.

In [6] the Empirical Force to Stress (EFS) model and the Modified Chakrabarty (MCH) model was shown to robustly estimate the equivalent creep stresses for equal creep rupture times of SPC and uniaxial creep tests. The MCH is a simplification of the EFS model that can be recalculated for different test set-ups since the model parameters can be determined analytically using the CHA as base.

The Ψ_{MCH} is:

$$\Psi_{MCH} = A + B \cdot v \ [\text{N/MPa}] \tag{4}$$

where v is the displacement (or deflection) and A and B are test set-up dependent constants. In the case of small punch creep v is replaced by u_{min}, i.e. the deflection where a minimum deflection rate is reached in a test. The SPC data determined constants (from [6]) for A and B which are applied unchanged on the SP test data with the standard test-setup and specimen thickness, i.e. A=0.6143 and B=1.2954 for the S_{NR}#1 set-up. For the curved specimen, the miniature sample and the 0.45 mm thick standard SP specimen the constants have been recalculated using the methodology given in [6]. For the curved specimen further correction factors have to be applied as described in section 3.2 in this paper.

In Figure3a it is shown that the calculated F_i and v_i (and corresponding u_i) from [3] that was the base for Eq. (3) are in good agreement with the Ψ_{MCH} curve for the standard specimen and standard test-set up. In Figure3b it can be seen that for the miniature specimen the MCH slope is representative of the F_i/v_i (and F_i/u_i) but the analytically calculated MCH intercept is somewhat high. It is to be noted that Ψ_{MCH} curve for this specimen size and test-setup (S_{NR}#4) has not been verified up to now by creep tests and the few SP tests indicate that the model overpredicts the UTS (see section 4). The discrepancy is likely to be caused by the assumed fixed point for the MCH set by the CHA model v_{max}, i.e. $\Psi_{MCH}(v_{max})= \Psi_{CHA}(v_{max}) \cdot (1+h/r)$. This factor was optimized on P91 steel [18]. If another more reliable fixed point can be found, such as using the ALT data or actual test data (both SP and SPC data) it is foreseen that the MCH model for the miniature specimen can be improved. It is to be emphasized that the MCH model is not restricted to the location of maximum force as the CLA model even if it has been used that way in this paper. It can be used as the ALT model at lower displacements. This feature will be studied in future work.

All the above stress conversion models for the SNR#1 test-setup are shown in Figure4 with P91 SP data from the MATTER project.

Unification of reference stress estimation between SPC and SP tests would have a beneficial effect on the credibility of the SP and SPC determined material properties.

(a)   (b)
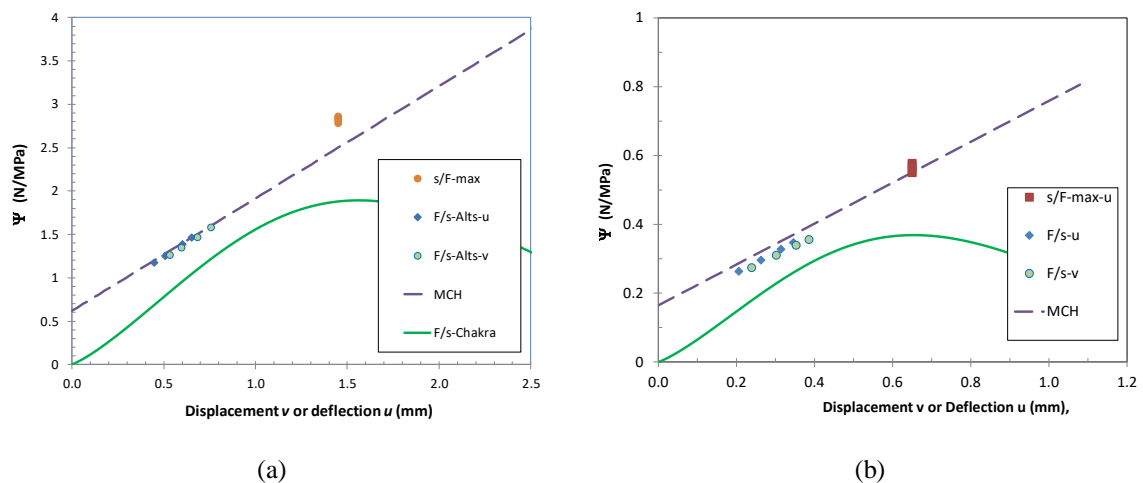
Figure 3. Force over stress (Ψ) as a function of v or u according to the classical Chakrabarty (CHA) and the MCH model for SP and SPC reference creep stress determination. The F_i / R_m and F_{max} / R_m of the simulated materials from the ALT model [3] are also shown for a) set-up S_{NR}#1 and b) S_{NR}#4.
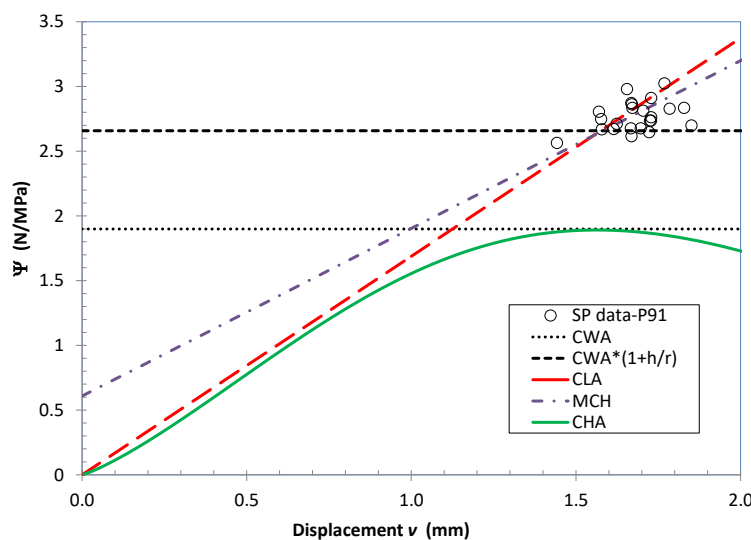
Figure 4. Force over stress (Ψ) for the SPC and SP models, Eqs. (1,2, 4) as a function of *v*. The shown F_{max}/R_m data are from the MATTER project.

3.1 Correction for curvature for thin walled tube samples

When SP testing curved samples [11,21] it is evident that the force-displacement curves are different from those of flat specimens. To find the right way of correcting the deflections (and marginally the force) a number of 3D FEA simulations using ABAQUS [22] have been performed on ¼ of the geometry for simulated flat and curved specimens. The curved sample studied in this paper is a section of the aforementioned SCK-CEN tube. The geometrical configuration consisting of the top die (red), specimen (blue), bottom die (grey) and the spherical punch (green) is shown in Figure 5. Example of computed force-displacement curves for the studied materials is shown in Figure 6. A more detailed description of the methodology and resulting correction factors are given in [23].
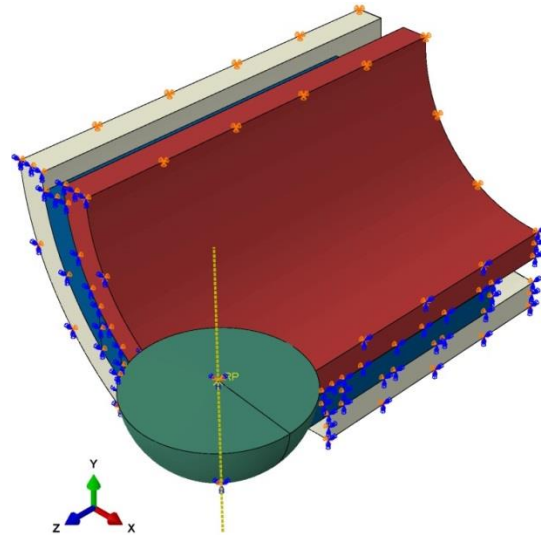
Figure 5. Quarter symmetry FEA model of the SP test on curved (cladding tube) specimen [23].
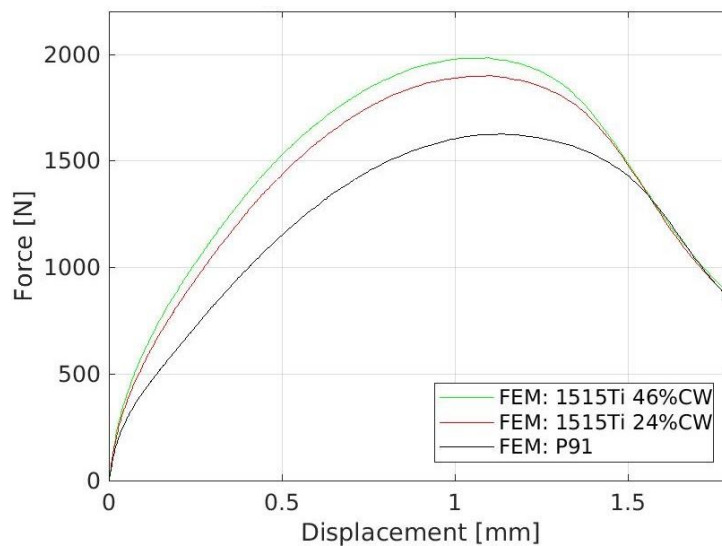
Figure 6. FEA computed force-displacement responses for P91, 24%CW and 46%CW 15-15Ti curved samples from cladding tubes. The friction coefficient, $\mu = 0.2$ and the specimen thickness 0.45 mm.

To obtain the equivalent force and displacement of a flat specimen, the measured force and displacement of a SCK·CEN tube specimen should be divided by a factor of 1.07 and 0.71, respectively. The given factors are averages on the results acquired from the two 15-15Ti materials and the reference material P91.

4. Results

The ultimate tensile strengths estimated by SP tests are given in Tables 5-7 as relative errors of the uniaxial UTS values given in Tables 2-4.

The relative error E_{rel} is calculated as:

$$E_{rel} = \frac{R_{m-SP}}{R_{m-UA}} - 1 \tag{4}$$

Where R_{m-UA} is the uniaxial tensile strength, R_{m-SP} the estimated UTS calculated by the CLA, ALT and MCH models.

Note that for the curved samples there are currently no calculated v_i values at which one could extract the F_i values for the ALT model. Potentially the same correction factors could be used as for correcting the v_{max} and F_{max} but this has not been attempted in this work.

Table 5. The UTS estimate relative errors, Eq. (4), for the ASTM round robin materials at RT.

Material and designation	CLA[1]	ALT (v)	MCH (v)
A533B	-9%	-1%	-9%
A533B (batch 2)	-10%	-1%	-9%
COST F	-7%	2%	-7%
22K	-4%	-7%	-2%
10Kh11N20T3R	-5%	-3%	-5%
08Kh18N10T	6%	-24%	13%
15Kh2MFA	-17%	-9%	-17%

1) Correlation constant for CLA model ($\beta_{Rm-CLA}=0.297$, Eq. (2)) from MATTER, optimized on P91 by JRC.

Note that the R_m estimates from CLA and the MCH are more or less the same. This is to be expected if the displacement at maximum is around 1.6 mm. The ALT estimates are for some materials more accurate but the model seems to be prone to larger deviations, especially for ductile material.
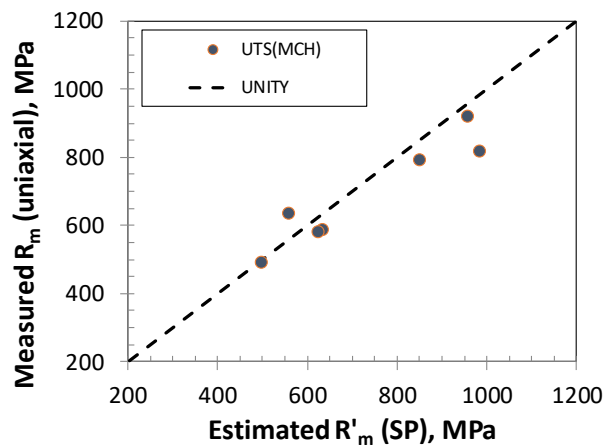
Figure 7. Estimated vs measured uniaxial axial strength at RT for all ASTM materials in Table at RT using the MCH model.

Table 6. Calculated relative errors, Eq. (4), for JRC tests at RT for the ECISS/TC101/WG1 materials.

Material and designation	CLA[1]	ALT (v)	MCH (v)
P92– as received	7%	3%	3%
P92– Heat treatment 1	9%	-2%	6%
P92– Heat treatment 2	13%	-7%	8%
P92– Heat treatment 3	12%	-5%	6%
P92– Heat treatment 4	6%	0.3%	2%
316L – miniature	-3% [2]	23%	14% [3]
316L	10%	-26%	18%

1) Correlation constant for CLA model ($\beta_{Rm-CLA}=0.297$, Eq. (2)) from MATTER, optimized on P91 by JRC
2) Correlation constant from miniature specimen CLA model by HZDR ($\beta_{Rm-CLA}=0.26$, Eq. (2))
3) MCH model parameters as in Figure 7.

The ALT and MCH models are for these sets of data better than the CLA model, except for the miniature specimen estimate. It is to be noted that the MCH is generally over-predicting the stress though less so than the CLA model.

Table 7. Calculated relative errors, Eq. (4), for JRC tests at RT for the TASTE materials.

Material and designation	CLA	MCH
15-15Ti CW24% CURVED	3%	-2%
15-15Ti CW46% CURVED	10%	-1%
P91–CURVED (0.45 mm thick)	-8%	-6%
P91 standard specimen (0.45 mm thick)	-5%	-2%
P91 standard specimen (0.5 mm thick)	-2%	-2%

In addition to the RT tests the MCH method was also applied to the full range of test temperatures, i.e. RT-800°C. The results are very encouraging as can be seen in Figure 8. In the previous assessments on the TASTE data [11] the SP estimates were based on a displacement corrected CLA model, with inherently more scatter in the estimated UTS. The CLA model also predicts somewhat lower strengths for P91 and clearly over-predicts the RT strength for the 46%CW 15-15Ti steel.

(a)   (b)
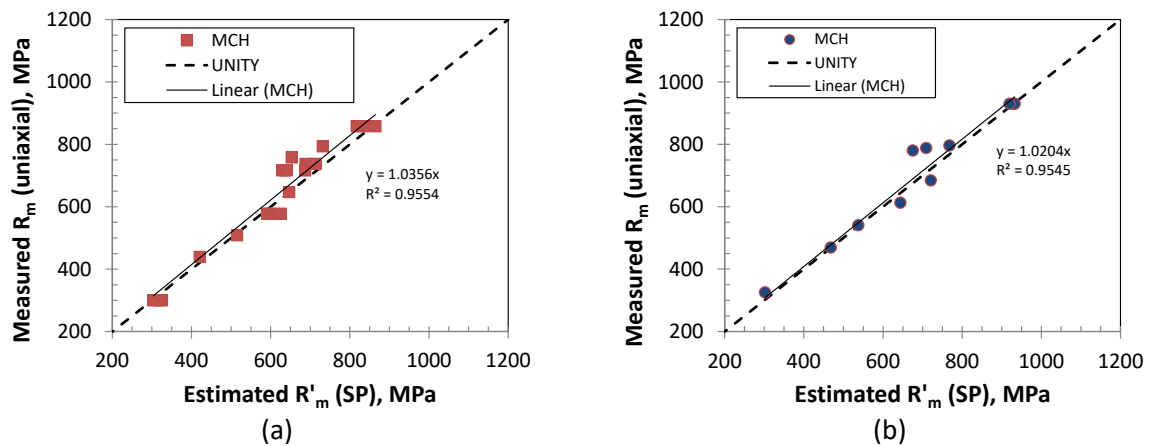
Figure 8. Estimated vs measured uniaxial axial strength for **a)** 24%CW and **b)** 46%CW 15-15Ti using the MCH model in the temperature range RT-800°C.

In Figure 9 the reference P91 SP estimates are plotted against the measured uniaxial strength for the temperature range RT-650°C. It can be seen that the P91 flat specimens give robust predictions and the spark erosion manufactured curved samples show more scatter. The MCH seems to under-predict the tensile strength for the curved P91 samples. This could be an artefact caused by the manufacturing route, i.e. the inner surface was not polished.

a   b
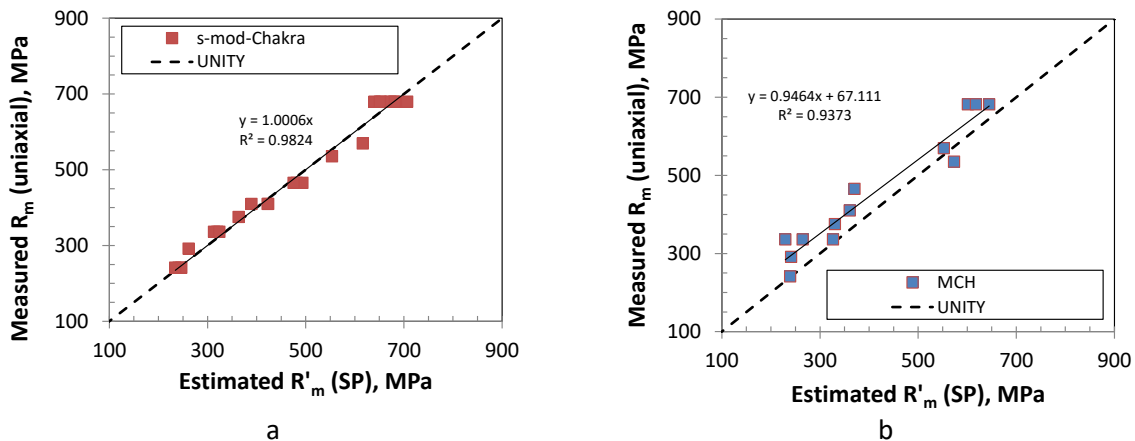
Figure 9. Estimated vs measured uniaxial axial strength for P91 steel a) standard flat specimen and b) EDM cut curved samples in the temperature range RT-650°C.

In Figure 10 and Figure 11 the SP estimated strengths are plotted as a function of temperature together with both uniaxial UTS results and hoop direction ring tension results for 24%CW and 46%CW samples correspondingly.
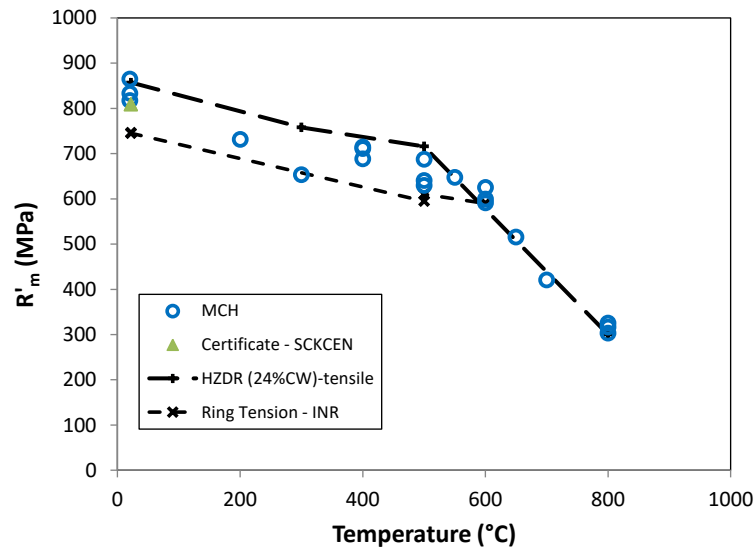
Figure 10. Comparison of RT-800°C tensile strength estimates for 24%CW 15-15Ti from sub-sized axial specimen, Ring-Tension and the new estimates based on the SP data [24] assessed with the MCH model.
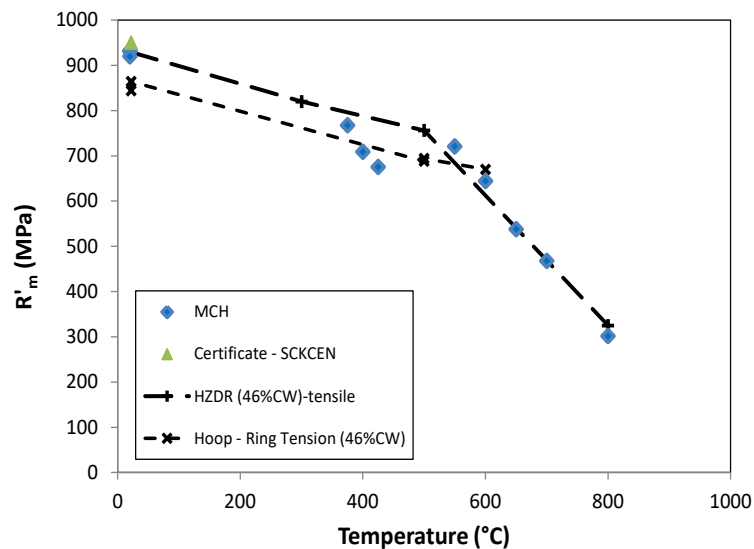
Figure 11. Comparison of RT-800°C tensile strength estimates for 46%CW 15-15Ti from sub-sized axial specimen, Ring-Tension and the new estimates based on the SP data [25] assessed with the MCH model.

5. Discussion

The models compared in this paper for SP estimation of the UTS include a model originally optimized for SPC creep data assessment. It is encouraging to find that the same formulation gives good estimates also when applied on SP data for estimating the tensile strength. In Figure 12 the SPC data from the ECISS/TC101/WG1 round robin [6] show the $\Psi = F_{SPC}/\sigma_{c-UA}$ ratio as a function of the measured deflection at minimum deflection rate (u_{min}) for 3 different materials, i.e. a P92 pipe, a F92 forging and a 316L plate. The MCH line is calculated on the standard test-setup and a 0.5 mm specimen thickness. In Figure 13 the SP data from the TASTE project (assessed in this paper) is presented as $\Psi = F_m/R_{m-UA}$ as a function of displacement v_m (v at F_m). In this case the MCH was modified to fit the standard test-setup with a 0.45 mm specimen.
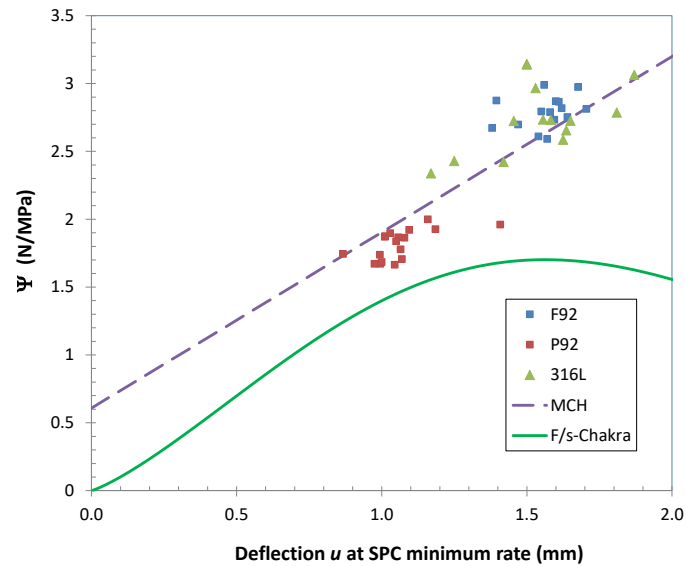
Figure 12. The SPC creep data from the ECISS/TC101/WG1 round robin [6] plotted as Ψ at u_{min} together with the CHA and the MCH models. Note that the P92 SPC samples were suffering from early cracking and failure. The predicted uniaxial creep stress at equal rupture time will therefore be increased and Ψ decreased. The specimen thickness $h_0=0.5$ mm.
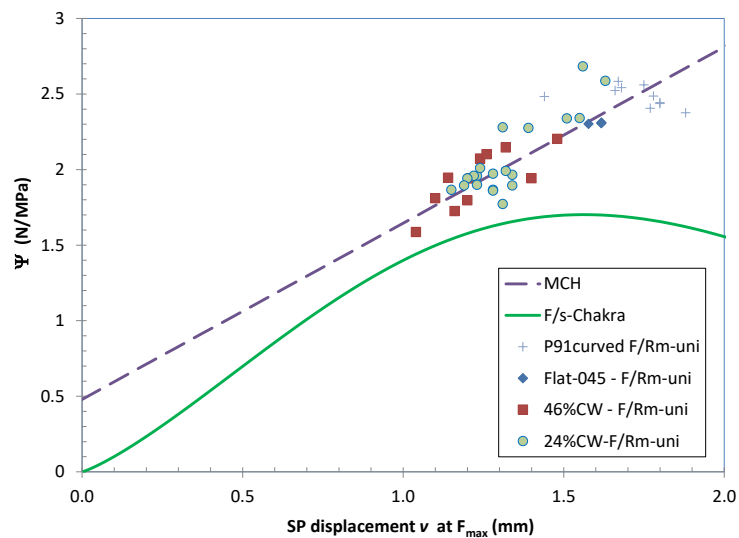
Figure 13. The SP test data from the TASTE project plotted as F_{max}/R_{m-UA} at the test specific v_{max}. Note that $h_0=0.45$ mm.

It could be concluded from the above figures that the MCH could be given a slightly steeper slope, perhaps pivoting around a displacement of 1 to 1.25 mm. However, the slope should not be as steep as CLA model, having a slope of h_0/β_{Rm-CLA} going through the origin. The CLA model is not giving an optimal solution if applied on SPC data replacing v_{max} for u_{min}.

As stated earlier, the optimization of the MCH model parameters using both SPC and SP data would most likely improve the understanding and accuracy of predictions for both small punch test types.

Studying the F_i/R_m for the ALT model, as seen in Figure 14, for the ASTM steels it is evident that some of the materials with low proof strength did not give the expected Ψ as was indicated by the FEA simulated SP tests on "synthetic" materials. It could be concluded that for low proof stress materials the R_m cannot be estimated at this (low) displacement. Maybe this information can instead be used for improving the SP estimates for proof strength.
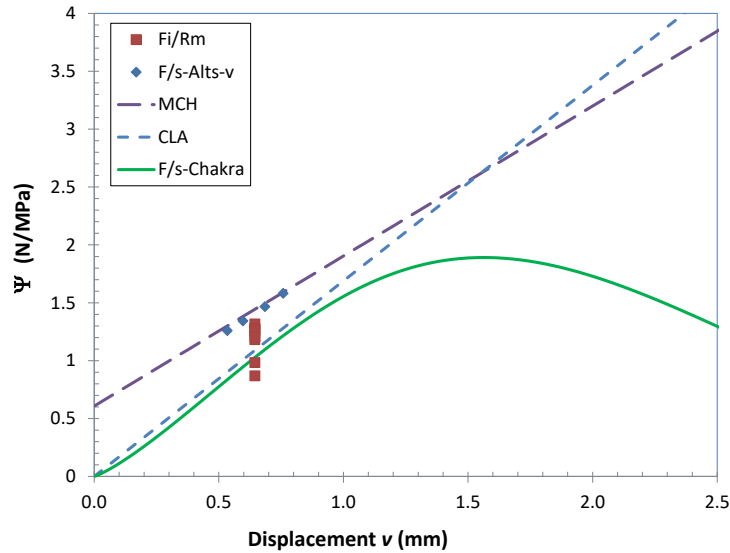
Figure 14. Room temperature F_i/R_m data from the ASTM materials extracted from the force displacement curve at $v_i = 0.645$.

One of the remaining main challenges for increasing the applicability of the SP tests technique in general is to establish ductility limitations for successful assessment of both SP and SPC data. For instance what is the impact of material "necking" on the SP test curve. For some low ductility materials this could happen already at small displacement [26]. The material properties beyond the uniaxial engineering ultimate tensile strength, i.e. after necking, will naturally have an effect on v_{max} and F_{max}. In Figure15a a SP tested 15-15Ti specimen clearly failed by plastic collapse whereas the SPC specimen in Figure15b has cracked open in a star shaped manner. The change in fracture behavior is linked to the deformation rate and differences in tensile and creep ductility.

(a)   (b)
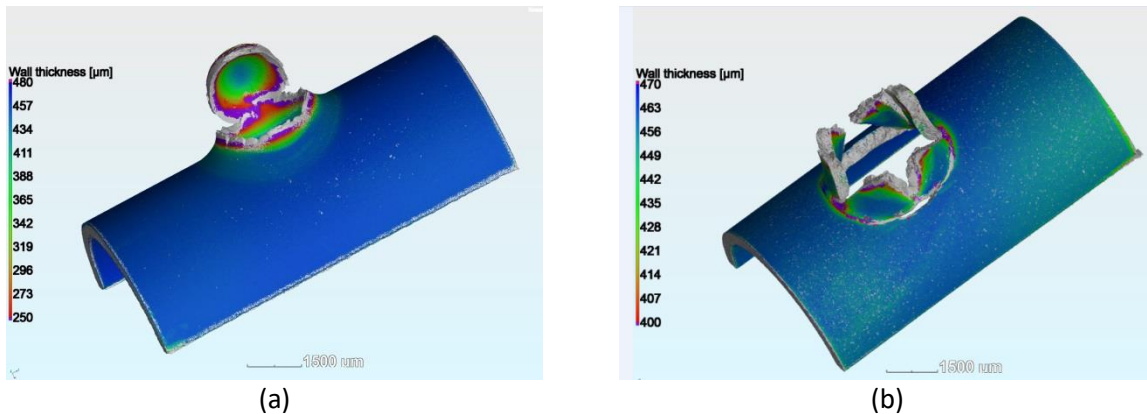
Figure 15. Difference in fracture mode of a 24%CW 1515Ti A) SP "tensile" specimen after test at 600°C and B) SPC creep specimen ruptured after 22 h at 600°C/400N.

6. Conclusions

A range of different materials with differing tensile strengths have been analyzed with three different models. SP data from test set-ups that are non-standard in nature such as the curved samples from fuel cladding tubes have also been successfully assessed. The conclusions to be drawn from results from the here presented assessments are:

- Good estimates on the tensile strength can be acquired by the existing conversion models, e.g. the ALT model developed for SP data and the MCH model initially developed for SPC data.
- The force to stress conversion of SP and SPC test can be unified by optimizing models like the MCH.
- Curved samples such as cladding tubes can be tested by SP and analyzed successfully using curvature corrections calculated by FEA.

- Tensile strength estimates for less ductile materials should be done on forces extracted at low displacement, for instance using an ALT type model.
- Challenges remain in the field of improving the estimates on proof strength and ductility.

It could be claimed that the usability of the SP testing has been improved greatly by the new assessment methods, such as for estimating tensile strength in general and for nuclear claddings in specifically.

References

1. Chakrabarty, J., A theory of stretch forming over hemispherical punch heads, *International Journal of Mechanical Sciences* 12(4), pp.315-325, 1970.
2. García, T.E.; Rodríguez, C.; Belzunce, F.J.; Suárez, C., Estimation of the mechanical properties of metallic materials by means of the small punch test. *Journal of Alloys and Compounds* 582:708–717, 2014.
3. Altstadt E.; Houska M.; Simonovski, I.; Bruchhausen, M.; Holmström, S.; Lacalle, R., On the estimation of ultimate tensile stress from small punch testing, *International Journal of Mechanical Sciences* 136, pp. 85–93, 2018.
4. Bruchhausen, M.; Austin, T.; Holmström, S.; Altstadt, E.; Dymacek, P.; Jeffs, S.; Lancaster, R.; Lacalle, R.; Matocha, K.; Petzova, J., European standard on small punch testing of metallic materials. In Proceedings of the ASME 2017 Pressure Vessels & Piping Conference, Volume 1A-2017, Waikoloa Village, USA, July 16-20 2017.
5. CEN Workshop Agreement CWA 15627: Small Punch Test Method for Metallic Materials: European Committee for Standardization, CWA 15627: 2007.
6. Holmstrom et. Al, Creep strength and minimum strain rate estimation from Small Punch Creep tests, MSEA-2018-01831, to be published.
7. Lancaster, R.; Davies, G.; Illsley, H.; Jeffs, S.; Baxter,G. 2016. "Structural integrity of an electron beam melted titanium alloy". *Materials*, 9(6), p. 470.
8. [Catalog] Holmstrom, S.; La-Petite, J-M.; De Haan, F.; SP tests at room temperature on 316L, version 1.0, European Commission JRC, 2018, http://dx.doi.org/xx.yyyy/zz, to be published.
9. Standard for Small Punch Creep Test, Estimation of Residual Life for High Temperature Component, The Committee on High Temperature Strength of Materials JSMS, The Society of Materials Science, ISBN: 978-4-901381-38-3, Japan, 2012.
10. Altstadt, E.; Ge, H.E.; Kuksenko, V.; Serrano, M.; Houska, M.; Lasan, M,; Bruchhausen, M.; Lapetite, J.-M.; Dai, Y. Critical evaluation of the small punch test as a screening procedure for mechanical properties. *Journal of Nuclear Materials*, vol. 472, pp. 186-195, 2016, https://doi.org/10.1016/j.jnucmat.2015.07.029.
11. Holmström, S., et. al, Determination of high temperature material properties of 15-15Ti steel by small specimen techniques, EUR 28746 EN, https://dx.doi.org/10.2760/259065.
12. Holmström, S., et. al., Test methodologies for determining high temperature material properties of thin walled tubes, EUR 28642 EN, https://dx.doi.org/10.2760/702821.
13. Holmström, S.; Simonovski, I.; Ripplinger, S.; Altstadt, E.; Delville, R.; Serrano, M.; Radu, V., Tensile and creep property determination of 15-15Ti fuel cladding steel by small punch testing, International Conference on Life Management and Maintenance for Power Plants, VTT TECHNOLOGY 261, 2016.
14. Delville, R.; Stergar, E.; and Verwerft, M., Results of a new production of nuclear-grade 1.4970 15-15Ti stainless steel fuel cladding tubes for GEN IV reactors in 22nd International Conference on Nuclear Engineering ICONE22. Prague, Czech Republic July 7-11, 2014. ASME.
15. [Catalog] Altstadt, E.; Houska, M (2018): Uniaxial tensile tests at room temperature on 24%CW 1515Ti, version 1.0, European Commission JRC, http://dx.doi.org/10.5290/28.
16. [Catalog] Altstadt, E.; Houska, M (2018): Uniaxial tensile tests at room temperature on 46%CW 1515Ti, version 1.0, European Commission JRC, http://dx.doi.org/10.5290/29.
17. [Catalog] Holmström, S. (2016): Uniaxial tensile data for P91 in the temperature range 20°C to 600°C, version 1.0, European Commission JRC Institute for Energy and Transport, http://dx.doi.org/10.5290/6.
18. ASTM work item WK61832, "New Test Method for Small Punch Testing of Metallic Materials", https://www.astm.org/DATABASE.CART/WORKITEMS/WK61832.htm.

19. Bruchhausen, M.; Holmström, S.; Simonovski, I.; Austin, T.; Lapetite, J.-M.; Ripplinger, S. and F.de Haan, Recent developments in small punch testing: Tensile properties and DBTT. *Theoretical and Applied Fracture Mechanics*, vol. 86, Part A, pp. 2-10, 2016, https://doi.org/10.1016/j.tafmec.2016.09.012.

20. Holmstrom, S, et Al. Small punch creep testing for material characterization and life time prediction, 10th Liege Conference: Proc. Materials for Advanced Power Engineering 2014, ISSN 1866-1793, pp. 627-635 (2014).

21. Simonovski, I.; Holmström, S.; Bruchhausen, M. Small punch tensile testing of curved specimens: Finite element analysis and experiment. *International Journal of Mechanical Sciences*, vol. 120, pp. 204-213, 2017, https://doi.org/10.1016/j.ijmecsci.2016.11.029.

22. ABAQUS 6.14-2, Dassault Systemes, 2015.

23. Simonovski, I. et Al., Determining the Ultimate Tensile Strength of Fuel Cladding Tubes by Small Punch Testing, JNM_2018_131, To be published.

24. [Catalog] Holmström, S (2018): Small Punch tests on 24%CW 1515Ti (curved samples) RT-800°C, version 1.0, European Commission JRC, http://dx.doi.org/10.5290/27.

25. [Catalog] Holmström, S (2018): Small Punch tests on 46%CW 1515Ti (curved samples) RT-800°C, version 1.0, European Commission JRC, http://dx.doi.org/xx.yyy/zz to be published.

26. Campitelli, E.N., et Al, Assessment of the constitutive properties from small ball punch test: experiment and modeling, Journal of Nuclear Materials 335 pp. 366–378, 2004.

Effect of anisotropic microstructure of ODS steels on small punch test results

E. Altstadt [1, *], M. Houska [2] and A. Das [3]

[1] Helmholtz-Zentrum Dresden-Rossendorf, Germany; e.altstadt@hzdr.de
[2] Helmholtz-Zentrum Dresden-Rossendorf, Germany; m.houska@hzdr.de
[3] Helmholtz-Zentrum Dresden-Rossendorf, Germany; a.das@hzdr.de
[*] Correspondence: e.altstadt@hzdr.de; Tel.: +49-351-260-2276

Abstract: Oxide dispersed strengthened (ODS) steels can exhibit a strongly anisotropic microstructure leading to anisotropic mechanical properties. The ductile to brittle transition temperature in the small punch (SP) test is therefore dependent on the specimen orientation. Three ODS steels with 13-14 mass percent Cr, manufactured through hot extrusion and hot rolling respectively, were investigated by means of SPT in different orientations. Existing microstructural data (EBSD) are used to discuss the anisotropic fracture behavior observed in the SPT. In addition, the SPT results are compared with those from existing fracture mechanics tests based on sub-sized C(T) samples. The applicability of the empirical conversion of SPT based transition temperatures into Charpy transition temperatures – well established for isotropic homogeneous metals – is investigated for materials with anisotropic microstructure.

1. Introduction

Oxide dispersion strengthened (ODS) steels are candidate materials for fuel claddings of Gen-IV sodium cooled fast reactors as well as for the first wall and blanket structures of fusion reactors [1–3]. The envisaged operation temperature is up to 650 °C. The focus of ODS materials development was put on superior creep and swelling properties. However, sufficient tensile and fracture mechanical properties are required for safety relevant structural applications in the whole range from room to operation temperature. Lindau et al. demonstrated that yield stress and ultimate tensile stress (UTS) of ODS-EUROFER are significantly higher in comparison to the non ODS EUROFER steel for temperatures up to 750 °C [4]. The creep resistance at 750 °C is also significantly improved. However, the ductile-to-brittle transition temperature (DBTT) was found to be significantly higher than that of non-ODS-EUROFER. Chaouadi et al. [5] found a significant crack resistance degradation of Eurofer ODS when the test temperature increases. In particular, at 550 °C and 650 °C, the crack resistance is very low. Nevertheless, Byun et al. [6] have demonstrated that high temperature fracture toughness could be significantly improved by appropriate thermo-mechanical treatments.

The fracture behavior of ODS materials is governed by grain morphology. Chao et al. [7] found a grain size anisotropy for a 20Cr ODS alloy manufactured as a tube by hot rolling. The grains were found to be elongated along the rolling direction. KLST impact tests and subsequent EBSD analyses of the crack region revealed intergranular cracks along the elongated grain boundaries which constitute weak interfaces. The term "delamination" originating from laminated composite materials was adopted for this type of intergranular cracking. The delamination phenomenon had earlier been reported for ultrafine grain structure steels by Kimura et al. [8]. Depending on the orientation of the weak planes in the impact specimen, they discriminated a "crack arrester" and a "crack divider" situation. The impact of two different fabrication routes (hot rolling and hot extrusion) on the grain morphology and thereby on the fracture toughness in different orientations was investigated in detail by Das et al. [9,10].

The small punch (SP) test has long been accepted as a method to estimate mechanical properties from small quantities of materials. In particular the ductile to brittle transition temperature, the yield stress, the ultimate tensile stress and creep strength can be extracted for homogeneous and isotropic metals [11–19]. The SP test is not intended to replace conventional tests such as tensile tests, Charpy impact tests or fracture mechanical testing, but to be used as screening procedure [17]. The SP test is especially useful in one or more of the following cases: (i) the available amount of material is limited, (ii) the material is highly activated by neutron irradiation, (iii) material properties are non-homogeneous and exhibit significant gradients. Therefore it is generally useful to include this technique in the characterization of ODS alloys. So far, the effect of the above mentioned anisotropic microstructure on SP test

results has only rarely been investigated [20,21]. A systematic comparison with impact tests and fracture mechanics tests is needed. In this paper we investigate one hot rolled and two hot extruded ODS steels by means of SP testing. The SP results are discussed in the view of existing fracture mechanics tests for the same materials. The paper aims at relating fracture mechanisms depending on grain morphology and orientation to features of SP force-displacement curves and SP based DBTTs.

2. Materials and Methods

Three different ODS steels were selected for testing, one hot-rolled and two hot-extruded. The denomination in this paper is ODS-HR, ODS-HE-1, ODS-HE-2. The bulk chemical composition of the materials is given in Table 1.

- **ODS-HR** is a 13%Cr ODS steel hot rolled plate provided by Karlsruhe Institute of Technology, Germany (KIT). The main production steps include: mechanical alloying in an attritor ball mill, encapsulation of the powder, hot isostatic pressing at 1100 °C and 100 MPa and rolling at 1100 °C from a diameter of 80 mm to a plate of 8 mm thickness in 5 runs [9,22].
- **ODS-HE-1** is a hot extruded 13% Cr ODS steel round bar also provided KIT. The main fabrication steps include: mechanical alloying in an attritor ball mill, encapsulation of the powder, evacuation of the capsule and hot extrusion at 1100 °C [10,22].
- **ODS-HE-2** is a hot extruded 14% Cr ODS steel round bar provided by Centro Sviluppo Materiali, Italy (CSM). Gas atomized pre-alloyed steel powder was mixed with 0.3% Y_2O_3 and dry ball milled in an environment of Ar and H. After canning, direct hot extrusion was performed at 1150 °C with an extrusion ratio of 22.5. A heat treatment at 1050 °C was applied for one hour with subsequent cooling in the furnace [10].

Table 1. Chemical composition of the tested ODS steels (wt%) [9,10,22].

Material	C	Si	P	Ti	Cr	Ni	W	Y_2O_3 *
ODS-HR	0.21	-	-	0.151	13.10	0.09	1.11	0.3
ODS-HE-1	0.028	0.051	0.01	0.138	12.99	0.101	1.03	0.3
ODS-HE-2	0.010	0.371	0.006	0.238	13.76	0.239	0.84	0.3

* Nominal Y_2O_3 content of the powder composition

Small punch tests were executed in three orientations for ODS-HR (S - thickness direction, L - rolling direction and T - transverse direction) and in two orientations for ODS-HE-1 and ODS-HE-2 (L - extrusion direction, R/C - radial/circumferential direction). The orientation refers to the normal direction of the specimens. In case of ODS-HE-1 and ODS-HE-2, it is assumed that the directions R and C are equivalent because of the axial symmetry of the extrusion process. Moreover, plane samples cut from a round bar in axial direction always exhibit a combination of R and C orientation for geometrical reasons. One can assume a plane stress state in a SP test, i.e. the stress components in thickness direction are much smaller than the in-plane stress components. Therefore the S oriented specimens represent the mechanical behavior of the LT plane, the T oriented specimens those of the LS plane and the L oriented specimens those of the TS plane [21].

Specimens of ⌀8 x 0.5 mm were manufactured by electrical discharge machining and subsequent grinding to final thickness with grit 2500. The maximum accepted thickness tolerance was ±5 μm. The thicknesses of all specimens were measured by laser micrometer with an accuracy of ±1 μm. Specimens with a thickness outside the tolerance were not used. The main parameters of the SP set-up are: punch diameter $d = 2.5$ mm, receiving hole diameter $D = 4$ mm, receiving hole edge radius $R_E = 0.5$ mm (cf. Fig. 1). The edge size is larger than proposed in the upcoming standard [23]. While the effect of the edge size on the estimation of tensile properties (in particular the yield stress) is significant, it can be neglected for the estimation of the ductile to brittle transition temperature [17].

The punch displacement v was measured by an inductive sensor with an accuracy of ±1 μm and corrected for the device compliance. The punch force was measured by means of a load cell placed between the puncher and the cross head of the testing machine with an accuracy of ±5 N.

In total a number of 168 tests were performed. The temperature range was from -188 °C to +350 °C. The subsequent fractographic analysis of the tested SP specimens was done by SEM using a Zeiss EVO 50 device.
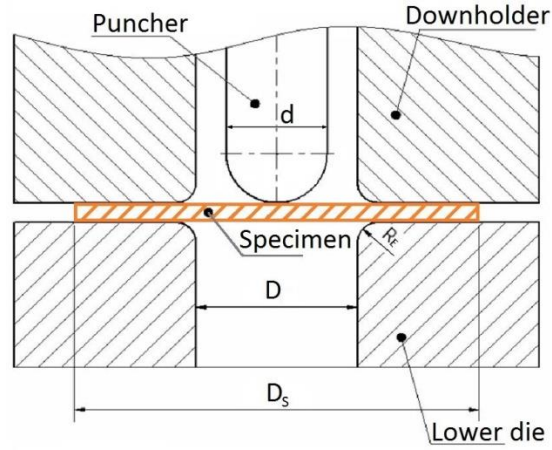
Figure 1. Geometry of the SP set-up.

The SP based ductile-to-brittle transition temperature T_{SP} is determined on the basis of normalized energies $E_n = E_{SP}/F_m$ [24] of the different tests. E_{SP} is the area under the force-displacement curve up to the displacement v_m at maximum force F_m:

$$E_{SP} = \int_0^{v_m} F(v)dv \approx \sum_{k=2}^{k_{max}} (F_k + F_{k-1})(v_k - v_{k-1}) \tag{1}$$

A tanh-fitting procedure was applied for the $E_n(T)$ dependence based on the following equation:

$$E_n(T) = A + B \cdot \tanh\left[\frac{T - T_{SP}}{C}\right] \tag{2}$$

A least square procedure was used to determine the coefficients A, B, C, and T_{SP}. The Charpy transition temperature T_{CVN} can be recalculated by the well-known correlation $T_{SP} = \alpha \cdot T_{CVN}$ (temperatures in K) [14]. For our set-up we used $\alpha = 0.43$ [17]. This value was further validated for a number of ferritic-martensitic steels and reactor pressure vessel steels. However, these results are no yet published.

In case of discontinuous load drops (pop-ins) in the force-deflection curve, caused by crack initiation and subsequent crack arrest [21], the procedure for the energy calculation Eq. (1) is modified so that v_m and F_m are replaced by displacement v_{1p} and force F_{1p} of the first significant pop-in (cf. Fig. 2). A load drop is considered as significant, if $\Delta F/F_m \geq 0.1$.
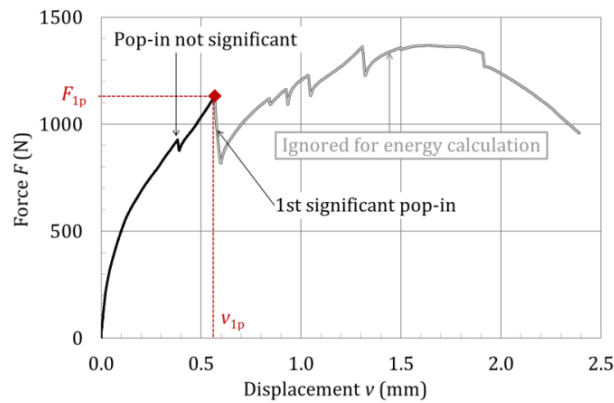
Figure 2. Energy calculation in case of load-drops.

3. Results

3.1. Force-displacement curves

Selected force-displacement curves are shown in Figs. 3-5. For the hot-rolled material ODS-HR, there are significant differences between the orientation L and T on the one hand and orientation S on the other hand. The maximum forces F_m and corresponding displacements v_m are smaller in L/T-oriented samples. Moreover, load-drops (pop-ins) are observed at low test temperatures (below -70 °C) for orientation L/T but not for orientation S. For room temperature, the parameters v_m and F_m are summarized in Table 2.
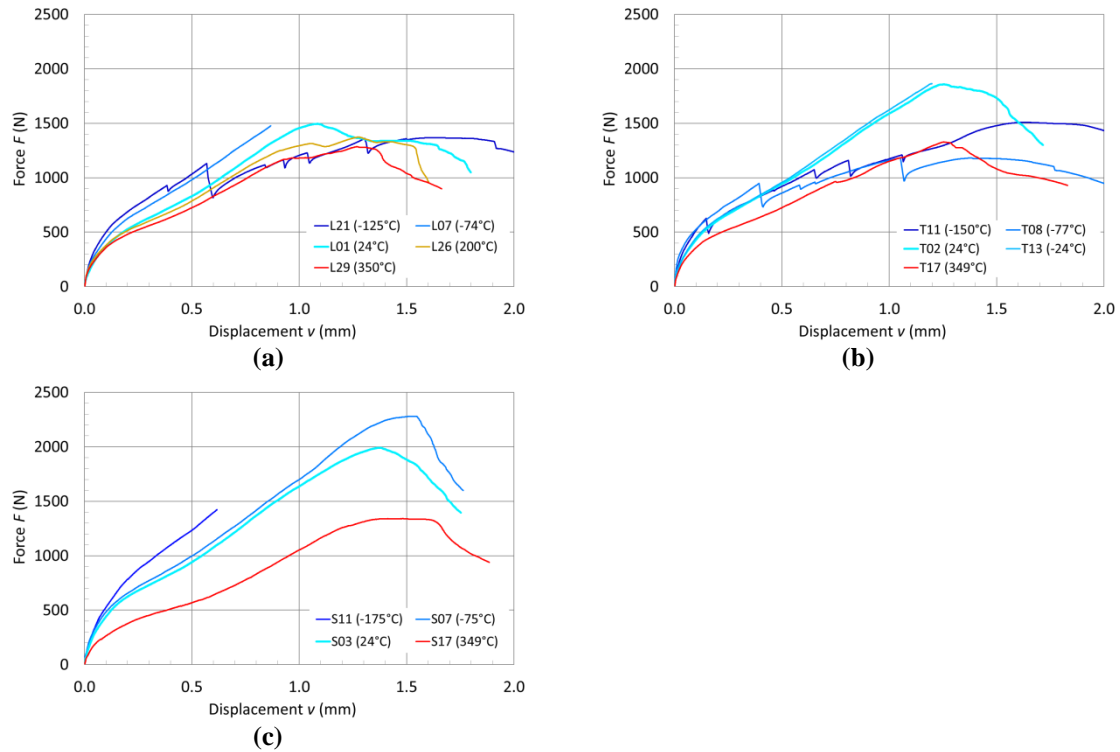
Figure 3. Force-displacement for material ODS-HR; **(a)** orientation L, **(b)** orientation T, **(c)** orientation S.

For the hot extruded materials, pop-ins do not occur in either orientation. The maximum forces F_m and corresponding displacements v_m are slightly smaller in C/R oriented samples as compared to orientation L. There is, however, a pronounced difference between the two materials ODS-HE-01 and ODS-HE-2 in that the latter one exhibits significantly lower absolute values.
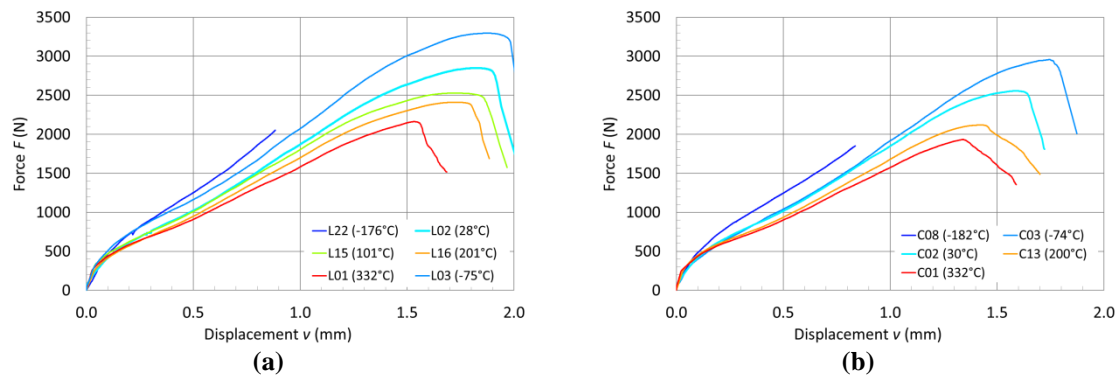
Figure 4. Force-displacement for material ODS-HE-1; **(a)** orientation L, **(b)** orientation C/R.
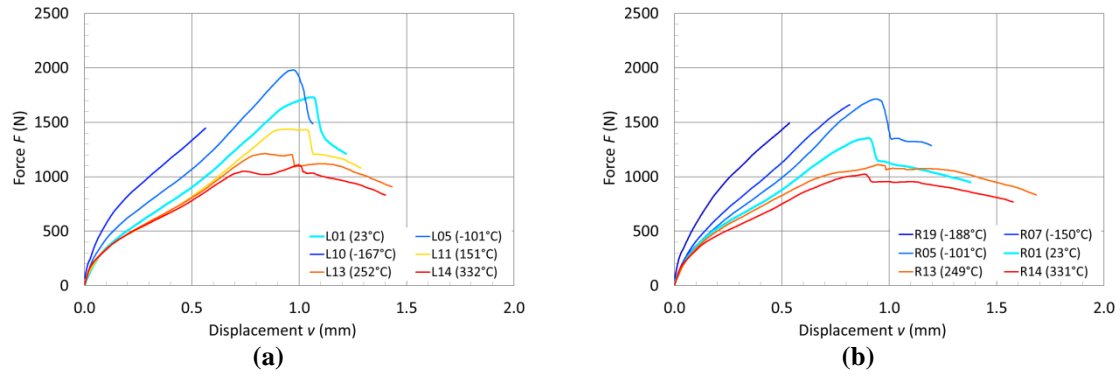
Figure 5. Force-displacement for material ODS-HE-2; **(a)** orientation L, **(b)** orientation C/R.

Table 2. Parameters of the force-displacement curves at room temperature.

Material Orientation	ODS-HR L	ODS-HR T	ODS-HR S	ODS-HE-1 L	ODS-HE-1 C/R	ODS-HE-2 L	ODS-HE-2 C/R
v_m (mm)	1.08	1.26	1.37	1.82	1.59	1.05	0.90
F_m (N)	1494	1857	1991	2848	2556	1730	1355

3.2 Ductile-to-brittle transition temperatures

The SP ductile-to-brittle transition temperature were determined for all materials and orientations as described in section 2. Two examples of the dependence of the normalized SP energy E_n on temperature are shown in Fig. 6. The full set of SP transition temperatures T_{SP} and the corresponding recalculated Charpy transition temperature T_{CVN} are given in Table 3.
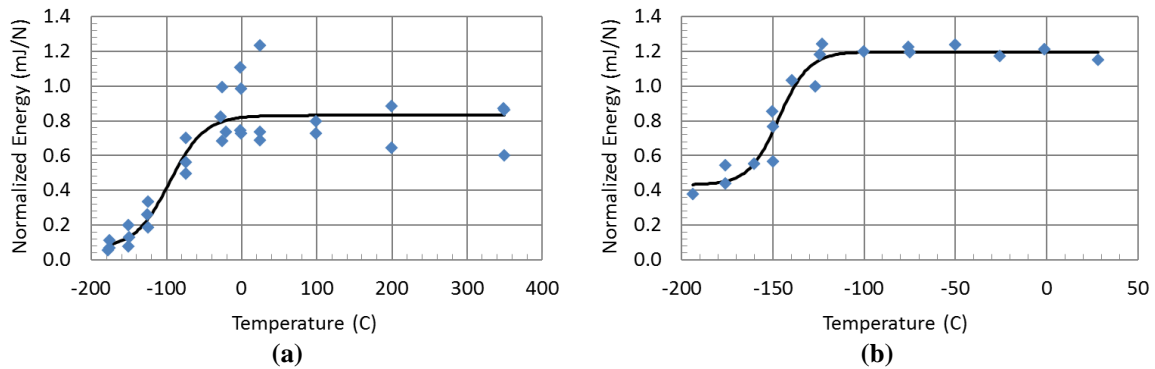
Figure 6. Example of $E_n(T)$ fit curves: **(a)** ODS-HR orientation L, T_{SP} = -96 °C; **(b)** ODS-HE-1 orientation L, T_{SP} = -147 °C.

Table 3. Ductile-to-brittle transitions temperatures.

Material Orientation	ODS-HR L	ODS-HR T	ODS-HR S	ODS-HE-1 L	ODS-HE-1 C/R	ODS-HE-2 L	ODS-HE-2 C/R
T_{SP} (°C)	-96	-70	-157	-147	-130	-144	-154
T_{CVN} (°C) *	+139	+199	-2	+21	+59	+26	+4

* Recalculated from: $T_{SP}[K] = 0.43 \cdot T_{CVN}[K]$

4. Discussion

The microstructure of the investigated ODS steels is characterized by fine and coarse grained regions. In the hot-rolled material ODS-HR the coarse grained regions exhibit elongated pan-cake shaped grains [9] (cf. Fig. 7a, whereas cigar shaped elongated grains were observed in the hot extruded materials ODS-HE-1 and ODS-HE-2 [10] (cf. Fig. 7b).
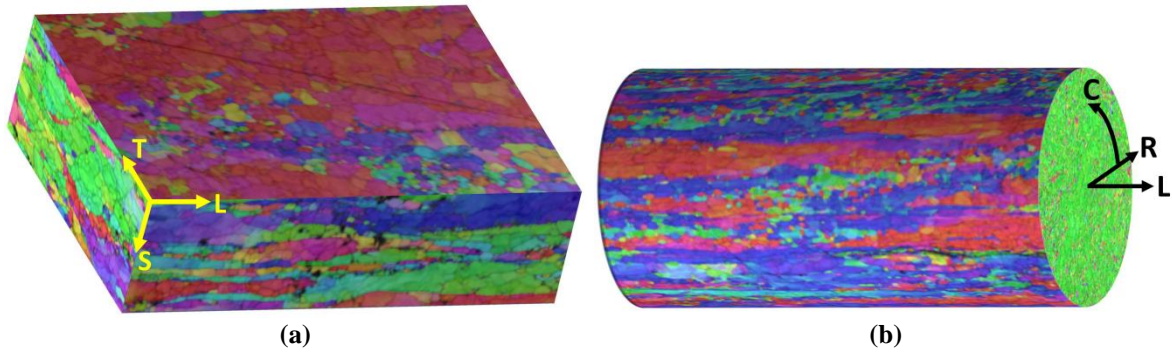
Figure 7. EBSD images from [9,10]: **(a)** pan-cake shaped coarse grains in ODS-HR; **(b)** Cigar shaped coarse grains in ODS-HE-1.

It was reported that in the hot rolled material crack extension is preferred through fine grained regions or through the interface between fine grained and coarse grained regions [9]. The large area grain boundaries and the interfaces between coarse and fine grained regions constitute weak interfaces leading to delamination under tensile stress [9,21]. This is the reason why pop-ins are observed in the $F(v)$ curves of L and T oriented samples. The fracture process is characterized by an interplay of stable transgranular crack growth and unstable intergranular crack. Crack arrest occurs when the crack tip arrives at a coarse grain which is extended perpendicularly to the crack propagation direction. The fracture in the SP specimen is preferentially oriented in radial direction and the fracture surface exhibits lamella (cf. Fig 8a). Their formation can be associated with the pop-ins in the $F(v)$ curves. By contrast, such a mechanism does not exist in S oriented samples as the weak interfaces are not loaded by tensile stress. Therefore the crack appearance is the same as for ductile isotropic materials (cf. Fig. 8b).

In hot-extruded materials, the coarse grains are extended only in one direction (L). Thus the SP samples are less susceptible to unstable intergranular cracking and subsequent crack arrest for pure geometrical reasons. Consequently pop-ins cannot be observed in the $F(v)$ curves.

In fracture mechanics investigations by means of 0.25C(T) compact tension samples it was found that the ODS-HR material is susceptible to secondary cracking, i.e. cracks in planes perpendicular to main crack plane were observed [9]. By contrast, the hot-extruded materials ODS-HE-1 and ODS-HE-2 were found to be unsusceptible to secondary cracking [10]. Obviously the occurrence of pop-ins in the SP $F(v)$ curves corresponds with the occurrence of secondary cracks in fracture mechanics testing.

The large differences between ODS-HE-1 and ODS-HE-2 with respect to the v_m and F_m parameters (Table 2) correspond to the different values of fracture toughness reported in [10]. A detailed comparison is given in Table 4.
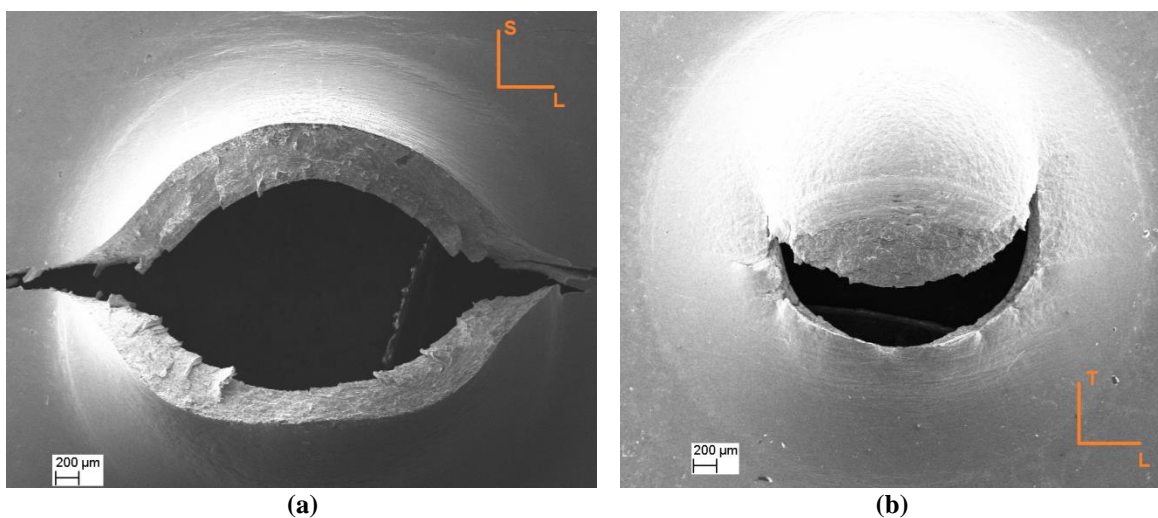
Figure 8. SEM pictures of the fracture modes of samples from ODS-HR: **(a)** orientation T; **(b)** orientation S.

Table 4. SP parameters and fracture toughness (from [10]) at room temperature for the hot-extruded materials.

Parameter Orientation	v_m (mm) L	F_m (N) L	v_m (mm) C/R	F_m (N) C/R	J_Q (kJ/m²) L-C	J_Q (kJ/m²) C-R
ODS-HE-1	1.82	2848	1.59	2556	486	97
ODS-HE-2	1.05	1730	0.90	1355	64	35

The existence of coarse Si-rich particles in ODS-HE-2 was identified as main reason for the significantly lower fracture toughness values as compared to ODS-HE-1 [10], also cf. Si content in Table 1. Obviously, the higher values of v_m and F_m in the SP test correspond with higher fracture toughness values J_Q in fracture mechanics testing.

The ductile-to brittle transition temperatures T_{CVN} recalculated from T_{SP} gives reasonable values for the hot-extruded materials (all orientations) and for the hot-rolled material tested with S oriented samples, cf. e.g. [4,21]. The DBTT values between 0 and 60 °C were also found in classical Charpy impact tests and KLST impact tests. In contrast the tests with samples from ODS-HR in orientations L and T give unrealistic high DBTTs. In conclusion, it is suggested that the correlation $T_{SP} = \alpha \cdot T_{CVN}$ can be applied for SP tests without pop-ins in the $F(v)$ curves.

5. Conclusions

- In hot-rolled ODS steel, the occurrence of pop-ins in the SP $F(v)$ curves corresponds with the susceptibility to secondary cracks in fracture mechanics testing.
- In hot-extruded ODS steel, higher values of F_m and v_m in the SP test correspond with higher fracture toughness values J_Q in fracture mechanics testing.
- The application of the established correlation between DBTTs from SP test and Charpy impact test ($T_{SP} = \alpha \cdot T_{CVN}$) is questionable for L/T oriented SP specimens of hot-rolled ODS material.

References

1. Lindau, R.; Möslang, A.; Rieth, M.; Klimiankou, M.; Materna-Morris, E.; Alamo, A.; Tavassoli, A.-A.F.; Cayron, C.; Lancha, A.-M.; Fernandez, P.; Baluc, N.; Schäublin, R.; Diegele, E.; Filacchioni, G.; Rensman, J.W.; v. d. Schaaf, B.; Lucon, E;. Dietz, W. Present development status of EUROFER and ODS-EUROFER for application in blanket concepts, *Fusion Eng. Des.* 75–79 (2005) 989–996. doi:10.1016/j.fusengdes.2005.06.186.

2. Klueh, R.L.; Shingledecker, J.P.; Swindeman, R.W.; Hoelzer, D.T. Oxide dispersion-strengthened steels: A comparison of some commercial and experimental alloys, *J. Nucl. Mater.* 341 (2005) 103–114. doi:10.1016/j.jnucmat.2005.01.017.

3. McClintock, D.A.; Sokolov, M.A.; Hoelzer, D.T.; Nanstad, R.K. Mechanical properties of irradiated ODS-EUROFER and nanocluster strengthened 14YWT, *J. Nucl. Mater.* 392 (2009) 353–359. doi:10.1016/j.jnucmat.2009.03.024.

4. Lindau, R.; Möslang, A.; Schirra, M.; Schlossmacher, P.; Klimenkov, M. Mechanical and microstructural properties of a hipped RAFM ODS-steel, *J. Nucl. Mater.* 307–311, Part 1 (2002) 769–772. doi:10.1016/S0022-3115(02)01045-0.

5. Chaouadi, R.; Coen, G.; Lucon, E.; Massaut, V. Crack resistance behavior of ODS and standard 9%Cr-containing steels at high temperature, *J. Nucl. Mater.* 403 (2010) 15–18. doi:10.1016/j.jnucmat.2010.05.021.

6. Byun, T.S.; Yoon, J.H.; Wee, S.H.; Hoelzer, D.T.; Maloy, S.A. Fracture behavior of 9Cr nanostructured ferritic alloy with improved fracture toughness, *J. Nucl. Mater.* 449 (2014) 39–48. doi:10.1016/j.jnucmat.2014.03.007.

7. Chao, J.; Capdevila, C.; Serrano, M.; Garcia-Junceda, A.; Jimenez, J.A.; Pimentel, G.; Urones-Garrote, E. Notch Impact Behavior of Oxide-Dispersion-Strengthened (ODS) Fe20Cr5Al Alloy, *Metall. Mater. Trans. A.* 44 (2013) 4581–4594. doi:10.1007/s11661-013-1815-7.

8. Kimura, Y.; Inoue, T.; Yin, F.; Tsuzaki, K. Delamination Toughening of Ultrafine Grain Structure Steels Processed through Tempforming at Elevated Temperatures, *ISIJ Int.* 50 (2010) 152–161. doi:10.2355/isijinternational.50.152.

9. Das, A.; Viehrig, H.W.; Bergner, F.; Heintze, C.; Altstadt, E.; Hoffmann, J. Effect of microstructural anisotropy on fracture toughness of hot rolled 13Cr ODS steel – The role of primary and secondary cracking, *J. Nucl. Mater.* 491 (2017) 83–93. doi:10.1016/j.jnucmat.2017.04.059.

10. Das, A.; Viehrig, H.W.; Altstadt, E.; Heintze, C.; Hoffmann, J. On the influence of microstructure on the fracture behaviour of hot extruded ferritic ODS steels, *J. Nucl. Mater.* 497 (2017) 60–75. doi:10.1016/j.jnucmat.2017.10.051.

11. Misawa, T.; Adachi, T.; Saito, M.; Hamaguchi, Y. Small punch tests for evaluating ductile-brittle transition behavior of irradiated ferritic steels, *J. Nucl. Mater.* 150 (1987) 194–202. doi:10.1016/0022-3115(87)90075-4.

12. Mao, X.; Takahashi, H. Development of a further-miniaturized specimen of 3 mm diameter for tem disk (ø 3 mm) small punch tests, *J. Nucl. Mater.* 150 (1987) 42–52. doi:10.1016/0022-3115(87)90092-4.

13. Jia, X.; Dai, Y. Small punch tests on martensitic/ferritic steels F82H, T91 and Optimax-A irradiated in SINQ Target-3, *J. Nucl. Mater.* 323 (2003) 360–367. doi:10.1016/j.jnucmat.2003.08.018.

14. Fleury, E.; Ha, J.S. Small punch tests to estimate the mechanical properties of steels for steam power plant: I. Mechanical strength, *Int. J. Press. Vessels Pip.* 75 (1998) 699–706. doi:10.1016/S0308-0161(98)00074-X.

15. Kameda, J.; Mao, X. Small-punch and TEM-disc testing techniques and their application to characterization of radiation damage, *J. Mater. Sci.* 27 (1992) 983–989. doi:10.1007/BF01197651.

16. Dymáček, P.; Milička, K. Creep small-punch testing and its numerical simulations, *Mater. Sci. Eng. A.* 510–511 (2009) 444–449. doi:10.1016/j.msea.2008.06.053.

17. Altstadt, E.; Ge H.E.; Kuksenko, V.; Serrano, M.; Houska, M.; Lasan, M.; Bruchhausen, M.; Lapetite, J.-M.; Dai, Y. Critical evaluation of the small punch test as a screening procedure for mechanical properties, *J. Nucl. Mater.* 472 (2016) 186–195. doi:10.1016/j.jnucmat.2015.07.029.

18. Altstadt, E.; Houska, M.; Simonovski, I.; Bruchhausen, M.; Holmström, S.; Lacalle, R. On the estimation of ultimate tensile stress from small punch testing, Int. J. Mech. Sci. 136 (2018) 85–93. doi:10.1016/j.ijmecsci.2017.12.016.

19. Vivas, J.; Capdevila, C.; Altstadt, E.; Houska, M.; San-Martín, D. Importance of austenitization temperature and ausforming on creep strength in 9Cr ferritic/martensitic steel, *Scr. Mater.* 153 (2018) 14–18. doi:10.1016/j.scriptamat.2018.04.038.

20. Okuda, N.; Kasada, R.; Kimura, A. Statistical evaluation of anisotropic fracture behavior of ODS ferritic steels by using small punch tests, *J. Nucl. Mater.* 386–388 (2009) 974–978. doi:10.1016/j.jnucmat.2008.12.265.

21. Altstadt, E.; Serrano, M.; Houska, M.; García-Junceda, A. Effect of anisotropic microstructure of a 12Cr-ODS steel on the fracture behaviour in the small punch test, *Mater. Sci. Eng. A.* 654 (2016) 309–316. doi:10.1016/j.msea.2015.12.055.

22. Hoffmann, J.; Rieth, M.; Commin, L.; Antusch, S. Microstructural anisotropy of ferritic ODS alloys after different production routes, *Fusion Eng. Des.* 98–99 (2015) 1986–1990. doi:10.1016/j.fusengdes.2015.05.002.

23. Bruchhausen, M.; Austin, T; Holmström, S.; Altstadt, E.; Dymacek, P.; Jeffs, S.; Lancaster, R.; Lacalle, R.; Matocha, K.; Petzová, J. European Standard on Small Punch Testing of Metallic Materials, in: ASME, 2017: p. V01AT01A065. doi:10.1115/PVP2017-65396.

24. Bruchhausen, M.; Holmström, S.; Lapetite, J.-M.; Ripplinger, S. On the determination of the ductile to brittle transition temperature from small punch tests on Grade 91 ferritic-martensitic steel, *Int. J. Press. Vessels Pip.* 155 (2017) 27–34. doi:10.1016/j.ijpvp.2017.06.008.

Tensile property evaluation of a Japanese reactor pressure vessel steel by Shear punch test technique

T. Kobayashi [1,*], Y. Miura [2] and M. Yamamoto [3]

[1] Central Research Institute of Electric Power Industry; k-tomo@criepi.denken.or.jp
[2] Central Research Institute of Electric Power Industry; ymiura@criepi.denken.or.jp
[3] Central Research Institute of Electric Power Industry; masatoy@criepi.denken.or.jp

* Correspondence: k-tomo@criepi.denken.or.jp; Tel.: +81 70-6450-8448

Abstract: Shear punch test specimen, whose dimensions are small as 8 mm-diameter × 0.5 mm thickness, is recently closed up as one of the alternative for tensile specimen. In this study, a Japanese reactor pressure vessel steel as well as several kinds of steels for mechanical structures were subjected to the shear punch tests at R.T. using a shear punch test frame developed in CRIEPI and the capability of the test technique for uniaxial tensile property evaluation was investigated. In addition, the disk shape specimens were machined along different orientations in the Japanese reactor pressure vessel steel and effect of specimen orientation on the shear punch properties was investigated. Shear punch yield stress and Shear punch strength for the tested materials could be obtained from stress – strain curves and they have reasonable linear relationships with uniaxial tensile yield stress and ultimate tensile strength. The shear punch yield stress for the specimens with the different orientations were not so different and the effect of specimen orientation was small.

Keywords: Reactor pressure vessel steels; Shear punch test; Hardness test; Tensile property

1. Introduction

As number of long-term operated nuclear power plants increases, the demand to ensure their structural integrity increases. Neutron irradiation embrittlement of reactor pressure vessels (RPV) is one of the most important material aging phenomena to be monitored during the operation period of RPV. The Japanese surveillance test program [1] takes the role of this monitoring, and change in mechanical properties, such as fracture toughness and tensile properties, of RPV steels are periodically evaluated via Charpy impact test and uniaxial tensile test. However, increase in number of the surveillance test is required with expand of operation period of nuclear power plants, and shortage of the surveillance test specimens is one of the key concerns.

Shear punch (ShP) test specimen, whose dimensions are small as 8 mm-dia × 0.5 mm thickness or TEM disk size (3 mm-dia.), has recently been proposed as one of the alternatives for the uniaxial tensile specimen [2,3]. The advantages of use of ShP specimen is reduction of volume of specimen and also radiation exposure from the specimens. In addition, ShP test technique has a potential to evaluate location by location variability of material properties such as a RPV weld and heat affected zone.

In order to confirm the capability of the ShP test for tensile property evaluation, we developed a ShP test frame which can be install into a common material fatigue testing machine. A Japanese RPV steel as well as common structural steels were subjected to the shear punch tests at R.T. using the shear punch test frame and the relationships between tensile property and ShP property were investigated. In addition, disk shape specimens were machined along different orientations in the Japanese RPV steel block and effect of specimen orientations on ShP properties were examined.

2. Materials and Methods

2.1 Materials

The materials used in this study are Japanese RPV steel (SQV2A), the European reference material; JRQ (ASTM A533 Grade B Class 1), carbon steel for mechanical structure (S45C), and precipitation hardening stainless steel (630SS). Chemical compositions of these tested materials are shown in Table 1.

Table 1. Chemical composition of tested materials.

Material	Chemical composition (wt.%)											
	C	Si	Mn	P	S	Cu	Ni	Cr	Mo	Nb	V	Al
Carbon steel (S45C)	0.44	0.19	0.73	0.18	0.13	0.01	0.02	0.15	-	-	-	-
Precipitation hardening stainelss steel (630SS)	0.04	0.24	0.86	0.35	0.02	3.33	4.24	15.68	-	0.24	-	-
JRQ (A533B Cl.1)	0.18	0.24	1.42	0.017	0.004	0.14	0.84	0.12	0.51	-	0.002	0.014
SQV2A	0.22	0.25	1.46	0.002	0.002	-	0.69	0.11	0.57	-	-	-

2.2 Shear Punch Test

ShP test specimens were machined from the tested materials. ShP test specimens with a final surface polishing using a #2000 paper have a dimension of 8 mm-diameter and 0.5 mm thickness. In the case of SQV2A, to investigate effect of specimen orientation on ShP properties, the ShP specimens were machined along L (rolling direction of plate), T and S (thickness of plate) at 1/4 thickness location of SQV2A plate.

A ShP test frame developed in CRIEPI was installed into a material fatigue testing machine (Figure 1). Upper and lower fixtures generate clamping force, which is translated to the ShP specimen through a guide bushing and a die. A puncher gives compressive load to center of the specimen and then the shear stress is generated in the specimen between the puncher and the die. The ShP test will be continued at R.T. in stroke control mode (0.25 mm/min) until the load remarkably drops at the specimen failure. Compressive load and specimen deflection are measured through the test. The engineering shear stress; S_e is calculated by the following equation.

$$S_e = \frac{P}{\pi \cdot D \cdot t}$$ (1)

Where, P is punch load, D is the average of the puncher and the die diameter (D = 3.1 mm) and t is specimen thickness. ShP properties were evaluated in accordance with procedures reported by Milot [3]. In this procedure, ShP yield stress (S_{ey}) and ShP strength (S_{em}) are evaluated based on cross point between the stress of stress (S_e) – strain (d/t) curve and 0.2% strain offset line parallel to the linear portion, and the maximum S_e in S_e – d/t curve, respectively (Figure 2). At small strains S_{ey} is associated with shear yielding stress; τ_y [3].
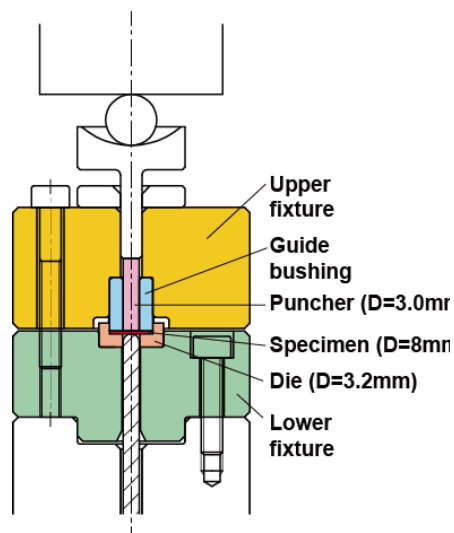
Figure 1. Shear punch test frame and principle of measurement of specimen displacement.
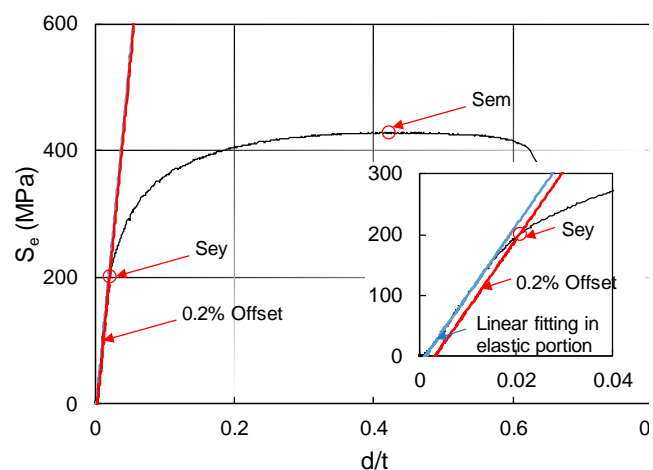
Figure 2. Typical stress–strain curve obtained by ShP test.

Vickers hardness tests of the surveillance materials were also conducted with test loads of 9.81 N (1 kgf) according to Japanese Industrial Standards (JIS Z 2244 [4]) using a Vickers hardness tester. Specimens after ShP

tests were used for the hardness test. Grinding and lapping by an emery paper followed by electro-polishing were applied for the surface preparation of the specimens. The lengths of diagonals for the Vickers indentations were measured using the reader system equipped with the test machine, and Vickers hardness values; HV1 were evaluated.

3. Shear Punch Test Results

Figure 3(a) – (e) shows S_e – d/t curves obtained for the tested materials with S_{ey} and S_{em}. For each material, three specimens were subjected to ShP test. As shown in the Figures, the S_e – d/t curves exhibit features typical of stress – strain curves obtained in uniaxial tensile tests. When we look at the S_e – d/t curves obtained for 630SS and JRQ-2, deflection of S_e – d/t curve due to moving specimen in the frame were observed. This phenomenon may lead an increase in ShP yield stress. The average values of S_{ey} and S_{em} for the tested materials are summarized in Table 2.

Figure 4 shows comparison of S_{ey} with the SQV2A specimens sampled from L (rolling direction, T-S plane), T (L-S plane) and S (L-T plane) directions. As shown in Figure(d) and Figure4, their tensile properties are almost the same. From these results, it was clarified that effect of the sampling orientation (rolling direction of plate) was small.

Table 2. Uniaxial tensile property, hardness and ShP property data of tested materials.

Material	ID	Uniaxial tensile test		Vickers hardness, HV1	Shear punch test	
		σ_y (MPa)	UTS (MPa)		S_{ey} (MPa)	S_{em} (MPa)
S45C	S45C	778[1]	871[1]	281	399	549
630SS	630SS	1112	1150	375	537	733
JRQ	QT_057	480[2]	630[2]	197	205	435
	QT_216			200	219	423
SQV2A	SQV2A-L	485[3]	625[3]	197[3]	210	421
	SQV2A-T				200	420
	SQV2A-S				200	420

1) Average values of JRQ plate A and B [5]
2) Estimation based on relationship between uniaxial tensile yield stress (σ_y), ultimate tensile strength (UTS) and HV1 obtained for JRQ, 630SS and SQV2A
3) σ_y, UTS and Vickers hardness reported in [6, 7]

4. Relationship between Uniaxial Tensile Properties and Shear Punch properties

Figure 5 shows relationships between uniaxial tensile yield stress (σ_y) and S_{ey}, and ultimate tensile strength (UTS) and S_{em}. The uniaxial tensile σ_y and UTS of S45C (Δ, $\blacktriangle$) was estimated from relationships of σ_y – HV1 and UTS – HV1 obtained for 630SS ($\square$, $\blacksquare$), JRQ ($\diamond$, $\blacklozenge$) and SQV2A ($\circ$, $\bullet$) materials. As shown in Figure 55, there are reasonable linear relationships of σ_y – S_{ey} and UTS – S_{em}. As mentioned above, S_{ey} at small strain is associated with the shear yielding stress τ_y and τ_y has a following relationship with uniaxial tensile σ_y under an ideal shear dominated condition; the von Mises criteria.

$$\sigma_y = \sqrt{3} \cdot \tau_y \qquad (2)$$

A slope of the σ_y – S_{ey} relationship is similar to the value of $\sqrt{3}$ and this indicates that a stress state in deformation process in ShP test is mainly shear [2]. It is interesting to note that a correlation coefficient of 1.71 similar to $\sqrt{3}$ was observed for UTS – S_{em} relation.

In previous studies on ShP test for various metals, uniaxial tensile σ_y and S_{ey} could be expressed as

$$\sigma_y = A \cdot \tau_y + B \qquad (3)$$

Where, coefficient A which values are in range of 1.6 – 2.6 [3] is considered as deviations from the ideal stress state [3] and $\sqrt{3}$ of A has been reported with B ≈ 0 in the previous studies [3]. In our case, A = 1.83 with B = 101 MPa was observed.
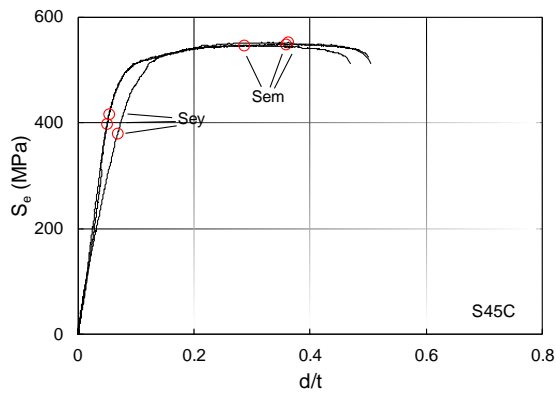
(a) S45C
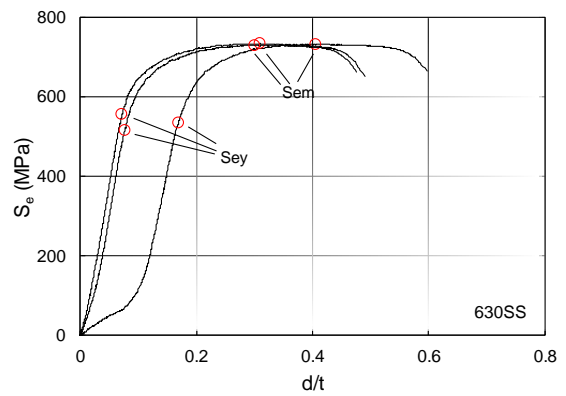
(b) 630SS
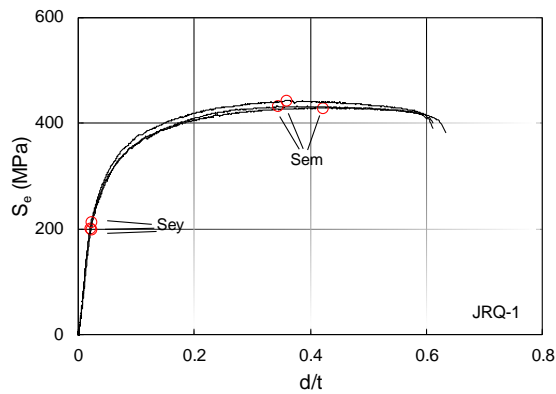
(c) JRQ-1
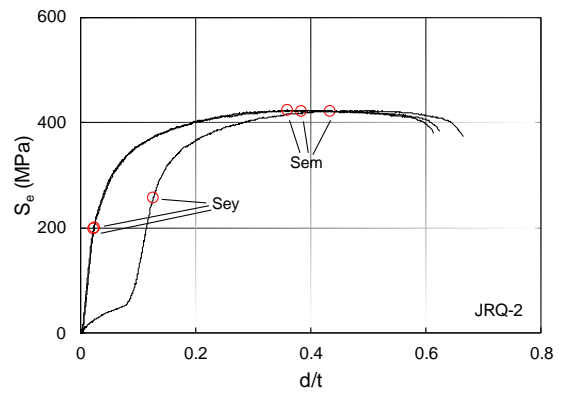
(d) JRQ-2
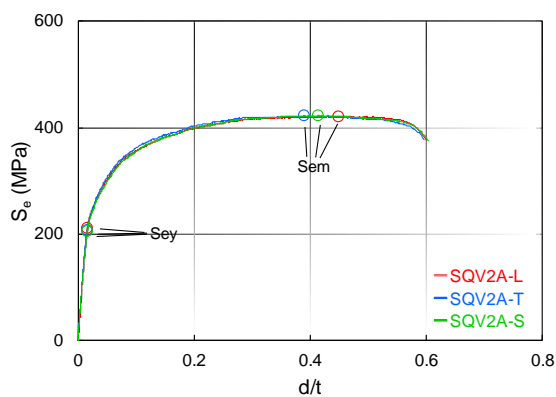
(e) SQV2A-L, SQV2A-T, SQV2A-S

Figure 3. S_e – d/t curves obtained for the tested materials; (a) carbon steel (S45C), (b) precipitated hardening stainless steel, (c) JRQ-1, (d) JRQ-2, and (e) SQV2A machined from the different orientation. JRQ-1 and JRQ-2 specimens were machined from same block by different facilities.
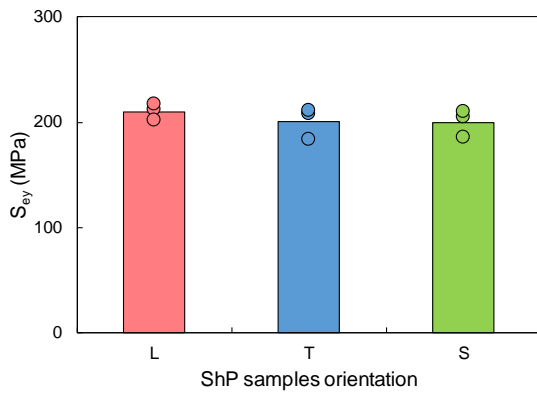
Figure 4. Comparison of S_{ey} for SQV2A-L, SQV2A-T and SQV2A-S.
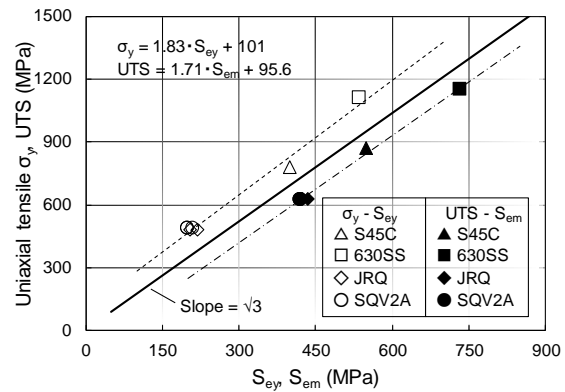
Figure 5. Relationships between uniaxial tensile properties (σ_y and UTS) and shear punch properties (S_{ey} and S_{em}) obtained by ShP test.

5. Summary

Shear punch tests could be executed a Japanese RPV steel as well as common structural steels at R.T. and stress – strain curves, ShP properties can be successfully obtained. ShP yield stress and strength for the tested materials have reasonable linear relationships with uniaxial tensile yield stress and UTS, respectively. However, small deviation of their relationships from the ideal shear stress states was observed. In future, we will perform ShP test for various steels with a wide range of yield stress and UTS and physical meaning of this deviation will be investigated in detail based on data set of tensile and ShP tests. In addition, temperature dependence of ShP properties of RPV steels will be examined.

References

1. Japan Electric Association Code, *Method of Surveillance Tests for Structural Materials of Nuclear Reactors*, JEAC4201-2007, 2007.
2. Lucas, G.E.; Sheckherd; J.W.; Odette; G.R.; Panchanadeeswaran, S.; Shear Punch Tests For Mechanical Property Measurements In Tem Disc-Sized Specimens, *Journal of Nuclear Materials*, **1984**; 122 – 123, 429 – 434.
3. Milot, T.S. Establishing Correlations for Predicting Tensile Properties Based on the Shear Punch, *A Thesis submitted in partial satisfaction of the requirements for the degree Master of Science in Mechanical Engineering*, University of California Santa Barbara, 2013.
4. JIS Z 2244, *Vickers Hardness Test – Test method*, Japanese Industrial Standard, 2009.
5. Tecdoc International Atomic Energy Agency, Reference Manual on the IAEA JRQ Correlation Monitor Steel for Irradiation Damage Studies, *IAEA-TECDOC-1230*, Vienna, 2001.
6. Miura, N.; Soneda, N. Evaluation of Fracture Toughness by Master Curve Approach Using Miniature Specimens, *CRIEPI report (Q08025)*, 2009.
7. Yamamoto, M.; Takahashi, S.; Nomoto, A.; Nishida, K.; Miura, N.; Soneda, N. Development of Low Temperature Hardness Tester for the Irradiation Embrittlement Monitoring, and Low Temperature Hardness Property of Reactor Pressure Vessel Steel SQV2A, *CRIEPI report (Q10016)*, 2011.

Interim results of the reactor pressure vessel materials evaluation within the framework of the implemented Advanced Surveillance Specimen Programme

M. Kapusňák [1],*, **J. Petzová [1], M. Březina [1] and M. Adamech [1]**

[1] VUJE, a.s., Okružná 5, 918 64 Trnava, Slovakia

* Correspondence: Michal.Kapusnak@vuje.sk; Tel.: +421-033-599-1564

Abstract: The reactor pressure vessel (RPV) is the most critical component of every nuclear power plant (NPP) and continuous evaluation of its mechanical properties is a necessity for long and safe operation. Standard tests require a collection of large-dimension samples coming from the precious and archive materials, usually produced as control segments. Since SPT testing samples are quite small, high activity of irradiated materials is no longer an issue. The SPT technique therefore represents a very useful and effective method applied for characterization of mechanical properties such as ultimate tensile strength (R_m), yield strength (R_e), and fracture appearance transition temperature (FATT). Monitoring of structural components in nuclear power plants receives much attention, particularly, in the context of long term operation (LTO) of current plants where the amount of material available for destructive testing is considerably limited.

1. Introduction

This paper gives an overview of the mechanical SPT test results, acquired within the evaluation of SPT samples that were irradiated in the commercial nuclear power reactor at NPP Bohunice, unit no.4, for a period equal to seven fuel-campaigns. Herein presented results are just partial that participate and correspond to a very complex reporting system for all irradiated samples of the irradiation chain, as a part of currently running Advanced Surveillance Specimen Programme (ASSP). To evaluate mechanical properties of the RPV materials within irradiation chain of the ASSP, SPT samples of the following materials were chosen and tested:

1. HAZ-I of weld no.4 from the RPV,
2. HAZ-II of weld no.4 from the RPV,
3. Underclad HAZ-I of the RPV,
4. Underclad HAZ-II of the RPV,
5. Transversely-orientated underclad HAZ from the RPV,
6. Original weld metal from RPV of unit no.4,
7. Austenitic cladding (AC)-I from the RPV,
8. Austenitic cladding (AC)-II from the RPV,
9. Transversely-orientated AC from the RPV,
10. Austenitic type 08Ch18N10T corrosion resistant steel of reactor internal components.

2. Materials and Methods

2.1 Advanced Surveillance Specimen Programme

ASSP is specially designed for monitoring of the neutron irradiation effects on RPV materials' mechanical properties that change due to the operation. Project ASSP meets the requirements of the national supervisory by Nuclear Regulatory Authority of the Slovak Republic (NRASR), IAEA's recommendations and the need of Slovak NPPs operator operated nuclear power reactors of the VVER 440/213 type. During the ASSP realization, irradiation induced changes are continuously compared with the results obtained in the initial state and after defined time of irradiation, in this case, precisely after seven fuel-campaigns. The presented results serve for demonstration of the real RPV state during exposure up to the end-of-life neutron irradiation fluencies, still considered under the LTO. The ASSP represents one of the most important parts for the currently operating NPPs in Bohunice-3 and 4, Mochovce-1 and 2 units, in light of their continuous LTO support [1, 2]. A design of the ASSP program is based on long-term experience in the field of monitoring of radiation degradation to VVER-440 type RPVs not only in Slovakia but also in the world and represents the fifth generation of Surveillance Specimen Programs (SSPs) in

Slovakia. The philosophy of this program is based on the need to continuously monitor trends in changes of the properties of RPV structural materials throughout their planned life.

The RPV is the most important part of the design in terms of operational safety of NPP. The current objective for the majority of nuclear power plants is the planned LTO. For LTO it is important to know the mechanical properties of RPV materials and their changes due to operation. The ASSP in four NPP units presents continuation and completion of the originally designed Standard Surveillance Specimen Program (SSSP) and Extended Surveillance Specimen Programme (ESSP). The main aim of the ASSP monitoring program is to acquire reliable technical argumentations for the power plant long term operation by performing continuous monitoring of RPV materials irradiation embrittlement.

The effect of irradiation depends on the type and state of the crystal lattice of an irradiated material. Predominant effects also have characteristic parameters of the real irradiation environment. These parameters include the quantities describing RPV ionizing radiation where the most important parameters are [3, 4]:
- Neutron fluence,
- Irradiation temperature.

2.2 Experimental materials

Mentioned important parameters and irradiation induced changes in materials' mechanical properties during ASSP application are to be measured and evaluated. The aim of this paper is to present the partial results of mechanical properties in the as-irradiated state and evaluated by SPT method and to bring comparison between the results of experimental materials used. The specimens used in this paper were prepared from ten main experimental material types of the RPV and internal components. The representative microstructures and SPT orientation of the above mentioned materials, taken from the reference RPV material "control segment" of identical chemical composition and production technology as for the operated RPV unit, can be seen in the next Figure 1. Samples of the original weld metal were taken from pre-prepared surveillance programme Charpy-V impact test specimens by using electro-discharge wire cutting machine. Samples were irradiated at a max. temperature of 285°C and to a neutron fluence of up to 3.81×10^{24} [n/m^2].
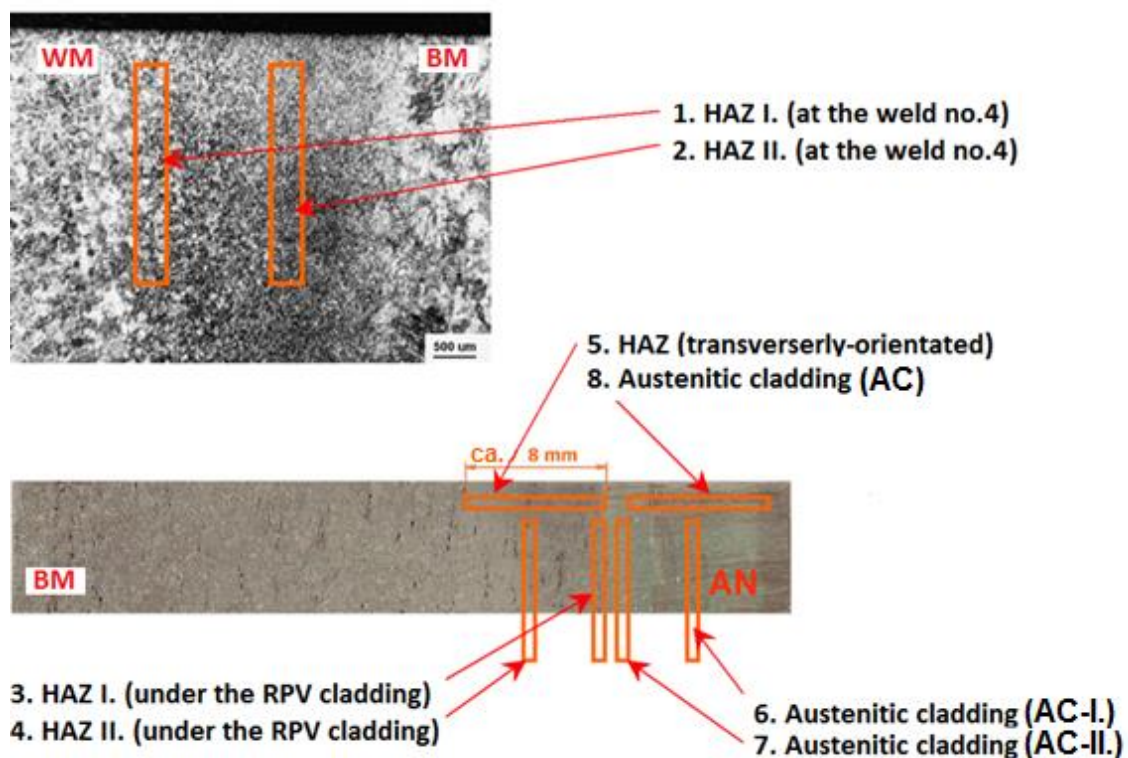
Figure 1. Sampling scheme for HAZ and AC SPT type samples from RPV and internal components.

In the ASSP program two different types of specimens to analyze and monitor RPV steel radiation degradation are used. They are:

- Insert-type specimens for reconstitution to the original standard specimens to assess static fracture toughness and Charpy-V impact toughness of materials,
- Small punch test specimens (SPT).

The ASSP program includes in addition to RPV material irradiation damage monitoring, the measurements of irradiation temperature and neutron fluence inside of irradiation capsules as well. Irradiation capsules are filled with samples made of the original material with specified geometry and also melting monitors as well as neutron fluence activation monitors (see Figure 2).
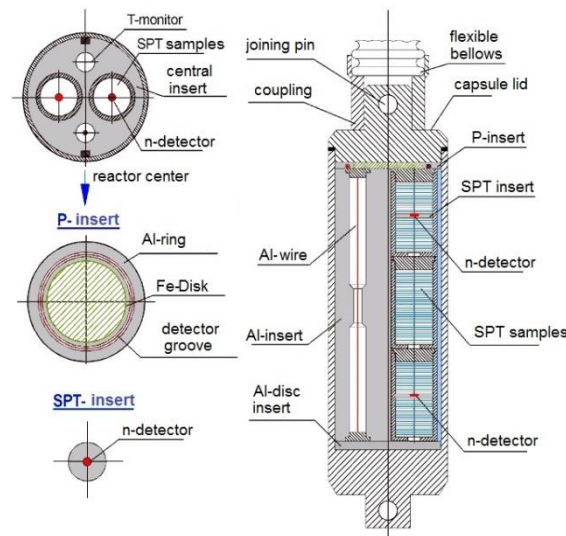
Figure 2. SPT irradiation capsule with samples, detectors, and all other related structural parts.

The design of irradiation chains, measuring of irradiation temperature and neutron fluence is based on the experience from the realized surveillance specimen programs. The innovations in this project are [5]:
- Besides the standard tests of mechanical properties there was included in the material degradation monitoring also the new testing method - Small Punch Test, all the SPT samples are inserted into the special capsules, as can be seen in Figure 2 above,
- Preparation of SPT type samples in order to monitor the new RPV materials that were formerly not included within any of the previous SSP generations. This idea has given us a possibility to assess mechanical properties of mostly irradiated RPV structural parts made of underclad HAZ, austenitic cladding (AC), and austenitic type 08Ch18N10T corrosion resistant steel of reactor internal components.

2.3 Small Punch Test

The standard tests need relatively high amount of the original RPV material and after irradiation, the samples must be tested in the special hot laboratories due to their very high induced activity. In order to study irradiation damage, small samples are preferred because there are limitations of sample size in irradiation channels and great lack of original RPV materials. SPT practice requires a small volume of tested materials what substantially reduces the total activity of the individual irradiated specimen. There's no need for special hot cells when testing SPT sample, a simple lead brick shielding of a testing machine is adequate [6, 7]. Because there is a lack of RPV experimental materials, the great advantage is using the SPT methods for evaluation of their basic mechanical properties [8].

The principle of SPT testing procedure used in VUJE, a.s. is penetration of a disk specimen by a hemispheric rod. The small punch experimental configuration is presented in the Figure 3. The disk shaped specimen is 8 mm in diameter and 0.5 mm in thickness. The specimen holder consists of a lower and upper die and holder body. Using this specimen holder, the specimens are prevented from cupping upward during punching, and therefore, plastic deformation is concentrated in the region below the punch rod. Using relatively simple system with recorders of the load and deflection values, we can obtain the following data of basic mechanical properties [6, 7]:
- The yield stress R_e and ultimate tensile strength R_m, which are well correlated with the parameters P_y, P_m, and d_m which is displacement at maximum load P_m (see Figure 4),

- Ductile-to-brittle transition temperature (DBTT) measured by using the Charpy-V impact test is determined as the fracture appearance transition temperature (FATT at a value of 50-% of shear fracture portion). $FATT_{50\%}$ can be estimated from the results of temperature dependence of small punch energy determined from the area under the load-deflection curve up to the fracture load at displacement, $\mathbf{d^*}$, corresponding to the specimen fracture. The $FATT_{50\%}$ correlates to transition temperature of SPT tests, $DBTT_{SPT}$, according to the following equation (1):

$$DBTT_{SPT} = \alpha \times FATT_{50\%} \tag{1}$$

where α is a correlation coefficient of approximately of 0.4, or, in the range of 0.35 up to 0.45. The α coefficient is an empirically derived constant to a very particular tested material. A sufficiently large number of SPT specimens (approx. 20 pcs) from reference materials allowed also evaluating a transition temperature of ferritic steels. The testing procedure, parameters, and the estimation of transition temperature were performed in accordance with [9]:
- Type of puncher - rod or ball of a diameter of 2 mm,
- Punch displacement velocity: 0.5 mm/min for tensile tests, 2 mm/min for tests performed at low and high temperatures,
- SPT specimen geometry: diameter 8.00 - 0.05 mm, thickness 0.500 ± 0.005 mm,
- Total number of SPT specimens used to determine transition temperature - 20 pcs per SPT energy-temperature curve.

To prepare SPT samples the method of an electrical discharge machining (EDM Cutting) followed by wet grinding on abrasive paper with a grit size of P320 unto P1200 is used. By this way the VUJE, a.s. laboratories have prepared several thousands of SPT specimens.

(a)   **(b)**
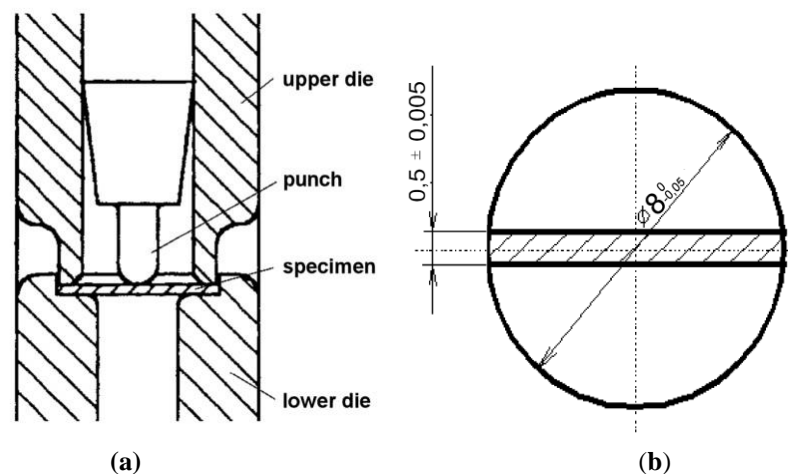
Figure 3. (**a**) Schematic of the setup for the SPT; (**b**) SPT specimen geometry with given tolerances [8].

The testing is usually performed on a standard tension test machine, equipped with load and crosshead feed gauges and a data recorder for the registration of load-deflection curves. Special testing rigs, depending on the testing temperature, are used for the realization of SPT tests. Tests at low temperatures are carried out in a special thermo-insulated chamber. The specimen is cooled using liquid nitrogen vapors or directly by liquid nitrogen. The temperature of the specimen is measured by a calibrated thermocouple. For tests at elevated temperatures a special furnace is used. The SPT method is also used for such evaluation of mechanical properties for lifetime predictions of service components by the authors [10–12].
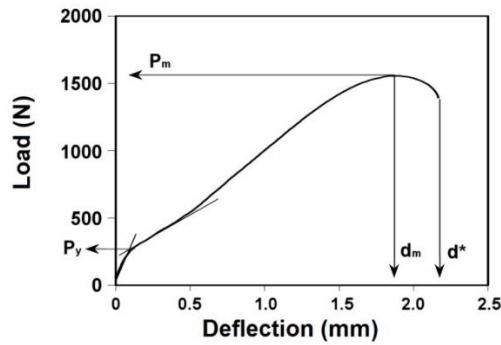
Figure 4. Typical SPT load-deflection curve [8, 9].

3. Results

In the following part of the paper, there are summarized results of the SPT evaluation applied to the as-irradiated state of materials in the frame of the ASSP. For the ASSP project there were prepared 1500 pieces of SPT samples per reactor unit totally and of that number the 750 pieces have already been tested, and other 750 pieces of different types of RPV materials are planned to be tested in as per ongoing program schedule. There are presented the SPT results of tensile evaluated properties and transition temperature determination for steels exhibiting transition behavior (carbon and low carbon steel). For the austenitic steels and their welds, which do not have a ductile-brittle transition, the temperature dependence of SPT energy has been determined. Partial results of determined tensile properties are clearly summarized in the following Table 1. In this table, the values are found after irradiating for a period of effective 7 fuel-campaigns. The graphical demonstration of the changes that occurred as a result of neutron irradiation is given in Figures 5 and 6. It can be seen from the figures that after the irradiation, the strength characteristics of all the evaluated materials slightly increased [5].

Table 1. Tensile properties evaluated using SPT tests before and after irradiation of R 4BZ3 chain [5].

Material	"0"-state		Chain R 4BZ3		Figure
	R_m	R_e	R_m	R_e	
	[MPa]		[MPa]		
HAZ-I of weld no.4 from the RPV	650	543	910	733	*5a*
HAZ-II of weld no.4 from the RPV	664	532	922	703	*5b*
Underclad HAZ-I of the RPV	648	509	1097	856	-
Underclad HAZ-II of the RPV	548	389	927	667	-
Transversely-orientated underclad HAZ from the RPV	570	404	947	691	-
Original weld metal from RPV of unit no.4	551	399	784	618	-
Austenitic cladding (AC)-I from the RPV	618	387	820	526	-
Austenitic cladding (AC)-I from the RPV	634	379	807	468	-
Transversely-orientated AC from the RPV	649	423	723	546	*6a*
Austenitic type 08Ch18N10T corrosion resistant steel of reactor internal components	600	278	888	399	*6b*
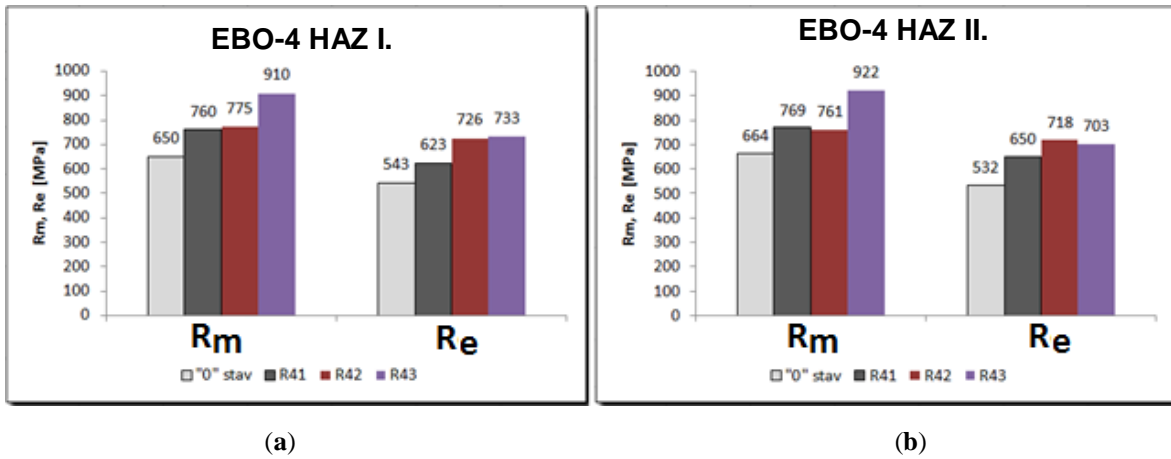
Figure 5. (**a**) Change in tensile and yield strengths of HAZ I.; (**b**) Change in tensile and yield strengths of HAZ II. [5]
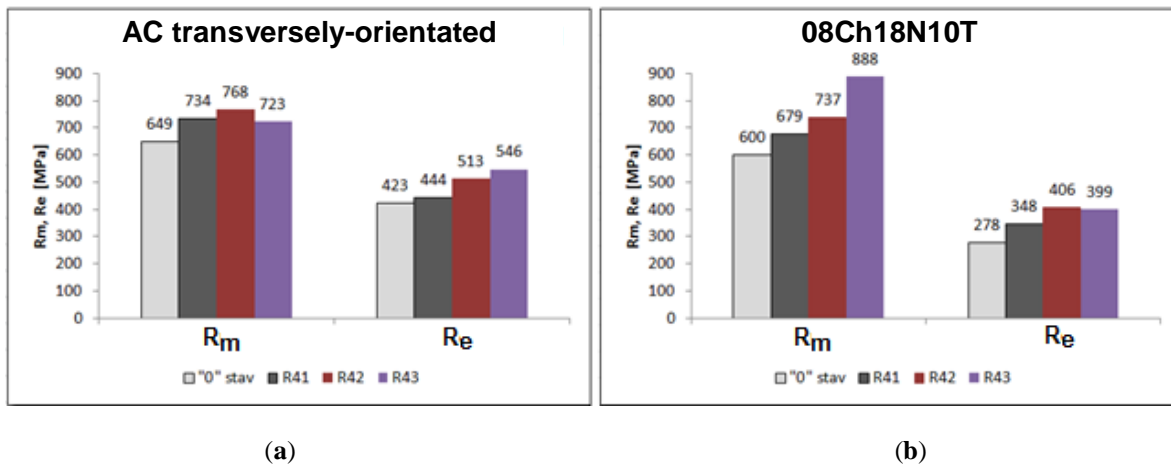
Figure 6. (**a**) Change in tensile and yield strengths of AC; (**b**) Change in tensile and yield strengths of 08Ch18N10T [5].

The DBTT$_{SPT}$ transition temperature values determined by the SPT test for ferritic materials are summarized in Table 2. The SPT energy as a function of temperature for these materials is shown in Figure 7, and for the austenitic materials in the Figure 8. The transition temperature of ferritic steels rises with increasing irradiation level. For austenitic steel 08Ch18N10T in contrast there is no transition temperature and no effect of the irradiation; the SPT energy decreases with increasing temperature [5].

Table 2. Results of DBTT$_{SPT}$ evaluated using SPT tests after irradiation of R 4BZ3 chain [5].

Material	Transition temperature [°C]		Figure
	"0"-state	**R 4BZ3**	
HAZ-I of weld no.4 from the RPV	-13.9	55.1	*7a*
HAZ-II of weld no.4 from the RPV	-6.6	34.0	*7b*
Underclad HAZ-I of the RPV	-24.2	59.4	-
Underclad HAZ-II of the RPV	-24.6	50.1	-
Transversely-orientated underclad HAZ from the RPV	-25.7	43.5	-

Original weld metal from RPV of unit no.4	14.4	74.6	
Reference weld metal	-2.2	-	-
Note: R41 - 1 fuel campaign, **R42** - 3 fuel campaigns, **R43** - 7 fuel campaigns			

(**a**)   (**b**)
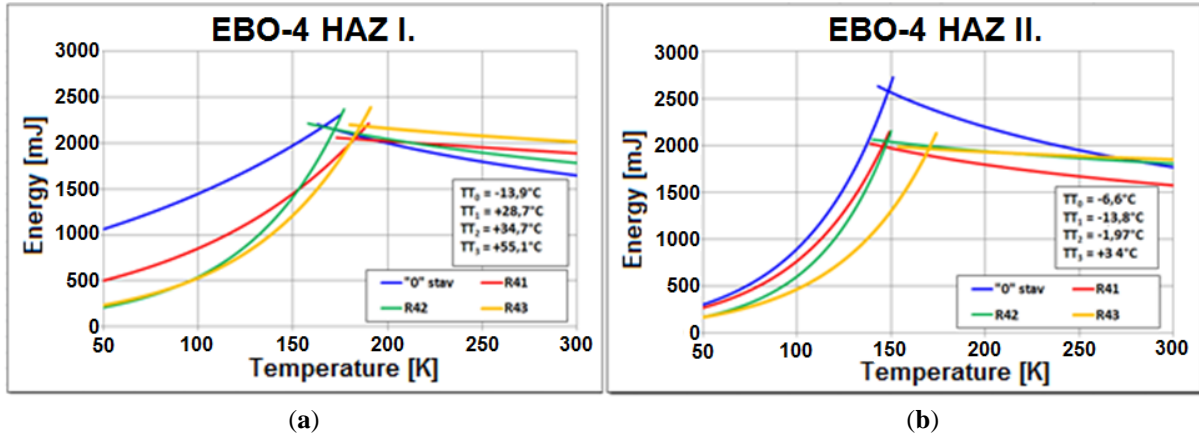
Figure 7. (**a**) Rise in DBTT$_{SPT}$ of HAZ I.; (**b**) Rise in DBTT$_{SPT}$ of HAZ II. [5].

(**a**)   (**b**)
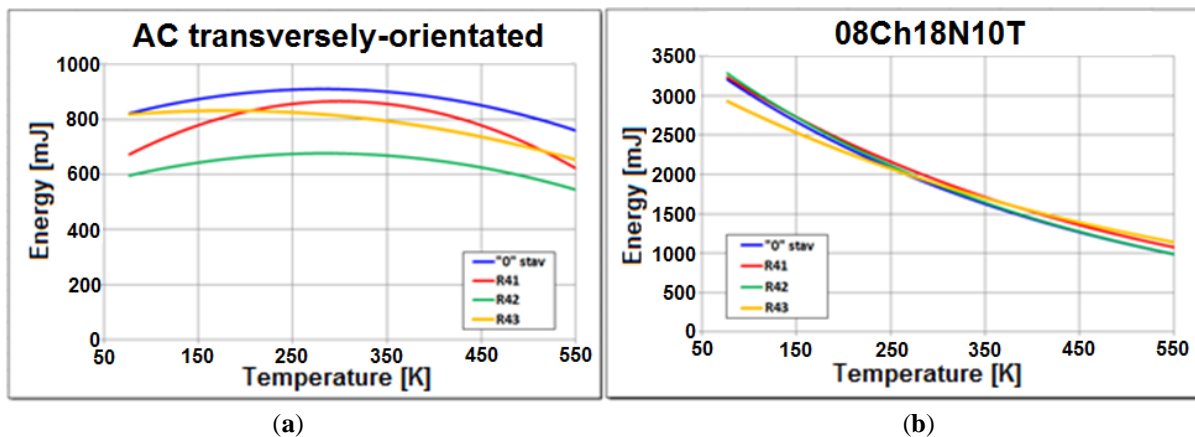
Figure 8. (**a**) SPT energy run for AC; (**b**) SPT energy run for 08Ch18N10T [5].

4. Discussion

By comparing the SPT experimental results of tensile properties for four representative materials with the values of mechanical properties as-tested by exactly the same SPT procedure, but in four different states,"0"-state and three irradiation levels (cf. Figures 5 and 6); it can be discussed the following:

- the values of tensile strengths for HAZ-I and HAZ-II confirmed the expected changes that are clearly manifested by the incremental trend in both Figures 5a and 5b,
- considering all the results, changes in the yield strengths for HAZ-I and HAZ-II as a result of irradiation by neutrons can also be well noticed, and the increase of R_e is still around 30%,
- changes in the values of tensile strengths for austenitic cladding AC and 08Ch18N10T type steel also confirmed the expected incremental behavior for both materials as given in Figures 6a and 6b,
- after the irradiation at different neutron fluences, the austenitic cladding AC in Figure 6a generally revealed slightly higher tensile and yield strengths than that of the 08Ch18N10T type steel in Figure 6b, nevertheless, the maximum tensile strength reached value was recorded for this type of structural material,
- the transition temperature curves shown in Figure 7 for the both HAZs indicate the larger shifts ascertained and the established values presented in Table 2, confirmed this as to the underclad HAZ-I and transversely-orientated underclad HAZ as well,

- the SPT energy curves for austenitic type in-vessel structural materials, as given in Figure 8, still document very high irradiation resistance to neutron induced damaging processes under the VVER-440/213 type reactor operating conditions,
- in terms of energy change, titanium-stabilized austenitic type 08Ch18N10T corrosion resistant steel can in overall be characterized as less sensitive to irradiation than the material of austenitic cladding AC, most probably for the reason of microstructural differences as claddings are in fact two-layered weldments, produced by using two different material weld tapes.

5. Conclusions

- In general, the tensile properties are higher for all HAZ types then for other material types tested,
- Further monitoring of materials properties continuous as per defined irradiation schedule,
- The most irradiation sensitive is the material of HAZ-I, and conversely the most irradiation resistant are the austenitic-type materials used for in-core and in-vessel RPV structures, such as claddings,
- The published results achieved in the evaluation of irradiated materials states are an essential part of the ASSP program and are used as the input data in calculation so as to determine the residual lives of all operating RPVs,
- The ASSP project is approved by the NRASR according to IAEA's recommendations, and has already been launched for all RPVs of the NPP Bohunice, and Mochovce units 1 and 2.

References

1. Kupča, Ľ. et al. Design project for the Advanced Surveillance Specimen Program, VUJE, a.s.'s report, reg. no. VÚJE 0360/15/2007, July, 2007 (in Slovak).
2. Kupča, Ľ. et al. Advanced Surveillance Specimen Program for VVER-440 type reactor pressure vessel materials - assembling and installation of chains for irradiation, VUJE, a.s.'s report, reg. no. VÚJE 0360/14/2009, October, 2009 (in Slovak).
3. Alekseenko, N. N.; Amaev, A.; Gorynin, I.; Nikolaev, V. A. *Radiation Damage of Nuclear Power Plant Pressure Vessel Steels*, 1st edition; Illinois, American Nuclear Society, 1997, ISBN 978-0-89448-564-0.
4. Beskorovajnyj, N. M.; Kalin, B. A.; Platonov, P. A.; Chernov, I. I. *Structural materials for nuclear power reactors*, 1st edition; Moscow, Energoatomizdat, 1995, ISBN 5-283-03819-X (in Russian).
5. Adamech, M.; Kapusňák; M. Advanced Surveillance Specimen Program for VVER-440 type reactor pressure vessel materials - determination of mechanical properties on SPT samples of R 4BZ3 irradiation chain, VUJE, a.s.'s report, reg. no. VÚJE 0360/16/2017, October, 2017 (in Slovak).
6. Petzová, J.; Březina, M.; Kupča, Ľ. Evaluation of mechanical properties of the reactor pressure vessel materials changes by small punch test application. In Proceedings of the 2013 *ASME Pressure Vessels and Piping Conference*, July 14-18, 2013, Paris, France, Volume 1A: Codes and Standards, American Society of Mechanical Engineers (ASME), 28 Feb 2014 Fairfield, United States, ISBN 978-0-7918-5563-8, Paper No. PVP2013-97171, 5 pages, doi:10.1115/PVP2013-97171.
7. Březina, M.; Petzová, J.; Kupča, Ľ. Evaluation of mechanical properties of primary circuit components using SPT technique. In Proceedings of the 2013 *ASME Pressure Vessels and Piping Conference*, July 14-18, 2013, Paris, France, Volume 1A: Codes and Standards, American Society of Mechanical Engineers (ASME), 28 Feb 2014, Fairfield, United States, ISBN 978-0-7918-5563-8,
Paper No. PVP2013-97170, 5 pages, doi:10.1115/PVP2013-97170.
8. Petzová, J.; Březina, M.; Kapusňák, M.; Kupča, Ľ. Application of small punch testing methods for thermal ageing monitoring at primary circuit components in nuclear power plant. In Proceedings of the 2015 *ASME Pressure Vessels and Piping Conference*, July 19-23, 2015, Boston, USA, Volume 1A: Codes and Standards, American Society of Mechanical Engineers (ASME), Fairfield, United States, ISBN 978-0-7918-5692-5, Paper No. PVP2015-45539, 6 pages, doi: 10.1115/PVP2015-45539.
9. CEN, "Small Punch Test Method for Metallic Materials", CEN workshop agreement CWA 15627:2006, 2007.

10. Blagoeva, D.; Hurst, R. *The Small Punch Test for Creep and Fracture Prediction: Development of a Lifetime Prediction Methodology for Creep and Fracture Behaviour of Ferritic-Martensitic Steels using Small Punch Testing Technique*, 1st edition; VDM Verlag, 2009, ISBN 978-3-6391-9118-9.

11. Small Punch Testing for Nuclear Reactor Embrittlement Assessment, EPRI, Palo Alto, CA: TR-111116, 1998.

12. Kopřiva, R.; Kytka, M.; Eliášová, I.; Lašan, M.; Siegel, J.; Haušild, P.; Matocha, K. Small Punch Test Specimen in Determination of Tensile Properties for Nuclear Power Plant Components. In Proceedings of *the 3rd International Conference SSTT 2014*, September 23-25, 2014, Graz, Austria, pp. 225-233, editors: K. Matocha, R. Hurst, W. Sun, Ocelot s.r.o., Ostrava-Vítkovice, Czech Republic.

Small Punch Technique Used to Evaluate the Radiation Damage in SS316L Thin Foils Due to Proton Bombardment

D. Moreno [1], S. Haroush [2], A. Turgeman [2] and I. Silverman [1]

1 Soreq Nuclear Research Center, Yavne 70600, Israel

2 Nuclear Research Center-Negev, P.O. Box 9001, Beer-Sheva 84190, Israel

  Affiliation 1; dmoreno@netvision.net.il

  Affiliation 2; monih6655@gmail.com

  * Correspondence: dmoreno@netvision.net.il; Tel.: +972-50-629-2406

Abstract: The mechanical properties characterization of thin foils to be used as target in high intensity accelerator requires non standards techniques. Previous studies, focused on foils after annealed, cold rolled and heat treatment after rolled, in addition to foils at different thickness, have been carried out to estimate the sensitivity of the small punch test (SPT) technique in foils. In this research we studied the degradation of the mechanical properties of foils due to irradiation damage by high intensity proton beams. For this new study, two samples of SS316L foils have 25 µm thickness were exposed to proton bombardment at 3.6 MeV, and approximately 300 µA of current for a period of 3 hours and 40 hours, separately. The SPT technique revealed that the un-irradiated specimens exhibited the largest load and deformation before failure, rather than the irradiated foils. The electron microscopy observations (SEM) revealed high cross slips and pseudo-cleavage density combined with multiple deformation twinning after irradiation to high energy. The mechanical behavior can be explained by the microstructure. The crack propagation path is in a zigzag fracture mode when multiple deformation twinning occurs close to the stretched zone of the foil and failure. Changes of the SPT measurements were found and the degradation from ductile to brittle crack mode is attributed to radiation damage effects.

---

1. Introduction

The Soreq Applied Research Accelerator Facility (SARAF) is a multi-user and versatile particle accelerator facility located at the Soreq Nuclear Research Center [1]. The beam operation on the thin-foil target is the subject of interest in the present work.

Thin foils (25µm) are used in cyclotron accelerators as a window for liquid and gas targets. Irradiation of targets by proton or deuteron beams is carried out at various energies and occasionally at high currents and for long time durations, up to a few hours. During such irradiation conditions, the foil might be damaged; its microstructure and mechanical properties can be degraded and, therefore, the window life-time can be significantly reduced.

The changes in the foils mechanical properties due to proton irradiation requires the characterization of its properties before and after the irradiation process in order to analyze the alloy's ability to withstand the process. The goals of the current stage of the research were to study the SS316L foil mechanical behavior in two different conditions of irradiation.

Small Punch Test (SPT), Ball Punch Test (BPT), Disk Bend Test (DBT) [4], and Shear Punch Test are common mechanical techniques for the characterization of small dimension or thin specimens [2–7]. These testing methods are usually conducted on specimens that are too small to undergo standard tension tests. The SPT concept is based on locking a thin sheet-like specimen between two dies and pushing a punch against it with a spherical cap, up until failure. During the test, the load and the punch stroke are monitored simultaneously until the end-test criterion (e.g., maximal or failure load) is achieved. Many of the common standards, including the E-643 ASTM standard, are valid for specimens whose thickness ranges from 200 to 2000 µm [8]. In many research publications focusing on mechanical characterization the specimen thickness is greater than 200 µm [9–13].

Haroush et al. [14] have shown that for specimens having a thickness greater than 300 µm, classical plate equations can be used to estimate the yield stress, while for thinner specimens yield stress estimation from SPT is a very complex issue, since it is a function of the specimen thickness.

To correlate between yield stress and ultimate stress obtained by SPT to tensile test, Finite Element Analysis (FEA) was applied using damage model as shown in [14]. To validate the FE model, the computed load displacement curves obtained from the FE computation were compared to the experimental curves. Interrupted SPT

experiments in which the experiment was terminated prior to specimen failure were conducted for the observation of deformed but un-cracked specimens that were cut and examined under a microscope.

In the present study we report the SPT results, the energy to fracture and the fracture modes by SEM observation of SS316L, 25 μm foils that were exposed to proton bombardment at 3.6 MeV, 300μA for 3 and 40 hours irradiation in the SARAF. The results show mechanical properties degradation and ductile to brittle fracture attributed to the radiation damage effects.

2. Materials and Methods

This study was carried out on foils of SS316L as targets. The foils following irradiation exhibited high activation as shown by auto radiography of the foil in figure 1b. Because the high activation we had to wait 5 years until the activation decreases and the foils return to the background level. Schematic apparatus for SPT is shown in figure 2a [15].

The SARAF accelerator was operated at 250 and 310 μA, 3.6 MeV CW beam of 4 W/mm^2 heat flux on a thin foil target of 25μm. Beam operation was focused on the thin foil target as shown in the calculation of the temperature in figure 1a. The main beam current limit was the foil surface maximum temperature that was limited to 500±50 °C. This was achieved owing to the following two factors; development and improvement of the target design and improvement of the beam diagnostics system and the tuning procedures. Pattern on the foil at the higher current is due to the convection process in the cooling liquid NaK metal.

The temperature in the target region, the collected beam currents on the electrodes and neutron dose rates were monitored during operation. The temperatures were monitored using thermocouples probes and an optical pyrometer.

The small punch specimens were cut by scissors to W= L = 8 mm dimensions (figure 2a). The SPT was conducted using the apparatus shown in figure 2a by clamping of the specimen between the dies under 600 N, pre load up to 20 N and balance the stoke transducer (Instron COD), and finally pushing the ball into the specimen under stroke control at a speed of 0.2 mm/min up to failure [14-15]. The end test criterion was the drop from the maximal loads, this happening very sharply. The dimensions of the SPT apparatus are: the corner radius of the dies in the internal cylinders (close to de samples) $R_D = 0.2$ mm; the ball diameter $2r_b = 2.4$ mm; the lower die internal cylinder diameter, $2R_{LD} = 3$ mm and upper die cylinder diameter $2R_{UD} = 3.1$ mm.

Following specimen failure, indicated by the load drop, the specimen shape, dimensions, and fracture mode were characterized by scanning electron microscopy (SEM). In addition, Cross section metallography using SEM reviled that considerable number of equiaxed grains presence across the thickness.
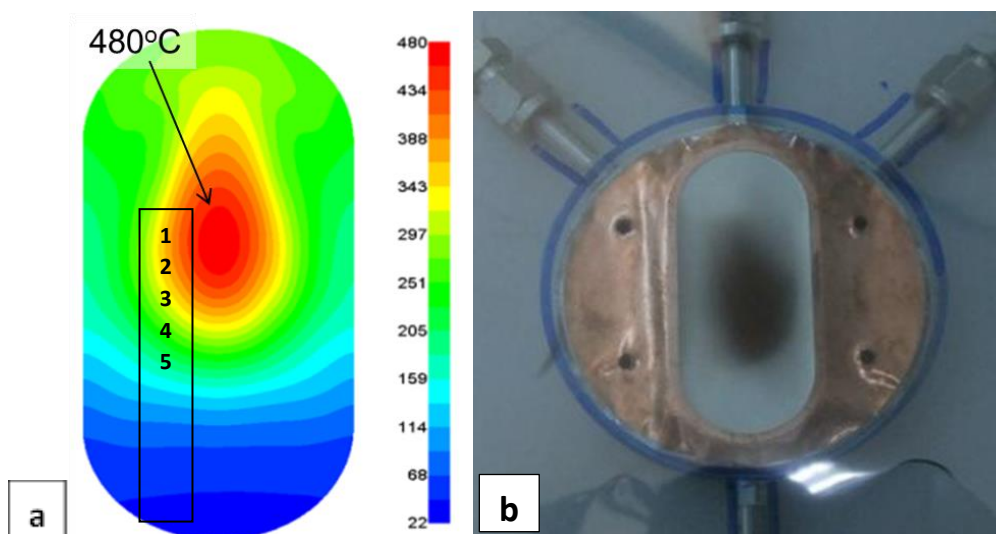
Figure 1. (a) Simulated foil temperature during irradiation and **(b)** auto-radiography of the irradiated foil on the target holder after irradiated.
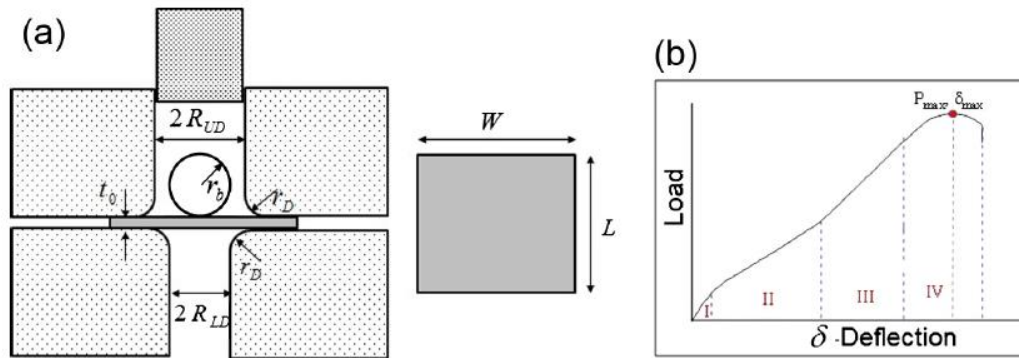
Figure 2. (a) Schematic apparatus for SPT, **(b)** typical curve of load vs. deflection; I—Elastic behavior, II—Plastic behavior (strain hardening), III—Plastic membrane stretching, and IV—plastic instability.

3. Results

The SPT load & displacement curves are shown in Figures 3, for the un-irradiated foil; the irradiated foil at 3.6 MeV, 310 μA of protons during 3 hours (case 1), and the irradiate foil at 3.6 MeV, 250 μA of protons during 40 hours (case 2). Figure 4 shows respectively energy to fracture for each case. The displacement per atom (DPA) per collision for the 3.6 MeV proton energy of approximately 8.5/Angstron is 0.044 for case 1 and 0.477 for case 2.
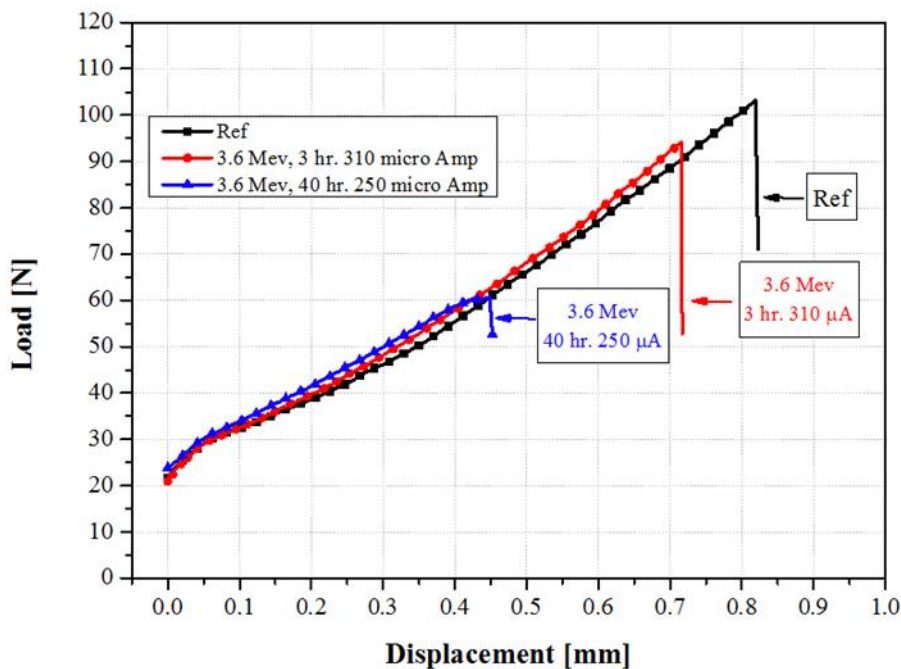
Figure 3. Comparison of the Small Punch Test results presenting load vs. displacement of as received foil and the irradiated foils in zone 1 as shown in figure 1a.

It can be seen in figure 2b that the curve obtained by SPT technique for each one of the foils condition, three regions were apparent: I—elastic, II—strain hardening, and III—membrane stretching up to failure which indicates plastic instability. When the failure occurs in the membranes the load dropped sharply. Cross section metallography using SEM reviled that more than 10 equiaxed grains presence across the thickness.

(a) (b) (c)
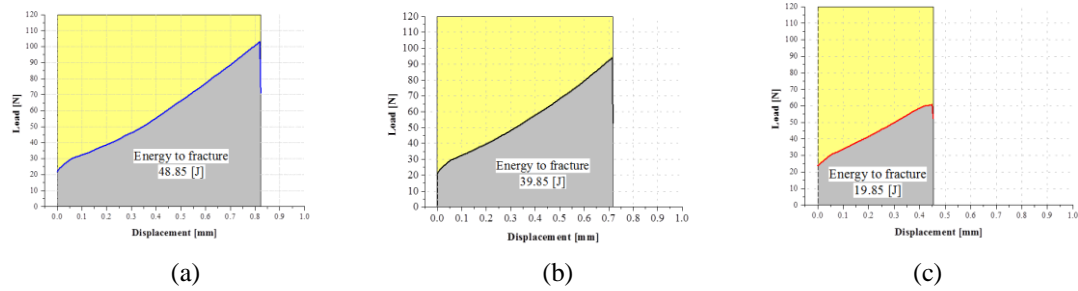
Figure 4. Energy to fracture: **(a)** for the as received foil - un-irradiated, 48 [J], **(b)** – 3.6 MeV, 310 μm proton during 3 hours, 39.85 [J], and **(c)** .6 MeV, 250 μm proton during 40 hours, 19.85 [J].

The maximal load for the SS316L un-irradiated foils with 25 μm thickness achieved the highest value of 100 N as shown in figure 3. Figure 5a-c exhibits the fracture failure area close to the stretching zone of the un-irradiated foil (5a) and for the low irradiated foil (5b - 3 hours). The characteristics of the rupture are consistent with the failure of a membrane as shown in previous works [14-15]. In contrast, the foil that was exposed to 40 hours of radiation (5c), the rupture was started on the center top of the cap (none shown).

The irradiated foils figure 5 (b) and (c) shown dislocation channels intersecting the surface of the austenitic stainless steel 316L attributed to the plastic strain and the irradiation. Furthermore, for the high irradiated sample in figure 5c, the fracture was developed in the channels by a zig-zag fracture mode (see red circle).
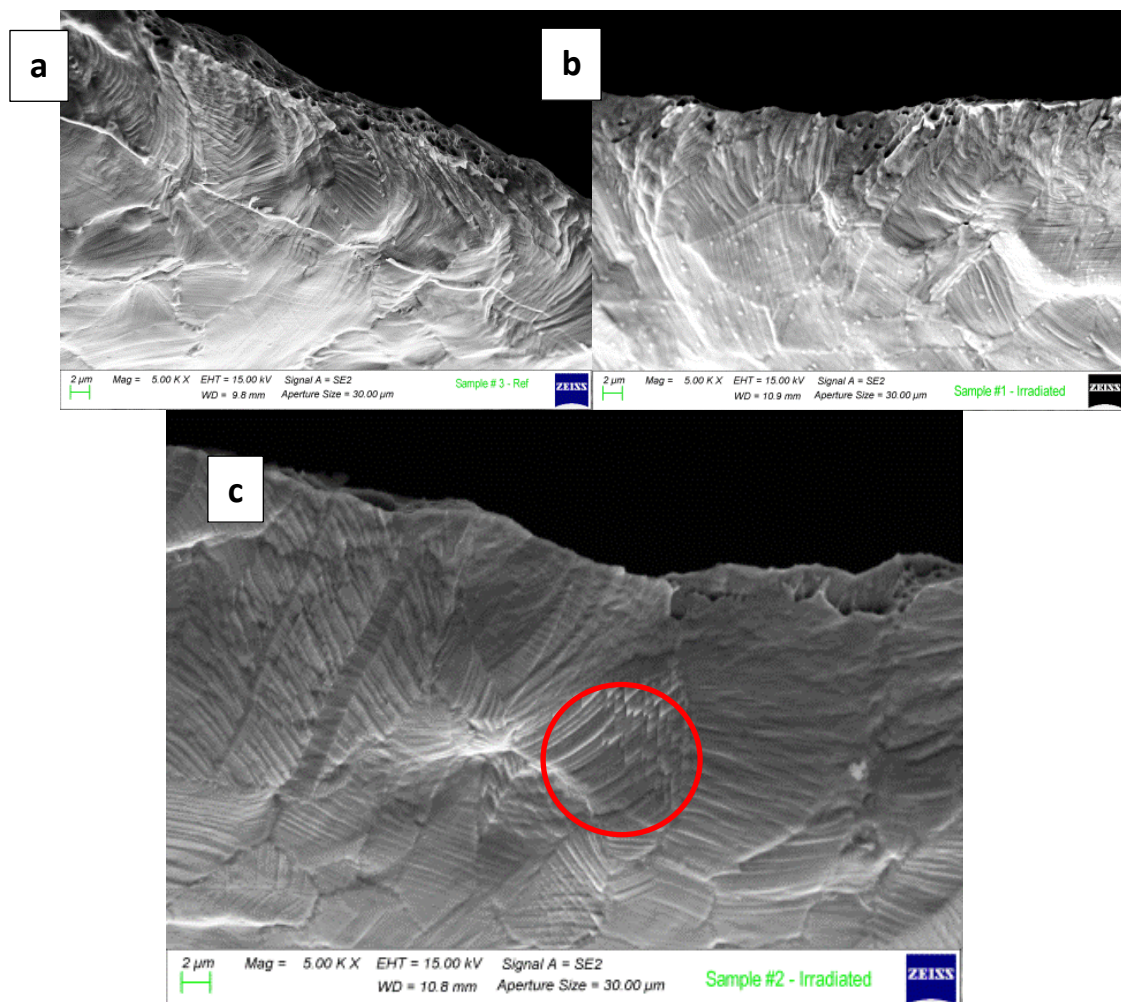
Figure 5. Zoom in on the stretched area close to the cross section fracture for the as received foil **(a)** - un-irradiated foil, **(b)** – 3.6 MeV, 310 μm proton during 3 hours, and **(c)** 3.6 MeV, 250 μm proton during 40 hours.

4. Discussion

Microstructure evolution during irradiation of a metal is controlled by the migration defect fractions of vacancies and interstitials. Irradiated metals exhibit a loss of ductility and a loss of work hardening. The loss of uniform ductility and the work hardening are due to the interaction between dislocations and the irradiated microstructure. Dislocation loops resulting from vacancy and interstitial condensation are created from clusters of defects and either shrink or grow depending on the flux of defects reaching the critical defect volume due to the radiation. Once the critical defect volume has been reached, the critical size under irradiation, the dislocation loops interacts with the network dislocation density. Deformation twinning or mechanical twinning is a localized deformation mechanism caused by partial dislocations. The low stacking fault energy in FCC metals and the deformation by twins contribute to the glide of Shockley partial dislocation on the same sign on successive {111} planes. By high shear strain, the defects due to the radiations are cleared by glide of the partial dislocations. Koyama et al. [16] report that the presences of hydrogen bring about quasi-cleavage fracture behavior in a single crystalline type of SS316L that has FCC structure. The deformation induced plate like products along the two specific planes in the <111> orientation with hydrogen charging. Some of the fracture edges are very similar to the fracture observed in figure 5c. They report [16], that the plate like products along the two specific planes are identified as the deformation twins along the two different {111} twinning plates. The study concluded that the obtained fracture surface depend on the crystallographic orientation and the degree of degradation on the tensile properties in the <111> tensile direction that is larger than the obtained in the <001> tensile orientation. They attribute this change to the higher flow stress and the formation of martensite at the intersections of the deformation twins. In this study the crack propagation path obtained is with a zigzag shape as observed in figure 5c. This effect is due to multiple deformation twinning and smooth when only a small amount of deformation twins appear on a single {111} twinning plane. We assume that in irradiated samples there are similar behavior as shown in figure 5b (zigzags in the pre-crack stage) and in figure 5c (zigzags after the crack was created), attributed by the accumulation of interstitials, vacancies and remained protons or hydrogen due to the irradiation damage that effects on the partial dislocation glide and reduces the ductility of the metal. The electron microscopy observations (SEM) revealed high cross slips and pseudo-cleavage density after irradiation to high energy.

Future research on TEM characterization should be done to define the deformation mechanism on two axes as evolved in the SPT technique and to characterize the proper mechanism that leads to loss of ductility and a loss of work hardening in the irradiated materials.

5. Conclusions

The changes in microstructure due to the expose of the SS316L under proton irradiation can explain the major changes in the mechanical properties obtained by the SPT technique.

The irradiated samples show consistent degradation on the mechanical behavior in comparison to the non-irradiated sample. Maximum load, ductility and work hardening range decrease by irradiation. The highest degradation was observed in the foil exposed to 3.6 MeV, 250 µm of proton during 40 hours.

The fractography shown dislocations and twins attributed by the accumulation of interstitials, vacancies and remained protons due to the irradiation damage that effects on the partial dislocation glide and reduces the ductility of the metal.

References

1. Mardor, I.; Aviv, O.; Avrigeanu, M.; Berkovits, D.; Dahan, A.; Dickel, T.; Eliyahu, I.; Gai, M.; Gavish-Segev, I.; Halfon, S.; Hass, M.; Hirsh, T.; Kaiser, B.; Kijel, D.; Kreisel, A.; Mishnayot, Y.; Mukul, I.; Ohayon, B.; Paul, M.; Perry, A.; Rahangdale, H.; Rodnizki, J.; Ron, G.; Sasson-Zukran, R.; Shor, A.; Silverman, I.; Tessler, M.; Vaintraub, S.; and Weissman, L.; "The Soreq Applied Research Accelerator Facility (SARAF) – Overview, Research Programs and Future Plans", [*physics.ins-det*] (submitted as an invited review to *European Physics Journal A*, on 19 Jan 2018 (*v1*), last revised 23 Jan 2018) Available online: arXiv:1801.06493 (accessed on 23 Jan 2018).

2. Guduru, R.K.; Darling, K.A.; Kishore, R.; Scattergood, R.O.; Koch, C.C.; Murty, K.L. Evaluation of mechanical properties using shear–punch testing. *Mater. Sci. Eng. A*, **2005**, *vol. 395*, 307–314.

3. Guduru, R.K.; Wong, P.Z.; Darling, K.A.; Koch, C.C.; Murty, K.L.; Scattergood, R.O. Determination of activation volume in nanocrystalline Cu using the shear punch test. *Adv. Eng. Mater.* **2007**, *vol. 9*, 855–859.

4. Hamilton, M.; Toloczko, M. Effect of low temperature irradiation on the mechanical properties of ternary V–Cr–Ti alloys as determined by tensile tests and shear punch tests. *J. Nucl. Mater.* **2000**, *vol. 283*, 488–491.

5. Toloczko, M.B.; Kurtz, R.J.; Hasegawa, A.; Abe, K. Shear punch tests performed using a new low compliance test fixture. *J. Nucl. Mater.* **2002**, *vol. 307*, 1619–1623.

6. Hankin, G.L.; Toloczko, M.B.; Hamilton, M.L.; Garner, F.A.; Faulkner, R.G., Shear punch testing of 59 Ni isotopically-doped model austenitic alloys after irradiation in FFTF at different He/dpa ratios. *J. Nucl. Mater.* **1998,** *vol. 258*, 1657–1663.

7. Goyal, S.; Karthik, V.; Kasiviswanathan, K.V.; Valsan, M.; Rao, K.B.; Raj, B. Finite element analysis of shear punch testing and experimental validation. *Mater. Des.* **2010,** *vol. 31*, 2546–2552

8. ASTM- American Society for Testing and Materials. Ball Punch Deformation of Metallic Sheet Material; ASTM-E643; American Society for Testing and Materials: West Conshohocken, PA, USA, 1987; pp. 885–888.

9. García, T.E.; Rodríguez, C.; Belzunce, F.J.; Suárez, C. Estimation of the mechanical properties of metallic materials by means of the small punch test. *J. Alloys Compd*. **2014**, *vol. 582*, 708–717.

10. Baik, J.-M.; Kameda, J.; Buck, O., Development of small punch tests for ductile-brittle transition temperature measurement of temper embrittled Ni-Cr steels. *The Use of Small-Scale Specimens for Testing Irradiated Material*; Corwin, W.R., Lucas, G.E., Eds.; ASTM-STP 888; American Society for Testing and Materials: West Conshohocken, PA, USA, 1983; pp. 92–111.

11. Mao, X.; Takahashi, H. Development of a further-miniaturized specimen of 3 mm diameter for TEM disk (ø 3 mm) small punch tests. *J. Nucl. Mater.* **1987**, *vol. 150*, 42–52.

12. Klein, M.; Hadrboletz, A.; Weiss, B.; Khatibi, G. The 'size effect' on the stress–strain, fatigue and fracture properties of thin metallic foils. *Mater. Sci. Eng. A*, **2001**, *vol. 319*, 924–928.

13. Matoca, K.; Hurst, R. The European Code of Practice for Small Punch testing—where do we go from here. In Proceedings of the 1st International Conference on Determination of Mechanical Properties of Materials by Small Punch and other Miniature Testing Techniques, Ostrava, Czech Republic, 30 August–2 September 2010.

14. Haroush S., Priel E., Moreno D., Busiba A., Silverman I., Turgeman A., Shneck R., and Gelbstein Y., Evaluation of the mechanical properties of SS-316L thin foils by small punch testing and finite element analysis. *Mater. Des*. **2015**, *vol. 83*, 75–84.

15. Haroush S., Moreno D., Silverman I., Turgeman A., Shneck R. and Gelbstein Y., The Mechanical Behavior of HAVAR Foils Using the Small Punch Technique, *Materials* **2017**, *vol. 10*, 491; DOI:10.3390/ma10050491.

16. Koyama M., Akiyama E., Sawaguchi T., Ogawa K., Kireeva I. V., Chumlyakov Y.I. and Tsuzaki K., Hydrogen Assisted Quasi-Cleavage Fracture in Single Crystalline Type 316 Austenitic Stainless Steel, *Corrosion Science* **2013** *vol. 75*, 345-353.

Using of SPT method for estimation of mechanical properties changes of RPV steels after irradiation in the Halden reactor

M. Adamech[1*], J. Petzová[1], M. Březina[1], M. Kapusňák[1]

[1] VUJE, a.s., Okružná 5, 918 64 Trnava, Slovakia

* Correspondence: marek.adamech@vuje.sk; Tel.: + 421 33 5991519

Abstract: The paper deals with experimentally estimation and comparison of the mechanical properties changes of RPV steels before and after irradiation of samples in Halden reactor in Norway coming from Unit #3 and #4 of NPP Mochovce (still under construction). Altogether 180 SPT and 30 mini-tensile samples in two sets were prepared for irradiation, obtained from weld metal material (Sv10ChMFT) and base material (15Ch2MFA). In general, a good agreement between results obtained by SPT technique and using mini-tensile specimens was found. Both, base and weld metals of RPVs were found to be bainitic. After that, the first set of samples was irradiated in Halden reactor at temperature T_{irr} = 270 - 280°C with intention to use two fluence values: $\sim 1.0 \times 10^{24}$ n/m^2 and $\sim 2.0 \times 10^{24}$ n/m^2 (> 1 MeV), respectively. Specimens after 1st irradiation were successfully tested and preliminary results show small increase of the strength characteristics (R_e, R_m) if compare to "zero condition" testing results. FATTs, evaluated by the temperature dependence of the SPT energy, exhibit transition behaviour and shift towards higher temperatures.

Keywords: small punch test; RPV steels; Halden reactor

1. Introduction

The reactor pressure vessel (RPV) is the most crucial component of every nuclear power plant (NPP) and continuous evaluation of its mechanical properties is necessary for safe operation. During the standard operation of NPP, RPV is subjected to various types of degradation processes. The wall of the RPV around the reactor core is exposed to high doses of neutron flux and the steel becomes brittle [1]. The neutron radiation causes changes of mechanical properties; in the first place, it is the shift of the ductile-brittle transition temperature towards higher values. Changes of tensile properties and fracture toughness are considerable too. Standard tests require collection of large-dimension samples coming from the precious materials, usually obtained after exposure to radiation. Since samples for SPT testing are quite small, high activity of irradiated materials is no longer an issue. The SPT technique therefore represents a very useful and effective method applied for characterization of mechanical properties such as ultimate tensile strength (R_m), yield stress (R_e) and fracture appearance transition temperature (FATT) [2, 3].

The main aim of the actual VUJE – Halden project includes irradiation and testing of materials from RPVs of unit #3 and unit #4 of NPP Mochovce. These two units are still under construction and the expected start of the operation will be soon. The results of the project are therefore highly relevant for the assessment of the safe operation of both units.

2. Materials and Methods

The principle of SPT testing procedure which has been applied in VUJE is the penetration of a disk shape specimen by a hemispheric rod and recording of loads and deflections during the test. The specimen has 8.00 mm in diameter and 0.50 mm in thickness. The receiving die bore diameter is d= 4 mm, and a punch tip radius r = 1.0 mm. The chamfer edge of the receiving die is recommended to be with radius R=0.2 mm. Polynomial function, as a result of compliance correction measurements, was introduced into system. The testing is performed on a standard tension test machine, equipped with load and crosshead feed gauges and a data recorder for the registration of load-deflection curves. Using relatively simple testing system and with one type of specimen only, it is possible to estimate yield stress and ultimate tensile strength, and fracture appearance transition temperature (FATT) based on the results of temperature dependence of small punch energy determined from the area under the load – deflection curve. The SPT testing procedure is accepted by the Nuclear Regulatory Authority of the Slovak Republic [4] and currently, it is under the process of standardization into the form of both EN and ASTM standards [5].

Altogether 180 SPT and 30 mini-tensile samples in two sets were prepared for irradiation as it is shown in Table 1. Prepared sets consist of two types of bainitic RPV steels: weld material (Sv10ChMFT) and base material

(15Ch2MFA) from two units (#3 and #4) of Mochovce NPP. After irradiation in the Halden reactor, the samples were tested in hot labs of IFE in Kjeller, Norway. Testing and evaluation of samples after their irradiation bring knowledge about irradiation behaviour of these reactor structural steels before putting the units into operation.

Table 1. List of prepared samples.

Material / Marking	Number of specimens for irradiation 1		Number of specimens for irradiation 2		Total number of specimens	
	SPT	Mini tensile	SPT	Mini tensile	SPT	Mini tensile
Weld metal RPV - MO3	22	4	22	3	44	7
Base material RPV - MO3	23	4	23	4	46	8
Weld metal RPV - MO4	22	3	22	4	44	7
Base material RPV - MO4	23	4	23	4	46	8
Total	**90**	**15**	**90**	**15**	**180**	**30**

The irradiation condition requirements were proposed with respect to the irradiation conditions of the surveillance samples program designed by VUJE for Slovak nuclear power plants. The irradiation temperature should be T_{irr} = 270 - 280°C. Melting monitors, placed into special thermometric case, were used to provide information about irradiation temperature. They were made of eutectic alloys with specific chemical compositions (usually contain Pb, Ag, and Sb) correspond to exact melting temperature. After all, the melting (i.e. reaching melting temperature of alloy) was evaluated by visual control. By the melting monitors the irradiation temperature of the first capsule was identified above 282.6 °C and below 292°C. The neutron fluence is planned to two different levels: $F_1 = 1.0 \times 10^{24}$ n/m² – comparable to one campaign of irradiation in the power reactor – marked as "Irradiation 1" (tested in June 2017); and $F_2 = 2.0 \times 10^{24}$ n/m² – comparable to three campaigns of irradiation in the power reactor – marked as "Irradiation 2" (to be tested in May 2018).

The properties of the experimental materials in the initial state were also described in [6]. Table 2 summarizes chemical compositions of used experimental materials. Both, base and weld metals of RPVs are bainitic steels. Typical microstructures are shown in Figure 1a, b.

Table 2. Chemical composition of used materials.

Material	Element content [mass. %]										
	C	Mn	Si	P	S	Cr	Ni	Mo	V	Cu	Co
BM3	0.160	0.54	0.32	0.010	0.010	2.87	0.09	0.69	0.30	0.045	0.005
WM3	0.042	1.10	0.55	0.010	0.011	1.36	---	0.55	0.20	0.060	0.003
BM4	0.150	0.52	0.29	0.009	0.013	2.69	0.03	0.67	0.31	0.043	0.005
WM4	0.032	1.04	0.63	0.009	0.010	1.35	---	0.55	0.20	0.050	0.005
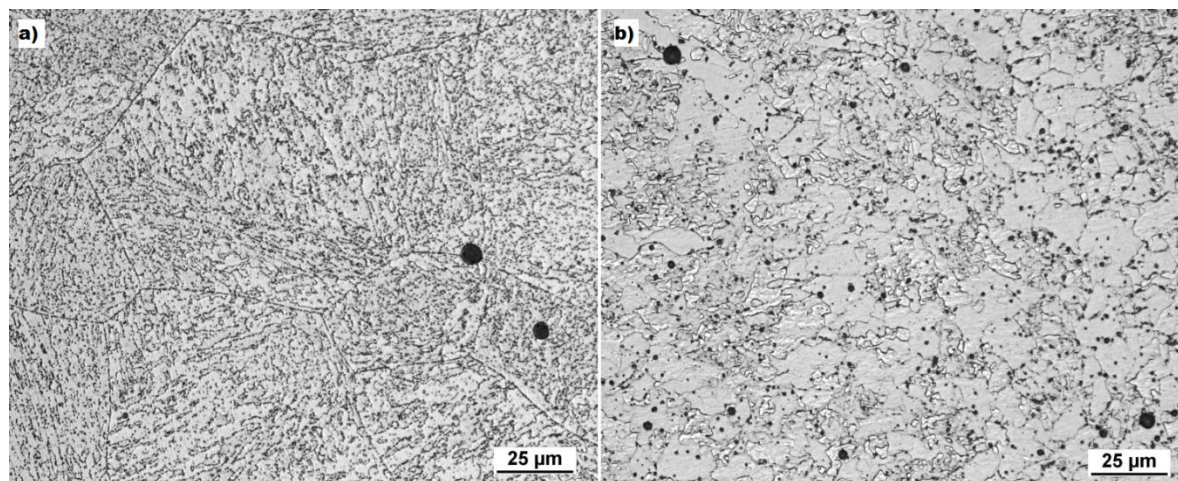
Figure 1. Microstructure of (**a**) base metal and (**b**) weld metal.

3. Results and Discussion

3.1. Tensile properties

Testing results of SPT and mini-tensile specimens before and after 1st irradiation in the Halden reactor are summarized in Table 3. The table shows the yield stress (R_e) and the ultimate strength (R_m) for each material. For determine Rm and Re, linear correlation functions $R_e(Rp_{02}) = \beta.F_e/h^2$ and $R_m = \beta.F_m/(h.u_m)$ were used, where β stands for empirical coefficient, h is initial specimen thickness, and u_m corresponds to displacement. Tensile properties were tested at the room temperature. The values R_e and R_m in Table 3 are the average values of three measurements. Graphical representations of the results given in Table 3 are in Figures 2a-d being chosen as the most convenient to emphasize trend in mechanical properties values.

Table 3. Mechanical properties before and after 1st irradiation.

| Material | Initial state | | | | After 1st irradiation | | | |
| | SPT | | Standard | | SPT | | standard | |
	R_e [MPa]	R_m [MPa]	R_e [MPa]	R_m [MPa]	R_e [MPa]	R_m [MPa]	R_e [MPa]	R_m [MPa]
BM3	470	569	478	601	527	598	557	654
WM3	485	620	490	606	504	629	519	620
BM4	457	600	495	547	526	675	539	653
WM4	509	609	467	590	511	636	507	612

From the Table 3 and Figures 2a-d it is possible to specify trend of base and weld metals in terms of mechanical properties values (Rm, Re). It was found that irradiation leads to a slight increase in strength characteristics, especially in case of base materials, and results obtained by SPT and standard method correlate with each other very well.
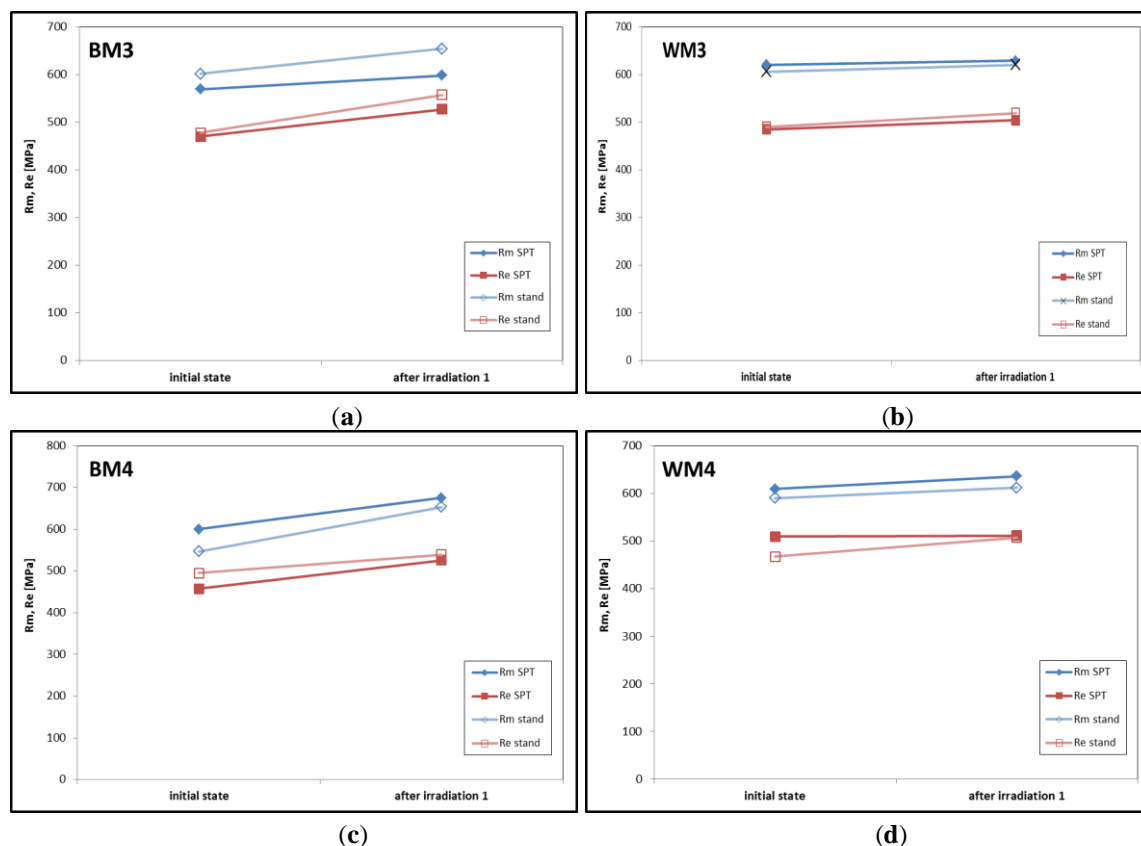
Figure 2. Tensile properties of RPV materials before and after irradiation; (**a**) base metal EMO 3, (**b**) weld metal EMO 3, (**c**) base metal EMO 4, (**d**) weld metal EMO 4.

3.2. Transition temperature and fracture properties

The values of the transition temperatures (FATT) evaluated by the temperature dependence of the SPT energy are listed in Table 4. Energies are obtained from SPT tests at various test temperatures for all evaluated materials. The SPT energy is calculated from a single load-deflection curve needed to deform and crack the SPT sample. By doing this for several different temperatures, the TT_SPT was constructed. This curve consists of two fits, the first one describes the brittle and transition regime (lower energy plateau corresponds to or is extrapolated to a temperature of 50 K), and the second one the ductile regime. Exponential and power functions are used. The intersection of the two curves (upper energy plateau) marks the maximum of the fitted energy, E_{max}. The SPT transition temperature is then defined as temperature where $DBTT_{SPT} = (SP_{max} + SP_{min})/2$. For comparison of the SPT results, TT_{KCV50} and TT_{FATT} values from standard Charpy-V tests in the initial state are given, where TT_{KCV50} stands for transition temperature determined by Charpy-V test for 50 J/cm^2, TT_{FATT} is transition temperature determined by Charpy-V test for 50% of brittle fracture, and TT_{SPT} represents transition temperature determined by SPT.

Table 4. SPT and standard results of transition temperature evaluation for RPV materials.

Material	Initial state			After 1st irradiation
	SPT	standard		SPT
	TT_{SPT} [°C]	TT_{FATT} [°C]	TT_{KCV50} [°C]	TT_{SPT} [°C]
BM3	- 20.2	- 24.7	- 39.6	+ 12.1
WM3	- 18.0	- 16.0	- 23.2	+ 31.5
BM4	- 2.9	- 59.4	- 86.0	+ 15.6
WM4	+ 14.9	+ 13.2	- 12.4	+ 19.9

The obtained temperature dependences of the SPT energy for all tested materials are illustrated in Figures 3a-d.

(a)

(b)

(c)

(d)
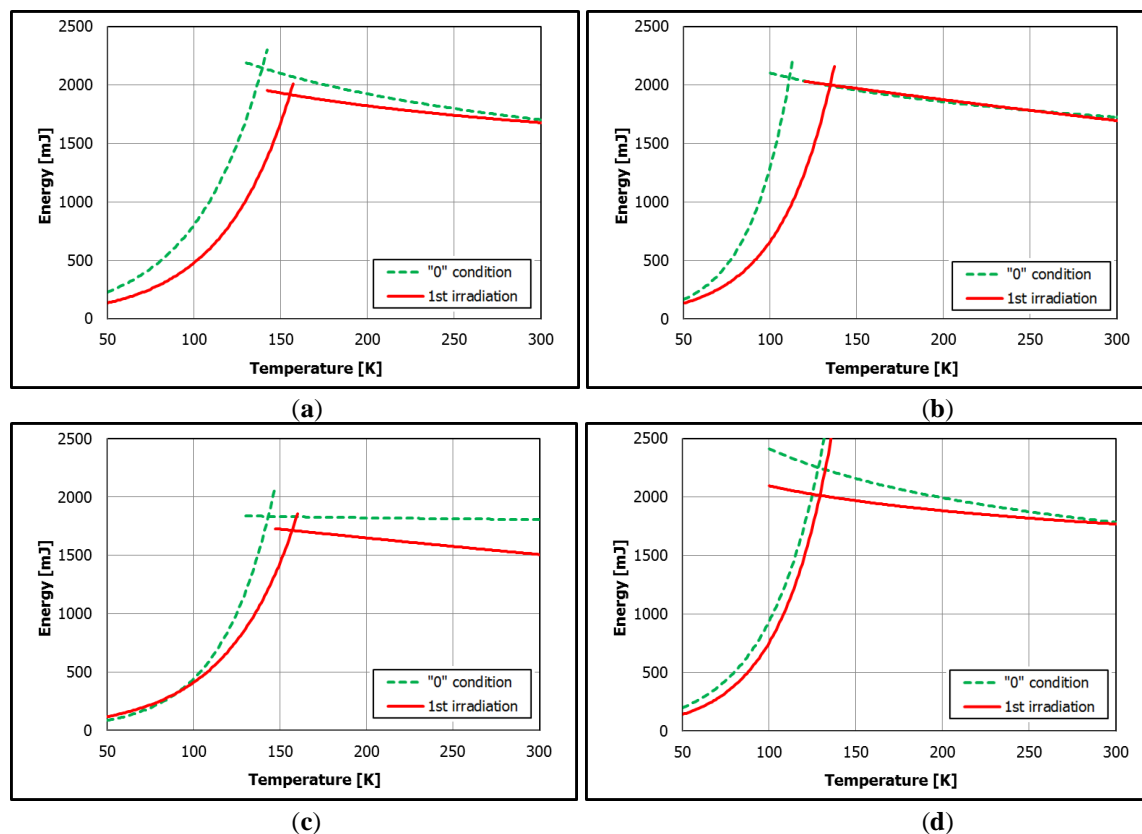
Figure 3. Temperature dependence of the SPT energy for RPV before and after 1st irradiation; (**a**) BM3, (**b**) WM3, (**c**) BM4, (**d**) WM4.

4. Conclusions

The results can be summarised as follows:

- All SPT specimens, as well as mini-tensile specimens after 1st irradiation in the Halden reactor, were successfully tested and obtained values evaluated.
- A small increase in the strength characteristics of all materials after their irradiation in the Halden reactor was observed.
- Good agreement between the results obtained by SPT technique and using mini-tensile specimens was confirmed.
- Neutron irradiation was found to shift of TT_{FATT} towards higher temperatures for base and weld metal.
- The presented results are only preliminary, after the evaluation of the second capsule they will be completed and the current VUJE - Halden project will be finalized.

References

1. IAEA: TECDOC-1442 "Guidelines for prediction of irradiation embrittlement of operating WWER-440 reactor pressure vessels", Vienna, Austria, June 2005.
2. IAEA: "Integrity of Reactor Pressure Vessels in Nuclear Power Plants: Assessment of Irradiation Embrittlement Effects in Reactor Pressure Vessel Steels", IAEA Nuclear Energy Series No. NP-T-3.11, Vienna, Austria, April 2009.
3. Safety guide: The rules on design, manufacture and operation of the degradation monitoring systems of classified equipment of nuclear installations Part 3. Monitoring of irradiation embrittlement of structural materials of nuclear installations. The Nuclear Regulatory Authority of the Slovak Republic, BNS II.3.6/2016.
4. Safety guide: Evaluation of mechanical characteristics of materials of the classified engineering-technology components by the Small Punch Test method. The Nuclear Regulatory Authority of the Slovak Republic, BNS II.9.2/2016.
5. Bruchhausen, M. et al Recent developments in small punch testing: Tensile properties and DBTT. Theoretical and Applied Fracture Mechanics 86 (2016) 2–10.
6. Březina, M.; Petzová, J.; Kupča, Ľ. Samples Preparing and Determination of RPV Steel Properties before Irradiation in the Halden Reactor, EHGP Meeting 2016.

Study on fracture toughness with different thicknesses CT specimen

S. Fan, J. Zhang, Q. Wang, K. Guan*

School of Mechanical and Power Engineering, East China University of Science and Technology, 130 Meilong Road, Shanghai, China 200237; fansining22@163.com

* Correspondence: guankaishu@ecust.edu.cn; Tel: +86-131-662-13046

Abstract: The material selected for this study was a WELDOX 900 steel plate. This paper analyzed the size effect of fracture toughness based on experimental results and finite element numerical simulation results. In addition, J-integrals of different thicknesses were investigated and the relational expression between them was acquired in this study. The main conclusions are as follows: Firstly, the formula between the ductile fracture toughness $J_{0.2}$ and the specimen thickness was obtained. It proposed a method for predicting the fracture toughness of plane strain state using thin specimens of several thicknesses based on this formula. Secondly, the fracture toughness values of the materials were obtained by finite element numerical simulation. And it was found that the distribution of stress triaxiality near the crack tip could well explain the variation of fracture toughness with thickness.

Keyword: fracture toughness; J-integral; reverse finite element method; stress triaxiality

1. Introduction

The fracture toughness of materials is an important reference for the safety evaluation of equipment and life prediction. The sample of conventional methods for measuring fracture toughness was required to have larger size specimens. But many in-service equipment couldn't meet this requirement. It is an effective way to make the sample thinner in order to evaluate fracture toughness of in-service equipment. J-integral was an index for fracture toughness, which was used to characterize the stress strain field in the leading edge of crack [1]. Therefore, it is great engineering significance to study the effect of thickness of specimen on J-integral.

The stress triaxial factor represented the triaxial stress state and determined the degree of restraint, which was used by many literatures to explain the influence of size on fracture toughness [2]. The stress state in the front of the crack tip was changed with the thickness. With the specimen size decreasing and reaching to the plane stress state, the fracture toughness would increase [3]. Although the value of the fracture toughness was related to the size of specimen, the fracture toughness could be considered to be dimension independent when the specimen thickness was large enough to reach the plane strain state [4].

2. Experimental procedure

2.1 Material

The materials used in this series of experiments were WELDOX900, which was applied to fan blower compressor. The chemical composition of weldox900 low-alloy high strength steel under investigation in wt% was shown in Table 1. The results were shown that the material met the standard of EN10025. In addition, yield strength and tensile strength of metallic materials were necessary for fracture toughness test, which were acquired by uniaxial tensile test [5] (Table 2).

Table 1. Chemical composition of WELDOX 900 (wt%).

Element	C(max)	Si (max)	Mn(max)	P (max)	S (max)	Cr (max)	Mo(max)
Measured value	0.20	0.21	1.37	0.01	0.002	0.25	0.52
EN10025	0.20	0.51	1.60	0.02	0.01	0.70	0.70
Element	Ni(max)	Al(min)	Cu (max)	V(max)	Ti(max)	Nb(max)	B (max)

Measured value	0.05	0.058	0.01	0.02	0.001	0.017	0.0013
EN10025	2.0	0.018	0.30	0.06	0.04	0.04	0.05

Table 2. Tensile mechanics of WELDOX 900.

No.	$R_{p0.2}$(MPa)	Rm(MPa)	δ_5 (%)	ϕ (%)
1	890.5	947.0	15.78	69.10
2	889.3	949.1	14.56	68.19
3	890.1	948.2	15.23	68.29
Average	890.0	948.1	15.19	68.53

2.2. Experimental methods

In fracture toughness testing, the Compact Tension (CT) specimen that was recommended as one of the standard specimen was adopted in this study [6]. On the basis of the load-displacement curves which were obtained by the experimentation, J-integral was worked out.

In addition, multi-specimen method and single-specimen method were the main methods to determining J resistance curves. Multi-specimen method means a series of specimen of the same size are used to gain different levels of displacement. In contrast, different levels of displacement were acquired by only one specimen for single-specimen method. Single-specimen method was used in this study.

The experimental materials were got from a sheet material whose thickness was 18mm with 240mm width. Sampling direction was shown in Figure 1 which was the same as tensile samples.

The sizes of these specimens were designed as follows: width was invariable which was 50mm and the thickness was set into five levels which were 16mm, 12.5mm, 8mm, 4mm and 2mm (Figure 2).
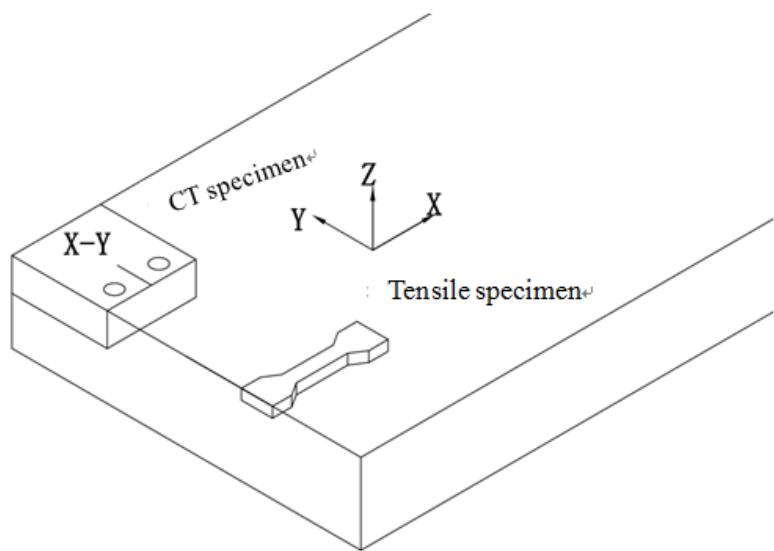
Figure 1. Sampling direction.
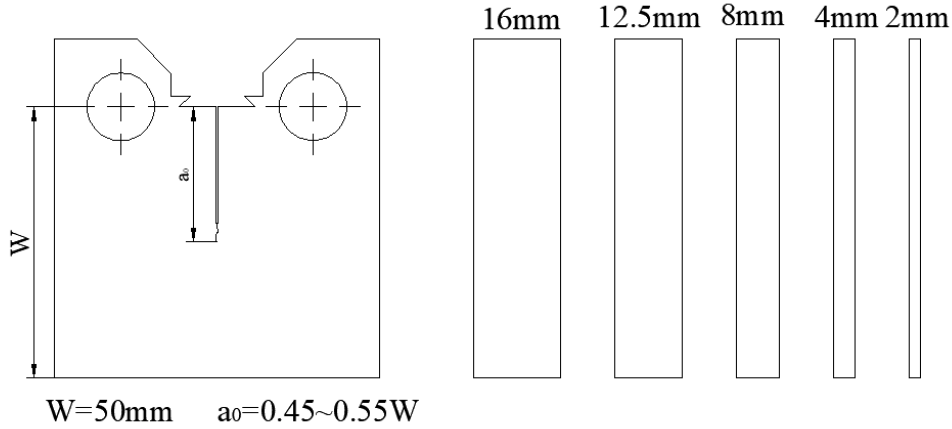
Figure 2. CT samples with different thickness.

2.3. Method of gaining J resistance curves

According to GB/T 21143-2014, J-integral was obtained by the follow formula for CT specimen:

$$J=\left[\frac{F}{\left(BB_N W\right)^{0.5}}\times g_2\left(\frac{a}{W}\right)\right]^2\left[\frac{\left(1-v^2\right)}{E}\right]+\left[\frac{\eta_P U_P}{B_N\left(W-a\right)}\right]\left\{1-\left[\frac{\left(0.75\eta_P-1\right)\Delta a}{W-a}\right]\right\} \qquad (1)$$

$$\eta_P=2+0.522\left(1-a_0/W\right) \qquad (2)$$

$$a=a_0+\Delta a \qquad (3)$$

Where n_p was plastic factor. $g_2(a/W)$ could be acquired in GB/T 21143-2014. BN meat the thickness between side groove and here $BN = B$.

The output data of the test machine was the force-displacement curve while using single sample unloading flexibility technology. J-integral was calculated by iterative algorithm.

3. Results and discussion

3.1. Experiment

The results of different thickness samples where shown in Table 3 which including initial crack length a_0, end crack length a_f and fracture toughness $J_{0.2}$. J resistance curves of the samples of different sizes were shown in Figure 3. The results of samples with different thickness were shown in Figure 3(f). Blunting line equation was as follow:

$$J = 3.75\times 948\Delta a \qquad (4)$$

Where Δa was the length of crack propagation.

Table 3. Test data of fracture toughness of CT specimen.

NO.	Thickness /mm	Width /mm	a_0/mm	a_f /mm	$J_{0.2}$ KJ/m^2	Notes
CT-T16-1	16.00	49.98	24.31	26.33	311.46	Pin bending
CT-T16-2	16.00	50.02	24.30	26.03	175.53	
CT-T16-3	16.00	49.99	24.29	26.25	180.45	
CT-T12.5-1	12.51	50.02	24.38	25.78	186.12	
CT-T12.5-2	12.49	50.02	24.28	25.62	179.61	
CT-T12.5-3	12.50	50.00	24.32	25.71	177.85	
CT-T8-1	7.95	50.01	24.45	26.12	202.43	
CT-T8-2	7.96	50.01	24.51	25.96	196.86	
CT-T8-3	7.98	50.00	24.48	26.07	200.02	
CT-T4-1	3.96	50.01	25.31	26.06	218.57	
CT-T4-2	3.97	50.01	25.02	25.96	220.88	
CT-T4-3	3.98	50.02	25.15	25.89	220.32	
CT-T2-1	1.98	50.01	24.96	26.01	null	Sample distortion
CT-T2-2	1.97	50.01	25.38	26.13	210.56	
CT-T2-3	1.86	50.07	24.61	26.52	211.15	
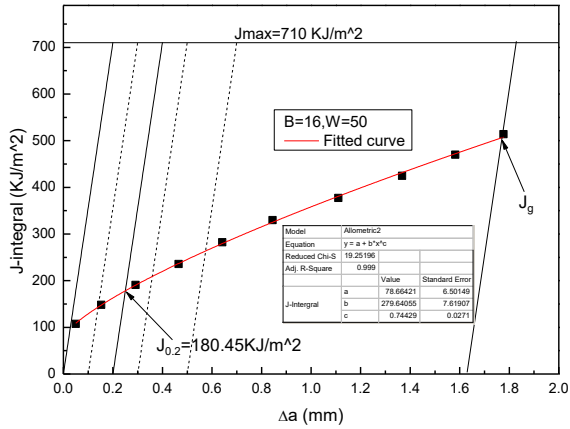
(a) B = 16mm, W = 50mm
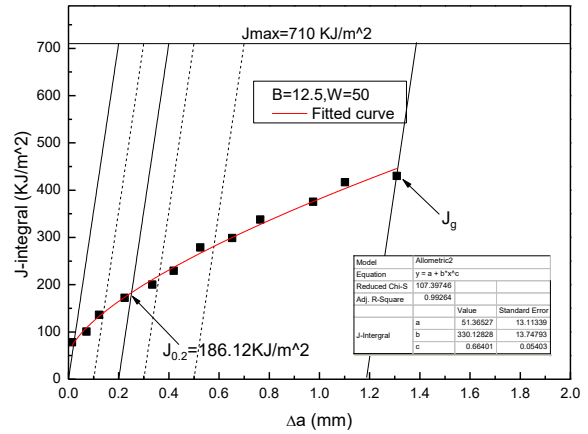
(b) B = 12.5mm, W = 50mm
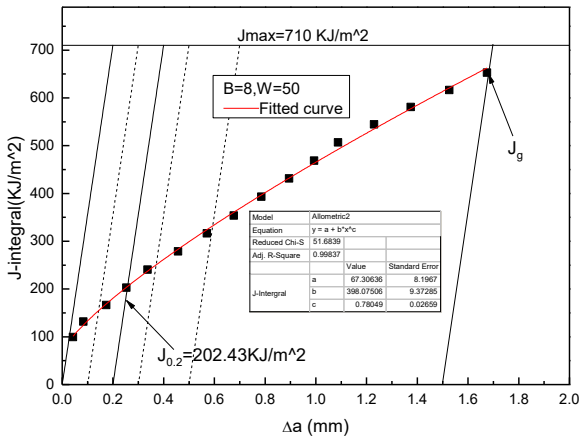
(c) B = 8mm, W = 50mm
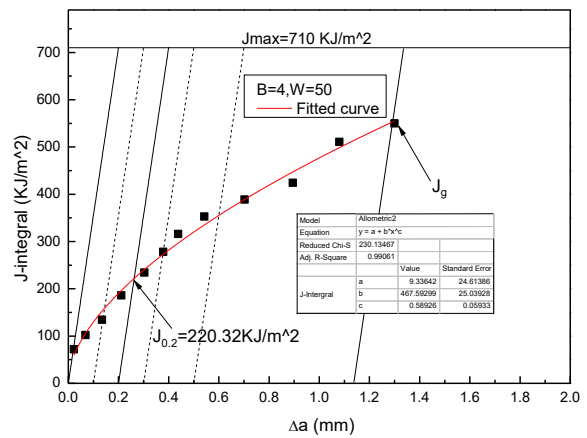
(d) B = 4mm, W = 50mm
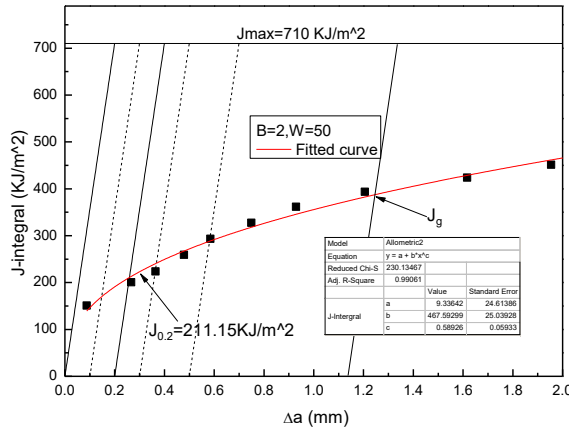
(e) B = 2mm, W = 50mm
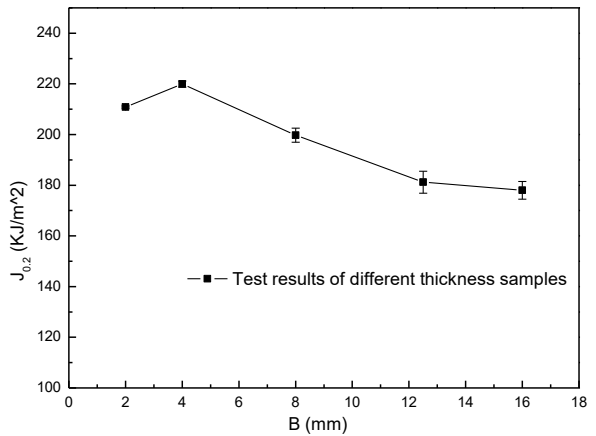
(f) Test results of samples with different thickness

Figure 3. JR curve and J0.2 value obtained by single sample method.
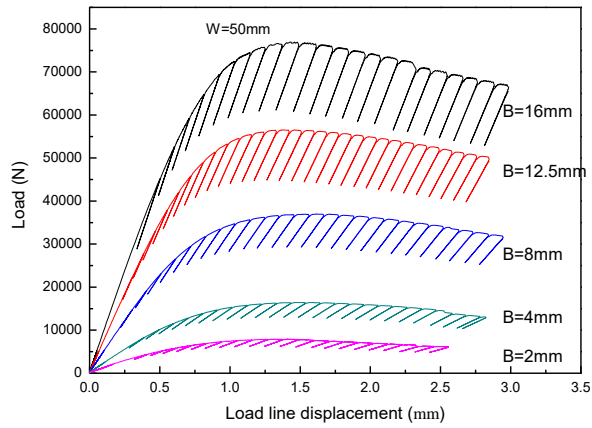
Figure 4. Load and displacement curves of specimens with different thickness.

Figure 5. CT specimens of different thickness after test.

Load and displacement curves of specimens with different thickness were shown in Figure 4. And CT specimens of different thickness after test were shown in Figure 5.

It was shown that increasing thickness resulted in rising fracture toughness, except for the specimen of 2mm. And the results of last two specimens were very close. It is important to note that to calculate the plane strain fracture toughness, the thickness of the sample should be larger while in the case of plane stress fracture toughness test, small thickness of the sample is sufficient. That meant that the process of changing the plane stress state to the plane strain state was relevant with thickness. And finally, the J integral value of fracture toughness was determined and had no relation with thickness when the thickness was larger enough.

The relationship between fracture toughness and thickness of high strength titanium alloy had been researched by Ji [7]. The following formula was given by them.

$$K_C = \xi B^{1/2} e^{-kB} + K_{IC}\left(1 - e^{-kB}\right) \tag{5}$$

Where, B was thickness of sample, Kc was stress intensity factor and KIC was stress intensity factor. ξ and k were material constant.

The relationship between J-integral and stress intensity was obtained by many researchers [8].

$$J = \begin{cases} \dfrac{1}{E} K^2 & \text{plane stress state} \\[2mm] \dfrac{1-\nu}{E} K^2 & \text{plane strain state} \end{cases} \tag{6}$$

On the basis of the two formulas, the following relationship was acquired.

$$J = \alpha B e^{-\beta B^n} + J_{IC}\left(1 - e^{-\beta B^n}\right) \tag{7}$$

Where *n* was used to improve the accuracy of fitting curve.

The result of fitting curve was closed to experimental data and the goodness- of-fit was 0.97195 which indicated that the variation of fracture toughness and thickness of low alloy and high strength steel could be described well by the formula.
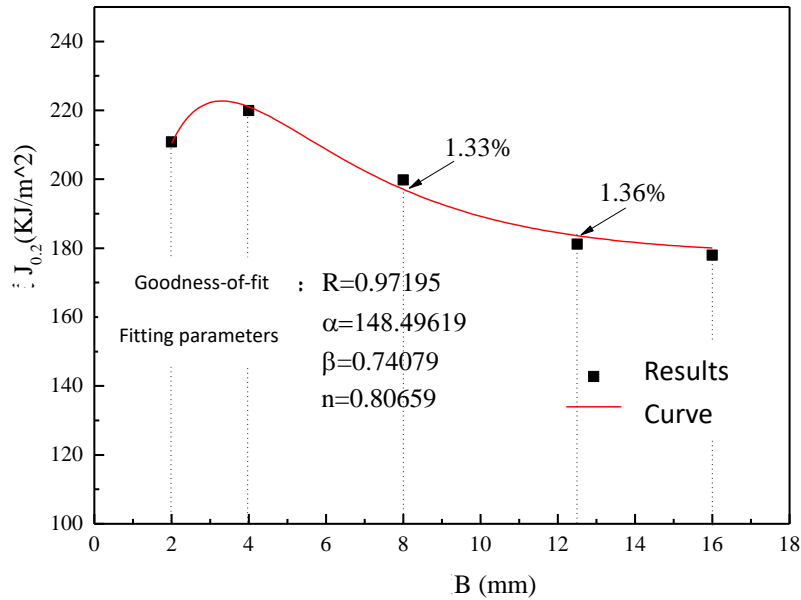
Figure 6. The formulae (3-6) are used to fit the result of the test.

3.2. Simulation

The fracture toughness parameters and true stress strain curve of material were necessary for finite element modeling (FEM). GTN model which was aimed at simulating ductile fracture process was chosen in this study. The parameters of GTN and true stress strain curve were obtained by means of small punch test which was based on inverse finite element [9]. Above results were used to obtained fracture toughness of specimens with different thickness by FEM [10].

Table 4. Fracture toughness of specimens with different thicknesses obtained by FEM.

B (mm)	2	4	8	12.5	16	25
Simulated results $J_{0.2}$ (KJ/m$_2$)	207.44	216.97	193.92	174.83	162.82	165.65
Test results $J_{0.2}$ (KJ/m$_2$)	210.56	218.57	196.86	177.85	180.45	170.94
Deviation %	1.48	0.73	2.94	1.15	9.78	6.02
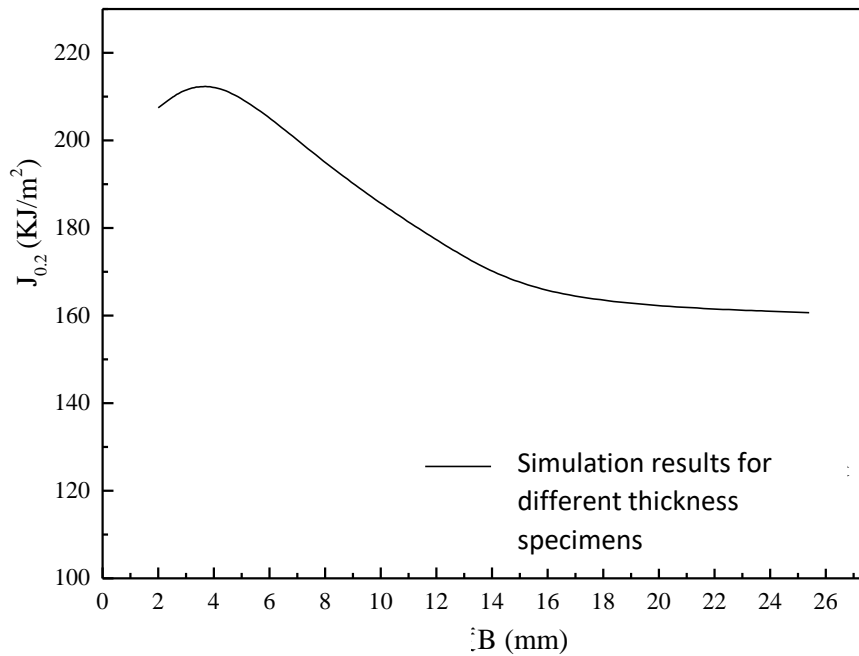
Figure 7. Simulation results for different thickness specimens.

Figure 7 was shown that the simulation results for specimens with different thickness were closed to the results of testing. It was indicated that the backward simulation using FEM which was used to get fracture toughness parameters and true stress strain curve of material was able to simulate the fracture toughness of specimens with different thickness.

In addition, many researchers found that the fracture of ductile material was divided into void-mode fracture and shear-mode fracture [11]. There was a critical stress state between the two kinds of fracture which was represented by stress triaxiality. Fracture morphology of sample was dimple, which was conformed to the characters of stress triaxiality in this study (Figure 8). Furthermore, growth and polymerization of material void were affected by stress triaxiality, which was related to GTN because GTN was based on theory of void damage of materials. Therefore, the relationship between stress and thickness of specimen was discussed in this study.
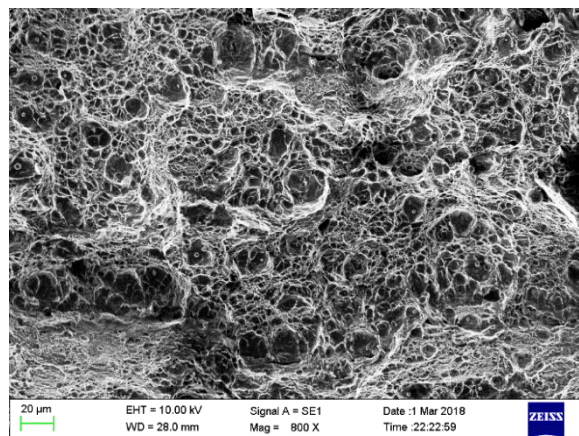
Figure 8. Topography of crack tip extension.

The time of beginning the phenomenon of unit reduction was defined as the rev. crack moment. The distribution of Von Mises stress was shown in Figure 9.

(a) B = 2mm (b) B = 4mm (c) B = 8mm

(d) B = 12.5mm (e) B = 16mm (f) B = 25.4mm
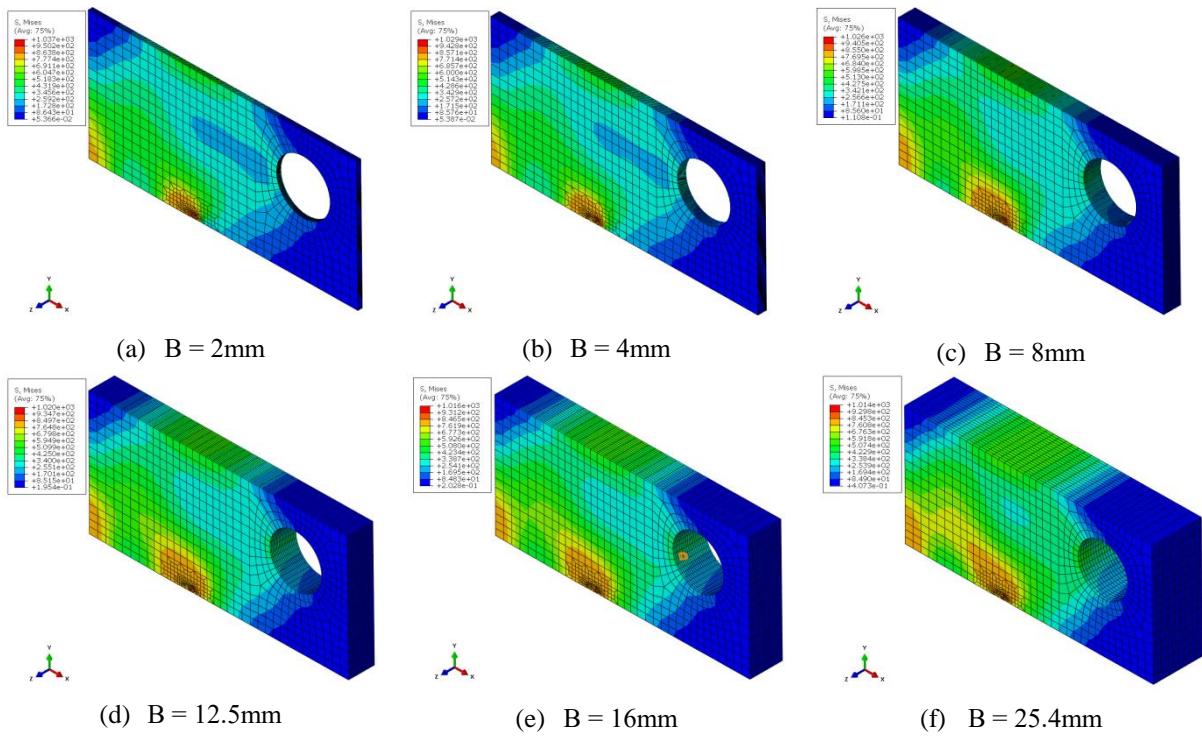
Figure 9. Von Mises stress distribution of samples with different thicknesses.

It was shown that six specimens reached the balance of stress at the rev. crack moment. Von Mises stress was increased slightly with the increase of thickness.

(a) B = 2mm (b) B = 4mm (c) B = 8mm

(d) B = 12.5mm	(e) B = 16mm	(f) B = 25.4mm
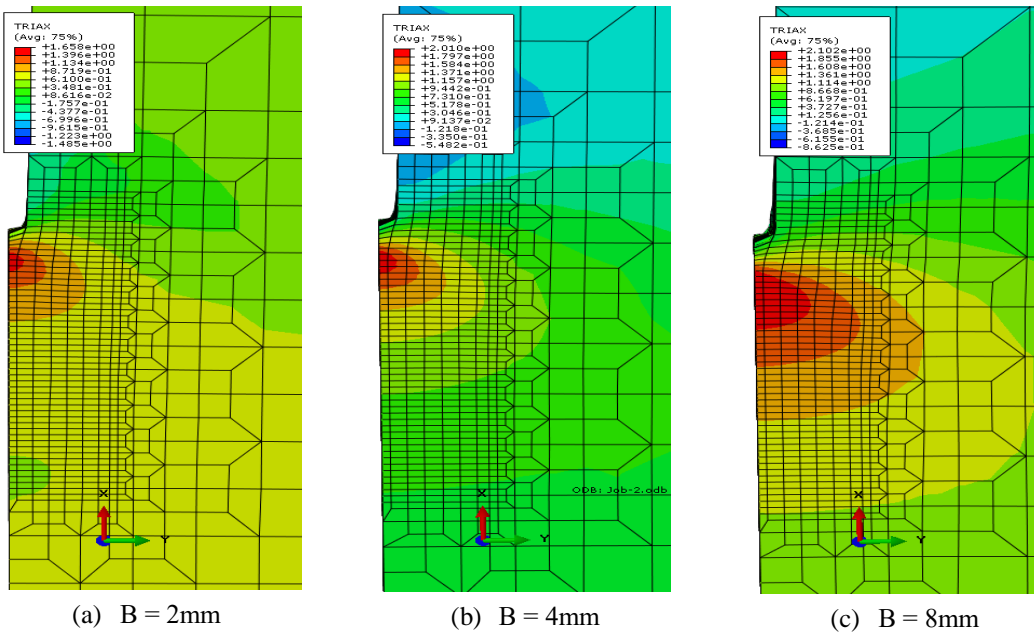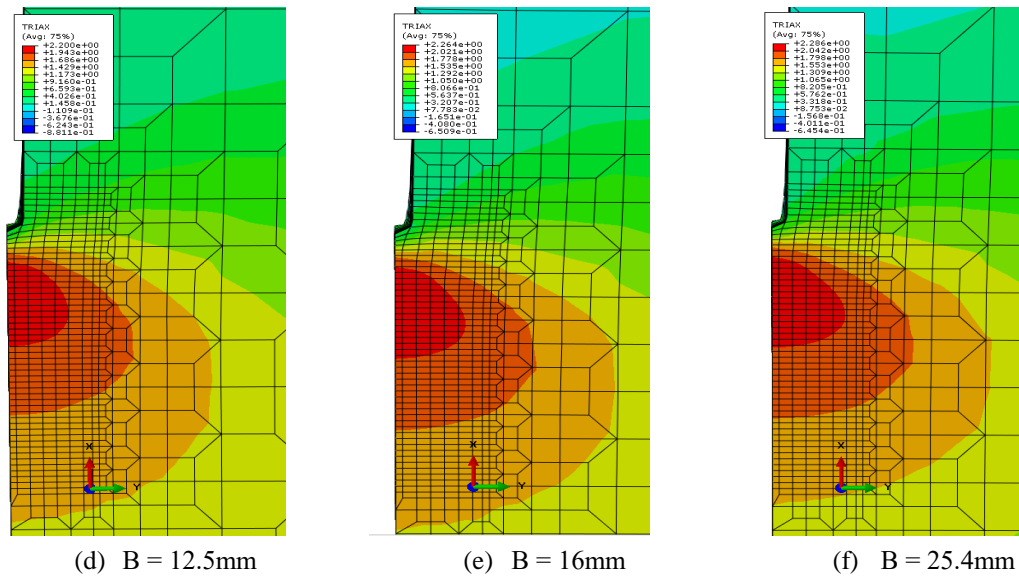
Figure 10. Stress triaxiality distribution of specimens with different thicknesses.

Stress triaxiality distribution of specimens with different thickness was shown in Figrue 10. It indicated that stress triaxilaity was raised with the increase of thickness and the area of maximum value was also expended.
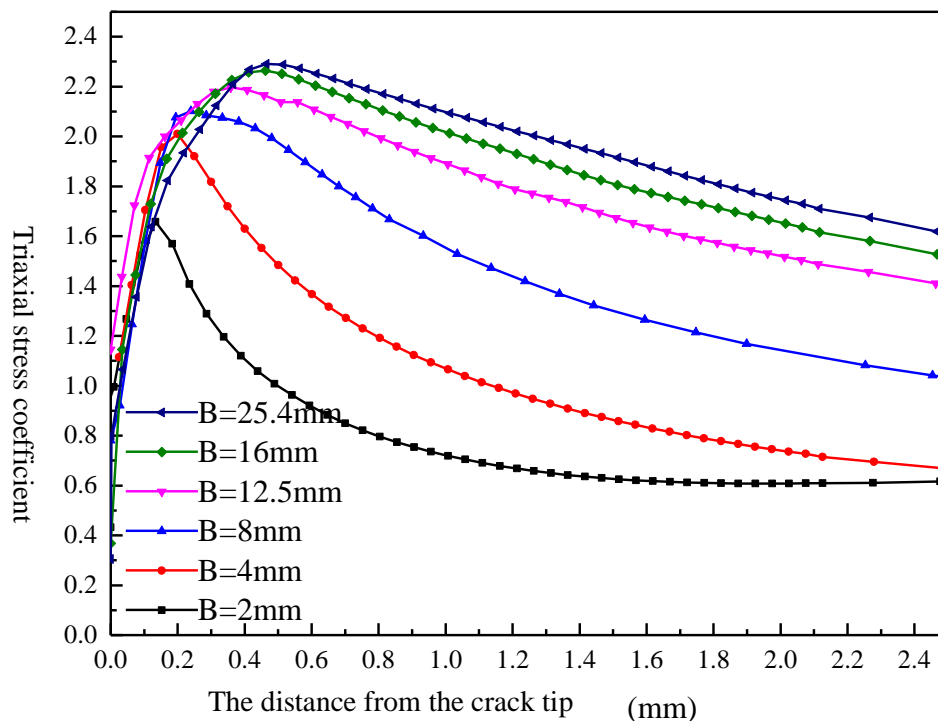
Figure 11. Stress triaxiality distributions in front of crack tips.

Stress triaxiality distribution in the front of crack tips was shown in Figure 11. It revealed that stress triaxiality was higher when the thickness of specimen was larger and the result of specimen with 16mm was closed to 1T, which was illustrated that the specimen with 16mm was more closed to plane strain state.

In addition, the specimen with 2mm was different with others in not only stress cloud charts but curve graphs (Figure 10 and Figure 11). It illustrated that the maximum stress triaxality couldn't be used to reflect fracture toughness when the thickness of sample was too small to close to plane stress state.

4. Conclusions

An experimental program was carried out to study the fracture toughness and dimensional effect. The results were shown that specimens of different sizes were relevant and guidelines for further practice were proposed. The main outcomes are the following:

1) Based on the testing results of samples with different thickness, a larger number of data was obtained and $J_{0.2}$ was calculated by series of formulas. According to the relationship between ductile fracture toughness ($J_{0.2}$) and thickness, the specific mathematical expression was given by derivation and limit analysis which was $J = \alpha B e^{-\beta B^n} + J_{IC}\left(1 - e^{-\beta B^n}\right)$. The expression could fit the relationship between fracture toughness $J_{0.2}$ and specimen thickness well.

2) The fracture toughness values of the materials were obtained by finite element numerical simulation. Compared with the experimental results, it is found that the numerical error of $J_{0.2}$ obtained by reverse finite element method was only 9.7%. That was indicated that the results of tests were valid and the formula that was based on the results was reliable.

References

1. Ku M. Analysis engineering method of elastic-plastic fracture analysis [M]. National Defense Industry Press. 1985.
2. Huiru D.; Wanlin G. Experimental method of three-dimensional composite fracture [J]. Experimental mechanics. 2002, 17(4):497-503.
3. Tahtinen S.; Laukkanen A.; Singh B.N. Damage mechanisms and fracture toughness of GlidCop (R) CuAl25IG0 copper alloy [J]. Journal of Nuclear Materials. 2000,283:1028-32.
4. Ono H.; Kasada R.; Kimura A. Specimen size effects on fracture toughness of JLF-1 reduced-activation ferritic steel [J]. Journal of nuclear materials. 2004,329:1117-21.
5. GB/T 228-2002. Metallic materials tensile testing at ambient temperature[S].2002.
6. Lx C. GB T21143-2014. Uniform test method for the quasi-static fracture toughness of metal materials [J]. 2015.
7. Jiyun Y.; Xing Z. Study on the relationship between material fracture toughness and sample thickness [J]. Mechanical strength. 2003, 25(1):76-80.
8. Hai L. J integral plane stress state and K_I relationship is derived [J]. Journal of chongqing jiaotong university (Natural Science). 2006, 25(2):35-7.
9. Xiaocheng Z. The fracture toughness parameters of the materials were obtained by the inverse finite element method in the small punch test. Thesis, East China University of Science and Technology. 2014.
10. Linling G. Research about the fracture toughness of materials based on small size CT specimen and small punch test. Thesis, 2018.
11. Jien C. Study on material failure based on stress triaxiality. HuaZhong University of Science and Technology. Thesis, 2012.

Rate effects on the estimation of fracture toughness by Small Punch tests in hydrogen embrittlement scenarios

B. Arroyo [1,*], J.A. Álvarez [1], R. Calle [1,2] and F. Gutiérrez-Solana [1]

[1] LADICIM, Universtiy of Cantabria, Avda. Los Castros 44, 39005, Santander, Cantabria, Spain
[2] INESCO INGENIEROS, CDTUC Módulo 9, Avda. Los Castros 44, 39005, Santander, Cantabria, Spain
* Correspondence: arroyob@unican.es; Tel.: +34-942-201-837

Abstract: In this paper, different techniques to test notched Small Punch (SPT) samples for the estimation of the fracture properties in aggressive environments are studied, based on the comparison of the micromechanisms at different rates. Pre-embrittled samples subsequently tested in air at conventional rates (0.01 and 0.002 mm/s) are compared to embrittled ones tested in environment at the same rates (0.01 and 0.002 mm/s) and at a very slow rate (5E-5 mm/s); a set of samples tested in environment under static loads that produce very slow rates complete the experimental results. As a conclusion, is recommended to test SPT notched specimens in environment at very slow rates, of around E-6 mm/s, when characterizing in Hydrogen Embrittlement (HE) scenarios, in order to allow the interaction material-environment to govern the process.

Keywords: Small Punch Test; hydrogen embrittlement; punch rate, fracture toughness

1. Introduction

A critical aspect concerning high strength steels is their resistance to Stress Corrosion Cracking (SCC) and Hydrogen Embrittlement (HE) phenomena, both of which lead to degradation of the mechanical properties of these steels when facing aggressive environments [1,2]. The effect of hydrogen is especially significant in high-strength steels exposed to aqueous environments under cathodic protection (such as off-shore platforms) or those typical of H2S presence (as in gas transport pipelines). Both phenomena, HE and SCC, are similar, resulting in brittle failures in the presence of an aggressive environment and maintained stress. Both phenomena are dependent on the crack deformation rate, and may even disappear at very high rates, while at very slow strain rates hydrogen continues to exert an embrittling effect [3]. The recommendations presented by various research groups over the last few decades have been collected in the standard ISO 7539 [4]. It establishes requirements concerning specimen size and solicitation rate, but does not specifically define the procedure to follow in numerous applications. Also, there are particular situations where standards cannot be followed to perform characterizations on in-service components, mostly due to the impossibility of machining specimens fitting the dimensions, or mainly the thickness required. One of those situations is usually present in the welded joints of any type of structure.

To find a solution for these types of scenarios, among these alternative techniques, the Small Punch Test (SPT) is one of the most notables [5]. The SPT, based on punching a reduced dimensions plane specimen, allows the estimation of parameters such as the yield stress, ultimate tensile strength and fracture toughness of metallic materials with high reliability. Over the last years, some authors have proved the validity of the SPT when used in HE and SCC characterization [5-12]. In order to reproduce accurately the micromechanisms taking place in HE failures, as it is imposed by standardised environmental characterizations, the test rates should be very slow, or even quasi-static [5,11]. The ultimate research in the SPT field [11,12] indicates that tests performed in environment, under static load applied to the specimen, should be one suitable option to reproduce the micromechanisms of real subcritical processes, despite the time and samples requirements are higher.

In this paper a review of all possible SPT testing techniques and rates for its application to HE scenarios is carried out, form pre-embrittled samples tested in air at conventional rates to tests submerged in environment under static load, going by submerged tests at different punch rates from 0.01 mm/s to 5E-5 mm/s.

2. Materials and Methods

The material used in this study is a Cr-Ni-Mn high-strength steel, which is employed in the manufacture of large anchor chain links for off-shore platforms. It is obtained by quenching and tempering processes, which give the tempered martensite microstructure showed in Figure 1. This steel is received in the factory in bars, which are then forged to conform the links by bending forces.
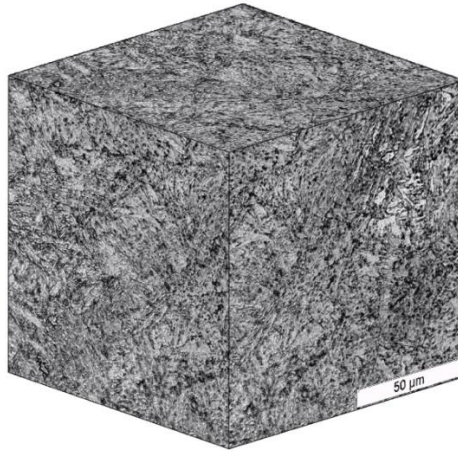
Figure 1. Microstructure of the steel used.

Compact specimens for fracture mechanics according to [13] and Small Punch notched samples according to [5,14] were obtained from a chain link for the subsequent labors. Also, in order to determine the mechanical behavior of the material as received [13,15,16] some other tensile and fracture specimens were machined to obtain the results shown in Table 1. The Hydrogen content of the material as received was measured by the hot extraction technique in a LecoR analyser, obtaining the value of 0,84 ppm showed in Table 1.

Table 1. Mechanical properties of the steel.

Parameter		Value
Yield Stress	(MPa)	920
Ultimate Stress	(MPa)	1015
Young's Modulus	(GPa)	205
R.O. parameter	N	14,5
R.O. parameter	α	1,15
J0,2	(KN/m)	821
KJ0,2	(MPa*m^1/2)	410
H2 content	(ppm)	0,84

An environmental condition known as cathodic charge (CC), or anodic polarization, has been employed in this study. It is used to protect against corrosion structures that operate in aggressive environments, or to reproduce local situations where a high amount of hydrogen is present. It causes substantial embrittlement on the steel by the action of the hydrogen going through and getting trapped in it.
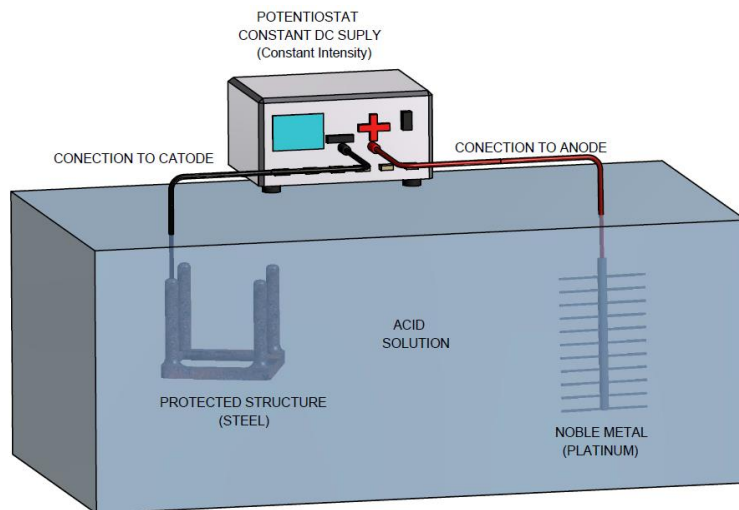
Figure 2. Cathodic charge method. [5,11].

Figure 2 shows a set-up of the method used in this work [5,11]. It consists of the interconnection, via an acid electrolyte, of a noble material (platinum in this case) and the steel, which will be protected due to the fixed current interposed [1,17,18]. In this study, for the cathodic charge situations, an environmental condition in accordance [7,10,11,17,18,19] was proposed, consisting of an 1N H2SO4 solution in distilled water containing 10 drops of CS2 and 10mg of As2O3 dissolved per liter of dissolution. The solution of As2O3 was prepared using Pessouyre's method [17,19]. A platinum grid was used as an anode. The PH was controlled in the range 0,65 - 0,80 during the tests and at room temperature 20ºC - 25ºC. An embrittlement level of 5mA/cm2 was employed. The Hydrogen content of the material resulting from its exposition to this environment was 5,86 ppm (vs 0,84 ppm as received).

The SPT, that is in a pre-standard state, has been successfully employed in the evaluation of tensile [20] and fracture [21] properties of different materials. Because of its reduced dimensions and simplicity, this technique has been applied to characterize embrittlement situation on steels, such as the evolution of materials properties with neutron irradiation [22], the brittle-ductile transition temperature of metallic materials [23], or environmental embrittlement [5-12]. A schematic of the device used in this work for the performance of these tests is represented in Figure 3; during the test the force and the punch displacement were registered continuously.
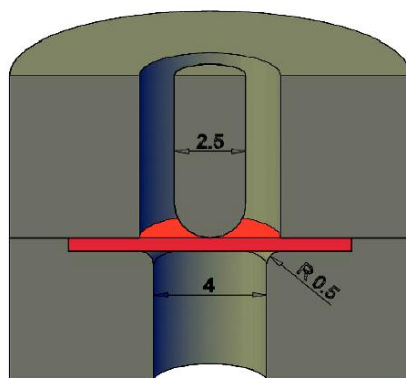
Figure 3. SPT device and samples used.

From SPT tests at standard rates, curves like the ones shown in Figures 4.a and 4.b [24] are obtained. In brittle materials or embrittlement situations (Figure 4.b), the membrane stretching (zone III) does not exist, moving from a yielding plastic behaviour directly to the final plastic instability. It can be observed that while in ductile situations the specimen rupture surface has a semicircular shape and its deflection is higher meanwhile (figure 4.a), in brittle scenarios the breaking typology is a star (figure 4.b) and the specimen deflection lower, so the energy under the register is also lower [5].
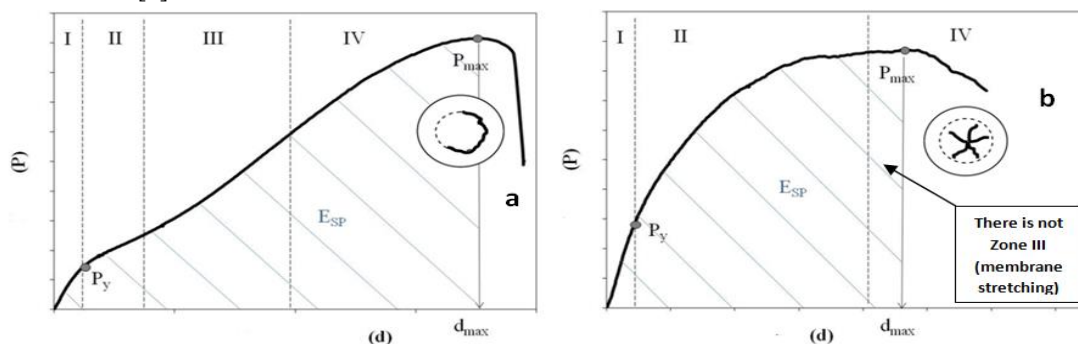
Figure 4. Schematic of SPT curves at conventional rates [24]; (**a**) ductile materials; (**b**) brittle scenarios.

When characterizing materials in HE situations the testing rate is an important parameter to take in account [3,5,12], as far as it will govern the micromechanism taking place. In environmental subcritical processes very low rates, or even static tests, are commonly employed [4], being the Slow Strain Rate Tests (SSRT) and the tests under constant load the most widely used [25] for conventional characterizations. By using these testing conditions, hydrogen will have enough time not just to diffuse form reversible tramps to the new cracking areas subsequently generated during the test, but also to escape form irreversible tramps helped by plastic deformation and diffuse to the new cracking areas [26,27]. The ultimate research for the Small Punch test in HE characterizations [5,11,12] advises that static load tests, or very low punch rates (Slow Small Punch Test, SSPT), should be used, in order to

allow hydrogen to cause all of its embrittling power; in the same way as advised for standardized tests. In [11] the punch displacement vs time SPT curve resulting from static load tests in environment (d-t register) was studied, resulting in the three zones shown in figure 5.
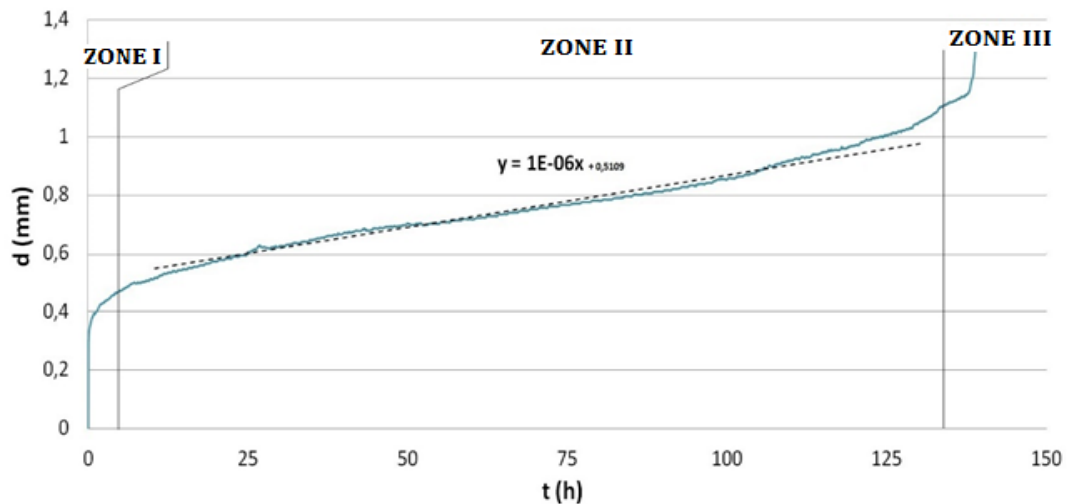
Figure 5. Displacement-time curve for static load tests in environment [12].

- Zone I consists of the punch indentation and settlement.
- In zone II a quasi-constant punch rate takes place, caused by the variation on the flexibility of the system produced by an increasing cracking in the specimen in both radial and thickness directions.
- Finally, in zone III the damage level of the system is so high that the punching load can't be supported anymore and the specimen leads to final instability and fails.

In a first attempt fracture mechanics tests were carried out in the environmental condition described (cathodic polarization at a level of 5mA/cm2) in order to determine the micromechanisms of fracture by SEM images, as well as the K_{IEAC} value. Prior to the test, the specimens were subjected to hydrogen absorption by exposing them for 48 hours to the same environment and aggressiveness conditions as the test itself, that was performed subsequently by applying the corresponding loading rate using a slow strain rate machine. Two loading rates were employed in order study their effect, one test was performed at 6E-9 m/s of constant solicitation rate and another 10 times faster, at 6E-8 m/s, following the recommendations of the Standard ISO-7539 [4]. The methodology proposed by ASTM E-1820 [13] was employed for the K_{IEAC} value calculation. Figure 6 shows a test while being carried out.
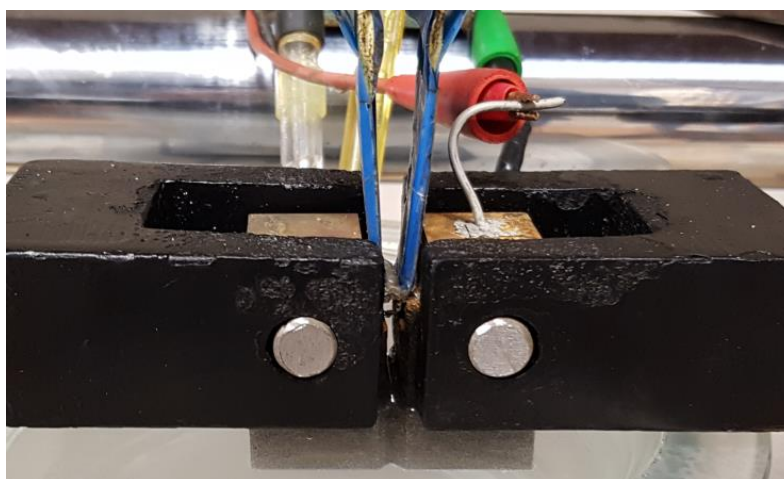
Figure 6. Fracture mechanics test carried out.

The sample geometry employed for SPT, according to [5,14,28,29], is presented on Figure 7, it consists on a plane 10mmx10mm of section and 0.5±0.01mm of thickness including a lateral notch machined by wire electro-

erosion of 0,15 mm radius. The orientation of the notches in SPT and C(T) samples was the same, in order to reproduce the same material orientation in both cases.
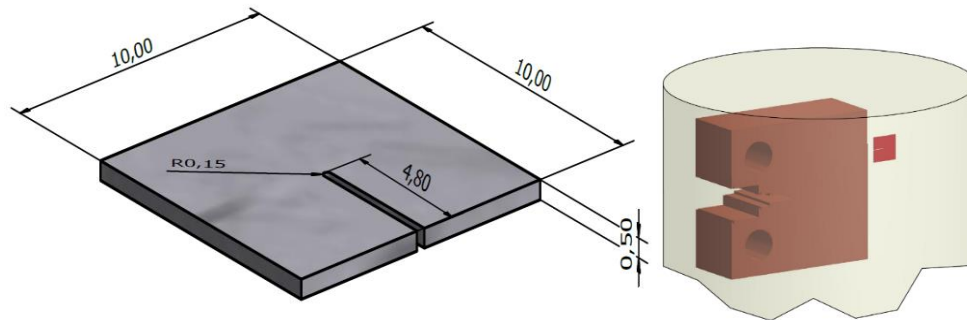
Figure 7. SPT notched samples employed and its orientation compared to C(T)'s one.

Prior to the test, the specimens were subjected to hydrogen charging by exposing them for 2 hours to the corresponding environment, a period of time considered sufficient for a proper and complete diffusion of the hydrogen inside the material [5], then the mechanical testing was applied. In the case of the SPT, four mechanical testing conditions were employed in order to produce the different punch rates on the sample to be studied:

- Pre-embrittled samples tested in air at the conventional 0.01mm/s punch rate recommended by [14,21] and widely employed by authors, and another rate of 0.002 mm/s, five times slower, in order to compare their effect. For this purpose, the samples were charged, as shown in Figure 8, and immediately extracted, dried and tested in air environment in an electric machine.

Figure 8. SPT pre-embrittled specimens during its hydrogen absorption.

- Embrittled samples tested in continuous exposition to the environment at the conventional rate of 0.01 mm/s, and five times slower of 0.002 mm/s. For this purpose, the samples were charged and tested in a device was specifically designed, built and patented [30] for this purpose that is presented in Figure 9; in this case the punching is applied in the horizontal direction.
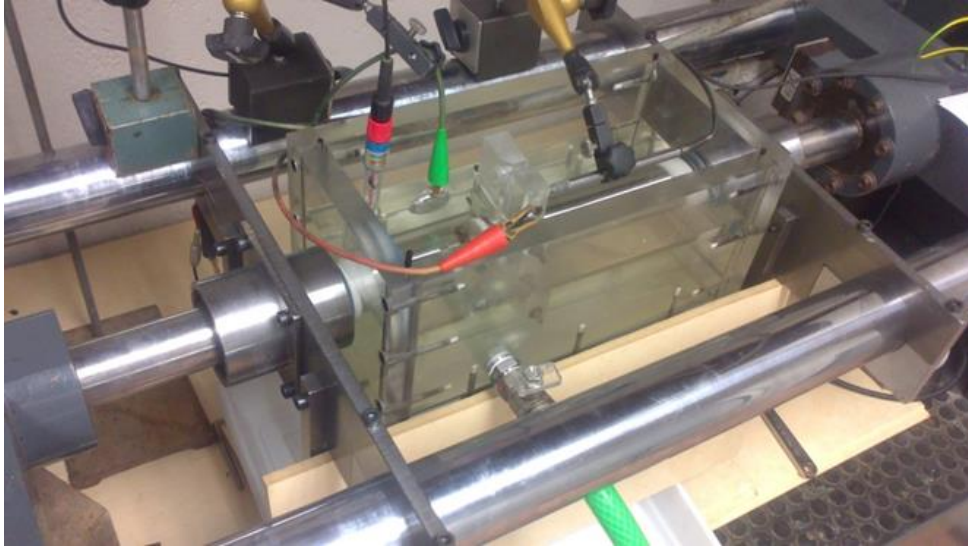
Figure 9. SPT specimen while being tested in environment in the device designed.

- Embrittled samples tested in continuous exposition to the environment at a very slow rate, 500 times lower than the conventional rate, of 5E-5 mm/s that has been previously employed by some authors [5,6,9,10]. These tests were carried out in the device presented in Figure 9, a detail is shown in Figure 10.
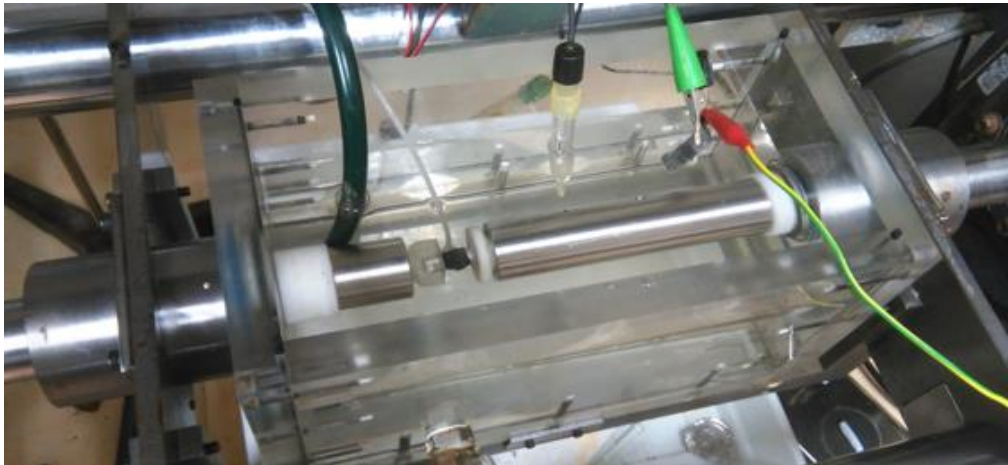
Figure 10. SPT device for testing samples submerged in environment.

- Embrittled samples tested in continuous exposition to the environment under static loads. A set of samples were tested using decreasing imposed loads, which produced decreasing punch rates in the zone II of the curve, up to that load that was not enough to produce any cracking departing from the edge of the notch. After embrittling, the load was softly applied by an endless screw system on the specimen subjected to the environment. For the purpose of this test, the experimental device presented in Figure 11 was designed and built.
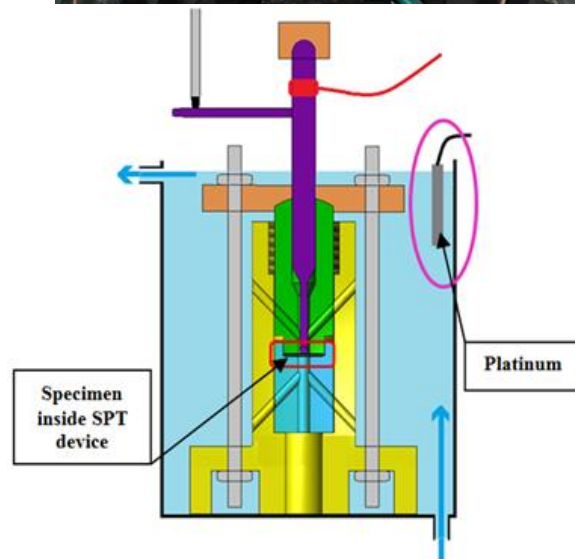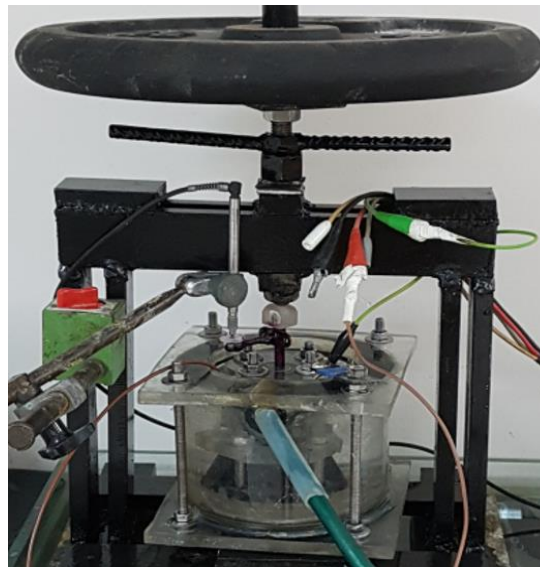
Figure 11. Experimental device and schematic for performing SPT tests in environment under static load.

3. Results

3.1. Standard Fracture Mechanics tests on C(T) specimens at slow rates

Figure 12 shows the load-COD registers and the fractographic images obtained from the C(T) samples tested in environment. By applying [13,16] values of KIEAC=32.62MPA*m1/2 and KIEAC=30.08MPA*m1/2 were obtained from the samples tested at 6E-8 and 6E-9 m/s respectively. The curves shape tends to lower maximum loads and COD values (lower energy) when the testing rate is slower. There is just a slight influence on the fracture toughness due to a similar crack initiation micromechanism, as presented in the fractography, but the sample at the lower rate develops more brittle processes during propagation, which explains such a mechanical difference between both curves. The slower the rate, the higher enough the time for Hydrogen trapped in the material to get activated and diffuse to the new cracking areas, allowing all the embrittling capacity of the environment. A clear environmental effect can be appreciated in the material, as a result of brittle fracture in a mixed mode of transgranularity and grain boundaries separation by cracking. It can also be observed a slightly more brittle cracked system in the most aggressive situation.
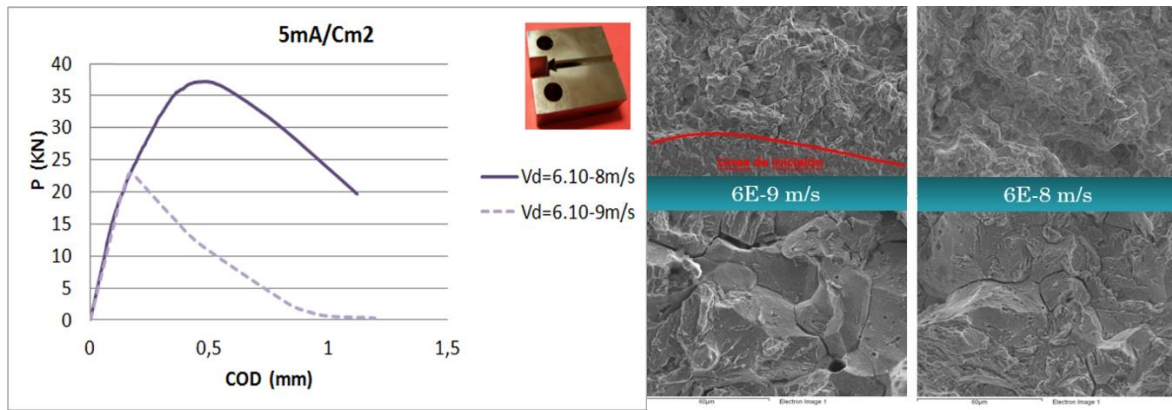
Figure 12. Experimental curves and fractographic images from conventional fracture mechanics tests.

3.2. SPT tests on pre-embrittled samples tested in air at conventional rates of 0.01 and 0.002 mm/s

Figure13 presents the curves and fractography form the SPT tests performed on pre-embrittled samples tested in air at conventional rates (0.01 and 0.002 mm/s). The register form an SPT test of the material as received is superposed for comparison (black line). It can be observed that the exposition to the environment caused an important embrittlement in the material traduced in loss of mechanical properties. The shape of the curve, that was the typical form a ductile material (black line) is now of a total brittle typology. Comparing the curves from tests at 0.01 and 0.002 mm/s, as well as its fractography, a clear difference cannot be found.
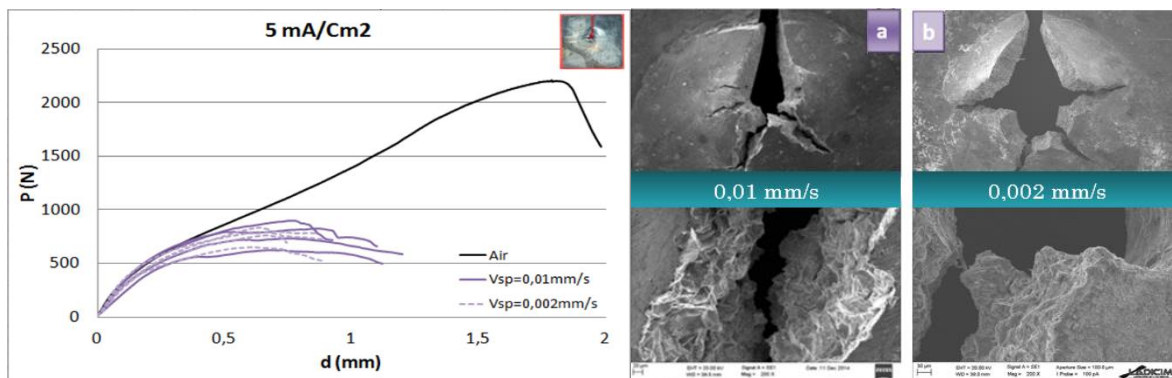
Figure 13. SPT curves and fractographic images from pre-embrittled SPT samples tested in air at conventional rates. SPT curve of as-received SPT test is superposed for comparison (in black).

3.3. SPT tests on embrittled samples tested in environment at conventional rates of 0.01 and 0.002 mm/s

Figure 13 presents the curves and fractography form the SPT tests performed on embrittled samples tested in environment at conventional rates (0.01 and 0.002 mm/s). The register form an SPT test of the material as received is superposed for comparison (black line). In this case, the environment produced again an important embrittlement, showing the SPT curves a typical brittle shape and a decrease of properties compared to the as received curve (black line). Regarding the fractography for this case, a mixed mode can be observed for both rates (0.01 and 0.002 mm/s), but slight differences can be found between them. The lower punch rate, 0.002 mm/s, shows a more brittle system that presents a slightly higher transgranularity and grain boundaries separation than 0.01 mm/s sample, and it is nearly as brittle as the one presented by fracture mechanics tests (Figure 12).
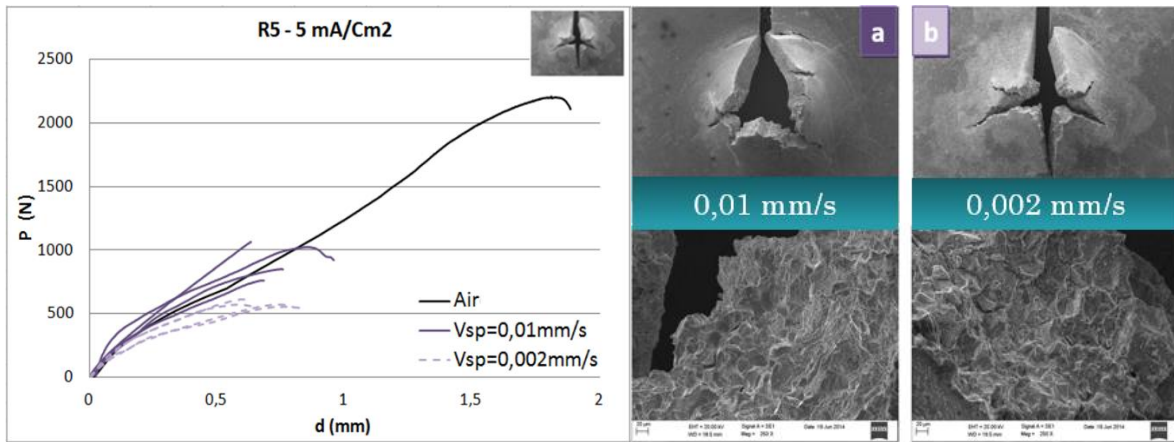
Figure 14. SPT curves and fractographic images from embrittled SPT samples tested in environment at conventional rates. SPT curve of as-received SPT test is supperposed for comparison (in black).

3.4. SPT tests on embrittled samples tested in environtment at very low rate of 5E-5mm/s

Figure 15 presents the curves and fractography form the SPT tests performed on embrittled samples tested in environment at a very low rate proposed by [6] (5E5-5 mm/s). The register form an SPT test of the material as received is superposed for comparison (black line).
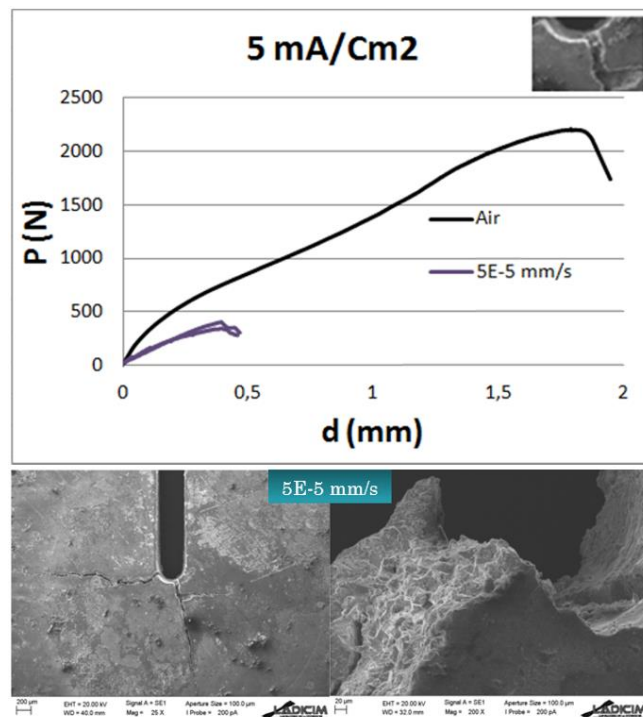
Figure 15. SPT curves and fractographic images from embrittled SPT tested in environment at very slow rate.

The registers exhibit once more a brittle typology, that is enhanced by the very slow rate (5E-5 mm/s), which gives the Hydrogen time enough to develop all of its embrittling and damaging power to the microstructure. From the fractographic images, it can be stated that a clearly brittle pattern in a mixed mode is presented, showing transgranularity and grain boundaries separation in a similar magnitud to the one presented on conventional fracture mechanics tests on C(T) samples (Figure 12).

3.5. SPT tests on submerged samples tested in environtment under static load

Figure 16 shows the registers displacement-time, and presents the macrographic pictures of the samples tested by this methodology. The imposed loads produced a punch rate developed by the flexibility variation of the cracked sample when developing new cracking areas, due to its exposition to the combination of aggressive environment and applied load, as stated in [11]. The two highest loads produced the failure in 5 minutes and less than 4 hours developing rates around E-4 and E-5 mm/s. The rest of the samples reached a quasi-stable zone II of cracks evolution, resulting this in rates in the range of E-6 to E-7 mm/s. Due to the conclusion obtained from Figure 15, where the micromechanism shown seemed to be equivalent to the one presented for conventional fracture mechanics tests, no fractographic analysis were carried out.
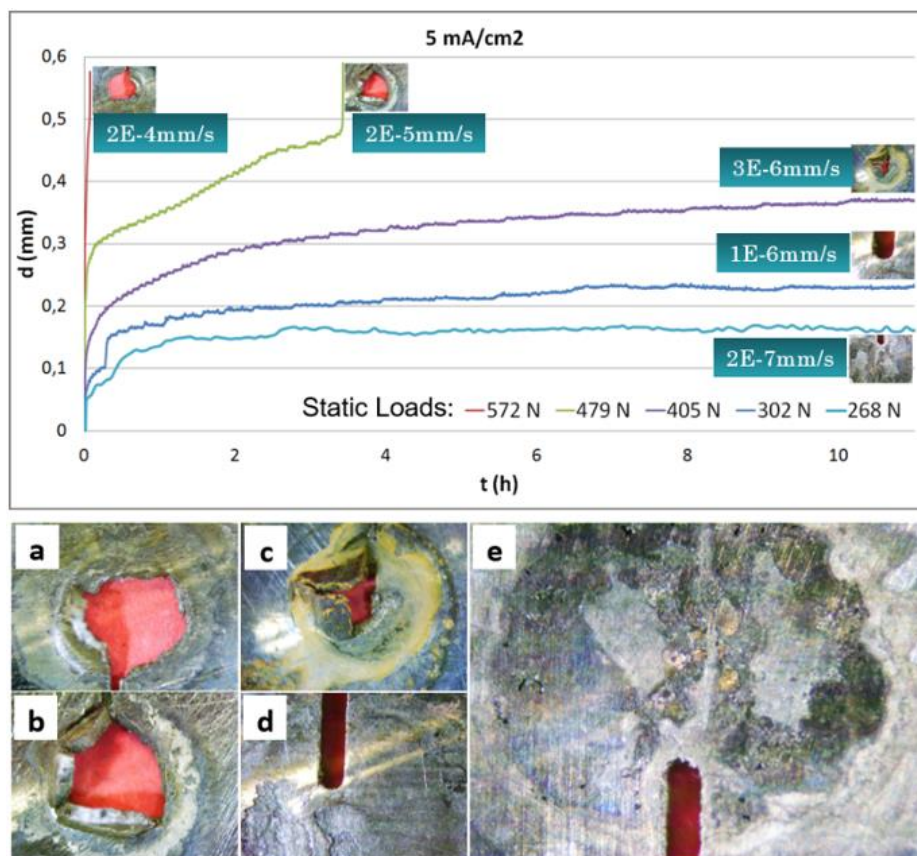
Figure 16. Displacement-time curves and macrographs from embrittled SPT samples tested in environment under static loads.

4. Discussion

A brittle fracture mixed mode can be observed for pre-embrittled samples at both rates (0.01 and 0.002 mm/s), but its intensity seems to be less brittle than the cracked system presented on Figure 12 for conventional fracture mechanics tests. There is a competition between two effects taking place. On the one hand, the lower the punch rate is, the more time given to the trapped hydrogen to diffuse to the new cracking areas and its close zones of plasticity causing its embrittling effect. But on the other hand, the lower the rate is, the more time takes the test to be performed, so a higher quantity of Hydrogen can diffuse out of the sample due to its reduces thickness (0.5mm), not being able to cause any embrittlement any more. Ergo, the profit by lowering the punch rate is compensated by the diffusion out of the sample; this dual effect will be in function of the material microstructure and hydrogen trapping net [31].

Even if is clear that the SPT pre-embrittled samples are capable of reproducing HE situations, the aforementioned fact points clearly that a more accurate way to reproduce the micromechanisms from conventional fracture mechanics tests is needed. A way to solve this situation was performing SPT tests on samples exposed to a continuous source of Hydrogen, by submerging them in the environment. Despite the 0.01 mm/s SPT curves don't differ much from the SPT pre-embrittled samples (Figure13) and tested in environment ones (Figure14), for tests in

environment a clearer difference between both rates (0.01 and 0.002 mm/s) can be appreciated (Figure 14). Slower punch rate curves (0.002 mm/s) show a clear reduction of their mechanical properties (lower maximum load and displacement) from 0.01 mm/s ones, being also placed lower than their homologous at 0.002 mm/s pre-embrittled curves (comparing Figures 13 and 14). Thus, it can be stated that carrying out the test submerged in the environment has a clear influence. It seems that submerging the embrittled samples during the test, and reducing the punch rate in order to allow the Hydrogen time enough to diffuse to the cracking plastic zones, is the way to reproduce the micromechanisms taking place during conventional fracture mechanics test accurately.

In a further step, SPT embrittled samples were tested in environment at a very low rate (5E-5 mm/s). At the first look at the graphs, its mechanical response results poorer than the samples tested in environment at conventional rates and a lot poorer than the SPT test of the material as received (Figure 15). The registers exhibit once more a brittle typology, that is enhanced by the very slow rate (5E-5 mm/s), which gives the Hydrogen time enough to develop all of its embrittling and damaging power to the microstructure. From the fractographic images, it can be stated that a clearly brittle pattern in a mixed mode is presented, showing transgranularity and grain boundaries separation in a similar magnitude to the one presented on conventional fracture mechanics tests on C(T) samples (comparing Figure 15 and Figure 12). Thus, the rate imposed by this methodology (5E-5 mm/s) can reproduce the same micromechanisms taking place during conventional fracture mechanics tests.

In order to study the effects for lower values of the rate, submerged SPT tests in environment under static load were performed. A set of samples was tested using decreasing imposed loads, which produced decreasing punch rates in the quasi-constant punch displacement zone (zone II from Figure 5), up to the load that was not enough to produce any cracking departing from the edge of the notch. As presented in Figure 16, the two highest loads produced the failure in 5 minutes and less than 4 hours developing rates around E-4 and E-5 mm/s, but the rest of the samples reached a quasi-stable zone II of cracks evolution, resulting this in rates in the range of E-6 to E-7 mm/s. For the punch rates developed of E-6 to E-7 mm/s, Hydrogen will have time enough to cause all of its embrittling capacity, so micromechanisms will be alike to those from Figure 15.

Thus, it can be stated that the static load SPT test is an appropriate methodology to reproduce HE situations. Allowing the system to be auto-cracked by the load imposed, it is assured the application of a rate slow enough to produce the HE micromechanisms present in real scenarios. On the other hand, the disadvantage of this method is the need to test several samples, up to finding the one that does not produce any cracking from the edge of the notch of the specimen.

5. Conclusions

A mechanical analysis of the curves together with a fractographic study of the micromechanisms presented by the samples tested at different rates was carried out. Pre-embrittled SPT notched samples were tested in air at conventional rates of 0.001 and 0.002 mm/s, and embrittled samples were tested in environment from rates of 0.01 mm/s to static load tests, that reached up to E-7 mm/s. Form this study, it is concluded that:

- Very slow rates are necessary to perform SPT characterizations in environment.
- This makes necessary the continuous exposition of the sample to the embrittling environment, i.e. being submerged during the hole test.
- Tests at rates of 5E-5 mm/s, or lower, showed similar micromechanisms than those from conventional fracture mechanics tests on C(T) samples for the same environment.
- Static load tests developed punch rates of around E-6 to E-7 mm/s, as a result of the system's flexibility variation assisted by the environment. Even if this technique seemed suitable, it demands an excessive amount of material and time, as it needs to tests a set of samples for each environmental condition. Tests in environment at punch rates around E-6 mm/s seem to be a more suitable option, ergo rates 10,000 times slower than the conventionally used for SPT tests in air [14,32].

As a general conclusion, to perform SPT applications to HE scenarios, is recommended to employ embrittled notched samples tested completely submerged in the environment at a range of rates of around E-6 mm/s. By doing so, it will be assured to reproduce the micromechanisms taking place during real processed.

References

1. Hamilton J.M., "The challenges of Deep-Water Artic Development", International Journal of Offshore and Polar Engineering, 21 (4), (2011), 241-247.
2. Tiwari G.P.; Bose A.; Chakravartty J.K.; Wadekar S.L.; Totlani M.K.; Arya R.N.; Fotedar R.K., "A study of internal hydrogen embrittlement of steels", Materials Science And Engineering A, 286 (2000) 269-281.
3. Rehrl J.; Mraczek, K.; Pichler, A.; Werner, E. "Mechanical properties and fracture behavior of hydrogen charged AHSS/UHSS grades at high- and low strain rate tests", Materials Science & Engineering A, 590 (2014) 360-367.
4. ISO 7539:2011; Parts 1 to 9 "Corrosion of metals and alloys"
5. Arroyo B., "Caracterización mecánica de aceros de alta y media resistencia en condiciones de fragilización por hidrógeno mediante ensayos Small Punch", Doctoral Thesis, University of Cantabria, 2017.
6. Tao B.; Kaishu G., "Evaluation of stress corrosion cracking susceptibility of stainless steel 304L welded joint by small punch test", Material and Design, 561 52 (2013), 849-860.
7. García T.E.; Rodríguez C.; Belzunce F.J.; Peñuelas I.; Arroyo B. "Development of a methodology to study the hydrogen embrittlement of steels by means of the small punch test", Materials Science & Engineering A, 626 (2015), 342-351.
8. García T.E.; Rodríguez C.; Belzunce F.J.; Cuesta I.I., "Effect of hydrogen embrittlement on the tensile properties of CrMoV steels by means of the small punch test", Materials Science & Engineering A, 664 (2016), 165-176.
9. Arroyo B.; Álvarez J.A.; Lacalle R., "Study of the energy for embrittlement damage initiation by SPT means. Estimation of KEAC in aggressive environments and rate considerations", Theoretical and Applied Fracture Mechanics, 86 (2016), 61-68.
10. García T.E.; Arroyo B.; Rodríguez C.; Belzunce F.J., Álvarez J.A., "Small punch test methodologies for the analysis of the hydrogen embrittlement of structural steels", Theoretical and Applied Fracture Mechanics, 86 (2016), 89-100.
11. Arroyo B.; Álvarez J.A.; Lacalle R.; Uribe C.; García T.E.; Rodríguez C., "Analysis of key factors of hydrogen environmental assisted cracking evaluation by small punch test on medium and high strength steels", Materials Science and Engineering A, 691 (2017), 180-194.
12. Arroyo B.; Álvarez J.A.; Lacalle R.; González P.; Gutiérrez-Solana F., " Using Small Punch tests in environment under static load for fracture toughness estimation in hydrogen embrittlement", IOP Conference Series: Materials Science and Engineering, Volume 272, Issue 1, (2017), Article number 012033.
13. ASTM E-1820-01, "Standard Test Method for Measurement of Fracture Toughness", Annual Book of ASTM Standards, 2001.
14. CWA 15627, "Small Punch test method for metallic materials, Part A: Code of practice for Small Punch creep testing, Part B: Code of practice for Small Punch testing for tensile and fracture behavior", Documents of CEN WS21, Brussels, 2007.
15. ASTM E-8-11. "Standard test methods for testing of metallic materials".
16. ASTM E399-12. "Standard test methods for Linear-Elastic Plane-Strain Fracture Toughness KIc of Metallic Materials ". An ASTM designation number identifies a unique version of an ASTM standard.
17. Álvarez J.A., "Fisuración inducida por hidrógeno de aceros soldables microaleados. Caracterización y modelo de comportamiento", Doctoral Thesis, University of Cantabria, 1998.
18. Álvarez J.A.; Gutiérrez-Solana F., "An elastic-plastic fracture mechanics based methodology to characterize cracking behaviour and its applications to environmental assisted processes", Nuclear engineering and design, vol. 188, Pp. 185-202, 1998.
19. Pressouyre G.M.: PH.D. Thesis, Carnegie Mellon University, 1977.
20. Eskner M.; Sandstrom R., "Mechanical property using the small punch test", Journal of Testing and Evaluation, vol 32, Nº 4, January 1995, pp. 282-289.
21. Lacalle R.; Álvarez J.A.; Gutiérrez-Solana F., "Use of small punch notched specimens in the determination of fracture toughness", ASME 2008 Pressure Vessels and Piping Conference, 66 (2008), 1363-1369.
22. Finarelly D.; Roedig M.; Carsughi F., "Small Punch Tests on Austenitic and Martensitic Steels Irradiated in a Spallation Environment with 530 MeV Protons", Journal of Nuclear Materials 328, 2004, pp. 146-150.

23. Kim M.C.; Oh Y.J.; Lee B.S., "Evaluation of ductile-brittle transition temperature before and after neutron irradiation for RPV steels using Small Punch tests" Nuclear Engineering and Design 235, 2005, pp. 1799-1805.
24. Lacalle R., "Determinación de las propiedades en tracción y fractura de materiales metálicos mediante ensayos Small Punch". Doctoral Thesis, University of Cantabria, 2012.
25. Sedriks A.J., "Stress corrosion cracking test methods", National association of corrosion engineers, 1989.
26. Pressouyre G.M., "A classification of hydrogen traps in Steel", Metallurgicall transactions A, 10 (1979), 1571-1573.
27. Gutiérrez-Solana F.; Valiente A.; González J.J.; Varona J.M., "Strain-based fracture model for stress corrosion cracking of low-alloy steels", Metallurgical and Materials Transactions A, 27A (1996), 291-304.
28. Lacalle R.; Álvarez J.A.; Gutiérrez-Solana F., "Use of small punch notched specimens in the determination of fracture toughness", ASME 2008 Pressure Vessels and Piping Conference, 66 (2008), 1363-1369.
29. Arroyo B.; Álvarez J.A.; Lacalle R., "Analysis of the small punch test capability to evaluate the response of high strength steels facing HIC or SCC", American Society of Mechanical Engineers, Pressure Vessels and Piping Division (Publication) PVP, Volume 6B-2016, (2016), Code 125172.
30. Arroyo B.; Álvarez J.A., "Dispositivo para la realización de un ensayo de punzonado en condiciones de sumersión en un solución líquida", Spanish patent, University of Cantabria, 2015.
31. Pressouyre G.M.; Bernstein, I.M. "An example of the effect of hydrogen trapping on hydrogen embrittlement", Metallurgical transactions, vol. 12, nº A, pp. 835-844, 1981.
32. EN Standard Working Draft WI, "Metallic materials - Small punch test method" Documents of ECISS/TC 101, AFNOR. 2018.

Evaluation of ductile-brittle transition temperature of anisotropy material by small punch test with U-shaped notch

K. Guan [1]*, D. Wang [1], J. Dobrovska [2], K. Matocha [2]

1 School of Mechanical and Power Engineering, East China University of Science and Technology, 130 Meilong Road, Shanghai, China 200237; guankaishu@ecust.edu.cn
2 Faculty of metallography and material engineering, Technical university of Ostrava
* Correspondence: guankaishu@ecust.edu.cn; Tel: +86-131-662-13046

Abstract: Miniature and standard specimens, were cut from the anisotropy materials with axial, central and radial directions to study the mechanical property. In the paper, main research focused on the small punch test (SPT) with un-notched and U-shaped notched specimen in low temperature. Through the small punch energy variation with temperature, the ductile-brittle transition temperature by the small punch test (T_{SP}) can be determined. The results indicated that there was no obvious difference among three different directions in transformation temperature of SPT with un-notch specimens, and it cannot represent upper plateau impact energy of three different directions. And the SPT with U-shaped notched specimens can determine the differences of upper plateau fracture energy of three different directions. Therefore, SPT with U-shaped notch specimens was more useful to evaluate the material anisotropy.

Keywords: Small punch test; Low temperature; Ductile-brittle transition temperature; U-notch grooves specimens; Anisotropy

1. Introduction

The small punch test (SPT) originated in the 1980s and was proposed by Baik [1] et al, by which various material properties could be obtained from a fairly small disk specimen with an almost nondestructive. The small-punch testing method has been applied successfully to evaluate a variety of material mechanical properties, such as yield strength, rupture strength, ductile-brittle transition temperature, fracture toughness [2] and creep performance [3]. The index of material embrittlement commonly was represented by the ductile-brittle transition temperature by the small punch test (T_{SP}), which is associated with standard ductile to brittle transition temperature by Charpy Impact test (T_{CVN}) [4]. Due to the bidirectional force, the specimens were insensitive to the anisotropy by SPT. The mechanical properties of each anisotropic material cannot be obtained in different directions by SPT. This paper study the A350 flanged forging by changing the conventional pattern specimens of SPT, in order to effectively characterizing the anisotropic materials, which has certain guiding significance for evaluating the toughening brittle characteristics of anisotropic materials and also has a certain help for the improvement of the technology of small punch test in the future research.

2. Test procedure

2.1 Chemical composition and mechanical performance test

In order to compare the correlation with the small punch test, the chemical composition analysis, tensile test and impact test of the material must be carried out.

2.1.1. Chemical composition analysis

The test material in this paper is A350 flanged forging, and its chemical composition was shown in Table 1, which conformed to the ASTM A350 standard.

Table 1. Chemical composition of A350 steel (wt％).

Material	C	Mn	Si	Cr	Mo	Ni	Cu	V	Nb	S	P
A350	0.20	0.86	0.2	0.12	0.05	0.098	0.14	< 0.001	< 0.001	0.015	0.025
Standard	≤ 0.30	0.60~ 1.35	0.15~ 0.30	≤ 0.030	≤ 0.12	≤ 0.040	≤ 0.040	≤ 0.030	≤ 0.02	≤ 0.040	≤ 0.035

2.1.2. Tensile test

Tensile test specimens were respectively carried along the axial direction L, circumferential direction C and radial direction R. According to Table 2, the mechanical properties on the materials of circumferential and radial basic are quite, while properties of axial direction on mechanical are the worst. The axial yield strength and tensile strength are slightly smaller, and the percentage elongation after fracture is obviously inadequate.

Table 2. The properties comparison of A350 flange material for three different directions.

	Yield Strength （Rel）	Tensile Strength （Rm）	Percentage elongation after fracture A (%)
Axial direction L	240.9	474.5	10.8
Central direction C	261.8	502.2	26.4
Radial direction R	258.4	498.6	25.6
Standard A350-LF2-1	≥250	485~655	≥22

2.1.3. Impact test

In order to investigate the anisotropy of the impact toughness of A350 flanged forging, the flange should be sampled according to the fracture surface with different notch direction. For the impact samples, the axial direction (L), circumferential direction (C) and radial direction (R) are respectively used to the length direction of the impact sample. The Charpy impact test specimens sampling are shown in Figure 1, which cover the impact toughness of flange in all directions.

Figure 2 showed that CVN curves at three different temperatures of A350 samples. The Boltzmann function was used to fitting the ductile-brittle transition temperature curve. The ductile-brittle transition temperature in the three different directions of the A350 material was determined:

C-L direction T_{CVN}=205.4K;

R-L direction T_{CVN}=193.8K;

L-C direction T_{CVN}=199.4K.

From the ductile-brittle transition temperature, the result was R-L > L-C > C-L, which had a little difference. From the upper shelf impact energy, the result was C-L > R-L > L-C, which had obvious difference.
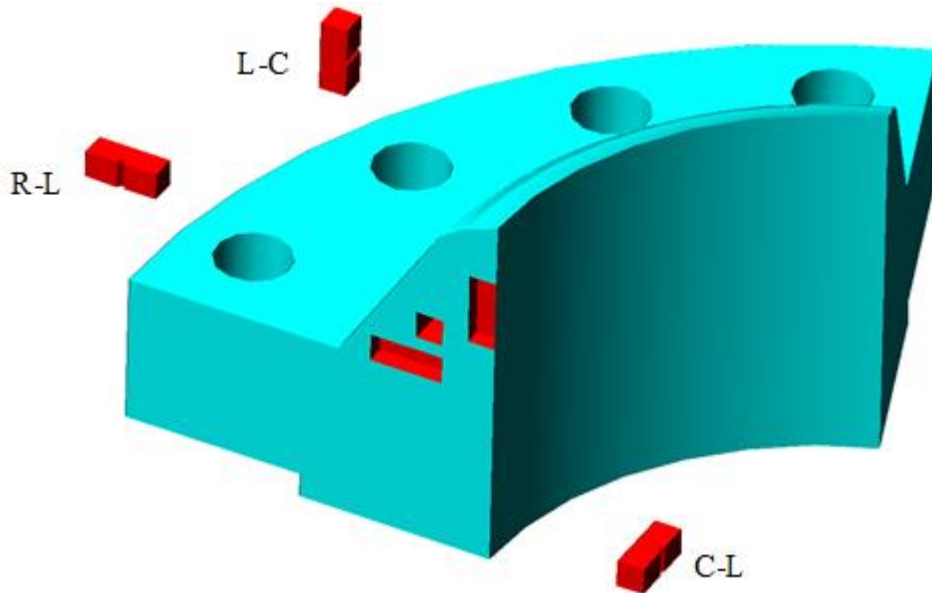
Figure 1. The Charpy impact specimen sampling number.
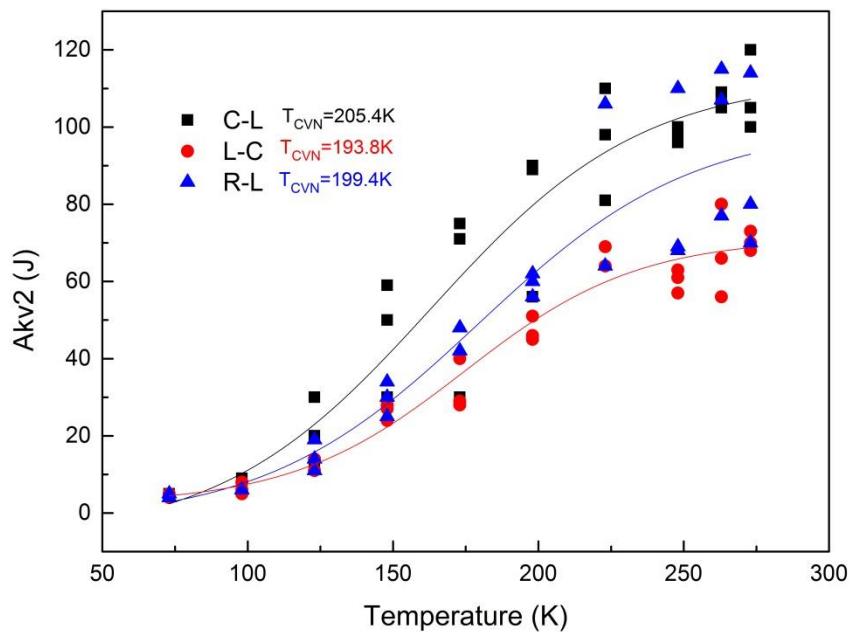
Figure 2. CVN curves at three different temperature of A350 samples.

2.2 Disk samples of SPT

SPT samples are disks with a diameter of 10 mm and thickness of 0.5 ± 0.005 mm with a good finish (P1200). Figure 3 showed the specimen with U-shaped notch. Both surfaces are parallel. The specimen with U-shaped notch was processed by Electric discharge method on the basis of sample without gap with a diameter of 0.18 mm. The size of the sample with U-shaped notch was shown in Figure 4.
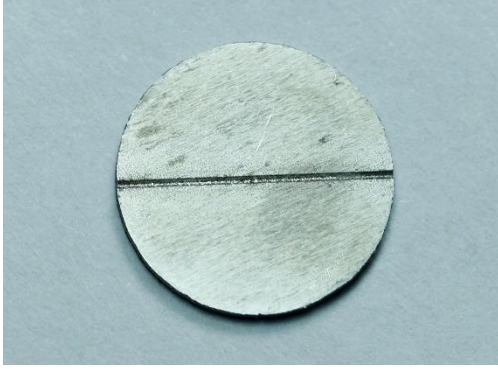
Figure 3. U-notched specimen of SPT.
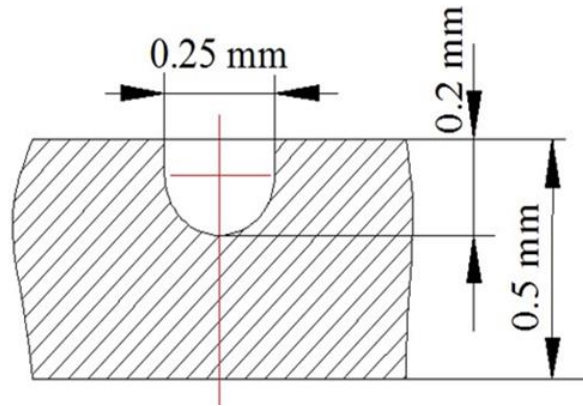
Figure 4. Size of U-notched specimen.

2.3 SPT at low temperature

The experiments were carried out in three different directions at low temperature (0°C, -25°C, -50°C, -50°C, -75°C, -100°C, -125°C, -135°C, -145°C, -155°C, -155°C, -175°C, -175°C, -185°C and -196°C), and the experimental results were processed.

As shown in Figure 5, the samples of the small punch were carried out in three different directions of the A350 material respectively, and the directions were the same as that of the Charpy impact sample.

Finarelli [5] observed that in the process of the small punch test, the crack appears near the peak load point (F_m) and gradually expand, until the break. According to the GB for SPT [6], the fracture energy of small punch test specimen is abbreviated as E_{SP} is commonly derived from integrating the load-displacement curve along the X axis with defining 80% of F_m point for integral upper limit. In the impact test, the relationship between impact energy and test temperature is more commonly used by Boltzmann function and hyperbolic tangent function [7]. Some studies showed that the former has a good correlation coefficient and a little error. Therefore, Boltzmann function is used to fit the relationship between the fracture energy of the small punch and the experimental temperature.

(**a**) Axial direction

(b) Central direction

(c) Radial direction
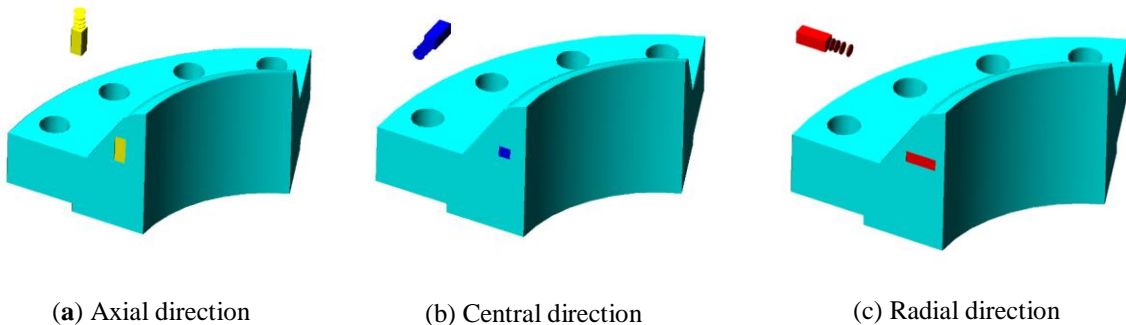
Figure 5. Small punch sampling of A350 flange material in different directions.

Boltzmann function is $A = \dfrac{A_1 - A_2}{1 + e^{\frac{(x - x_0)}{dx}}} + A_2$

Among them:

A_2 is the upper shelf of the ductile-brittle transition curve.

A_1 is the lower shelf of the ductile-brittle transition curve.

X_0 represents the energy transition temperature ETT50.

There are two methods to determine the ductile-brittle transition temperature of the small punch test [8-10].

1. T_{SP} is identified as the half of peak energy point in the energy curve.

2. T_{SP} is identified as the temperature of the average value of the peak energy and the lower shelf if the lower shelf can be appeared.

The first determination was used in this article. And the first half of the curve was fitted with Boltzmann function, and the second half was fitted with a straight line. The fracture energy fitting curve of three different directions was shown below.
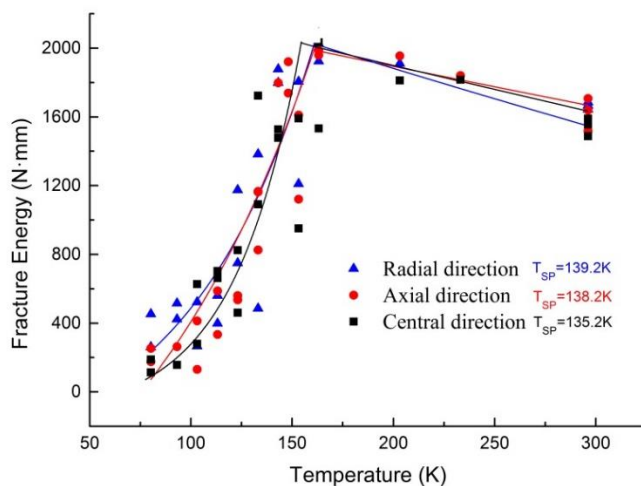
Figure 6. Temperature dependence of fracture energy for A350 material with disk specimens.

Figure 6 showed the fracture fitting curves in three different directions with disk specimens. And the T_{SP} of A350 material was determined by the energy curve method.

Axial direction: T_{SP}=138.2K;

Central direction: T_{SP}=135.2K;

Radial direction: T_{SP}=139.2K.

As shown in Figure 6, the curves in three different directions of the A350 materials are almost the same. And the upper shelf energy and T_{SP} have a little deference in three different directions.

2.4 U-notched samples of SPT at low temperature

Due to conventional small punch test results cannot evaluate the variation of the upper shelf energy for anisotropic material, the small punch test at low temperature was carried out by using the U-notched shape samples.
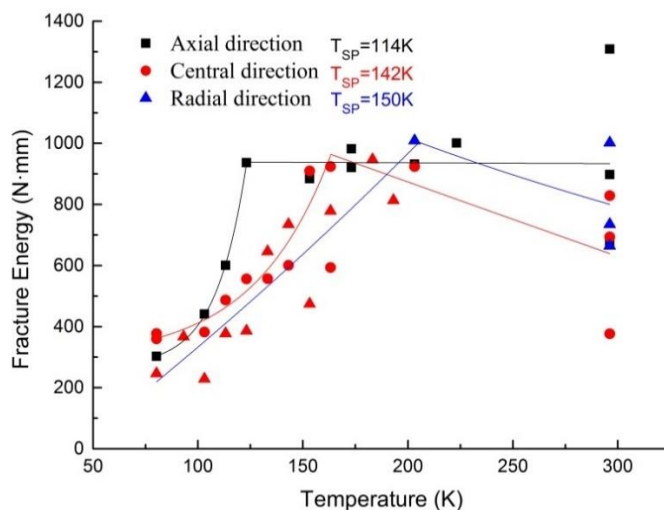
Figure 7. Temperature dependence of fracture energy for A350 material with U-notched specimens.

Figure 7 showed the fracture fitting curves in three different directions with U-notched specimens. And the T_{SP} of A350 material was determined by the energy curve method.

Axial direction: T_{SP}=114K;

Central direction: T_{SP}=142K;

Radial direction: T_{SP}=150K.

As shown in Figure 8, the upper shelf energy and T_{SP} in three different directions of the A350 materials are significantly different.

Figures 8-10 are respectively the fracture energy-temperature relationship curves of the A350 material in three different directions. As can be seen from the Figures, the fracture energy-temperature curves of the U-notched and un-notched specimens are similar. Both have the upper shelf and the transition zone, and the samples of the three different directions have no lower shelf. With the U-notched sample, the fracture energy of the sample reduced, especially on the upper shelf. The fracture energy decreases as the temperature decreases. The difference of the two samples is that the range of transition zone is widened with the U-notched sample.
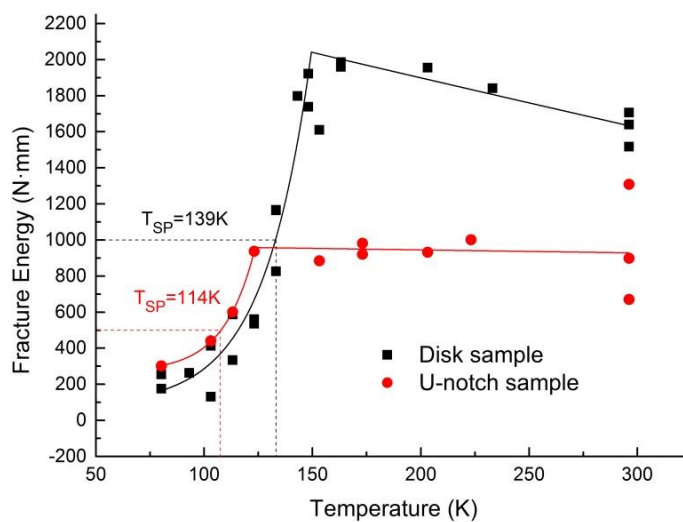
Figure 8. Temperature dependence of fracture energy in axial direction for A350 material.
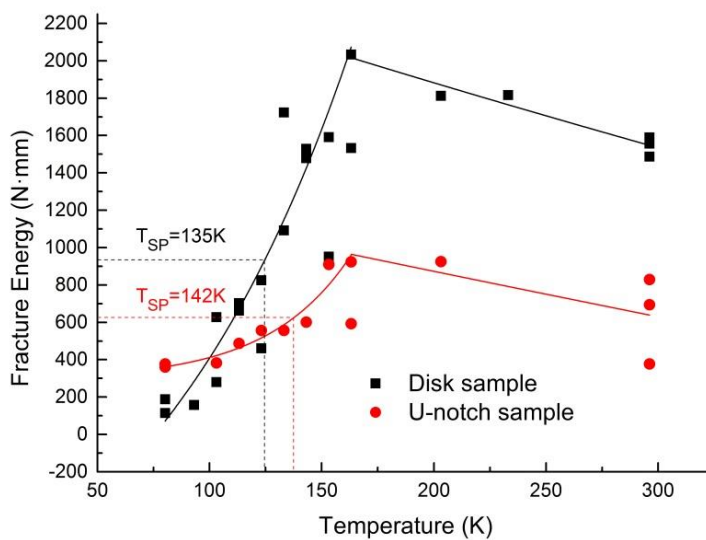
Figure 9. Temperature dependence of fracture energy in central direction for A350 material.
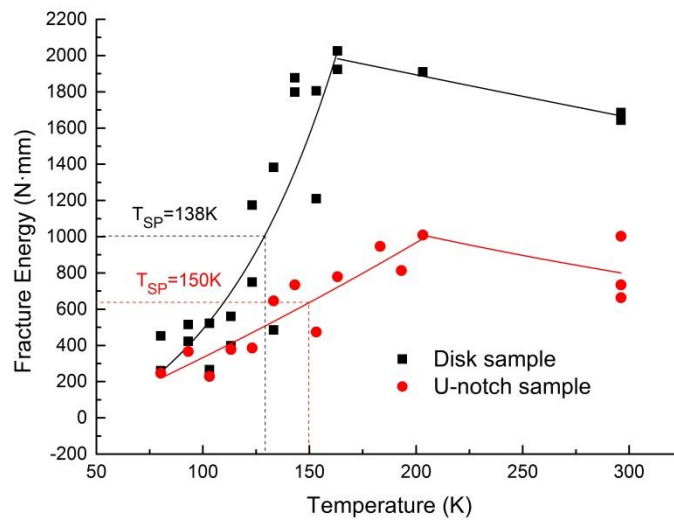
Figure 10. Temperature dependence of fracture energy in radial direction for A350 material.

2.5 Comparison and correlation of small punch test and standard impact test

Table 3 was the results of the T_{SP} of small punch test and T_{CVN} of Charpy impact test for the A350 material. With U-notched specimens, the differences of transition temperature among three different directions are larger than disk specimens. Especially the transition temperature of axial direction is much smaller than the other two different directions, which means the axial direction performance is best. In this case, the force of axial specimen is the combined force of radial and circumferential tensile stress, which is exactly the same as the tensile strength. The transition temperature obtained by small punch test with disk specimens can only be used in empirical correlations with the ductile-brittle transition temperature by the Charpy Impact test [11] and is unable to evaluate the upper shelf impact energy on impact test curves. However, the small punch test with the U-notched specimens can show the difference in the ductile-brittle transition temperature of anisotropic materials in different directions.

Table 3. The comparison of SPT transition temperature of A350 by disk and U-notched specimens and impact transition temperature.

Material	Disk samples T_{SP}/K	U-notched samples T_{SP}/K	Impact test samples T_{CVN}/K
A350 Axial direction (L-C)	139.2	114	199
A350 Central direction (C-L)	135.2	142	205
A350 Radial direction (R-L)	138.2	150	194

3. Discussion

1. The results of conventional tensile test in three different directions of the A350 showed that the A350 has obvious anisotropy and the axial tensile properties is the worst, but the results of Charpy impact test showed that the difference in ductile-brittle transition temperature is a little among three different directions, while the upper shelf impact energy have obvious differences, which is the lowest in axial direction, and is consistent with the tensile properties.

2. The transition temperature and upper shelf impact energy obtained by small punch test and Charpy impact test are consistent in three different directions. So the conventional small punch test can be used to link the T_{SP} and the T_{CVN}.

3. The force of small punch specimens in three different directions is complex. The force of axial direction is the combined force of the radial direction and circumferential direction tensile stress. The force of radial direction is the resultant force of the axial direction and circumferential direction tensile stress. The force of circumferential direction is the combined force of the radial direction and axial direction tensile stress. According to the tensile results, the intensity in axial direction is weaker than the circumferential direction and the radial direction, so the axial sample has a good performance, and the axial T_{SP} should be the lowest. The fracture energy of the sample decrease with the U-notched specimens and the tendency of decline is getting smaller. The fracture energy of the U-notch specimens shifted to the right with the temperature changing, and the transition temperature of the U-notch specimens is obviously changed.

4. Conclusion

1) The study for the anisotropy of A350 material found that the small punch test with disk specimens can be used to link the T_{SP} and the T_{CVN}.
2) The fracture energy of the U-notch specimens shifted to the right with the temperature changing, and the transition temperature of the U-notch specimens is obviously changed.
3) The small punch test with U-notched specimens can effectively reflect the differences of the impact energy in three different directions.

Reference

1. Baik, J.M.; Kameda; J. and Buck, O. "Small punch test evaluation of intergranular embrittlement of an alloy steel." Scripta Metallurgica 17.12(1983):1443-1447.
2. Misawa, T.; et al. "Fracture toughness evaluation of fusion reactor structural steels at low temperatures by small punch tests." Journal of Nuclear Materials 169.12(1989):225-232.
3. Li, Y. and Ŝturm, R. "Determination of Creep Properties From Small Punch Test." ASME 2008 Pressure Vessels and Piping Conference 2008:739-750.
4. Linse, T., et al. "Usage of the small-punch-test for the characterisation of reactor vessel steels in the brittle–ductile transition region." Engineering Fracture Mechanics 75.11(2008):3520-3533. D
5. Finarelli, D.; Roedig, M. and Carsughi, F. "Small punch tests on austenitic and martensitic steels irradiated in a spallation environment with 530 MeV protons." Journal of Nuclear Materials 328.2–3(2004):146-150.
6. GBT 29459.1-2012. "Metallic material- Small punch testing for in-service pressure equipment in Chinese." 2012.
7. Huang, Q. "Fitting Curves to Impact Toughness Date of Nuclear Structure Steel by Computer Program." Journal of Sichuan Union University (1995).
8. Zhao, J.P.; Zhang, X.M. and Shen, S.M. "On the method of data processing for ductile-brittle transition temperature." Petro-chemical Equipment (2004).
9. Zhou, C. and Xia, X. "Regression Analysis of Ductile -Brittle Transition Temperature Curve for CrMo Steel." Pressure Vessel Technology 20.6(2003):13-18.
10. Matsushita, T.; et al. "DBTT Estimation of Ferritic Low Alloy Steels in Service Plant by means of Small Punch Test." Key Engineering Materials 51-52(1991):259-264.
11. Matsushita, T.; et al. "Correlation Between a Charpy V-notch Impact Test and a Small Punch Test in Ductile-Brittle Fracture Mode Transition Behavior." Nihon Kikai Gakkai Ronbunshu A Hen/transactions of the Japan Society of Mechanical Engineers Part A 55.515(1989):1619-1622.

Numerical Investigations of Small Punch Tests for Determining Tensile Properties

M. Kamaya [1]*

[1] Institute of Nuclear Safety System, Inc.

* Correspondence: kamaya@inss.co.jp; Tel.: +81-50-7105-0096

Abstract: Small punch tests were conducted for carbon steel specimens prepared with and without cold working. A digital image correlation technique was applied to measure displacement. Finite element analyses using the true stress-strain curves including post-necking strain could reproduce the load-displacement (LD) curve. Use of the nominal stress-strain curve obtained by the conventional tensile test was not enough to simulate the maximum load. It was found that the maximum load did not depend on the ultimate strength. Therefore, the ultimate strength prediction using the maximum load in the LD curve may not be valid for the general case. On the other hand, the yield strength correlated well with the deflection point in the LD curve. A new equation was proposed to estimate the yield strength that takes into consideration the influence of the specimen thickness.

1. Introduction

The small punch (SP) test has been applied to estimate tensile properties such as the yield and ultimate strengths [1-3]. Since a tiny specimen is used for the SP test, it is possible to determine the tensile properties for a small piece taken from an actual component. The local properties of inhomogeneous materials such as welds also can be obtained by the SP test. The tensile properties are determined from the load-displacement (LD) curve, which consists of four regions [2]: the elastic bending, plastic bending, membrane stretching and failure regions. The LD curve exhibits linear (elastic) deformation at the beginning of the SP test, and then, deflects due to yielding. After yielding, the curve increases almost linearly and peaks before an abrupt load drop due to fracture of the specimen. The deformation of the specimen has been correlated to the stress-strain curve. The yield strength has been correlated to the initial deflection of the LD curve and the ultimate strength has been determined using the maximum load during the SP test [1,2].

Since the deformation of a specimen during the SP test is quite different from that of tensile tests, it is difficult to find a clear correlation between the LD curve and the stress-strain curve. Therefore, determination of the tensile properties from the LD curve has been rather empirical. Finite element analysis (FEA) for various conditions can be an effective tool to get a generalized and comprehensive correlation between the tensile properties and the LD curve. Although it is relatively easy to simulate the elastic and plastic bending regions, it is difficult to reproduce the peak of the LD curve by FEA [3,4]. Since the specimen deforms largely during the SP test, the stress-strain curve over the necking strain is required for precise simulation of the SP test.

In this study, SP tests were conducted for cold worked and non-cold worked carbon steel specimens. Then, FEAs were performed to simulate the tests using stress-strain curves obtained in a previous study [5], in which true stress-strain curves including post-necking strain were determined by an iterative process using FEAs and the local strain measurement technique. By performing FEAs for various conditions, influences of the stress-strain curve and specimen thickness on the determination of the yield and ultimate strengths were discussed.

2. Small punch tests

2.1. Material

The material used for the SP tests was carbon steel plate for welding structures (SM490A in JIS), whose alloying constituents (in wt%) were: C, 0.16; Si, 0.31; Mn, 1.35; P, 0.019; S, 0.004; and V, 0.033. A rolling process was applied to the plate to induce cold working at room temperature. The degree of cold working was quantified from the nominal thickness change of the plate and it was 5%, 10% or 20%. The cold-worked specimens were respectively designated as SM5, SM10 and SM20, while SM0 denoted the specimen free of cold working. The

tensile properties are shown in Table 1 and they were obtained using specimens taken along the rolling direction. The yield strength for the cold-worked specimens was defined by the 0.2% proof strength.

The stress–strain curves are shown in Figure 1. Although the uniform elongation of SM0 was 14.7%, it was only 2.1% for SM20. Therefore, the stress-strain curves for the cold worked specimens are not sufficient to simulate specimen deformation during SP tests. In the previous study [5], the stress-strain curve of the materials was obtained using the iterative procedure as schematically shown in Figure 2. By using the digital image correlation (DIC) technique, the local strain at the root of the hourglass shaped specimen was measured. Then, the stress-strain curve which reproduced the change in load with the local strain was determined by an iterative FEA. Finally, true stress-strain curves were obtained as shown in Figure 1(b).

Table 1. Mechanical properties of carbon steel (room temperature).

Material	Cold working (%)	Yield Strength (MPa)	Ultimate strength (MPa)	Elongation (%)	Reduction in area (%)	Young's modulus (GPa)
SM0	0	365	534	29.7	74.6	208
SM5	5	494	572	24.0	75.6	209
SM10	10	547	592	19.3	71.6	208
SM20	20	607	640	15.0	69.8	207
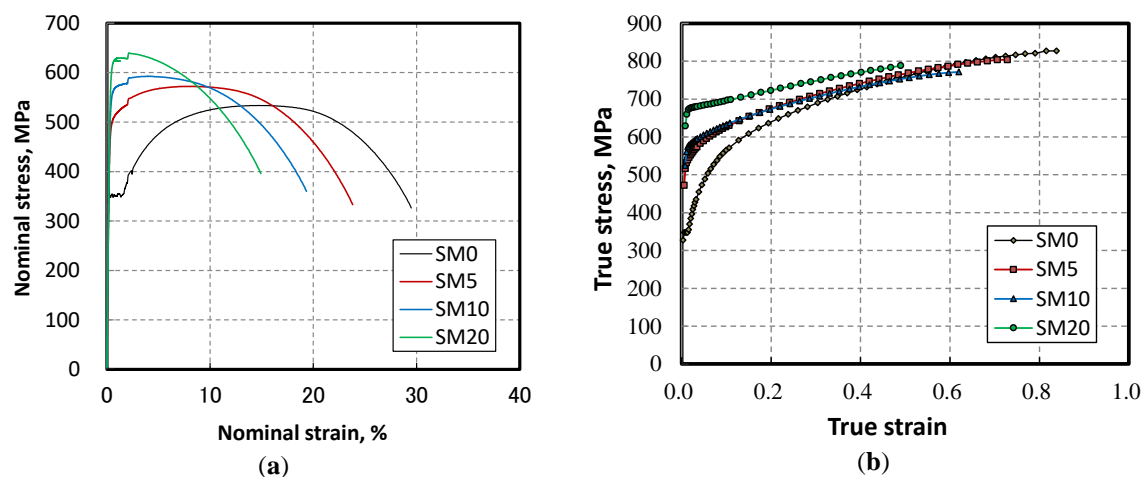
Figure 1. Stress-strain curve of test materials. (a) Nominal stress-strain curve; (b) true stress-strain curve obtained by iterative procedure.

2.2. Test procedure

Disc-type specimens, with a diameter of 8 mm, were used for SP tests. The normal direction of the disc specimen was the same as that of the plate. A single specimen was prepared for SM0, SM5, SM10 and SM20. The thicknesses of the specimen t were 0.4994 mm (SM5), 0.5015 mm (SM20), 0.5041 mm (SM10) and 0.5214 mm (SM0) and the surface was finished using #1200 emery paper.

The specimens were subjected to the SP tests at room temperature using the test device shown in Figure 3. The specimen was fixed by upper and lower dies. The inner diameter of the lower die was 4 mm. No lubrication was applied to reduce friction between the specimen, ball and dies. The ball of 2.3812 mm diameter was indented into the specimen surface at a constant rate of 0.2 mm/m at the cross-head of the tensile test machine.

The displacement was measured using the DIC technique. The lower surface of the specimen was observed by two cameras. In this measurement procedure, the compliance of the test device could be excluded from the displacement measurement.
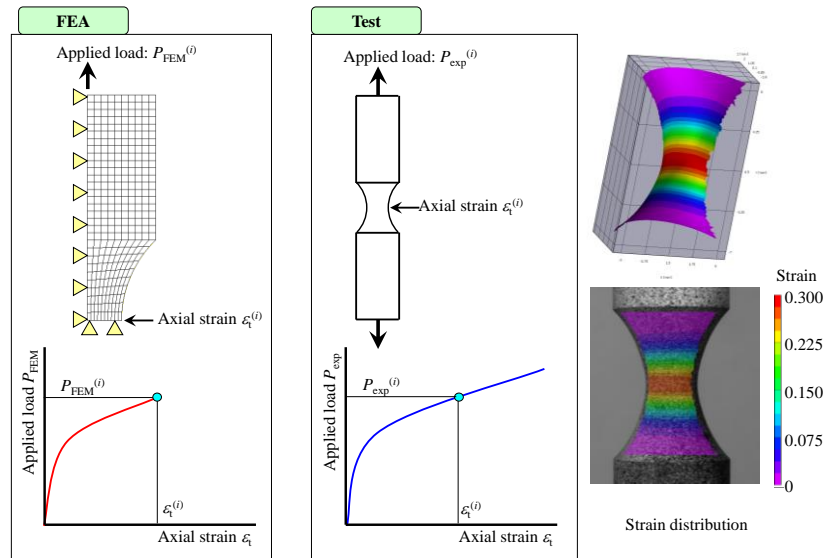
Figure 2. A schematic drawing for the procedure to determine the stress-strain curve using an hourglass shaped tensile specimen (to determine $\sigma_t(i)$ at $\varepsilon_t(i)$).
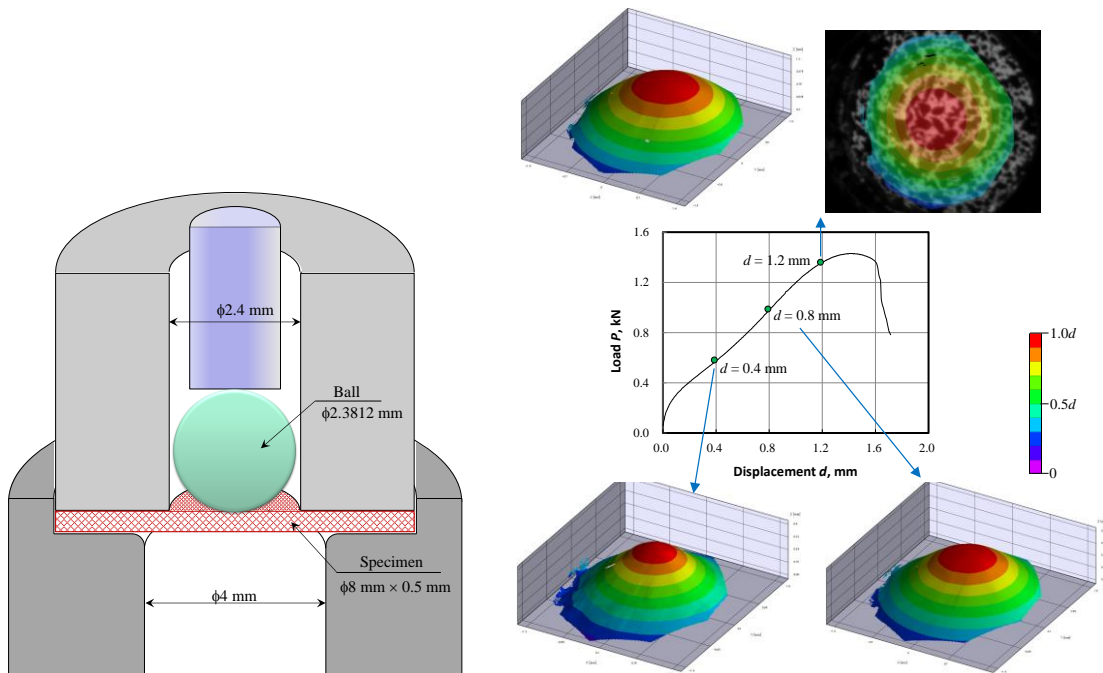
Figure 3. Schematic drawing of SP test device.

Figure 4. Load displacement curve obtained by the SP test using SM0 specimen. The displacement was measured using the DIC technique.

2.3. Test results

Figure 4 shows the LD curve obtained in the test using the SM0 specimen. The DIC technique could successfully measure the displacement field and the maximum peak of the displacement was quantified as the displacement d. The LD curves obtained for each material are shown in Figure 5. The cold working increased the load for the same displacement. Since the SM0 specimen was relatively thick, it showed a relatively large maximum load.

From the LD curve, the yield strength σ_y and ultimate strength σ_u were estimated using the following equations:

$$\sigma_y = \alpha \frac{P_{t/10}}{t^2} \tag{1}$$

$$\sigma_{\mathrm{u}} = \beta \frac{P_{\max}}{t \cdot d_{\max}} .$$

(2)

A line having an inclination that was parallel to the LD curve of the elastic bending region was drawn so that it passed through the point of $d = 0.1t$ at $P = 0$. Then, the load of the cross point of the line and the LD curve was defined as $P_{t/10}$ [1]. The constant $\alpha = 0.364$ was obtained in Ref. [1]. The ultimate strength was estimated using the maximum peak load $P_{\max}$ and the displacement at $P_{\max}$, which is noted as $d_{\max}$. It was shown that $\beta = 0.277$ gave a good estimation for various materials [1]. The estimated yield and ultimate strengths were compared with the tensile test results in Figure 6. Although the estimated ultimate strengths agreed well with the tensile test results, the yield strengths exhibited smaller values.
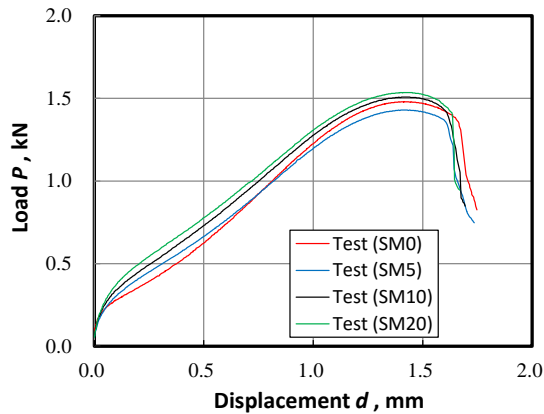
Figure 5. Load displacement curves obtained by the SP tests.
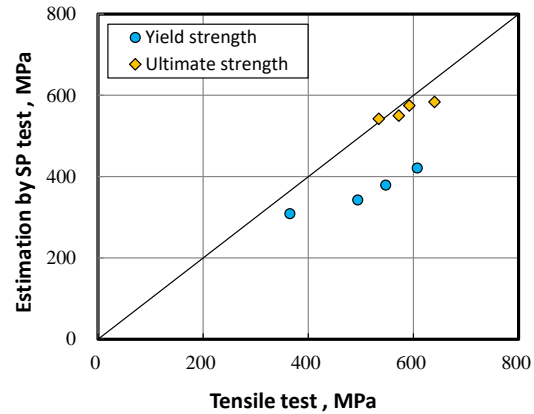
Figure 6. Estimation of the yield and ultimate strengths from load-displacement curves obtained. by the SP tests.
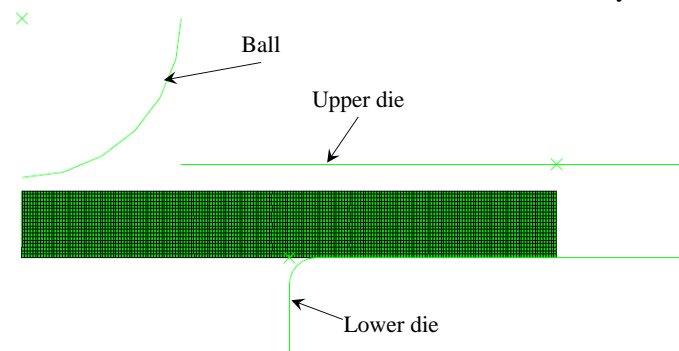
Figure 7. Finite element model for simulating SP tests.

3. Finite element analyses

3.1. Analysis procedure

Isotropic hardening elastic–plastic FEAs were performed using the finite element model shown in Figure 7 together with the stress-strain curves shown in Figure 1(b). The true stress-strain curve was extrapolated to 2.0 in true strain to simulate large deformation. The SP test specimen was modeled with axisymmetric linear reduced integration elements (CAX4R). Due to geometrical symmetries, only one half of the specimen was modeled with the displacement boundary conditions on the plane of symmetry. The upper and lower dies for fixing the specimen and indentation ball was modeled using rigid bodies, which were non-deformable bodies.

First, axial force was applied to the upper die to fix the specimen as done in the test. Then, the ball was moved to press into the specimen. The friction coefficient between the ball and specimen was set to 0.1. ABAQUS standard Version 6.14 was applied as the FEA solver. To simulate large inelastic deformation during the test, the nonlinear geometry option with ABAQUS (the NLGEOM option) was invoked.

3.2. Analysis results

Figure 8 plots LD curves obtained by FEAs together with test results. The FEA simulated well the change in the load with the displacement at the lower surface. Particularly, the result for SM0 specimen was almost identical to the test result. The load of the FEA tended to be larger for the cold-worked specimens, although the maximum load was almost the same as the test results.
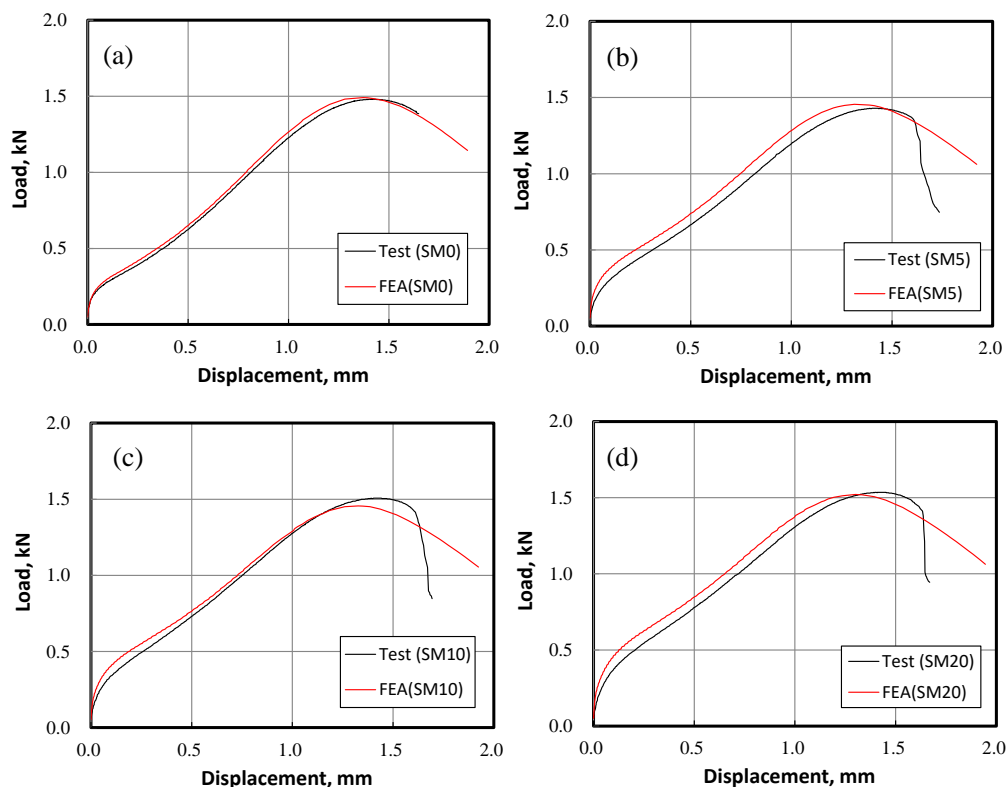
Figure 8. The load-displacement curves simulated by FEAs. (a) SM0; (b) SM5; (c) SM10; (d) SM20.

4. Discussion

4.1. Estimation of ultimate strength

The maximum load P_{max} and the displacement d_{max} were used to estimate the ultimate strength in Equation (2). In order to investigate the correlation between P_{max}, d_{max} and the ultimate strength, FEAs were performed for the various stress-strain curves shown in Figure 9. The curves were modified from that of SM0. The maximum stress of the stress-strain curve used for the previous analysis was sufficiently large, being 1500 MPa corresponding to the true strain of 20. Meanwhile, in Figure 9, it was assumed that the true stresses could not be more than the set values, which were 827, 792, 732 and 649 MPa. It should be noted that these stresses were more than the ultimate strength, which was 612 MPa in the true stress.

Figure 10 shows the LD curves obtained using the stress-strain curves assuming the specimen thickness of t = 0.5 mm. P_{max} and d_{max} were almost the same when the maximum true stress was more than 792 MPa. However, P_{max} and d_{max} decreased apparently when the maximum stress was 732 or 649 MPa, which corresponds to true strain of 0.41 or 0.21, respectively. Since the ultimate strength was 612 MPa, the change in P_{max} and d_{max} was not brought about by the change in the ultimate strength. The peak position seemed to depend not on the ultimate strength as discussed in Kumar et al. [6].

As shown in Figure 6, the ultimate strength can be predicted well by Equation (2) using P_{max} and d_{max}. However, it is just an empirical correlation. It is difficult to say that Equation (2) is valid for a general case.
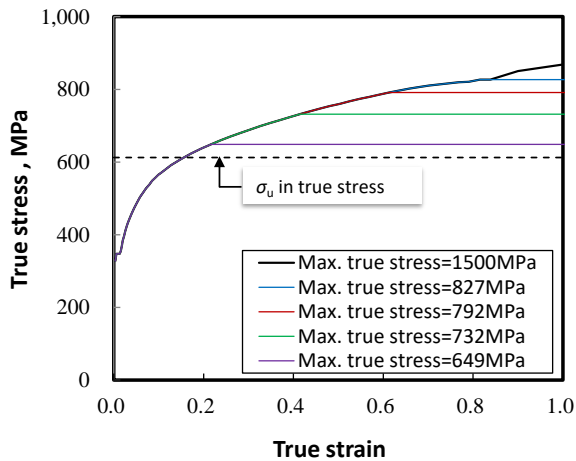
Figure 9. Modeled stress-strain curves used for FEAs. The maximum true stresses were no more than the set values.
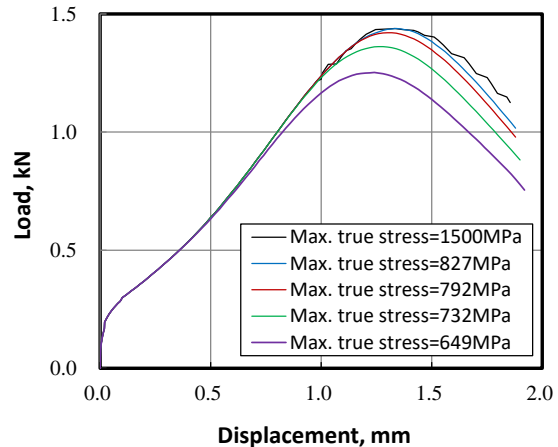
Figure 10. Load-displacement curves obtained using various stress-strain curves (t = 0.5 mm).

4.2. Estimation of yield strength

The yield strength was estimated using $P_{t/10}$ in Equation (1). To investigate the validity of the estimation procedure, the estimation was conducted for the modeled stress-strain curves shown in Figure 11. Simplified bi-linear stress-strain curves were defined using the plastic slopes of E_p = 0, 500, 1000, and 1500 MPa, while the elastic slope (Young's modulus) of 200,000 MPa and yield strength of 200 MPa were assumed to be the same. Figure 12 shows the yield strength estimated by Equation (1) using the LD curve obtained by the simulation. Although the estimated yield strength should be 200 MPa regardless of E_p, it slightly depended on E_p. An almost identical value was obtained when E_p = 1500 MPa, and it was 171 MPa when E_P = 0. Since the change in estimated yield strength was relatively small compared with the wide variation of E_P, it can be concluded that the deflection point in the LD curve correlates well with the yield strength.
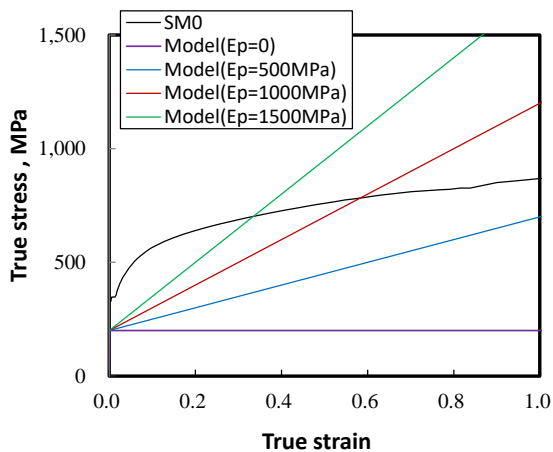
Figure 11. Modeled stress-strain curves used for FEAs.
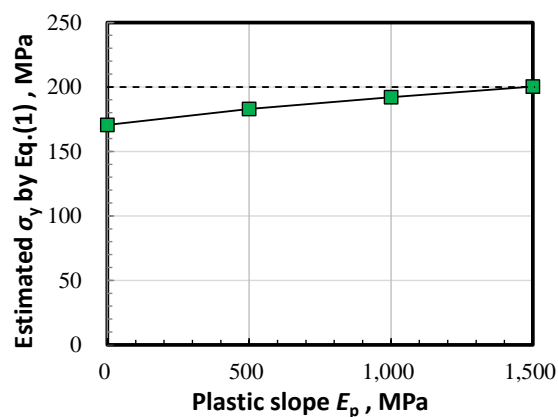
Figure 12. Estimated yield strength obtained using different stress-strain curves (t = 0.5).

The specimen thickness was used to estimate the yield strength in Equation (1). It was pointed out that the use of t^2 was better for correcting influence of the specimen thickness on the estimation. Figure 13 shows the constant α obtained for various stress-strain curves and specimen thicknesses. The value of α was calculated from Equation (1) by substituting the assumed yield strength σ_y and $P_{t/10}$ obtained by the simulation. The obtained α was larger than the value proposed in Ref. [1]. Therefore, the accuracy of the yield strength can be improved by applying a larger α. However, α depends on the specimen thickness.

In order to exclude the influence of the specimen thickness on the yield strength estimation, various definitions of the deflection point in the LD curve were investigated. Finally, it was found that the deflection point of $P_{0.3mm}$ was better than $P_{t/10}$. As shown in Figure 14, the offset displacement of 0.3 mm was quoted for determining $P_{0.3mm}$. Then, the yield strength was estimated by:

$$\sigma_{y(0.3mm)} = \alpha_{0.3mm} \frac{P_{0.3mm}}{t^2}. \tag{3}$$

The constant $\alpha_{0.3mm}$ was obtained by substituting the assumed yield strength into the expression for $\sigma_{y(0.3mm)}$. Figure 15 shows the change in $\alpha_{0.3mm}$ with the specimen thickness. An almost constant $\alpha_{0.3mm}$ was obtained regardless of the specimen thickness. The average value for all data shown in Figure 15 was $\alpha_{0.3mm} = 0.229$. By performing the simulations for various stress-strain curves, it is possible to determine a better value for the constant $\alpha_{0.3mm}$.
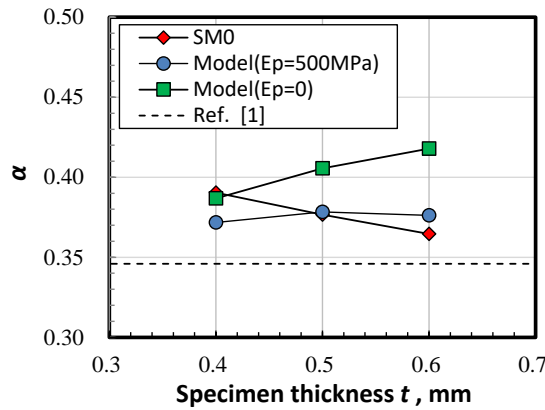
Figure 13. Constant α to estimate the yield strength obtained for various specimen thicknesses and stress-strain curves.
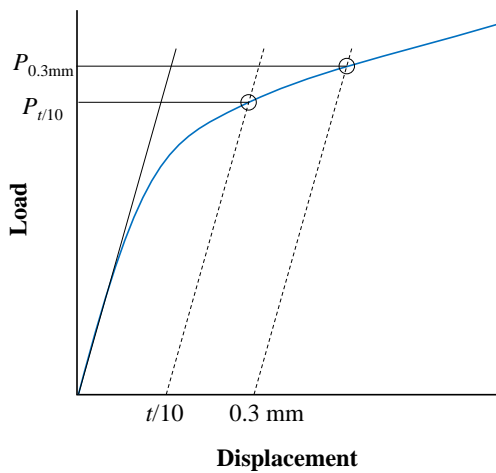
Figure 14. Definition of deflection points $P_{y(t/10)}$ and $P_{y(0.3mm)}$.
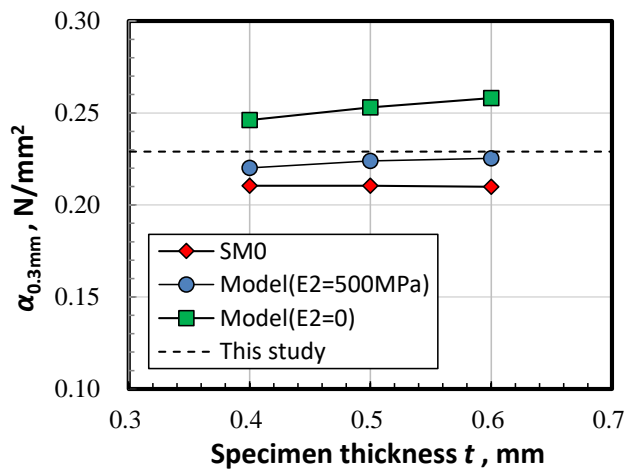
Figure 15. Constant $\alpha_{0.3mm}$ to estimate the yield strength obtained for various specimen thicknesses and stress-strain curves.

5. Conclusions

The SP tests were conducted for carbon steel specimens with and without cold working. The DIC technique was applied to measure the displacement. Then, by using the true stress-strain curves including post-necking strain, detailed FEAs were carried out for the SP tests. The following conclusions were drawn.

- The DIC technique enabled measurement of the specimen displacement free from compliance of the test device.

- Detailed FEAs using the stress-strain curves including the post-necking strain could reproduce the LD curve. Use of the nominal stress-strain curve obtained by the conventional tensile test was not enough to simulate the maximum load P_{max}.
- Although the empirical ultimate strength estimation obtained by Equation (2) worked well for the current material, it was shown that the maximum load P_m and displacement d_{max} quoted in Equation (2) did not have a direct correlation with the ultimate strength.
- The deflection point in the LD curve correlated with the yield strength.
- The yield strength estimated by Equation (1) depended on the specimen thickness. It was shown that the thickness dependency on the yield strength estimation could be excluded by using $P_{0.3mm}$.

References

1. García, T.E.; Rodríguez, C.; Belzunce, F.J.; Suárez, C. Estimation of the mechanical properties of metallic materials by means of the small punch test. *Journal of Alloys and Compounds* 2014, Vol. 582 (2014), pp.708-717.
2. Mao, X.; Takahashi, H. Development of a further-miniaturized specimen of 3 mm diameter for TEM disk (ø 3 mm) small punch tests. *Journal of Nuclear Materials* 1987, Vol.150, pp.42-52.
3. Fleury, E.; Ha, J. S. Small punch tests to estimate the mechanical properties of steels for steam power plant: I. Mechanical strength. *International Journal of Pressure Vessels and Piping* 1908, Vol.75, pp.699-706.
4. Sainte Catherine, C. S.; Messier, J.; Poussard, C.; Rosinski, S.; Foulds, J. Small Punch Test: EPRI-CEA Finite Element Simulation Benchmark and Inverse Method for the Estimation of Elastic Plastic Behavior, Small Specimen Test Techniques: Fourth Volume, ASTM STP 1418, M. A. Sololov, J. D. Landes, and G. E Lucas, Eds., (2002), pp.350-370.
5. Kamaya, M.; Kawakubo, M. A procedure for determining the true stress-strain curve over a large range of strains using digital image correlation and finite element analysis. *Mechanics of Materials* 2011, Vol. 43, pp.243-253.
6. Kumar, K.; Pooleery, A.; Madhusoodanan, K.; Singh, R. N.; Chakravartty, J. K.; Shriwastaw, R. S.; Dutta, B. K.; Sinha R. K. Evaluation of ultimate tensile strength using miniature disk bend test. *Journal of Nuclear Materials* 2015, Vol.461, pp.100-111.

Development of an improved correlation method for the yield strength of steel alloys in the small punch test

J. Calaf Chica [1]*, P.M. Bravo Díez [2] and M. Preciado Calzada [3]

[1] Universidad de Burgos; jcalaf@ubu.es
[2] Universidad de Burgos; pmbravo@ubu.es
[3] Universidad de Burgos; mpreciado@ubu.es
* Correspondence: jcalaf@ubu.es; Tel.: +34-660040883

Abstract: The Small Punch Test (SPT) is a miniaturized test to characterize the mechanical properties of the materials. The load-displacement curve obtained by this test does not directly provide the material parameters, and linear correlations between data obtained from SPT curve and each mechanical property are necessary. The main difficulty of these correlation methods is the high level of scattering showed when analyzing a wide set of materials in the same study. In this paper, a finite element analysis focused on steel alloys was performed to understand the specimen behavior in the early stages of the SPT. Present methods to correlate the material yield strength with the data obtained from the SPT curve were also analyzed via this FEM study to discover the meaning of the current correlation scattering for this mechanical property. This numerical research also proved the accuracy of the proposed correlation method for the yield strength via the SPT. The maximum slope of zone I (Slopeini) of the SPT curve showed an accurate correlation with this mechanical property. Focusing on steel alloys, experimental tensile tests and SPT's were performed to validate the numerical analysis and to demonstrate the suitability of the proposed Slopeini versus yield strength correlation method.

Keywords: Small Punch Test; SPT; yield strength.

---

1. Introduction

In the early 1980s an innovative Miniaturized Disk Bend Test (MDBT) was developed as a cost-effective method to test the post-irradiated state of materials used in thermonuclear reactor applications [1-2]. Many researchers have investigated and improved this test, developing the Small Punch Test (SPT) as a test method for characterization. It consists of a punch which deforms a firmly gripped specimen between two dies until fracture (see Fig. 1(a)). Research and investigation in the SPT were focused on the evaluation of material properties, including the elastic modulus, yield strength and tensile strength [3-5], ductile-brittle transition [6], fracture properties [7-10], etc. The significant interest shown by researchers in this testing procedure motivated the development of a CEN Code of Practice for the application and use of the small punch test method for metallic materials [11].

Results data recorded during SPT are the load/displacement curves (see Fig. 1(b)). Zones distinguished in this curve are [12]:

Zone I: elastic bending.
Zone II: transition between elastic and plastic bending.
Zone III: plastic hardening.
Zone IV: softening due to material damage initiation.
Zone V: crack growth with a circular shape around the center of the specimen until failure.
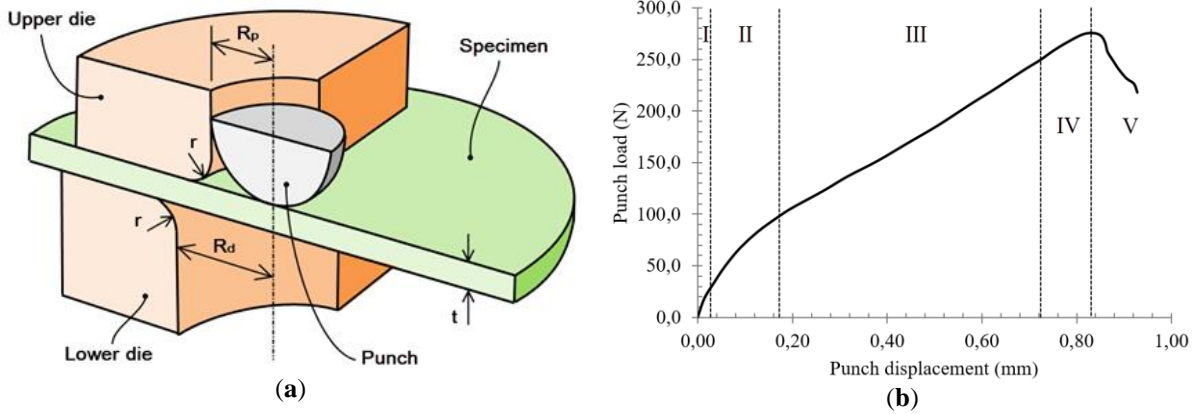
Figure 1. (**a**) Small Punch Test geometry; (**b**) Main behavior zones in the SPT curve.

Nowadays, there are four different methods to obtain the yield strength from the SPT curve:

a. Mao's method [7]. Also referred to as the "two tangents" method, the yield load P_y is obtained from the intersection between two lines: a tangent to the elastic zone I of the SPT curve and another tangent to the plastic zone III of the SPT curve. Both zones I and III do not show any linear behavior so, the tangent to zone I is calculated for the point with the maximum slope, and the tangent to zone III for the point with the minimum slope.

b. Modified Mao's method [13]. The point obtained from the previous "two tangents" method is projected vertically to the SPT curve to obtain the yield load P_y.

c. t/10 method [14]. The yield load P_y is obtained in a way that is similar to σ_y (offset: 0.2%) in standard tensile tests. A parallel line with the tangent to the elastic zone I of the SPT curve is drawn with an offset equal to $t/10$ in the displacement axis. The intersection of this line with the SPT curve is identified as the yield load P_y.

d. CWA method [11]. Also referred as the "two secants" method, it is like the "two tangents" or Mao method, except for the use of secants instead of tangents. Yield load P_y is calculated by the intersection of two linear functions (two secants), which are calculated minimizing the error between these functions and the SPT curve. CWA [11] recommends the vertical projection of this intersection point to the SPT curve to obtain the most reliable P_y value via this method.

In the early days of SPT research, the SPT curve was performed with the displacement measured using an extensometer installed between upper and lower arms of the assembly (hereinafter referred to as δ_{ext}). Later, an LVDT (Linear Variable Differential Transformer) sensor installed in contact with the lower face of the specimen was used to obtain the displacement data (hereinafter referred to as δ_{lower}). The main differences between these two displacements are:

a. The plastic indentation between the punch and the upper face of the specimen in the initial stages of the zone I of the SPT curve is suppressed in δlower. Thus, zone I becomes a pure elastic region.

b. Non-linear contact deformations between all parts involved in the punch configuration influence the displacement measurement δext.

Point (b) is solved with a correction in the extensometer measurement. The lower die of the SPT is substituted by a tungsten cylinder with an outer diameter and height equal to the lower die dimensions. After a first loading step to a maximum load, which should not be surpassed in the subsequent SPTs, some unloading-loading cycles are performed until the stabilization in the load-displacement δ_{ext} curve is reached. The last loading step of this calibration test is recorded, and a 5th order polynomial regression from this data is established as a calibration function. This curve is used to correct the δ_{ext} obtained from the SPT tests, and it results in a new displacement δ_{upper} equal to the displacement of the upper face of the specimen.

Point (a) is considered by some researchers as the main reason to consider δ_{lower} as more reliable data than δ_{upper} to measure the displacement for the SPT curve [13]. The non-linear behavior of the initial stages of zone I of the SPT curve when δ_{upper} is used is the main reason to discard this method.

2. Materials and Methods

In this article, a first investigation is focused on FEM analyses to:

a. Demonstrate that the accuracy of the correlation obtained from both displacements (δ_{upper} and δ_{lower}) is similar.

b. Perform a detailed analysis of the dependency of the yield load P_y of the SPT curve with more than one plastic property to demonstrate the arbitrary character of the current P_y - σ_y correlations.

c. Validate numerically an alternative method for obtaining the yield strength σ_y with the SPT which shows a high level of dependency on the yield strength of the material and no significant alterations with the rest of the plastic properties.

Finally, as a second part of this investigation, experimental tests (uniaxial tensile tests and SPTs) were performed to demonstrate the suitability of the previous numerical study.

FEM simulations were performed with Abaqus FE software, taking into consideration 36 hypothetical materials. The plastic behavior for all materials was simulated with an isotropic hardening model following the Ramberg-Osgood equation (see Equations 1 and 2 [15]):

$$\varepsilon = \frac{\sigma}{E} + \varepsilon_{offset} \left(\frac{\sigma}{\sigma_y} \right)^n \tag{1}$$

$$n = \frac{\ln\left(\frac{\varepsilon_m - \sigma_m/E}{\varepsilon_{offset}} \right)}{\ln\left(\frac{\sigma_m}{\sigma_y} \right)} \tag{2}$$

where $\varepsilon_{offset} = 0.002$ is the offset strain used to calculate the yield strength.

The elastic properties of all these materials were fixed to $E = 200000$ MPa and $v = 0.3$, and plastic properties were selected to have nine families (M1.y to M9.y) with different yield strengths (100, 250, 400, 550, 700, 850, 1000, 1200 and 1400 MPa). Each of these families had four different Ramberg-Osgood coefficients n (6.95, 8.95, 14 and 35). Table 1 shows the plastic properties assigned for each hypothetical material.

Table 1. Plastic properties of the hypothetical materials

Material	σ_y (MPa)	n^*	Material	σ_y (MPa)	n^*
M1.1	100	6.95	M5.3	700	14
M1.2	100	8.95	M5.4	700	35
M1.3	100	14	M6.1	850	6.95
M1.4	100	35	M6.2	850	8.95
M2.1	250	6.95	M6.3	850	14
M2.2	250	8.95	M6.4	850	35
M2.3	250	14	M7.1	1000	6.95
M2.4	250	35	M7.2	1000	8.95
M3.1	400	6.95	M7.3	1000	14
M3.2	400	8.95	M7.4	1000	35
M3.3	400	14	M8.1	1200	6.95
M3.4	400	35	M8.2	1200	8.95
M4.1	550	6.95	M8.3	1200	14
M4.2	550	8.95	M8.4	1200	35
M4.3	550	14	M9.1	1400	6.95
M4.4	550	35	M9.2	1400	8.95
M5.1	700	6.95	M9.3	1400	14
M5.2	700	8.95	M9.4	1400	35

Material	σ_y (MPa)	n^*	Material	σ_y (MPa)	n^*

(*) Hardening coefficient of equations (1) and (2)

In FEM simulations, the specimen thickness was set at 0.5 mm. The rest of the geometric parameters were: R_d=2.0 mm, R_p=1.25 mm and r=0.5 mm (see Fig. 1).

In the experimental tests, six different steels were selected to obtain a wide range of yield strengths from 160 MPa to 1215 MPa. Table 2 shows the mechanical properties of these materials.

Table 2. Mechanical properties of the experimental materials

Material	E (MPa)	σ_y (MPa)	σ_{u_eng} (MPa)	ε_{fract} (mm/mm)
DC04 (1.0338)	203000	160	288.00	0.47
HC300LA (1.0489)	206000	322	411.00	0.31
DC01 (1.0330)	208000	229	353.00	0.35
F1110 (1.0401)	216430	550.60	615.60	0.19
F1140 (1.1191)	204910	745.00	922.67	0.10
15-5PH H900 (1.4545)	194926	1215.00	1310.00	0.16

3. Results

3.1. Numerical analyses

Abaqus was the software selected to perform the numerical analyses for this research. SPT simulation was done with an implicit method in an axisymmetric model (see Fig. 2). The specimen was meshed with quadrilateral elements with reduced integration and hourglass control (CAX4R) and with a global size of 0.025 mm per cell. The spherical punch and upper and lower dies were simulated as analytical rigid bodies. Interaction between each part was simulated with the standard surface-to-surface contact algorithm with a friction coefficient of $\mu = 0.18$ (typical value for steel-steel contact). Elastic and plastic material properties used for each analysis are shown in Table 1.
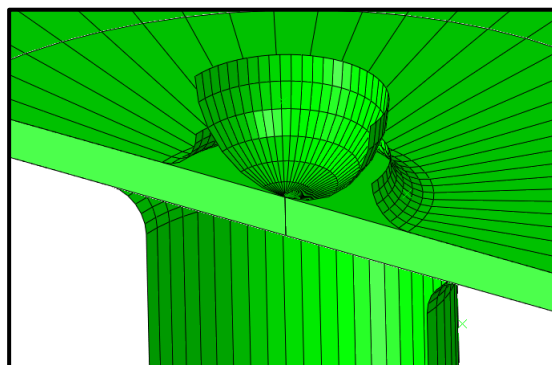
Figure 2. SPT FE model.

Thirty-six hypothetical materials M1.1 to M9.4 (see Table 1 for the mechanical properties of these materials) were simulated with the same FE model used in the previous section. Fig. 3 represents the load-displacement SPT curves for four hypothetical materials M1.1 to M1.4. Two types of SPT curves are shown: left graphs represent the displacement of the punch vs. load; right graphs represent the displacement of the lower face of the specimen vs. load (typical measurement obtained from an LVDT placed in this location).
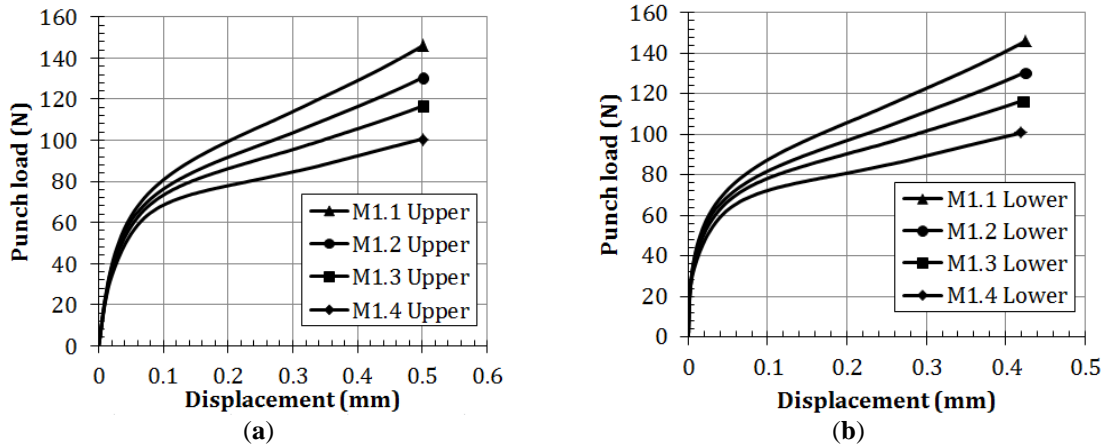
Figure 3. SPT curves, (**a**) with displacement of the punch, and (**b**) with specimen lower face displacement.

The four methods currently used to obtain the elastic limit of the material via the SPT curves (Mao, Mao-projected, t/10 and CWA methods) were applied in all of the previous hypothetical materials. Two types of displacement were used: upper (the displacement of the upper face of the specimen center); and lower (the displacement of the lower face of the specimen center).

Figs. 4 and 5 show the correlation between the normalized yield loads (P_y/t^2; where t is the specimen thickness) and the yield strength σ_y of the material.
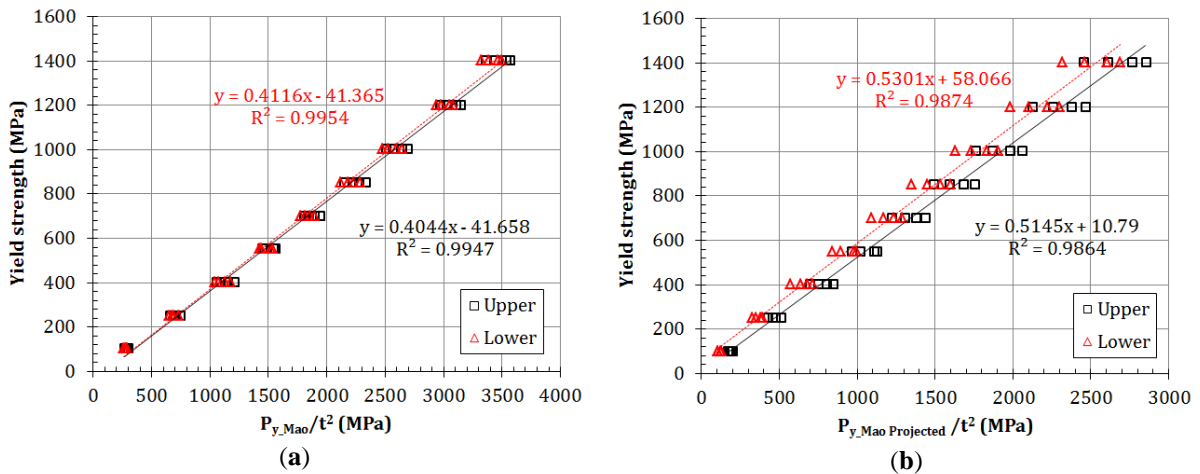
Figure 4. (**a**) P_{y_Mao} correlation; (**b**) $P_{y\_MaoProjected}$ correlation.
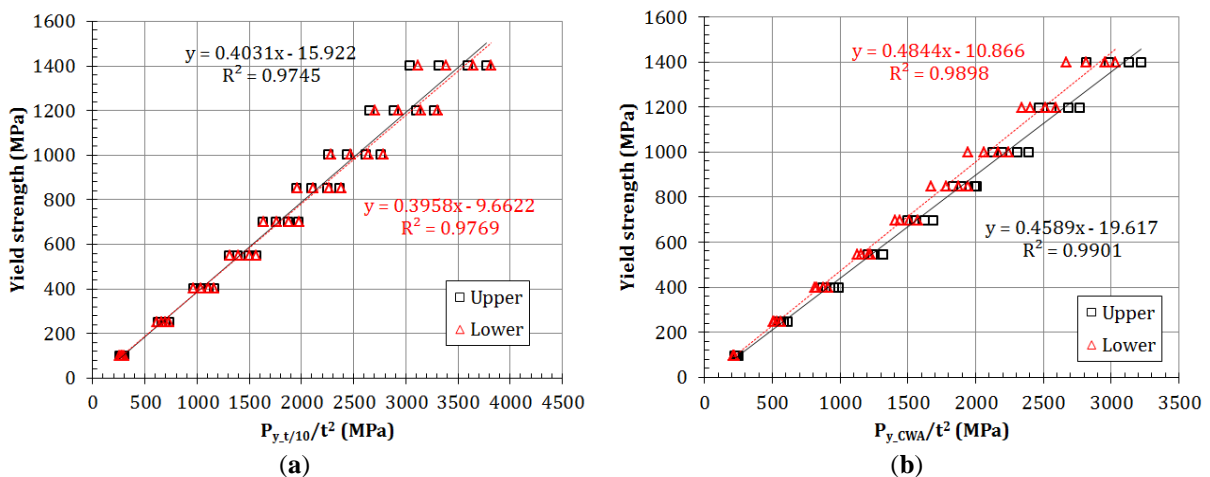
Figure 5. (**a**) $P_{y\_t/10}$ correlation; (**b**) P_{y_CWA} correlation.

The SPT specimen showed a high level of plasticization in the numerical analyses for punch displacements between 0.1 mm and 0.5 mm (values used for P_y calculation in the correlation methods seen before). Thus, the hardening coefficient n had an important role in the behavior of the SPT specimen.

In zone I of the SPT curve, the FEM analysis showed that the beginning of the plastic zone was located just below the punch on the upper face of the sample. The yielded volume grew until reaching the lower face of the SPT specimen. This event matched with the maximum slope of the zone I of the SPT curve ($Slope_{ini}$). Thus, $Slope_{ini}$ could show a high dependence on the yield strength and low deviations due to the hardening coefficient n.

Fig. 6 shows the correlation between the normalized $Slope_{ini}$ ($Slope_{ini}/t$; where t is the thickness of the specimen) and the yield strength of each material.

$$y = 4.741E+01e^{1.736E-04x}$$
$$R^2 = 9.944E-01$$
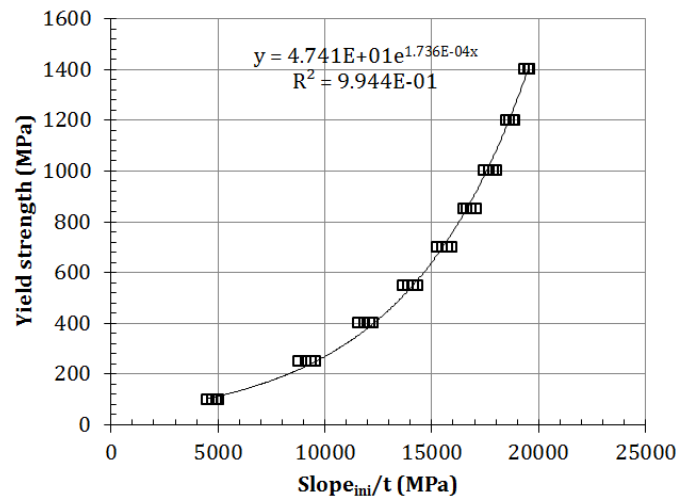
Figure 6. *Slope$_{ini}$* correlation.

3.2. Experimental analyses

Six steels, DC01, DC04, HC300LA, F1110, F1140 and 15-5PH H900 were tested using standard tensile tests (ASTM E8M) and small punch tests to confirm the numerical results previously shown. Table 2 shows the mechanical properties for all tested materials, and Fig. 7 shows the SPT curves obtained from the experimental tests. The geometry and the setup of the SPT were the same as the one analyzed in the previous numerical calculations.
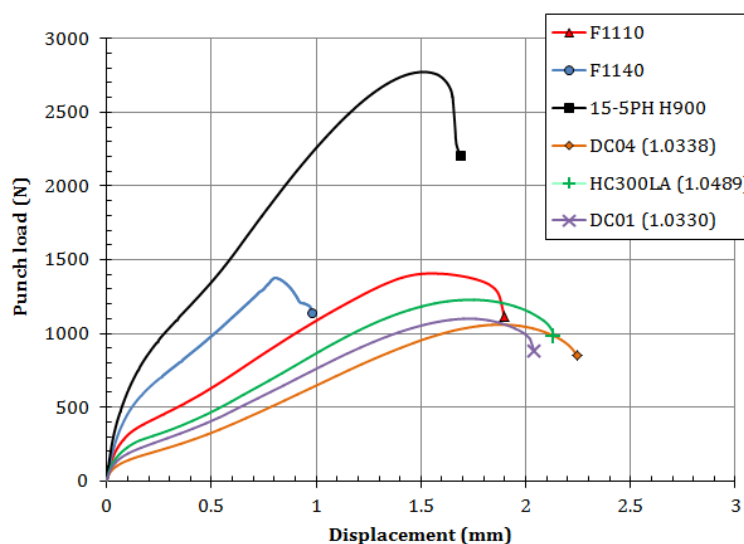
Figure 7. SPT curves of the experimental tests.

Figs. 8 to 10 show the correlation for each method with the yield strength of each alloy (obtained from the tensile tests). Fig. 11 shows the deviations between the calculated yield strengths from the experimental correlation

equations and the yield strengths obtained from the tensile tests. The most precise and reliable method was the proposed $Slope_{ini}$ method, with the CWA and t/10 methods following far behind.
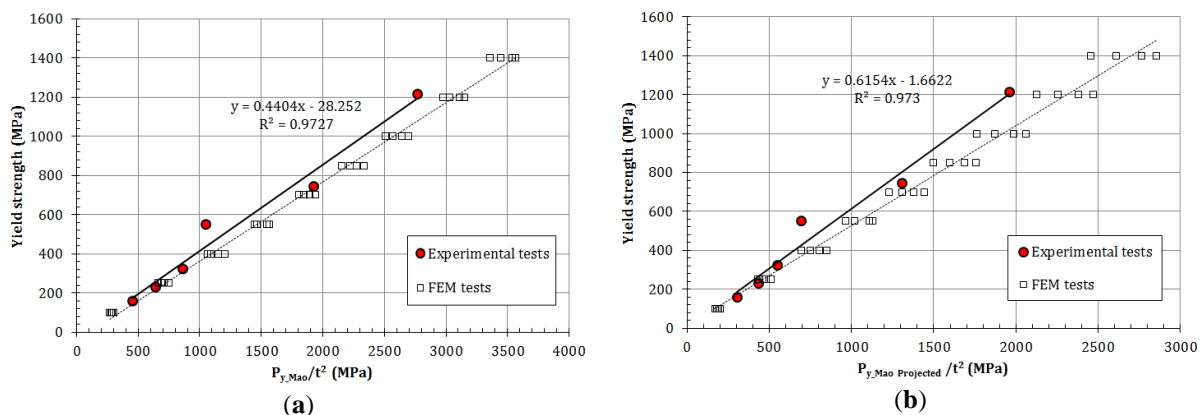
Figure 8. (**a**) Mao's method correlation; (**b**) Mao Projected method correlation.
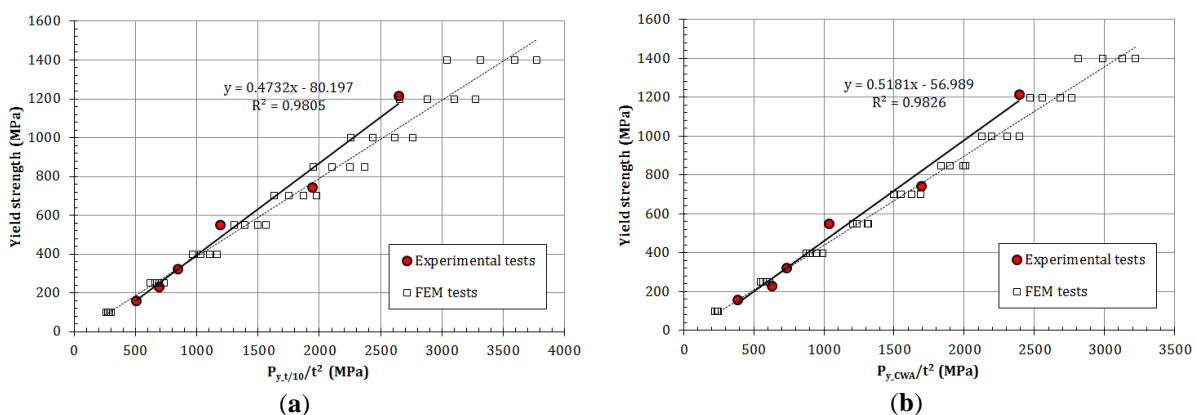
Figure 9. (**a**) t/10 method correlation; (**b**) CWA method correlation.
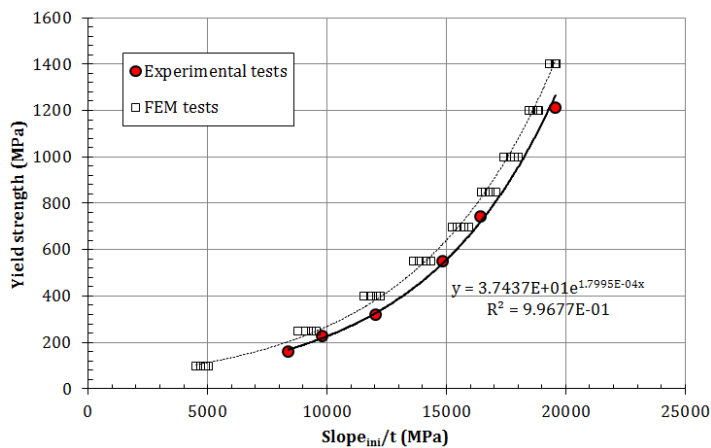
Figure 10. $Slope_{ini}$ method correlation.
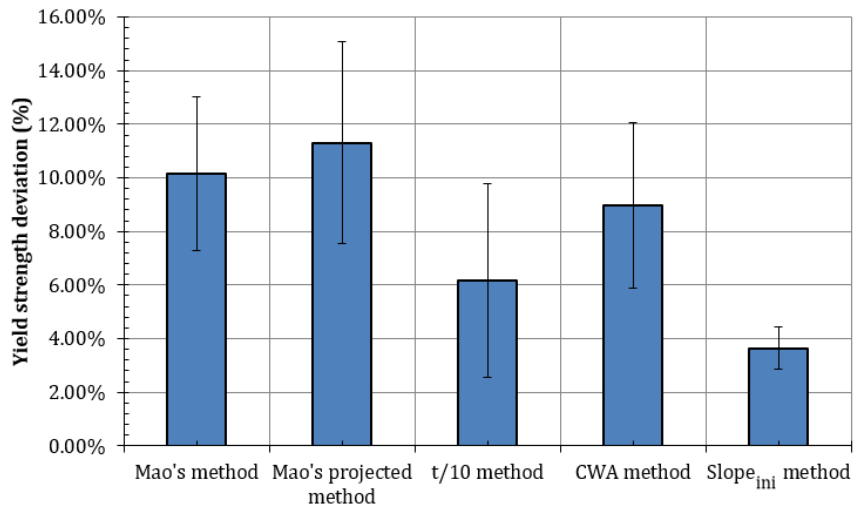
Figure 11. Deviations of the yield strength calculation.

4. Conclusions

A numerical analysis and a set of experimental tests (uniaxial tensile tests and SPTs) were performed in this research obtaining following conclusions:

a. There are two methods for measuring the displacement data for the SPT curve: the upper and the lower methods. This research demonstrated numerically that both had the same accuracy level for the yield strength correlation. The upper method is the best method for obtaining the SPT curve considering its simplicity (lower method needs the installation of an LVDT supported in the lower face of the specimen).

b. Current methods to correlate the yield strength with the SPT curve showed numerically an important dependency on the hardening coefficient *n*. Only the Mao's method showed in FEM calculations less dependency compared to the other methods, but the reason for this accuracy was based on a geometrical coincidence and not on the mechanical properties of the material. Experimental tests showed that Mao's method had a deviation level similar to the rest of the current methods. Thus, Mao's method was not more accurate than the rest of the correlation methods.

c. An improved correlation method for the yield strength σ_y was obtained using the $Slope_{ini}$ of the SPT curve. This method showed, both numerically and experimentally, a lower level of deviations and standard error compared with the current methods (Mao, Mao projected, t/10 and CWA). The "$Slope_{ini}$ method" only needs the load-displacement data from zone I and the initial part of zone II of the SPT curve to be obtained. This is much less information compared with the current methods, which need data from zones I, II and III of the SPT curve. This adds another advantage for the proposed method for materials which show brittle behavior and premature failures.

d. The "$Slope_{ini}$ method" depends on the elastic properties of the material. This investigation shows the correlation equation for steel alloys but other materials with different elastic properties should be correlated with its own correlation parameters obtained in a similar way of this research.

References

1. Manahan, M.P.; Argon, A.S.; Harling, O.K. The development of a miniaturized disk bend test for the determination of postirradiation mechanical properties. *Journal of Nuclear Materials* **1981**, 103 & 104, 1545-1550, DOI: 10.1016/0022-3115(82)90820-0

2. Huang, F.H.; Hamilton, M.L.; Wire, G.L. Bend testing for miniature disks. *Nuclear Technology* **1982**, 57.2, 234-242, DOI: 10.13182/NT82-A26286

3. Lucas, G.E.; Okada, A.; Kiritani, M. Parametric Analysis of the Disc Bend Test. *Journal of Nuclear Materials* **1986**, 141-143, 532-535, DOI: 10.1016/S0022-3115(86)80096-4

4. Lucas, G.E. Review of Small Specimen Test Techniques for Irradiation Testing. *Metallurgical Transactions A* **1990**, 21A, 1105-1119, DOI: 10.1007/BF02698242

5. Calaf Chica, J.; Bravo Díez, P. M.; Preciado Calzada, M. Improved correlation for the elastic modulus prediction of metallic materials in the Small Punch Test. *International Journal of Mechanical Sciences* **2017**, 134, 112-122, DOI: 10.1016/j.ijmecsci.2017.10.006

6. Baik, J.M.; Kameda, J.; Buck, O. Development of Small Punch Tests for Ductile-brittle Transition Temperature Measurement of Temper Embrittlement Ni-Cr Steels **1986**, *ASTM STP 888*, 92-111, DOI: 10.1520/STP32997S

7. Mao, X.; Takahashi, H. Development of a further-miniaturized specimen of 3 mm diameter for tem disk small punch tests. *Journal of Nuclear Materials* **1987**, 150, 42-52, DOI: 10.1016/0022-3115(87)90092-4

8. Misawa, T.; Adachi, T.; Saito, M.; Hamaguchi, Y. Small punch tests for evaluating ductile-brittle transition behavior of irradiated ferritic steels. *Journal of Nuclear Materials* **1987**, 150, 194-202, DOI: 10.1016/0022-3115(87)90075-4

9. Mao, X.; Saito, M.; Takahashi, H. Small punch test to predict ductile fracture toughness JIc and brittle fracture toughness KIc. *Scripta Metallurgica et Materialia* **1991**, 25, 2481-2485, DOI: 10.1016/0956-716X(91)90053-4

10. Mao, X.; Takahashi, H.; Kodaira, T. Supersmall punch test to estimate fracture toughness JIc and its application to radiation embrittlement of 21/4Cr-1Mo steel. *Materials Science and Engineering A* **1992**, I50, 231-236, DOI: 10.1016/0921-5093(92)90116-i

11. CEN Workshop Agreement. *Small Punch Test Method for Metallic Materials*, CWA 15627:2007 D/E/F; CEN: Brussels, Belgium, 2007.

12. Abendroth, M.; Kuna, M. Determination of deformation and failure properties of ductile materials by means of the small punch test and neural networks. *Computational Materials Science* **2003**, 28, 633-644, DOI: 10.1016/j.commatsci.2003.08.031

13. Moreno, M.F; Bertolino, G.; Yawny, A. The significance of specimen displacement definition on the mechanical properties derived from Small Punch Test. *Materials and Design* **2016**, 95, 623-631, DOI: 10.1016/j.matdes.2016.01.148

14. Rodríguez, C.; García, J.; Cárdenas, E.; Betegón, C. Mechanical properties characterization of heat-affected zone using the small punch test. *Welding Research* **2009**, 88, 188-192.

15. Ramberg, W.; Osgood, W.R. Description of stress-strain curves by three parameters. *NACA Technical Note* **1943**, 902.

Influence of the notch length on the estimation of the reference temperature by means of the small punch test

D. Andrés [1],*, R. Lacalle [2], S. Cicero [3], J.A. Álvarez [4] and M. Pinzón [5]

[1]   LADICIM (Laboratory of Materials, Science and Engineering), University of Cantabria; andresd@unican.es
[2]   LADICIM (Laboratory of Materials, Science and Engineering), University of Cantabria; lacaller@unican.es
[3]   LADICIM (Laboratory of Materials, Science and Engineering), University of Cantabria; ciceros@unican.es
[4]   LADICIM (Laboratory of Materials, Science and Engineering), University of Cantabria; alvareja@unican.es
[4]   LADICIM (Laboratory of Materials, Science and Engineering), University of Cantabria; manuel.pinzon@alumnos.unican.es
*   Correspondence: andresd@unican.es; Tel.: +34-942-200-928

Abstract: The Master Curve approach has been widely applied to characterize the ductile to brittle transition region of ferritic steels. In order to further optimise the available material to be tested, great efforts have been recently performed to combine it with miniature testing techniques. One of the most promising is the small punch testing technique, currently under standardisation process in Europe. In this paper, small punch modified specimens with a lateral notch for the estimation of fracture toughness have been employed to obtain the reference temperature, T_0, of a pressure vessel steel. The influence of the applied notch length has been analysed and a valid range has been proposed. In addition, the validity criterion of the tests for the estimation of T_0 has been further verified, confirming its suitability. Finally, results have been compared with those obtained with conventional fracture mechanics specimens and previous works. As a result, a methodology to estimate the reference temperature by means of small punch tests with notch lengths of approximately 4.4 mm has been proposed, turning it into a promising candidate for the characterisation of the transition regime.

Keywords: small punch; reference temperature; master curve, notch, fracture toughness, transition region

---

1. Introduction

The Master Curve (MC) approach enables a full characterisation of the ductile to brittle transition region of pressure vessel steels, or in general, ferritic steels, with a single parameter: the reference temperature. Developed at the VTT [1], the method has been successfully applied to a large number of ferritic steels and, thanks to its numerous advantages, has already been incorporated in several standards and codes, such as ASTM E1921 [2], BS 7910 [3], API 579/ASME FFS [4] or FKM Guideline [5].

One of its main features is the material optimisation: the reference temperature can be determined with a reduced number of tests. For challenging applications with reduced available material, such as the extension of the operating life of nuclear power plants, the MC approach has been combined successfully with miniature testing techniques to further reduce the material to be tested. For instance, micro compact tension specimens have been applied, employing a volume of only 10x10x4 mm per test [6].

The small punch technique is another promising miniature testing technique, which is currently under standardisation process in Europe [7]. It requires reduced volumes of material to estimate its properties, with specimens of only 0.5 mm-thickness and 8mm-diameter. Thanks to its potential, it has been employed in a wide range of applications, although its origins are directly related to the assessment of the embrittlement of pressure vessel steels [8].

One of its most appealing applications is the estimation of fracture toughness, given the size of the specimens employed. Several approaches have been proposed, such as the use of the equivalent fracture strain [9] or finite element modelling [10], among which the use of lateral notches results highly remarkable [11, 12]. This geometry has been recently applied to the estimation of the reference temperature on several ferritic and pressure vessel steels with promising results [13, 14]. In these previous works, a fixed notch length has been employed, which might have had some influence on the results obtained. Consequently, the main goal of this paper is to analyse its effects on the estimation of the reference temperature by means of small punch specimens with a lateral notch. To achieve it, a pressure vessel steel has been analysed and different usually employed notch-length values have been tested, in a range from 4.2 mm to 4.5 mm. In addition, the validity criterion for the tests has been confirmed, by analysing the differences in the estimations with tests exhibiting pure cleavage fractures and mixed fractures.

2. Materials and Methods

2.1. Experimental device

The small punch tests have been performed according to the recommendations of CWA 15627:2008 [15] in a universal mechanical testing machine with a load capacity of 2.5 kN. Given the scope of the research, the testing rig has been assembled inside an environmental chamber cooled by means of liquid nitrogen, which guaranteed the attainment of the testing temperatures required to characterise the ductile to brittle transition region.

Square 10x10 mm specimens have been employed with a lateral notch on it [11, 12], as it can be seen on Figure 1, which enables the use of analytical approaches to estimate fracture toughness and that will be included in the future European Standard for small punch testing of metallic materials. Other notches have been proposed, such as the use of through thickness central notches [16], blind longitudinal notches [17] or sharp circular notches [18], but the lateral notch has been selected for this research given its accurate results, its ease of machining by means of wire electron cutting and the possibility of characterising any orientation of the material.
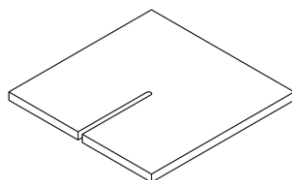
Figure 1. Scheme of a small punch specimen with a lateral notch machined on it.

To prepare the specimens, firstly the notch has been machined on 10x10 mm prisms. After this first step, it has been cut into pieces of approximately 0.55 mm thickness by means of a liquid-cooled cut-off machine. The samples have then been ground to at least 2000 grit on both sides until achieving the desired thickness of 0.5 ± 0.005 mm, according to the recommendations of CWA 15627:2008 [15].

The notch length has been corrected during the specimen preparation by grinding, if needed, until achieving the desired length. During the tests, the use of and adjustable lower matrix has enabled the reduction of the possible clearance between the matrix and the specimen, which could misalign the notch or vary its length. It is a novel design, which has been manufactured and validated for testing this specific geometry of specimen. It counts with a mobile piece, as shown in Figure 2, which can be adjusted to the length of each specimen, enabling the correction of the notch length if needed, something impossible to achieve by means of the conventional small punch testing rigs.

Figure 2. Adjustable lower matrix.

2.2. Material

A pressure vessel steel, HSST A533B PLATE 13B, has been tested. Its tensile properties have been obtained by means of conventional full-scale testing techniques, as well as its reference temperature. It has a yield strength, σ_y, of 480 MPa, a tensile strength, σ_u, of 608 MPa and a reference temperature, T_0, of 250 K [19].

2.3. Estimation of fracture toughness

The estimation of fracture toughness by means of small punch specimens with a lateral notch is based on the Crack Tip Opening Displacement (δ) concept [20]. According to it, cracks experience a certain degree of blunting before fracture, which can be related to the toughness of the material. Shih provided evidence of a unique

relationship between δ and J by evaluating the displacements at the crack tip implied by the HRR solution under elasto-plastic fracture mechanics conditions [21]:

$$\delta = \frac{d_n J}{\sigma_y}, \tag{1}$$

where d_n is a is a dimensionless constant with a strong dependence on the strain hardening exponent of the material [21].

During a small punch test on a modified specimen with a lateral notch, the notch is deformed in a similar way to notch blunting, until a certain point, where a crack usually initiates. This point can be easily identified on the Force-Displacement curve as a sudden change on its slope [11, 12]. If the tests are simulated by means of finite element models, it can be seen that a material independent relationship between the degree of crack blunting or δ_{SP} and the punch displacement can be obtained for a given notch geometry, as seen in Figure 3. Consequently, δ_{SP} can be easily obtained at the point of crack initiation after the test has been performed, by simply identifying the punch displacement correspondent to the crack initiation and then by simply applying the abacus shown in Figure 3.
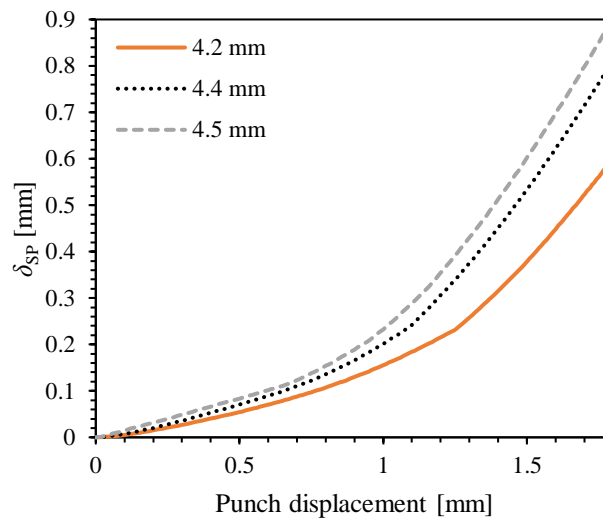
Figure 3. Relationship between δ_{SP} and punch displacement obtained by means of finite element models for notch lengths in between 4.2 and 4.5 mm.

If the tensile properties have already been obtained, by means of small punch tests or any other technique, equation (1) can be applied to obtain J_{SP}. Once it has been determined, equation (2) can be employed to estimate the equivalent K_J^{SP} value at the point of crack initiation [2, 20, 22]:

$$K_J = \sqrt{\frac{EJ}{1-\nu^2}}, \tag{2}$$

where E represents the Young modulus of the material and ν is the Poisson's coefficient.

2.4. Master Curve approach

The Master Curve approach is a statistical, theoretical, micromechanism based, analysis method for fracture toughness in the ductile to brittle transition region (DBTR) [1]. It enables the full characterisation of the DBTR with a single material-dependent parameter, the reference temperature, which can be defined as the temperature corresponding to a K_{Jc} value of 100 MPam^0.5 for a failure probability of 50%, obtained with a 25 mm-thickness specimen [1T].

The MC method also takes into account the scatter of the results at the DBTR, as well as the size effects and the temperature dependence of the fracture toughness [2]. Consequently, T_0 can be obtained with a reduced number of tests with limited volumes of material by applying equation (3):

$$K_{Jc} [1T] = 20 + \left[11 + 77e^{[0.019(T-T_0)]}\right]\left(\frac{25}{B}\right)^{\frac{1}{4}}\left[\ln\frac{1}{1-P_f}\right]^{\frac{1}{4}}, \tag{3}$$

where T represents the temperature in Kelvin, B is the thickness of the specimen and P_f is the probability of failure [2].

3. Results and discussion

3.1. Results of the small punch tests

The small punch tests have been performed at several temperatures, ranging from 143 to 158 K, for the estimation of the reference temperature. As it can be seen in Table 1, notch lengths of approximately 4.2, 4.3, 4.4 and 4.5 mm have been tested. The length values have been measured after the test, taking into account the possible deviations that the specimens might have suffered during the test, which introduce some scatter to the values. In addition, K_J^{SP} values have been estimated according to the methodology aforementioned.

Table 1. Results obtained from the small punch tests.

Temperature [K]	Notch length [mm]	K_J^{SP} [MPam$^{0.5}$]	Sudden force drop
158	4.19	110	
158	4.19	103	
153	4.22	105	×
158	4.22	103	
158	4.24	84	
158	4.24	110	
148	4.25	82	×
148	4.27	119	
153	4.29	108	
153	4.29	104	
153	4.29	128	
153	4.30	110	
158	4.38	121	
148	4.39	129	
143	4.40	99	×
148	4.43	105	
153	4.43	133	
143	4.45	122	×
148	4.46	122	
153	4.46	116	
148	4.49	125	
153	4.51	119	×
148	4.53	98	×

3.2. Analysis of the validity criterion

According to previous works [13, 14], to guarantee the applicability of the MC approach, the onset of cleavage cracking is the criterion of validity. After performing analysis of the micromechanisms present at the crack initiation, it has been proven that those tests exhibiting a sudden drop of the force at maximum force or those tests with a discontinuity on its slope on the proximity of maximum force exhibit pure cleavage or mixed fracture mechanisms respectively, being both valid for the determination of T_0^{SP} [13, 14].

In this paper, the effect of using the most restrictive case (sudden drop load during the test) on the reference temperature has been analysed. Consequently, the reference temperature has been estimated by applying equation (3). In one case, by only taking into account those tests with a sudden drop load and, in the other, taking into account all of the tests, as shown in Figure 4. T_0^{SP} from pure cleavage fractures has been 146 K, while the reference temperature obtained from the whole of the tests has been 147 K.

As a result, it can be seen that the use of only pure-cleavage-fracture tests does not introduce nearly any change on the estimation of the reference temperature, being it of only 1 K in this case, in good agreement with previous analysis.
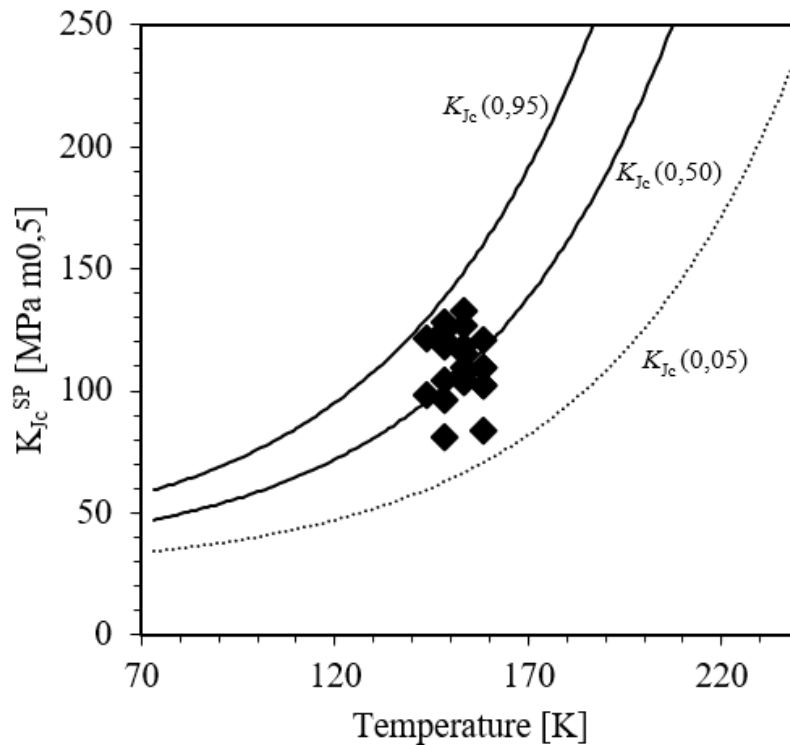
Figure 4. Small punch Master Curve obtained for all the tests performed.

3.3. Influence of the notch length on T_0^{SP}

To analyse the influence of the notch length on the estimation of the reference temperature by means of small punch tests, T_0^{SP} has been determined by applying equation (3) on groups of tests of different notch lengths, organised as following:

- 4.2 mm: tests with a notch length between 4.15 and 4.25 mm (average value: 4.22 mm).
- 4.3 mm: tests with a notch length between 4.25 and 4.35 mm (average value: 4.28 mm).
- 4.4 mm: tests with a notch length between 4.35 and 4.45 mm (average value: 4.41 mm).
- 4.5 mm: tests with a notch length between 4.45 and 4.55 mm (average value: 4.48 mm).

The reference temperature values obtained for each notch length are shown in Figure 5. It can be clearly seen that for the shorter notches, higher small punch reference temperatures have been obtained, with a maximum difference of 20 K. On the other hand, an apparent estabilisation of the temperature seems to occur for the lengths in between 4.4 and 4.5 mm, for which practically the same T_0^{SP} value has been obtained. This effect could be due to a possible influence of the notch length on the estimations of fracture toughness for the shorter values. According to the obtained results, the use of notches shorter than 4.4 mm (for this material) leads to lower estimations of fracture toughness values, which could have risen the estimation of the reference temperature. Further research should be performed in order to achieve a better understanding of its influence.
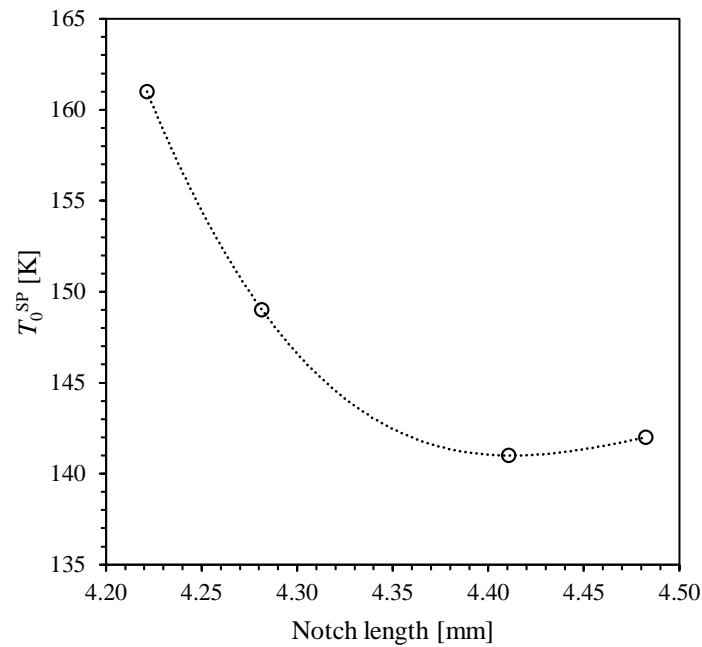
Figure 5. Small punch reference temperature obtained for each notch length.

The obtained reference temperatures for the different notch lengths have been compared with previous research [13, 14], where S275JR and S460M steels had been tested with a notch length of approximately 4.4 mm and a correlation factor between T_0^{SP} and T_0 of 0.52 had been established. It can be seen that the relationship provides accurate results for all the materials tested at the same notch length, of approximately 4.4-4.5 mm. On the other hand, shorter notches lead to higher correlation values, which would increase the error of the estimation, proportional to the reduction of the notch length.

As a result, special attention should be paid to the notch length for the estimation of the reference temperature. According to the obtained results, different relationships between T_0^{SP} and T_0 should be established for each specimen geometry or a single geometry should always be used. In the latter case, values in between 4.4 and 4.5 mm seem to be the most appropriate for this material, since both lengths have led to similar results.
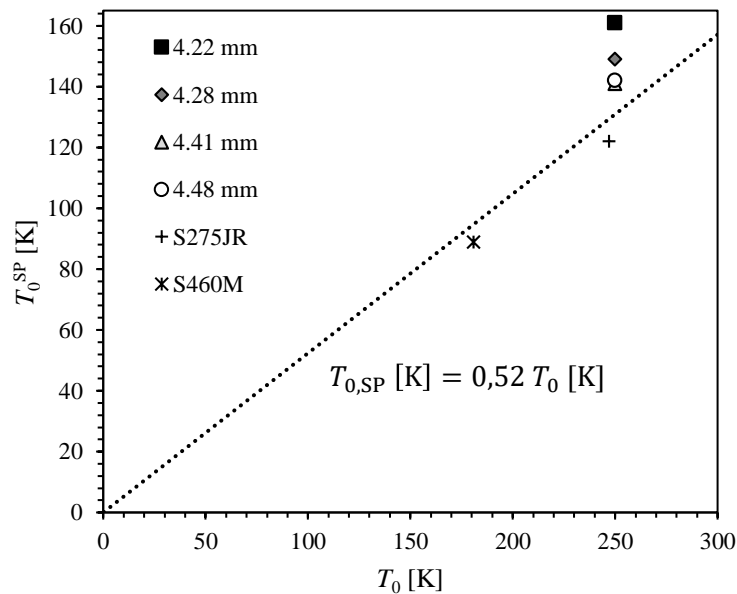
Figure 6. Relationship between the reference temperature obtained by means of small punch tests and full-scale conventional tests for several notch lengths on A533B and for a length of 4.4 mm for S275JR and S460M.

5. Conclusions

In this paper, the small punch testing technique has been successfully applied to the characterisation of the ductile to brittle transition region of pressure vessel steel, in combination with the Master Curve approach. Since it is a model based on the direct estimation of fracture properties, small punch specimens modified with a lateral notch have been employed to estimate K_J^{SP}. It has been proven that the notch length can influence the estimated reference temperature, leading to higher values of T_0^{SP} for lengths shorter than 4.4 mm for A533B. The use of values between 4.4-4.5 mm has shown an apparent estabilisation of T_0^{SP}, with a similar correlation coefficient T_0^{SP}-T_0 to the one obtained in previous works. This could suggest that material-independent relationships between T_0 and T_0^{SP} can be determined for the different notch lengths.

In addition, the test validity criterion has been further validated. It has been proven on A533B steel that both mixed fractures and pure cleavage fractures can be used to estimate T_0^{SP} without any influence on its value. Consequently, small punch tests exhibiting a discontinuity on the slope of the Force-Displacement curve or a sudden force drop can be regarded as valid. However, in case of doubt, a micromechanism analysis is encouraged to guarantee the validity of the results.

Briefly, this new approach results in a promising candidate for the characterisation of the ductile to brittle transition region of ferritic steels with an optimised use of the material. Further research is required on different materials to confirm the trends observed and achieve a better understanding of the influence of the different parameters.

References

1. Wallin, K. *Master Curve analysis of ductile to brittle transition region fracture toughness round robin data*; Technical Research Centre of Finland (VTT): Espoo, Finland, 1998.
2. ASTM E1921-17a. *Standard Test Method for Determination of Reference Temperature, T_0, for Ferritic Steels in the Transition Range*; ASTM International: West Conshohocken, PA, 2017, DOI: 10.1520/E1921-17A.
3. BS 7910:2013+A1:2015. *Guide to methods for assessing the acceptability of flaws in metallic structures*; British Standards Institution: United Kingdom, 2013.
4. API 579-1/ASME FFS-1. *Fitness-for-Service*; American Petroleum Institute/The American Society of Mechanical Engineers, Washington, D.C., 2016.
5. FKM-Guideline. *Fracture Mechanics Proof of Strength for Engineering Components*, 2nd revised edition; VDMA Publ. House: Germany, 2004.
6. Yamamoto, M.; Kimura, A.; Onizawa, K.; Yoshimoto, K.; Ogawa, T.; Chiba, A.; Hirano, T.; Sugihara, T.; Sugiyama, M.; Miura, N.; Soneda, N. A Round Robin Program of Master Curve Evaluation Using Miniature C(T) Specimens: First Round Robin Test on Uniform Specimens of Reactor Pressure Vessel Material. Proceedings of the ASME 2012 Pressure Vessels and Piping Conference, Toronto, Canada, July 15-19 2012; PVP2012-78661, 73-79, DOI: 10.1115/PVP2012-78661.
7. Bruchhausen, M.; Austin, T.; Holmström, S.; Altstadt, E.; Dymáçek, P.; Jeffs, S.; Lancaster, R.; Lacalle, R.; Matocha, K.; Petzová, J. European Standard on Small Punch Testing of Metallic Materials. Proceedings of the ASME 2017 Pressure Vessels and Piping Conference, Waikoloa, USA, July 16-20 2017; PVP2017-65396, DOI: 10.1115/PVP2017-65396.
8. Manahan, M.P.; Argon, A.S.; Harling, O.K. The development of a miniaturized disk bend test for the determination of postirradiation mechanical properties. *J. Nucl. Mater* **1981**, *103-104*, 1545-1550, DOI: 10.1016/0022-3115(82)90820-0.
9. Mao, X.; Takahashi, H. Development of a further-miniaturized specimen of 3 mm diameter for TEM disk (φ 3 mm) small punch tests. *J. Nucl. Mater.* **1987**, *150:1*, 45-52.
10. Abendroth, M.; Kuna, M.; Identification of Ductile Damage and Fracture Parameters from the Small Punch Test using Neural Networks. *Eng. Fract. Mech.* **2006**, *73*, 710-725, DOI: 10.1016/j.engfracmech.2005.10.007.

11. Lacalle, R.; Álvarez, J.A.; Arroyo, B.; Gutiérrez-Solana, F. Methodology for fracture toughness estimation based on the use of Small Punch notched specimens and the CTOD concept. Proceedings of the 2nd International Conference SSTT, Ostrava, Czech Republic, 2012.

12. Lacalle, R.; Álvarez, J.A.; Gutiérrez-Solana, F.; Use of small punch notched specimens in the determination of fracture toughness. Proceedings of the ASME 2008 Pressure Vessels and Piping Conference, Chicago, USA, July 27-31 2008; DOI: 10.1115/PVP2008-61537.

13. Lacalle, R.; Andrés, D.; Álvarez, J.A.; Gutiérrez-Solana, F. Transition Region of Nuclear Vessel Steels: Master Curve Approach Using Small Punch Notched Specimens. *Key Eng. Mater.* **2017**, *734*, 77-86, DOI: 10.4028/www.scientific.net/KEM.734.77.

14. Andrés, D.; Lacalle, R.; Cicero, S.; Álvarez, J.A.; Pinzón, M. Estimation of the reference temperature, T_0, by means of the small punch testing technique. Proceedings of the ASME 2018 Pressure Vessels and Piping Conference, Prague, Czech Republic, July 15-20 2018, PVP2018-84250.

15. Documets of CEN WS21. *Small Punch Test Method for Metallic Materials, CWA 15627:2008. Part A: Code of Practice for Small Punch Creep Testing and Part B: A Code of Practice for Small Punch Testing for Tensile and Fracture Behaviour.* European Committee for Standardization, Brussels, Belgium, 2007.

16. Ju, J.B.; Jang, J.I.; Kwon, D. Evaluation of fracture toughness by small-punch testing techniques using sharp notched specimens. *Int. J. PVP* **2003**, *80-4*, 221-228.

17. Martínez-Paéda, E.; García, T.E.; Rodríguez, C. Fracture toughness characterization through notched small punch test specimens. *Mater. Sci. Eng. A* **2016**, *657*, 422-430.

18. Turba, K.; Gülcimen, B.; Li, Y.Z.; Blagoeva, D.; Hähner, P.; Hurst, R.C. Introduction of a new notched specimen geometry to determine fracture properties by small punch testing. *Eng. Fract. Mech.* **2011**, *78-16*, 2826-2833.

19. Sokolov, M.; McCabe, D.; Davidov, Y.; Nanstad, R. Use of precracked Charpy and smaller specimens to establish the master curve. *Small Specimen Test Tech.* **1998**, *STP1329*, DOI: 10.1520/STP1329-EB.

20. Anderson, T.L. *Fracture Mechanics: Fundamentals and Applications*, 3rd ed.; Taylor and Francis Group, 2005.

21. Shih, C.F. A Path Independent Integral and the Approximate Analysis of Strain Concentration by Notches and Cracks. *J. Appl. Mech.* **1968**, *35*, 379-386.

22. ASTM E1820-17a. *Standard Test Method for Measurement of Fracture Toughness*. ASTM International: West Conshohocken, PA, 2017, DOI: 10.1520/E1820-17A.

Neural network utilization for evaluation of the steel material properties

J. Špička [1], L. Kander [2] and P. Čížek [2]

[1] Research and Testing Insitute Plzeň, Tylova 1581/46, 301 00, Plzeň, Czech Republic; spicka@vzuplzen.cz
[2] Material and Metallurgical Research, Ltd., Pohraniční 31/639, 703 00 Ostrava-Vítkovice, Czech Republic; ladislav.kander@mmvyzkum.cz

Abstract: The aim of this work is to develop and test a new method for identification of material properties of the steel. This work deals with application of the small punch test for evaluation of material degradation of power station in the ČEZ company (main Czech energetic company) within the project TE01020068 "Centre of research and experimental development of reliable energy production, work package 8: Research and development of new testing methods for evaluation of material properties". The main effort is here an improvement of empirical correlation of selected steel materials used in power industry for manufacturing of the critical components (rotors, steam-pipes, etc.). The effort here is on the utilization of the finite element method (FEM) and the neural network (NN) for evaluation of mechanical properties (Young modulus of elasticity, yield stress, tensile strength) of the selected material, based on SPT results only.

Keywords: Small Punch Test, Neural Network, Power Plant Steel, Mechanical properties

1. Introduction

Currently, there is an effort to maximize the service life of nearly worn out operating components while maintaining the conditions for reliable and safety operation. Consequently, the new test methods for evaluation of residual service life or for determination of the actual strength values and brittle fracture properties of the exploited components are being developed. One of the methods used to evaluate the current state of mechanical properties is the small punch test (SPT) [1-4]. Such experimental method is used for both assessing the current condition of the material as well as evaluating the so-called zero states of newly manufactured power plants components.

The main aim of this paper is to create a numerical tool, which could estimate material parameters of the particular steel, on basis of already performed experiments for penetration test (SPT) and tensile test. There will not be a requirement to perform the tensile test with the currently tested material and to identify from this test these parameters. Only SPT and database of previously performed (SPT and tensile test) tests is used together with the Neural network tool. This approach can significantly reduce time and cost of the material parameters assessment.

The standard process of identifying yield stress, tensile strength is to perform tensile test and based on this test, the material properties can be evaluated [5, 6]. Moreover, fracture toughness [7] needs to be also evaluated from the individual test. However, tensile test as well as fracture toughness assessment requires large specimen of the material and it could be financially and time demanding task. The small punch test has advantage of small specimen required for the test and relatively cheap cost, but it does not allow us to directly evaluate the material properties. To ensure the safe operation of the component, it is necessary to find out the actual values of the material parameters. With the advantage of this work, one would avoid the necessity to perform an expensive tensile test. It would be sufficient to perform just a penetration test and using a suitable mathematical apparatus identified such mechanical parameters. This newly developed approach could facilitate identification of the actual material parameters of steel in a timely and economical manner.

2. Methods

A neural network (NN) was chosen as a suitable mathematical apparatus. The neural network is a computational system originally inspired by nature and the human brain. Dr. Robert Hecht-Nielsen defined the neural network as follows:

"...a computing system made up of a number of simple, highly interconnected processing elements, which process information by their dynamic state response to external inputs.
In "Neural Network Primer: Part I" by Maureen Caudill, AI Expert, Feb. 1989 [8].

The original idea of the neural network was to solve the problems in a way that human brain would do. However, over time many other applications were discovered for this method. The main idea is that the network can be trained/taught using input and output data to give reasonable outputs for new inputs. The structure of the neural

network is seen in Figure 1, where the first layer is the input; the last layer is the output and between them is (optional) number of the hidden layers. Each layer contains mutually connected nodes, and these are further connected to other nodes in the next layer. In this way, we get to the last layer, i.e. to the output data. However, it is necessary to properly train the network in order to create suitable connections between the layers and the nodes. There should be several hundred to several thousand input/output pairs required to properly train the network [9, 10].
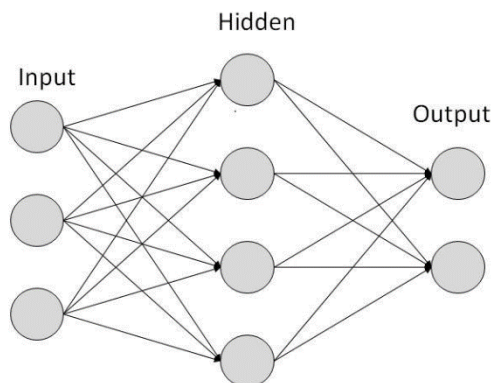
Figure 1. Structure of the neural networks.

In this case, the network would have the data from the penetration test (curve of Force versus Strain) as input and one of the following material parameters as an output: Young's modulus of elasticity E, yield stress R_{p02} and tensile strength R_m, see Figure 2. For each material value, one single network was created.

Figure 2. Diagram of the neural network based program.

The neural network has to be trained with a known data pair set (input-output). Here, experimental testing of SPT and tensile test of the given material were considered. From the standard tensile test, the material parameters were identified using standard identification method in company MATERIÁLOVÝ A METALURGICKÝ VÝZKUM, s.r.o. and directly used for the neural network as a training output. The input here was the force curve measured during SPT experiment. Consequently, the training dataset for the neural networks consist of the material parameters (E, R_{p02} and R_m) as an output and SPT curve as an input. The reference values of these material parameters come from experimental tensile test. The neural network must not only be trained, it is always necessary to test it with the use of some known pair of the input-output, which was not used in the training process. Here only one dataset of 100 specimens was available for the material 10GN2MFA. Number of 99 pairs was used for network training and one remaining pair for testing. This was done gradually with all 100 values (each of this will become ones a testing value). The final error of the neural network prediction was then evaluated. However, this process of training with the relatively small data set (100 pcs.) of only one material would predict reasonable results only for this particular material or similar one. To build a robust algorithm for prediction of any kind of material properties, one would need to build very large database of the reference specimens. Such database should contain various materials in a various state of residual life. Thus, to build the database, one must perform the SPTs as well as tensile tests, from which the reference material properties are determined. Since the database is filled up, you will only perform a SPT with the new/monitored material and the experimental curve will be used in the neural network to predict Young's modulus of elasticity, yield stress or tensile strength.

2.1 Experimental methods

In order to obtain experimental data, structural steels 10GN2MFA were used. This particular material is exploited in nuclear power engineering on a long term basis and particularly in the nuclear power engineering for power station of type VVER 1000 and MIR 1200. It was subjected to real heat treatment procedures in order to achieve real level of mechanical properties and to provide thus enough experimental data for the neural networks.

For investigated state the tensile tests was performed with subsequent determination of the curve of actual stress-strain (current state of the material), SPT or fracture toughness tests that resulted in the R curves. Since the characteristic feature of the fracture behaviour at the laboratory temperature for all of the above materials and their states after heat treatment was a stable growth of a ductile crack.

Due to the fact that both tensile and fracture toughness tests are standardized and adequately described in the literature [9,10], the next paragraph will deal only with the method of the SPT penetration tests.

The SPT method belongs to advanced testing methods developed on the long term basis in the company MATERIÁLOVÝ A METALURGICKÝ VÝZKUM, s.r.o. This method makes possible to obtain a number of mechanical properties with the use of the relatively small size of the test specimen. This method is used mainly for evaluation of the current state of mechanical properties of the components exploited in standard power engineering. In the recent past, this method was newly used also for determination of the impact of the sigma phase on the brittle fracture properties of steels used for the USC parameters [11-13].

The main advantage of the SPT method lies in the low volume of the experimental material and also in the fact that it is possible to obtain from the conducted SPT tests a number of properties. The SPT principle is illustrated in Figure 3. The test corpuscle is a disc with a diameter $d_1 = 8$ mm and a thickness $h = 0.5$ mm, which is penetrated by a hemispherical punch with a radius $r = 1$ mm till the failure. The diameter d_2 of the hole in the lower die is 4 mm. Record of the SPT test is shown in Figure 4. Such curve can be further used for the neural network to obtain the required values of mechanical properties [4]. In this experimental SPT, the deflection was controlled value, and thus remains very similar across the measurements and thus it was not used for the analysis.
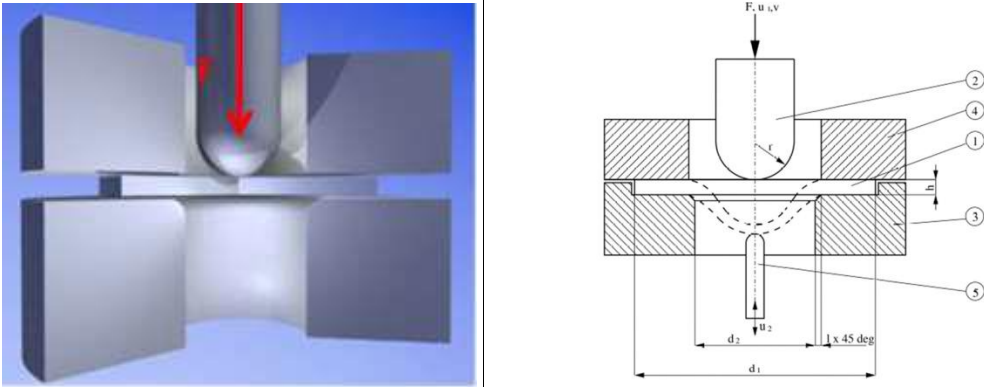
Figure 3. Principle of small punch test.
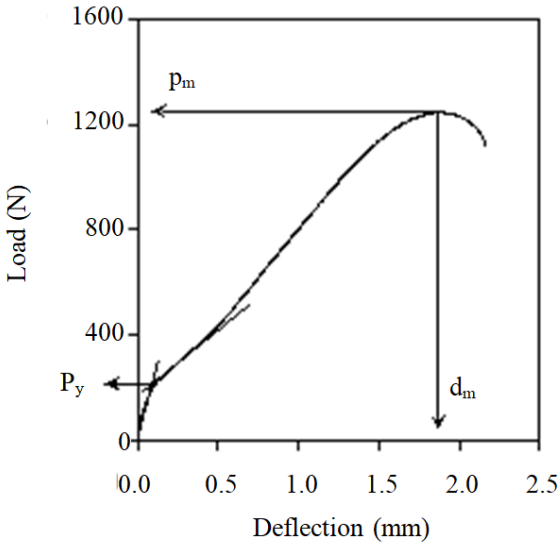
Figure 4. Record of the Small Punch Test.

3. Results

One investigated material 10GN2MFA was tested within the algorithm for evaluation of the steel material properties based on the Small Punch Test and neural network. The given 100 experimental pairs were gradually used for the training and testing of the neural network. There were always 99 pairs for the training of the network and one for the testing. The pair changes in the way, that each pair was ones a testing and 99 times a training one. The neural network provides a prediction of the material values (output) for the testing input (force vs displacement). Since these values are known (from the experiment), but not used for the training, the quality of such prediction can be assessed just with the comparison of the predicted and real values (output – E, R_{p02} and R_m). The error was calculated in absolute (MPa) and relative (%) values and the mean error was evaluated.

Table 1. Results of the Neural Network simulation of the mechanical properties.

		Mean Absolu	Max Absolu	Mean Relati	Max. Relati
		[MPa]		[%]	
10GN2MF A	E	516	45190	0.0663	20.5
	R_p	-0.09	61.6	-0.07	11.18
	R_m	0.291	51.2	-0.016	7.87

The obtained results summarised in Table 1 show good quality of the predicted values for the Young modulus of elasticity E. Maximal error of the estimation is about 20% while the mean error is less than 0.1%. Moreover, the 20% error of the prediction is still significant value. The maximal error of the predicted values for the yield stress and tensile strength is about 10%. Such estimation is considered as a good estimation, since we have only 99 training examples. For each three cases, the mean relative error is less than 0.1% and this indicates the reasonability of this approach. The complete results of the neural network (reference values, predicted values and the error is the Appendix A). Where, the name *SIM* (E_sim) refers to a simulated (predicted) value, while the *ORIG* (E_orig) refers to reference one.

4. Discussion

It follows from the obtained results summarized in Table 1, that the simulations here have good agreement with the experimental results. In our previous work started 3 year ago only limited number of data set do not exceeding 18 results was available. Such number of data set was found to be not acceptable as the scatter was too high. After improving NN methodology and increasing number of experimental data, the good agreement was found. Further work will be focused on the continuing of the experimental tests and building the material database using material like P91, P92 and A508 to get more relevant data.

5. Conclusions

The work describes the essence and the results obtained within the framework of the TAČR project TE01020068, work package 8. The project is focused on the use of the Small Punch Tests for evaluation of material degradation of critical components of conventional power plants. The aim of this work consists, in the creation of a connection between the SPT tests performed within the frame of evaluation of the actual material properties of the exploited and newly manufactured components and numerical calculation using neural networks. The first results indicate the possible application of the neural network method, especially for determining the values of mechanical properties. This work exploited the results obtained in [1], where authors tested such method on the three materials, with the maximal number of 18 values. Here, only one material, but with the larger number of specimens (100) were used. The results given here indicate/prove that the higher number of the training pairs can build better neural network with the better estimation. However there is still quite high maximal error. Moreover, the material 10GN2MFA is homogeneous material and the dispersion and quality of tested specimen was good. When the particular material would have non-linear behaviour and the scatter of the experimental data would increase, the prediction based on 100 examples only would vary significantly.

Achievement of consistent results when estimating material characteristics using neural networks would surely require a much bigger number of training samples. This is consistent with the literature, which states the need for at least several hundred or thousands pairs, for the proper functioning of the neural network. Consequently, this method

would require a wide database of the experiments for each material used in the real power plants. One could not assume that building one wide database for any kind of material will bring much more reasonable results.

References

1. Kander, L.; Špička, J. Utilization of Neural Networks for Evaluation of Material Properties of Structural Steels based on SPT Results, *Hutnické listy* č. 4/2017, ISSN 0018-8069, In press.
2. Catherine, C. S.; Messier, J.; Poussard, C.; Rosinski, S.; Foulds, J. Small punch test: EPRI-CEA finite element simulation benchmark and inverse method for the estimation of elastic plastic behaviour. In: *Small Specimen Test Techniques*: Fourth Volume. ASTM International, 2002.
3. Li, Y.; Hurst, R.; Matocha, K.; Čížek, P.; Blagoeva, D. New Approach to Determine Fracture Toughness from the Small Punch Test, In: *Metallurgical Journal*, vol. LXIII p. 94-102
4. Small Punch Test Method for Metallic Materials. CEN WORKSHOP AGREEMENT CWA 15627, December 2007
5. ČSN EN ISO 9862-1 Geosynthetics - Sampling and preparation of test specimens.
6. ASTM E 1820 Standard Test Method for Measurement of Fracture Toughness.
7. Abendroth, M.; Meinhard, K. Determination of ductile material properties by means of the small punch test and neural networks. *Advanced Engineering Materials* 6.7 (2004): 536-540.
8. "Neural Network Primer: Part I" by Maureen Caudill, AI Expert, Feb. 1989.
9. https://en.wikipedia.org/wiki/Artificial_neural_network
10. https://www.tutorialspoint.com/artificial_intelligence/artificial_intelligence_neural_networks.htm
11. Kander, L.; Korčáková, L. The Influence of Sigma Phase Precipitation on Mechanical Properties of Tp347H Austenitic Steels after 100.000 Hours Service in Coal-fired Power Plant. In *Metal 2015*, Brno, Czech Republic.
12. Stejskalová, Š.; Kander, L.; Hermanová, Š. The Change of the Structure and Mechanical Properties of the Austenitic Steels after Exposure at the Critical Temperature. *In Metallography 2016*, p. 100, Stará Lesná, Slovak Republic.
13. Kander, L. Precipitation of Sigma Phase in Austenitic Steels Used in Supercritical Conditions. In *Metal 2016*, p. 103, Brno, Czech Republic.

Appendix A

E_sim	E_orig	Error abs	Error rel [%]	Rp02_sim	Rp02_orig	Error abs	Error rel [%]	Rm_sim	Rm_orig	Error abs	Error rel [%]
	E				Rp02				Rm		
179913,2	208210	28296,81	135,905,124	507,928	526	1,807,197	3,435,736,134	6,145,796	630	1,542,037	2,447,678,383
233975,4	205032	-28943,4	-1,411,652,112	5,176,012	545	2,739,879	5,027,300,114	6,215,438	651	2,945,617	4,524,757,372
226773	206161	-20612	-9,997,987,142	4,881,569	532	4,384,307	8,241,177,815	5,943,482	635	4,065,182	6,401,861,211
190918,9	216967	26048,11	1,200,556,442	5,614,051	537	-244,051	-4,544,704,631	6,562,859	639	-172,859	-2,705,151,531
230873	204562	-26311	-1,286,213,871	5,086,515	527	1,834,851	348,168,978	6,179,982	630	1,200,183	1,905,052,805
188447,6	209460	21012,42	1,003,171,166	5,247,508	554	2,924,922	527,964,192	6,276,305	655	2,736,949	4,178,548,641
186267,3	196472	10204,7	5,193,969,254	5,271,693	527	-0,16926	-0,032117495	6,342,406	630	-424,065	-0,673118279
236676,5	207245	-29431,5	-1,420,128,505	4,822,892	543	6,071,081	111,806,272	5,942,317	645	5,076,834	787,106,123
197911	197288	-623,003	-0,315783684	5,249,188	532	7,081,153	1,331,043,847	6,317,164	635	3,283,628	0,517106831
212447,6	188409	-24038,6	-1,275,874,449	5,206,245	554	3,337,546	602,445,176	6,329,842	657	2,401,584	3,655,379,415
211581,8	201989	-9592,8	-4,749,171,487	5,165,961	524	7,403,882	1,412,954,654	6,261,159	627	0,884123	0,141008403
213250,6	209138	-4112,63	-1,966,467,337	5,350,972	525	-100,972	-1,923,266,671	633,703	628	-570,301	-0,908122105
208166,4	209269	1,102,599	0,526881222	5,064,671	529	2,253,291	4,259,530,068	6,179,101	632	1,408,994	2,229,420,477
187632,6	213394	25761,42	1,207,223,178	5,236,989	527	3,301,143	0,626402809	6,326,192	632	-0,61922	-0,097978003
180621,1	204331	23709,93	1,160,368,625	5,455,465	529	-165,465	-3,127,883,283	6,431,316	631	-121,316	-1,922,599,509
198497	211102	12605,03	5,971,062,395	5,930,581	525	-680,581	-1,296,345,527	6,873,436	627	-603,436	-9,624,177,277
211921,6	207148	-4773,59	-2,304,436,817	5,012,594	530	2,874,062	5,422,758,616	608,972	632	2,302,802	3,643,674,706
183953,5	205995	22041,53	1,070,003,125	5,596,594	526	-336,594	-6,399,117,929	6,526,686	631	-216,686	-3,434,014,915
235105,6	202846	-32259,6	-159,034,931	5,669,878	542	-249,878	-4,610,291,015	6,579,645	647	-109,645	-1,694,660,798
190593,3	207234	16640,74	8,029,926,243	5,617,689	529	-327,689	-6,194,501,745	663,534	633	-30,534	-4,823,693,537
193640,8	192917	-723,842	-0,375208961	5,433,297	524	-193,297	-3,688,882,021	6,368,811	625	-118,811	-190,097,251
210604,3	203093	-7511,33	-3,698,469,206	5,128,104	548	3,518,956	6,421,453,052	6,113,299	650	3,867,007	5,949,241,952
229383,5	213038	-16345,5	-7,672,553,218	5,602,281	547	-132,281	-2,418,307,154	6,647,267	648	-167,267	-2,581,283,666
179847,8	209388	29540,15	141,078,545	5,282,795	541	1,272,047	2,351,288,066	6,332,808	645	1,171,917	181,692,605
205263,1	198437	-6826,12	-3,439,941,019	4,895,332	524	3,446,681	6,577,636,173	5,989,544	627	2,804,557	4,472,977,972
200586,4	202338	1,751,616	0,865688034	5,739,383	525	-489,383	-932,157,434	670,62	628	-42,62	-6,786,629,048
187550	183553	-3996,99	-2,177,566,366	5,232,996	529	5,700,385	1,077,577,458	6,241,304	630	5,869,633	0,9316877
222861,9	209070	-13791,9	-6,596,799,449	5,580,009	554	-400,093	-0,72218966	6,477,652	652	4,234,814	0,64951128
196619,6	207160	10540,37	5,088,033,853	541,115	526	-15,115	-2,873,575,536	6,476,453	629	-186,453	-2,964,274,666
209494,5	193015	-16479,5	-8,537,962,062	5,417,419	522	-197,419	-3,781,979,981	6,426,773	625	-176,773	-2,828,367,997
230684	204939	-25745	-1,256,228,093	5,183,378	528	9,662,184	1,829,959,104	6,189,704	629	1,002,957	1,594,525,531
188285,6	201281	12995,45	6,456,370,613	523,655	524	0,34504	0,065847324	6,270,419	627	-0,04185	-0,006674837
208786	188583	-20203	-1,071,307,052	5,735,515	535	-385,515	-7,205,891,565	6,655,038	638	-275,038	-4,310,933,868
204809,1	218831	14021,86	6,407,620,857	5,502,414	524	-262,414	-5,007,910,041	6,398,768	624	-158,768	-2,544,357,605
231810,7	210726	-21084,7	-1,000,572,393	6,421,729	522	-120,173	-2,302,162,065	7,145,464	622	-925,464	-1,487,883,818
201111,1	231772	30660,93	1,322,891,923	5,377,606	529	-876,057	-1,656,062,461	6,445,123	631	-135,123	-2,141,405,008
218103,5	200009	-18094,5	-9,046,847,856	5,544,928	543	-114,928	-2,116,528,684	6,515,677	648	-356,773	-0,550575484
193851,7	202870	9,018,258	4,445,338,511	4,769,222	521	4,407,781	8,460,231,321	5,953,283	622	2,667,169	4,288,053,243
221342,2	200141	-21201,2	-1,059,312,437	5,280,504	530	1,949,564	0,367842194	623,605	633	9,394,966	1,484,196,782
223157,2	199641	-23516,2	-1,177,925,805	5,206,901	520	-0,69012	-0,132715715	6,262,869	621	-528,687	-0,851347633
168189,4	199786	31596,64	1,581,524,215	5,102,884	525	1,471,164	2,802,217,118	6,120,495	628	1,595,051	2,539,890,827
249630,5	204644	-44986,5	-2,198,280,451	566,358	527	-39,358	-7,468,314,975	6,584,338	628	-304,338	-484,614,422
204380,8	198889	-5491,84	-2,761,260,855	5,478,675	528	-198,675	-3,762,782,059	6,519,982	633	-189,982	-300,128,981
200119,5	202833	2,713,457	1,337,778,837	5,600,127	537	-230,127	-4,285,427,798	6,531,132	639	-141,132	-2,208,645,678
170792,7	194506	23713,32	1,219,156,473	550,379	535	-15,379	-2,874,575,951	6,498,462	639	-108,462	-1,697,375,403
254903,9	208131	-46772,9	-2,247,281,199	5,828,848	554	-288,848	-5,213,856,569	6,802,488	655	-252,488	-3,854,785,301
248400	211650	-36750	-1,736,355,382	5,369,283	523	-139,283	-2,663,155,023	6,387,111	625	-137,111	-2,193,780,184
194348,8	207607	13258,18	6,386,191,982	5,554,302	524	-314,302	-599,812,029	6,515,223	628	-235,223	-3,745,592,023
160825,5	198477	37651,49	1,897,020,131	5,124,028	525	1,259,715	2,399,457,174	6,230,338	627	3,966,191	0,632566346
180454,3	194188	13733,7	7,072,375,069	5,207,419	528	7,258,099	1,374,640,006	6,221,686	632	9,831,435	1,555,606,877
235871,6	201996	-33875,6	-1,677,042,068	5,582,566	547	-112,566	-2,057,873,314	6,562,146	649	-721,457	-1,111,643,878
232413,8	194549	-37864,8	-1,946,285,854	5,241,144	548	2,388,563	435,869,211	623,586	649	2,541,398	3,915,867,922
170588,4	205391	34802,62	1,694,456,934	5,145,674	536	2,143,263	3,998,624,254	6,220,891	637	1,491,092	2,340,803,726
192684,7	195737	3,052,293	1,559,384,809	5,422,667	542	-0,26668	-0,04920219	6,543,707	644	-103,707	-1,610,353,009
185548,5	191539	5,990,456	3,127,538,669	5,306,261	543	1,237,389	2,278,800,661	6,337,079	646	1,229,207	1,902,796,922
235466,8	188853	-46613,8	-2,468,259,102	5,626,476	530	-326,476	-6,159,923,482	654,181	630	-24,181	-3,838,259,996
176521,1	190114	13592,86	7,149,849,123	5,262,361	574	4,776,389	8,321,235,328	6,367,429	665	2,825,708	4,249,185,162
195259,9	202145	6,885,147	3,406,043,878	5,479,812	528	-199,812	-378,432,198	6,305,603	632	1,439,663	0,227794782
193159,8	193158	-18,107	-0,000937418	5,755,788	536	-395,788	-7,384,096,601	6,708,026	640	-308,026	-4,812,901,412
209172,8	199534	-9638,76	-4,830,633,557	503,205	540	3,679,504	6,813,896,553	6,219,127	647	2,508,729	38,774,791
238190,1	198473	-39717,1	-2,001,133,411	5,576,939	540	-176,939	-3,276,645,664	6,505,954	641	-959,543	-1,496,947,371
181370	225170	43799,98	1,945,196,131	5,588,256	561	2,174,392	0,387592214	6,544,907	657	2,509,267	0,381927934
206828,2	201420	-5408,16	-2,685,018,861	5,876,725	529	-586,725	-1,109,121,213	6,828,526	632	-508,526	-804,630,361
217058,7	192430	-24628,7	-1,279,878,757	5,374,176	528	-941,762	-1,783,640,571	6,373,852	630	-738,522	-117,225,784
205316,6	201203	-4113,59	-2,044,497,596	5,353,858	545	9,614,161	1,764,066,278	6,328,857	646	1,311,434	2,030,083,022
160858,3	194265	33406,69	1,719,645,317	5,474,477	543	-444,775	-0,819106699	6,545,851	645	-95,851	-1,486,062,306
232433,1	198775	-33658,1	-1,693,276,776	5,074,934	529	2,150,665	4,065,528,397	6,155,072	631	1,549,279	2,455,275,357
231559,1	190135	-41424,1	-2,178,666,993	5,387,267	533	-572,673	-10,744,338	6,329,305	634	1,069,513	0,168692912
206712,8	218591	11878,16	5,433,966,166	5,568,154	535	-218,154	-4,077,644,132	6,641,138	639	-251,138	-3,930,172,602
194925,8	214243	19317,2	9,016,489,352	540,538	544	3,462,009	0,636398741	6,444,597	644	1,540,313	0,238438544
198760	231048	32288,05	1,397,460,492	5,418,732	527	-148,732	-2,822,238,264	6,407,231	628	-127,231	-2,025,968,707
191690,7	226558	34867,34	1,539,002,723	5,045,173	546	414,827	7,597,563,556	6,101,878	645	3,481,219	539,723,886
205575,6	199838	-5737,65	-2,871,149,826	5,343,134	551	1,668,657	3,028,414,728	639,162	652	1,283,801	1,969,020,212
193955,6	213632	19676,44	9,210,435,767	5,232,118	522	-12,118	-0,232145343	6,252,334	623	-223,342	-0,358494827
218079,9	203513	-14566,9	-7,157,720,159	5,063,266	550	4,367,338	7,940,614,966	6,076,995	649	4,130,052	636,371,636
189728,7	203062	13333,32	6,566,132,892	5,312,211	546	147,789	2,706,759,055	6,295,762	646	1,642,384	254,239,043
219953,8	215356	-4597,84	-2,134,995,158	5,573,919	538	-193,919	-3,604,436,987	6,561,465	640	-161,465	-2,522,893,667
223493,2	212287	-11206,2	-5,278,801,869	5,562,468	525	-312,468	-595,177,505	6,514,494	628	-234,494	-3,733,979,682
216836,8	206597	-10239,8	-49,564,122	5,099,771	535	2,502,291	4,677,179,339	6,160,856	635	1,891,438	2,978,641,759
183589,2	214685	31095,81	1,448,438,664	5,414,244	573	3,157,561	5,510,577,398	6,447,845	664	1,921,549	2,893,898,792
223831,2	216369	-7462,22	-3,448,838,912	5,143,952	576	6,160,478	10,695,275	6,158,165	667	5,118,349	7,673,687,205
209876,7	191879	-17997,7	-9,379,733,815	535,746	537	1,253,959	0,233511889	6,357,728	638	2,227,203	0,349091396
201810,8	199357	-2453,83	-1,230,873,566	5,623,783	538	-243,783	-4,531,291,381	6,558,978	642	-138,978	-2,164,765,528
171184,9	198085	20900,07	1,055,106,212	5,033,026	535	3,169,742	5,924,751,121	6,126,942	637	243,058	3,815,667,611
206221,7	204633	-1588,7	-0,776365801	5,314,273	533	1,572,716	0,295068638	6,354,973	634	-149,726	-0,236160935
174005,8	206631	32625,19	1,578,910,474	5,404,479	534	-644,785	-1,207,462,832	6,443,181	638	-631,808	-0,990294218
183801,7	201161	17359,29	8,629,552,407	5,441,141	529	-151,141	-2,855,218,487	6,426,791	633	-967,909	-1,529,081,584
186090,5	198138	12047,51	6,080,364,082	5,229,774	550	2,702,259	4,913,197,851	6,312,367	651	1,976,325	3,035,829,865
221182,3	204128	-17054,3	-8,354,694,233	523,626	541	17,374	3,211,459,905	6,231,044	644	2,089,558	3,244,655,694
196279,2	204377	8,097,786	396,218,072	5,468,314	545	-183,138	-0,336033172	6,436,565	647	3,343,451	0,516762207
224197,7	194995	-29202,7	-1,497,612,641	5,097,194	548	3,828,057	698,550,565	6,162,519	650	3,374,808	5,192,012,259
172879,3	201938	29058,67	1,438,989,671	5,696,189	553	-166,189	-3,005,219,228	6,680,889	650	-180,889	-2,782,907,805
187698,5	196942	9,243,519	4,693,523,601	555,372	529	-26,372	-4,985,261,995	6,544,349	631	-234,349	-3,713,937,141
217126,3	210404	-6722,32	-3,194,957,516	5,286,569	555	2,634,314	4,746,510,886	6,327,082	654	2,129,179	3,255,624,628
183895,8	203511	19615,18	9,638,388,957	5,170,417	543	2,595,833	4,780,540,086	618,127	644	2,587,297	4,017,541,528
171716,6	208930	37213,4	1,781,141,903	5,295,821	542	1,241,789	2,291,123,365	6,353,856	647	1,161,443	1,795,120,916
208574,9	218060	9,485,052	4,349,743,912	5,633,616	580	1,663,845	2,868,697,783	6,522,427	671	1,875,727	2,795,420,001
188791,3	184786	-4005,3	-2,167,533,537	5,741,544	533	-411,544	-7,721,284,741	6,752,926	635	-402,926	-6,345,291,255
193665,8	201820	8154,2	4,040,332,895	5,601,703	533	-271,703	-5,097,611,527	6,522,466	636	-162,466	-255,449,585
174377,8	219568	45190,17	2,058,140,026	4,925,919	548	5,540,809	1,011,096,599	6,184,844	650	3,151,561	4,848,555,083
	Average	5,159,602	0,066375834		Average	-0,09595	-0,07324758		Average	0,291442	0,016639919
	Max	45190,17	2,058,140,026		Max	6,160,478	111,806,272		Max	5,118,349	787,106,123

Comparative study between small punch test and hydraulic bulge test

H. Wang [1*], T. Xu [2] and J. Zou [3]

[1] China Special Equipment Inspection & Research Institute; dearwhk@foxmail.com
[2] China Special Equipment Inspection & Research Institute; xutong@csei.org.cn
[3] School of Mechanical and Power engineering, Nanjing Tech University; 645060741@qq.com

* Correspondence: dearwhk@foxmail.com; Tel.: +86-105-906-8595

Abstract: The systematically comparison between small punch test and hydraulic bulge test is carried out, which include specimen geometry, the test device, testing procedure, testing results interpretation. The specimen geometry, test device and testing procedure are three major aspects of the experiments. Both the testing fixtures of SPT and HBT are redesigned to meet the specimen geometry. The testing procedure of SPT is similar to strain-controlled tension test, which control the displacement of the puncher and measure the corresponding reaction load. The testing procedure of HBT is similar to stress-controlled tension test, which control the pressure of the hydraulic oil and measure the displacement of the deformed specimen. The finite element method is used to study the deformation pattern of the specimen. The initial plastic zone distribution is different. The plastic zone of SPT is concentrated in a small area under the puncher and the initial plastic zone is a circle around the corner of the fixture for HBT. The deformation pattern play an important role in the yield stress interpretation, it is suggest that the interpretation method should include the parameters from the testing fixtures for HBT, and radius of the puncher for SPT.

Keywords: Small Punch Test; Hydraulic Bulging Test; comparative study; small specimen

1. Introduction

Small specimen testing is a technology to get the mechanical properties from a small volume material. There is big demand in the market and industry for these kinds of methods. Small specimen techniques have been developed for almost 50 years. Lots of testing methods have been inverted for small specimen, which include specimen miniaturization, indentation test, small punch test and hydraulic bugle test etc.

Small punch test (short as SPT) is one of the most popular small specimen testing techniques which was developed for nuclear power plant in the 1970s to assessment the safety of critical components [1-2]. After more than 40 years development, there are some codes to instruct to carry out the small punch tests, such as ASTM-F2183, GB/T-29459, and CEN CWA-15627 [3-5].

Hydraulic bugle test (short as HBT) is newly developed small specimen test method. HBT has been used in car industry for plate forming. Recently, HBT is used for small specimen whose width is with 10.0mm and thickness is 0.5mm [6]. HBT use hydraulic oil to make specimen deformation. There is no punch-specimen friction, and there is no puncher related influence, such as the radius of the puncher. The most important advantage is that theoretical derivation could be used to get yield stress and ultimate tensile stress of the specimen. The HBT is sensitive to the environment, for the hydraulic system. High or low temperature will cause the system fail.

Although HBT and SPT are two type of testing method with some similarity, the idea behind the two testing procedure is exactly the same, which is use something to make the specimen deformation, and get the apply force or pressure and the displacement curve. The rigid puncher is used for SPT to make the specimen deformation while high pressure hydraulic oil is used for HBT to make the specimen deformation. So there is no puncher related error factors such as the geometry of the puncher, the puncher axis and friction between the puncher and the specimen in the final testing results. Hydraulic oil which acts same as puncher is used to make the specimen deformation. The puncher related error factors are eliminated due to the fact that there is no puncher in the HBT. The testing device is much more complicated in HBT for the hydraulic system.

Generally, there are four steps in the small specimen testing procedure, which are sampling the specimen from the structure, machining the specimen to specific geometry, testing the specimen and data processing. For HBT and SPT comparison, there is no difference between them in the first step and the second step, and the same sampling machine and sampling procedure could be used. The machining method is slightly different due to the testing specimen geometry. The testing and data processing procedure is different. In this paper, a special design fixture

and a load frames is needed for SPT to get the load force and corresponding displacement, and a high pressure pump and a specimen holdings is used for HBT to get the hydraulic oil pressure-displacement curve.

The testing device, specimen deformation, testing procedure is the major aspect of the comparison. The finite element analysis is used to explain the fundamental difference.

2. Materials and Methods

The material used in the testing is P91 and Q420. P91 play a key role in the energy industry for high temperature application, and Q420 is usually in the structure. The chemical composition and mechanical properties are listed in the table blow. The geometry of the specimen is 10mm by 10mm with thickness 0.5mm.

Two testing methods which are HBT and SPT are used to test the specimen. The pressure of the hydraulic oil increase rate is 0.5MPa/s, and the punch speed is 0.2mm/min.

Table 1. Chemical composition (wt %).

Material	C	Si	Mn	P	S	Cr	Ni	Mo
P91	0.098	0.329	0.499	0.014	0.0041	8.84	0.060	0.94
Q420	0.142	0.235	1.182	0.013	0.0052	0.14	0.036	0.02

Table 2. Mechanical properties.

Material	Yield Strength (MPa)	Ultimate tensile strength (MPa)	A (%)	Z (%)
P91	747	877	22.0	70.63
Q420	489	551	26.5	76.48

3. Comparison between HBT and SPT

3.1. Testing device

For steel properties, small specimen testing method is not a standard testing procedure now, so there is no vendor to supply the testing device to carry out SPT or HBT. Most of the time, we have to design the testing fixture and assemble the testing device. Generally, there are three major parts for the testing device, which are load, fixtures and sensors, as shown in Figure 1, and detail comparison listed in table 1.

There are many differences in the device. The hydraulic oil pump is used to generate high pressure to make the specimen deform, and the puncher is driven by screw. The displacement of the specimen is measured by no-contact video extensometer for HBT for reliability. The fixture is more complicated for HBT, for the fixture should be designed with seal ring to keep the high pressure oil in the fixture chamber. The testing device are shown in figure 2.
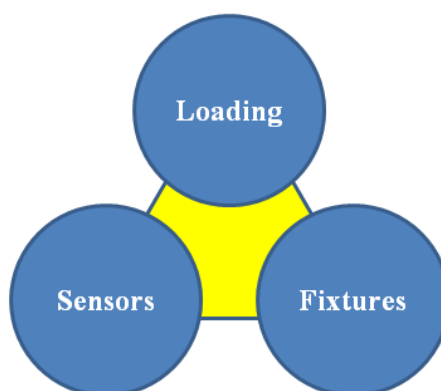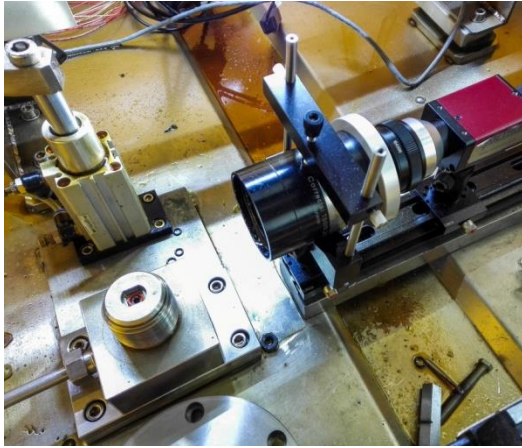

Figure 1. The testing system of HBT and SPT.

Table 3. The testing system comparison.

Title 1	HBT	SPT
Loading system	Hydraulic pump	Servo Motor
Sensors	Video extensometer	Extensometer
	Pressure Gauge	Force Gauge
Fixtures	Shown in figure 2(a)	Shown in figure 2(b)

(**a**) The test device for HBT   (**b**) The test device for SPT

Figure 2. Device comparison (**a**) The test device for HBT; (**b**) The test device for SPT.
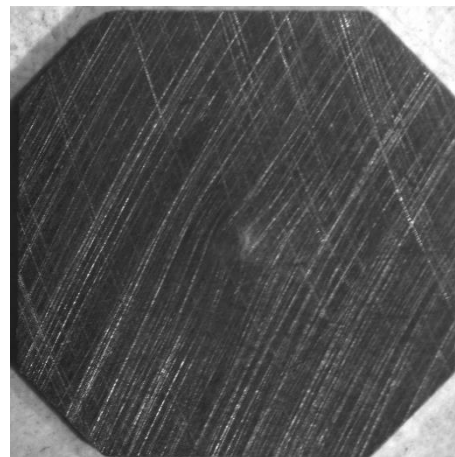
3.2. Specimen deformation

For better comparison between the SPT and HBT, the fixtures of HBT and SPT are redesigned to satisfy the geometry of the specimen.

The geometry of the specimen is shown in the figure 3, which is octagon for HBT and SPT. The width and height of the specimen is 10.0mm, and the thickness is 0.5mm. Four corner of the specimen is removed to make sure that the specimen is perfect contact with the fixtures surface. The specimen is deformed under the load. After the maximum dislocation of the specimen reach 0.1mm , the pressure of the hydraulic oil and the force on the puncher is unload to zero. The deformation of the specimen is shown in Figure 3.

The deformation character is different for HBT and SPT. There is a plastic circle around the boundary of the specimen for HBT, and there is a plastic deformation point at the centre of the specimen for SPT. The different deformation marks indicate that the initial plastic zone is different for HBT and SPT, which indicates that the initiate test curve of HBT is sensitive to the geometry of the fixtures while the curve of SPT is sensitive to the radius of the puncher. This different indication could be further explained by numeric simulation.
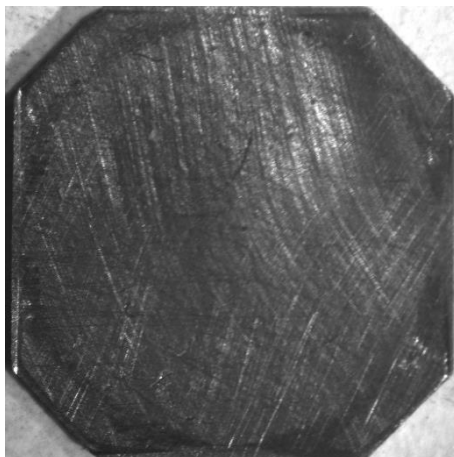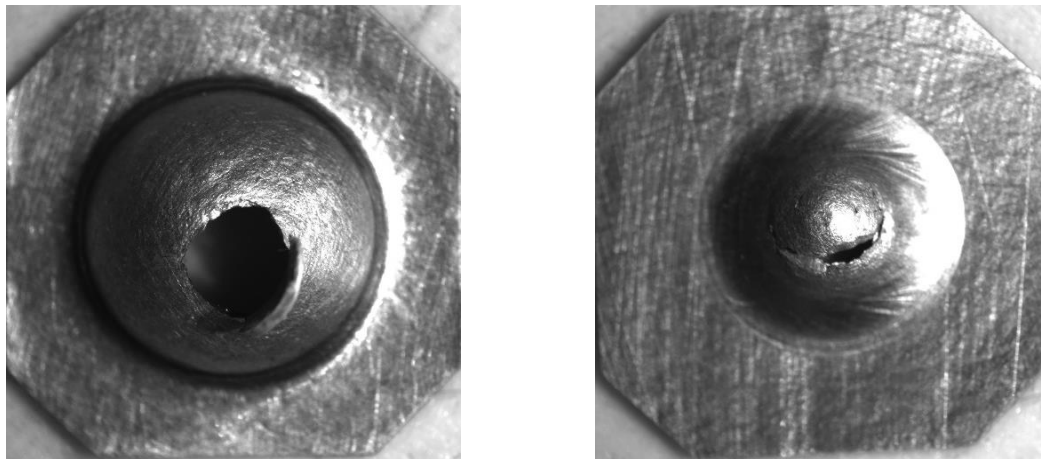

(**a**) HBT   (**b**) SPT

Figure 3. The specimen deformation comparison, the maximum displacement is 0.1mm. The surface of the specimen is sanded to make the deformation more obvious.
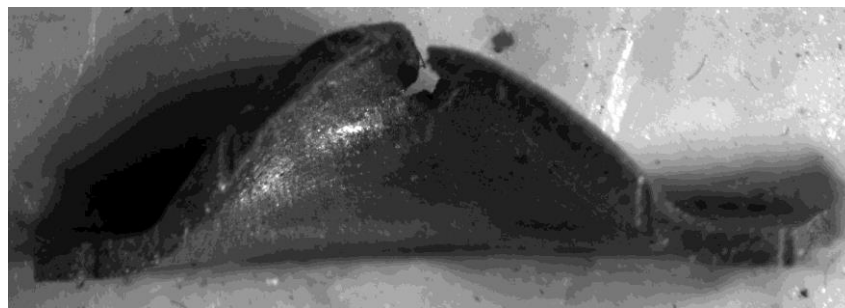
(a) HBT   **(b)** SPT

Figure 4. The fractured specimen deformation comparison.

The specimen after break is different, as shown in figure 4. For HBT, the deformation is similar to sphere, and the radius of the sphere is decrease with the increase of the hydraulic pressure. At the final moment, the initial break area is at the top of the sphere. For SPT, the deformation is similar to cone, and the height of the cone is raise with the increase of the load. Not like HBT, the initial break area is at the skirt of the cone, not at the top of the specimen. The friction between the puncher and the specimen play an important role in determining the location of the initial break. The specimen cut into two parts by electron discharge machining. The section of the specimen is illustrated in figure 5.

(a) HBT
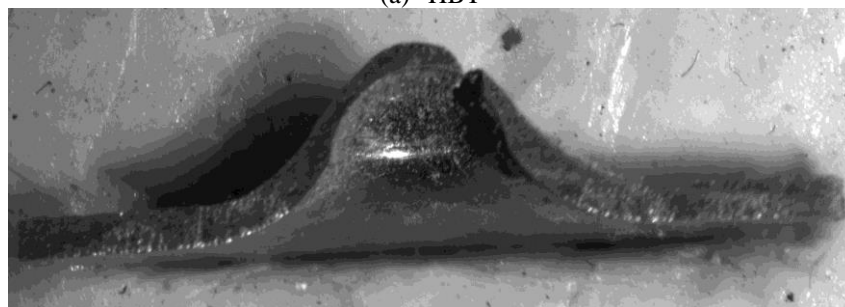
(b) SPT

Figure 5. The cross sections of the broken specimens.

3.3. Loading and deformation

At one level, SPT is a strain-controlled testing method, while HBT is a stress controlled testing method. For SPT, the puncher move to the specimen with a constant speed and a load sensor connected the puncher measures the load to get the displacement-load curve of the test. For HBT, the pressure of the hydraulic oil increase with a constant rate, the displacement of the specimen is transmitted outside of the fixtures and measured by a digital camera. The data for the pressure-displacement curve is from the hydraulic system pressure sensor and the computer digital camera. After the break of the specimen, the pressure of the hydraulic oil decrease to zero immediately and hydraulic oil pour out from the broken specimen, while the load on the puncher will decrease but not to zero. The

SPT and HBT are similar to the two kinds of testing procedure to the uniaxial tension test, which are strain-controlled tension test and stress-controlled test. Usually, the tension test machine drive by servo motor use strain-controlled testing procedure and electro-hydraulic servo use stress-controlled testing procedure.

The most import difference between HBT and SPT is the loading and its distribution on the specimen. The hydraulic pressure distribute on the specimen evenly for HBT, while the puncher is only contact with the specimen within a small area for SPT. With increase the pressure of the hydraulic oil, the contact geometry of the hydraulic oil and specimen changes from plate to spherical cap, and the radius of the spherical cap decrease with the increase of the pressure. During the testing, the contact area is always one side of the surface, and the pressure is distributed evenly on the contact area. For SPT, the contact geometry of the puncher and specimen is just a point at the beginning, and with the increase of the loading force, the contact geometry transform from a point to a spherical cap, and the radius of the spherical cap is a constant which is determined by the radius of the puncher. The intact force distribute on the specimen is not evenly and the will change with the deformation of the specimen. The plastic strain and stress distribution could be simulated by finite element method, and the simulation results are show in figure 6 and figure 7.
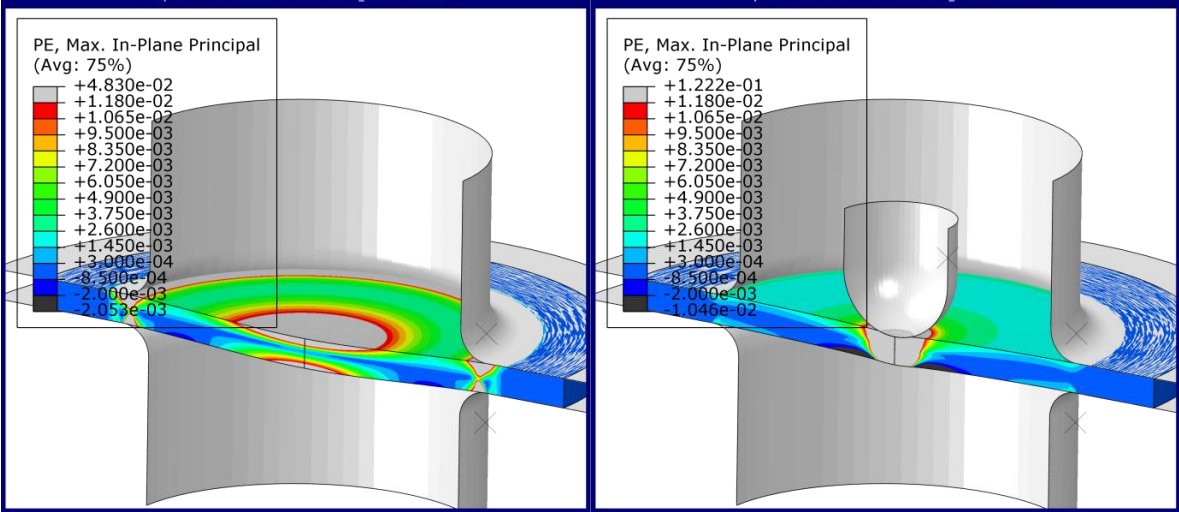

Figure 6. The initial plastic zone(the maximum displacement is 0.1mm.Left:HBT, right:SPT).

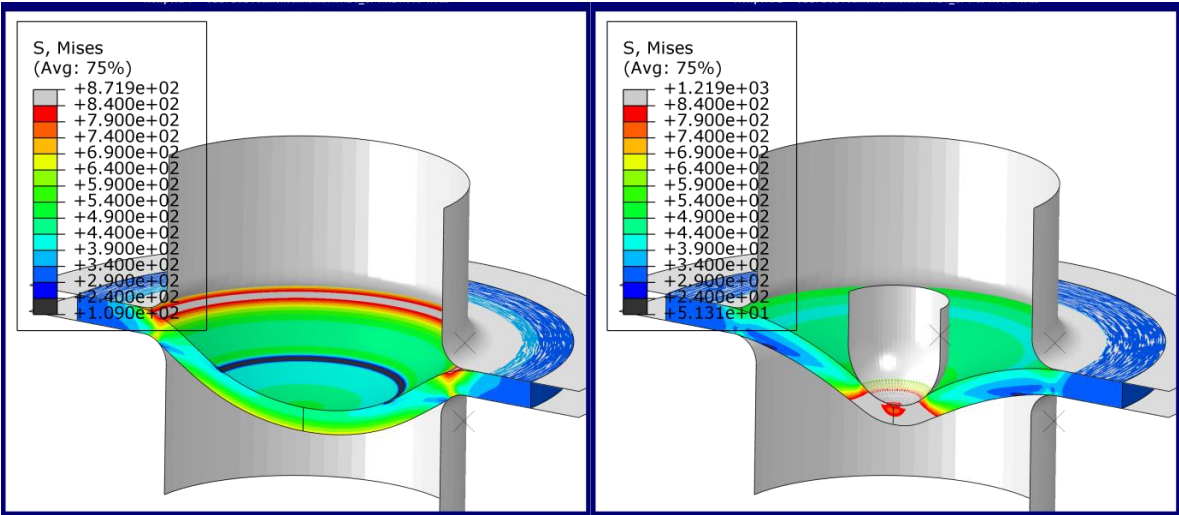**Figure 7.** The stress distribution(the maximum displacement is 1.2mm.Left:HBT, right:SPT).

From a general point of view, if we regardless of the friction between the puncher and the specimen, HBT could be seen as a special kind of SPT whose puncher radius decrease with the deformation of the specimen. SPT could also be seen as a special case of HBT whose hydraulic pressure is limited to a small area with unevenly distribution.
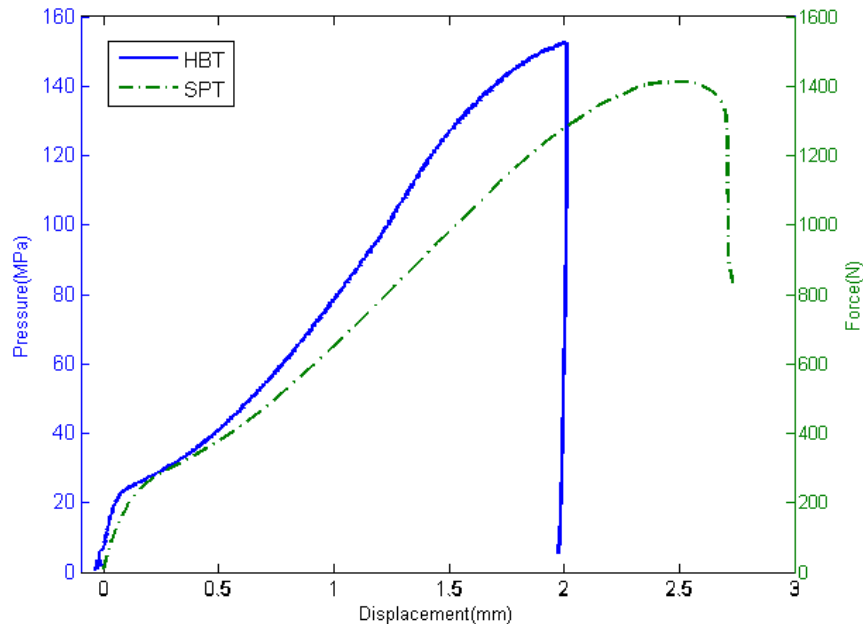
Figure 8. The testing curve of Q420.

The pressure-displacemnt curve from HBT and the load-displacement curve from SPT is drawn in figure 8. Both curve have turring point at low pressure or load, but the mechanism of the turning point is different. It is related the initial plastic zone, as shown in figure 6.

4. Conclusion

Due to the similarity between HBT and SPT, these two methods could be seen as one type of testing method.Those two testing methods could learn from each other in all aspects.

The test devices, test procedure and the results are systematically compared. All of them will greatly influence the test results. A universal test platform is designed for the comparison result. Two kinds of materials P91, Q420 is tested for comparison. The fracture location of small punch test and hydraulic bulge test is compared based on the profile of ruptured specimens, and the fracture mechanism of them are analyzed. The testing data interpretation methods should be further optmized to get a uniform formation.

References

1. Manahan, M. P., The development of a Miniaturized Disk Bend Test for the Determination of Post-Irradiation Mechanical Behavior, Sc. D. Thesis, MIT, Cambridge, Massachusetts, 1982.
2. Manahan, M.P.; Argon, A.S.; Harling, O.K., The development of a Miniaturized Disk Bend Test for the Development of Post-Irradiation Mechanical Properties, Journal of Nuclear Materials, Vol. 103 and 104, 1981, pp. 1545-1550.
3. ASTM F2183-02, Standard Test Method for Small Punch Testing of Ultra-High Molecular Weight Polyethylene Used in Surgical Implants.
4. GBT 29459-2012, Small punch test methods of metallic materials for in-service pressure equipment.
5. CEN Workshop Agreement CWA 15627:2007, Small Punch Test Method for Metallic Materials, Dec. 2007
6. Wang, H.; Xu, T.; Shou B. Determination of Material Strengths by hydraulic bugle test, Materials, Vol 23, 2017.

Miniature creep tests using plate specimens bonded by electron beam welding

K.I. Kobayashi [1], H. Aoki [1,2], T. Kawashima [1,3], M. Takemoto [1,4], Y. Takayama [1,5] and Y. Yamazaki [1]

[1]   Chiba University; k-cobayashi@faculty.chiba-u.jp
[2]   JXTG Holdings, Ltd
[3]   Citizen Watch Co. Ltd
[4]   MITI Japan
[5]   ISUZU Motor Co. Ltd
*   Ken-ichi Kobayashi: k-cobayashi@faculty.chiba-u.jp; Tel.: +81-43-290-3205

Abstract: Many aged thermal power plants restarted to supply sufficient electricity for Japanese industries and daily activities after the seismic earthquake. Reasonable guidelines for assessment of their integrity and estimation of remaining life have been required to operate them with a safety margin. Miniature Creep (MC) test is recognized as a semi-destructive technique to examine the degradation level of aged high temperature components. The MC thin plate specimen of 2.25Cr-1Mo steel and the similar one welded by Electron Beam (EB) for gauge length were employed to evaluate the validity of the EB welded MC thin plate specimen. A series of creep tests using the MC thin plate specimens were conducted in vacuum at 600ºC. Then, following conclusions were obtained: (1) Creep rupture lives of the MC thin plate specimens welded by the EB were nearly the same as those of standard ones. (2) Vickers' hardness in the welded zone decreased in a short time after the test started and reached almost the same as or below that in the base metal. (3) Rupture lives of the EB welded MC thin plate specimen at higher stress levels were longer than those of the standard MC thin plate specimen.

1. Introduction

Great East-Japan earthquake which magnitude was 9.0 happened on March in 2011. Within only an hour, a giant Tsunami generated by the earthquake hit the Japan's east coast. The maximum height of tsunami was about 20 meter, which was much higher than ever expected. Many atomic power plants were located along east coastline of the main island of Japan. Three of them were severely damaged, because they lost cooling systems that were installed under the ground. Unfortunately, two atomic power plants caused meltdown/melt-through due to overheat of the main reactor. After the disaster, all atomic power plants in Japan had completely stopped the generation of electricity for several years. About 30 % of total electricity in Japan were supplied by the nuclear plants at that time. However, a certain amount of electricity has been required to maintain daily lives and industrial activities using other alternative means, even if the atomic power plants stopped. There were many suspended fossil power plants, but some of them were not able to perform the full performance because they were a bit old and not always guaranteed to operate safely. Then, some reasonable guidelines were required to generate the electricity using these old fossil power plants.

There are two main methodologies to evaluate the integrity of high temperature power plants, *i.e*., destructive test and non-destructive test (NDT). Although the destructive test shows higher reliability comparing with the NDT, it has some drawbacks; much more labor and time are taken to conduct these tests. Furthermore, specimens in the destructive test usually require a relatively large volume to sample from actual components. However, sampling large volume specimens sometimes damage target components, and it is also difficult to collect the standard uniaxial specimen from thin plates or grooves/edges with sharp angles. Furthermore, examined components would not be able to reuse even if its integrity was guaranteed after the inspection. Thus, another new testing method using a smaller volume of specimen has been required. Small Punch Creep (SPC) test has been recently proposed to fit these requirements, and their test results have been proved profitable [1-4]. However, the SPC test has an inevitable issue; how to convert test load in the SPC test to stress in the uniaxial creep test? Some significant interpretations and/or useful transformations have been proposed [5-6].

In order to avoid this issue, a miniature creep (MC) test has also been proposed as one of the semi-destructive tests [7-8], where the uniaxial stress can be employed as an index. Since the uniaxial stress as a parameter is the same as that in the standard creep test, uniaxial creep test data accumulated so far will be widely utilized to evaluate

the integrity of aged components. Although the volume of specimen for the MC test is smaller than that of the standard uniaxial one, much less volume specimen should be introduced to examine restricted zones in the components. If only limited zones can be employed as a gauge length (GL) in the MC specimen, the volume for inspection could be greatly reduced. In this paper, an electron beam (EB) welding method was introduced to bond the GL with grip ends using the same material. A series of creep tests were performed employing two standard uniaxial round bar, the standard MC thin plate and the EB welded MC thin plate specimens. Then, it was shown that creep rupture lives of the MC specimens with the EB welding were nearly the same as those of the standard round bar and the standard MC thin plate specimens.

2. Materials and Testing Methods

2.1. Test Material and Specimens

A low alloy heat-resistant steel, SCMV termed as 2.25Cr-1Mo steel in general, was employed here. It is a rolled thick plate with a thickness of 32 mm, 163 mm wide, and 233 mm long. Vickers' hardness test was performed on each section of the material; longitudinal rolling direction and two transverse sections. Then, it was shown that the hardness was independent on each section. The grain size number of the test material was #8 to #9.

Tensile axes of all specimens were cut along the rolling direction of the thick test plate. Two standard round bar specimens were employed, which have diameters of 8 mm and 5 mm, and these corresponding gauge lengths were 38 mm and 20 mm each. These specimens were machined from a usual lathe processing.

Configuration and dimensions of the standard MC and the EB welded MC thin plate specimens are illustrated in Figure 1. The EB welded MC thin plate specimens were welded using three subdivided plates, and then cut to the prescribed shape using an electric discharge machine. Two red lines shown in Figure 1 indicate the EB welded parts. The normal standard MC plate specimen requires at least the area of 50 mm x 13 mm. On the other hand, the area for the EB welded MC plate specimen can be reduced to 15 mm x 7 mm, and then its area ratio is nearly below a sixth. Thickness of each MC thin plate specimens is 1.00 mm. Both surfaces of the MC thin plate specimens were carefully polished with the emery paper of up to # 2000 fine grit before the tests.

Figure 2 show distributions of Vickers' hardness along the loading axis in the vicinity of the EB welding joints. In the horizontal axis, the area indicated from $x = 14.5$ mm to 18.5 mm is the welded zone and the GL is located in over $x= 18.5$ mm. Initial distributions of Vickers' hardness are depicted as the solid squares. Width affected by the EB welding is about 4 mm, and its hardness is twice harder than that of the base metal. The hardness of exposed area in an electric furnace including the GL is almost the same as that of the base metal.

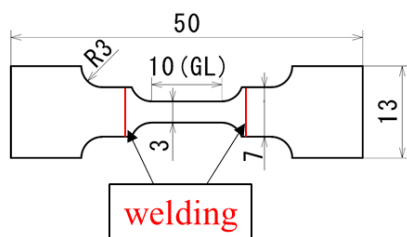**Figure 1.** Configuration and dimensions of Miniature Creep (MC) thin plate specimen. Red lines show the zones welded by Electric Beam (EB), and the thickness of the specimen is 1 mm.
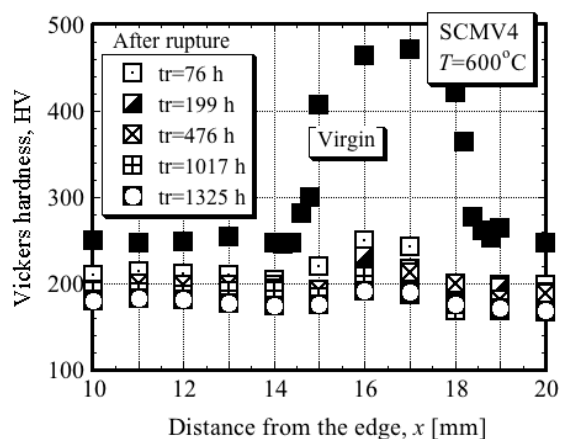

Figure 2. Distributions of Vickers' hardness on MC thin plate specimen around the EB weld lines. Solid squares were measured before the test, and other open symbols show the values measured after the creep tests.

2.2. Testing Apparatus and Procedures

Uniaxial creep tests using the round bar specimen were performed in air with a standard single lever creep machine. Test temperature was set to 600°C. The creep machine for the MC thin plate specimens were newly developed and shown in Figure 2 (a). Here, an enlarging load lever system was not adopted in this machine, because the testing load was very small, so the load was directly applied to the specimen. In order to avoid oxidation of the MC thin plate specimens, this machine equips with a vacuum chamber. The specimens are set up inside this chamber that provided 2×10^{-4} Pa vacuum degree (Figure 2 (b)). An extra guide rod was inserted between the upper and the lower grip ends to prevent bending the specimen during the tests.

If the thermocouple for controlling the test temperature were welded on the MC thin plate specimen, welded spots would have been damaged, and the rupture life would have been shortened. Thus, a difference of temperature between the MC thin plate specimen and a fixed spot inside the chamber was measured in advance, and the temperature at the fixed spot was always controlled through the tests.

All the creep tests were started after 12 hours later when the temperature of the specimen reached 600°C. Displacement of the loading rod was monitored with a linear gauge to measure the deformation between the grip ends and recorded on a chart recorder till rupture. Since the total deformation in the MC thin plate specimen includes rounded zones besides the GL, the deformation of GL was distinguished from the total one using the FE analysis. Thus, the creep strain and its rate in the MC tests were calculated. The actual equation, the theta projection, employed in the analyses is expressed as follows;

$$\varepsilon = \theta_1\{1- \exp (-\theta_2\, t)\} + \theta_3\{1- \exp (-\theta_4\, t)\} \tag{1}$$

$$\theta_1 = 7 \times 10^{-8}\sigma^{2.46},\ \ \theta_2 = 3 \times 10^{-20}\sigma^{8.20},\ \theta_3 = 5 \times 10^{-8}\sigma^{2.60},\ \theta_4 = 4 \times 10^{-21}\sigma^{8.51}$$

(ε: mm/mm, *t*: hour, σ: MPa)
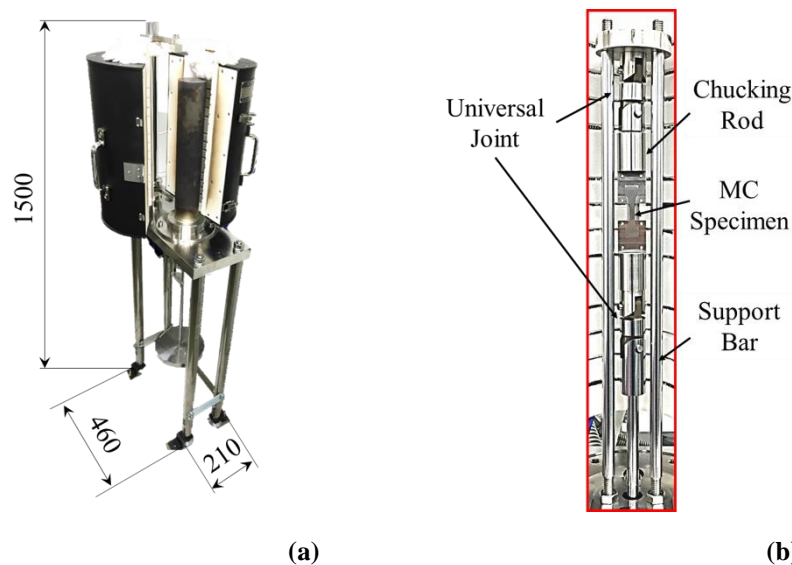

(a)   (b)

Figure 3. Creep machine newly developed for the Miniature Creep (MC) test. **(a)** Total view of the testing machine; **(b)** Set-up of the MC thin plate specimen inside the vacuum chamber.

3. Creep Test Results and Discussions

3.1. Results of the round bar specimens

Figure 4 shows creep test results employing the round bar specimens of 5 mm and 8 mm in diameter. Two solid lines are drawn using a least-square method. In this figure, *R* denotes a correlation factor. It seems that there is a bit larger variation on rupture lives in the tests of 8 mm round bar specimen, shown as the open circles. This may be caused by the fact that these specimens were sampled from different individual plates.

Figures 5 (a) and (b) show appearances of 5 mm round bar specimen at rupture. These creep tests were conducted in air, so some oxide films were formed on the surface of specimens. Especially, severe ring-type oxide
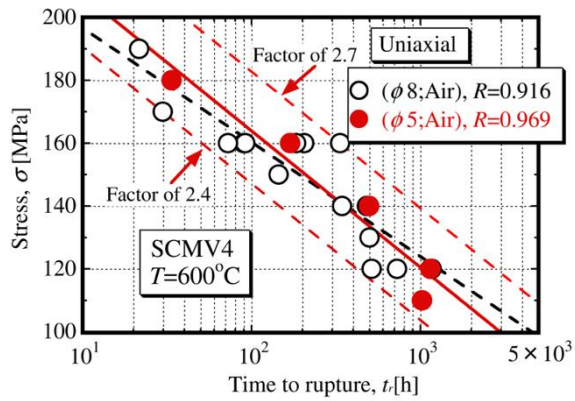
Figure 4. Relationship between the applied stress and time to rupture using round bar uniaxial specimens. All tests were performed in air.
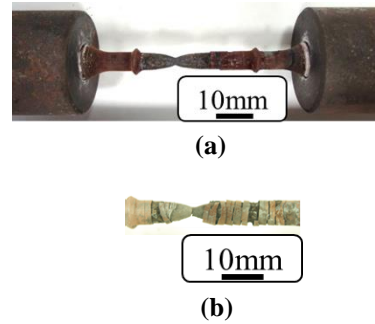

Figure 5. Appearance of ruptured round bar specimens of 5 mm in initial diameter.

(a) Stress is 120 MPa, tr =1,146 hours;

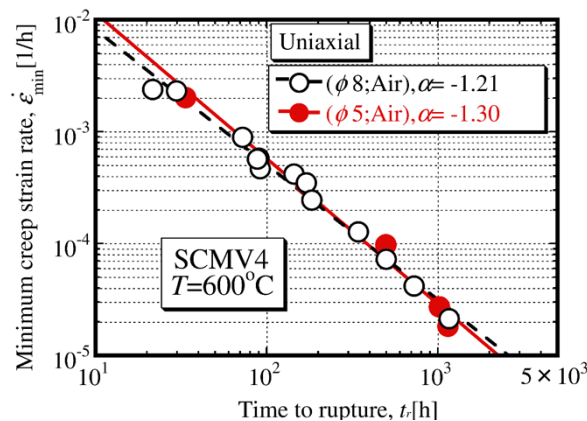**(b)** Stress is 110 MPa, tr =1,022 hours.

Figure 6. Monkman-Grant relation in the creep test employing the round bar specimens. Each solid line is drawn by using the least-square method.

films were found on the specimen tested at the stress of 110 MPa (Figures 5 (b)) due to long exposure. These thick oxide films reduced the diameter of round specimens, and then the actual stress on the net section was increased; the rupture life at 110 MPa was a little shorter than the statistically predicted solid red line.

Monkman-Grant relationships are shown on Figure 6. Slope α in this relation is a bit steeper comparing with other literatures [9]. However, there was little dependency on whichever the specimen was employed.

3.2. Results of the MC thin plate specimens

In this section, the creep test results using the MC thin plate specimens were shown and discussed dividing into two items; (1) standard MC thin plate and (2) EB welded MC thin plate specimens.

3.2.1. Case #1; Standard MC Thin Plate Specimen

Creep curves employing the standard MC thin plate specimens exhibited nearly the same manner as the those of the round bar specimens; the primary stage of creep rarely appears, the secondary and the tertiary stages of creep occupies most of creep life.

Creep rupture data employing the standard MC thin plate specimen are plotted in Figure 7 as blue open triangles. The MC thin plate specimen at higher stress levels has a tendency to extend its rupture time a little longer than that of the round bar specimens, but the lifetime at lower stress levels sometimes become to be shortened. Especially one specimen at the stress of 110 MPa broke in a very short time. Although the reason why this causes has currently been unclear so far, rupture lives of the round bar specimens at lower stress levels are also shorter than the solid red least-square line derived from the test results using MC thin plate specimens.
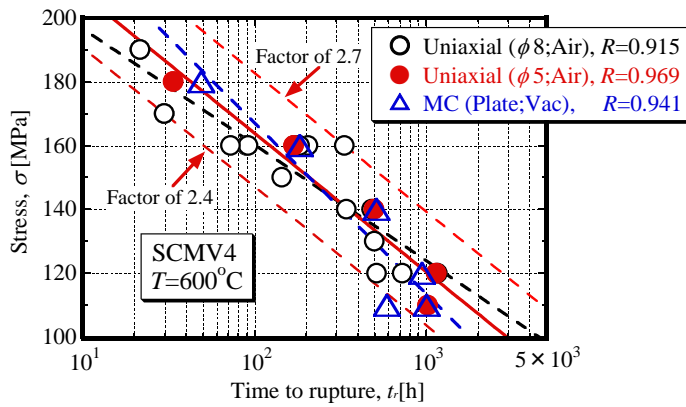
Figure 7. Relationship between the applied stress and time to rupture for the standard MC thin plate specimens.
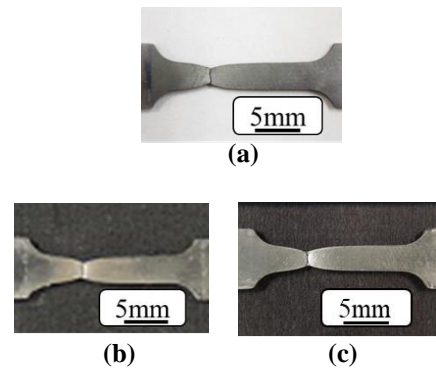

Figure 8. Appearance of standard MC thin plate specimens at rupture.

(a) Stress is 120 MPa, tr = 970 hours;

(b) Stress is 110 MPa, tr = 1,006 hours;

(c) Stress is 110 MPa, tr = 591 hours.

Figures 8 (a) to (c) show appearances of the standard MC thin plate specimens at rupture. These tests were conducted in vacuum. Little oxide film was observed on the surface of specimens, and superficially there was little differences between the specimens at the stress of 110 MPa even if the rupture time was significantly different (Figures 8 (b) and (c)). In order to calculate the creep strain and its rate on the GL of the MC thin plate specimen, the theta projection was applied in the FE analysis, where the creep data obtained in Section 3.1 were employed [10].

3.2.2. Case #2; EB Welded MC Thin Plate Specimen

Relations between the rupture time and the applied stress for the EB welded MC thin plate specimens are added in Figure 7, and they are displayed as green open squares in Figure 9. Their rupture lives are plotted near those using the standard MC thin plate specimens or a little longer than them, and variations fall within nearly a factor of two based on the solid red line. This relation may be caused by the reason why the welded zone had higher strength than the base metal. Figure 2 demonstrates that Vickers' hardness around the welded zone decreases in a short time soon after the test starts, and the welded zone gradually softens with time. In Figure 9 a test result at the stress of 110 MPa using the MC thin plate specimen depicted in brackets is excluded to recalculate the least square line, because its rupture time was extremely short.
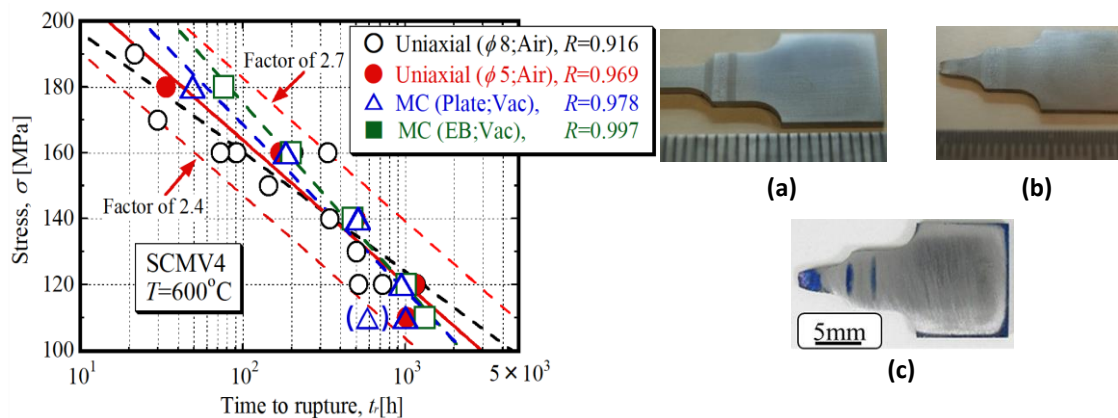

Figure 9. Relationship between the applied stress and time to rupture for MC thin plate specimens.

Figure 10. Appearances of the welded MC thin plate specimens around the welded zone.

(a) Before the creep test, **(b)** After the test, tr=76 hours, **(c)** Dents along HAZ after the test.

A general view before the test around the welded zone in the EB welded MC thin plate specimen is shown in Figure 10 (a), where two lines in the HAZ can be distinguished clearly. Figure 10 (b) is another photo of the same specimen at rupture. It seems that the two lines disappeared at first glance. After coloring in blue on the surface with an oily marker ink, the specimen was polished and wiped. Dents along the HAZ remain in blue colored in Figure 10 (c). Since the HAZ area was a bit softer than the other ones, it might deform unexpectedly during the creep test.

(a)

(c)

(c)

(d)
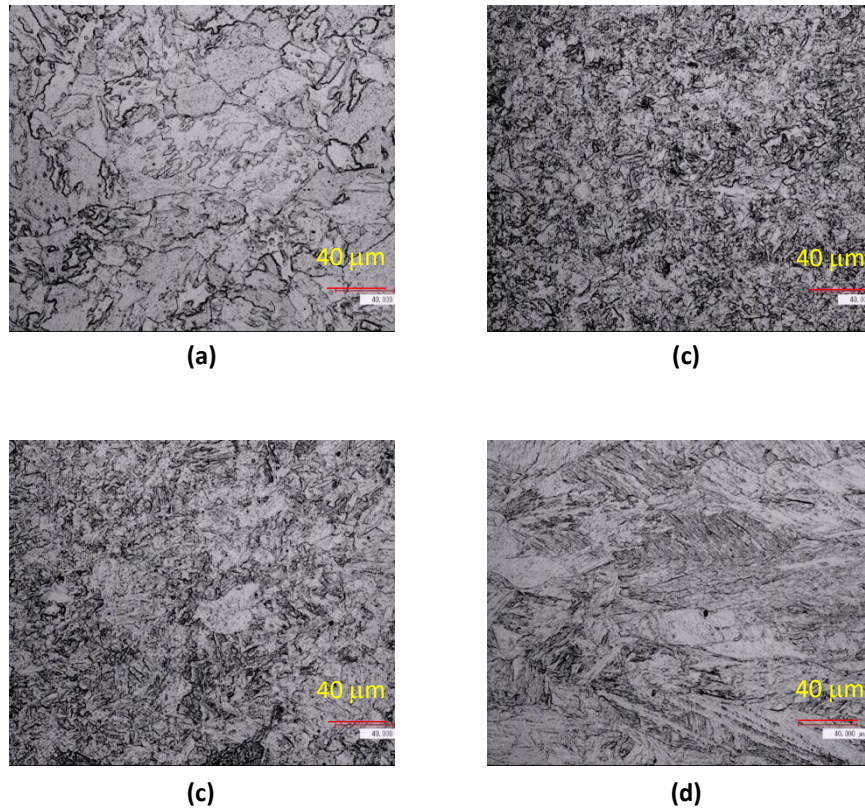
Figure 11. Microstructures in the EB welded MC thin plate specimen.
(a) Base Metal; **(b)** FGHAZ; **(c)** CGHAZ; **(d)** Weld Metal.
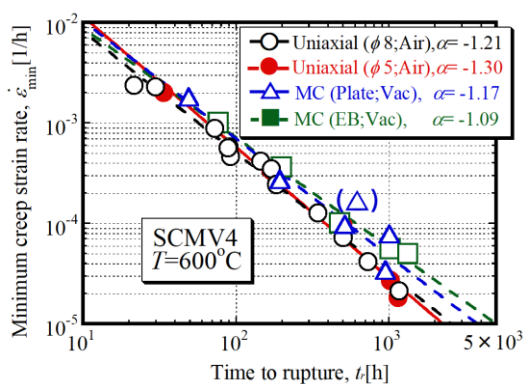
Figure 12. Monkman-Grant relations obtained in this study employing round bar and MC thin plate specimens. Each line is drawn using the least-square method.
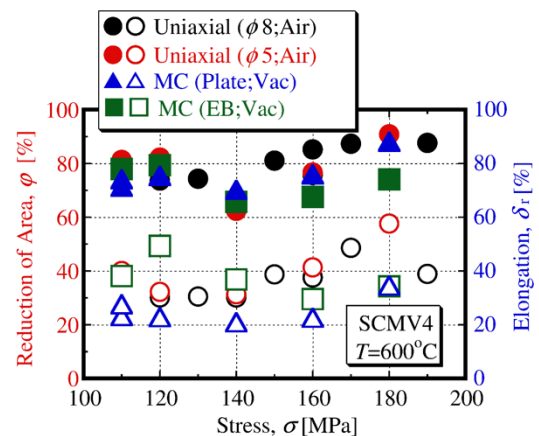
Figure 13. Relationship between elongation / reduction of area (RA) and applied stress. Open symbols show the elongation, and solid ones RA.

Microstructures of the EB welded specimen before the test are shown in Figures 11. They are (a) Base Metal, (b) Fine Grain HAZ, (c) Coarse Grain HAZ, and (d) Weld Metal. Here, the contents of a corrosion liquid are; 250 mL of Ethanol, 0.9 g of Picric acid, and 1 mL of Nitric acid. It can be seen that each zone has different structures. Every fracture surface of the specimens at rupture was also examined with a laser microscope, and it was found that

dimple patters covered all fracture surfaces. The diameter of dimples generally depended on the time to rupture: the longer the rupture time, the larger the diameter of dimple was.

All Monkman-Grant relationships acquired here are illustrated in Figure 12. Each dashed and solid lines are drawn using the least-square method. This picture indicates that the slopes in blue and green dashed lines based on the MC plate specimens exhibit a little gentler than those employing the round bar ones. In Figure 9 there is a difference in the creep rupture time at higher stress levels, but in Figure 12, apparent contrast in the minimum creep strain rate can be found at longer rupture lives / in the lower stress levels. This may be caused by conversion results of creep strain in the MC plate specimens. In these creep tests, only the creep deformation between both grip ends of the specimen was measured. In order to calculate the creep strain in the MC plate specimens, the creep deformation of GL must be separated from that of grip ends. Thus, the deformation ratio of the GL to the total one was introduced. FEA results explain that this ratio gradually increases with time; it starts from 0.60, 0.85 at t/t_r=0.2, and 0.93 at t/t_r =0.8. However, the creep deformation of the GL in the MC plate specimen at lower stress levels may be calculated a little greater than the actual deformation, because the creep data below the stress of 120MPa were not employed in the FEA due to a lack of those creep data.

Figure 13 displays changes of elongation and reduction of area (RA) with the applied stress, where the elongation depicted as open symbols, and the RA as solid ones. As the results of examining precisely, each index may depend on the type of specimens. However, from a broad viewpoint it seems that both values a bit decrease with the decrease of stress similarly, and round bar specimens indicate a little more ductile failure comparing with the plate specimens. Thus, creep properties, *i.e.*, rupture time and ductility of the EB welded MC thin plate specimens, show nearly the same as those of the standard MC thin plate ones and/or the round bar specimens.

Then, if a very small volume were sampled from target components, its creep properties could be estimated employing the EB welded MC thin plate specimen. Henceforth, it would be studied whether this methodology could be suitable to examine the residual life of aged components or other heat-resistant materials.

4. Conclusions

In order to minimize the uniaxial creep specimen, Individual three parts, *i.e.*, parallel gauge length and grip ends in the plate specimen, were bonded using the electron beam (EB) welding method. The target area can be limited, and then the volume of EB welded MC thin plate specimen can be reduced below a sixth comparing with the standard MC one. In addition to the standard MC thin plate and the standard round bar specimens, a series of creep tests were conducted to examine the validity of EB welded MC thin plate specimen. Then, following results were obtained.

(1) Creep rupture lives of the EB welded MC thin plate specimens were nearly the same as those of the standard MC thin plate specimens and the round bar ones.

(2) Vickers' hardness in the welded zone decreased in a short time after the test started, and reached almost the same as or below that in the base metal.

(3) Rupture lives of the EB welded MC thin plate specimen at higher stress levels were longer than that of the standard MC thin plate specimen.

References

1. Parker, J.D.; James, D.J., Creep Behaviour of Miniature Disc Specimens of Low Alloy Steel, Proceedings of ASME Development in a Processing Technology, PVP-Vol.279, 1994.

2. Parker, J.D.; Stratford, G.C.; Shaw, N.; Spink, G.; Metcalfe, H., The Application of Miniature Disc Testing for Assessment of Creep Damage in CrMoV Rotor Steel, Baltica IV, Plant Maintenance for Managing Life & performance, Vol.2, pp.477-488, 1998.

3. Komazaki, S.; Hashida, T.; Shoji, T.; Suzuki, K., Development of Small Punch Tests for Creep Property Measurement of Tungsten-Alloy 9%Cr Ferritic Steels, *Journal of Testing Evaluation*, ASTM, Vor.28, No.4, pp.249-256, 2000.

4. Kobayashi, K.; Kajihara, I.; Koyama, H.; Stratford, G.C., Deformation and Fracture Mode during Small Punch Creep Tests, *Journal of Solid Mechanics and Materials Engineering*, Vol.4, No.1, pp.75-86, 2010.

5. Komazaki, S., Development of Remaining Life Assessment Technology Using SP Creep Test, The Frontier of Technology Development in Remaining Life Assessment for High Temperature Components Chapter II, *Journal of JSMS*, Volume 61, No.12, pp.980-986, 2012 (in Japanese).

6. The Society of Materials Science, Japan, Miniature Creep Tests Method - For the Assessment of High Temperature Equipments-, pp.172-177, 2012 (in Japanese).

7. Kadoya, Y.; Goto, T.; Date, S.; Yamauchi, T.; Karato, H.; Sada, T.; Assessment of Remaining Life Using Miniature Creep Tests for Fossile Plant Parts, *Journal of JSMS*, 1990, Volume 39, No.445, pp.1373-1379.

8. Sonoya, K; Kitagawa, M., Evaluation of Creep Rupture Properties Using Miniature Specimens, *Journal of JSMS*, 1992, Volume 41, No.460, p.112 (in Japanese).

9. Viswanathan, R., *Damage Mechanics and Life Assessment of High-Temperature Components*, ASM International: Ohio, USA, 1989; p.82, ISBN 0-87170-358-0.

10. Evans, R.W.; Wilshire, B., *Creep of Metals and Alloys*, The Institute of Metals: London, England, 1985; p.204, ISBN 0-904357-59-7.

Determining the temperature dependent fracture toughness of carbon-bonded alumina using chevron-notched specimens

H. Zielke [1],*, M. Abendroth [1], M. Kuna [1]

[1] Institute for Mechanics and Fluid Dynamics, TU Bergakademie Freiberg, Germany
* Correspondence: henry.zielke@imfd.tu-freiberg.de; Tel.: +49-3731-39-3371

Abstract: Open cell ceramic foam filters are used for metal melt filtration. The aim is to reduce the number of non-metallic inclusions and therefore to enhance the quality of the cast product. A new generation of multifunctional filters, which is investigated within the collaborative research center CRC920, is made of fine grained carbon-bonded alumina. The filter manufacturing process leads to hollow struts with sharp edge cavities, which could act as a crack tip. To evaluate the integrity of the filter, a fracture mechanical characterization of the bulk material at different temperatures is necessary. In the applied chevron-notched beam method (CNB) the small specimens (5 x 6 x 25 mm^3) are loaded with a four-point bending test set-up until failure occurs. The test set-up offers the possibility of testing at temperatures up to 1000°C. With the help of the measured load-displacement curve the fracture toughness is calculated. Additionally, an analysis of the microstructure of the fracture surface of the specimens is presented.

Keywords: chevron-notched beam method; carbon-bonded alumina; fracture toughness

1. Introduction

The presence of non-metallic inclusions is an important question for the quality of cast products. A low number of these inclusions increase the properties of the cast product. This is the reason, why open cell ceramic filters are utilized during metal melt filtration. Furthermore, a reduction of turbulences in the melt flow, which also leads to an enhancement of the quality of the cast product, is achieved. An essential requirement for industrial application is the integrity of the filter with respect to the applied loading by the metal melt during the casting process. The filter has to withstand the mechanical loading at elevated temperatures without any failure to avoid additional impurities of the cast product.

Within the scope of the collaborative research center CRC 920 "Multi-Functional Filters for Metal Melt Filtration – A Contribution towards Zero Defect Materials" at TU Bergakademie Freiberg, Germany, an new generation of filters are made of fine grained carbon-bonded alumina [2]. The filter manufacturing process is based on the Schwartzwalder replica technique [3]. This technique uses polyurethane foams which define the topology and the geometry of the filter. The ceramic slurry is produced and applied to the polyurethane foam as a coating. After a drying process the foam is heat treated. The polyurethane pyrolizes during the heat treatment. The result of the manufacturing process is a filter structure with hollow struts. The hollow struts have sharp-edged cavities which can act as crack tips. Consequently, a fracture mechanical characterization is required.

A standardized method to evaluate fracture toughness of ceramics [4, 5] is the chevron-notched beam test (CNB), which is the applied testing technique in this study. Experimental bending test set-ups with specimens possessing a chevron notch have been introduced and standardized since the 1960's [6–8]. The advantage of this test set-up is that no sharp pre-crack has to be introduced at the beginning of the test [1] because a sharp crack is formed during loading. Additionally, no crack length measurement is required and a stable crack growth can be reached due to the geometry of the notch [9] because of the increasing crack front with increasing crack length. The challenge in the present work is to qualify the CNB test for high temperature testing at 800°C and to use a non-standard specimen geometry. Therefore, a special test set-up is developed to handle the specimen under high temperature environment. The set-up and the function of each component is explained and described.

2. Materials and Methods

2.1. Carbon-bonded alumina

One of the filter materials is a fine grained carbon-bonded alumina Al2O3-C, usually applied to steel filtration. It consists of different raw materials which are 99.8%-pure alumina (Martoxid MR 70, Martinswerk, Germany, d_{90}

≤ 3.0 μm) and three different carbon sources. The carbon sources are named modified coal tar pitch powder (Carbores® P, Rütgers, Germany, $d_{90} \leq 0.2$ mm), fine natural graphite (AF 96/97,Graphit Kopfmühl, Germany, 96.7wt% carbon, 99.8wt% ≤ 40 μm), and carbon black powder (Luvomaxx N-911, Lehmann & Voss & Co., Germany, ≥ 99.0 wt.% carbon, > 0.01 wt.% ash content, primary particle size of 200 – 500 nm). The mass fraction of the residual carbon content is about 30%. The chemical composition of the slurry with a total solid mass fraction of 60% can be found in Table 1.

Table 1. Chemical composition of Al2O3-C slurry.

Raw material	Mass fraction in %
Martoxid MR 70	66.0
Cabores® P	20.0
AF 96/97	7.7
Luvomaxx N-991 2	6.3
Additives[a]	
Castament VP 95 L	0.3
Contraspum K 1012	0.1
C12C	1.5

[a] Related to total solid content

To produce the slurry, the powdery raw materials are mixed together with deionized water. Afterwards, the slurry is used to manufacture the filter or the specimens. The next steps are a mixing and a drying process followed by a heat treatment. This coking regime runs through a stepwise heating up to 800°C and is described in detail by Emmel et al. [10]. Carbores® P is acting as the binding phase during the heat treatment. Hence, the alumina is bonded in a carbon matrix. Approximately 80% of the mass fraction of the Carbores® P remains inside the material, the other 20% are volatile organic components. The porosity of the material is about 40%.

The slurry of the material is slip cast into rectangular blocks (25 x 25 x 150 mm³), dried and heat treated according to their specific heating regime. Specimens with final dimensions are cut from these blocks after the heat treatment. Finally, the triangularly shaped notch is cut into the specimens made of carbon-bonded alumina using a precision diamond wire saw (Well, Mannheim, Germany) with a wire diameter $d = 0.3$ mm (Well, Type A3-3. The final dimensions of the specimens amount to length $L = 25$ mm, width $W = 6$ mm, and thickness $B = 5$ mm.

2.2. Chevron-notched beam method

In order to determine the fracture toughness K_{Ic} of the brittle filter bulk material, the chevron-notched beam method is applied. Different configurations of chevron-notched specimens are available in literature, for example the short bar [8, 11], short rod [12, 13], and four-point-bending specimens [9]. The triangular shaped notch which is cut into the specimen offers the following advantages: Firstly, no pre-crack is necessary because a sharp crack develops from the tip of the notch during loading. Secondly, no crack length measurement is required because only the maximum load is necessary to calculate the fracture toughness of the specimen after testing. For further investigations, the notch parameters crack length a, chevron tip dimension a_0 and chevron dimension a_1, see Fig. 1b, are normalized with respect to the specimen width W leading to $\alpha = a/W$, $\alpha_0 = a_0/W$ and $\alpha_1 = a_1/W$, respectively.

In the present study, a four-point-bending set-up is applied to the chevron-notched specimen which differs slightly from the geometry of the standardized method [4, 5]. Figure 1 shows the geometrical parameters and the developed test set-up [14]. One roller of loading and supporting span are replaced by a ball, which is in contrast to DIN-Norm application at which two roller pairs are used. The balls in test set-up are used to fulfill the DIN-requirements of the rotatable support and to offer the possibility of high temperature testing. Both rollers (m) and balls (k) have diameters of $D = 5$ mm. A cage structure is assembled to the lower sealing of the testing machine (i). This cage structure was constructed in order to ensure the alignment of the specimen (k) by specimen positioning bolts (g) as well as the loading and bearing components. The cage structure is guided by a housing (d) and consists of three rings, namely lower (h), middle (f) and upper cage ring (c). The upper and lower spacers and guiding rods, which are not visible in Figure 1a, provide the correct distance between the cage rings. The load from the upper punch (a) is transferred to the inner ball-cylinder pair via loading plate (e) and loading ball (b).
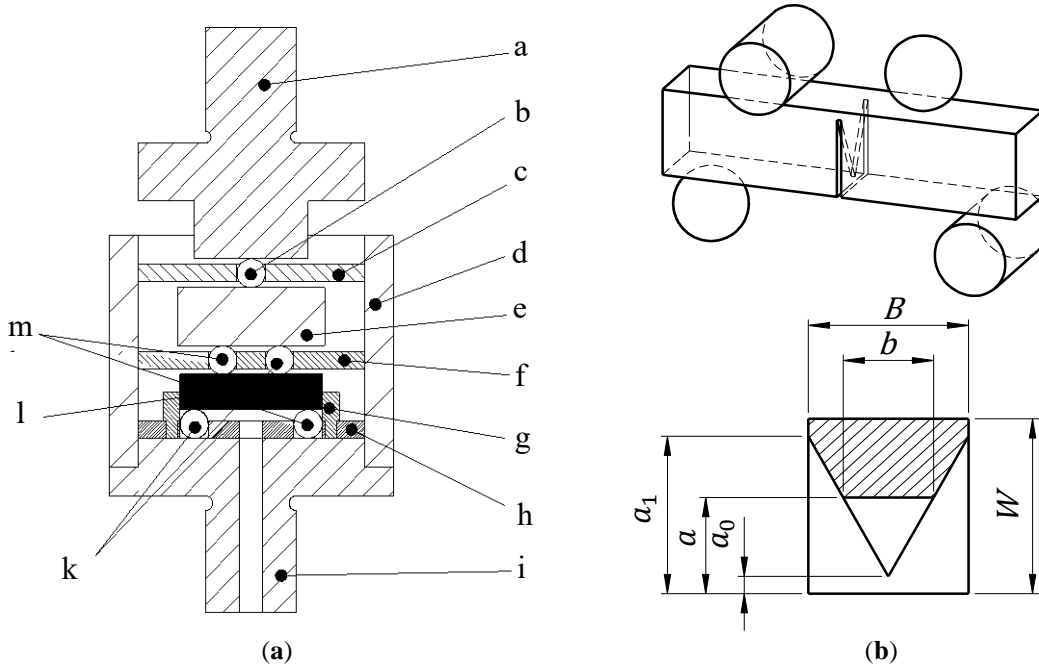
Figure 1. CNB test set-up: (**a**) Schematic of constructed set-up, (**b**) Details of specimen and geometrical parameters (S_1 – supporting span, S_2 – loading span, b – length of crack front).

The loading of the chevron-notched specimen is displacement controlled, with a constant displacement rate of $\dot{u} = 0.01$ mm/min until the specimen fails. The test set-up is assembled into a universal testing machine (inspekt table 10, Hegewald & Peschke, Nossen, Germany) that enables the measurement of a load-displacement curve with a 1 kN load cell. A very stiff testing machine is required in order to get valid test results. The experiments are performed at room temperature and 800°C under inert gas atmosphere with argon. For the elevated temperature tests, a three zone furnace (STE-13, Hegewald & Peschke) is used. The crack initiates at the tip of the notch and while propagating the compliance of the specimen increases. Additionally, the crack front b and the necessary energy for crack extension Δa increase continuously during crack growth. This results in a non-linearity at the load-displacement curve. The minimum of the geometry function of the specimen Y^*_{min} and the maximum of the load-displacement curve coincides with each other. With the help of the maximum load F_{max} the fracture toughness is calculated. A test is not valid, if the load-displacement curve exhibits only a sudden decrease of the load without a smooth maximum. Hence, no crack arrest is reached and the crack propagates unstably. In that case, no fracture toughness can be calculated. Some other restrictions due to the symmetry condition of the notch can also lead to an invalid test [4].

The fracture toughness is finally calculated with

$$K_{Ic} = \frac{F_{max}}{B\sqrt{W}} Y^*_{min},\tag{1}$$

at which F_{max} is the maximum measured load and Y^*_{min} the minimum of the geometry function of the specimen. Munz et al. [1] provides an empirical formula based on compliance measurements and FEM simulations for the minimum of the geometry function:

$$Y^*_{min} = (3.08 + 5.00\alpha + 8.33\alpha^2)\left(1 + 0.007\sqrt{\frac{S_1 S_2}{W^2}}\right)\frac{\alpha_1 - \alpha_0}{\alpha - \alpha_0}\frac{S_1 - S_2}{W}.\tag{2}$$

The validity area for this formula is given by $0.12 \leq \alpha_0 \leq 0.24$ and $0.9 \leq \alpha_1 \leq 1$.

3. Results and Discussion

The fracture toughness of the filter material carbon-bonded alumina is calculated with Eq. (1) and Eq. (2) and the measured maximum load of the CNB tests. The experiments were performed at room temperature and 800°C. A number of 15 specimens were tested at each temperature, but not every specimen shows a valid load-displacement

curve. Consequently, the number of valid experiments is 14 and 10 at room temperature and elevated temperature, respectively. Examples for measured load-displacement curves of valid tests for each temperature are plotted in Figure 2.
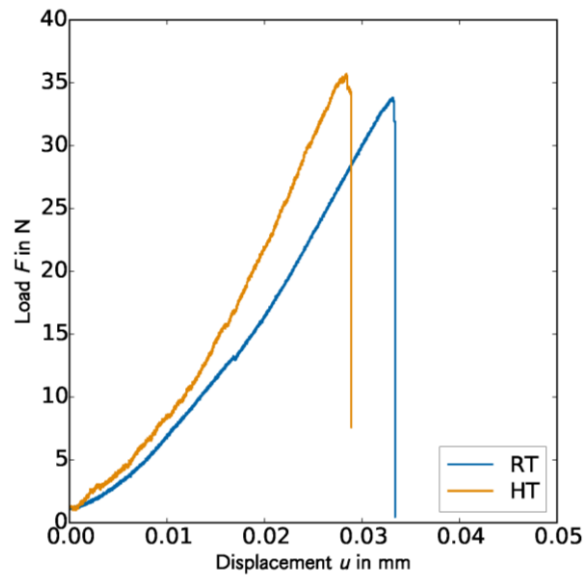

Figure 2. Measured load-displacement of CNB test at room temperature (RT) and 800°C (HT).

The curves start with a running-in characteristic followed by a linear section and a maximum until the specimen fails and a sudden load drop occurs. The load drop starts close to the load maximum because of the low fracture toughness of the material. Nevertheless, a small section of stable crack growth can be obtained. The difference between the curves at both temperatures can be explained by the change of Young's modules with respect to the temperature [15, 16]. The results of all valid tested specimens and the geometry parameters of the notch are shown Table 2. The analysis of the results points out that the testing temperature shows no significant influence on the fracture toughness of carbon-bonded alumina.

Table 2. Temperature dependent fracture toughness of carbon-bonded alumina.

Testing Temperature in °C	F_{max} in N	W in mm	B in mm	α_0	α_1	K_{Ic} in MPa$\sqrt{m}$
25	31,42	5,93	4,89	0,20	0,90	0,552
	30,76	6,03	4,93	0,22	0,90	0,543
	33,82	6,07	5,01	0,20	0,90	0,561
	35,83	6,04	4,94	0,18	0,89	0,577
	26,76	6,03	4,98	0,29	0,96	0,576
	29,64	5,87	4,91	0,27	0,97	0,660
	32,82	6,07	5,05	0,22	0,93	0,579
	31,76	5,92	4,98	0,21	0,94	0,589
	28,97	5,86	4,88	0,27	0,97	0,648
	29,19	6,05	4,99	0,22	0,93	0,526
	29,92	6,02	4,92	0,25	0,95	0,598
	27,53	6,01	4,83	0,25	0,96	0,565
	27,08	5,96	4,90	0,24	0,94	0,531
	32,98	6,12	4,99	0,21	0,92	0,562
800	38,05	5,99	4,85	0,16	0,86	0,587
	31,65	5,93	4,80	0,18	0,87	0,529

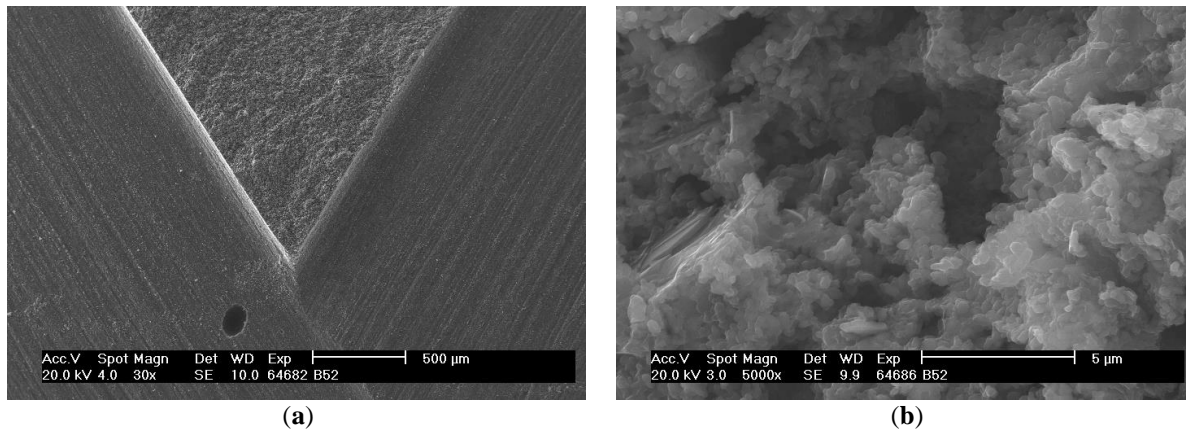| Testing Temperature in °C	F_{max} in N	W in mm	B in mm	α_0	α_1	K_{Ic} in MPa$\sqrt{m}$
	41,45	6,07	4,83	0,17	0,83	0,611
	34,77	5,80	4,95	0,16	0,87	0,567
	42,79	5,99	4,89	0,11	0,81	0,562
	33,32	5,94	4,80	0,18	0,83	0,527
	35,72	5,98	4,83	0,20	0,88	0,610
	41,45	6,07	4,94	0,15	0,86	0,602
	42,79	6,01	4,85	0,11	0,82	0,566
	43,31	6,00	4,75	0,13	0,80	0,594

Figure 3. SEM-micrograph of the fracture surface of carbon-bonded alumina: (**a**) 30-times magnified; (**b**) 5000-times magnified.

Additionally, the crack surface topologies are analyzed for the carbon-bonded alumina. Figure 3 illustrates the microstructure of the crack surfaces obtained by a scanning electron microscope (SEM), Philips XL 30 (Phillips, Germany) with different magnifications. The fracture surfaces of the material at higher temperatures are equal to those at room temperature and therefore not shown in the present paper. Carbon-bonded alumina exhibits a homogeneous microstructure and a macroscopically flat fracture surface. No plastic deformations and a smooth fracture surface indicate a brittle fracture at both temperatures. Figure 3b shows the alumina particles that are embedded in the carbon matrix. An intergranular fracture can be obtained because of the visible grain boundaries at this magnification.

5. Conclusions

The chevron-notched beam test with a non-standardized specimen geometry was applied to a carbon-bonded alumina at different temperatures. The fracture toughness was determined using the empirical formula proposed by Munz et al. [1]. Carbon-bonded alumina shows a constant value up to the elevated testing temperature of 800°C. A fractographic analysis revealed smooth crack surfaces without plastic deformations and with visible grain boundaries as a result of an intergranular cleavage fracture.

References

1. Munz, D.; Shannon, J. L.; Bubsey, R. T. Fracture Toughness Calculation From Maximum Load in Four Point Bend Tests of Chevron Notch Specimen. *International Journal of Fracture*, Vol. 16, pp. R137–R141, 1980.
2. Voigt, C.; Zienert, T.; Schubert, P.; Aneziris, C.G.; Hubálková. J. Reticulated Porous Foam Ceramics with Different Surface Chemistries. *Journal of the American Ceramic Society*, Vol. 97 (7), pp. 2046–2053, 2014.
3. Schwartzwalder. K. Method of making porous ceramic articles, Patent US 3,090,094, 1963.
4. DIN EN 14425-3 Advanced technical ceramics - Test methods for determination of fracture toughness of monolithic ceramics - Part 3: Chevron notched beam (CNB) method, 2010.
5. ASTM C-1421-01b Standard Test Methods for Determination of Fracture Toughness of Advanced Ceramics at Ambient Temperature, 2001.
6. Nakayama. J. Direct Measurement of Fracture Energies of Brittle Heterogeneous Materials. *Journal of the American Ceramic Society*, Vol. 48 (11), pp. 583–587, 1965.
7. Tattersall H.G.; Tappin. G. The work of fracture and its measurement in metals, ceramics and other materials. *Journal of Materials Science*, Vol. 1 (3), pp. 296–301, Aug 1966.
8. Munz, D.; Bubsey, R.T.; Srawley. J.E. Compliance and stress intensity coefficients for short bar specimens with chevron notches. *International Journal of Fracture*, Vol. 16 (4), pp. 359–374, 1980.
9. Munz, D.; Bubsey, R. T.; Shannon. J. L. Fracture Toughness Determination of A12O3 Using Four-Point-Bend Specimens with Straight-Through and Chevron Notches. *Journal of the American Ceramic Society*, Vol. 63 (5-6), pp. 300–305, 1980.
10. Emmel, M., Aneziris. C.G. Development of novel carbon bonded filter compositions for steel melt filtration. *Ceramics International*, Vol. 38 (6), pp. 5165–5173, 2012.
11. Barker, L.M. Short Bar Specimens for K_{Ic} Measurements. In *Fracture Mechanics Applied to Brittle Materials*. ASTM International, 1979.
12. Barker, L.M. A simplified method for measuring plane strain fracture toughness. *Engineering Fracture Mechanics*, Vol. 9 (2), pp. 361– 369, 1977.
13. Munz. D. Determination of fracture toughness of high strength aluminum alloys with chevron notched short rod and short bar specimens. *Engineering Fracture Mechanics*, Vol. 15 (1), pp. 231 – 236, 1981.
14. Zielke, H.; Abendroth M.; Kuna. M. Fracture Toughness Characterization of Carbon Bonded Alumina Using Chevron Notched Specimens. *Key Engineering Materials*, Vol. 754, pp. 71-74, 2017
15. Werner, J.; Aneziris, C.G.; Dudczig, S. Young's Modulus of Elasticity of Carbon-Bonded Alumina Materials up to 1450°C. *Journal of the American Ceramic Society*, Vol. 96 (9), pp.2958-2965, 2013.
16. Werner, J.; Aneziris, C.G; Schafföner, S. Influence of porosity on young's modulus of carbon-bonded alumina from room temperature up to 1450°C. *Ceramics International*, Vol. 40 (9, Part A), pp. 14439-14445, 2014.

Determination of plastic properties using instrumented indentation test with hybrid particle swarm optimization

L.Y. Huang [1], K.S. Guan [1,*], T. Xu [2], J.M. Zhang [1], Q.Q. Wang[1]

[1] East China University of Science and Technology, Xuhui District, Shanghai, China, 200237.
[2] China Special Equipment Inspection & Research Institute, Shunyi District, Beijing, China, 100013.
* Correspondence: Guankaishu@ecust.edu.cn; Tel.: +86-64253055

Abstract: instrumented indentation test is a promising non-destructive method to determine mechanical properties. This paper proposes a new approach to determine the plastic properties of bulk metal materials (including yield stress, strain-hardening exponent (n) and strain-hardening rate (K)), which couples an experimental load-displacement curve with finite element method. The load–displacement curve was obtained from continuous instrumented indentation test. Then a hybrid particle swarm optimization was employed to minimize the deviation between experimental and simulated load-displacement curves. As a combination of particle swarm optimization and simulated annealing, the simulated annealing particle swarm optimization is an economical and effective algorithm to identify plastic parameters. It was observed that the maximum error of strain-hardening rate extracted from the macro indentation test was 8.2 percent contrast to that determined by the conventional tensile test, and the maximum error of strain-hardening exponent was 4.7% respectively.

Keywords: continuous indentation test; optimization algorithm; plastic properties;

1. Introduction

Indentation tests have been employed to estimate material characteristics extensively. The indentation test was originally used to measure material hardness(H) by dividing maximum indentation load to the contact area[1]. Then the load-displacement curve obtained from indentation test was used to determine Young's modulus(E), based on Hertzian contact theory [2] and Sneddon's axisymmetric elastic contact problem. With the development of high-resolution, depth-sensing instruments, Doerner and Nix[3] determined both hardness and Young's modulus based on the indentation load-depth curve(P-h curve) of thin films. Further improvements were made by Oliver and Pharr [4] , They induced Young's modulus and hardness from the indentation load-displacement and demonstrated the possibility of using data directly from the indentation test to determine the area function and mechanical properties without images of indentation. Thereafter instrumented indentation was well developed to obtain material properties such as yield stress, ultimate tensile strength, flow characteristics [5-12], fracture toughness [13-21], creep property [22, 23] and fatigue property [24, 25] because of its convenience, non-destruction and economy.

After several decades' research, varieties of data processing with P-H curve led to varieties theories. Most studies focused on the relationship between hardness (H) and mechanical properties of materials. It has been proved that the P-h curve is sensitive to the material properties [26]. Generally, P-h curve is a function of uniaxial stress-strain, although an accurate prediction of its relationship is sophisticated due to the three-dimensional stress-strain state. Moreover, high nonlinearity due to large deformation beneath the indenter made the characterization process very difficult.

Based on experimental results of spherical indentation test, Meyer found an empirical relationship between force (P) and contact diameter (D) as equation (1):

$$P = \alpha \times D^{\beta} \tag{1}$$

Where α β are material constant. In 1951, Tabor [1] found that the material constant in equation (1) had a relationship with work-hardening exponent (n) according to a power-law stress-strain behavior and it can be expressed as equation (2) as below:

$$n = \beta - 2 \tag{2}$$

This equation is valid especially when applied load is large enough to form a plastic zone near the indenter.

Doerner and Nix proved that the unloading curve can be described with a linear equation as below:

$$P=S(h-h_c) \tag{3}$$

Where h_c is the true contact indentation depth which takes pile-up and sink-in into account. The top one third of the unloading data should be used to obtain best-fit results.

Oliver and Pharr analyzed six materials to establish the combination of hardness and Young's modulus using Berkovich indenter. It has been shown that the unloading curve of indentation test can be nonlinear and it can be fitted in the form of exponent as below:

$$P=A(h-h_f)^m \tag{4}$$

Where h is the maximum indentation depth during one load-unloading cycle, h_f is impressed depth after unloading. A and m are fitting coefficients responding to given materials.

In 2006, Luo J and Lin J [27] extracted mechanical properties from P-h curves using an optimization approach. They minimized the errors between the simulated curves and experimental curves with an objective function using Bates and Watts' optimization method. This approach could deduce material properties (E, σ_y, n) effectively, but it had to preset a lot of initial values. Thus it was not intelligent and efficient enough. Zhang Tairui [28] proposed a method to determine the optimal constitutive model through spherical indentation test. Dimension analysis and finite element method were employed to determine the constitutive model of materials (linear hardening or power-law) and its parameters. However, too many fitting coefficient are utilized and no specific physical meaning was given.

To deduce material properties from indentation P-h curves, presentative strain was also employed. Ahn and Kwon presented a representative stress and strain method to derive plastic stress–strain relationship from the P-h curves of ball indentation [29]. They made a new definition of strain and investigated the ratio of mean contact pressure to representative stress in indentation. However, it is hard to determine the contact depth because of pile-up and sink-in processing around the indenter. With the help of finite element method (FEM), Jian Lu defined a new presentative strain which is a function of the representative stresses and reduced Young's modulus [5]. Combined with dimension analysis and inverse approach, the plastic properties of given material had been derived. The presentative strain had been defined in various ways, but this approach was based on the numerical estimations of empirical parameters.

It has been shown that the pile-up and sink-in had an obvious influence on the precision of determined material characteristics. To avoid the effect of pile-up and sink-in on the contact area edges, an intelligent optimization algorithm named a simulated annealing particle swarm optimization algorithm and finite element simulation were employed to derive mechanical properties of materials from P-h curves directly. This novel approach can obtain material characteristics regardless of any inspection of indentation morphology or various definition of representative strain. The uniqueness of identified parameters was discussed and the stress-strain curves were also verified.

2. Optimization Algorithm

PSO algorithm, a kind of intelligent algorithm created by Eberhart and Kennedy [30, 31], is originally inspired by the social behavior of birds swarm prey. PSO algorithm is widely applied to solve global optimization problems. For this algorithm, particles which have no mass and volumes are regarded as birds. The position of particle i, denoted as $x_i(t) = [x_{i,1}(t), x_{i,2}(t), ... x_{i,D}(t)]^T$ at the t-th iteration, is represented as potential solution to optimization problem in a D-dimensional space. The flight direction and speed of particle i are determined by the velocity, denoted as $v_i(t) = [v_{i,1}(t), v_{i,2}(t), ... v_{i,D}(t)]^T$. During searching for the optimum solution, particles move around randomly in the multidimensional solution space and record their own previous best position simultaneously. After each iteration, particle i changes its velocity and position according to $P_i(t)$ and P_g, shown in equation (5) and (6). $P_i(t)$ was the best position of particle i which fits the objective function F best after the t-th iteration. The particle with the smallest objective function value which is the best position of particles swarm is denoted by P_g. The set of each particle's best position is marked as P, and $P = [P_1(t), P_2(t) ... P_n(t)]^T$. P_g is an element of set P. Particles keep flying until the iteration criterion is satisfied. The iteration process is introduced in detail as below. Step 1, n particles are randomly generated in the solution space. x_i and v_i represent the position and velocity of particle i (i=1,2…n). Then its fitness for the objective function F of optimization problem was evaluated and $P = [P_1(t), P_2(t) ... P_n(t)]^T$ and P_g are obtained. Steps 2, initial velocity and position of particles get changed

according to the following formulas:

$$v_{i,j}(t+1) = wv_{i,j}(t) + c_1 r_1 [p_{i,j} - x_{i,j}(t)] + c_2 r_2 [p_{g,j} - x_{i,j}(t)] \tag{5}$$

$$x_{i,j}(t+1) = x_{i,j}(t) + v_{i,j}(t+1), \quad j = 1,2,...,D \tag{6}$$

Where w is inertial weight that controls the impact of previous velocity of particle on current one; positive constant c_1 and c_2 are learning factor; r_1 and r_2 are random numbers within the range [0, 1]. Step 3, fitness of each particle in new position is evaluated. Then P and P_g are updated. If the fitness meets the requirements or iteration times exceed the permitted times, P_g will be recognized as the final solution, otherwise turn to step 2.

Although PSO algorithm has a strong ability to find global optimum solution, it may lead to premature convergence because P_g is the exclusive parameter used to update particles' velocity. Therefore the final solution may be affected by the initial position of particles [32, 33]. Simulated annealing (SA) algorithm, introduced by Kirkpatrick S[34], has a strong ability to search the local optimum solution while it is weak at finding global optimum solution. The core of SA algorithm is the introduction of annealing temperature T. In the process of annealing, SA algorithm not only accepts the best solution, but also accepts the poor solutions in a probability[35]. And the probability of accepting poor solutions drops with the decrease of annealing temperature T.

Considering the advantage of SA algorithm, the annealing temperature T is introduced into PSO algorithm. So, a new algorithm called simulated annealing particle swarm optimization (SAPSO) algorithm is created by combining PSO algorithm with SA algorithm. The updating of particles' velocity is modified in SAPSO algorithm and described as below.

$$v_{i,j}(t+1) = wv_{i,j}(t) + c_1 r_1 [p_{i,j} - x_{i,j}(t)] + c_2 r_2 [p_{g\_plus,j} - x_{i,j}(t)] \tag{7}$$

Where p_{g_plus} is an element of set P. Compared with the PSO algorithm, P_g is replaced by p_{g_plus} in SAPSO algorithm, which means not only the best solution but also a poor solution can be applied to update the new positions of particles. The determination of p_{g_plus} is based on the following inequality.

$$\exp(\Delta E_i / T) \geq \text{Random}(0,1) \tag{8}$$

Where $\Delta E_i = F(P_g) - F(P_i)$ is non-positive; T denotes the annealing temperature that is positive; Random (0,1) is a random number between 0 to 1. If the value of $\exp(\Delta E_i / T)$ is larger than Random(0,1), the best position of particle i is accepted as the current p_{g_plus}, as shown in Fig.1. As mentioned above, SA algorithm can accept poor solutions probability including the best solution. The SAPSO algorithm inherit this typical feature of SA algorithm when the annealing temperature is introduced. Initially, at large values of T, poor solutions will be accepted high probability; as T decrease, acceptance of poor solutions will become lower; finally, when the value of T approaches 0, poor solutions will not be accepted any more. This feature means that SAPSO algorithm, compared with PSO algorithm, can help escape from local minima while it still retains an excellent ability in searching global optimum solution. Note that the probability of accepting poor solutions is implemented by comparing the value of $\exp(\Delta E_i / T)$ with a random number generated from a uniform distribution on the interval (0, 1).

The calculation process of SAPSO algorithm was shown in Figure.1. Similar to the PSO algorithm, the SAPSO algorithm begins with initializing a group of random particles. The initial annealing temperature T_0 is determined based on the objective function F and the first best position of particles swarm P_g. The annealing time is denoted by t. New particles are obtained after transforming each particle's velocity and position according to the equation (7) and (8). If the termination condition is satisfied, P_g will be accepted as the final solution. Otherwise, the iteration will continue.
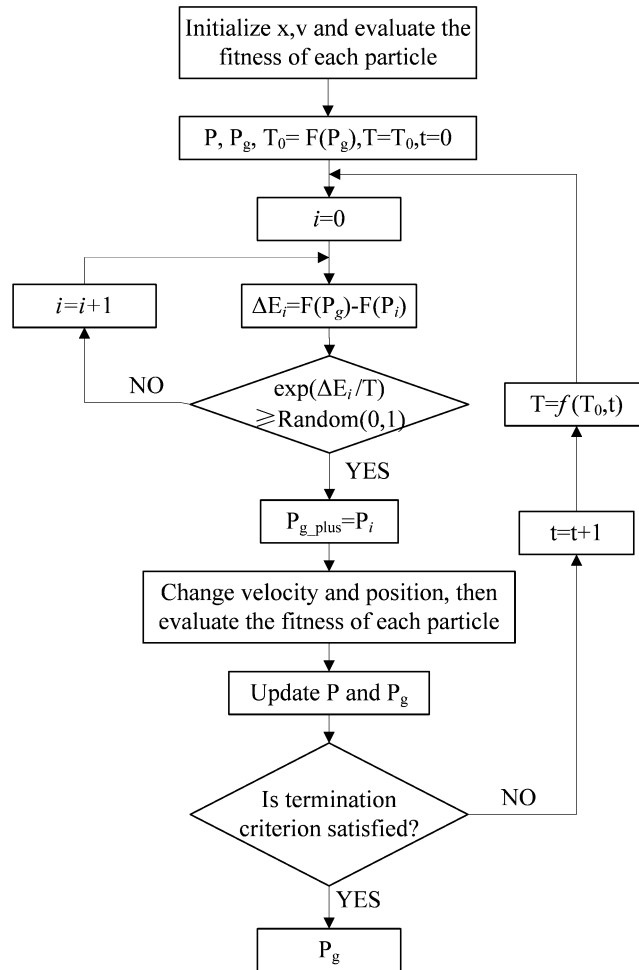
Figure 1. Schematic of HPSO algorithm.

3. Identification Procedure

In this work, SAPSO was employed to identify the material properties directly form P-h curves of indentation test. SAPSO is an optimization algorithm integrating particle swarm optimization and simulated annealing. It has a strong ability for searching the global optimal solution of multiple solution problems. Therefore, it can be applied to find the global optimal solution of the objective function efficiently. The procedure of deriving the plastic parameters including yield stress, strain strength coefficient (K) and strain hardening exponent (n) are described in Figure 2.
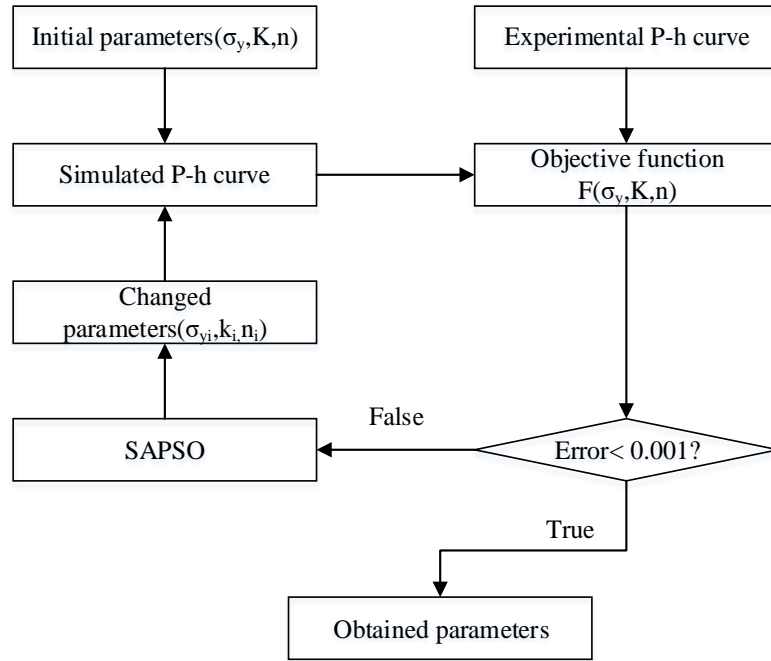
Figure 2. The procedure of identifying material property.

First, Young's modulus can be deduced from the conventional tensile test of a smooth round bar. It also can be deduced from the first unloading part of the P-h curve with Oliver and Pharr's method[26] if the material is difficult to machine into standard tensile specimen. Second, the indentation test with the same material is conducted and P-h curves of indentation are obtained. Numerical simulation of indentation test is performed by a commercial code ABAQUS (version 6.13) with Young's modulus and strain strength coefficient (K) and strain hardening exponent (n) deduced from standard tensile test to ensure that the simulation is valid. Third, preset a set of material parameters (k, n) and apply them to the simulation of indentation test. Then the simulated P-h curve is compared with the experimental curve. The error between the simulated and experimental curves is characterized by an objective function as shown in equation (9) as below.

$$F(E,K,n)=\frac{1}{N}\sum_{j=1}^{N}|\frac{F_j^{FE}-F_j^{exp}}{F_j^{exp}}| \tag{9}$$

Where F(x) is the objective function related to E, K, n. F_j^{FE} and F_j^{Exp} represent the simulated force and the experimental force at the same indentation depth. N is the total number of simulated force points in the loading process. It relies on output request intervals in ABAQUS. Change the value of K and n according to SAPSO and minimize the error between the simulated and experimental P-h curves until it is equal to or less than a preset value.

4. Experiment and Simulation

A continuous indentation test was carried out on the pressure vessel steel 16MnR and ASTM A193 B16 steel using a DDL 20 machine whose load and displacement resolution is 0.1N and 1um. The chemical composition of 16MnR and ASTM A193 B16 steel is shown in Table 1.All the specimens were machined into a size of Φ30×15mm and were mechanically ground and polished using emery paper (2000 grit) and 1 mm alumina powder respectively. The ball indenter with 0.5 mm diameter was made of tungsten carbide. Instrumented indentation tests were performed according to ISO/TR29381 standard using Instron 5965 system of 5 kN capacity. Specimens were restrained on the test bed by a clamp. The maximum depth was 0.1 mm, and 10 unloading procedure were conducted with a fixed loading and unloading rate (0.1mm/min) by displacement control. Three indentations per specimen were used to examine repeatability and the load-displacement curves were shown in Figure 3. To ensure the accuracy and decrease time consuming, only the middle P-h curves were utilized to compare with the simulated ones.
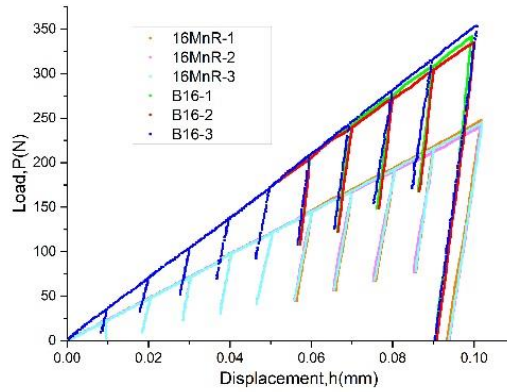
Figure 3. The indentation load-displacement curves of 16MnR and ASTM B16 steel.

To verify the tensile properties obtained through the instrumented indentation test, conventional tensile tests have been conducted at room temperature using Instron 8800 system of 100 kN capacity. The tests were conducted at crosshead speed of 1 mm/min for specimens with gauge length of 25 mm and diameter of 6 mm according to the ASTM E-8M standard.

Table 1. The chemical composition of 16MnR and B16 steel (wt-%).

Elements (%)	C	Mn	P	S	Si	Cr	Mo	Al	Ni	V	Nb	Ti	Cu
16MnR	0.17	1.48	0.022	0.004	0.26	0.004	0.005	0.022	0.02	-	0.004	0.013	0.03
B16	0.36	0.45	0.035	0.04	0.15	0.8	0.65	0.015	-	0.3	-	-	-

The commercial software ABAQUS was used to simulate the process of the indentation test. Figure. 4 shows the finite element model of the indentation test. The indenter was modeled as an analytic rigid and the specimens were modeled as deformable body respectively. 4-node axisymmetric linear reduced integral was utilized to mesh the specimen. The minimal mesh size in the contact region where it was under the indenter was 0.025mm. Away from the symmetry axis, the size became larger in order to save time. Because the plastic deformation didn't generate through whole specimen, it's not necessary to establish FE model according to practice size. 10 times of diameter in length and 5 times of diameter in height is sufficient. In this finite element model, the specimen's displacement was constrained in vertical direction (Y-axis). The displacement constraint at an increment of 0.01mm each step was applied to the reference point of the indenter. Surface to surface contact with finite sliding was established. The friction coefficients between the indenter and specimen was set to 0.2. Poisson's ratio was fixed at 0.3 which is proper for metals.
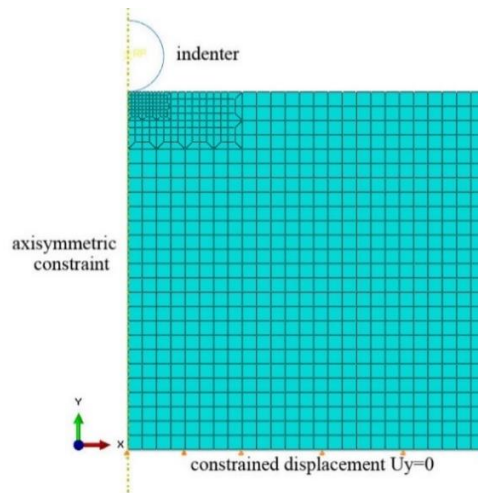

Figure 4. Finite element model of the indentation test.

5. Results and discussion

When the objective function was less than 0.01 in consideration of precision and time consuming. These simulation curves fit well with experiment curves, as shown in Figure 5. At the same time, a set of material properties (K, n) was determined which was close to the value derived from conventional tensile test, shown in Table 2. The maximal error between them was 8.2% which was reliable in engineering. The error introduced in this work mainly by three ways. Firstly, the processing of indentation test can't be accurately descripted by the elastic-plastic analysis because damage caused by plastic deformation was not taken into account. Secondly, power hardening model which is a simplified assumption of material constitutive relationship might introduce error especially where strain is relatively high. Thirdly, wear of experiment apparatus like indenter and precision of sensor also had effect on the accuracy of this approach.
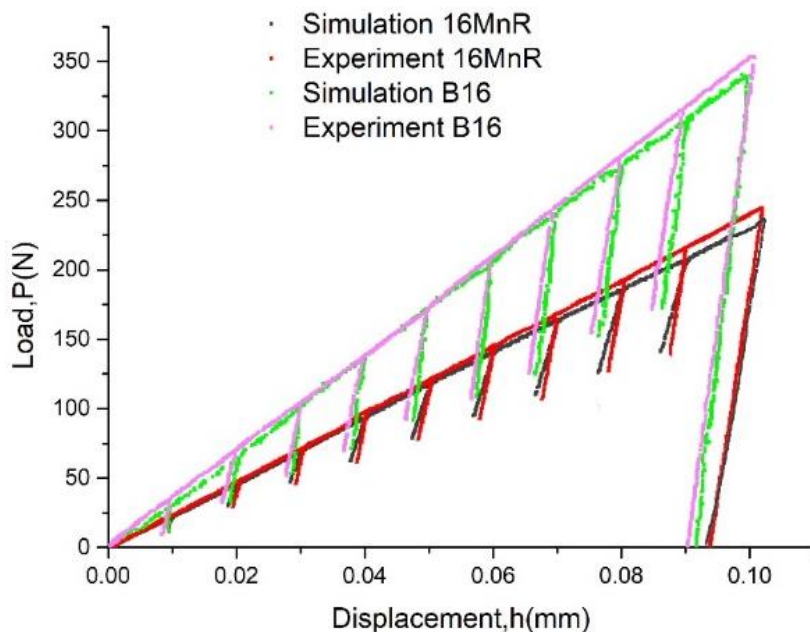

Figure 5. Simulated and experimental load-displacement curves.

Table. 2 Results of indentation test and tensile test.

	Indentation test			Tensile test			Error (%)		
	σ_y	K	n	σ_y	K	n	σ_y	K	n
16MnR	362.5	368.81	0.297	385.3	348.91	0.310	5.92	5.7	4.2
B16	380.7	384.78	0.315	402.7	355.54	0.301	5.4	8.2	4.7

It has been proved that the material properties can't be derived only from the P-h curves obtained from a single indentation test. Because many set of mechanical properties will result in the same P-h curve. To exclude the interference of the improper set of mechanical characteristics, continuous indentation test was utilized. Material strain hardening phenomenon which is affected by strain strength coefficient (K) and strain hardening exponent (n) can be reflect through more loading and unloading cycles. Large number of loading and unloading cycles will lead to precise identification of material properties while computation time will increase obviously. Since ten loading cycles can result in a unique and satisfying set of material parameters, continuous indentation test which has more than ten loading cycles were not carried out and identified.

In this work, power-hardening constitutive relationship was preset based on the premise that the material were coincident with the power-hardening model. However when the material's constitutive relationship is unknown, application of this approach may be restricted. More attention can be paid to the identification of unknown material constitutive relationships in further study.

6. Conclusions

SAPSO was an effective method to extracted plastic properties from load-displacement curve. The uniqueness and precision can be ensured. It was observed that the maximum error of strain-hardening rate extracted from the macro indentation test was 8.2 percent contrast to that determined by the conventional tensile test, and the maximum error of strain-hardening exponent was 4.7% respectively.

References

1. Tabor, D. The hardness of metals, Measurement Techniques 5(4) (1951) 281.
2. F.F.G. G., Hertz's Miscellaneous Papers, Nature 55(1410) 6-9.
3. Sneddon, I.N. The relation between load and penetration in the axisymmetric boussinesq problem for a punch of arbitrary profile, International Journal of Engineering Science 3(1) (1965) 47-57.
4. Oliver, W.C.; Pharr, G.M. An improved technique for determining hardness and elastic modulus using load and displacement sensing indentation experiments, Journal of Materials Research Home 7(06) (1992) 1564-1583.
5. Cao, Y.P.; Lu, J.A new method to extract the plastic properties of metal materials from an instrumented spherical indentation loading curve, Acta Materialia 52(13) (2004) 4023-4032.
6. Das, G.; Ghosh, S.; Sahay, S.K. Use of ball indentation technique to determine the change of tensile properties of SS316L steel due to cold rolling, Materials Letters 59(18) (2005) 2246-2251.
7. Ogasawara, N.; Chiba, N.; Chen, X. Measuring the plastic properties of bulk materials by single indentation test, Scripta Materialia 54(1) (2006) 65-70.
8. Yonezu, A. An algorithm to determine the plastic properties of materials based on the loading data in single sharp indentation, Mrs Proceedings 1049 (2007).
9. Das, M.; Das, G.; Pal, T.K. Use of Portable Automated Ball Indentation System to Evaluate Mechanical Properties of Steel Pipes, Transactions of the Indian Institute of Metals 65(2) (2012) 197-203.
10. Wu, S.B.; Guan, K.S. Evaluation of tensile properties of austenitic stainless steel 316L with linear hardening by modified indentation method, Materials Science & Technology 30 (2014) 1404-1409.
11. Shedbale, A.S.; Singh, I.V.; Mishra, B.K.; Sharma, K. Evaluation of mechanical properties using spherical ball indentation and coupled finite element–element-free galerkin approach, Mechanics of Advanced Materials and Structures 23(7) (2016) 832-843.
12. Hosseinzadeh, A.R.; Mahmoudi, A.H. Determination of mechanical properties using sharp macro-indentation method and genetic algorithm, Mechanics of Materials 114 (2017) 57-68.
13. He, M.; Shi, D.; Yang, F.; Zhang, N.; Guo, H.A method to determine fracture toughness using Berkovich indenter for bulk materials, 2013 International conference on process equipment, mechatronics engineering and material science, Wuhan(CN), 2013.
14. Lost, A. Fracture toughness evaluation of brittle or ductile materials by indentation testing, Revue De Metallurgie-Cahiers D Informations Techniques 110(3) (2013) 215-233.
15. Amiri, S.; Lecis, N.; Manes, A.; Giglio, M. A study of a micro-indentation technique for estimating the fracture toughness of Al6061-T6, Mechanics Research Communications 58 (2014) 10-16.
16. Feng, Y.; Zhang, T. Determination of fracture toughness of brittle materials by indentation, Acta Mechanica Solida Sinica 28(3) (2015) 221-234.
17. Hyun, H.C.; Rickhey, F.; Lee, J.H.; Kim, M.; Lee, H. Evaluation of indentation fracture toughness for brittle materials based on the cohesive zone finite element method, Engineering Fracture Mechanics 134 (2015) 304-316.
18. Li, J.; Li, F.; Ma, X.; Wang, Q.; Dong, J.; Yuan, Z. A strain-dependent ductile damage model and its application in the derivation of fracture toughness by micro-indentation, Materials & Design 67 (2015) 623-630.
19. Rickhey, F.; Marimuthu, K.P.; Lee, J.H.; Lee, H.; Hahn, J.H. Evaluation of the fracture toughness of brittle hardening materials by Vickers indentation, Engineering Fracture Mechanics 148 (2015) 134-144.
20. Moattari, M.; Sattari-Far, I.; Persechino, I.; Bonora, N. Prediction of fracture toughness in ductile-to-brittle transition region using combined CDM and Beremin models, Materials Science and Engineering: A 657 (2016) 161-172.
21. Yu, F.; Jar, P.Y.B.; Hendry, M.T. Indentation for fracture toughness estimation of high-strength rail steels based on a stress triaxiality-dependent ductile damage model, Theoretical and Applied Fracture Mechanics 94 (2018) 10-25.

22. Li, W.B.; Henshall, J.L.; Hooper, R.M.; Easterling, K.E. The mechanisms of indentation creep, Acta Metallurgica Et Materialia 39(12) (1991) 3099-3110.
23. Oyen, M.L. Spherical Indentation Creep Following Ramp Loading, Journal of Materials Research 20(8) (2005) 2094-2100.
24. Guiberteau, F.; Padture, N.P.; Cai, H.; Lawn, B.R. Indentation fatigue, Philosophical Magazine A 68(68) (1993) 1003-1016.
25. An, L. Indentation Fatigue in Random and Textured Alumina Composites, Journal of the American Ceramic Society 82(1) (2010) 178-182.
26. Pharr, G.M.; Oliver, W.C.; Brotzen, F.R. On the generality of the relationship between contact stiffness, contact area, and elastic modulus during indentation, Journal of Materials Research 7(3) (1992) 613-617.
27. Luo, J.; Lin, J.; Dean, T.A. A study on the determination of mechanical properties of a power law material by its indentation force–depth curve, Philosophical Magazine 86(19) (2006) 2881-2905.
28. Zhang, T.; Wang, S.; Wang, W. Method to determine the optimal constitutive model from spherical indentation tests, Results in Physics 8 (2018) 716-727.
29. Jeong-Hoon, A.; Dongil, K. Derivation of plastic stress-strain relationship from ball indentations: Examination of strain definition and pileup effect, Journal of Materials Research 16(11) (2001) 3170-3178.
30. Kennedy, J. Particle Swarm Optimization, Proc. of 1995 IEEE Int. Conf. Neural Networks, (Perth, Australia), Nov. 27-Dec. 4(8) (2011) 1942-1948 vol.4.
31. Eberhart, R.; Kennedy, J.A new optimizer using particle swarm theory, International Symposium on MICRO Machine and Human Science, 2002, pp. 39-43.
32. Liu, B.; Wang, L.; Jin, Y.H.; Tang, F.;. Huang, D.X. Improved particle swarm optimization combined with chaos, Chaos Solitons & Fractals 25(5) (2005) 1261-1271.
33. Lvbjerg, M.; Group, E.P.; Rasmussen, T.K.; Krink, T. Hybrid Particle Swarm Optimiser with Breeding and Subpopulations, 2001, pp. 469--476.
34. Kirkpatrick, S. Optimization by Simulated Annealing: Quantitative Studies, Journal of Statistical Physics 34(5-6) (1984) 975-986.
35. Van Laarhoven, P.J.M.; Aarts, E.H.L. Simulated Annealing: Theory and Applications, Sold and distributed in the U.S.A. and Canada by Kluwer Academic Publishers 1987.

The research and development of small-invasive sampling machine

J. Wang *, R. Chen, Q. Wang, S. Tu

(School of mechanical engineering and power, East china university of science and technology, Shanghai, China, 200237)

* Correspondence: wangjianwen@ecust.edu.cn; Tel.: +81-021-6425-3413

Abstract: The research and development of small-invasive sampling machine (SISM), which can be used to take out small dimensional samples from in-service equipment and to provide experimental materials for hydraulic bulging test and small punch test, has important application value in Engineering practice. This paper proposed a SISM and its design considerations. The sampling trajectory plan and small dimensional sample arrangement for improving sampling material utilization have been described. A unique semispherical machine tool was designed and the preparation method and performance characterization of the tool blade coating was studied. The tool rotary cutting motion and rotary feed motion were planned. A swing-level-type centering mechanism was designed as feeding mechanism. Samples of form of spherical crown with diameter 35mm and thickness 4mm can be take down from in-service equipment.

Keywords: Small-invasive sampling machine; Online sampling; small sample; spherical machine tool

---

1. Introduction

People usually have an urgent need to know clearly about the service status as well as the reliability, residual life and safety status of the special equipment, especially such as the power station equipment, process equipment and pipelines and chemical devices. Therefore, it has important theoretical significance, engineering value and social benefit to monitor and evaluate the status of the equipment in service.

It is impossible to remove large material from the in-service equipment to make standard samples due to the particularity of the special equipment. People developed the small punch test technique and hydraulic bulging technique in order to evaluate the material properties of the in-service equipment. These test methods only need to take a small piece of material on the body of the in-service equipment. The shallow pits because of the sampling will generate very low stress, the shallow pits' surfaces are smooth and the shallow pits are no need to be repaired. Therefore, this micro sampling method can be considered as a sampling method that does harm to the surface of the equipment.

The tiny material removed from the equipment can be made into a small circular specimen with the thickness of 0.5mm and the diameter of 5~10mm. Small surface cracks and grain boundary inclusions can be observed under a high power optical microscope or an electron microscope. The sample can be used to evaluate the properties of fracture toughness, hardness, radiation embrittlement and so on. The sample can also be used to test the change of material behavior in tensile, fatigue, creep, and corrosive environments.

The data obtained by the micro sample test method can be directly used to establish the design criteria of special equipment, safety evaluation of in-service equipment, equipment life extension, residual life estimation, failure mode analysis, and equipment maintenance and monitoring.

Consider the conditions of the sampling site according to the requirements of the sample for the micro damage test and determine the design constraints of the micro damage fast micro-sampling machine. Finish the design and verification of the dynamic system, transmission system, cutting system, coolant system and control system of the mechanical sampling machine in a narrow space. Design and test facilities to meet different sites and different sampling equipment. Study the special bowl cutter for the sampling machine, including high strength tool steel molding, cutter edge wear resistant coating, as well as the manufacturing process of bowl cutter, tool material, tool forming process and screening of the cutter edge wear coating combination process. Stability and safety design in sampling process of sampling machine and the selection of sampling parameters.

The size of the micro sampling is shown in Figure 1, the micro sampling is spherical cap shaped. The radius R and the thickness H are related to the diameter of spherical cap L. The thickness of the micro sampling is 5 mm, the diameter of spherical cap L=30~50 mm. Each micro sampling can be made of a number of micro specimens according to their size. If the thickness of the sampling is 2mm, two rows of specimens can be made in the direction of thickness. If the thickness is 4mm, 3 or 4 rows of specimens can be made. In the plane direction, L=40mm, micro

sampling can be made according to the arrangement in Figure 2. In this way, 15~35 micro specimens can be made from the removed tiny material.
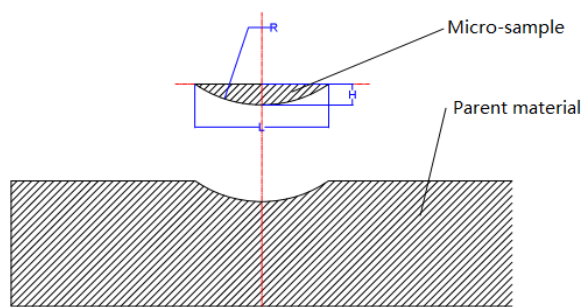

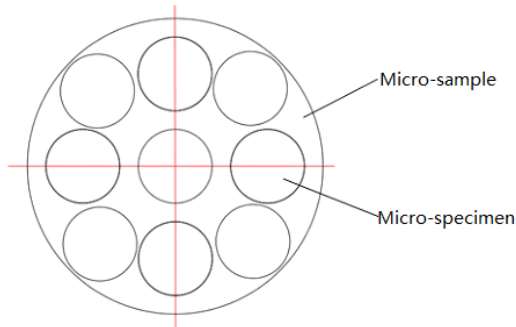**Figure 1.** Size and structural shape of micro-sample.

Figure 2. Arrangement of micro-specimens in the sampling.

2. Research process and overall plan

Consider the conditions of the sampling site according to the requirements of the sample for the micro damage test and determine the design constraints of the micro damage fast micro-sampling machine. Finish the design and verification of the dynamic system, transmission system, cutting system, coolant system and control system of the mechanical sampling machine in a narrow space. Facilities are designed and tested to meet different sites and different sampling equipment. Study the special bowl cutter for the sampling machine, including high strength tool steel molding, cutter edge wear resistant coating, as well as the manufacturing process of bowl cutter, tool material, tool forming process and screening of the cutter edge wear coating combination process. Stability and safety design in sampling process of sampling machine and the selection of sampling parameters. The project mainly involves the sampling machine's principle and model selection, key components research and development, mechanical components design, automatic control parameter optimization, field fixation and so on. Through debugging and improvement, manufacture a filed sampling machine with perfect function. Test the reliability of the sampling machine, analyze the material's changes of structure and performance before and after sampling, study the effect of different cutting rates on sampling efficiency and material properties, and finish the technique documents at the end.

According to the contents and ideas mentioned above, the structures and functions of the mechanical sampling machine designed and planned are shown in Figure 3.

The specific research contents are as follows:

2.1. Sampling requirements

The recommended sizes of the small punch test are 8 to 10mm in diameter and 0.25 to 0.5mm in thickness. At present, the size of the specimen in our country is usually 10mm in diameter and 0.5mm in thickness. Considering the use of EDM technology to machine micro specimens later, there will be heat affecting layers and processing lines on the specimens. So there must be machining allowances. Due to relatively more influence factors of the small punch test, enough specimens are needed to ensure the reliability of the experiments. At least 3 pieces of specimens can be taken out from each piece of sample removed to ensure the machining efficiency. Therefore, it is generally required that the minimum sampling thickness of the sampling machine should be guaranteed to be above 2-3mm (containing the heated cutting surface or mechanical damaged part). Increase the utilization of the material removed as much as possible, it is hoped that the utilization rate can reach more than 80%. In addition, the sampling

size must can be adjusted according to the size and shape of the micro specimen, the appearance of the equipment, and the size of the equipment.

2.2. Principle and structure design

There are two kinds of field sampling machines developed abroad at present, such as EDM type and mechanical type. Taking into account that the EDM type sampling cost is high and the time consuming is long, the field sampling is limited, so we use the mechanical type. As we can see from Figure 1, the following parts need to be considered during the development of a mechanical sampling machine: electric motors, spindle, cutter, fixing device, connection type, cooling methods and machining equipment after sampling. It can be roughly divided into six systems: power system, transmission system, cutting system, cooling system, control system and fixed system. The power system has the plug-in type and the mobile power type.

The cutting system and the transmission system of the sampling machine is relatively complicated. The cutting system includes the high speed rotation of the cutting tool and the low speed rotation of the tool along the sampling depth direction. The trajectory of the superposition motion of two independent motions must be calculated, so that we can implement its regular cutting function through the control system. The stability and reliability will reduced due to the vibration during the high speed cutting process. It will lead to reduction of the cutting system's life. Through the analysis and research of the sampling location , the optimal design of the motion mechanism and the life-span design of the motion structure, we can achieve the flexible, reliable and controllable motion system. Through finite element analysis and a large number of field tests, analysis and improvement of the stability and reliability of the motion system and the cutting system, we can improve the stability of the motion system and cutting system.

Mechanical cutting will generate a lot of heat. Reasonable cooling design for the cutter of the sampling machine is necessary to avoid excessive heat effect on equipment or material. The sampling machine should have advanced control system, not only can realize the cutting function, can also adjust cutting speed and coolant supply according to different materials and the change of the temperature. The stiffness of each structure and the balance of the whole structure must also be taken into account.

2.3. Research and development of special cutting parts

The components of the field sampling machine such as motors and spindles can be purchased. At least, through reasonable selection and overall design of the whole structure, the carrying function is easy to achieve. The cutter in the sampling machine is the most important component which needs to be developed by people.
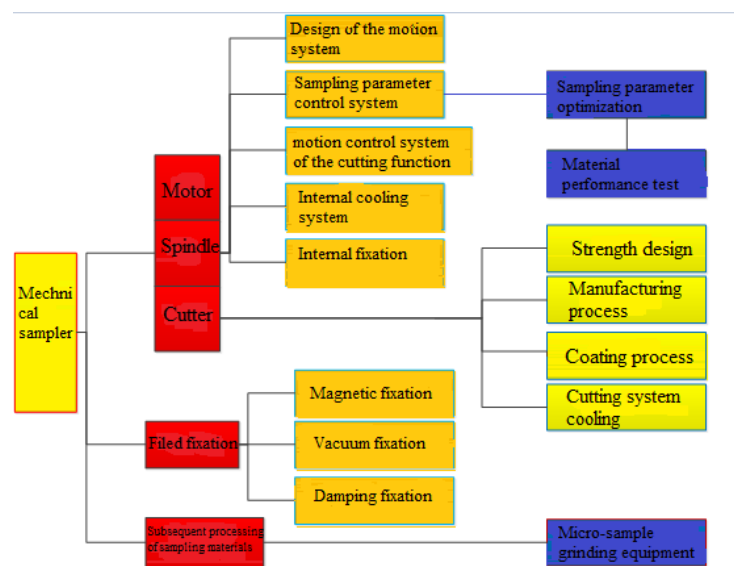

Figure 3. Structure and function of the mechanical sampling machine.

The sampling component of the sampling machine is based on the basic requirements of in-service equipment, the hemispherical cutting tool is used as the cutting tool. The hemispherical cutting tool is mainly subjected to the force of cutting and grinding, and may be subjected to the bending stress, the impact stress, the fatigue stress caused

by the vibration, etc. Firstly, it is necessary to study on the tool design, material selection, strength design and vibration analysis. Secondly, material heat treatment and processing technology of the cutting tool are essential. Lastly, the surface of the cutting tool must apply the surface preparation to improve the wear resistance and impact resistance of the surface. Through comprehensive performance test and life analysis of different combinations of high strength wear resistant tool steel and wear resistant coating to choose the optimized structure, material and coating combination to develop the cutting parts with high performance.

In the research and development of cutting parts, the most important is the shape design of grinding tools, the strength design of cutting tools, the manufacturing technology of cutting tools and the technology of abrasive coating.

2.4. Sample equivalence verification after sampling

Although there is no particular change in the micro-structure and macro-mechanical properties of the sample, but the micro-specimen is very small and susceptible to minor changes. Therefore, the issue of specimen equivalence verification after sampling must be taken into account. A small punch test or a hydraulic bulging test will be performed on the removed sample and the bulk material, and the influence of cutting on the mechanical properties of the material should be examined. The curved surfaces of different structures are separately sampled and compared on the mechanical properties of the sampling and bulk. At the same time, the micro-structure of the sample is observed for metallographic changes.

3. Results

In order to prevent the depth of the sampling from being too deep, it is necessary to strictly control the blade trajectory of the cutting tool. The cutting trajectory of the blade is shown in Figure 2.1.

According to the sampling size shown in Figure 1.1：

$$R = \frac{1}{2H}\left(H^2 + \left(\frac{L}{2}\right)^2\right)$$

（1）

In the above formula, R is the radius of the cutting trajectory; H is the height of the crown, H=2~4mm; L is the diameter of the bottom of the spherical cap, L=30~50mm. In order to reduce the size of the tool and increase the safety and reliability of the operation, initially take L = 33mm, H = 5mm, which can be obtained R = 30mm. The blade of the cutting tool completes the path shown in the figure and needs to rotate θ =69.7°. The overall rotation of the tool is 69.7°, which is almost impossible to achieve in the structure because it is constrained by other parts of the mechanism. On the other hand, such a large corner will inevitably lead to an oversized cutter. In order to reduce the size of the tool and the entire mechanism, consider two-way rotary cutting, so that the inclination angle of each side of the tool is 34.85°, reducing the possibility of interference.
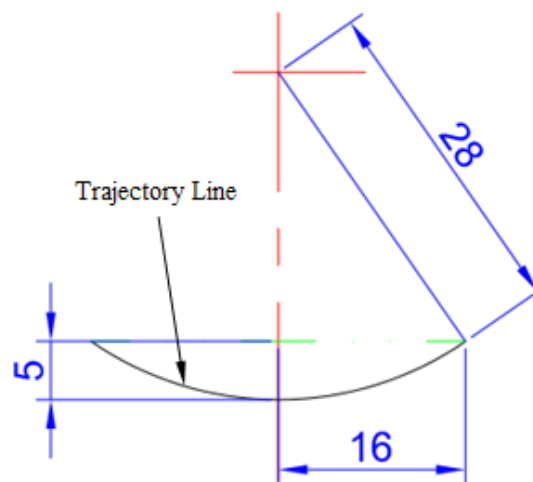

Figure 4. Tool Trajectory Line.

3.1. Tool Design and Blade Coating Preparation

The cutting edge of the tool and its subsequent part must match well with the cutting trajectory shown in Figure 4 to improve cutting efficiency, reduce interference and additional frictional resistance. The edge of the tool and the portion of the tool that is within 35° range should be as thin as possible. Other parts must maintain sufficient strength and stiffness to support the cutting motion of the tool.
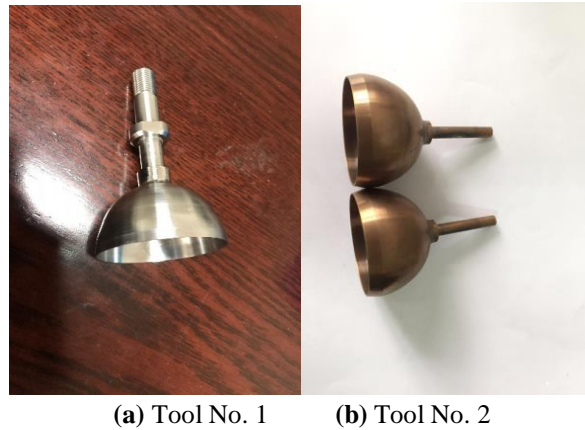

(a) Tool No. 1   **(b)** Tool No. 2

Figure 5. Designed cutting tools.

In order to test the cutting effect and determine the cutting parameters, two types of tools were preliminarily designed, such as the No. 1 and No. 2 tools shown in Figure 5.

The tool material is W6MoCr4V2 high speed steel. The material properties and chemical composition are shown in Table 1.

Table 1. High-speed steel material properties and chemical composition.

Material	Density g/cm^3	Flexural strength GPa	Hardness HRC	Chemical composition w/%				
				C	Cr	Mo	V	W
HSS	8.16	3.5~4.0	58-62	0.87	4.20	0.32	2.0	6.00

After ultrasonic cleaning of the finished tool, the tool is placed in a physical vapor deposition cathode arc ion plating apparatus, and a TiN film is formed on the blade edge as a wear-resistant layer.

Figure 6 shows the interface image of a multilayer coating substrate observed under scanning electron microscopy. It can be seen from the figure that the interface of the coating substrate is fuzzy, indicating that the bonding force is good.
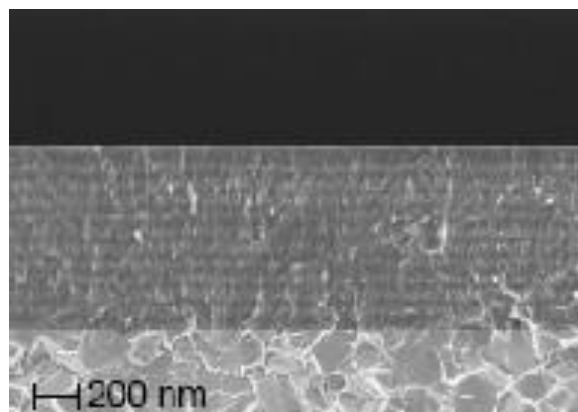

Figure 6. Photograph of the coated substrate observed under SEM.

Through using the WS-2005 automatic scratch tester that meets DIN EN ISO 14577-1:2003 "Metallic materials-hardness and material parameters of instrumental indentation test. Part 1: Test method" standard、HVS-1000 digital micro-hardness tester, kaloMAX ball mill manufactured by BAQ GmbH, Germany, and high-resolution microscopy to analyze coating thickness TiN coatings parameter wad obtained as shown in table 2.

Table 2. Parameters of Prepared TiN Coatings.

Coating type	Coating thickness （μm）	Micro hardness （ $HV_{0.05}$ ）	Deposition temperature （ ºC ）	Membrane-based binding force （N）
TiN	3	2800	180~450	60

3.2. Feed mechanism design

The cutting motion of the tool is a high-speed rotary motion around its own axis. The rotation speed is initially set at 12,000 rpm to achieve high speed cutting. At the same time, the entire tool is deflected and moved along the trajectory shown in Fig.4. This requires that the shape of the cutting edge and front end of the cutting tool should be completely consistent with the trajectory line. Therefore, the cutting portion of the cutting tool should be consistent with the trajectory line and be a spherical structure. The more important point is: During the feed process, the cutter must keep the ball center fixed. The design of the feed mechanism needs to ensure that the position of the center of the ball is fixed and it needs to consider special operating mechanisms.

After analysis and program discussion, two kinds of solutions that can keep the center of the tool center fixed are obtained, as shown in Figure 7.
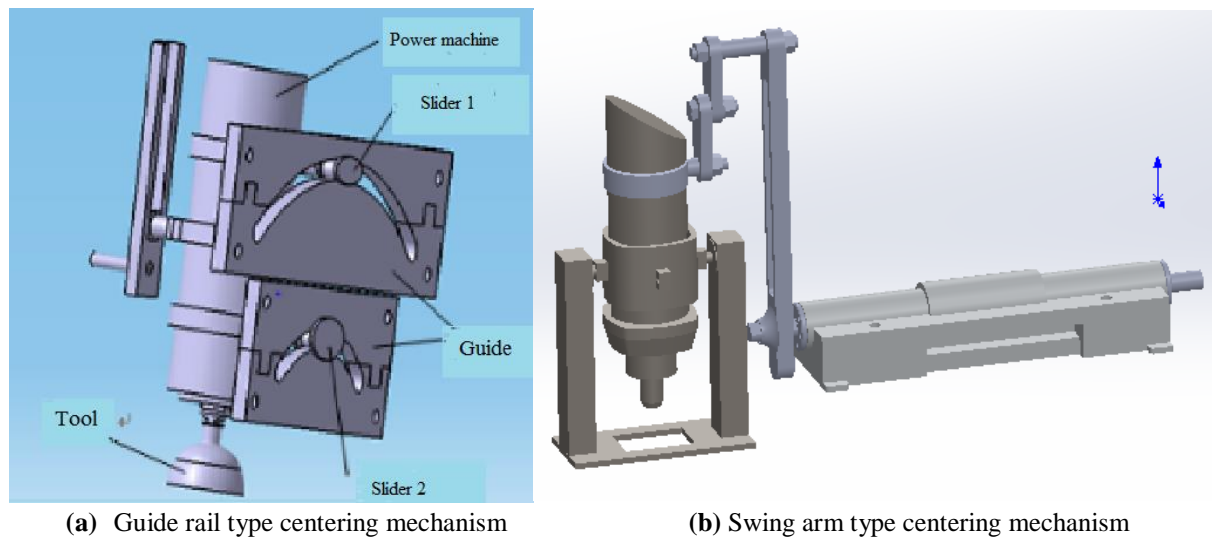

(a) Guide rail type centering mechanism   **(b)** Swing arm type centering mechanism

Figure 7. Cutting Feed Centering Mechanism.

In the guide rail type centering mechanism, on the one hand, the power machine drives the tool to rotate to perform cutting. On the other hand, the tool and the power machine make circular movements along the guide rails through the sliders 1 and 2 so as to ensure that the tool center is fixed. In the swing arm type centering mechanism, the swing arm swings around the rotation axis to complete the feed motion, keeping the tool center fixed. Both types have completed the design process and are under manufacturing.
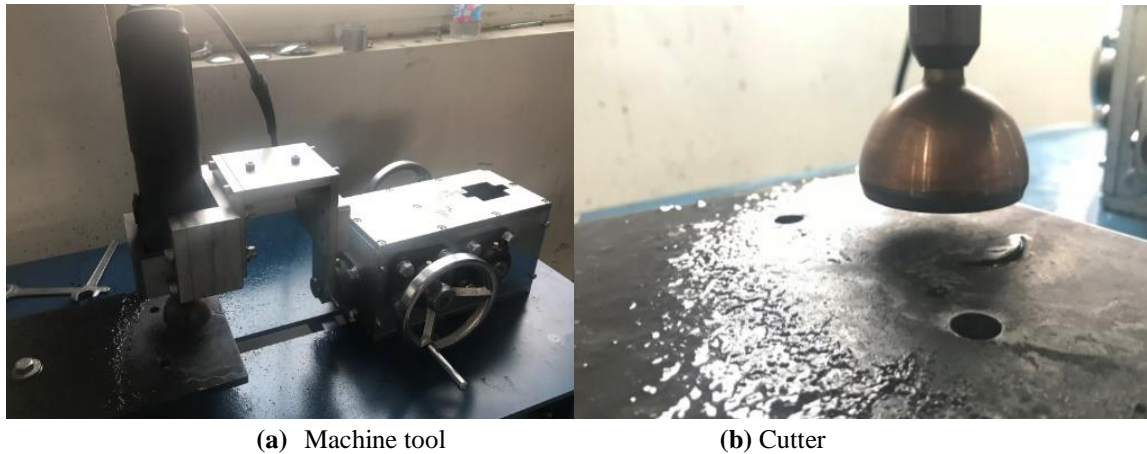
3.3. Small-invasive sampling machine

(a) Machine tool   (b) Cutter

Figure 8. Machine tool and cutter.

The small- invasive sample machine has been manufactured and tested to take out small dimensional samples from a plate of 20 carbon steel. The time of sampling is about 100 minutes.

4. Conclusions

Cutting mechanism and tool design are the most critical parts of all research tasks. In the initial stage of mission implementation, due to the lack of reference materials, everything started from scratch and we were front to several difficult troubles. Fortunately, adjustments and plans were made in a timely manner, and tool trajectory studies, tool design, and tool blade coating studies, as well as the design and drawing of the cutting feed centering mechanism were successfully completed.

304L stainless steel fatigue evaluation using dynamic mechanical analysis

D. Rao[1*], Y. Shen[2]

[1*] School of Mechanical Engineering, Shanghai Jiao Tong University; [*]Correspondence: raode@sjtu.edu.cn
  Tel.: +86 17717630065
[2] School of Mechanical Engineering, Shanghai Jiao Tong University; shenyz@sjtu.edu.cn

Abstract: In order to evaluate the fatigue effects on 304L Stainless Steel, the internal friction or damping of the material have been investigated by means of dynamic mechanical analysis (DMA), using single cantilever test modes. Before DMA measurement, the 304L plates are loaded with different cycle number and stress amplitude to simulate different fatigue condition. The amplitude dependant internal friction (ADIF) of 304L small sample is measured. It shows that the ADIF curves of DMA are associated with the pre-fatigue loading. One ADIF peak is observed near the critical strain amplitude. The DMA data of different pre-stressed samples (cyclic stress amplitude from ±80MPa to ±200MPa) show that the height of ADIF peak increases with the pre stress value. The mechanism of the peak is discussed in the paper. The results indicate that a clear correlation exists between fatigue condition and internal friction curve, so that the fatigue behaviour of 304L stainless steel can be evaluated from DMA measurements.

Keywords: Dynamic mechanical analysis (DMA); Fatigue; Amplitude dependant internal friction; 304L stainless steel

1. Introduction

Type 304L stainless steel, as its corrosion resistance and excellent mechanical properties, has always attracted attention of manufacturing industries, and it is widely used in industry of chemistry and nuclear energy. As one of main structure material, the 304L components are often exposed to severe conditions such as cyclic fatigue stresses, thus a detailed research on the fatigue behavior and fatigue life of the material is required.

Materials subjected to cyclic loading absorb energy, some of which may be stored as potential energy within the structure of the material, but most of which is dissipated as heat to surroundings. Energy dissipation in materials, termed damping or internal friction (IF), is caused by a wide range of physical mechanism, depending on the material, temperature, strain amplitude, and frequency of cyclic loading involved [1]. Dynamic Mechanical Analysis (DMA) methods have been widely used in the characterizations of viscoelastic materials, particularly in the polymer science. The DMA can determine changes in sample properties resulting from changes in five experimental variables: temperature, time, frequency, force, and strain. It can measure many properties of material, including: modulus (storage modulus and loss modulus), internal friction or damping, creep, stress relaxation, glass transitions, and softening points. Many studies have been performed on the effect of prior deformation on internal friction. To characterize the internal friction peak in cold deformed A316L stainless steel, the specimens with prior tensile strain 5% or 20% were used by Ivanchenko et al[2]. Liu et al explored the effects of cold working deformation on the internal friction of the 2.25Cr-1Mo steel [3]. The prior deformation was performed also on tensile loading and results show that the internal friction of the steel increases with the magnitude of cold working deformation. Li et al has been studied the internal friction of Fe-Ni based austenitic alloy with prior tensile deformation [4]. The IF of the austenitic alloy was explained by planar and wavy slip of dislocation. Mechanical spectroscopy of Co-Ni-Cr super-alloy was investigated by Cosimati et al[5]. The internal friction of cold worked and annealed Co-Ni-Cr super-alloy samples were interpreted based on the G-L theory. These research were based on the tensile loading or roll milling to produce cold working or prior deformation. However, structural materials failure due to fatigue loading is very common phenomenon. Therefore, it is of great importance in many engineering problems to measure the changes of the materials after fatigue. Few works are available on the internal friction of austenite steel after fatigue loading. In this study, type 304L stainless steel samples, which have been cyclic loaded, were tested on DMA. The amplitude-dependent internal frictions (ADIF) of different pre-stressed samples were measured. The relationship between the ADIF and cyclic stress amplitude was discussed.

2. Materials and Methods

304L plates are machined to dog-bone shape indicated in figure 1. To simulate the effect of fatigue or cyclic loading, the 304L plates are cyclic loaded on material testing system MTS810. The plates are loaded with stress control mode and the loading involves completely reversed (R= -1) cycling between constant stress limits.
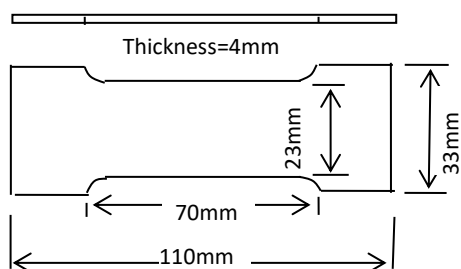

Figure 1. 304L plate with prior fatigue loading.

After cyclic loaded the dog-bone plates are cut in half. The small samples of DMA are extracted along length of the plate using electric spark cutting (figure 2) . Then the small sample surfaces are grinded and polished by hand. The final size of DMA small sample is shown in the right side of figure 2.
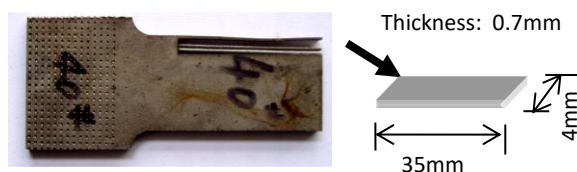

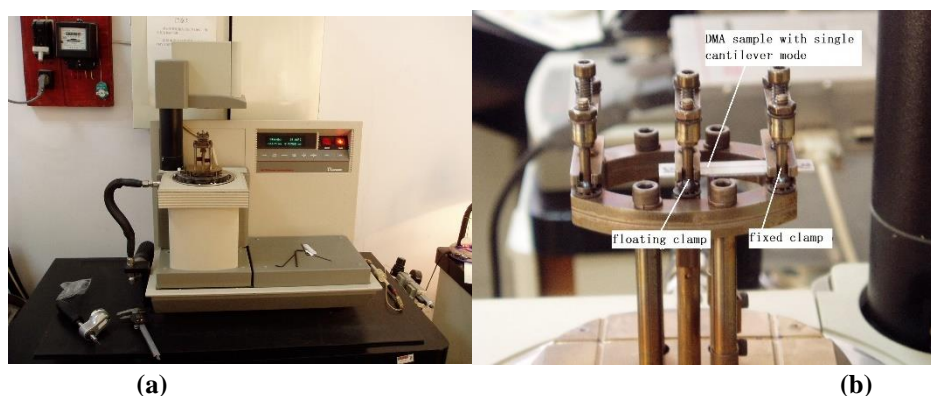**Figure 2**. The 304L plate and the small sample of DMA extracted.

Figure 3. (a) DMA2980 dynamic mechanical analyzer and **(b)** the single cantilever test mode.

Internal friction measurement is made on the Mechanical Analyzer type DMA 2980 of TA Company. The single cantilever test mode is used. The small sample undergoes a flexural deformation between the fixed clamp and floating clamp, see figure 3. During DMA testing the storage modulus E' (elastic response) and loss modulus E'' (viscoelastic/anelastic response) of 304L samples are measured as a function of strain/stress amplitude as the samples is deformed under an oscillatory load (stress) at a controlled frequency (f=1Hz) and temperature in a specified atmosphere. The storage modulus is related to stiffness, and the loss modulus to internal friction and energy dissipation. The relative amount of internal friction or energy loss in the material is given by the loss tangent, tanδ [6]

$$E''/E' = \tan \delta \qquad (1)$$

Anelastic deformation is the term used to describe the time-varying, hysteretic elastic behavior of metals. Anelasticity of metal can lead to mechanical hysteresis manifested by strain not being in phase with an oscillatory stress. The resulting energy loss or internal friction ($\tan\delta = Q^{-1}$) is related to the internal structure of the materials [7]. The internal structures of 304L samples change after cyclic loading and the DMA testing results may show the internal friction difference of samples which subjected to different cyclic loading amplitude and time.

3. Results and discussion

Figure 4 shows the amplitude-dependent internal friction of four samples which have been subjected to different number of cyclic loading while the prior fatigue stress amplitude of the samples is 150MPa. The ADIF of four samples are almost the same when the strain is below 0.1% and the ADIF increase with the increasing of strain. Cyclic number of prior fatigue has little influence on the ADIF or damping values. However, when the strain amplitude approach 0.2%, the effect of fatigue time (cyclic number) appears. The internal friction of original sample without pre stressed increase steadily as the plastic deformation increase. But the ADIF curves of the pre-stressed samples have a hump when strain amplitude is 0.2%, which agree with the yield strain of the samples. The more prior fatigue cycle the higher the ADIF curve hump. The plastic deformation is significant when the strain amplitude approach 0.2%, therefore, the hump is associated with the extent of plastic strain during DMA.
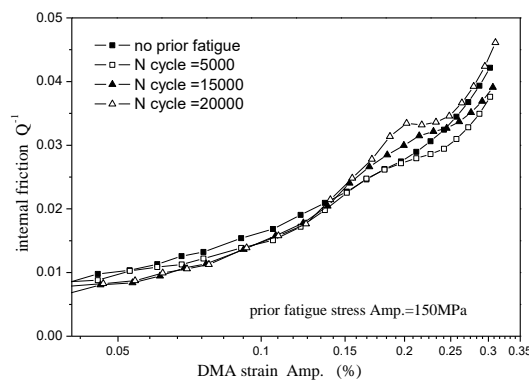

Figure 4. ADIF of four samples with different cyclic pre-stress number.

The ADIF of samples which have been loaded with different amplitude of loading are measured on DMA2980. The cyclic pre-stress amplitude is from ±80MPa to ±200MPa and the number of loading cycle is 10000. Five internal friction curves are shown in figure 5.
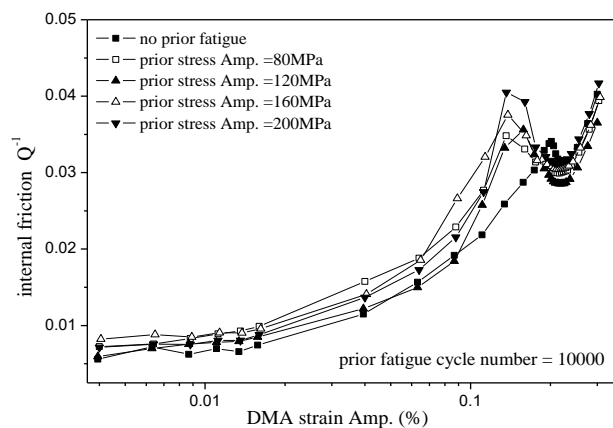

Figure 5. ADIF of samples with different pre-stress amplitude.

Figure 5 shows all ADIF curves have a peak when the strain amplitude is about 0.2%. The peak is not mentioned in many ADIF related literatures because the maximum strain amplitude is generally less than 0.1% during ADIF testing with DMA [8,9,10]. The peak in figure 5 shows an apparent association with the prior fatigue stress amplitude. The height of the ADIF peak increase with an increase of the prior fatigue stress amplitude. The

relationship between the ADIF peak and the prior fatigue stress amplitude indicate that the fatigue history of the 304L SS may reflect by the internal friction curves, thus, the fatigue life of the 304L SS may be predicted with the peak value of internal friction.

The ADIF curves can be explained by the Granato-Lucke mode (G-L) [11]. According to the mode, a crystal contains a network of dislocation lines. The network nodes are considered to be strong pinning points: under the small strain conditions during DMA testing, dislocation will oscillate between these nodes, but will not be torn loose from the dislocation intersections, therefore, the ADIF is low when the oscillation amplitude is small. Once the strain is over critical level, the attractive force between dislocation and point defect is overcome and the dislocation moves away from the pinning point. At still higher strain, long-range dislocation motion will result in dislocation multiplication and drastically alter the internal friction behavior [12]. An internal friction peak occurs which relates to the plastic deformation of the materials. Samples subjected to higher cyclic loading amplitude (pre-stress amplitude) have heavier dislocation density and the ADIF peak is higher. The agreement between G-L mode theory and the ADIF curves is obtained.

4. Conclusions

The study shows that dynamic mechanical analysis equipment can be applied for the internal friction or damping characterization of 304L SS. The fatigue history of 304L SS can be reflected by the internal friction curves. The ADIF of 304L SS samples are insensitive to the DMA strain amplitude when the strain amplitude is less than 0.1%. There is a peak in ADIF curves when the strain is about 0.2% which relates to the damping and plastic deformation. ADIF curves may indicate the dislocation pinning and unpinning from pinning point and dislocation multiplication, which are compliance with the Granato-Lucke mode. As the prior fatigue stress or cyclic loading is a strong influence on the distribution and density of dislocations, this work provides a means for the evaluation of fatigue status and residual life of 304L SS.

References

1. Dowling. N.E. Mechanical behavior of materials: engineering methods for deformation, fracture, and fatigue. Prentice-Hall, Inc, New Jersey, USA 1993
2. Ivanchenko, M.; Yagodzinskyy, Y.; Hanninen, H. Effect of plastic deformation on anelastic mechanical losses in multi component substitutional austenitic alloys, Materials Science and Engineering A **2009**, *521-522*: 121–123
3. Liu, X.; Shiwa, M.; Sawada, K.; Yamawaki, H.; Watanabe, M.; Yin, F. Effect of cold working deformation on the internal friction of 2.25Cr-1Mo steel, Materials Science and Engineering A **2010**, *527*: 6741–6744
4. Li Z.; Hu, X.; Zhao, M.; Rong, L. Effect of prior deformation on internal friction in a Fe-Ni based austenitic alloy, Materials Letters, **2013**, *98* :82–85
5. Cosimati, R.; Mari, D. Secondary hardening in Co-Ni-Cr super-alloy investigated by Mechanical Spectroscopy, Materials Science & Engineering A **2016**, *662*:426–431
6. Hertzberg. R.W. Deformation and fracture mechanics. John Wiley & Sons, Inc. USA 1976
7. Courtney. T.H. Mechanical behavior of Materials.2nd ed. McGraw-Hill Companies, Inc. 1990
8. Menard, K.P. Dynamic Mechanical Analysis: A Practical Introduction, CRC Press Boca Raton USA 1999.
9. Aruga, Y.; Morikawa, Y.; Tamaoka, S.; Nishino, Y. Scripta Materialia **2012**, *66* 686–689
10. Li, Q.; Li, J.; He, G. Materials Science & Engineering A **2017**, *680*: 92–96
11. Courtney, T.H. Mechanical behavior of Materials. McGraw-Hill Companies, Inc. 1990
12. Batist, R.D.E. Internal friction of structural defects in crystalline solids. North-Holland publishing Co. Netherlands, 1972

Small punch fatigue testing of a nickel superalloy

S.J. Davies [1], R.J. Lancaster [1,*], S.P. Jeffs[1], R.C. Hurst [1], G.J. Baxter [2]

[1] Institute of Structural Materials; Swansea University Bay Campus; Fabian Way; Swansea; SA1 8EN, UK
[2] Rolls-Royce plc, P.O. Box 31, Derby, DE24 8BJ, UK
* Correspondence: R.J.Lancaster@eswansea.ac.uk; Tel.: +44-1792-295965

Abstract: Miniaturised mechanical test approaches, specifically small punch testing, are now widely recognised as a means of obtaining useful mechanical properties to characterise the creep, tensile and fracture characteristics of numerous material systems from a range of industrial applications. Limited success has been found in replicating fatigue properties through the use of a small punch disc. This paper will discuss the ongoing research and progress in developing a novel small punch fatigue testing facility at the Institute of Structural Materials at Swansea University. Experiments have been performed on the nickel superalloy C263 at ambient room temperature, investigating three different alloy variants; two orientations produced through additive manufacturing and the cast equivalent. Fractographic analysis has been completed to interpret the complex damage mechanisms in the test method along with the differences in performance amongst the alloy variants.

Keywords: small punch; small punch fatigue; C263; additive manufacturing.

1. Introduction

A fundamental understanding of the mechanical performance of a material is essential when looking to implement them into any high temperature component, as is often the case within the aerospace industry. Advanced materials and processes are continuously under development in an attempt to improve performance whether through a reduction in weight, improved strength, enhanced temperature capability or streamlined design. An extensive assessment of mechanical performance of these advancements through traditional means is typically expensive and, coupled with the challenge of often limited material availability, has led to a commitment in developing more appropriate test techniques. The miniaturised test method being discussed here is the Small Punch (SP) test, the general arrangement for which is given in the European Code of Practice [1].

Primarily, the SP test is used to obtain creep, tensile and fracture data from small discs of material, providing useful mechanical property information from small material quantities [2,3]. The approach is carried out by deforming a disc specimen under an applied compressive load transferred through an indenter, where the test may be either constant load, which exhibits a creep type response, or constant displacement rate which promotes tensile type behaviour. During SP testing the specimens are considered to deform under a biaxial stress state and data sets for both the constant load and constant displacement rate regimes have been correlated to equivalent conventional test methods through various means [2,3]. The test method has been applied across a range of industries and alloy systems for different purposes including the residual life assessment of power plant steels [4], ascertaining local properties of welded joints [5] and ranking the performance of aerospace alloys [6]. As a result, SP testing offers a feasible option for determining mechanical properties at the early stages of development in novel alloys and processing, potentially assisting with down selection through means of ranking.

The advancement and worldwide implementation of the SP technique has highlighted the necessity to understand the behaviour of the arrangement under cyclic deformation, particularly in aerospace alloys where fatigue performance is a life limiting parameter. Thus far, efforts have seen a SP test with a cyclic loading capability [7,8] implemented using compressive loading ratios (R>0), whilst a second arrangement has been developed to accommodate positive loading regimes (R=0.1) and fully reversed cycles (R=-1) by means of a twin indenter layout [9,10].

This research discusses the progress made at the Institute of Structural Materials (ISM) at Swansea University in developing the aforementioned SP fatigue testing methodology. Experiments were performed on nickel superalloy C263, produced through different processes; either casting or built through additive layer manufacturing (ALM), over a range of maximum load conditions using a positive R ratio of 0.1. The differences in fatigue lives between the variants was assessed and post-test fractographic analysis was conducted to determine whether any evidence of fatigue crack growth could be identified.

2. Materials and Methods

2.1. Material

Nickel-based superalloy C263 is a commercial alloy used in the aero-engine industry for static components such as combustion chambers due to its performance at high temperature along with its resistance to creep and corrosion. The nominal composition for C263 is summarised in Table 1 [11].

Table 1. Chemical composition of C263 (wt%).

	Co	Cr	Mo	Al	Ti	C	B	Zr
C263	20.0	20.0	5.9	0.5	2.1	0.06	0.001	0.02

Its relatively low γ' content means that C263 has good weldability and lends the material well to ALM processes. ALM provides the opportunity to manufacture near net shape components, offering the potential for considerable benefits in terms of design capability and material wastage. Disadvantages of ALM include the inherent microstructural anisotropy due to the re-melting of previous layers as well as the possibility of the presence of features such as porosity or lack of fusion during the build. One such method is Laser Powder Bed Fusion (LPBF) in which a 3D component is built through successively melting layers of powder through a computer controlled laser. As a result, an understanding of the relationships that exist between the process, microstructure and mechanical properties is essential, especially when considering applications in structural components. This is where exploiting miniaturised test techniques proves valuable since multiple test samples may be extracted from much smaller quantities of material allowing a more cost-effective means of down selection in terms of LPBF process parameter input such as power, hatch spacing and velocity or post-process conditions such as orientation or heat treatments [12].

The microstructures for each of the variants of C263 under investigation are given in Figure 1, displaying the microstructure of the punch contact surface. In the first instance, LPBF variants were built as traditional round bar test specimens in two orientations under the same process parameters, either vertically (90°) where the gauge length is parallel to the build direction or horizontally (0°) SP specimens were extracted from the thread ends of larger test pieces in each orientation. The clear anisotropic microstructure produced by LPBF can be seen in Figure 1b and 1c, where elongating grains are present in the build direction. Cast C263 material was used as a reference material although the bi-modal grain structure makes the miniaturised sample challenging since the number of grains present in each sample can vary. Table 2 provides the grain sizes and aspect ratios of the corresponding microstructures.

Cast SP specimens were obtained by electrical discharge machining Ø9.5mm cylinders from a cast ring which were subsequently sectioned in to ~800 µm segments. The sections were then ground and polished to obtain a final thickness of 500 µm ± 5 µm with a 1200 grit finish. In the case of the LPBF specimen the Ø9.5 mm cylinders were obtained by the turning of threaded ends from larger test samples.
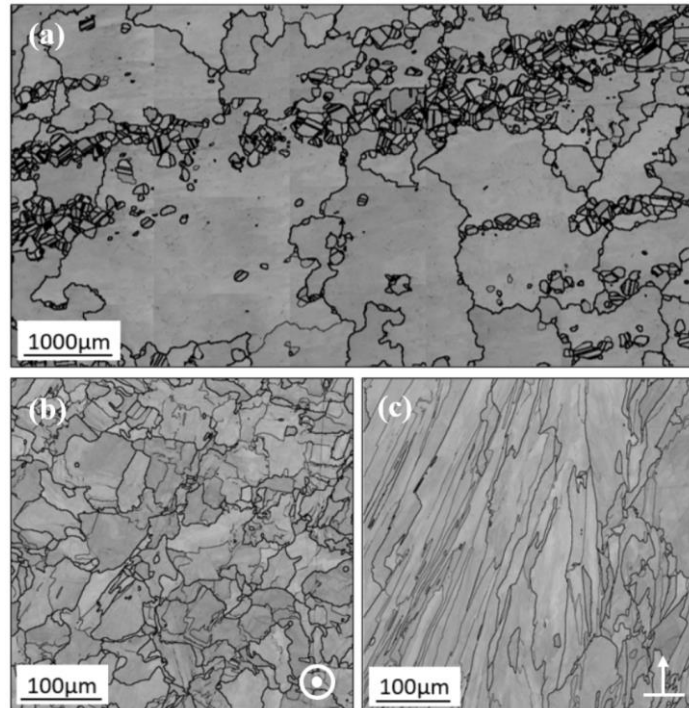
Figure 1. Microstructures of C263 alloys showing the punch contact face; (a) cast (b) LPBF vertical (90°) and (c) LPBF horizontal (0°).

Table 2. Grain sizes and aspect ratios.

C263 Variant	Average Grain Size [μm]	Aspect Ratio
Cast	101.7/921.8	0.55/0.52
LPBF 90°	22.8	0.99
LPBF 0°	29.6	0.23

2.2. Small Punch Fatigue

Figure 2 shows the SP fatigue test setup which for testing positive R ratios, as in the case in this research, is consistent with that of a traditional SP test under a constant displacement rate, as a result the dimensions are as those prescribed by the European Small Punch Code of Practise [1]. Previous work in the authors' research group has gone into more comprehensive detail regarding this unique test arrangement [9,10]. Tests were performed with an R=0.1 load ratio at a 1Hz frequency using a sinusoidal waveform.
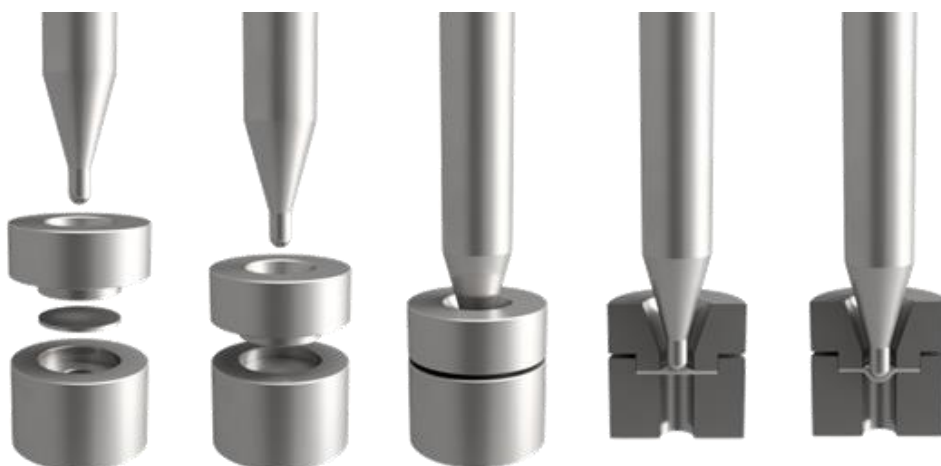

Figure 2. Small punch fatigue test configuration for an R > 0.

Figure 3 displays the commanded and actual load response for the first three cycles for two different maximum load tests, highlighting the control and repeatability of the setup to produce accurate and reliable fatigue cycles.
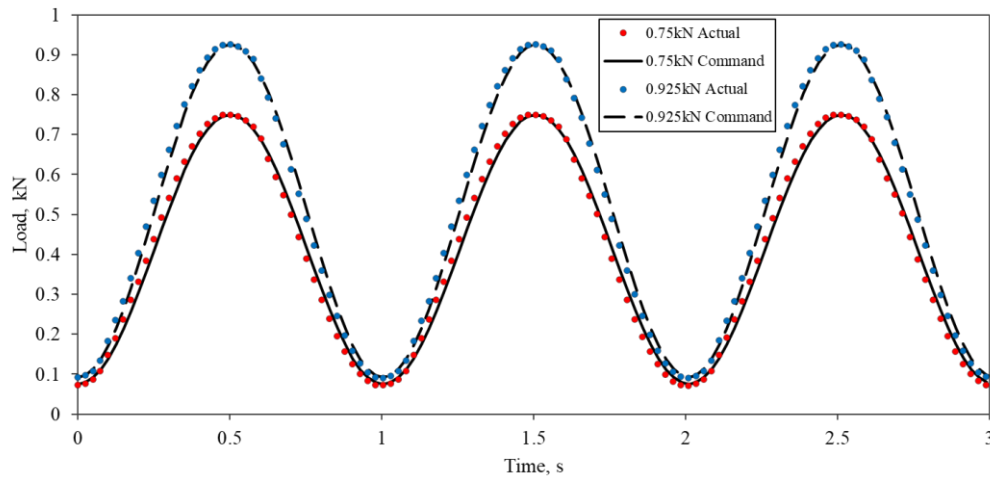

Figure 3. Commanded vs. Actual load response for the small punch fatigue test apparatus.

3. Results & Discussion

At the time of publication, a total of three SP fatigue tests have been performed on each of the material variants at different maximum load conditions to generate a series of representative load (L) – number of fatigue cycles to failure (N_f) curves, or an L-N curve. Figure 4 shows the L-N curves for the three C263 variants plotted as the maximum load against cycles to failure. The observed behaviour is akin to that from a series of uniaxial fatigue tests and the resulting uniaxial stress against number of cycles to failure curve, with an increasing maximum load reducing the number of cycles to failure. Nevertheless, the difference in stress state, biaxial in SP fatigue compared to uniaxial stress in conventional uniaxial fatigue, means any direct comparison requires a deeper understanding of the evolution of the stress and the material mechanisms that take place.

A key challenge in producing L-N curves for this arrangement comes from determining a consistent and repeatable failure criterion, since unlike a traditional uniaxial fatigue test there is no obvious or audible fracture that occurs. Therefore, the failure criteria need to be based upon the specimen displacement. From a series of initial interrupted trials, it was revealed that after 250 µm of displacement, a clearly defined fracture comparable to that seen in small punch tensile testing was observed. As such, this value was used as the failure criteria for all experiments.
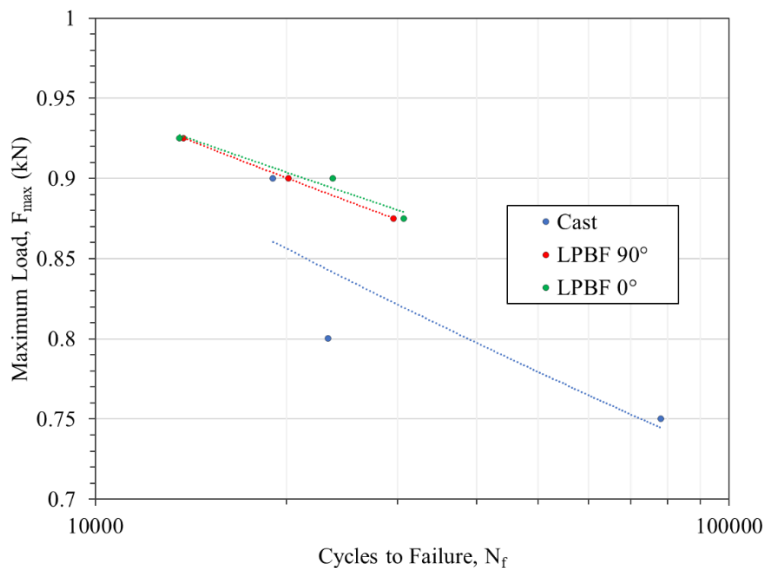

Figure 4. Room temperature small punch fatigue L-N curves (R=0.1, 1Hz sinusoidal waveform).

The L-N curves in Figure 4 clearly show that for the relatively limited data sets generated, LPBF materials outperform the cast material in this unique test type, with the LPBF 0° and 90° exhibiting near identical behaviour. It is believed these differences can be largely attributed to the grain size since the cast material has a grain size 5-50x greater than that of the LPBF materials and therefore fatigue life would be expected to decrease. The large scatter in the cast curve could then be attributed to the bi-modal grain structure which within a Ø9.5 mm x 500 µm specimen means the number of grains through thickness could potentially be just one. The LPBF 0° and 90° average grain sizes are within 5µm although there is a large difference in the aspect ratio due to the epitaxial grain growth from the additive process. Nonetheless, the grain size appears to be the dominant factor since the L-N response of the LPBF materials sit upon one another. Further SP fatigue tests with $N_f < 10000$ cycles and $N_f > 50000$ cycles may enhance the influence of the elongated grain structure further.

Figure 5 shows the load-displacement response for the first cycle and cycle 1000 for the three variants. The first load – displacement cycle helps to provide some means of confirmation as to whether the unique SP fatigue test setup is producing genuine results, in particular the displacement measurements being taken and how they compare to those from a small punch tensile test on the same material [13]. Furthermore, this explains the debit in performance seen the cast material when compared to the additive variants.
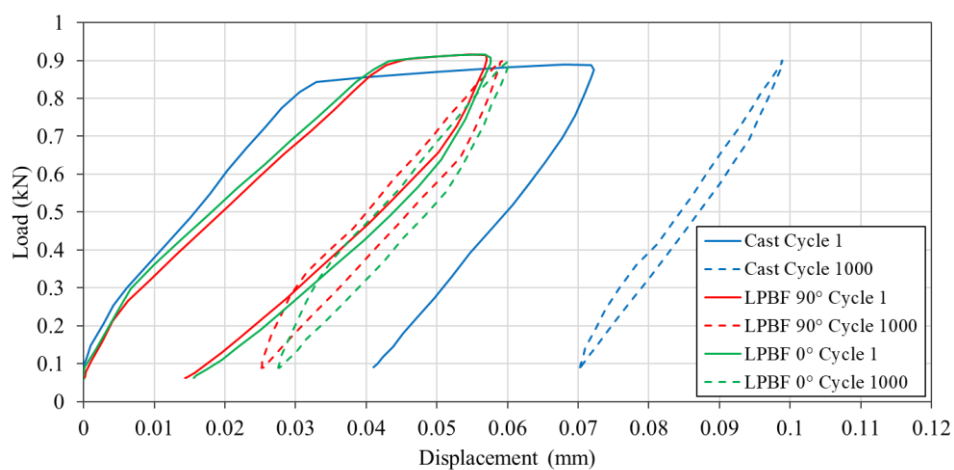

Figure 5. Load vs. displacement hysteresis response at F_{max} = 0.9kN; cycle 1 and cycle 1000.

3.1. Fractography

Fracture surfaces were assessed through scanning electron microscopy to determine the means and mechanisms by which the specimens had failed. Figure 6 shows the overall fracture morphology together with images taken at higher magnification of the through thickness for each of the C263 variants. Figures 6a), c) and e) show star-type cracking across the three materials where the cracks grow radially from the centre of the specimen. For the LPBF materials this is somewhat different to that observed in small punch tensile testing of these materials where a dominant circumferential crack occurs [13], therefore there must be a clear change in failure mechanism.

Figures 6b), d) and f) reveal features that relate to fatigue damage in each of the materials tested, specifically striations. Striations are features that occur along the crack path that represent the increment of crack growth that occurs in a single fatigue cycle as a result of the plastic blunting process. It is the presence of these features that gives confidence to the small punch fatigue testing methodology in terms of the mechanisms that are taking place, although a comprehensive understanding of the stress state is the next step moving forward.
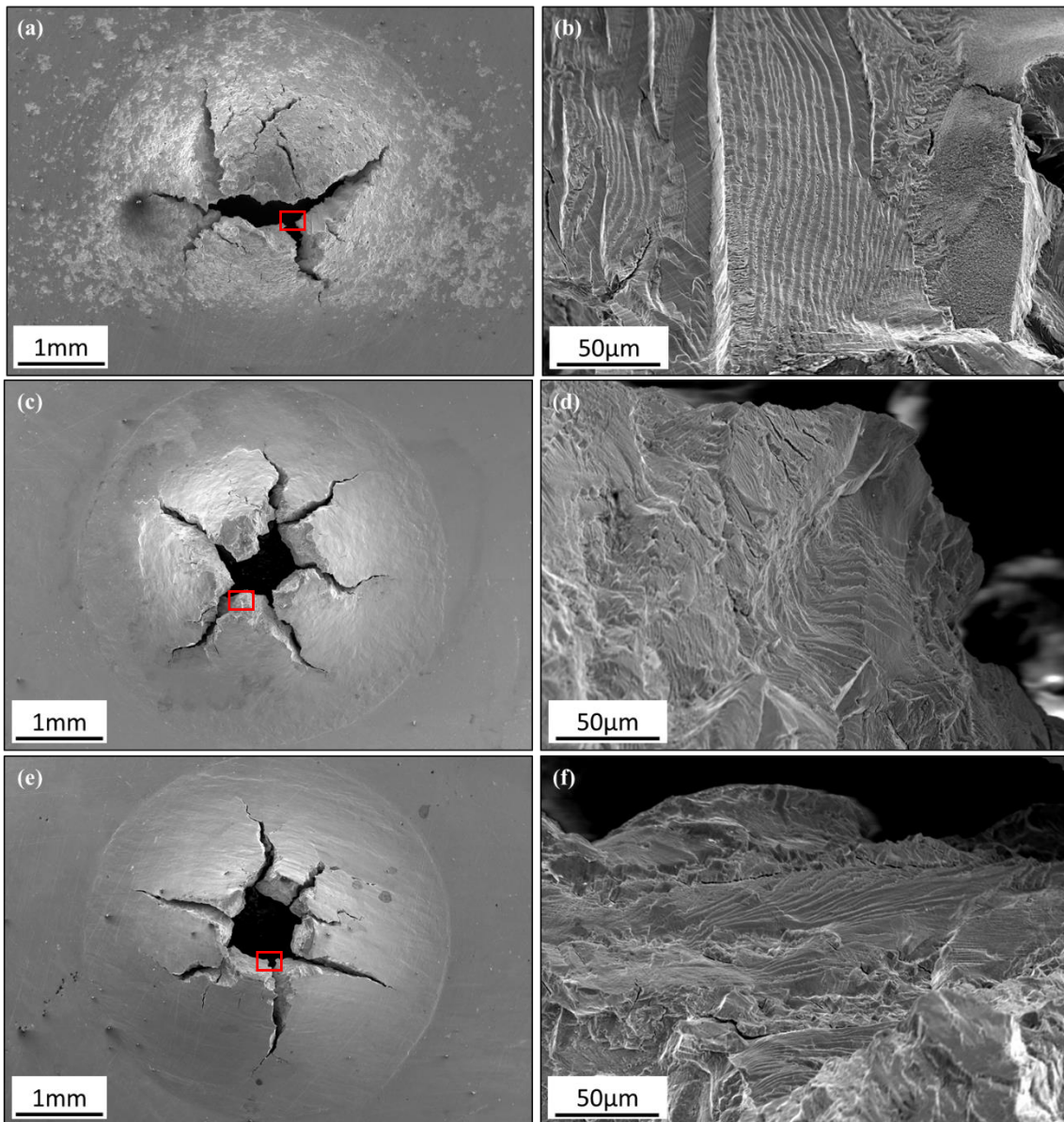
Figure 6. Fractographic images of small punch fatigue tests of (a-b) cast (c-d) LPBF 90° and (e-f) LPBF 0° C263 material showing clear evidence of striations.

4. Conclusions

Ongoing research into a bespoke small punch fatigue capability being conducted at Swansea University has been detailed in this paper resulting in the following conclusions:

- The small punch fatigue response of the C263 variants has shown a sensitivity to grain size in line with that expected under uniaxial fatigue conditions.
- Evidence of striations give confidence of the apparatus and the resulting fracture mechanisms that are taking place in the material variants.
- Further work into understanding the evolving stress state is a crucial step moving forward when aiming to compare or interpret the results with uniaxial fatigue data.

References

1. CEN Workshop Agreement CWA 15267 European Code of Practice: Small Punch Test Method for Metallic Materials 2007, 1–69.
2. Jeffs, S. P.; Lancaster, R. J.; Garcia, T. E. Creep lifing methodologies applied to a single crystal superalloy by use of small scale test techniques. *Mater. Sci. Eng. A* **2015**, *636*.
3. Bruchhausen, M.; Holmström, S.; Simonovski, I.; Austin, T.; Lapetite, J. M.; Ripplinger, S.; de Haan, F. Recent developments in small punch testing: Tensile properties and DBTT. *Theor. Appl. Fract. Mech.* **2016**, *86*, 2–10.
4. Kumar, J. G.; Laha, K. Small Punch Creep deformation and rupture behavior of 316L (N) stainless steel. *Mater. Sci. Eng. A* **2015**, *641*, 315–322.
5. Rodríguez, C.; García Cabezas, J.; Cárdenas, E.; Belzunce, F. J.; Betegón, C. Mechanical properties characterization of heat-affected zone using the small punch test. *Weld. J.* **2009**, *88*, 188s–192s.
6. Hurst, R. C.; Lancaster, R. J.; Jeffs, S. P.; Bache, M. R. The contribution of small punch testing towards the development of materials for aero-engine applications. *Theor. Appl. Fract. Mech.* **2016**, *86*.
7. Prakash, R. V. Study of fatigue properties of materials through cyclic automated ball indentation and cyclic small punch test methods. *Key Eng. Mater.* **2017**, *734 KEM*, 273–284.
8. Prakash, R. V. Investigation of Static and Fatigue Properties of Materials Through Small Specimen Test Methods. In *Proceedings of the 3rd International Conference on Small Scale Test Techniques*; 2014; pp. 339–347.
9. Lancaster, R.; Illsley, H.; Jeffs, S.; Hurst, R.; Baxter, G. Application of the small punch test to determine the fatigue properties of additive manufactured aerospace alloys. *MATEC Web Conf.* **2018**, *165*, 1–6.
10. Lancaster, R.; Illsley, H.; Hurst, R.; Jeffs, S.; Baxter, G. *A novel approach to small punch fatigue testing*; 2017; Vol. 734 KEM.
11. Reed, R. C. *The Superalloys: Fundamentals and Applications*; Cambridge University Press, 2006.
12. Vilaro, T.; Colin, C.; Bartout, J. D.; Nazé, L.; Sennour, M. Microstructural and mechanical approaches of the selective laser melting process applied to a nickel-base superalloy. *Mater. Sci. Eng. A* **2012**, *534*, 446–451.
13. Davies, S.; Jeffs, S.; Lancaster, R.; Baxter, G. High temperature deformation mechanisms in a DLD nickel superalloy. *Materials (Basel).* **2017**, *10*.

Fatigue response evaluation of stainless steel SS 304 L(N) and SS 316 L(N) through cyclic ball indentation studies

R.V. Prakash [1,*], K. Madhavan [2], A.R. Prakash [3], R. Sandhya [4] and G.V.P. Reddy [4]

[1]   Indian Institute of Technology Madras, Chennai 600036, India; raghuprakash@iitm.ac.in
[2]   SASTRA University, Thanjavur 613401, India; krishnamadhavan007@gmail.com
[3]   National Institute of Technology, Tiruchirappalli 620015, India; anirudh.kv.iit@gmail.com
[4]   Indira Gandhi Centre for Atomic Research, Kalpakkam 603102, India; san@igcar.gov.in; prasadreddy@igcar.gov.in
*   Correspondence: raghuprakash@iitm.ac.in; raghu.v.prakash@gmail.com; Tel.: +91-442-257-4694

Abstract: This paper presents the results of an experimental investigation of fatigue response of stainless steel SS 304 L(N) and SS 316 L(N) using cyclic ball indentation test method. A Tungsten Carbide (WC) spherical ball of 1.57 mm diameter is used for applying compression-compression fatigue cycling on the test specimen having a nominal thickness of 5 mm; the displacement response is monitored as a function of every cycle of loading. The study focused on cases where the stainless steel specimens were welded by two different welding processes – Activated flux TIG welding and conventional multi-pass TIG welding. Fatigue response was monitored at locations of weld zone, heat affected zone (HAZ) and base metal to identify the effect of microstructure variation on fatigue response. It is observed that there is a steady increase in depth of penetration of the spherical indenter due to fatigue cycling; however, after a number of cycles, there is a sudden increase in depth of penetration which indicates the failure of the material beneath the indenter. The specimens after cyclic ball indentation were examined using a scanning electron microscope and one could observe the presence of secondary cracking in the penetrated region of the specimen.

Keywords: Cyclic ABI testing; fatigue; failure life; weld and HAZ region; SEM observations.

1. Introduction

Life prediction of safety-critical components and structures is an important task where the accuracy of predictions, reliability and confidence level are critical parameters. One of the inputs that form the basis for life extension is the data on the present condition of the material. As the volume of material available for testing from working components is limited, recourse is taken to evaluate with reasonable level of confidence the mechanical behaviour of materials using small specimen test methods. The following mechanical properties are widely estimated using small specimen test methods: tensile properties [1-4], impact [5-6], fracture toughness properties [7-8] and in a few cases fatigue properties are evaluated through sub-size hourglass specimens [9]. Fatigue crack growth experiments have been carried out using miniature specimens [10-11] to estimate the degradation in performance due to irradiation. However, experimental techniques available to evaluate the fatigue properties through in-situ test methods are limited.

Welding is one of the most common engineering material joining methods over the past several decades. Despite many advances in welding technology, welded components pose difficulties when subjected to fatigue loading. This is due to the presence of different microstructures at the weld zones compounded with the presence of residual stresses in the weld region – typically the heat affected zone (HAZ). Estimation of fatigue properties at the weld region has been a topic of research over several decades. Specimens cut across the various sections are used to estimate the plain fatigue properties of welds. These are typically butt-welded joints. The purpose of this work is to assess the fatigue behavior of weld joints for a typical structural stainless steel material through a novel cyclic ball indentation test method.

The cyclic ball indentation technique can be considered as an extension of the automated ball indentation (ABI) test technique proposed by Haggag et al [12-13] to evaluate the static properties of materials. ABI test method employs a series of programmed load-unload segments to derive the stress-strain properties, but the indentation depth keeps varying as a function time. Hence, it cannot be considered as cyclic indentation testing. Under Cyclic ABI, the cyclic indentation load is held constant. In such a case, the depth of penetration would vary with the number of cycles of loading, and this forms the basis for prediction of failure life.

Dynamic indentation studies on foam material using flat cylindrical indenters has shown that if a material is cyclically loaded using an indenter, the force-displacement response changes as a function of the number of cycles of loading [14]. A drop in displacement has been considered as the material failure parameter during cyclic indentation. A similar approach is used in cyclic ball indentation studies carried out through the experimentation route. Details such as total depth of penetration as a function of applied cycles and loading/unloading compliance derived from the force vs. displacement response, offer the scope for the assessment of fatigue behavior of a material.

2. Materials and Methods

Structural stainless steel SS 304 L(N) and SS 316 L(N) in base metal form, as well as in welded form are considered for this study. Cyclic ABI (fatigue) tests were carried out on a 100 kN MTS closed-loop servo-hydraulic test system (Fig. 1a) that has a computer interface for test automation and data acquisition. The working range of the force and displacement transducer was scaled down to $1/10^{th}$ of its full scale range and the system tuned for reduced working ranges. A spherical tungsten carbide (WC) indenter of nominal diameter, 1.57 mm (1/16"), was inserted into a specially formed cup, and the cup was attached to a plunger. The plunger arrangement ensures that there is no-back lash at the WC indenter interface during cyclic loading of the specimen. The other end of the plunger is mounted into the standard grips of test system. The base platen that holds the specimen was mounted on the bottom grip of the test system. To measure the local displacements close to the indenter, a set of knife edges were mounted on the test fixture and a clip-on-displacement gage, having a full scale range of +/- 2.5 mm was used to measure the local displacements (Fig. 1b). The range of displacement transducer was electronically scaled down in the test controller for measurement purposes.
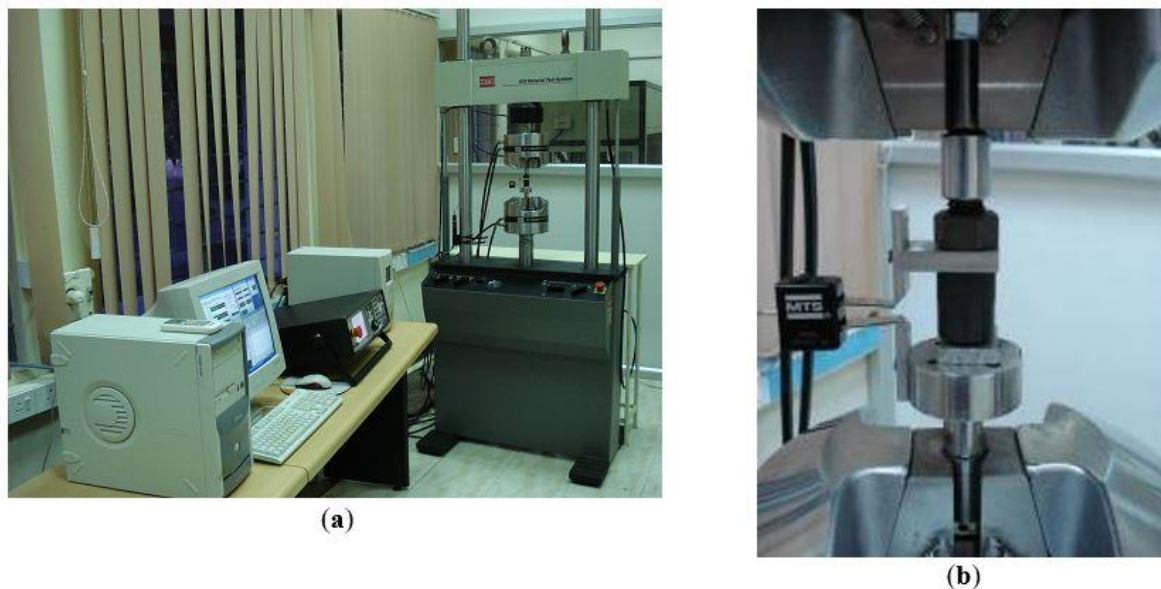

Figure 1. (a) Photograph of cyclic ball indentation test set-up; **(b)** close-up view of the spherical indenter along with clip-on-displacement gage that was used to measure local indenter depth of penetration.

The fatigue properties are estimated under compression-compression cyclic loading using sinusoidal wave form under force control mode. Test sequence for cyclic indentation was programmed to conduct tests in force control mode at a stress ratio (ratio of minimum to maximum load applied) of R=0.1. The test was conducted under constant amplitude loading investigating the cyclic load-displacement response for the base metal, Activated TIG welded region and Multi-Pass TIG welded regions of the stainless steel materials. As the plastic strain beneath the indenter is a function of the depth of penetration, different load amplitudes were chosen to obtain the plastic strain versus failure life data.

3. Results and Discussion

Figure 2a presents the typical load-indenter displacement response for SS 316 L(N) base metal (BM) subjected to 1000 N of peak compressive force and 100 N of minimum compression force. Also shown in the same graph is

the data for a cyclic indentation test conducted with 1250 N and 125 N as maximum and minimum force. Figure 2b presents the first cycle load-displacement data for SS 304 L(N) in base metal (BM) and Multi-Pass TiG (MP-TIG) welded conditions. It can be noted that the depth of penetration increases with an increase in peak load applied for SS 316 L(N) material. By comparing the graphs 2(a) and 2(b), one can say that the depth of penetration in SS 316 L(N) base material for the same 1000 N compressive load is lesser than that of SS 304 L(N) base material. The indentation depth is less for MP-TIG weld region of SS 304 L(N), which has a finer grain microstructure.
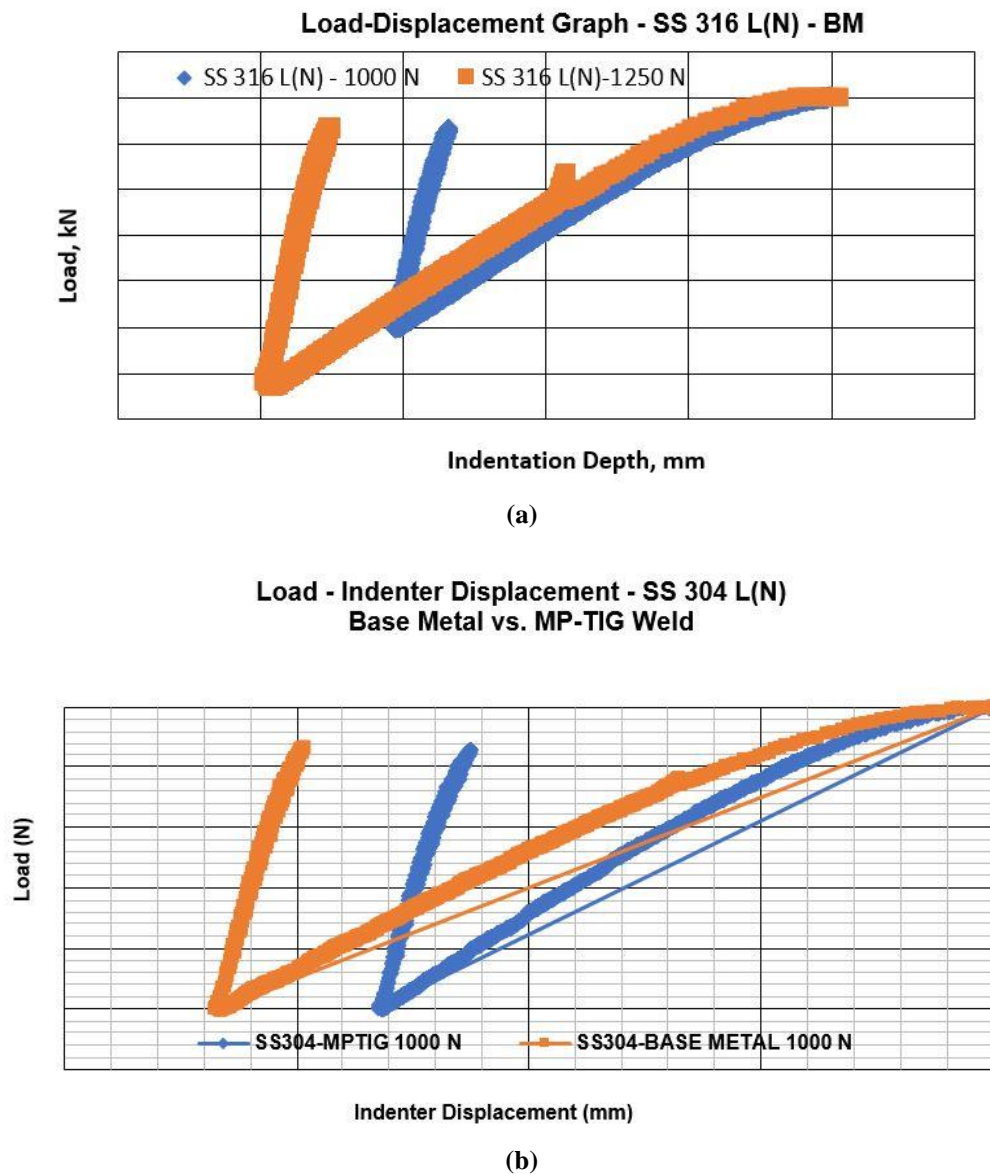

(a)

(b)

Figure 2. (a) Load-indentation depth for SS 316 L(N) material in base metal condition at two different loads; **(b)** comparison of load-indentation depth response for SS 304 L(N) material in base metal and Multi-pass TIG welded condition.

As indicated earlier, the indentation depth was monitored continuously during the test and the load-indenter depth data was logged. From this data, the unloading slope over a window covering 90-50% of peak compressive load was used for extracting the plastic depth of penetration data. Figure 3 presents the slope vs. number of cycles data for a SS304 L(N) MP-TIG weld region. It can be seen that at cycles close to N=2400, there is a change in the slope response from the previous cycles, with a sudden increase that is followed by a decrease in slope of the load-displacement data. This is characteristic of cyclic ABI testing and represents the failure of the material beneath the indenter. To understand this aspect, the specimens were electro-polished prior to the start of the experiment and after this event the specimen was examined under an optical and a scanning electron microscope to obtain details

of material beneath the indenter. Presence of extensive slip around the periphery of the spherical indenter and secondary cracking in the depth direction was observed from the SEM observations. Figure 4 presents a typical SEM image of the specimen after it was tested under cyclic ball indentation testing.
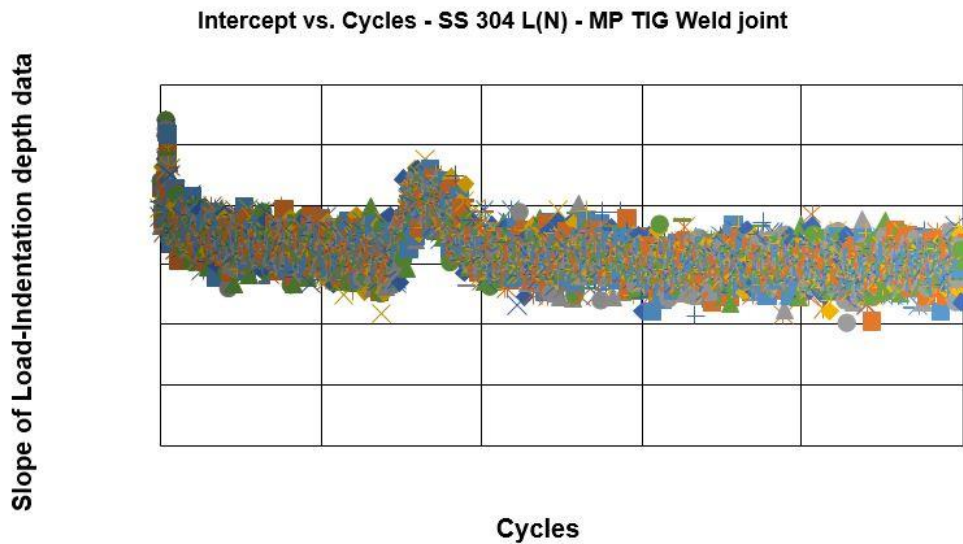

Figure 3. Slope of load-indentation depth data vs. cycles for SS 304 L(N) MP-TIG weld joint tested under cyclic ball indentation testing at 1500 N.
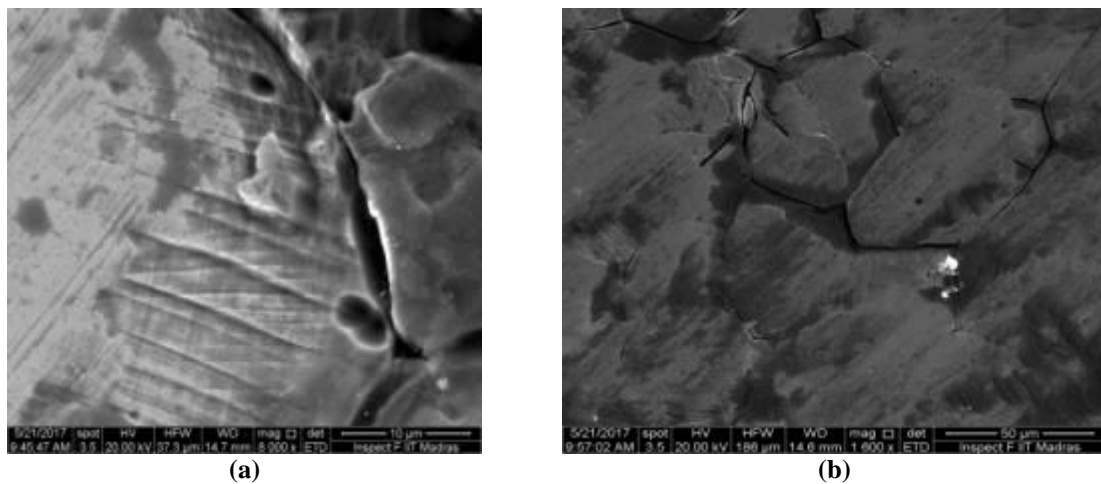

Figure 4. (a) Typical SEM Image near the periphery of indenter and specimen flat surface for SS 304 L(N) Base metal tested under cyclic ball indentation testing at 1250 N; **(b)** Typical SEM image near the mid-thickness region of indentation. Secondary cracks along the depth direction can be seen.

The cycles corresponding to the change in response of slope during cyclic indentation is collected for a number of experiments conducted at different load levels and for different microstructures. For a better consistency in tracking such data, the number of the cycles corresponding to such a shakedown has been tracked using a 2% offset from the mean intercept data and the same has been correlated with plastic strain. Figure 5 presents the graph of average true strain (obtained using Haggag's equation [12-13] for true strain from plastic penetration depth) versus the failure cycles for the variety of cyclic ABI experiments conducted. It can be seen that there is a good strain life linear plot between the (peak) plastic strain and failure cycles as estimated through cyclic ball indentation.
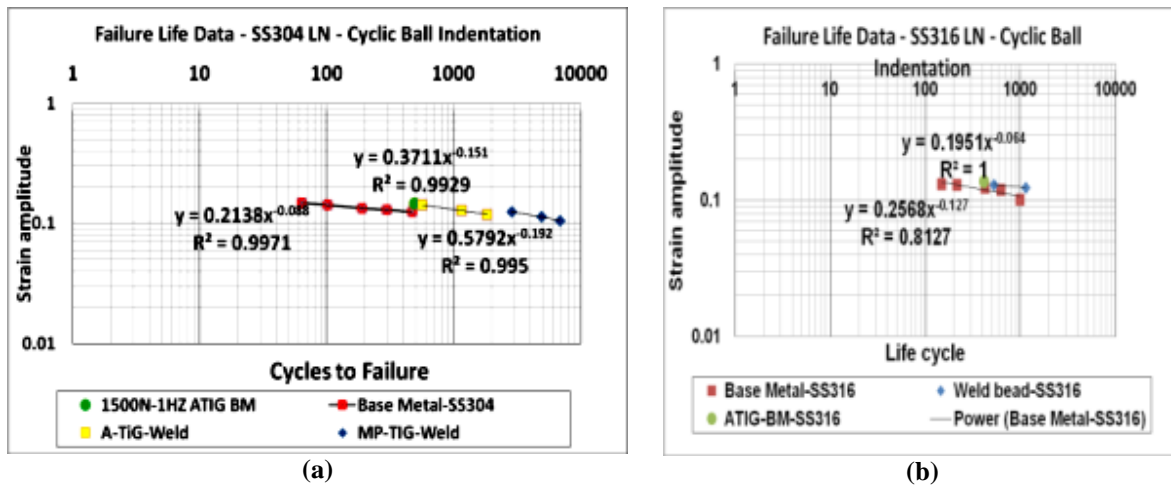
Figure 5. (a) Plastic strain vs. failure life data for SS 304 L(N) material in base metal, A-TIG and MP-TIG conditions; **(b)** Plastic strain vs. failure life data for SS 316 L(N) material in base metal, A-TIG weld conditions.

Figure 5a presents the failure life data plot as a function of strain amplitude for SS 304 L(N) material under various conditions: base metal, Activated flux-TIG (A-TIG) weld and MP-TIG weld. It is noted from the figure that the strain ductility coefficient for the MP-TIG weld region is the highest (0.579) compared to the A-TIG weld (0.371) and the least strain ductility coefficient was found for the base metal (0.2138). The strain ductility exponent for the MP-TIG weld is also the highest, thus indicating that the material is sensitive to low cycle fatigue. Figure 5b presents failure life information obtained from SS 316 L(N) material for the base metal and weld bead. The fatigue ductility coefficient of base metal is superior compared to the weld bead (based on the limited data analysis). Further experimentation is in progress to characterize the fatigue data for various strain levels.

Many of the experimental data reported here are from tests conducted at a select set of test frequencies, such as 0.1 Hz, 0.5 Hz and 1 Hz. The test results suggested that the failure life is not influenced by the test frequency. The reason for conducting experiments at different test frequencies was to ascertain if strain rate had an effect on failure life. The reason that test frequency did not show an influence could be the low rate of test frequency and possibility of heat dissipation from the specimen deformation zone to the surroundings, which annulled the strain rate effect on failure life.

It is further noted that though the failure life data is plotted in a conventional manner, the local stress ratio is not the same as the global loading stress ratio (R=0.1) as the local deformations are very different from the global deformations. Thus, a mean stress and mean strain correction may be required to correlate this data with those obtained from fully reversed low-cycle fatigue experiments. Work is in progress to obtain such a correlation through finite element simulations of cyclic ball indentation as well as through empirical relationships. Furthermore, it is proposed to explore the cyclic ball indentation tests under displacement control, as the depth of penetration varies with the number of cycles in the present load control mode; this affects the pin-pointing of strain for failure life determination, though the drop in displacement serves as a useful indicator for failure. In case of displacement controlled fatigue, the drop in load would hopefully serve as an indicator of failure.

4. Conclusions

This paper presented the results of an experimental study of cyclic ball indentation on base metal, weld region of two structural stainless steel materials: SS 304 L(N) and SS 316 L(N). From the experiments conducted at various load levels, it has been established that a typical plastic strain versus failure life data can be constructed; further, the distinction in failure life response between base metal and weld region can be clearly seen. The presence of secondary cracking as observed through SEM studies could correlate with failure tell-tale evidences from load-depth of penetration.

References

1. Manahan, M.P.; Williams, J.; Mariakanitz, R.P., *ASTM STP1204*, ASTM International, West Conshohocken, PA, 1993, pp. 62–76.
2. Nunomura, S.; Nishijima, T.; Higo, Y.; Hishinuma, A., *ASTM STP 1204*, 1993, pp 256–266.
3. Jitsukawa, S.; Kizaki, M.; Umino, A.; Shiba, K.; Hishinuma, A., *ASTM STP 1204*, ASTM International, West Conshohocken, PA, 1993, pp. 289–307.
4. Garner, F.A.; Hamilton, M.L.; Helnisch, H.L.; Kumar, A.S., *ASTM STP 1204*, ASTM International, West Conshohocken, PA, 1993, pp. 336–355.
5. Kryukov, A.M.; Sokolov, M.A.; *ASTM STP 1204*, 1993, pp. 417–423.
6. Rosinski, S.T.; Kumar, A.S.; Cannon, S.; Hamilton, M.L., *ASTM STP 1204*, International, West Conshohocken, PA, 1993, pp. 405–416.
7. Alexander, D. J., *ASTM STP 1204*, ASTM International, West Conshohocken, PA, 1993, pp. 130–142.
8. Tomimatsu, M.; Kuwaguchi, S.; Iida, M., *ASTM STP 1329*, ASTM International, West Conshohocken, PA, 1998, pp. 470–483.
9. Hirose, T.; Tanigawa, H.; Ando, M.; Suzuki, T.; Kohyama, A.; Katoh, Y.; Narui, M., *ASTM STP 1418*, ASTM International, West Conshohocken, PA, 2002, pp. 181–194.
10. Murase, Y.; Nagakawa, J.; Yammamoto, N., *ASTM STP 1418*, ASTM International, West Conshohocken, PA, 2002, pp. 211–220.
11. Li, M.; Stubbins, J.F., *ASTM STP 1418*, ASTM International, West Conshohocken, PA, 2002, pp. 321–335.
12. Haggag, F.M.; Server, W.L.; Lucas, G.E.; Odette, G.R.; Sheckherd, J.W., *J. Test. Eval.*, Vol. 1, No. 1, 1990, pp. 62–69.
13. Haggag, F.M.; Wang, J.A.; Sokolov, M.A.; Murty, K. L., *Non-Traditional Methods of Sensing Stress, Strain and Damage in Materials and Structures, ASTM STP 1318*, G. Lucas and D. Stubbs, Eds. ASTM International, West Conshohocken, PA, 1997, pp. 85–98.
14. Olurin, O.B.; Fleck, N.A.; Ashby, M. F., *Scr. Metall.*, Vol. 43, 2000, pp. 983–989.

Fatigue strength assessment of SUS316 by small bulge fatigue (SBF) test

S. Komazaki [1],*, R. Jojima [1], N. Muraoka [2], S. Nogami [3] , M. Kamaya [4] , C. Hisaka [2] , M. Fujiwara [2] and A. Nitta [2]

[1] Kagoshima University
[2] Kobe Material Testing Laboratory Co., Ltd.
[3] Tohoku University
[4] Institute of Nuclear Safety System, Incorporated
* Correspondence: komazaki@mech.kagoshima-u.ac.jp; Tel.: +81-99-285-8245

Abstract: A new fatigue test apparatus with a small disk-type specimen (8 mm in diameter) was developed in the authors' group. This testing technique was termed "Small Bulge Fatigue (SBF) test". Unlike the small punch (SP) test, a hydraulic bulging method was adopted for avoiding problems attributable to the contact or the friction between ball and specimen. A cyclic oil pressure could be alternatively applied to both specimen surfaces at the frequency of 10 Hz. The specimen thickness of central region (gauge area) was relatively reduced to avoid cracking at the edge of specimen, and the characteristic small disk-type specimen with flat and concave surfaces was proposed considering machinability and handleability. Austenitic stainless steel SUS316 was subjected to the preliminary test using this newly developed testing technique. The obtained results indicated that this SBF test had a potential for fatigue strength assessment.

Keywords: small sample testing technique; small punch test; fatigue; hydraulic bulging method

1. Introduction

The unplanned outage in fossil power plants is caused by various types of damage or materials degradation such as a fatigue, creep, erosion/corrosion, oxidation, wear, etc. [1-4]. The low cycle fatigue is the most critical issue in high temperature components. As can be clearly seen in Figure 1, the fatigue damage causes almost one third of the outages in the industrial boiler, gas turbine and industrial steam turbine, respectively. In the case of commercial boiler, sixty percent is attributable to this fatigue damage. Therefore, it is very important to evaluate the change in fatigue property of in-service components with higher accuracy for maintaining their integrity for a long period of time and preventing their premature failure.
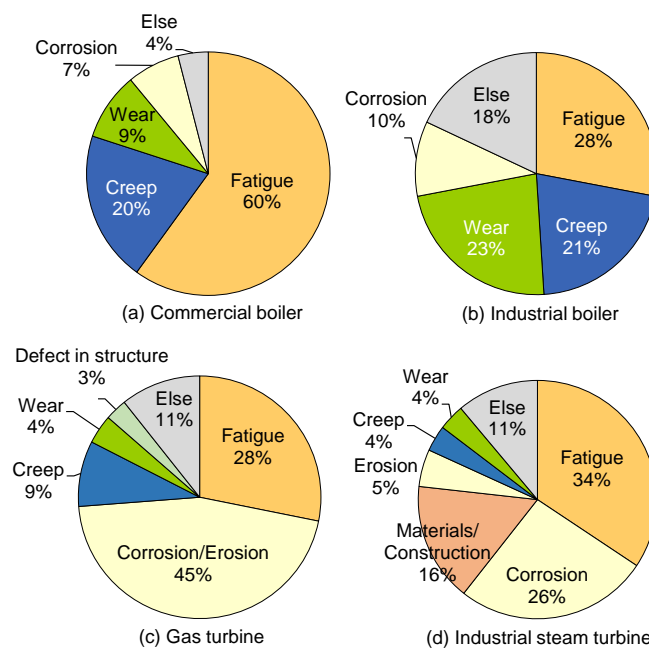

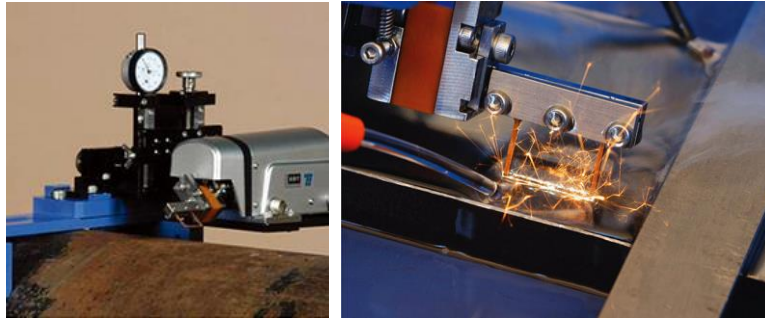**Figure 1**. Causes of unplanned outage in fossil power plants.

Figure 2. On-site electric discharge sampling equipment with copying mechanism.

In the late 1970s and early 1980s, the small punch (SP) testing technique using a miniaturized disk-type specimen was developed for determining post-irradiation mechanical properties. This technique has been widely used for evaluating various material properties, such as tensile property, ductile-brittle transition behavior, fracture toughness, hydrogen embrittlement, and stress corrosion cracking. It has also been successfully employed in evaluating high temperature creep property. This SP creep test is expected as a strong tool for assessing the heat-to-heat variation of in-service USC boiler pipings, because it requires only a small amount of sample [5]. This can minimize the damage caused by removing the sample from the components. In recent years, a novel on-site electric discharge sampling equipment with copying mechanism has been also developed for this purpose (Figure 2 [6]). This equipment is capable of taking a small plate-type sample as thin as 1 mm from the component's surface.

If the SP testing technique was made applicable to fatigue strength assessment also, almost all material strength tests could be conducted using the same or similar small disk-type specimen. This would be very beneficial from practical and engineering viewpoints. Under those things as background, the authors' group have developed a new fatigue testing technique with a small disk-type specimen, namely, "Small Bulge Fatigue (SBF) Test" [7]. In this SBF test, a hydraulic bulging method is adopted for avoiding several problems attributable to the contact or the friction between ball and specimen. Some results obtained from the preliminary tests using austenitic stainless steel SUS316 are briefly reported in this paper.

2. Testing Vessel and Specimen Developed for SBF Test

Figure 3 shows the testing vessel, which has been newly manufactured for the SBF test. The vessel is connected to the existing hydraulic servo-type material testing machine. As illustrated in Figure 4, the vessel consists of two hydraulic chambers, and the pressure gauge is connected to each chamber. A connector for drawing a lead wire of strain gauge is attached to one of the chambers (chamber 1), and a space for setting dummy strain gauge is also prepared in that chamber. A quartz glass window is installed in the other chamber (chamber 2) for the measurement of displacement with a laser sensor and the direct observation of specimen surface with a borescope. A small disk-type specimen is placed between those two chambers using gaskets and clamping screws, and a cyclic oil pressure is alternatively applied to both chambers.
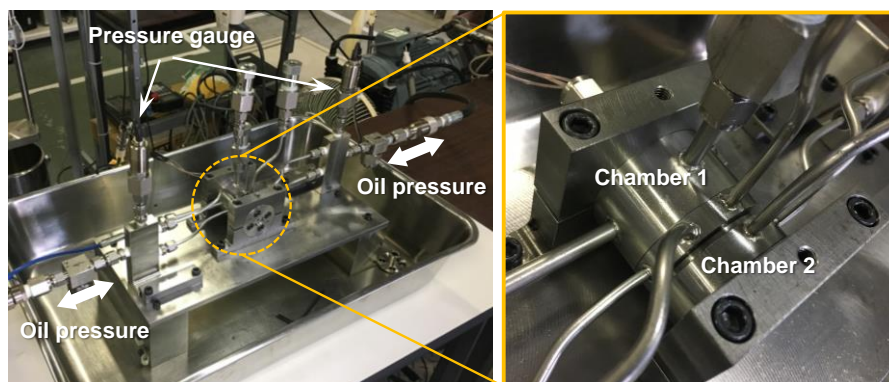

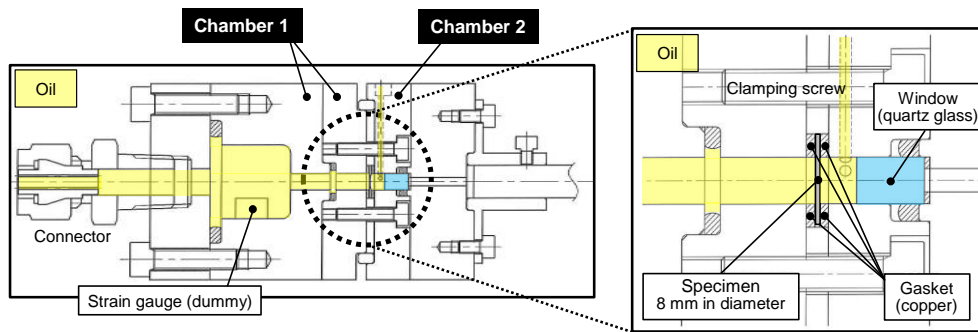**Figure 3**. Testing vessel newly manufactured for SBF test.

Figure 4. Testing vessel consisting of two hydraulic chambers.

It was revealed from the finite element analysis (FEA) that the equivalent strain was concentrated at the edge of unclamped area when the conventional SP specimen (8 mm in diameter, 0.5 mm in thickness) was subjected to the test, as shown in Figure 5. Therefore, the thickness of central region was relatively reduced for avoiding the fracture at around edge of unclamped area. Finally, as shown in Figure 6, the shape and dimension of small disk-type specimen with flat and concave surfaces were determined as follows; diameter of gauge area: 1.6 mm, thickness of gauge area: 0.15 mm, length of clamped area: 2 mm, thickness of clamped area: 0.4 mm, radius of fillet: 3 mm. This SBF specimen was placed in the testing vessel so that the concave side faced the quartz glass window.

3. SBF Test Results of SUS316

The material used in this study was austenitic stainless steel SUS316. The chemical composition is given in Table 1. The on-off pressure-controlled tests were conducted at room temperature and under several different
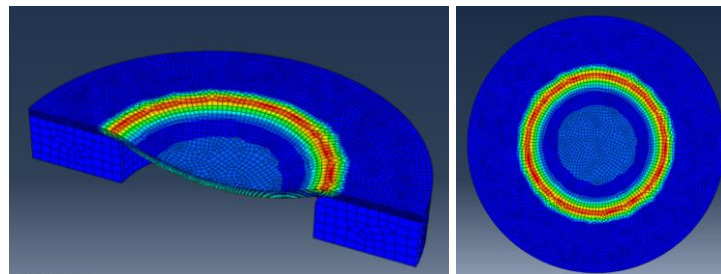

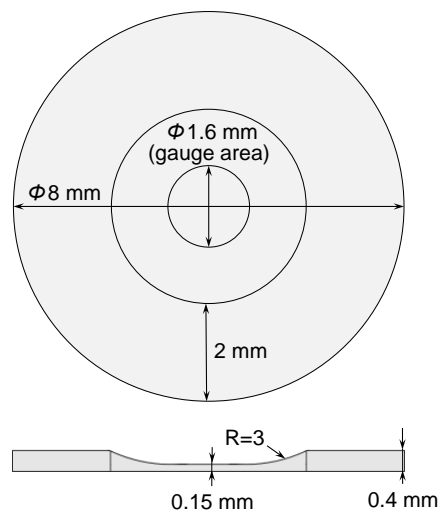**Figure 5**. Strain distribution of SP test specimen subjected to SBF tests.

Figure 6. Small disk-type specimen with flat and concave surfaces for SBF test.

Table 1. Chemical composition of SUS316 (mass%).

| Fe	C	Si	Mn	P	S	Ni	Cr	Mo
Bal.	0.05	0.41	0.84	0.026	<0.001	10.20	16.10	2.11

Table 2. Maximum pressure, equivalent strain, strain range and fatigue life [7].

Pressure, MPa	$\pm\varepsilon$, %	$\Delta\varepsilon$, %	N_f, cycles
10.5	0.26	0.52	21100
	-0.26		
12.0	0.36	0.75	46100
	-0.39		
12.5	0.42	0.90	7600
	-0.48		
13.2	0.52	1.20	3500
	-0.67		
13.5	0.58	1.37	6300
	-0.79		

maximum pressure levels (10.5, 12.0, 12.5, 13.2, 13.5 MPa) using the above-mentioned testing vessel and specimen. The oil pressure was alternatively applied to the flat and concave sides at the frequency of 5 or 10 Hz. The FEA was carried out for determining the strain on specimen surface. As a result, it was revealed that the strain state was a complete equi-biaxial ($\varepsilon_r/\varepsilon_\theta$=1) at the center of specimen, and the strain ratio deceased with increasing distance from the center. The equivalent strain and strain range on the specimen center of flat side are summarized in Table 2.

Figure 7 shows the change in oil pressure in two hydraulic chambers at the maximum pressure of 13.5 MPa and the frequency of 5 Hz. It can be clearly seen that the pressure is alternatively applied to the concave and flat sides. But, the pressure wave shape is slightly different between them. This difference is likely to result from the different shape of specimen surface. It has been also confirmed that the oil pressure could be successfully applied to both chambers even when the frequency was increased up to 10 Hz.

The SBF test was periodically interrupted to investigate the initiation and propagation behaviors of surface crack. Figure 8 shows examples of surface cracks observed on the specimen tested at the maximum pressure of 12.5 MPa. Some small cracks were initiated at around the center of gauge area on the flat side after 2000 cycle. But, there was no crack on the concave side at that time. When the number of cycles was 3000, the cracks of flat side were longer and some cracks pierced through the specimen into the concave side. The oil pressure of chambers was abruptly decreased and the test was automatically stopped, when the number of cycles reached 7600. The SEM
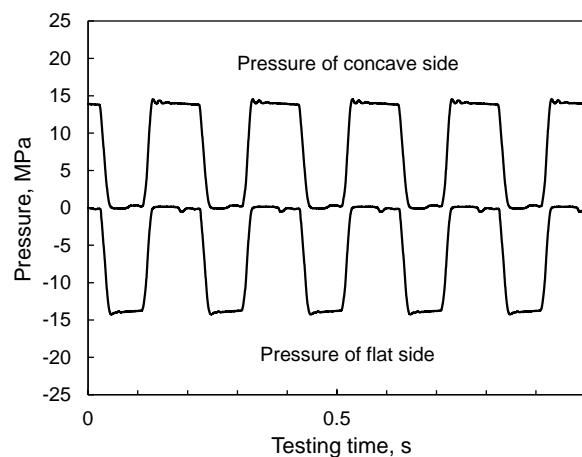
Figure 7. Changes in oil pressure in two hydraulic chambers during SBF test.
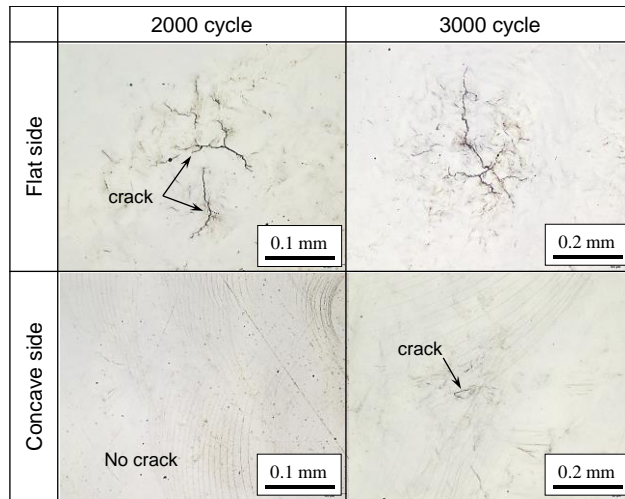
Figure 8. Examples of surface cracks observed on specimen tested at 12.5 MPa.
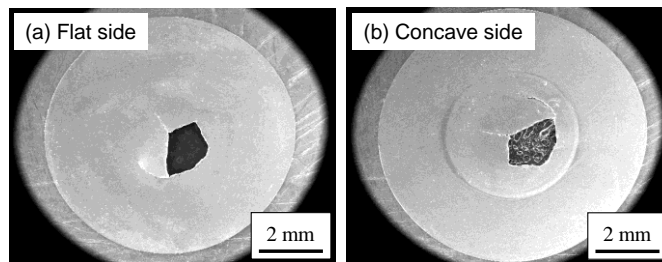

Figure 9. SEM micrographs of SBF specimen fractured at 12.5 MPa.

observation revealed that a part of gauge area was broken and dropped out after that number of cycles (Figure 9). The specimen always had a chip in the gauge area (1.6 mm in diameter, 0.15 mm in thickness) after the sudden drop in oil pressure, irrespective of test conditions.

The fatigue test results obtained in this preliminary study is given in Figure 10, where the fatigue life is plotted against the equivalent strain range determined by FEA. In this paper, the fatigue life is defined as the number of cycles to the drop in pressure due to fracture. The fatigue lives measured at five different maximum pressures are given in Table 2, along with the equivalent strain range. The fatigue life as a whole has a tendency to increase with decreasing strain range, although some scattering results can be seen. This result may indicate that the present SBF test has a potential for fatigue property assessment. In the presentation, the correlation between the results of the
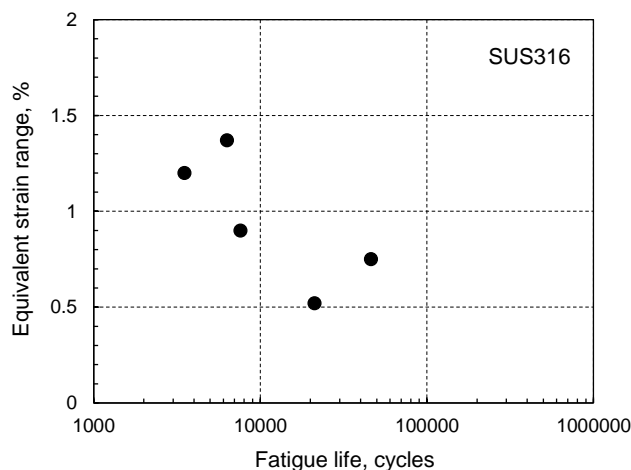

Figure 10. Fatigue life plotted as a function of equivalent strain range.

SBF test and the conventional uniaxial and plate bending fatigue tests will be introduced in addition to the results of strain and displacement measurements.

4. Summary

A new fatigue test apparatus with a small disk-type specimen was newly developed in the authors' group. This testing technique was termed "Small Bulge Fatigue (SBF) test". A cyclic oil pressure could be alternatively applied to both specimen surfaces at the frequency of 10 Hz by adopting hydraulic bulging method. The shape and dimension of small disk-type specimen with flat and concave surfaces were finally determined as follows; diameter of gauge area: 1.6 mm, thickness of gauge area: 0.15 mm, length of clamped area: 2 mm, thickness of clamped area: 0.4 mm, radius of fillet: 3 mm. Austenitic stainless steel SUS316 was subjected to the preliminary test using this newly developed testing technique. As a result, the initial cracking occurred at around the center of gauge area on the flat side, and the specimen always had a chip in the gauge area after the sudden drop in oil pressure irrespective of test conditions. In addition, the fatigue life as a whole had a tendency to increase with decreasing strain range, although some scattering results could be seen.

References

1. Thermal and Nuclear Power Engineering Society, "Guideline for Extending the Periodical Inspection Interval of Power Boilers", p. 1(1999) (in Japanese).
2. EPRI Report, "Combustion Turbine Materials Problems", EPRI AP-4475 (1986).
3. Thermal Power Research Working Group of Middle Japan Utilities Technical Committee, "Report of Maintenance Technology for Turbine Components in Thermal Power Stations", p. 38(1991) (in Japanese).
4. Yamanouchi, H.; Nakamura, M. and Setoguchi, K. "Life of Component and Its Materials: Boiler and Turbine", Journal of "The Thermal and Nuclear Power", Vol. 34, No. 10, pp. 1169-1185 (1983) (in Japanese).
5. Komazaki, S.; Obata, K.; Tomobe, M.; Yaguchi, M. and Kumada, A. "SP Creep Properties of Gr.91 Boiler Pipings Service-Exposed in Different USC Power Plants", SSTT2018, to be presented.
6. Okamoto, K.; Kitagawa, H.; Kusumoto, J.; Kanaya A. and Kobayashi, T. "Development of Electric Discharge Equipment for Small Specimen Sampling", International Journal of Pressure Vessels and Piping, Vol. 86, pp. 633-636 (2009).
7. Komazaki, S.; Jojima, R.; Muraoka, N.; Nogami, S.; Kamaya, M.; Hisaka, C.; Fujiwara M. and Nitta, A. "Development of Small Bulge Fatigue Testing Technique Using Small Disk-Type Specimen", International Journal of Fatigue, to be submitted.

Post-test impression creep evaluation methods and findings for improved code of practice

A. Bridges [1,*], D. Purdy [1]

[1] Electric Power Research Institute, 1300 W. W.T Harris Blvd, Charlotte, NC 28262 USA

* Correspondence: abridges@epri.com; Tel.: +1-704-595-2950

Abstract: The impression creep test is a small sample testing technique that has been used mostly for qualitative assessments intended for risk ranking of in-service components. Electric Power Research Institute (EPRI) has conducted testing to determine the limitations of the test method. This involved extensive analytical and physical posttest assessments that have led to recommendations to improve the current code of practice. Analytical assessments for determination of minimum strain rates suggest that having a standard procedure would be very beneficial to the testing community. Physical assessments that involve indentation depth measurements, hardness mapping and grain structure evaluations have provided methods for determining the affected area of deformation under the indentation surface. These methods may help in validating and revising current FEA models. Additional FEA modeling may also help answer further questions regarding applicable indentation range and appropriate testing conditions (stresses and temperatures). EPRI will continue to conduct impression creep testing to further evaluate the limitations of the test method and address questions from the work discussed in this paper.

Keywords: Impression creep, small sample testing, code of practice, hardness, FEA

1. Introduction

Coal-fired steam generation plants are reaching ages over 50+ years and are still operating with original materials that are well beyond their initial design life. This has led to an increase in the use of small sample testing at elevated temperatures for evaluations of in-service material. The impression creep (IC) test method uses minimal material and is considered a 'non-invasive' technique. Traditional creep testing methods (uni-axial creep) use a much larger volume of material, about 100-200 times more than impression creep and is considered a 'destructive' technique that generally requires weld repair or replacement of the extracted volume of material. The main steam (MS) and hot reheat (HRH) steam piping segments are typically evaluated using both methods. Scoop sampling can be used to extract material from the MS and HRH piping segments and impression creep specimens can be cut from the corresponding scoop samples [1].

Impression creep tests typically run until a 'steady state' creep rate is obtained and held for 100 hours. This usually leads to a total testing time of 300-500 hours depending on the material and testing conditions used. The test is also used for performing both stepped loads (isothermal) and stepped temperature (isostress) tests. The current code of practice does not address how long a test should be ran or the requirements for isothermal and isostress testing. This paper will address some of these concerns through an assessment of recent impression creep tests and posttest evaluations.

Posttest evaluations can be performed on impression creep samples for alignment checks, indentation depth measurements and evaluation of changes in grain orientation under the indentation deformation zone. Specimens can be cut in half perpendicular to the indent to examine the microstructure beneath the indent. A review of posttest evaluation methods and analytical findings has provided valuable information that can be used to revise a more rigorous code of practice for impression creep testing.

2. Materials and Methods

2.1. Standard Method Sample Preperation and Testing

The impression creep test uses a 1mm x 10mm rectangular indenter (a) to form an impression on a rectangular 10mm x 10mm x 2.5mm sample (b), as shown in Figure 1. The use of the rectangular indenter has lower localized deformation constraints than circular indenters [2] and has been adopted as the standard choice of indenter in the current code of practice. Finite element analysis work by Hyde et. al. [3] has led to the standard geometries currently adopted by the ECCC code of practice [4] which includes smaller specimens as well. A reference stress approach

has been used to convert stress relationships from traditional uniaxial testing to testing stresses used in impression creep testing [2]. It is also important to note that this approach is based solely upon sample geometry and has shown to be material independent based on published research of CrMoV, stainless steels, 9Cr steels, 2.25Cr1Mo steels and a variety of filler weld metals [5-9].
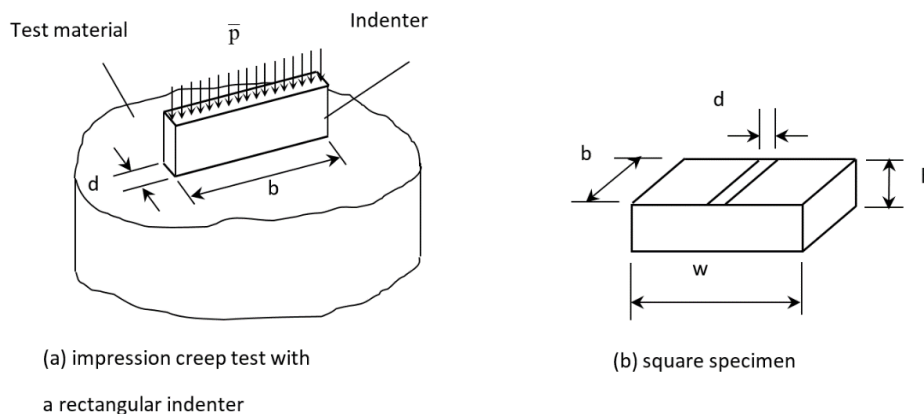

(a) impression creep test with

a rectangular indenter

(b) square specimen

Figure 1. Standard Impression Creep Indenter and Test Specimen.

Samples are typically cut to ~2.55-2.60 mm thickness using electric discharge machining (EDM) before being grounded to a final thickness of 2.50 ± 0.02 mm, finishing 600 grit sandpaper. Electric Power Research Institute (EPRI) is currently using a Tinius Olsen twin-screw servo-mechanical (H25KS) loading frame with a high temperature ceramic shell furnace using kanthal windings. A software program has been specifically designed for controlling a static load with a signal input for linear variable differential transformers (LVDTs) to measure strain accumulation during the entire duration of the test. The independent three zone furnace uses type N thermocouples for control of temperature, but the sample temperature is measured with an external data acquisition system using three type K thermocouples. A high strength nickel based superalloy (Waspaloy) was chosen as the material indenter, as it has a much higher creep strength than that of the materials being tested and negligibly contributes to measured strain. These specifications are outlined in the current code of practice [4].

2.2. Metallographic Preperation for Posttest Evaluations

EPRI has conducted posttest evaluations of impression creep specimens for further examination of each test. This, along with more rigorous data analysis, has led to further questioning to the limitations of impression creep testing and recommended revisions to the current code of practice. Posttest evaluations include measuring the indentation profile in three dimensions using a confocal laser microscope (Keyence VK-X105), hardness testing of cross sections perpendicular to indent surface using a Vickers automated hardness tester (LECO AMH43), and evaluations of microstructure.

After testing, specimens are cut in half perpendicularly to the indentation surface. These are mounted and polished using standard metallographic techniques. Figure 2 shows the how the cross section cut is taken and mounted in a clear epoxy hot mount in preparation for physical posttest evaluation methods.
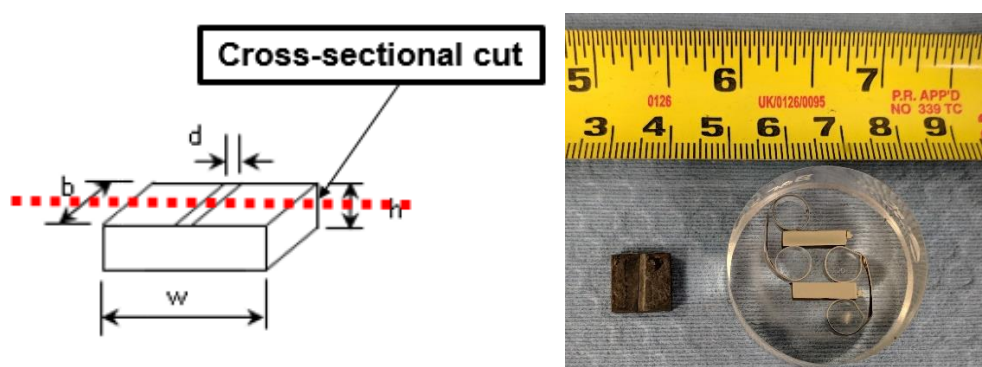

Figure 2. Preparation of Impression Creep Sample for Posttest Metallurgical Evaluation.

2.2. Standard Stress Conversions and Typical Impression Creep Curves

In the EPRI setup, the accumulated strain in an impression creep test is continuously captured by two water cooled LVDTs. The extensometry consists of upper and lower legs that are held between ridges on the upper and bottom half of the indenter. The legs move with the indenter during the test and translate movement to the LVDTs. Initial strain rates are high that quickly diminish to a somewhat constant rate. There is typically no acceleration regime after constant rates have been established, as the test is loaded with a compressive force and does not experience a change in the cross-sectional load-bearing area. The reference stress used to convert the mean pressure under the indenter (p) to a corresponding uniaxial stress (σ) is represented by:

$$\sigma = \eta p \tag{1}$$

The impression indentation displacement (Δ^c) is also converted to a uniaxial creep strain (ε^c) using:

$$\varepsilon^c = \frac{\Delta^c}{\beta d} \tag{2}$$

The reference parameters can then be represented by η and β, which are conversion factors, and d is the width of the rectangular indenter. To determine reference parameters using finite element analysis, Norton's creep power law is used [6]:

$$\dot{\varepsilon}^c = A\sigma^n \tag{3}$$

The reference stress approach allows impression creep testing to be used as an alternative to uniaxial creep testing when only a limited amount of material may be available for testing. Typical impression creep strain and strain-rate curves are shown in Figure 3.
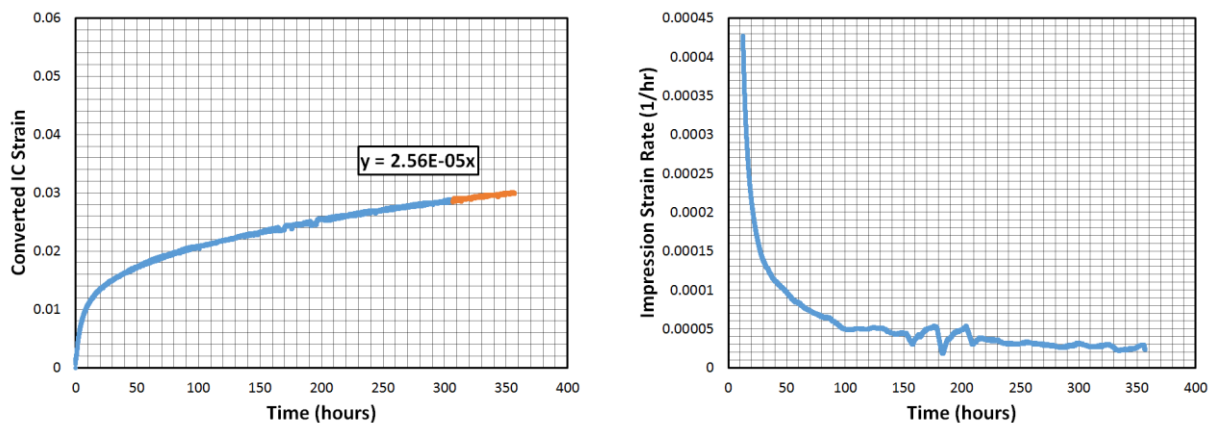

Figure 3. Typical Impression Creep Strain and Strain Rate Curves (Service Exposed Grade 22 Tested at 570°C and 80 MPa.

3. Results

3.1. Impression Creep Results

A Grade 91 sample was tested at 100 MPa and 625°C for about 475 hours. These strain and strain rate curves are shown in Figure 4. The strain rates were calculated using ±12.5-hours, ±25-hours, and ±50-hour increments, respectively. A ±50-hour increment that occurs 50 hours before the test terminates would be equivalent to the average rate in the last 100 hours of testing.
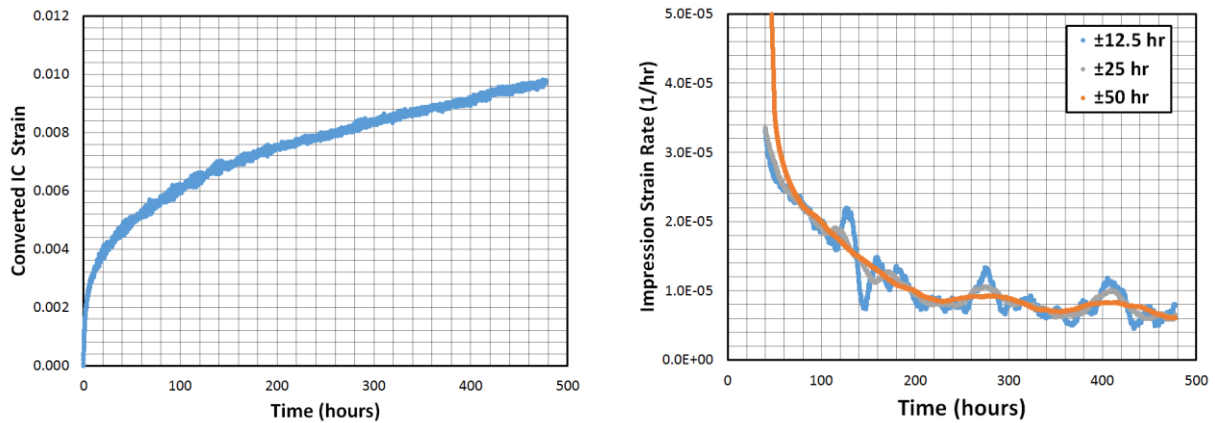
Figure 4. Impression Strain Curve and Strain-Rate Curves (using different averaging increments) for a Tempered Martensitic Grade 91 Steel Tested at 100 MPa and 625°C.

Another set of tests for tempered martensitic Grade 91 steel were tested at 625°C for tests of 80 and 100 MPa. Duplicate tests were conducted for each stress with strain and strain rate plots shown in Figure 5. The strain rates were calculated using ±50-hour increments.
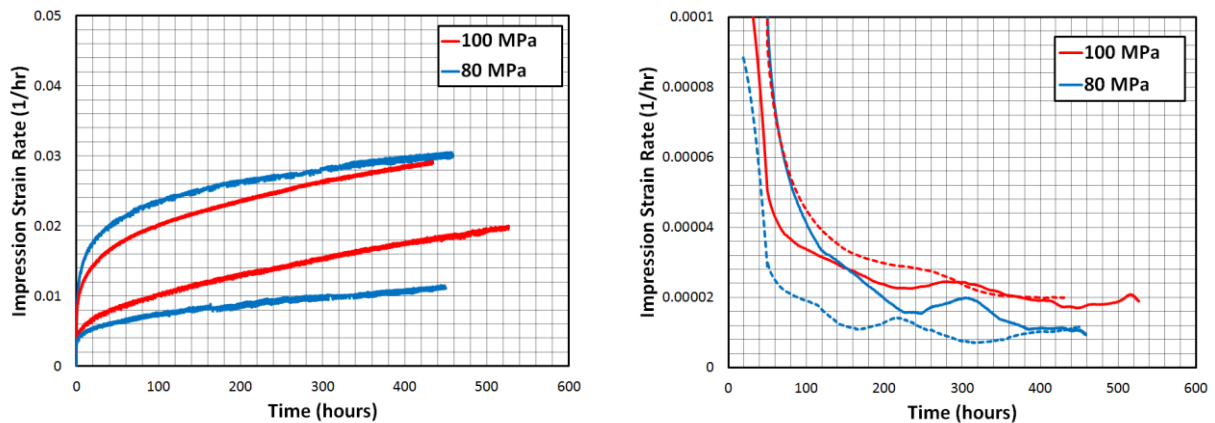

Figure 5. Comparison of Impression Strain Curve and Strain-Rate Curves for Grade 91 Samples at 625°C and both 80 and 100 MPa.

The final set of impression creep tests were conducted on a low alloy service exposed Grade 22 material. The testing was conducted at the base metal, weld metal and heat-affected zone from an extracted plug sample in the hot reheat piping section of a fossil power plant. Impression creep tests were ran for 300 to 350 hours at sample testing conditions of 80 MPa and 570°C. Accumulated strain and strain rate plots for all three tests are shown in Figure 6. The strain rates were calculated using ±50-hour increments.
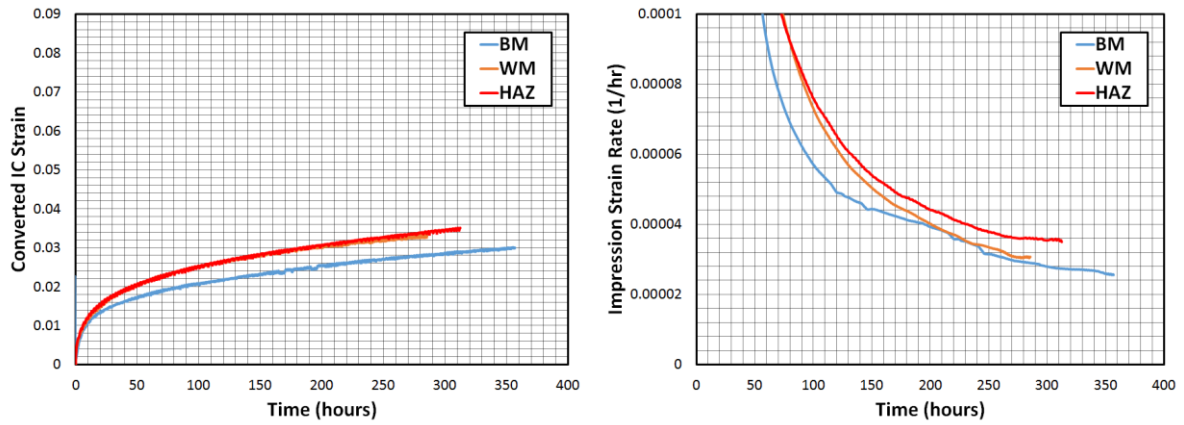
Figure 6. Comparison of Impression Strain Curve and Strain-Rate Curves for Ex-service Grade 22 Weld using ±50 hour increments (80 MPa and 570°C for each test).

3.2. Posttest Evaluation Results

After each impression creep test, measurements of the indent are made using the confocal laser microscope. Results can be compared to measurements from data files produced by the universal testing machine. Figure 7 shows the laser image with typical measurements and a depth measurement calculation using built in analysis software

Figure 7. Impression Creep Laser Scan with 150µm Depth Measurement.

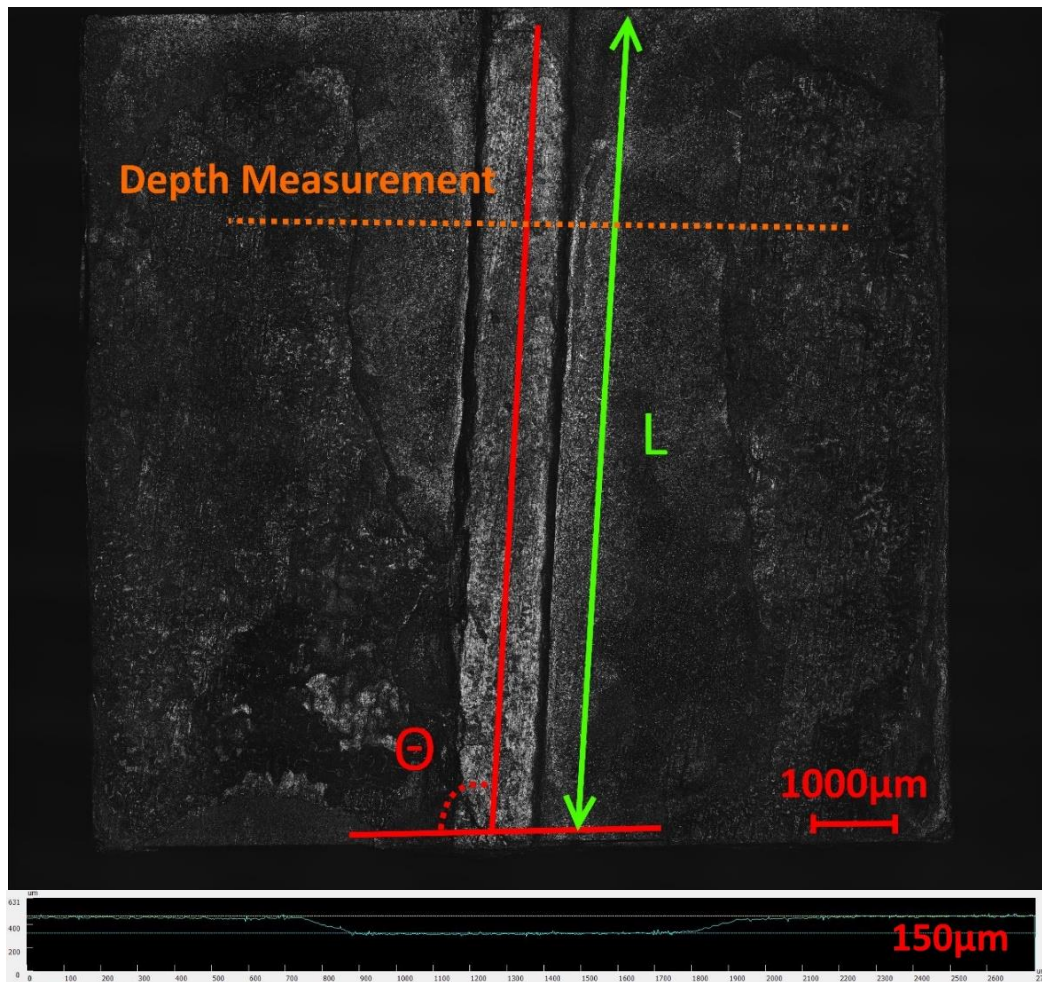Indent measurements can also be measured after the sample has been cut in half perpendicular to the indent, mounted and polished. Results have shown to be the same as measurements taken using the first method shown in Figure 7. Though, it is interesting to note that the measured indentation from the data file was 174µm. This measurement was taken at the end of the test, which was still at testing load and temperature. It seems reasonable that there was some elastic recovery (26µm) after unloading. Polished samples can also be used for hardness testing and etching for evaluation of microstructure and elongation of grains along the stress field. Figure 8 shows a hardness plot of a tempered martensitic grade 91 material that was tested to a 31µm indentation depth. It clearly shows a strain softening effect beneath the indentation (center of the sample), which is a known effect in uni-axial testing of the same material. The hardness plot was created using a 0.2 kg load with 100 µm spacing.
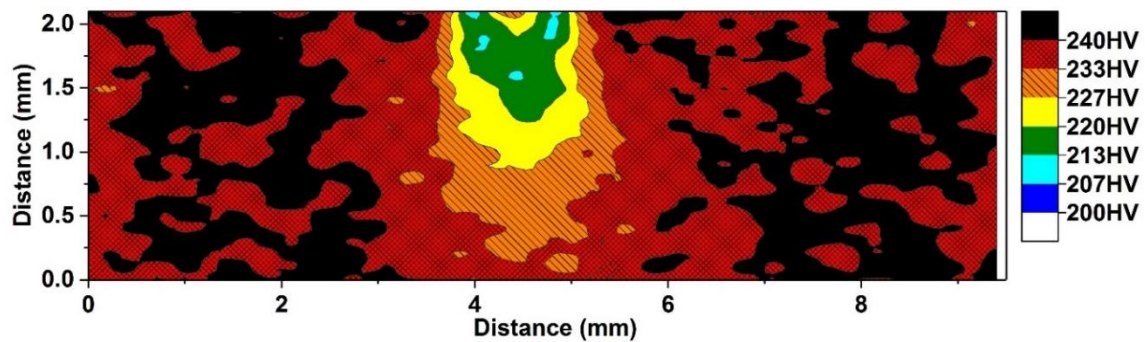
Figure 8. Hardness Plot of a Cross Section through an Impression Creep Sample of Tempered Martensitic Grade 91 Tested at a Temperature of 625°C and Stress of 100MPa; Overall Indentation Depth is 31 µm.

An example for an ex-service grade 22 seam weld is shown in Figure 9. The change in elongation of grains beneath the indent can been seen in the micrograph predominantly around the edges of the indentation. These results help visualize the effected stress field that is developed underneath the indent. The implications of these results are discussed in the next section.

Figure 9. Microstructure of Ex-service Grade 22 Posttest Impression Creep Specimen showing Elongation of Grain Structure beneath the Indenter.

4. Discussion

4.1. Proposal to add Calculation of Minimum Creep Rates in Code of Practice

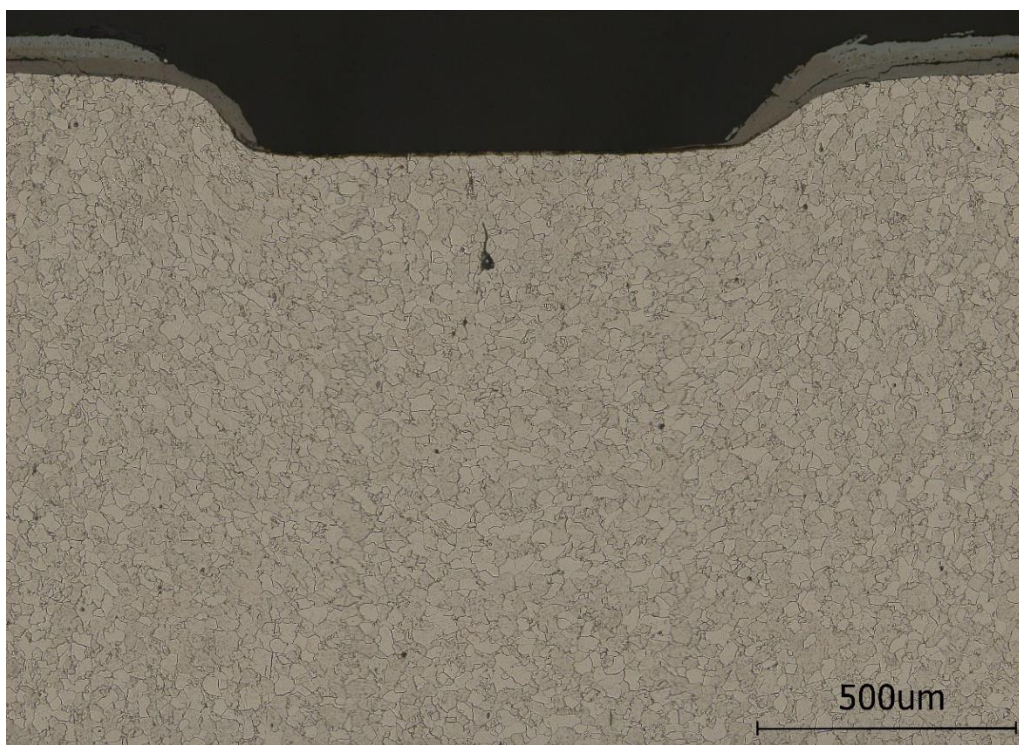The current code of practice does not address how long impression creep tests should be ran, as failure does not occur in this testing method and defining a minimum strain rate may seem arbitrary. There are many different analytical methods that can be used to determine the 'minimum creep rate'. Proposing set guidelines may help alleviate any discrepancy between different labs. Currently, without any standard, it is possible that large variations in reported creep rates between different testing labs may be due to the length of testing time and analytical method used for calculation of minimum rates. Above, in Figure 4, strain-rates were reported using ±12.5-hours, ±25-hours, and ±50-hour averaging increments. It has been clearly shown that a smooth strain rate vs. time plot can be accomplished using longer averaging increments, such as ±50-hour increments. This also allows for more data to be used in the calculating the minimum creep rate. It essentially states that a 100-hour increment of strain values is used for calculating the minimum creep rate. In addition to this, the percent variation during the test is calculated to ensure adequate testing time to reach steady state creep. This is further explained in the proposed guidelines, below. It is also evident that the time needed to reach a steady state rate can be dependent on the material (Grade 22 > Grade 91), and that some materials have shown more fluctuations than others (Grade 91 > Grade 22), as shown in Figure 5. The potential material effects on strain rate due to loading and temperature changes are not discussed in this paper, but another in these conference proceedings [7].

The following guidelines are proposed for addendum to the current code of practice:
1. Impression Creep tests should be tested to a minimum of 300 hours, regardless of testing conditions and material
2. Strain-rates should be calculated using ±50-hour time increments
   a. It is acceptable to use only the last 50 hours for the final time stamp – if percent variation requirements are also met
   b. Strain-rates should be analyzed before termination of any test to determine if recommended criteria have been met, ex. >300 hours, within 10% variation
3. The very lowest value from the strain-rate vs. time curve (using ±50-hour time increments) should be used when reported 'minimum creep rate'
   a. This may not always be at the very end of a test, ex. Grade 91 in Figure 10
   b. The time-point where MCR is determined should *always* be reported
4. Percent variation should be calculated using ±10-hour time increments from the already calculated strain-rate vs. time curve, using the following equation:

$$\% \; Variation = \frac{(V_1 - V_{2)}}{\frac{(V_1 + V_2)}{2}} \, x \; 100 \tag{1}$$
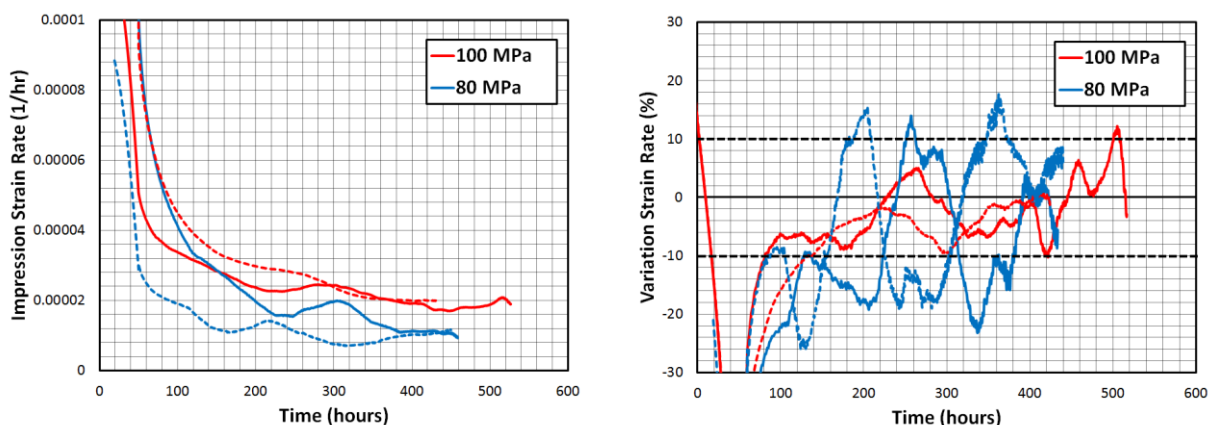

Figure 10. Example for Measurement of Minimum Strain-Rate and Percent Variation for Grade 91
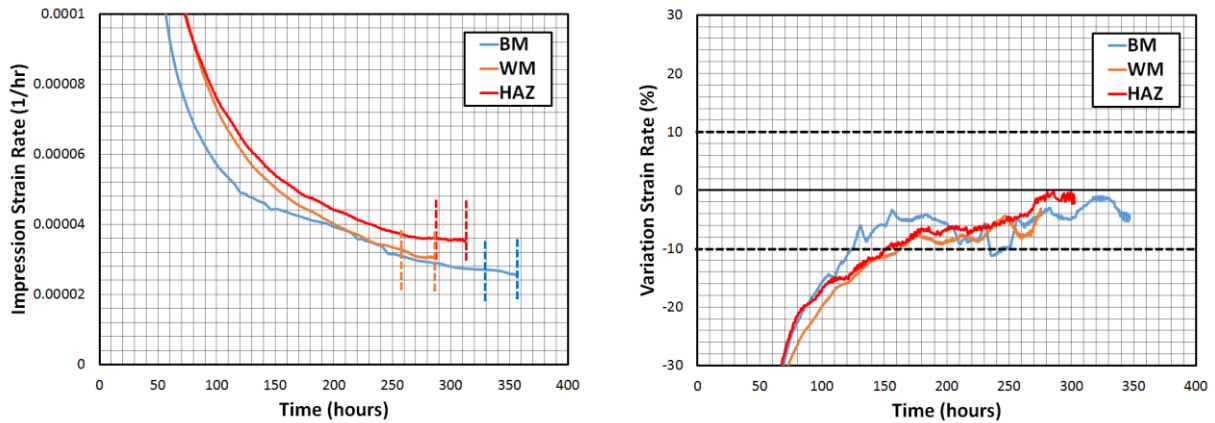
Figure 11. Example for Measurement of Minimum Strain-Rate and Percent Variation for Grade 22

The following comments are justification for recommended parameters in guidelines above:

1. It has been observed in some tests that significant fluctuations in strain-rates can occur up until and even after 300 hours of testing, even when using ±50-hour time increments for calculation of strain rate. Fluctuations appear to be less severe beyond 300 hours. The percent variations in Figure 9 and 10 were calculated using ±10-hour increments from the strain-rate vs time curve. It shows that the percent variations fluctuate more in the Grade 91 tests compared to the Grade 22 test. This question further explored in reference [7].

2. A minimum variation of 10% between ±10-hour increments from the strain-rate vs. time curve is a proposed guideline to provide ***consistency between labs***. 10% variation in strain-rates appears to be a reasonable target with limited test results. This number ***may change*** with additional results over time. In uni-axial testing there is usually a clear minimum before tertiary creep is reached, but there is no agreed upon standard that explains how to properly measure the creep rate. An exact number can be difficult to calculate due to the lack of knowledge of material effects during compressive loading and limited data to evaluate. This number should be re-considered as additional data is gathered and analyzed.

3. It is important to reiterate that the main purpose of these guidelines is to provide ***consistency*** between the different labs. Different individuals are currently using a variety of approaches to measure the minimum creep rate and open collaboration to set agreed upon guidelines is vital for further development of the testing technique.

4. Good engineering judgement should always be practiced when conducting impression creep tests. Any irregular findings and observations should be reported accordingly.

4.2. Considerations if Impression Creep is used as Quantative Assessment (IC-rates in lieu of uni-axial rates)

Uni-axial creep tests were also performed at 80 and 100MPa using a 625°C testing temperature for the same temper of Grade 91 shown in Figure 5. A comparison of results is shown in Table 2. [8]

Table 2. Comparison of Uniaxial Impression Creep Minimum Creep Rates for a Temper of Grade 91

Test Method	Testing Stress (MPa)	Measured Minimum Creep Rate (1/hr)	Time at Measured Minimum Creep Rate (hours)
Uniaxial	80	3.15×10^{-6}	-
Impression Creep	80	9.29×10^{-6}	456
Impression Creep	80	7.16×10^{-6}	320
Uniaxial	100	5.41×10^{-5}	-
Impression Creep	100	1.71×10^{-5}	445
Impression Creep	100	1.98×10^{-5}	434

The test results show that the duplicate impression creep rates were consistent (within 15-20%), but a factor of 2.5 to 3.5 greater than the corresponding uniaxial creep rates. In the uniaxial test, the creep rate at 100MPa was approximately 17 times greater than at 80 MPa. Comparison of impression creep tests from 100MPa to 80 MPa only show a factor of 1.5 to 2.5 times greater. If the impression creep test is to be used in as a direct relationship, these questions should be addressed and answered. The current conversion factors determined from FEA analysis [2] used to determine the converted IC strain rates may need to be revisited. There has also been work on an alternative approach to relating impression minimum creep rates to uniaxial rupture lives. Where it has been common to use traditional Monkman-Grant (MG) relationships in impression creep evaluations, Brett has proposed an Impression Monkman-Grant (Imp-MG) relationship [9]. A comparison of the relationships with actual data (from Table 2) is shown in Figure 12.
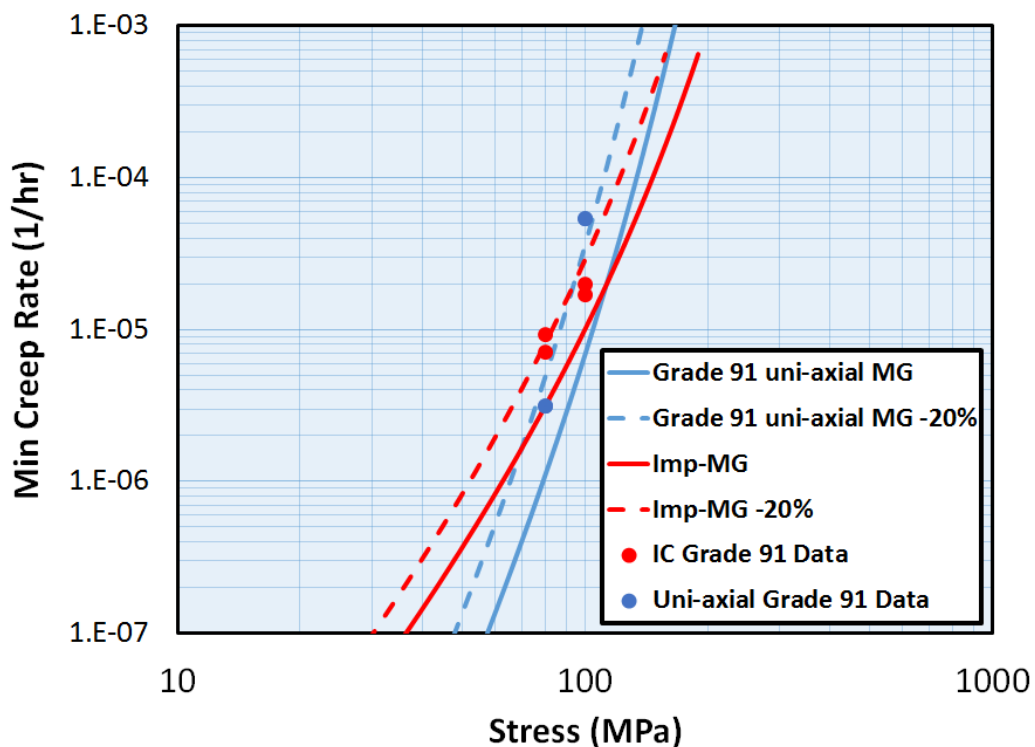

Figure 12. Comparison of Grade 91 uni-axial MG to Imp-MG relationship to actual data.

The Imp-MG relationship directly compares uniaxial rupture times to impression creep rates of the same testing condition. It is important to note that this relationship assumes that the impression creep minimum creep rates **are not the same** as expected uni-axial minimum creep rates, as shown in Figure 11. Improved and revised FEA models **may** also help further the use of impression creep rates in situ of uni-axial creep rates at the same 'testing conditions'. The findings discussed in this paper show that careful considerations must be made before directly comparing impression creep strain rates to uni-axial rates. Further testing for a variety of materials, rigorous analysis and additional FEA work will help further understand the implications of this.

4.3. Physical Methods for Determining Effected Deformation Area

Posttest evaluations methods shown in section 3.2 of the results section have provided tools for physically measuring the affected interaction volume. Testing of normalized and tempered Grade 91 has shown strain softening behavior, as shown in Figure 8. Strain hardening is expected in some alloys, which would demonstrate a very different reaction in the interaction volume. Even though some alloys have been shown to retain the same hardness throughout testing (neither softening nor hardening), samples can be etched to reveal microstructure. Elongation of grains have been noticed at the edges beneath the indentation. It is also possible that TEM and SEM work could be explored to further characterize these materials after testing to examine dislocation pileup formation, grain orientation effects, etc. Further FEA work may be needed to address some of the additional questions regarding applicable indentation range and testing conditions (appropriate stresses and temperatures) and the impact of an increasing softened zone as the test progresses in strain softening materials. Physical findings from hardness plots and evaluation of elongated grains may help validate and improve current FEA models.

5. Conclusion

These findings led by EPRI have shown additional testing parameters that should be considered for the current code of practice to improve consistency in test results across multiple labs. There should be a more consistent approach to determining the minimum creep rate and a proposed set of amendments to the current code of practice are discussed in this paper. A guideline that requires the test to reach a 'steady-state' for a given number of hours appears to be the most appropriate guideline for testing of all materials, and the term 'minimum creep rates' was defined for the impression creep test. It was determined that each test should be ran to a minimum of 300 hours and creep rates are to be calculated using ±50-hour time increments. A 10% variation in strain-rate was determined to be a reasonable target with limited test results. Observations showed that the time needed to reach a steady state rate can be dependent on the material (Grade 22 > Grade 91), and that some materials have shown more fluctuations in variation than others (Grade 91 > Grade 22). All testing was conducted using the exact same testing equipment.

EPRI has used additional assessment methods, such as analytical and physical posttest examinations, for determining the limits of the impression creep test. The test has currently been used in a qualitative manner, such as a risk ranking evaluation for main steam and hot reheat piping components [9-10]. The additional assessments and experiments conducted by EPRI have shown that there may be issues when using the impression creep test in certain quantitative assessments. Analytical posttest assessments have shown that a universal procedure for measurement of strain rate would be very beneficial to the testing community and likely lead to the having a more widely accepted test method. Physical posttest assessments, such as laser measurements, hardness testing and grain structure evaluations have shown that there are physical ways to measure the effected zone of deformation (interaction volume) under the indentation surface. These methods may help improve current FEA models and provide a better understanding of how different materials react under a compressive loading state. EPRI will continue to conduct a variety of tests on different materials with a goal of providing a **reliable test method** for both qualitative and semi-quantitative assessments.

References

1. Sun, W, et al. "Application of Impression Creep Data in Life Assessment of Power Plant Materials at High Temperatures." *Proceedings of the Institution of Mechanical Engineers, Part L: Journal of Materials: Design and Applications*, vol. 222, no. 3, Dec. 2008, pp. 175–182.
2. Hyde, T.H.; Yehia, K.A.; Becker, A.A. Interpretation of impression creep data using a reference stress approach, International Journal of Mechanical Sciences, Volume 35, Issue 6, 1993, Pages 451-462.
3. Hyde T.H.; Sun W.; Becker A.A. Analysis of the impression creep test method using a rectangular indenter for determining the creep properties in welds. Int J Mech Sci 1996;38:1089–102.
4. ECCC Guidelines for Impression Creep Testing; Discussion at 3th International ECCC Conference, 2014.
5. Recent Research Findings and Expanded Database for Impression Creep Testing: EPRI, Palo Alto, CA: 2017. 3002009056.
6. Hyde, T.H.; Sun, W.; Becker, A.A. Analysis of the impression creep test method using a rectangular indenter for determining the creep properties in welds, International Journal of Mechanical Sciences, Volume 38, Issue 10, 1996, Pages 1089-1102.
7. Bridges, A.; Purdy, D. Potential Implications of Step Loading in Impression Creep Testing; 5th International Conference SSTT, Swansea UK, 2018.
8. Life Management of Creep-Strength-Enchanced Grade 91 Steels – Atlas of Microstructures: Base Metal. EPRI, Palo Alto, CA: 2013. 3002000080.
9. A Guide to In-Service High Temperature Headers and Piping Materials Evaluation by Impression Creep Testing. EPRI, Palo Alto, CA: 2016. 3002009055.
10. Brennan, K.; Brett, S.J.; Eaton-Mckay, J. Impression Creep Testing of Aberrant Grade 91 Material Removed from Piping in Service; 4th International ECCC Conference, 2017.

Potential implications of step loading in impression creep testing

A. Bridges [1]*, D. Purdy [1]

[1] Electric Power Research Institute, 1300 W. W.T Harris Blvd, Charlotte, NC 28262 USA

* Correspondence: abridges@epri.com; Tel.: +1-704-595-2950

Abstract: The small sample impression creep test method has recently been of interest, as it can give a good indication of expected creep rates in uniaxial creep testing with minimal use of material. The compressively loaded test has also been shown to provide accurate results under multi-step loading conditions for a low alloy steel (½Cr½Mo¼V) to further extract value from a single test specimen. The Electric Power Research Institute (EPRI) has conducted step tests (step temperature and step loading changes) on another low alloy steel (Grade 22), as well as a tempered martensitic 9 Cr steel (Grade 91). Results have shown that there may be potential problematic areas when conducting step-up and step-down steps in these materials. Additional posttest evaluations have shown that material effects, such as strain hardening and strain softening, may add additional complexities when comparing strain rates of multi-stepped loaded stain rates. Hardness testing on posttest impression creep specimens have confirmed strain softening of tempered martensitic Grade 91 and no observed effect for an ex-service Grade 22 alloy. These findings have shown that careful considerations must be made before using creep rates obtained from multi-stepped loaded tests in situ of single loaded tests.

Keywords: Impression creep, strain softening, strain hardening, hardness, Grade 91, Grade 22

1. Introduction

In recent years, the impression creep test has gained interest in the testing community. The test method can be used as an alternative to standard uniaxial testing to determine steady state creep rates. Specifically, the test is used when an insufficient amount of material exists for uniaxial creep testing. Traditional uniaxial creep tests use a larger volume of material, about 100-200 times more than impression creep testing, which is considered a 'destructive' technique that generally requires weld repair or replacement of the extracted volume of material. Impression creep specimens can be machined from 'scoop' samples and is considered a 'non-invasive' testing technique. Scoop sampling has typically been used on main steam (MS) and hot reheat (HRH) steam piping components in fossil power plants [1]. Replications can be performed for microstructure evaluations, but the scoop can be machined into an impression creep specimen. The standard impression creep specimen geometry and an example of a scoop sample is shown in Figure 1.

Impression creep testing has shown to be useful for multi-step loading in service-aged ½Cr½Mo¼V low alloy steel [2]. Results showed that creep rates obtained under different loading histories were in good agreement with those of single loaded tests. It is also important to note that step up and step down testing was performed in this study. Recent testing by EPRI on two different materials has raised concern over the use of multi-step loading and multi-step temperature changes. Additional posttest assessments were also performed for further evaluation of the potential effects of step testing. This involved hardness testing at the cross-section perpendicular to the indentation formed during testing. Findings and potential implications are further expounded in the discussion section.
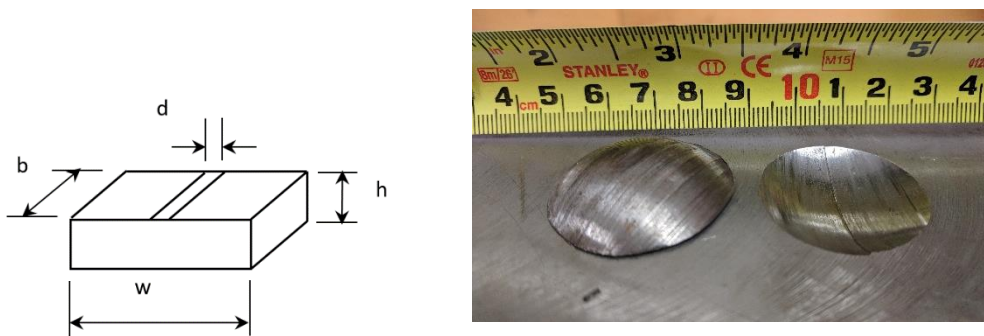

Figure 1. Standard Impression Creep Specimen (left) and Removed Scoop Sample (right).

2. Materials and Methods

After material has been removed (scoop sample, etc.) the impression creep specimen can be cut using electric discharge machining (EDM) to a thickness of ~2.55 to 2.60 mm. A final thickness of 2.50 ± 0.02 mm is achieved using 600 grit sandpaper. The standard tested specimens have samples dimensions of 10mm x 10mm x 2.50 ± 0.02 mm, as shown in Figure 1. Electric Power Research Institute (EPRI) is currently using a Tinius Olsen twin-screw servo-mechanical (H25KS) loading frame with a high temperature ceramic shell furnace using kanthal windings. A software program has been specifically designed for controlling a static load with a signal input for water cooled linear variable differential transformers (LVDTs) to measure displacement during the entire duration of the test. The independent three zone furnace uses type N thermocouples for control of temperature, but the sample temperature is measured with an external data acquisition (DAQ) system using three type K thermocouples. A high strength Waspaloy nickel based superalloy was chosen as the material for the indenter, as it has a much higher creep strength than that of the materials being tested. These specifications are outlined in the current code of practice [3].

Three different impression creep tests were carried out for a normalized and tempered martensitic Grade 91 steel. Test loads were varied (between 80-120 MPa) at a constant testing temperature of 625°C. After testing, the samples were cut in half perpendicular to the indentation that was formed. These were mounted using a hot mounting process and then polished using standard metallographic techniques. Hardness testing was performed at each of the three samples using a 0.2 kg load with 100 µm spacing. Figure 2 shows an impression creep sample before cutting with the two halves mounted (left) and a macro image of the sample after hardness mapping (right).
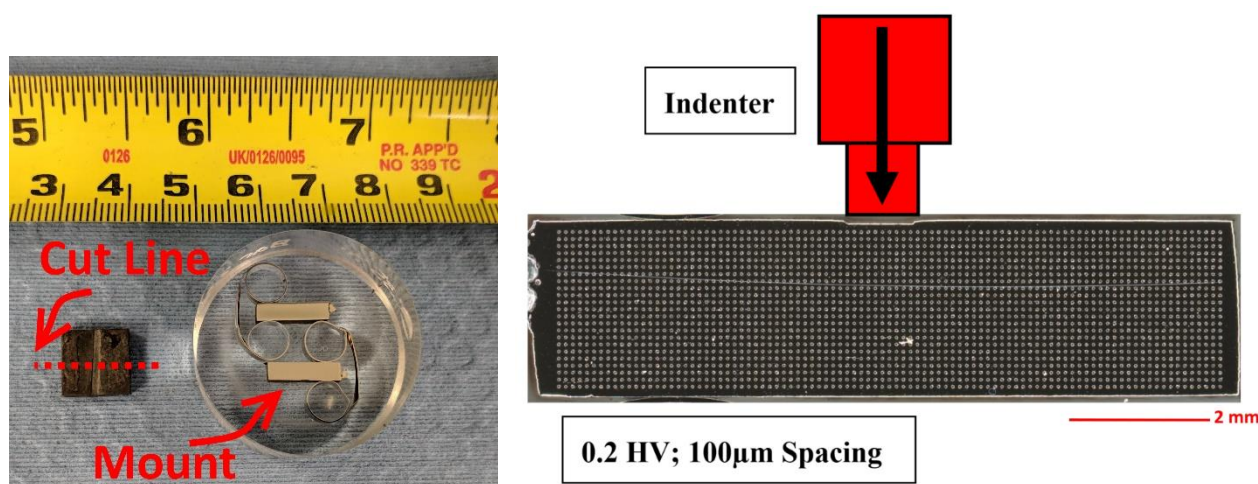

Figure 2. Impression Creep Metallographic Mounting (left) and Macro Image of Hardness Mapping Underneath Indentation Surface after Testing (right).

3. Results

3.1. Results for Normalized and Tempered Martensitic Grade 91

Three different impression creep tests were performed on the normalized and tempered martensitic Grade 91 material. Tests were conducted at 625°C and tested between a variation of stresses (80 to 120 MPa). The impression creep results are shown in Figure 3. The indentation depths for each test were measured using both the test results from the machine data files and confirmed with measurements from a confocal laser microscope (Keyence VK-X105). The measured depths were determined to be 7µm, 31µm and 40µm. It should also be noted that the 80 MPa test showed a decrease in strain around 300 hours because of a loss in furnace power. After testing, the samples were cut in half, mounted, polished and then tested using an automatic Vickers hardness tester (LECO AMH43). The hardness data is presented as color contour plots, shown in Figure 4 through 6.
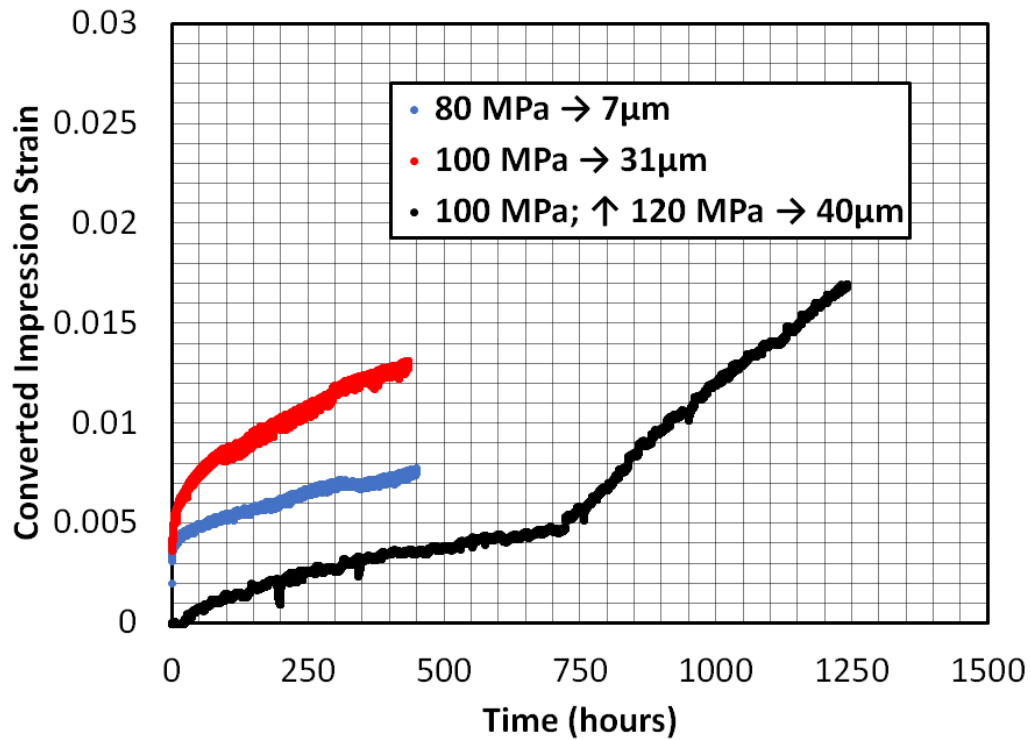
Figure 3. Comparison of Impression Creep Tests of a Normalized and Tempered Martensitic Grade 91 at 625°C and a Variety of Stresses (80 to 120 MPa)
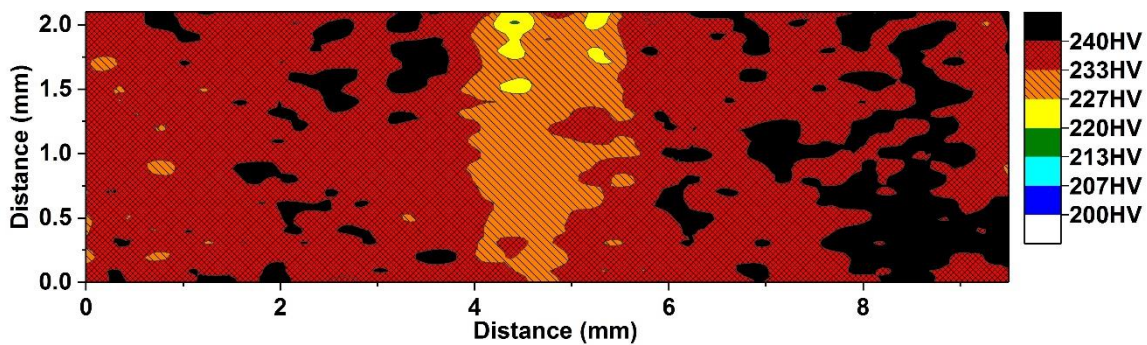
Figure 4. Hardness Plot of a Cross Section through an Impression Creep Sample of Tempered Martensitic Grade 91 Tested at a Temperature of 625°C and Stress of 80MPa; Overall Indentation Depth is 7 µm
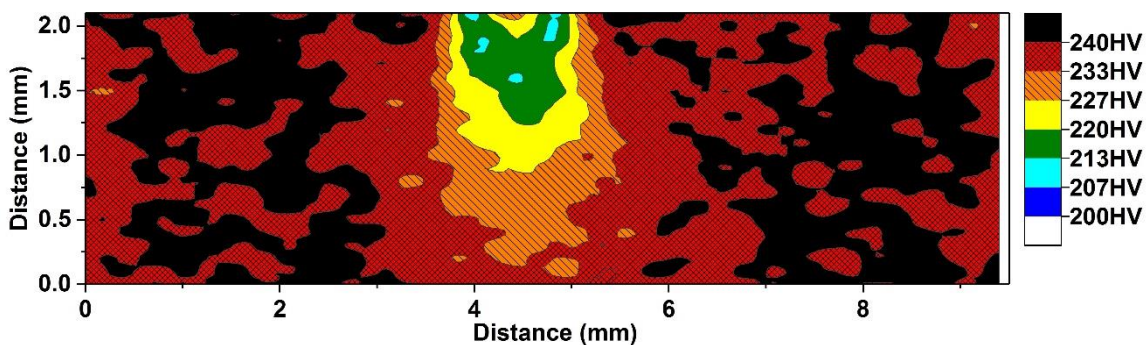
Figure 5. Hardness Plot of a Cross Section through an Impression Creep Sample of Tempered Martensitic Grade 91 Tested at a Temperature of 625°C and Stress of 100MPa; Overall Indentation Depth is 31 µm
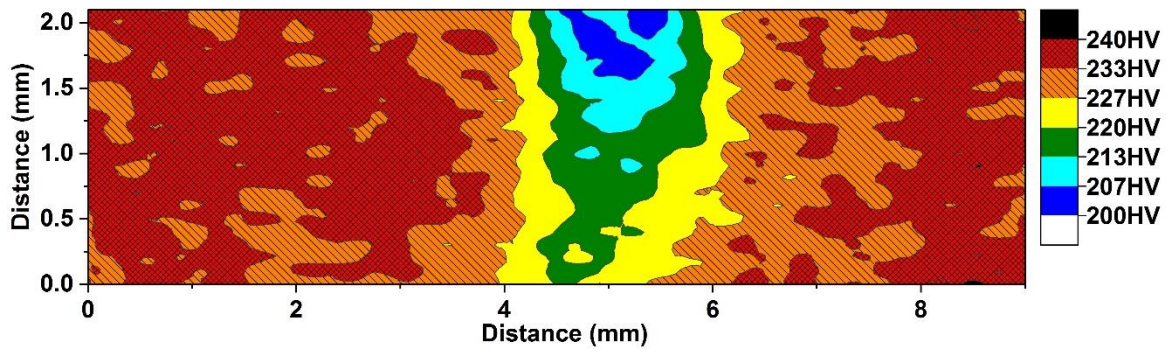
Figure 6. Hardness Plot of a Cross Section through an Impression Creep Sample of Tempered Martensitic Grade 91 after Stepped Loads from 100MPa to 120MPa at a Temperature of 625°C; Overall Indentation Depth is 40 µm.

Another normalized and tempered martensitic Grade 91 specimen was tested at a variety of loading conditions. The test started at 107 MPa for about 200 hours, stepped to 129 MPa for about 400 hours, then stepped back to 107 MPa for another 250 hours before finally being stepped to 145 MPa for about 175 hours. This is shown in Figure 7. The impression creep strain accumulated before the step to 145 MPa was about 0.030. The next step, 145 MPa, is shown in Figure 8.
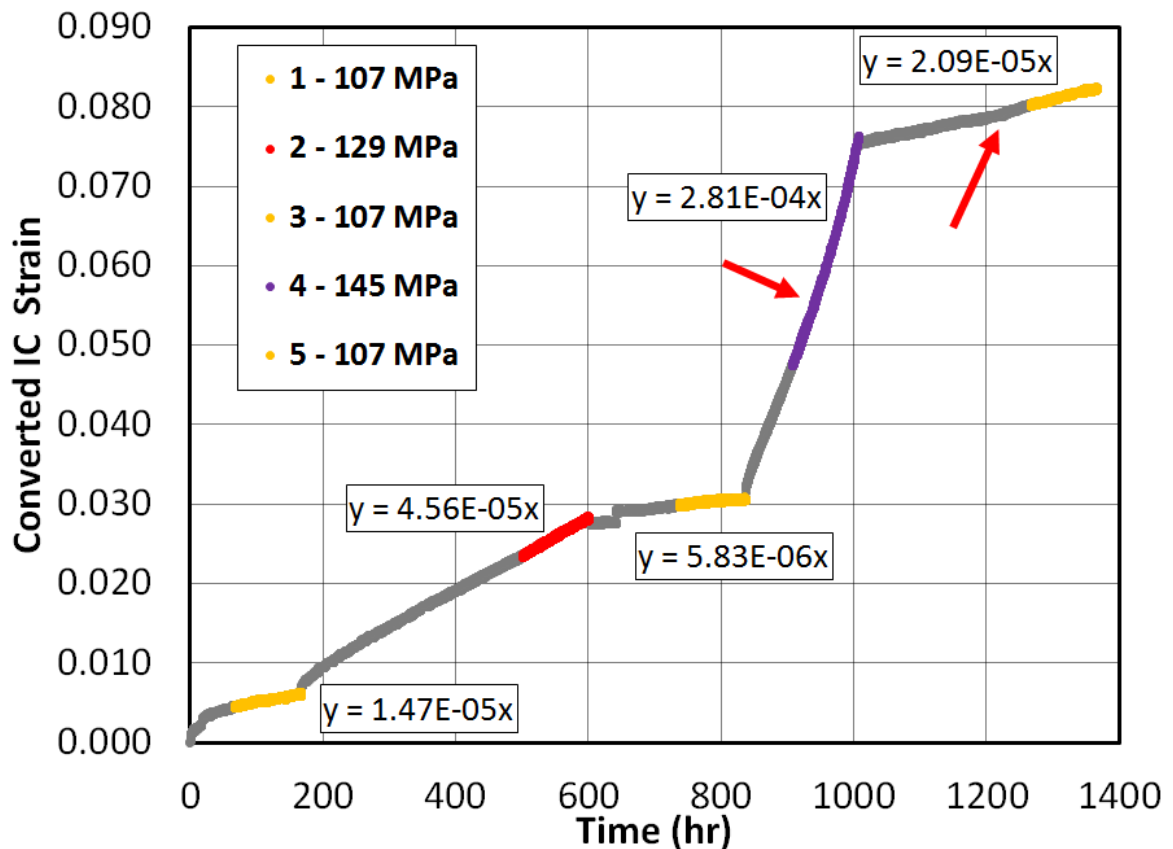
Figure 7. Impression Creep Curve for Stepped Load Test (625°C) of Normalized and Tempered Martensitic Grade 91 (107 to 145 MPa).
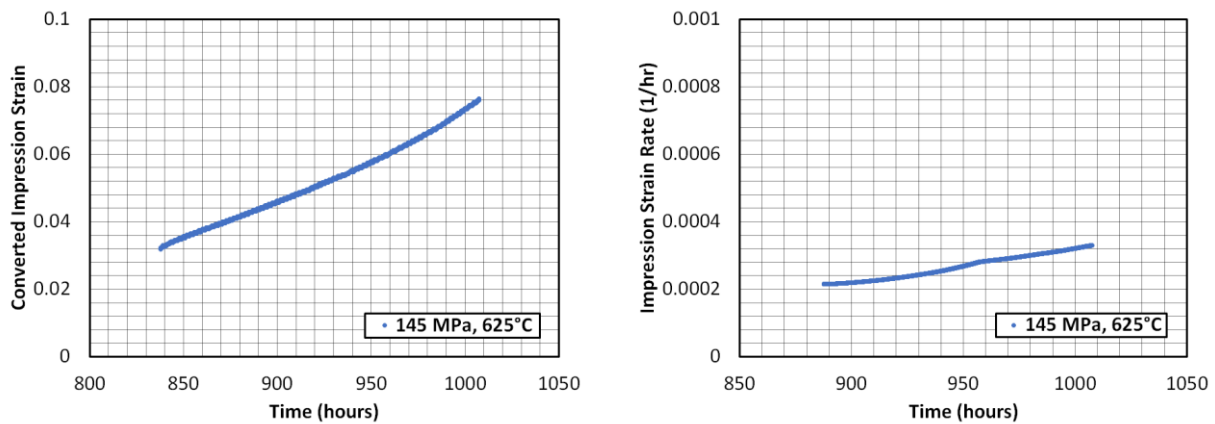
Figure 8. Impression Creep and Strain-Rate Curves for Stepped Load to 145 MPa (625°C) of Normalized and Tempered Martensitic Grade 91 after a Previous Strain History of 0.030.

The step load to a stress of 145 MPa clearly shows an initial steady-state creep rate that slowly increases with time. The reported strain rates were calculated using ±50-hour time increments. A ±50-hour increment that occurs 50 hours before the test terminates would be equivalent to the average rate in the last 100 hours of testing. It should also be noted that the testing stress of 145 MPa at 625°C is very close to reported yield stresses, which may be a possible reason for increasing strain rate behavior.

3.2. Results for Step Temperature Change in Service Exposed Grade 22

Service exposed Grade 22 base metal from a hot reheat piping system was tested at a constant stress of 80 MPa, but by stepping the temperature in 5 different increments. The test was initially started at 570°C for 300 hours, before being stepped up in 10-degree increments, up until 600°C. The final step was reduced to 570°C. The results are shown in Figure 9. The units for the comparison of the initial and final steps at 570°C are for comparison purposes only. The "primary creep zone" in the initial loading is also removed to better illustrate the difference.
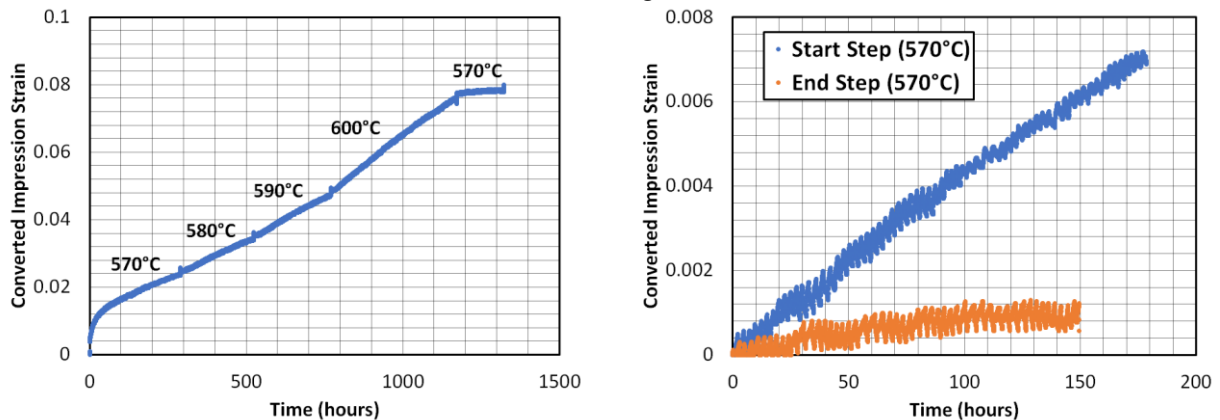
Figure 9. Impression Creep Results for Service Exposed Grade 22 Base Metal Tested at a Constant Stress of 80 MPa (left); Temperatures Stepped in Increments of 10-degrees (570°C to 600°); Comparison of Initial and Final Step at 570°C (right).

Although hardness testing was not performed on the stepped temperature test above (Figure 9), a hardness test was conducted on another impression creep test of the same service exposed base metal. To date, observations of hardness tests have shown that Grade 22 does not exhibit strain softening or hardening behavior under impression creep loading. The example of this is shown in Figure 10 below.

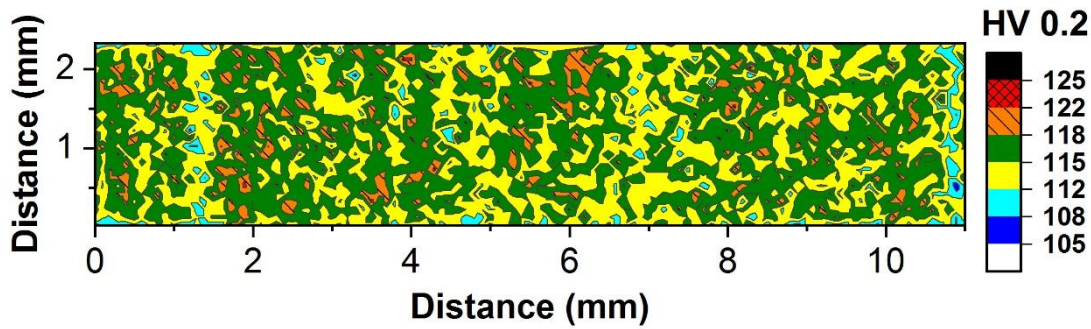**Figure 10.** Hardness Plot of a Cross Section through an Impression Creep Sample of Service Exposed Grade 22 Base Metal Tested at 80MPa and a Temperature of 570℃; Overall Indentation Depth is 86 µm.

4. Discussion

In martensitic steels, it has been observed that softening behavior is due to the disappearance of many of the microstructural subboundary characteristics and a decrease in the dislocation density in cyclic fatigue tests [4]. High temperature tensile tests at low strain rates, below 2.5×10^{-4} s^{-1}, have also confirmed the existence of a softening stage. Microstructural observations have revealed that softening mechanisms are based on annihilation of subgrain boundaries and mobile dislocations [4-6]. Impression creep results in this paper have shown that softening also manifests in compressively loaded samples at high temperatures and low strain rates in some alloys, such as martensitic Grade 91. This is particularly important when step loading tests are considered, as the material may have a reduction in overall creep strength with each increasing step and this can lead to faster creep rates than would have been measured on virgin material (e.g. in the first step). The last two steps in the impression creep test shown in Figure 7 show increasing strain rates, which were tested at higher indentation depths from prior loading history. Results in Figure 8 show a steady-state creep rate that slowly increases over time at the stress of 145 MPa, which may be due to excessive softening at such high impression depths. This also indicates that there may be an applicable range of indentation depth, regardless of step-up/step-down tests. The maximum level of softening that occurs in comparison to uni-axial creep testing of the same material is currently unknown. Further interrogation of these samples will provide a better explanation of the accelerating strain rates that occur. Microscopy evaluations and hardness testing will be conducted on this sample to confirm softening behavior.

The stepped temperature tests shown in Figure 6 showed that a sudden reduction in temperature (step down) caused creep rates to be drastically lower than the initial rates in service exposed Grade 22. The sudden reduction in strain-rates may be due to previously increased dislocation pile-ups at the much higher strain rates. To overcome the increased resistance to dislocation movement, it may be that only step-up tests can be performed.

If the impression creep test is to be used in a quantitative manner, these questions must be addressed. There appears to be competing mechanisms that are occurring and step testing has further complicated the matter. The intent of this paper is to raise concern over potential problematic areas in impression creep with the goal of finding the true limitations of the testing technique.

5. Conclusions

The findings in this paper have shown that there are problematic areas in stepped tests at certain testing conditions and changing material properties. It is important to highlight these findings, as stepped impression creep testing has been used for all materials. These findings are a first attempt to question the validity of stepped impression creep tests in all materials, as there appears to limitations, specifically in martensitic Grade 91. Impression creep tests to various indentation depths have shown that strain softening behavior exists for normalized and tempered Grade 91. Softening mechanisms have also been shown in previous literature for a variety of martensitic steels. Additional hardness testing will be conducted for a variety of materials to better understand softening and hardening mechanisms in impression creep testing. The stepped temperature test for Grade 22 showed a significant difference in strain-rates between the initial and final step. It is thought that increased dislocation pile-ups are caused at previous high strains rates, thus lower strain rates are due to the difficulties of overcoming these dislocations. These findings have shown that careful considerations must be made before using creep rates obtained from multi-stepped loaded tests in situ of single loaded tests.

References

1. Sun, W, et al. "Application of Impression Creep Data in Life Assessment of Power Plant Materials at High Temperatures." *Proceedings of the Institution of Mechanical Engineers, Part L: Journal of Materials: Design and Applications*, vol. 222, no. 3, Dec. 2008, pp. 175–182.
2. Hyde, T.H.; Sun, W. (2001). Multi-step Load Impression Creep Tests for a 1/2Cr1/2Mo1/4V Steel at 565°C. Strain, 37(3), 99-103.
3. ECCC Guidelines for Impression Creep Testing; Discussion at 3th International ECCC Conference, 2014.
4. Eisentrager, J.; et. al, Analysis of Temperature and Strain Rate Dependencies of Softening Regime for Tempered Martensitic Steel, SAGE Journals, Volume 52, Issue 4, Pages 226-238.
5. Alsagabi, S.; Shrestha, T.; Charit, I. High temperature tensile deformation behavior of Grade 92 steel, Journal of Nuclear Materials, Volume 453, Issues 1–3, 2014, Pages 151-157.
6. Wang, L.; Li, M.; Almer, J. In situ characterization of Grade 92 steel during tensile deformation using concurrent high energy X-ray diffraction and small angle X-ray scattering, Journal of Nuclear Materials, Volume 440, Issues 1–3, 2013, Pages 81-90.

Impression creep testing across a heat affected zone

J.H. Rantala [1]*, T. Andersson [1]

[1] VTT Technical Research Centre of Finland Ltd
* Correspondence: juhani.rantala@vtt.fi; Tel.: +358400570386

Abstract: Impression creep testing was applied for studying the creep strain rates in the heat affected zone of a P22 weld in order to support an FE analysis of a piping system. The specimen size recommendations for impression creep were violated in the sense that instead of a standard 10*10*2.5mm specimen an oversize 10*10*10 mm specimen was machined such that the heat affected zone was in the middle of the specimen. By grinding the specimen after each test cycle, the material combination from the base material through the HAZ to the weld metal was "scanned" as the specimen got thinner. The validity of the measured strain rates is supported by FE analysis, which showed that the creep deformation is very strongly concentrated in the immediate vicinity of the indenter while the underlying material remains unaffected. The effect of the previous loading was removed by grinding off the top layer. The strain rate distribution and primary strain component distribution vs. distance from the fusion line were determined. These results were applied in the FE analysis of full size piping components.

Keywords: impression creep, heat affected zone, FE analysis, stress analysis, piping

1. Introduction

In creep stress analysis of a live steam piping accurate material creep properties are needed. These can be obtained by traditional creep testing. However, for a detailed analysis of welded steam piping components also the properties of the heat affected zone would be needed. Uniaxial cross-weld testing would be useful, but the testing will not give the creep properties of the individual zones within the heat affected zone. Therefore, Impression Creep testing was applied in a research project [1] lead by Inspecta Technology, Sweden, and funded by Energiforsk AB (formerly Värmeforsk). By using an oversize specimen, it was possible to scan through the whole weldment from weld metal, across the heat affected zone, and to the base metal. In this way the creep properties of the heat affected zone were measured and implemented into an FE code, from this the critical locations in the piping system can be analysed in a more reliable manner.

2. Materials and Methods

Virgin 10CrMo910 (P22) tube 273*32mm was welded and post weld heat treated according to the welding procedure of the power plant Heleneholmsverket in Malmö, Sweden by using a matching consumable, TIG welding, preheat temperature 150-200°C, interpass temperature 350°C, PWHT 1h at 680-720°C. Samples were removed for uniaxial and Impression Creep testing as shown in Figure 1. From the weld cross-section an oversize 10*10*10mm Impression Creep "sandwich" specimen was removed as shown in Figure 2. The HAZ was parallel with the surface to be indented. The specimen was deliberately thicker than the recommended standard 2.5mm thick specimen to facilitate scanning of different material constituents within a specimen by grinding off 0.5mm after each test cycle and continuing with a fresh surface. By using an oversize specimen, it was assumed that the extra thickness would cause only minor error and most of the creep deformation of the previous test cycle is removed by grinding. The specimen was rotated by 90° after each test cycle, which also reduces the effect of the deformation under the indenter from the previous cycle.

Figure 1. Welded 10CrMo910 pipe (273*32mm) after removal of test specimens.
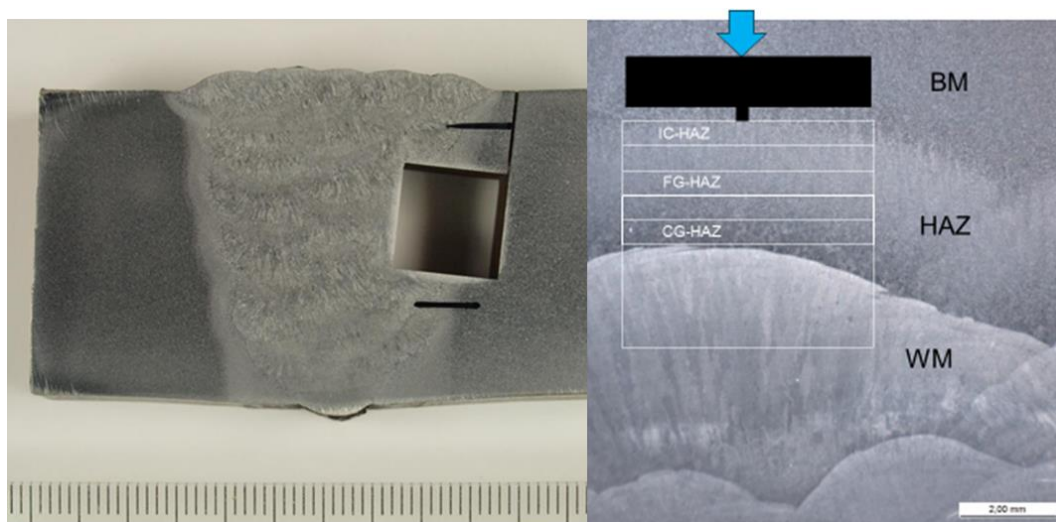

Figure 2. Left: Cross-section and the locations of the impression creep specimens and the hardness measurements across the HAZ (black lines), mm-scale at the bottom, right: schematic of the loading arrangement through different constituent of the weldment.

3. Results

The typical duration of an Impression Creep test is 500h. After each test cycle the minimum displacement rate was calculated and this was converted to a corresponding uniaxial strain rate by using a simple analytical equation established for Impression Creep to uniaxial conversion [2]. Also, the displacement curves (indentation depth) were converted to uniaxial strain curves as shown in Figure 3 where the curves of the nine first tests are shown. The continuous strain rate curves shown in Figure 4 were calculated by moving a 100 h "calculation window" from the beginning of the test to the end. It is seen that towards the end of each test the scatter increases when the strain rates become very small. In another project it was defined that below a strain rate of about $3*10^{-6}$ the accuracy will reduce [3]. This is also partly because towards the end of the test, the number of data points in the 100 h calculation window reduces and in fact, the last rate is calculated by a window of only 50 h. A linear trend line was fitted through the data of the last 100h of each test in order to calculate the corresponding uniaxial minimum creep rate of each test according to the standard conversion equation. By doing this, it was assumed that the reducing specimen thickness does not cause much error in the conversion calculation. To verify this a detailed FE analysis would be needed. The Impression Creep tests in this study were carried out at 530°C and an equivalent stress of 110 MPa. The measured creep rates are shown in Table 5.
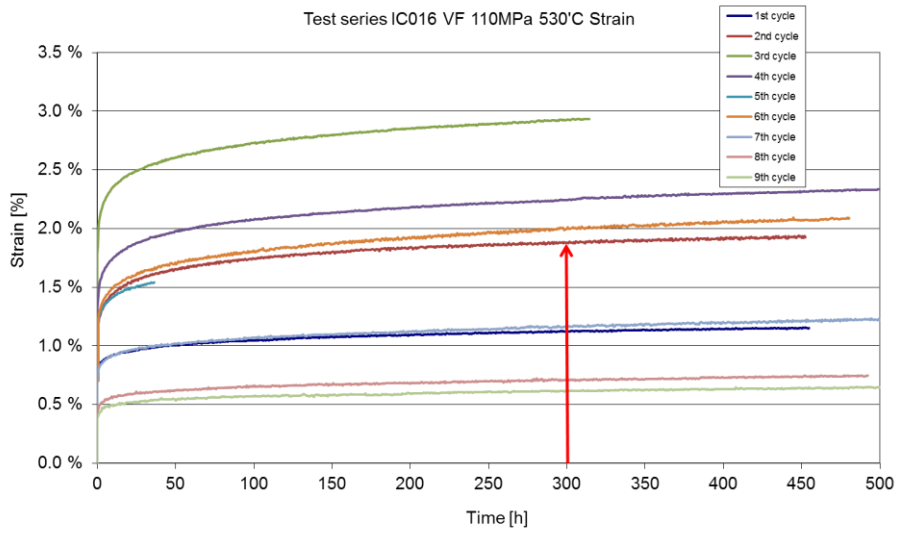
Figure 3. Corresponding uniaxial strain curves calculated from the Impression Creep test series at 110 MPa and 530°C.
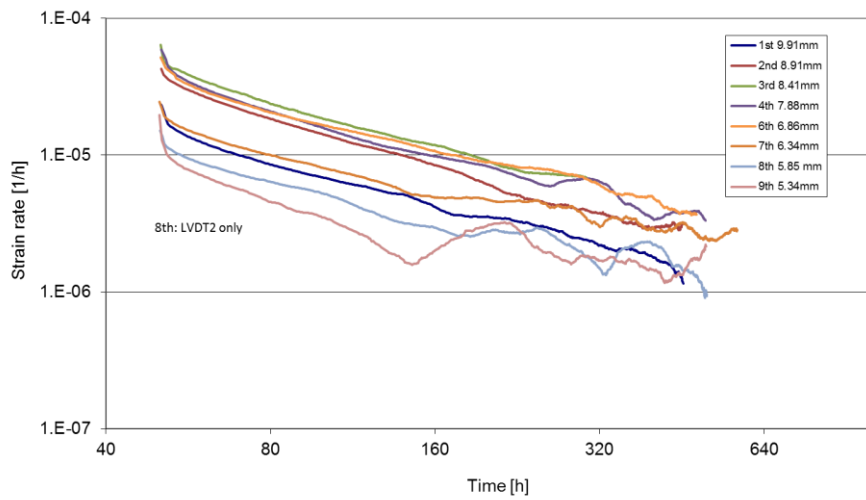
Figure 4. Continuous strain rate curves from the Impression Creep test data in Figure 3.

Table 5. Minimum linear strain rates at each specimen thickness at 110 MPa 530°C.

Specimen thickness [mm]	min. strain rate (corrected) [1/h]
9.91	1.75E-06
8.91	3.26E-06
8.41	3.90E-06
7.88	3.70E-06
6.86	4.58E-06
6.34	2.74E-06
5.85	1.65E-06
5.34	1.44E-06
4.85	1.79E-06
3.88	1.22E-06
3.09	9.47E-07
2.5	5.29E-07

The creep rate varied when moving from BM across the HAZ to the WM. The useful illustration of this behaviour is shown in Figure where the brown curve shows the corresponding uniaxial strain at a constant time value of 300 h, being a rough relative measure of the amount of primary creep at each material layer. However, the quality of the initial contact between the specimen and the indenter is not necessarily perfect in each test, so there is some uncertainly associated with this strain parameter. However, the strain value (brown curve) and the calculated minimum creep rate (blue curve) for each test seem to go roughly hand in hand. Standard deviation values were added on the strain rate curve as calculated at the same time period as the minimum strain rate.

The test series was started with the specimen thickness of 10 mm and at that thickness the tested surface was in base material. After the first test 1 mm was ground off and in the second test the measured minimum strain rate increased. After the following tests only 0.5 mm was ground off. However, two tests (at thicknesses 8.41mm and 4.85mm) were run to only about 300h instead of intended 500h test duration. Based on the general trend in Figure 4 it was estimated that the creep rate at 500h would be 0.54 times the rate at 300h. When these two test results are corrected, the maximum strain rate appears at a location which is likely to be the inter-critical (partially austenitized) zone, see Figure 5.

Based on the measurements from the cross-section of the weld in Figure 2 it can be estimated that on top of the 10*10mm hole the location of the fusion line is at 3.7 mm and at the bottom at 5.1 mm. The location of the IC-HAZ/BM transition is more difficult to define but is located roughly at 6.3 mm on top of the hole and at 7.0 mm at the bottom. The red inclined lines in Figure 5 illustrate the locations of the HAZ constituents on two opposite side of the specimen. From these measurements it can be estimated that the width of the HAZ is 2.6 mm on top of the hole and 1.9 mm at the bottom, which seem like rather small values. The CG-HAZ is the strongest zone and has the lowest creep rate. The minimum creep rate results in Table 5 and in Figure 5 show that the highest strain rate of $4.58*10^{-6}$ is only about 2.6 times higher than in the base material ($1.75*10^{-6}$). However, it was expected that the strain rate in the coarse-grained zone would have been considerably lower than in the base material, but this is not the case. The low creep rates measured from the WM as shown in Figure 5 indicate that the creep strength of the WM is slightly higher than of the BM. The weld is therefore overmatching.

The reported minimum strain rate values did not necessarily hit the lowest (intercritical zone) or the highest (coarse grained zone) values in the test specimen because the fusion line in a real weld is not straight and therefore the material under the indenter is not likely to contain just one thin layer of each constituent of the HAZ. Besides that, the selected grinding thickness of 0.5 mm was a compromise between two factors. First, the smaller the grinding thickness, the smoother the curve in Figure5 would have been (but would have increased the number of test cycles needed to scan through the specimen). Secondly, the smaller the grinding thickness, the more the deformation from the previous cycle would have influenced the following test. The FE analysis of the IC test specimen has shown that only very little deformation below the indenter will progress deeper than 0.5 mm. However, this is of course dependent on the stress level as shown in section 4.

When testing a HAZ specimen as described above it must be recognised that the sample is a sandwich structure in terms of material properties. At this point it is not known how the underlying different microstructures will affect the testing of the microstructure on the surface. This would require FE analysis which was not foreseen in the Energiforsk project.

Figure 5. Calculated minimum linear strain rate (with error bars) and the corresponding uniaxial strain at 300 h for each impression creep test at 110 MPa and 530°C.

3.1. Hardness measurement

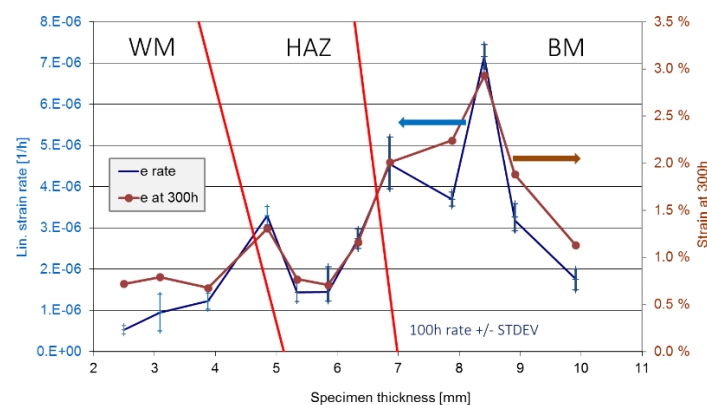Hardness was measured from the new weld and the results are shown in Figure 6. The locations of the hardness measurements are indicated in Figure 2. The hardness measurements suggest that the width of the HAZ is about 4 mm, which does completely coincide with the measurements taken from the specimen itself. The WM has much higher hardness (250 HV1) than the BM (160 HV1), which means that the WM is overmatching. The high hardness of the WM is in line with the finding that the creep rate of the WM in Figure 5 is lower than the creep rate of the BM although the correlation between hardness and creep strength is in most cases only coincidental.
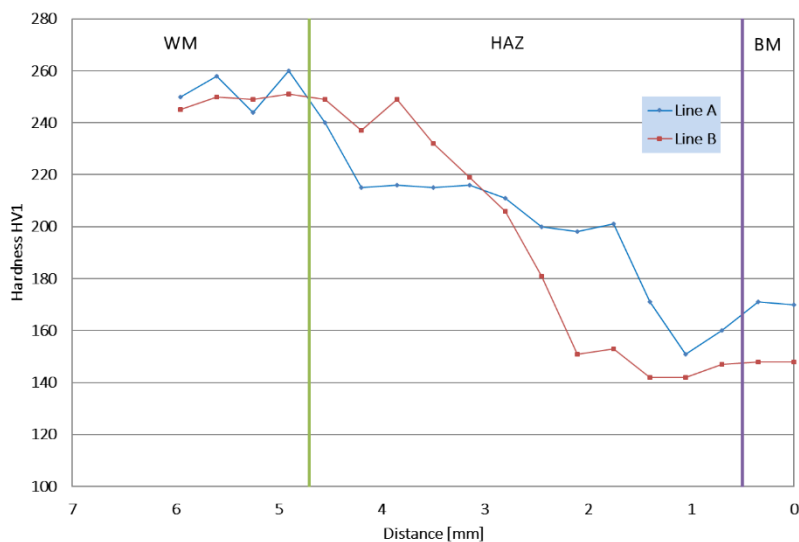

Figure 6. Hardness measurements across the HAZ of the weld.

4. FE analysis of impression creep test

The impression creep test was analysed by the FE method with Abaqus CAE software (version 6.14). A quarter model of the impression creep test for the 2.5mm thick standard specimen was used. For the 10mm thick specimen a different mesh was used. Specimens were meshed with 62500 and 48000 quadratic elements (C3D20R), respectively.

The LCSP creep model [4] for 10CrMo910 was used at 525°C with a contact pressure of 255.8 MPa, which corresponds to a uniaxial stress of 110 MPa, which was used in the IC test programme. The temperature of 525°C was used in the analysis instead of the real test temperature of 530°C, because the parametric LCSP model did not converge properly, but the LCSP model trimmed for 525°C was available and worked nicely. This difference in temperature leads to an error of less than 10% in strain rate.

The plots of the equivalent strain in Figure 7 and Figure 8 show that the maximum strain is located a short distance below the indenter edge and about 0.5mm below the indenter in the middle. This means that when 0.5mm of the 10mm thick specimen was ground after each test cycle, some strain (less than 0.08%) from the previous test was left on the surface of the ground specimen in the area directly under the indenter. The effect of this was however minimised by turning the specimen 90° along the vertical axis. After turning the specimen about 90% of the surface under the indenter is practically unstrained.

The strain distribution in the 10mm thick specimen in Figure 9 is rather similar to the 2.5mm thick specimen, but the strain in the thick specimen seems to spread deeper than in the standard specimen.

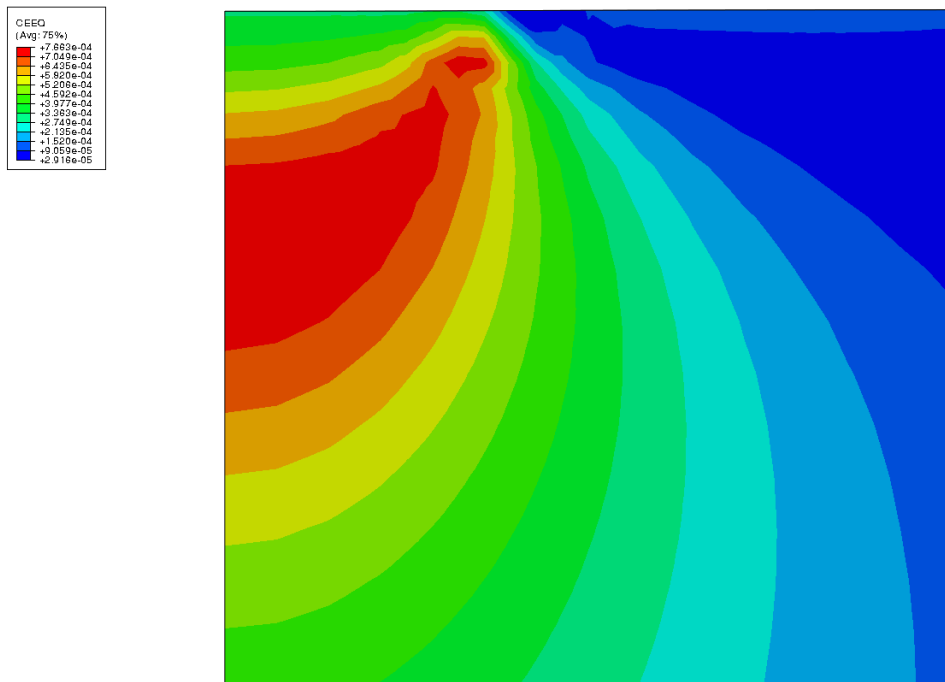**Figure 7.** Half model of the equivalent strain distribution in the 2.5mm thick specimen.

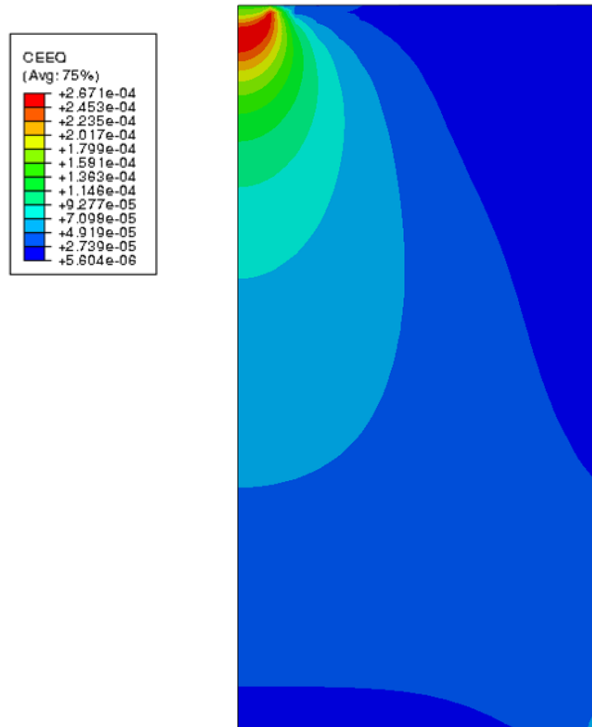**Figure 8.** Close-up of Fig. 18 (1.4*1.3mm).

Figure 9. The equivalent strain distribution in the 10mm thick specimen.

The displacement as a function of time was predicted by the FE analysis. The initial strain in the 10mm thick specimen was bigger by a factor of 1.84 than in the standard specimen, but the strain rate at 500 h in the 10mm specimen was 30% smaller than in the standard specimen. The expectation was that making the specimen thicker would not make much difference in the behaviour, because most of the strain should be concentrated just below the indenter. As shown in Figure 9, the strain level at the bottom of the thick specimen is small but sufficient to have an effect on the total strain and strain rate levels. When compared to the experimental strain rate measurements with the 10mm thick specimen, the FE predictions fell short by a factor of 5.

5. Conclusions

An innovative way of applying impression creep testing was used by manufacturing a "sandwich" type of specimen of a welded joint, which allowed the creep rates to be scanned from the base material across the HAZ to the weld metal. The highest creep rate in the inter-critical zone of the welded joint was, however, not as high as was expected: only 2.6 times higher than in the base material. The weld metal is slightly overmatching as compared to the base material. The measured HAZ creep rates were entered as part of material property data for the FE analysis of a live steam piping system and its components.

References

1. Storesund, J.; Steingrimsdottir, K.; Rantala, J.; Sollander, R.; Chen, Z.; Bolinder, T. Lifetime assessment of high temperature piping by stress analysis and testing, Report M12-218, Energiforsk AB, 2015.
2. Hyde, T.H.; Sun, W.; Brett, S.J. Some Recommendations on the Standardization of Impression Creep Testing, ECCC Creep Conference, 21–23 April 2009, Zurich.
3. Brett, S.J.; Rantala, J.H.; Holmström, S. Practical application of impression creep data to power plant, in proceedings of Baltica IX, Intl. Conf. on Life Management and Maintenance for Power Plants, 11-13 June 2013, Eds. Auerkari, P.; Veivo, J. Helsinki-Stockholm-Helsinki, 2013.
4. Holmström, S. Engineering tools for robust creep modeling. Doctor's dissertation, Aalto University, Espoo, 5 Febr. 2010. VTT, Publication 728 (2010), VTT, Espoo, 94 + 53 p, ISBN 978-951-38-7378-3.

The impression creep Monkman Grant relationship

S.J. Brett [1*]

[1] Nottingham University, UK
[*] Correspondence: steve.brett456@btinternet.com; Tel.: +44-124-981-1551

Abstract

Impression creep testing is an established small-scale testing technique in which the indentation rate of a rectangular indenter can be converted into equivalent creep strain rate. It is a versatile technique in that, once a stable indentation rate is established, either the stress, temperature, or both, can be varied to provide data under multiple test conditions on the same specimen. It does not however produce a specimen failure. In order to overcome this limitation, use can be made of an empirical relationship between the creep strain rate obtained in the impression test and the rupture life obtained in a conventional uniaxial creep test at the same stress and temperature. This relationship, termed the Impression Monkman Grant relationship, has been applied successfully to grade 91 steel where it has been shown that rupture life predicted from impression testing is in good agreement with actual rupture life obtained by conventional uniaxial testing. The relationship has proved particularly useful for plant application in situations where mis-heat treated grade 91 pipework with lower than expected creep strength has been encountered, requiring an estimate of creep strength to justify continued operation in service.

Keywords: Small Scale Creep Testing; Impression Creep Testing; Grade 91 Steel; Monkman Grant Relationship; Mis-heat Treatment

1. Introduction

Impression creep testing was originally developed at Nottingham University in the UK primarily to obtain creep data from different microstructural regions within weldments to be used in finite element modelling. As a result, the technique is supported by a substantial body of theoretical work and full details about specimen preparation and the testing technique are available [1]. In recent years it has become a useful method of evaluating the creep strength of grade 91 materials in high temperature steam pipework and headers, particularly where routine inspection/on-site metallography has indicated the possible presence of materials with inadequate properties [2][3].

As illustrated in Fig.1, the impression creep test uses a nickel base superalloy rectangular indenter of width **d** to load the specimen of dimensions **w** x **w** x **h** at high temperature. The most commonly used specimen dimensions are **w** = 10mm, **h** = 2.5mm, for which **d** = 1mm, or **w** = 8mm, **h** = 2mm, for which **d** = 0.8mm. Where, as is often the case, the material to be tested needs to be obtained from a plant component using a small-scale on-site sampling technique such as scoop sampling, the smaller size is often preferred, requiring as it does, less material removal.

Once the impression creep indenter is fully embedded in the specimen, the test generally achieves constant, or near constant, rate of indentation with time within a test time of 350-400 hours. The measured indentation rate, typically over the last 100 hours of the test, can then be converted into an equivalent creep strain rate using conversion factors calculated from a finite element model developed by Nottingham University (dividing by 2.180 for 10x10x2.5mm specimens or by 1.744 for 8x8x2mm specimens [4]). A useful advantage of this test method is that, after the creep strain rate has been obtained in this way, either the stress, temperature, or both, can be altered to provide additional creep strain rates at alternative test conditions. This means that creep strain rate data which might be obtained from a conventional uniaxial multi-specimen iso-stress or iso-thermal creep test programme can be obtained from a single impression creep specimen.
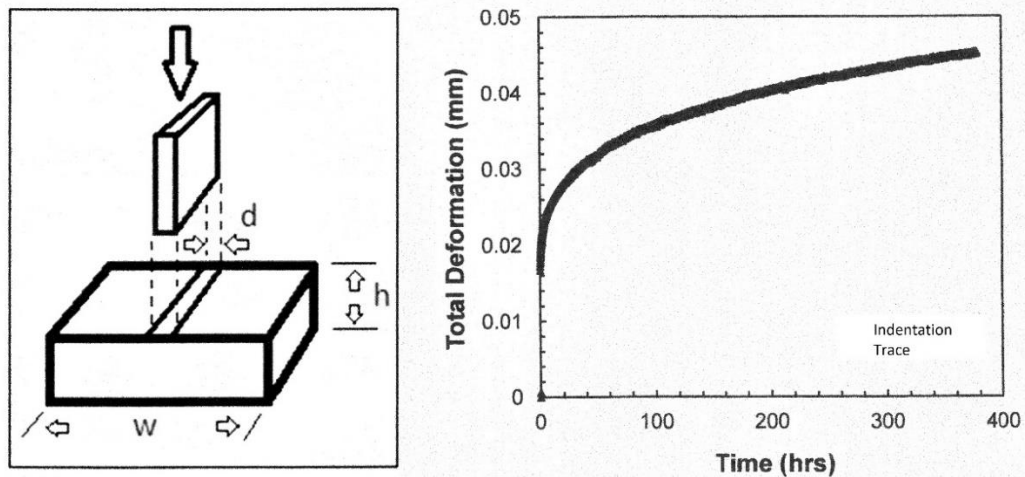
Figure 1. Geometric set-up of the impression creep test with a typical indentation trace.

2. Rupture Life Prediction using Impression Data and the Conventional Monkman Grant Relationship.

A potential disadvantage of the impression creep test is that it does not produce a specimen failure. However, the equivalent uniaxial rupture life corresponding to each impression creep strain rate measured can be estimated via an empirical relationship between creep strain rate and uniaxial rupture life, such as Monkman Grant. The requirements for this approach to be valid are: (a) that the uniaxial minimum creep strain rate and impression creep strain rate should be interchangeable and (b) that the material uniaxial minimum creep strain rate and the uniaxial rupture life must obey the particular Monkman Grant equation adopted.

A first attempt at this approach was made using the Monkman Grant relationship for P91 material derived by Parker [5]. Based on data produced by Spigarelli, Kimura and Ellis, this relationship was adopted because it was also found to provide a good fit to the present author's P91 uniaxial data:

$$\text{MCR} = 0.1 \, t_f^{-1.16} \tag{1}$$

where MCR is the minimum creep strain rate (per hour) and t_f is the rupture life (in hours) in conventional uniaxial creep testing.

A study looked at three different grade 91 materials with a wide range of creep strengths. For all three materials the rupture life predicted from impression creep data in combination with the Parker Monkman Grant relationship and the uniaxial rupture lives actually measured were found to be in good agreement [6].

3. Limitations to the use of the Conventional Monkman Grant Relationship

A limitation to the approach was however identified in that uniaxial minimum creep strain rates and impression creep strain rates were found to diverge at the highest stress levels. This is illustrated in Fig.2 below for one of the materials, Bar 257, a weak forging material which had been subjected to substantial investigation. It can be seen that the two measurements of strain rate are in good agreement, and arguably interchangeable, in the stress range 75-135MPa at 600°C. This is not necessarily so at higher stresses however, where the single impression strain rate obtained in this range falls significantly below the equivalent uniaxial minimum creep rates.
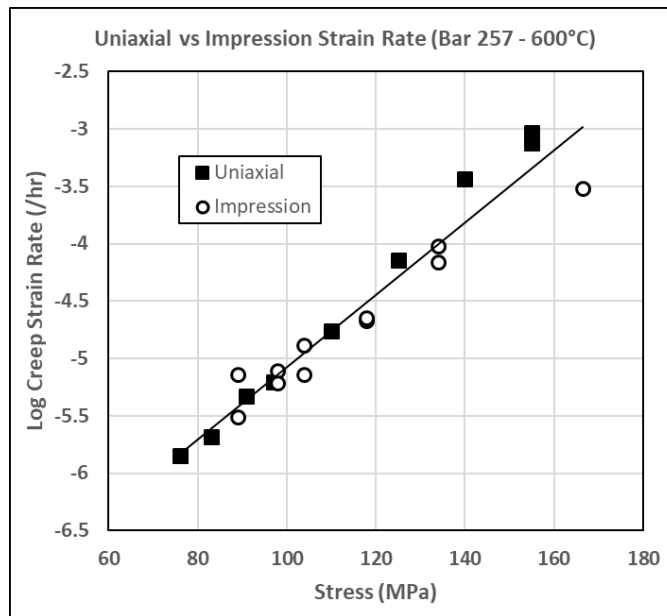
Figure 2. Uniaxial minimum creep strain rate and impression creep strain for Bar 257.

This region corresponds to the uniaxial tests with the highest elongations at fracture and is found to be a more generally observed effect when testing materials with high ductility. Two other examples of materials exhibiting high ductility at fracture are shown in Figs 3 and 4. Fig.3 shows uniaxial and impression data on ex-service 2Cr weld metal tested at a range of stresses at 570°C (a typical operating temperature for this material in the UK). The ex-service weld metal was found to be significantly weaker than weld metal of this type entering service. While impression creep strain rates and uniaxial minimum creep rates appear to be converging as stress approaches the relevant hoop stress typical of service (40MPa), they increasingly diverge as stress rises.
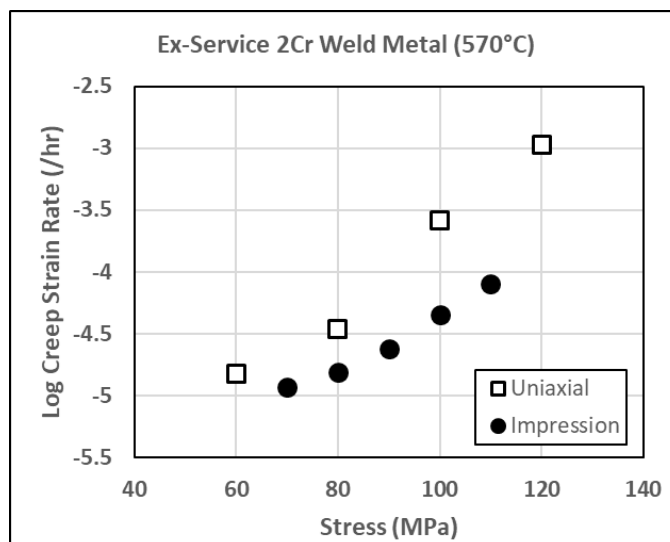
Figure 3. Uniaxial and impression strain rates for a ductile ex-service 2Cr weld metal.

Fig.4 shows uniaxial and impression data on a mis-heat treated grade 91 material in a 100% Ferrite metallurgical condition at a range of temperatures at 76MPa, a stress level typical of the hoop stress for grade 91 material in service in the UK. It can again be seen that, while impression creep strain rates and uniaxial minimum creep rates converge at the lowest strain rates, they increasingly diverge as the strain rates increase, in this case with increasing test temperature.

It should be explained that, while 100% Ferrite is clearly an aberrant material condition for grade 91, it is unfortunately of interest to plant operators because the widespread presence of such material in service has been established in the UK and elsewhere [2][3]. This type of microstructure can be created either where tempering of parent material or post weld heat treatment of a weld overshoots sufficiently into the austenitic range to remove

Martensite before falling back to the correct heat treatment temperature range. Under these conditions the Martensite is not reformed on cooling to ambient.
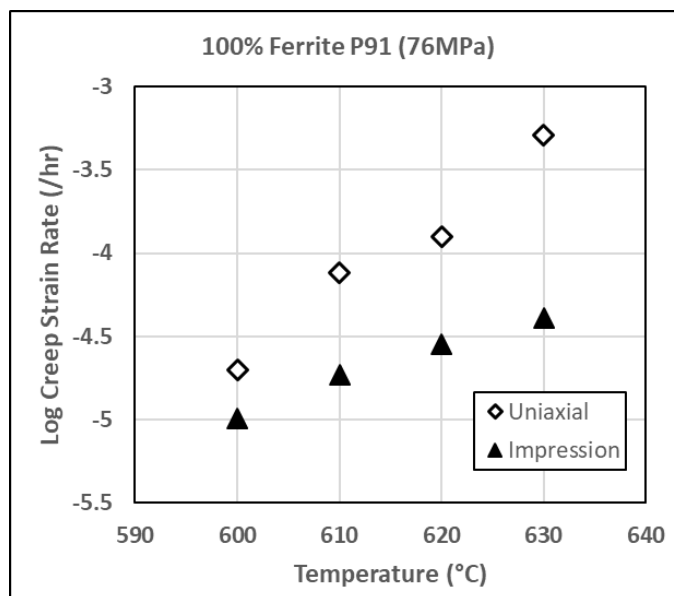
Figure 4. Uniaxial and impression strain rates for a mis-heat treated ductile 100% Ferrite grade 91 material.

An explanation of the behavior shown in Fig.3 and Fig.4 lies in the fact that the conventional uniaxial creep test is a constant load test in which the axial stress increases during the test as the specimen elongates and the cross section reduces. The impression test in contrast is a constant stress test. The uniaxial minimum creep strain rate and the impression creep strain rate are therefore being measured at different effective stress levels. As illustrated schematically in Fig.5, where the uniaxial ductility is low or moderate (e.g. where the strain at the point of measurement is less than 1%), the reduction of cross section at the point of measurement may be small enough to be ignored. In high ductility materials the reduction of cross section at the point of measurement may be more substantial.
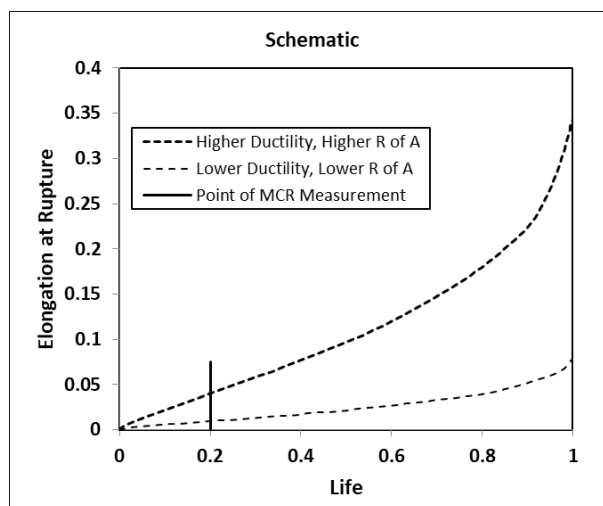
Figure 5. Measurement of minimum creep strain rate in uniaxial specimens of differing ductility.

The issue has particular relevance in the case of mis-heat treated grade 91 in a 100% Ferrite metallurgical condition. The high ductility of this type of material (generally >90% reduction of area at failure) means that the measured uniaxial minimum creep strain rates will always be significantly higher than the measured impression creep strain rates.

A further complication arising with 100% Ferrite grade 91 is that conventional uniaxial creep tests on material in this condition do not obey the conventional Monkman Grant relationship (equation 1 above). This is illustrated in Fig.6 below.

Figure 6. Conventional Monkman Grant data for two 100% Ferrite P91 materials compared to the Parker relationship for normal martensitic P91 (equation 1).

4. Rupture Life Prediction using Impression Data and the Impression Monkman Grant Relationship.

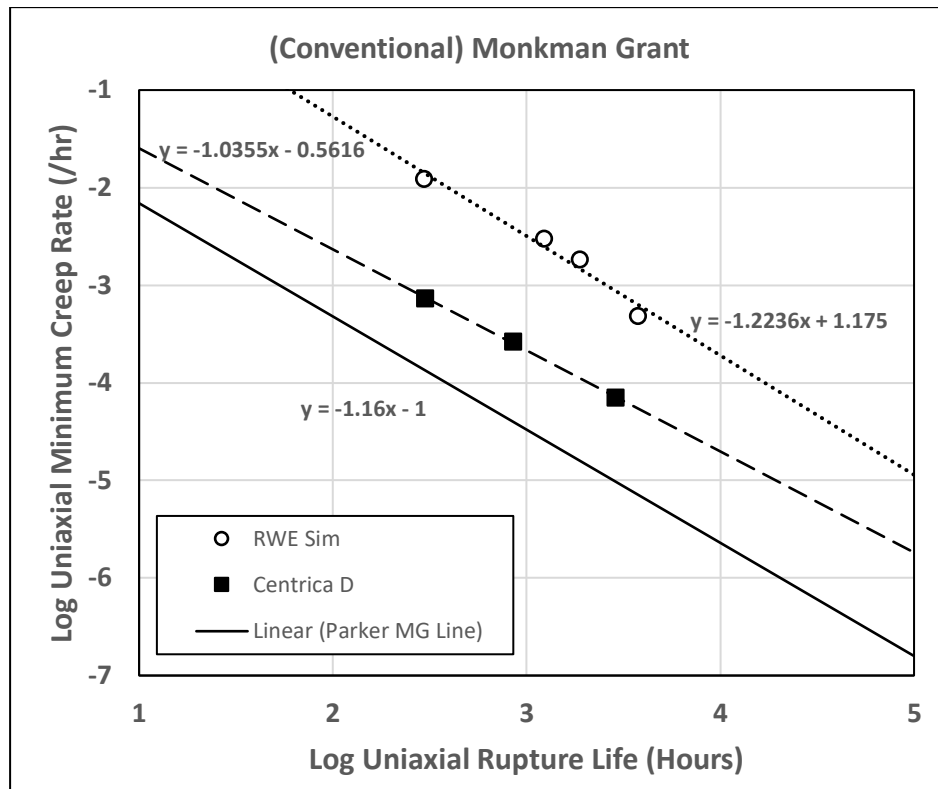Given these anomalies, it was clear that the use of impression creep strain data in lieu of uniaxial minimum creep strain rate and a conventional Monkman Grant relationship would not be a viable approach for 100% Ferrite grade 91. The widespread presence of this form of mis-heat treated material on plant however necessitated that an equivalent approach be developed. This led to the concept of an Impression Monkman Grant relationship, in which the measured impression creep strain rate could be correlated directly with uniaxial rupture life obtained at the same test conditions. It was argued that, provided a consistent relationship of this type could be demonstrated, it would no longer be necessary either for impression and uniaxial strain rates to be interchangeable or for the material to obey the conventional Monkman Grant relationship.

4.1. Impression Monkman Grant Utilising Martensitic Grade 91 Data

To generate an Impression Monkman Grant relationship ideally requires "paired values" of impression creep strain rate and uniaxial rupture life at each of the test conditions. In the absence of such data, provisional use was made of the Bar 257 data shown in Fig.2.

As a first step, the uniaxial rupture lives of the Bar 257 uniaxial tests were compared to those predicted for grade 91 material with mean properties. Although in principle any suitable assessment for mean rupture life could have been used, for the purposes of this exercise the Cipolla 2005 assessment was adopted (using the full version of the equation, as shown in [3]). The stress of each of the Bar 257 uniaxial tests was compared to the stress which would have produced failure in the same time for material of mean properties. The average strength level was found to be Mean-21%. The Cipolla equation, with this correction factor on stress, was then used to estimate a rupture life at each of the available impression creep strain rates for Bar 257 to produce Fig.7 below. This represents the

Impression Monkman Grant relationship for Bar 257, linking the impression creep strain rate directly to the corresponding uniaxial rupture life.
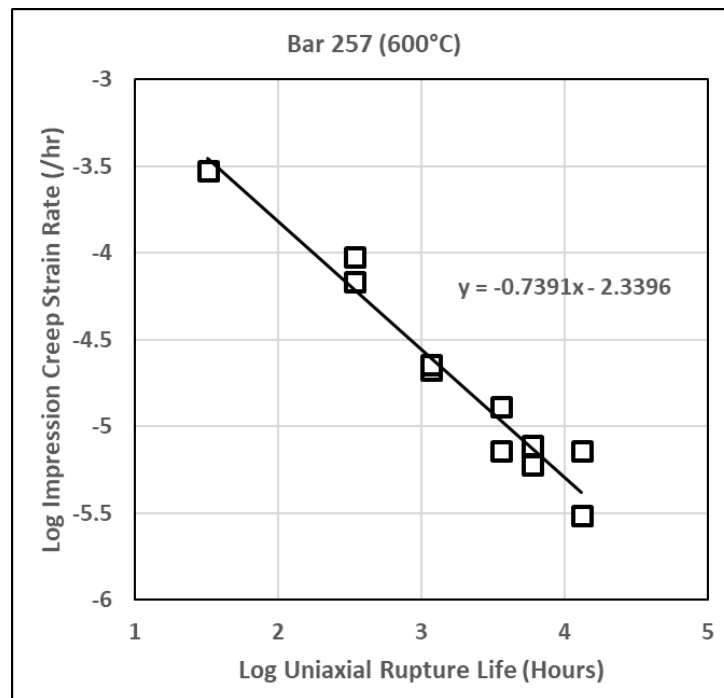
Figure 7. The Impression Monkman Grant relationship for Bar 257, comparing measured impression creep data to interpolated values of uniaxial rupture life at the same stress and temperature.

The equation derived for Bar 257 is:

$$ICR = 0.004575 \ t_f^{-0.7391} \tag{2}$$

where ICR is the impression creep strain rate (per hour) and t_f is the rupture life (in hours) in conventional uniaxial creep testing at the same stress and temperature.

This equation has been applied successfully to grade 91 materials sampled from plant and impression creep tested [2][3]. Additional data obtained for aberrant 100% Ferrite grade 91 materials has however allowed an alternative relationship to be produced using "paired" values, i.e. impression creep strain rates and uniaxial rupture lives for the same materials at the same test conditions. This is shown in the next section.

4.2. Impression Monkman Grant Utilising 100% Ferrite Grade 91 "Paired" Data

The currently available data for for 100% Ferrite materials using paired values are shown in Fig.8. The equation derived is:

$$ICR = 0.0057597 \ t_f^{-0.7265} \tag{3}$$

where ICR is the impression creep strain rate (per hour) and tf is the rupture life (in hours) in conventional uniaxial creep testing at the same stress and temperature.

This is very similar to equation 2, which is represented by the broken line in Fig.8. In fact, the lines are so close that it is possible that the underlying relationship is the same for both martensitic and 100% Ferrite materials, although further data will be required to demonstrate this. A key point to note is that the wide spread of data seen in Fig.6 for conventional Monkman Grant is not shown in Fig.8 for Impression Monkman Grant. The Impression Monkman Grant relationship appears to be far less sensitive to microstructural condition.
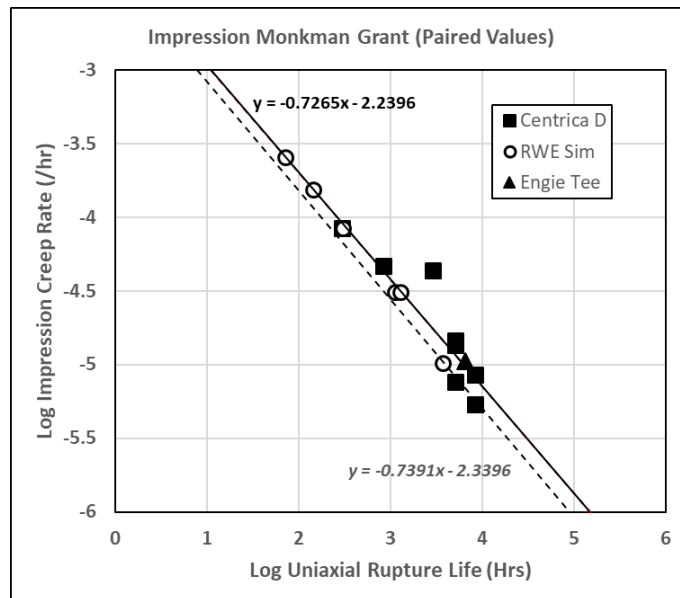
Figure 8. The Impression Monkman Grant relationship for 100% Ferrite grade 91 materials, using paired values of measured impression creep strain rate and measured uniaxial rupture life obtained at the same the same test conditions.

Equation 3 can be used as an alternative to Equation 2 to convert available impression data into predicted uniaxial rupture life to be compared to measured rupture life. This is shown in Fig.9 for two examples of aberrant 100% Ferrite grade 91 material and two examples of martensitic grade 91 material: Bar 257 and an as-received pipe material identified as 2328. The lines drawn for each material are the average strength levels relative to the mean derived from the uniaxial data. It can be seen that the uniaxial data points and those estimated from the impression data are scattered more or less uniformly around the lines and in good agreement.
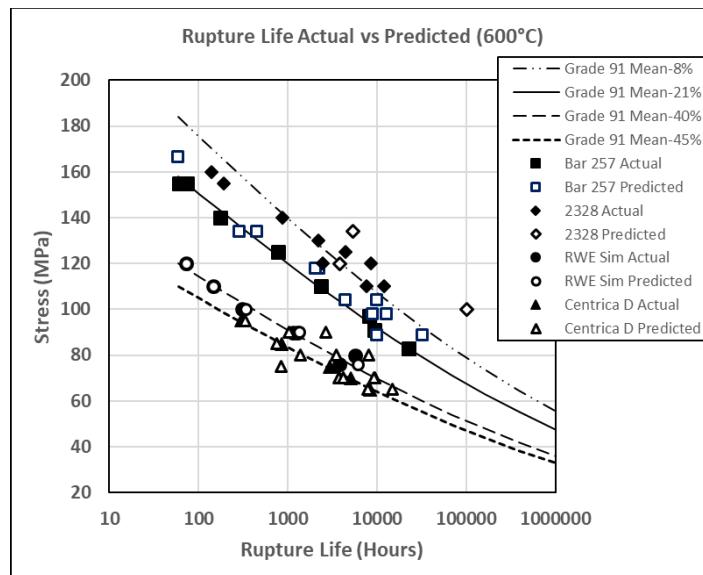
Figure 9. Uniaxial rupture life predicted from impression creep data and the Impression Monkman Grant relationship (equation 3) compared to measured values of uniaxial rupture life for two 100% Ferrite grade 91 materials, the martensitic material Bar 257, and a martensitic pipe material 2328.

An alternative comparison is shown in Fig.10, where the average strength values and standard deviations of the two sets of data are compared for each of the materials.
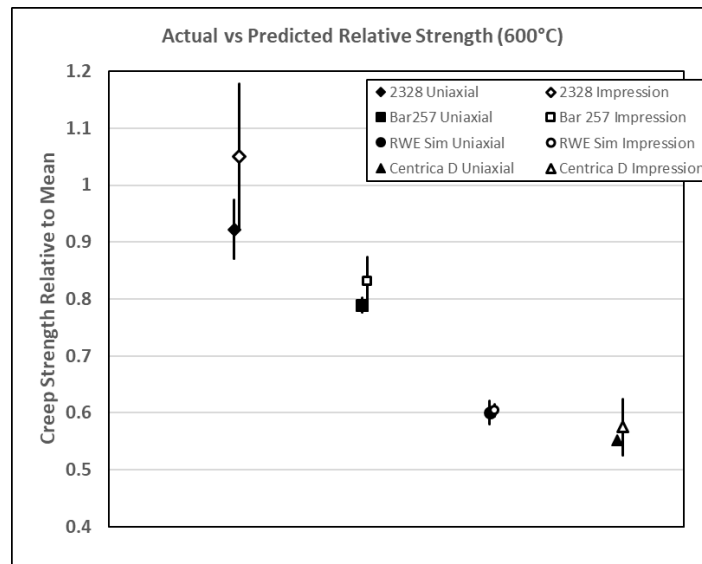
Figure 10. Creep strength relative to the (Cipolla 2005) Mean predicted from impression creep data and the Impression Monkman Grant relationship (equation 3) compared to measured values of uniaxial rupture life for two 100% Ferrite grade 91 materials, the martensitic material Bar 257, and a martensitic pipe material 2328.

Using the equation for mean grade 91 rupture life, either Equation 2 or Equation 3 can be used to predict corresponding lines of impression creep strain rate at different strength levels with reasonable accuracy. This is illustrated in Fig.11, which shows all the impression data currently available for 100% Ferrite grade 91 compared to predicted rates. The strength of this microstructural condition falls broadly within the range Mean-35% to Mean-50%, regardless of which Impression Monkman Grant equation is used.
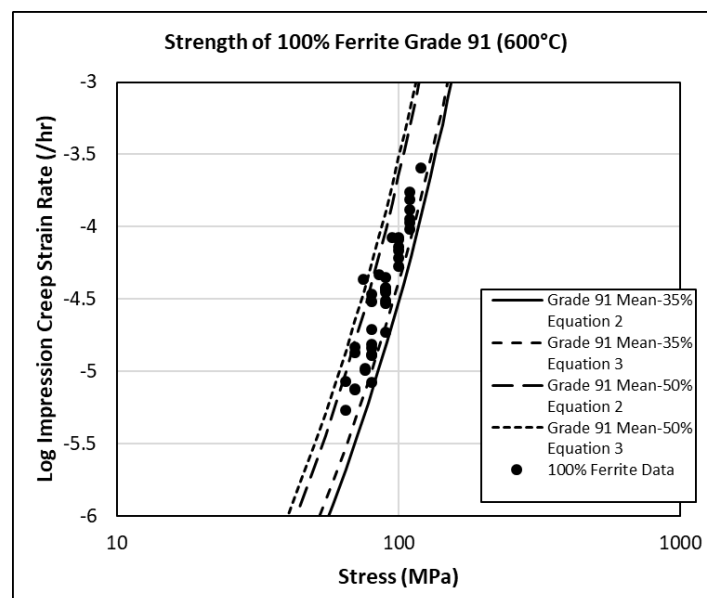
Figure 11. Impression creep data for 100% Ferrite grade 91 compared to impression creep strain rate predicted using Equations 2 and 3.

5. Discussion

The use of an Impression Monkman Grant relationship is a practical means of converting impression creep strain data into estimated uniaxial rupture life.

Under test conditions at which impression creep strain rate and uniaxial minimum creep strain rate can be regarded as interchangeable, the Impression Monkman Grant relationship and the conventional uniaxial Monkman Grant relationship will predict the same uniaxial rupture life from the same measured creep strain rate. This has been found to be the case for example both for ex-service CrMoV and grade 91 in the normal martensitic condition

in the lower stress and/or lower temperature test range. It is not however the case for these two materials in the higher stress and/or higher temperature test range, where impression strain rate is found to be lower than the minimum uniaxial minimum creep strain rate. These test conditions correspond to the shortest life uniaxial tests and to uniaxial specimens failing with high ductility.

This divergence between the strain rates is a greater problem for materials which fail generally with high ductility over the normal test range. This has been found to be the case for example both for ex-service 2Cr weld metal and grade 91 in the aberrant 100% Ferrite condition. The latter material is particularly important for plant operators because of the widespread presence of such material currently in service.

Focusing on grade 91, for the weaker end of the normal martensitic range, and the weak aberrant condition, both Equation 2 and Equation 3 will give reasonably accurate estimates of rupture life for both types of material using measured impression creep strain rates at 600°C. Where the material under investigation is martensitic, the previously published Equation 2, based on a weak martensitic material, may be more appropriate. This equation will give slightly conservative estimates of uniaxial rupture life for the 100% Ferrite condition. Where the material under investigation is 100% Ferrite, Equation 3, based on this type of microstructure, may provide a more accurate estimate of uniaxial rupture life.

References

1. Hyde, T.H.; Sun, W.; Brett, S.J.: Application of Impression Creep Test Data for the Assessment of Service Exposed Power Plant Components. 1st International Conference: Determination of Mechanical Properties of Materials by Small Punch and other Miniature Testing Techniques, Ostrava, Czech Republic, August 31 - September 2, 2010,
2. Lant, T.; Brett, S.J.; Clark, A.; Walton, R. Creep Testing of a Seam Welded Grade 91 Hot Reheat Bend with Aberrant Microstructure. 4th ECCC Conference: Creep & Fracture 2017, Dusseldorf, Germany, September 10-14, 2017.
3. Brennan, K.; Brett, S.J.; Eaton-Mckay, J. Impression Creep Testing of Aberrant Grade 91 Material Removed from Piping in Service. 4th ECCC Conference: Creep & Fracture 2017, Dusseldorf, Germany, September 10-14, 2017.
4. Hyde, T.H.; Sun, W.: Evaluation of Conversion Relationships for Impression Creep Test at Elevated Temperatures. International Journal of Pressure Vessels and Piping 86 pp.757-763, 2009.
5. Parker, J. EPRI, Personal communication.
6. Brett, S.J. The Practical Application of Small Scale Sampling and Impression Creep Testing to Grade 91 Components. EPRI – 7th International Conference on Advances in Materials Technology for Fossil Power Plants, Hawaii, October 22-25, 2013.

Commercialisation of impression creep testing

T. Gallacher [1*], J. Eaton-McKay [1], S. Brett [2], S. Jacques [1], C. Austin [1] and A. Wisbey [1]

[1] Wood plc, Walton House, Faraday Street, Birchwood Park, Warrington, Cheshire, UK, WA3 6GA
[2] Steve Brett Consultancy Ltd, UK
* Correspondence: tom.gallacher@woodplc.com; Tel.: +44-1925-462786

Abstract: Impression creep testing is a technique in which the deformation resulting from load applied via a rectangular indenter can be converted relatively straightforwardly into a proxy for creep minimum strain rate. This offers a valuable route to assess the creep performance ranking of in-service high temperature plant materials for a number of reasons: the small specimen size makes extraction feasible without significantly affecting the structural integrity of plant; the possibility to test a single specimen at several stresses or temperatures enables multiple assessments; and, increasingly, the maturity of underlying technical understanding and quality of results increases confidence in the technique. However, the method is not without challenges, in particular the capital and running costs associated with servo-electric test rigs. Development of a bespoke deadweight loaded testing system at Wood (formerly Amec Foster Wheeler) has enabled commercially sustainable impression creep testing, which has been successfully applied to ex-plant Grade 91 steel.

1. Introduction

The proposition to assess material creep properties and thus remnant life from small scale specimens is clearly attractive to high temperature plant operators, since it is possible to extract and test material without significantly affecting the structural integrity of in-service plant. However, there are some concerns regarding the transfer of such techniques into the commercial sector. Reservations broadly fall into two categories: underlying technical understanding of test methods and interpretation of results; and equipment, costs and other commercial drivers. Research into various techniques has been ongoing for many years [1]; several are now in the infancy of their application. Wood has focused on consolidating the considerable foundational understanding of the impression creep test technique, with the aim of developing the method to a level of maturity that enables initial sustainable commercial application.

2. Background to impression creep testing and potential advantages

There have been significant efforts on the provision of a sound theoretical and practical understanding of impression creep testing; much of this work has been led by Nottingham University in collaboration with UK power utilities, especially RWE nPower [1, 2, 3, 4].

Impression creep offers an alternative to conventional uni-axial creep testing to assess remnant life and determine material creep strength, using small-scale specimens. Typically, these specimens are 10x10x2.5mm, or 8x8x2mm, and so can be machined from samples extracted from plant components using scoop sampling or other on-site techniques. Importantly, when underpinned by appropriate engineering critical assessments (ECAs), specimen extraction need not significantly reduce the structural integrity of in-service plant.

A constant compressive load is applied to the centre of the specimen face, across the full width, via a 1mm or 0.8mm wide (depending on specimen geometry, above) rectangular indenter platen. It is important the indenter material has a significantly higher creep strength than the specimen. Thus for testing conventional power plant steels, the indenter has been produced from highly creep resistant nickel base superalloys (e.g. Nimonic 115) and no clear evidence for deformation of the indenter following testing has been observed. Generally, in laboratories around the world, this loading is carried out using servo-electric test frames [5]; Wood have also successfully designed, built and commissioned a bespoke deadweight-loaded impression creep rig, which is described below.

The indentation deformation in the specimen is measured throughout the test by high temperature extensometry; in Wood's laboratories, this uses a side-loaded extensometer with twin-arm ceramic probes mounted immediately adjacent to the top and bottom of the specimen and indenter, as shown in Figure 1.
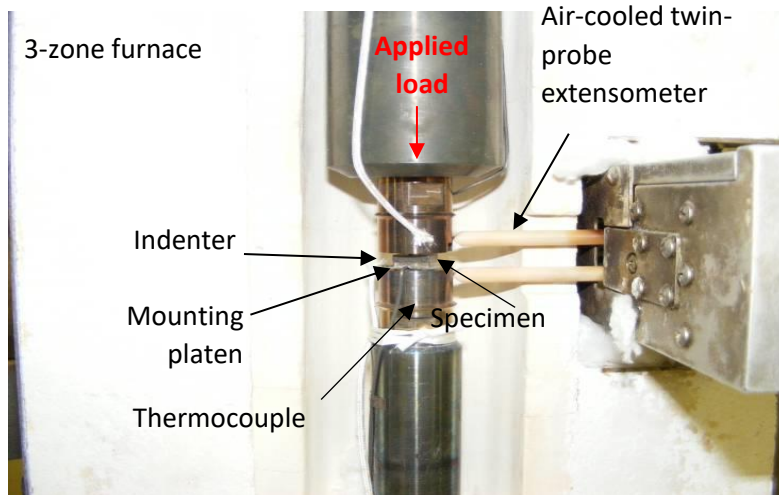
Figure 1. The impression creep testing arrangement used at Wood.

The specimen is heated to the test temperature; in Wood's arrangement using a three zone furnace and the temperature monitored with two calibrated N-type thermocouples, mounted vertically adjacent to the specimen on the loading bars. Specimen temperature is thus monitored and controlled throughout the test. Following a soaking time to permit the temperature to stabilise, typically one hour, the full test load is then applied to the specimen and the deformation measured.

Following loading and full mating of the indenter and specimen, a constant rate of indentation is achieved, typically within ~400 hours. This indentation rate, by convention measured over the final ~100 hours, has been correlated to the equivalent uni-axial creep minimum strain rate using conversion factors related to the specimen geometry, derived from finite element analysis (FEA) [4] and hence permitting direct comparisons. Thus the equivalent uniaxial stress is given by:

$$\sigma_{IC} = \eta P, \tag{1}$$

where P is the pressure under the indenter (MPa) and η is a specimen geometry specific constant derived from FEA. Similarly the equivalent uniaxial strain rate is given by:

$$\dot{\varepsilon}_{IC} = \dot{\Delta}_{IC}/\beta d, \tag{2}$$

where $\dot{\Delta}_{IC}$ is the linear indentation deformation rate (mm/hr) measured in the impression creep test, d is the indenter width (mm), and ß is a specimen geometry specific constant derived from FEA. The equivalence between impression creep and uni-axial creep is only between impression creep linear deformation rates and uni-axial creep minimum strain rates; no inference can be made more generally between impression creep data and uni-axial strain.

Typical values of the constants for the specimen geometries and indenter widths listed above are $\eta = 0.43$ and $\beta = 2.18$ [4]. It is worth noting that if the specimen geometry or material are changed significantly then further FEA is required to obtain the necessary constants for the correlations.

No formally recognized standards currently exist, but a code of practice [2] has been produced in an attempt to clarify the requirements of testing equipment and encourage a united approach to testing and subsequent analysis.

Once a stabilised indentation rate has been achieved and the associated equivalent uni-axial creep minimum strain rate derived, it is then possible to change either the test temperature or stress without interruption. Continued measurement of the indentation rate then provides additional analyses under alternative conditions; typically this can be repeated after 150 hours. Both changes in stress and temperature have been successfully applied to impression creep tests.

Recent tests at Wood have generally lasted 800 hours, comprised four 'steps', and provided four creep rate data points from each specimen, although some have produced up to eight. It is possible to continue testing until the total indentation deformation is approximately 10% of the specimen thickness, when it becomes clear the conversion to equivalent uni-axial creep data becomes invalid. An example of such an indentation vs time trace, taken from a recent test at 600°C and equivalent uni-axial stresses from 80 to 110MPa, on 100% ferritic Grade 91 material extracted from a combined cycle gas turbine plant component in the UK, is shown in Figure 2. It should be noted

that the four impression creep steps, each giving equivalent uni-axial creep minimum strain rates from which to assess material strength, were measured in approximately 800 hours, a time that could typically be required for an initial conventional creep rupture trial (or "sighter") test.
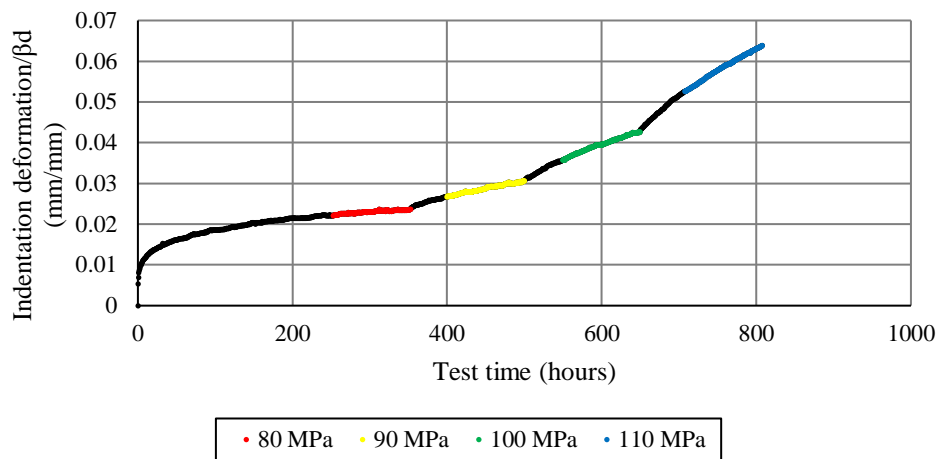
Figure 2. Four steps of indentation deformation scaled by geometric conversion factors such that the gradients of the coloured linear regions are equal to the equivalent uni-axial creep minimum strain rates, for the various equivalent uni-axial stress applications.

An example of changing temperatures during a number of impression creep specimens of ex-service (from UK nuclear power generation plant) austenitic 316H stainless steel is shown in Figure 3. Here tests were commenced at 525°C but once a uniform indentation rate was achieved, then the temperature was reduced to 480°C. The equivalent uniaxial creep rates were determined for each step, as noted above. This work showed consistent reductions in creep rate associated with the temperature reductions, as might be anticipated. Where the temperature was subsequently returned to the initial 525°C, then the creep rate was found to return the original creep rate.

A further potential benefit for impression creep, is the ability to evaluate specific regions of metallic structures, for example welds and their associated heat affected zones (HAZs).

These examples demonstrate a significant commercial benefit of the technique over conventional creep testing: the ability to produce results relatively quickly and for multiple loads and temperatures from a single sample.
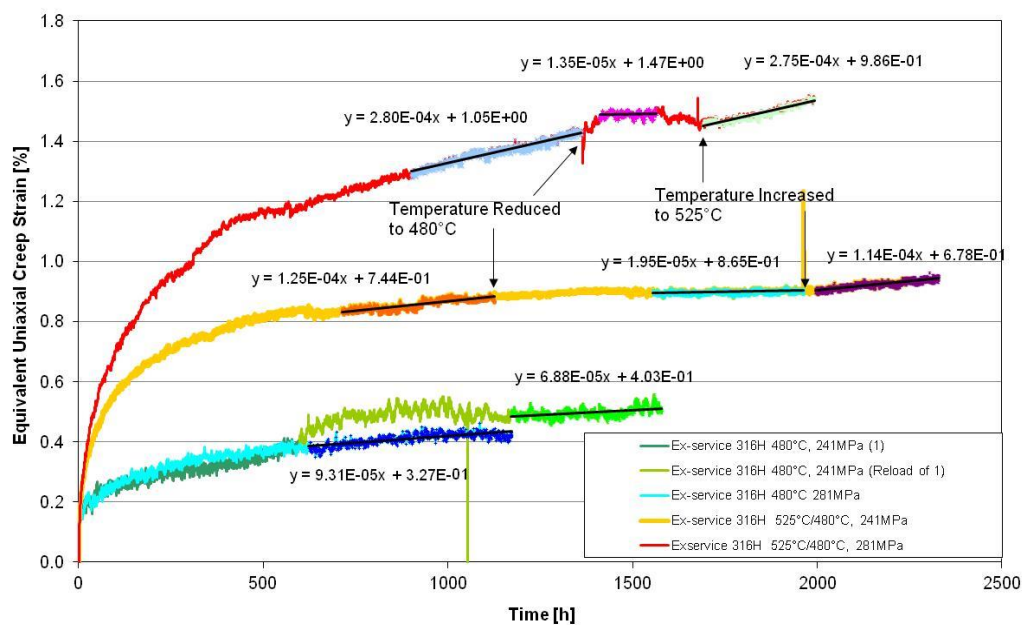
Figure 3. The equivalent uniaxial deformation behaviour for ex-service 316H stainless steel material, subjected to impression creep studies at 525°C, along with some temperature change trials to 480°C.

3. Commercial applications for impression creep testing

Assessment of in-service plant to determine remnant life is of obvious significant industrial interest, particularly to high temperature plant operators, where plant life extension or confirmation of existing plant life is needed. Impression creep testing offers an approach to such an assessment. An example of this type of work is the assessment of Grade 91 9Cr steel, one of the most widely used of a class of so-called Creep Strength Enhanced Ferritic (CSEF) steels within conventional power generation plant components in the UK and abroad. This material has been the focus of much study using impression creep testing [3, 6, 7]. One of the reasons for the interest in assessing this material has been the finding that Grade 91 steel in service in the UK was introduced in a number of microstructural conditions. In addition to the preferred martensitic structure, aberrant ferritic and mixed martensitic/ferritic microstructures have been observed [8]. The weaker ferritic material is worthy of particular scrutiny, since it severely limits creep performance. The widespread occurrence of this type of material has been established and poses a significant challenge to many plant operators [9].

For the assessment of remnant life the impression creep test is used to generate equivalent conventional uniaxial minimum creep rates. In turn these can be used with a Monkman-Grant type relationship to determine a rupture life, with the equation:

$$\dot{\varepsilon}_{min}{}^{\alpha}.t_r = C, \tag{3}$$

where $\dot{\varepsilon}_{min}$ is the minimum creep rate (mm/mm/hr), t_r is the rupture life (hr), and α and C are constants. The use of this approach has been validated by the undertaking of paired conventional creep rupture testing alongside impression creep tests [10]. A reasonably well established Monkman-Grant relationship for Grade 91 steel exists, based upon conventional creep testing, and this has been modified to give an Impression Monkman-Grant relationship, which has been shown to hold for impression creep testing of both martensitic and aberrant ferritic Grade 91 steel [11]:

$$\dot{\varepsilon}_{IC} = 0.004575 t_r{}^{-0.7391}, \tag{4}$$

where $\dot{\varepsilon}_{IC}$ is an equivalent uni-axial creep minimum strain rate derived via Equation 2 from an impression creep test (mm/mm/hr), and t_r is the equivalent uni-axial creep failure time (hr). This then permits the prediction of a conventional creep rupture life but based upon the much shorter duration impression creep tests. At the same time the fit of the experimental data to the established Monkman-Grant relationship can be determined and if acceptable, can provide confidence in the use of this approach. Where the correlation between the experimental and literature equations is not strong, further work is required to determine a better fit to the test data.

Clearly equations (3) and (4) only give rupture lives for the test temperature but the relationship between stress and life is also required to enable the impression creep data to be utilised more widely to assess plant specific creep rupture life times. Again with Grade 91 this has been enabled by an existing relationship between the rupture life, mean stress and temperature [12] of the form:

$$\log t_r = \left((263.8 + 217.1 \log \sigma - 212.8 (\log \sigma)^2 + 84.9 (\log \sigma)^3 - 13.2 (\log \sigma)^4).(T - 438.7)^{-0.27}\right) - 55.9 \tag{5}$$

where t_r is the rupture life (hr), σ is the mean stress (MPa) and T is the temperature (K). At the impression creep test temperature the result of equation (5) can be compared against the experimentally derived rupture data, as shown in Figure 4. Thence the stresses from equation (5), representing the mean performance of Grade 91 can be fitted to the experimental data to establish the level of difference in strengths between the experimental and predicted mean behaviour; in this case mean – 41.6%. This then allows equation (5) to be used to plot stress vs rupture time at more relevant plant operating temperatures and compared with the maximum stresses in the components of interest, hence the remaining creep endurance can be established and the potential further plant operating time.
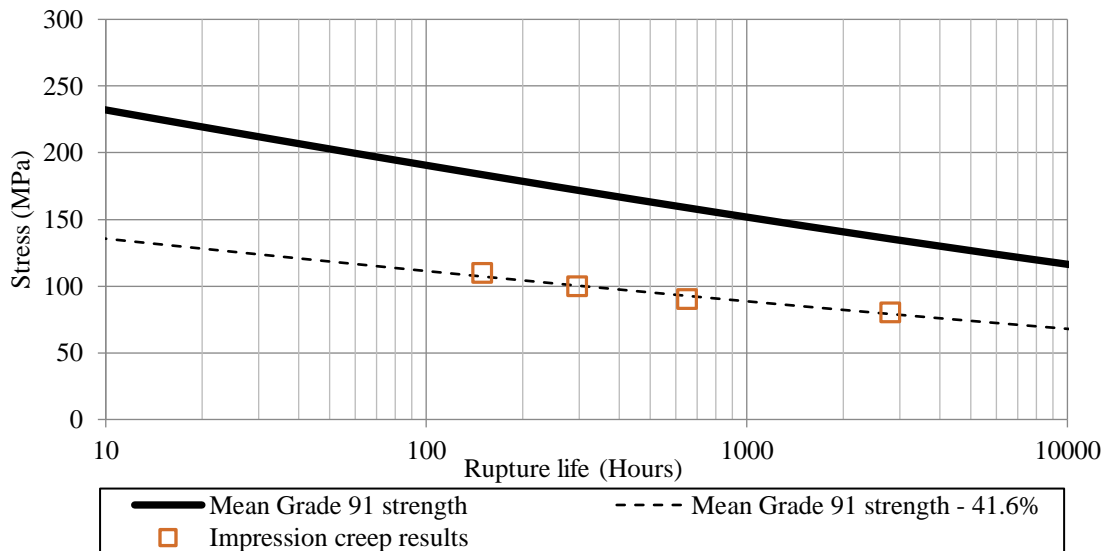
Figure 4. Comparison of impression creep derived Grade 91 rupture lives relative to mean performance for this material.

This type of assessment of creep strength relative to a known mean performance via impression creep test data can be powerful evidence for safe plant operation, and the ability to test a single specimen at multiple stresses or temperatures, maximises the value of extracted material. Where multiple specimens are available and can be tested over the same range of stresses, then such data should provide confirmation of a consistency in creep performance and confidence in the assessment of that material. To garner this type of understanding from conventional uni-axial creep testing, or other small-scale techniques, would require several tests on material from the same cast, which is not always commercially viable or indeed possible.

As with any small-scale test technique in relative infancy, concerns exist surrounding reliability of generating results and experimental scatter. However, impression creep testing is well placed to investigate and confront these concerns, since it is practical to examine creep properties of a single specimen at several conditions. Moreover, it is possible to reassess these properties by repeating steps from earlier in the test, for example by testing sequentially at 90MPa, 100MPa, 110MPa and then at 100MPa again. Previous work [13] has demonstrated that results from each step in a test are independent of previous steps, and so repeat steps are inherently expected to provide repeat results. This is a useful facet of the technique that simultaneously builds confidence in, and provides some measure of scatter of, results.

There are other potential commercial issues that drive the use of small scale testing techniques, including the ability to evaluate the limited material available in the early stages of material development activities, however, some caution is required in this area, as illustrated below in section 4.2.3.

4. Challenges to impression creep testing

4.1. Commercial challenges

Given the potential technical benefits of the impression creep test technique, and the level of maturity of underlying theoretical understanding described above, there is potential for industrial (e.g. the power utilities) appetite in increased application of the method. It is anticipated that the scope of this work will be beyond the interest of most academic and dedicated research organisations, and require take up by industrially focussed organisations, with conventional financial constraints on investment. Thus it is worth considering the financial credibility of an investment in an impression creep test station. Currently most of the impression creep test facilities have been developed around either existing servo-electric load applications frames or new low load capacity servo-electric test frames. Table 1 shows illustrative costs of procuring a new servo-electrically driven impression creep testing system. A total investment of £42,500 – 51,500 could be required to provide such a facility.

Table 1. Illustrative break-down of costs for a new commercial servo-electric impression creep facility.

Equipment	Typical cost (£)
Low load capacity servo-electric test frame	20,000
Furnace and controller	12,000
Extensometer, sensor and conditioning unit	6,000 – 15,000
Loading bars and indenter	3,000
Data recording system	1,500
Total cost	42,500 – 51,500

Set against these investment requirements, is potential income. Given the relationship to uni-axial creep tests, an initial assessment of potential income could be considered on the basis of current conventional creep strain measurement at similar temperatures (and excluding any specimen manufacturing and data reporting costs). This approach is likely reasonable given the tendency for conventional creep to set industrial expectations for impression creep testing. Recent commercial charges from a number of continental European laboratories for standard creep tests in the temperature regime of 500 – 650°C, including extensometry, indicated an hourly running rate of up to £0.70/hour. Additionally, there are costs associated with setting up creep tests; this could be up to ~£2000/year, assuming 4 – 5 tests are set up in a year. At these indicative rates, the earning capacity of a conventional creep test station would be ~£8,200/year. If it is assumed that a creep test achieves 10% profit, then a commercial organisation could expect to re-coup ~£820/year.

At a similar income level of current conventional creep testing then, it would take over 50 years to re-pay the capital investment in a new impression creep test facility. Even if higher profit levels were achieved (e.g. 20%), pay-back periods would still be significantly longer (e.g. 25+ years) than commercial organisations might require. With conventional financial constraints then, it would clearly not be feasible to make the investment required to produce a new test facility. The shorter duration of impression creep tests may allow for more test set-ups, which could supplement the testing income; this is still likely to be insufficient to achieve acceptable financial performance for most commercial organisations. A solution to this problem could be to increase the overall charges for impression creep testing.

Some consideration of aspects of the background to the current conventional creep test charges may be useful. Over the past two decades much commercial creep testing has been performed by laboratories that were originally set-up to support activities (e.g. material production, government research) other than commercial creep testing for third parties. However, as the requirement for the internal creep testing support within these organisations has diminished (e.g. as material production has declined), third party work has been attracted to supplement internal activities and help support the cost of the facility. In cases where the test facility already exists and is expected to be maintained, the charges levied for commercial creep testing for third parties did not need to reflect the level of original investment. Competition has driven prices down, to the point where one laboratory (now closed) was charging £0.14/hour for creep tests; which may not have even covered the cost of maintaining specimens at their test temperature. Such charging levels have inevitably started to set industrial expectations of costs but these suppressed prices are only sustainable whilst creep tests are required in a marketplace with excess capacity. There may be other factors that have also contributed to the relatively low current cost of creep testing but the above seems to be a strong contender to explain the testing charges now expected for creep. The unfortunate outcome now is the commercial difficulty of justifying investment in new creep equipment and modernisation of facilities. This background in conventional creep impacts small-scale creep test techniques, like impression creep, even if only by association and industrial expectation. There is thus a dual barrier to be overcome in the introduction of new creep assessments, with technical uncertainties but also financial difficulty in progressing the test technique from academia into widespread commercial operation.

To enable a more commercially practical return on investment than possible with servo-electric facilities, Wood has successfully designed, built and commissioned a bespoke deadweight loaded impression creep testing machine. This system, more akin to a conventional creep frame with an underslung lever and incrementally, manually loaded pan, incorporates a load cell to provide confidence that any frictional effects are overcome and the full test load is applied. Commissioning tests on a well-characterised cast of the 9Cr steel (Grade 91 - Bar 257) gave results consistent with those determined through servo-electric testing [5], as shown in Figure 5. Subsequent tests

on ex-service Grade 91 steel have confirmed this comparability with data previously generated using servo-electric loading frames.
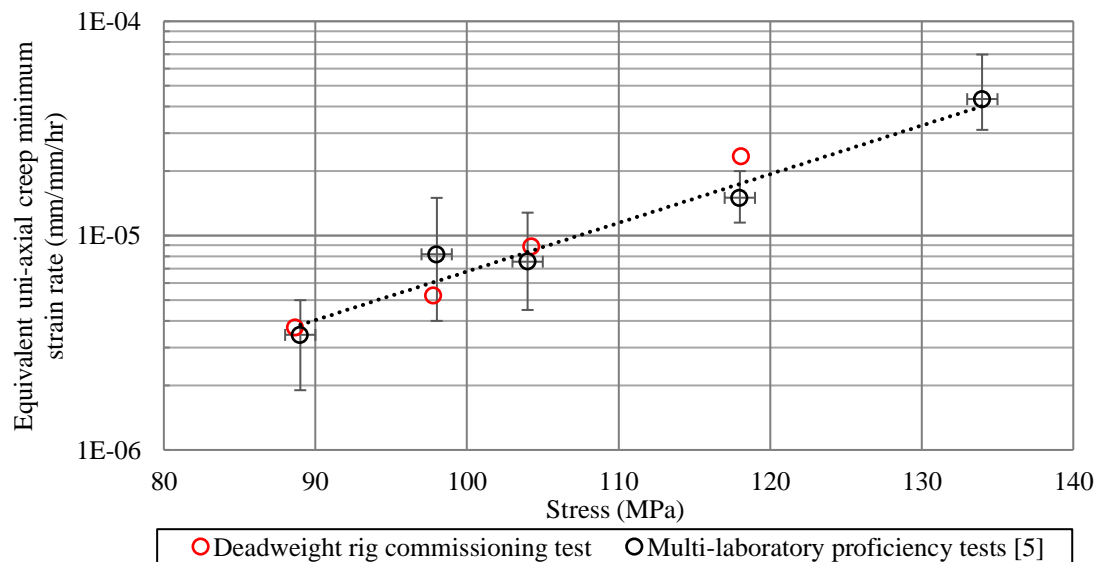

Figure 5. Bar 257 impression creep test results using Wood's deadweight loaded system and other servo-electric test frames.

4.2. Technical limitations

There are a number of potential limitations with impression creep testing, as with any small-scale technique, which must be recognised and which may inform the selection of the most appropriate test technique in different situations. Some of these issues are discussed below.

4.2.1 Compression testing

The impression creep test is only performed in compression and hence no fracture behaviour can be obtained. For materials with highly inhomogeneous deformation behaviour (especially brittle materials), alternative techniques to investigate tensile creep behaviour may be clearly advantageous.

The compressive nature of this test also leads to a limit on the depth of penetration of the indenter into a specimen where the deformation increases the effective load bearing area and hence reduces the applied stress significantly. It is currently thought that a maximum displacement of ~10% of the specimen thickness should be considered the practical limit for indentation penetration. There is not known to be an additional upper limit on test time, so long as the specimen material is unchanged due to exposure to high temperatures; tests at Wood have run for up to 2500 hours without any suggestion of test invalidity.

4.2.2 Correlation of indentation deformation to minimum creep rate only

There is a temptation to mis-interpret the indentation deformation vs time trace by associating the initial apparently reducing indentation rate (e.g. see Figure 3) with conventional uni-axial tensile primary creep deformation behaviour. However, FEA [14] has shown that the initial indentation deformation stages are more closely linked to small levels of mis-orientation between the indenter and sample surfaces, rather than primary creep. This is consistent with the observation that this initial stage of indenter deformation can be variable, even between nominally identical samples which produce similar equivalent uni-axial creep minimum strain rates. Impression creep does not provide a correlation to creep strain generally, only to the minimum creep rate of a material.

4.2.3 Material specific creep deformation behaviour

Wood has evaluated austenitic stainless steel 316H material using both uni-axial and impression creep testing. This material was tested in two conditions:

1.   Virgin tube material evaluated after cold work and simulated post weld heat treatment, and
2.   Ex-service tube material (from the UK nuclear power generation fleet).

Impression creep tests on the virgin tube material were undertaken at 525°C and a single equivalent uni-axial creep minimum strain rate was obtained from each specimen (i.e. no stepped stress tests). These creep rates are shown in Table 2 and produced no discernable trend. In some instances, increasing test stress resulted in apparently reduced deformation rates. Initially it was thought that this behaviour was associated with experimental scatter, although tests on other material, like Grade 91 steel, had shown that the general trends in deformation behaviour were well captured by impression creep testing.

Table 2. Applied equivalent uniaxial creep stress and creep rates for virgin 316H tube material, impression creep tested at 525°C.

Equivalent uni-axial creep stress (MPa)	Equivalent uni-axial creep minimum strain rate ($\times 10^{-6}$/hr)
240	0.20
240	1.77
240	2.64
240	1.82
280	0.90
320	1.69

The conventional creep deformation curves obtained from uni-axial creep tests on the same 316H tube material are shown in Figure 6. These reveal a double primary behaviour in a number of tests. Thus, the creep deformation behaviour in the initial stages of the tests was found to be highly variable, consistent with the unexpected and apparently misleading rates derived from the impression creep tests. The origin of the double primary behaviour in the virgin 316H material is not currently well understood, but may be attributed to microstructural instabilities in the as-manufactured material [15]. This hypothesis is to some extent substantiated by the uni-axial creep data obtained from the ex-service (i.e. thermally aged) material, which demonstrated a more conventional strain-time behaviour. Impression creep tests on this material are more readily understood, and the derived equivalent uni-axial creep minimum strain rates follow the ranking of applied stress, as demonstrated in Figure 3 for this material and consistent with the experience in Grade 91 steels.

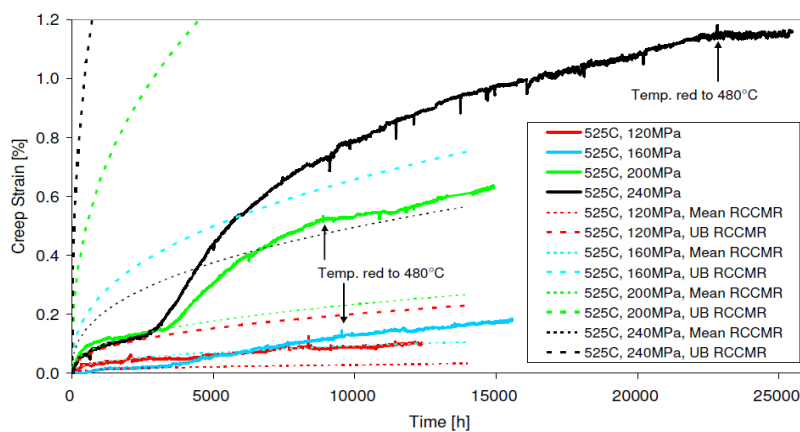**Figure 6.** Uni-axial creep deformation curves for virgin 316H material, some tests showing double-primary behaviour.

This experience emphasises the need to understand the conventional creep deformation behaviour of the test material before attempting to use relatively novel small-scale techniques. More generally, it may be that such techniques are best used to supplement, rather than replace, conventional creep testing.

4.2.4 Repeatability of data

There is currently limited direct experimental evidence of the level of repeatability, in terms of creep rates, that can be obtained from impression creep testing, thus this is an area for further development. Such information would be valuable in establishing the uncertainty of measurement for this technique.

5. Summary and Conclusions

There appear to be a number of motivating reasons to assess plant material using impression creep testing, in particular, the small specimen size and capability to test a single specimen at multiple conditions. Wood has attempted to resolve some commercial challenges associated with the method, and recognised some potential limitations. Development of a deadweight loaded testing arrangement has reduced costs sufficiently to enable commercially viable application of the technique. This has proved particularly successful in assessing ex-service Grade 91 steel in a variety of microstructural conditions from UK high temperature plant, and the underlying technical understanding of impression creep testing enables valuable creep strength assessment and remnant life determination.

References

1. Hyde, T.H.; Sun W.; Hyde C.J. "Applied Creep Mechanics". McGraw-Hill Education, 2014; pp.327-355, ISBN 978-0-07-182869-7.
2. Hyde, T.H.; Sun, W.; Brett, S.J. "Some Recommendations of the Standardization of Impression Creep Testing". Creep & Fracture in High Temperature Components Design & Life Assessment. 2, ECCC, 2009.
3. Sun, W.; Hyde, T.H.; Brett, S.J. "Application of impression creep data in life assessment of power plant materials at high temperatures". Proc IMechE Vol. 222 Part L:J. Materials: Design and Applications, 2008, pp.175-182.
4. Hyde, T.H.; Sun, W. "Evaluation of conversion relationships for impression creep rest at elevated temperatures". International Journal of Pressure Vessels and Piping 86, 2009, pp.757-763.
5. Brett, S.J.; Dyson, C.N.C.; Purdy, D.; Shingledecker, J.; Rantala, J.; Eaton-Mckay, J.; Sun, W. "Impression Creep Test of a P91 Steel: A Round Robin Programme" (under review).
6. Brett, S.J. "The practical application of small scale sampling and impression creep testing to grade 91 components". EPRI – 7th international conference on advances in materials technology for fossil power plants, Hawaii, USA, October 22-25, 2013.
7. Brett, S.J. "The application of small scale sampling and impression creep testing to power plant". ECCC conference: Creep & Fracture 2014, Rome, Italy, May 5-7, 2014.
8. Brennan, K.; Brett, S.J.; Eaton-Mckay, J. "Impression Creep Testing of Aberrant Grade 91 Material Removed from Piping in Service". 4th ECCC: Creep & Fracture 2017, Dusseldorf, Germany, Sept.10-14, 2017.
9. Brett, S.J. "Aberrant Grade 91 Pipework – Implications for Creep Life in Service". IMechE HRSG User Group presentation, Nottingham, November 21-22, 2017.
10. Brett, S.J.; Lant, T.; Clark, A. "Small scale impression creep testing of an ex-service mis-heat treated seam welded Grade 91 hot reheat bend". EPRI – 8th international conference on advances in materials technology for fossil power plants, Algarve, Portugal, October 10-14, 2016.
11. Brett, S.J. "Impression creep update", Presentation to the UK High Temperature Power Plant Forum, 39th Meeting, Arden Hotel, Solihull, UK, November 18, 2015.
12. Cipolla, L.; Gabrel, J.; "New creep rupture assessment of grade 91". ETD conference: Industry and research experience in the use of P/T91 in HRSGs/Boilers, IOM3, London, UK, December 7-8, 2005.
13. Hyde, T.H.; Sun, W. "Multi-step Load Impression Creep Tests for a 1/2Cr1/2Mo1/4V Steel at 565°C", Strain, Vol 37, 2001, pp.99-103.
14. Ren, J. "FEA study: sensitivity of initial deformation in impression creep testing to indenter and specimen alignment", private communication between LJMU and Wood.
15. Hyde, T.H. "Anomalous creep behaviour of 316 stainless steel at 550°C". High Temperature Technology 4, 1986 pp.25-29.

Impression creep testing for evaluation of grade 22 ex-service hot reheat piping seam weld

A. Bridges[1,*], J. Shingledecker [1], J. Siefert [1], D. Purdy [1], J. Foulds [2], C. Ferguson [3]

[1] Electric Power Research Institute, 1300 W. W.T Harris Blvd, Charlotte, NC 28262 USA
[2] Clarus Consulting, LLC, P.O. Box 470318 Charlotte, NC 28247 USA
[3] Kansas City Power and Light, 19950 Newton Dr., Kansas 66013 USA
* Correspondence: abridges@epri.com; Tel.: +1-704-595-2950

Abstract: U.S. electric power production is significantly dependent on the operation of coal-fired steam generation units and a large majority of these units are reaching ages over 50+ years with concerns for operating component integrity and remaining life. This paper discusses a small sample testing technique (impression creep) that was used to estimate the remaining life of a hot reheat seam welded piping system that saw about 322,000 hours of operation at nominally 4170 kPa (605psig) and 538°C (1000°F) steam conditions. Two different life assessments using experimental impression creep data are discussed and findings compared to a previous preliminary study of the same piping system using operational data, reported measured piping thickness values (from UT measurements), and published creep rupture data. Impression creep tests were conducted in unaffected base metal, weld metal and the heat-affected zone. Impression creep rates of the various zones showed no creep mismatch. Minimal creep mismatch, proper design, fabrication and operation, combined with proper metallurgy have successfully demonstrated that even low-alloy seam welds can operate 300,000+ hours and still exhibit useful remaining life.

Keywords: Impression creep; seam weld; small sample testing; CrMo steels; remaining life assessment

1. Introduction

The world's first commercial supercritical coal fired power plant was commissioned in 1957 in Philo, Ohio. This engineering accomplishment resulted in a significant increase in thermal efficiency in power generation [1]. From the 1960's to 1980's, supercritical units were constructed throughout the world with steam conditions of 538 to 565°C (1000 to 1050°F) and >221 bar (3205 psig).

Today, U.S. electric power production remains significantly dependent on the operation of a number of these steam generation units, including coal-fired ones that are now exceeding 300,000 hours of operation. In 2017, about 30% of the United States electricity was generated from coal sources [2,3]. With many of these aging units continuing to operate, there is a need for improved component integrity and life management strategies, including review of prior assessments in high energy piping and other critical components. The general movement to cleaner energy sources has further complicated life management strategies as these aging assets are now expected to cycle and operate outside their intended baseload operation.

Typically, the life management of high energy piping systems is inspection-based using a variety of non-destructive evaluation (NDE) techniques, such as phased array ultrasonics during planned outages, but this information does not, on its own, give a measure of remaining useful life. The accumulation of damage by creep remains a key area of concern in seam-welded high energy piping [4]. The factors affecting performance of a structure can be broadly grouped into design, operation, fabrication and metallurgy. Creep is a time-dependent mechanism that is affected by temperature, global stresses due to pressure and system loads, local stresses affected by geometry (weld cross section, out-of-roundness including peaking) and the aggravating effect of local mismatch in creep resistance between weldment zones. Metallurgical risk factors, including weld metal chemistry and cleanliness, and fabrication related issues further exasperate creep (e.g., [5-8]).

In the U.S., low alloy chromium molybdenum (CrMo) steels, Grades 11 (1.25Cr-0.5Mo) and 22 (2.25Cr-1Mo), have been the commonly used materials for main steam (MS) and hot-reheat (HRH) piping systems of older generating units. These materials have been used for boiler piping as HRH long seam-welded piping fabricated to ASTM A155: Electric-Fusion-Welded Steel Pipe for High-Temperature Service, beginning in 1952, and replaced circa 1975 with the use of ASTM A691: Specification for Carbon and Alloy Steel Pipe, Electric-Fusion-Welded for High-Pressure Service at High Temperatures. While the A691 standard specifically identifies three optional heat

treatments for the welds - subcritical post-weld heat treatment (temperature below the lower critical Ac1), normalizing, and normalize + temper (N&T), the older A155 standard only specified a minimum heat treat temperature of 593°C (1100°F), i.e., normalizing or N&T treatments were not a specific part of the standard, although not prohibited. The extent of weld metal-adjacent base metal or heat-affected zone mismatch in creep rate that affects creep life can, at least for an extended period immediately following installation, be significantly large in case of subcritically heat treated welds, far less so with N&T'd welds. In all cases of Grades 11 and 22, long seam-welded piping is fabricated from plate product specified by ASTM A387: Standard Specification for Pressure Vessel Plates, Alloy Steel, Chromium-Molybdenum.

Impression creep testing has been used as a qualitative assessment tool in the evaluation of CrMoV and Grade 91 piping systems (e.g., [9,10]). In this work, the usefulness of impression creep testing was assessed in the evaluation of a seam-welded Grade 22 hot reheat piping system. The principle focus of the work was to compare a global assessment based on steam conditions, service life, and component dimensions with targeted metallurgical studies and findings from impression creep testing performed on material removed from service. The impact on creep of mismatch between the base metal and weld metal including the analysis of the measured impression creep-rates will be discussed.

2. Materials and Methods

The impression creep test has been used for several decades and was first applied to the power industry in the UK in 1997. With the increasing age of coal-fired power plants, major components, such as the piping systems, need continuous evaluation to help ensure reliable, continued service. The results of uniaxial creep rupture tests are typically used to characterize material, predict long-term performance in high-temperature service, and develop rules for the use of these materials in design. This conventional approach to testing and performance evaluation is unfortunately not easily applied to operating equipment since the significant amount of material required for such testing is, at best, difficult to extract from the equipment. Additionally, rupture testing times limit the ability to derive useful information from such testing within a practical time frame. The impression creep test method uses a relatively small volume of material that may be obtained in a 'non-invasive' manner, such as by surface scoop sampling of the component. Figure 1 shows the amount of material that is typically removed for machining both uni-axial and impression creep test specimens. Since the test uses a strain rate based approach to estimate life, test durations can be short enough to produce useful information in a timely manner.
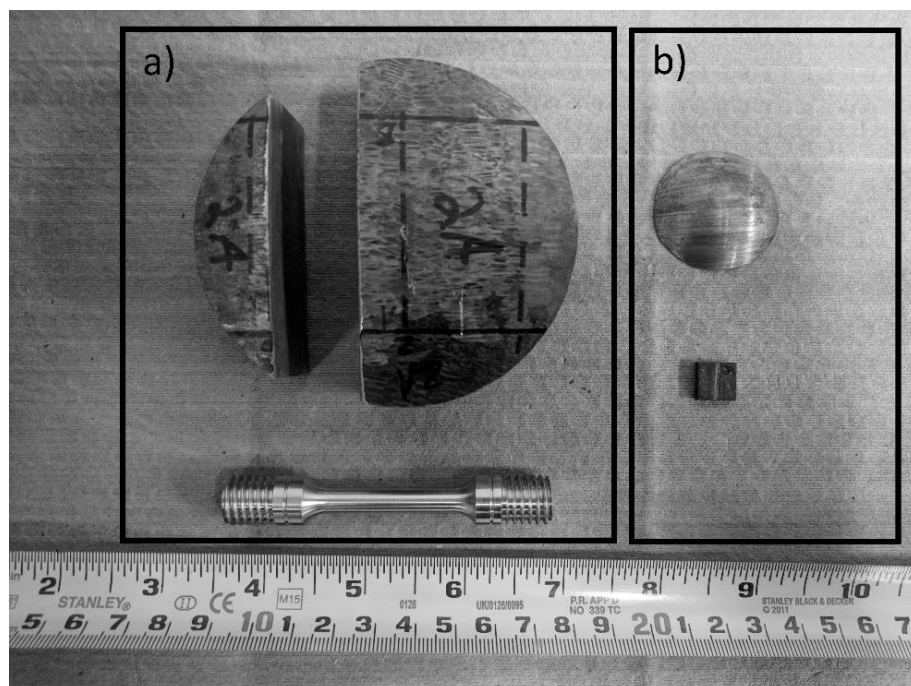

Figure 1. The uni-axial creep specimen is machined from a 'plug' sample (a) and the impression creep specimen is machined for a 'scoop' sample (b).

The material of interest in this study was removed from a Grade 22 HRH long seam-welded piping system of a coal-fired supercritical unit that experienced about 322,000 hours of operation since its original installation in 1969. The reported nominal HRH steam conditions were 4170 kPa (605psig) and 538°C (1000°F). In 1986 the utility reviewed the future prospective for the unit and elected to implement a condition assessment and replacement program with an objective to operate the plant through the year 2010 [11]. Many major components were evaluated and either repaired, replaced or determined to be in acceptable condition for continued operation. The HRH long seam-welded piping was inspected by visual examination, surface wet fluorescent magnetic particle testing, surface replication, ultrasonic testing (UT) for wall thickness, and volumetric inspection for damage by straight beam and shear wave UT. The inspections found no indications of damage or near-term failure risk. Lifetime calculations made at the time based on measurements of pipe dimensions and assumed creep rupture strength also did not indicate a significant concern for near-term failure.

In 2015, an EPRI-led review of the HRH piping system highlighted a need to adopt a risk-based approach to future prioritization of locations for NDE because the system had not been routinely and fully evaluated since the mid-1980s and since development of advanced UT methods suited for long seam welds. The EPRI assessment based on reported operating conditions, the results of prior inspections, and the plant-reported patterns of personnel traffic (for qualitatively considering exposure to personnel) provided a list of locations with a ranking of prioritization for inspection and testing [12]. Following the assessment, the utility removed a set of plug samples from several seam weld locations for laboratory testing and evaluation. These plug samples serve as the source of evaluated material for research that is summarized in this manuscript.

Six plug samples, as shown in Figure 1 a), were extracted by the plant at several straight segment long seam-weld locations in the HRH piping system at varying EPRI-estimated priority rank (risk) levels. The plug samples were ~80 mm (3.1 inch) in diameter with the seam weld nominally in the center of the sample. A portion of each sample was removed and polished using standard metallographic techniques. Hardness testing (0.5 kgf, 0.50mm spacing in weld metal, 0.25mm spacing in base metal) and assessment for the presence of creep damage was conducted on the as-polished samples using an automated Vickers microhardness tester (LECO AMH43) and a confocal laser microscope (Keyence VK-X105), respectively. Etching of the samples was performed for light optical microscopy using a 2% Nital solution (2 mL HNO_3 with 100mL of ethanol) following ASTM E407 [13].

Impression creep specimens were removed from two of the six plug samples using electric discharge machining (EDM) to a size of 10 x 10 x 2.6 mm. Specimens were sectioned from the base metal (BM), weld metal (WM) and heat-effected zone (HAZ) as shown for one of the samples (low risk, plug 1B) in Figure 2.
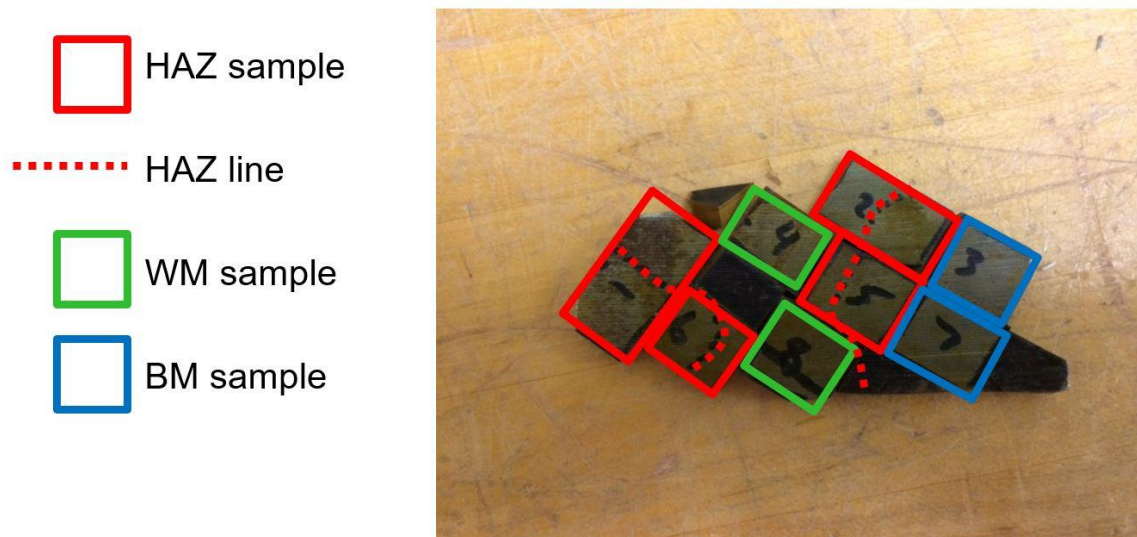
Figure 2. Extraction of impression creep specimens (BM, WM, HAZ) from low risk plug 1B using electric discharge machining (EDM) to cut specimens to ~ 10 x 10 x 2.5 mm in size.

The specimens were ground to a final thickness of 2.50 ± 0.02 mm using 240, 300 and 600 grit sandpaper. Impression creep test conditions were varied to include single stressed, multi-stressed and iso-stress (stepped temperature) testing to the ECCC guidelines for impression creep in reference [14]. The tests were conducted using a twin-screw servo-mechanical loading frame with a high temperature ceramic shell furnace using kanthal windings.

A software program was used for controlling the static load and type K thermocouples were used to control temperature to ± 1°C of the set point. The impression creep indenter was constructed of a high strength Waspaloy nickel based superalloy with creep strength more than 3 orders of magnitude that of the test material. Twin water cooled linear variable differential transformers (LVDT's) were used to measure displacement during the testing period. Impression creep tests were run for a minimum of 300 hours and the last 100 hours were used for determining the minimum creep rate.

Post-test evaluations were performed on all specimens after testing. This consisted of hardness mapping, measurement of indentation depth using a confocal laser microscope (Keyence VK-105) and evaluation of the microstructure.

3. Results

3.1. HRH Piping and Pipe Samples – Preliminary Study of Stresses and Lifetime

The 419MW unit had reported nominal 4170 kPa (605 psig), 538°C (1000°F) pressure-temperature HRH system steam conditions. The impression creep test material was from samples removed from a portion of the HRH system with nominal dimensions of 560mm (22 inch) OD and 28.6mm (1.125 inch) wall thickness. The current ASME B31.1 Power Piping Code material allowable stress at 538°C (1000°F), including with weld strength reduction factor of 0.82, is 44.1 MPa (6.4 ksi) [15]. The operational data for pressure and temperature and actual pipe wall thicknesses (by ultrasonic wall thickness measurements) showed that these straight sections operated well below the current B31.1 allowable stress limit. Table 1, adapted from Ref. [12], shows the estimated consumed life fraction for two sections analyzed (L2, L10) using the nominal steam conditions, pipe dimensions as shown, an ASME B31.1-calculated hoop stress, and an expectedly conservative, minimum rupture strength curve developed by EPRI from Grade 22 cross-weld stress rupture data.

Table 1. Findings from Preliminary Study of Two Straight Sections in the Hot Reheat Piping System [12].

Segment	D (in.)	t (in.)	T* (°R)	ASME B31.1-Calculated Hoop Stress, S MPa (psi)	Consumed Life Fraction (1968-2015)
L2 (straight)	22.0	1.005	1460	38.76 (5622)	0.582
L10 (straight)	22.0	1.040	1460	41.20 (5976)	0.478

The results from the preliminary study detailed in Ref. [12] indicated that there was an extensive amount of predicted remaining life at the two straight segments in the hot reheat piping system (≈231 kh, 351 kh). The ASME B31.1-calculated hoop stresses for the pipe sections of the two samples used for impression creep testing are shown in Table 2. These sections experienced similar temperature and pressure conditions to the straight section segments used in the preliminary study shown in Table 1, although lifetime calculations for these specific sampled sections were not performed as part of the preliminary study.

Table 2. Hoop Stresses for Two Plug Samples from Straight Sections in the Hot Reheat Piping System.

Sample	D (in.)	t (in.)	T* (°R)	ASME B31.1-Calculated Hoop Stress, S MPa (psi)
Plug 1B (low-risk)	22.0	1.068	1460	34.23 (5807)
Plug 3A (high-risk)	22.0	1.044	1460	41.02 (5950)

3.2 Metallographic Results

Etched macrographs of plug 1B and 3A are displayed in Figure 3. The seam welds were fabricated using a multi-pass weld with a double-vee. In this seam weld configuration, the highest susceptibility to the formation of damage is typically found at the cusp region of the weld and near the ID weld toes, based on previously summarized failures (e.g., [16]). No damage was observed in the low-risk (1B) sample and very little, low density, random,

homogenous cavitation damage was observed in the high-risk (3A) sample. The observed damage (as-polished samples) was captured using stitched images from the confocal laser microscope as shown in Figure 4.
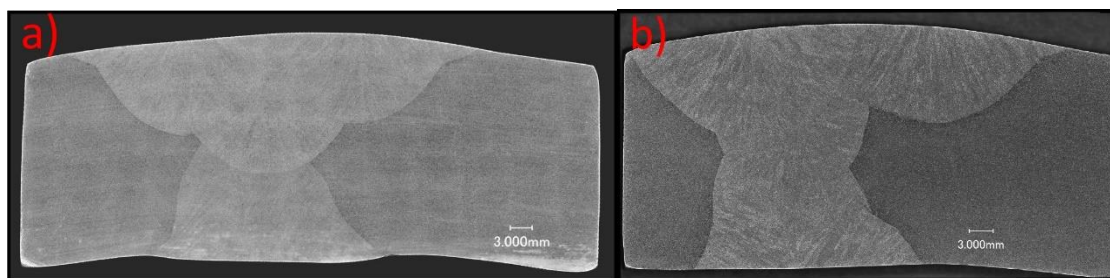
Figure 3. Etched macro image of low-risk plug 1B (a) and high-risk plug 3A (b).
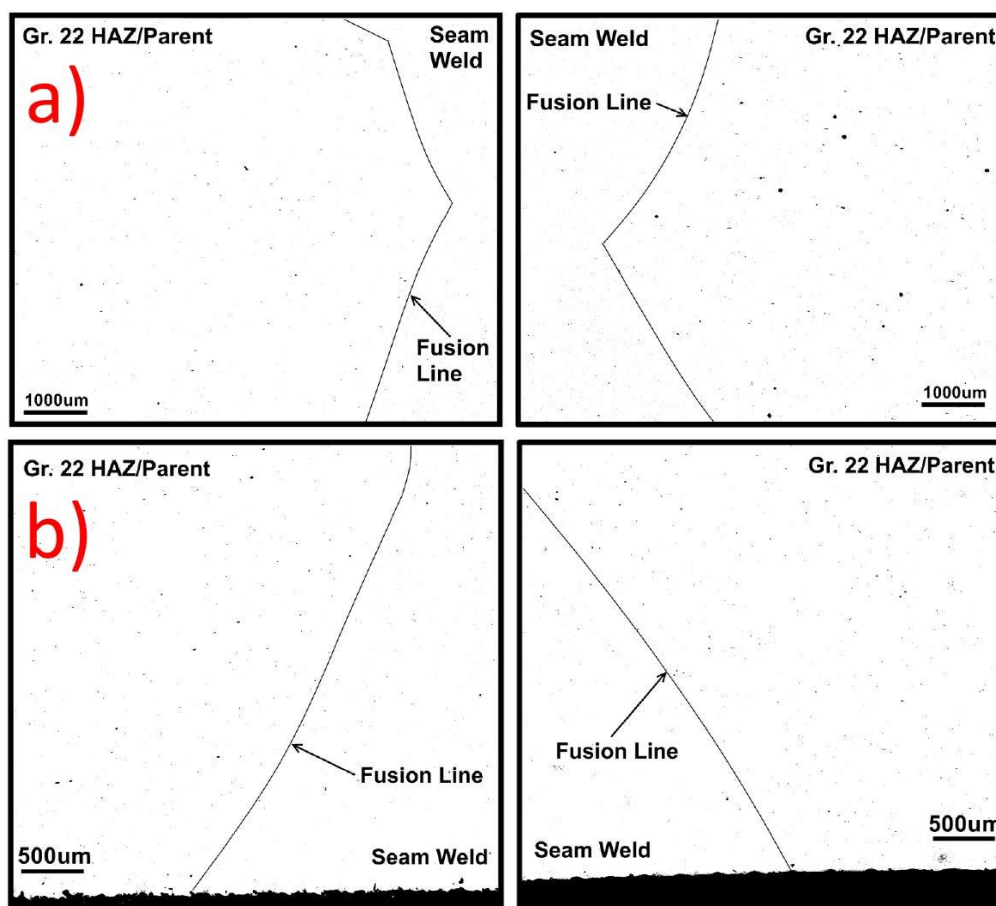
Figure 4. Observed damage/inclusions in high-risk plug 3A. Cusp region is shown at (a) and ID toe weld region is shown at (b).

Hardness testing was conducted across the welds with results shown in Figure 4-5 for sample 3A. The top hardness trace was from the left side parent material to the centerline of the weld in the lower portion of the macro of Figure 3B and the bottom hardness trace was from the centerline of the weld to the right side parent material in the upper portion of the macro. Results indicated similar hardness values in the weld metal and base metal with a moderate increase in the weld metal for the high-risk sample 3A. Hardness tests conducted on two other samples not included in this paper showed similar results.

Figure 5. Hardness testing for sample 3A at both the left and right sides show no signs of low strength in the weld (spacing of 0.50mm in weld, 0.25mm in HAZ/parent, 0.5 kg load).

3.3 Impression Creep

Impression creep testing consisted of single load tests (single temperature), stepped loading (constant temperature) and iso-stress (stepped temperature) testing. Hyde et al. (e.g., [9]) have shown that the measured minimum creep rates (MCRs) in multi-step load tests agree well with minimum creep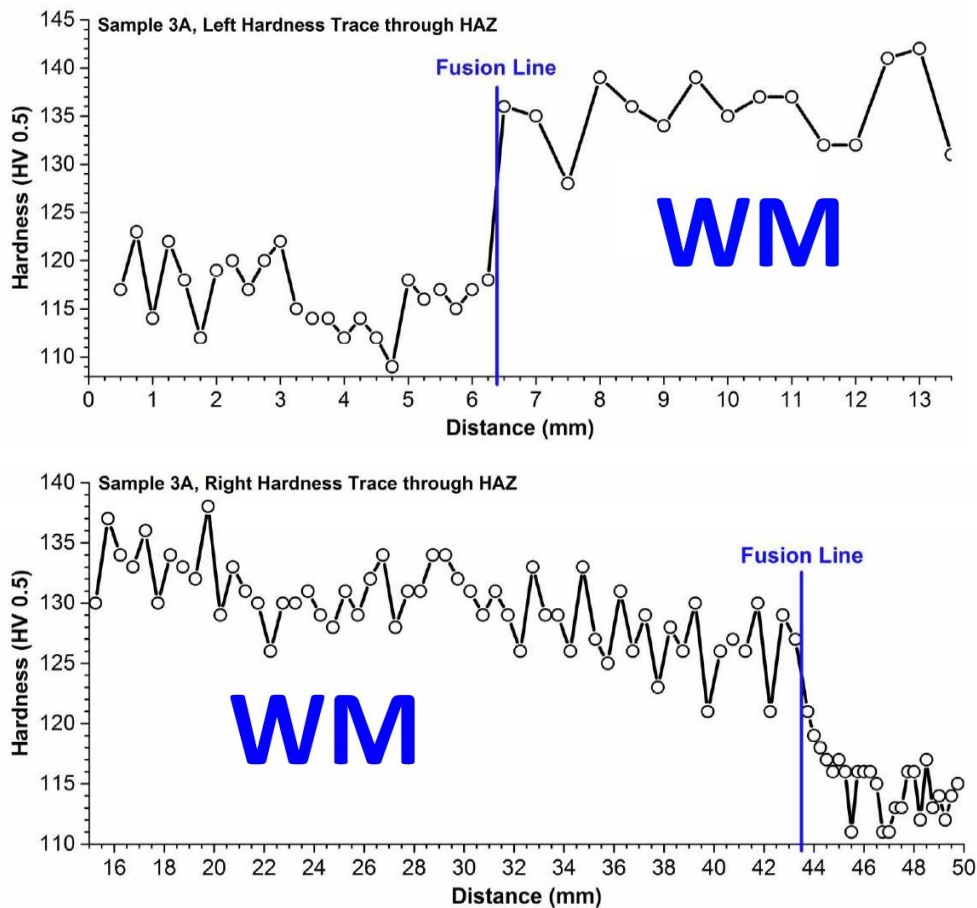 rates obtained in single load tests for low alloy CrMoV steels. The testing summarized in this manuscript assumes that each step can be represented by a single minimum creep rate (MCR) and corresponding representative rupture time. The impression creep test results for the evaluated plug samples are reported in Table 3. The (uniaxial) stress and MCR have been calculated from the indenter pressure and minimum displacement rate using the conversion factors and method of Hyde et al. (e.g., [9]). The rupture time is estimated from a Monkman-Grant, MCR-Rupture Time relationship as discussed below.

Table 3. Impression Creep Results for Service Exposed Grade 22 Hot Reheat Seam Weld

Sample	Zone	Temperature (°C)	Stress (MPa)	MCR (1/hr)	Rupture Time (hrs)*
Plug 1B (low-risk)[1]	BM	570	70	1.17E-5	2621
Plug 1B (low-risk)	BM	570	80	2.56E-5	1257
Plug 1B (low-risk)[1]	BM	570	90	3.05E-5	1067
Plug 1B (low-risk)	WM	570	80	3.07E-5	1060
Plug 1B (low-risk)	HAZ	570	80	3.50E-5	938
Plug 3A (high-risk)[2]	WM	570	80	3.61E-5	911
Plug 3A (high-risk)[2]	WM	580	80	4.08E-5	812
Plug 3A (high-risk)[2]	WM	590	80	4.52E-5	738
Plug 3A (high-risk)[2]	WM	600	80	6.14E-5	553
Plug 3A (high-risk)[2]	WM	620	45	2.07E-5	1535

Plug 3A (high-risk)[2]	WM	640	45	4.54E-5	735
Plug 3A (high-risk)[2]	WM	660	45	1.43E-4	250
Plug 3A (high-risk)	BM	570	80	4.32E-5	770

[1] Minimum Creep Rate from Stepped Loading Test (same temperature)

[2] Minimum Creep Rate from Stepped Temperature Test (same load)

*From a Monkman-Grant, MCR-Rupture Time relationship (see text)

One limitation of impression creep test is the lack of rupture time. The rupture times stated in Table 4 are estimated rupture times derived from a Monkman-Grant (MG) approach. The MG approach has been traditionally adopted for extrapolation of experimental creep rate data to assess remaining life (e.g., [17,18]). In this study, the MG relationship was used to relate the impression creep MCR to a rupture time. A key assumption in this approach is the applicability of the assumed MCR-Rupture Life MG relationship assumed. Published MCR data for 2.25CrMo steel is limited, with most coming from the 1971 ASTM dataset [19]. Not only are data limited, but MCR data for 'properly heat treated' versions of steel are even more limited. A MG relationship of all datasets was shown to have a wide scatterband possibly due to the wide range of heat treatments and temperatures used. The MG relationship used here was determined using uni-axial data from ASTM in material quenched between 927 to 954°C (1725F) and tempered at 621°C (1150°F) [19]. Equation (1) and Figure 6 show the calculated relationship using uni-axial data from ASTM plate material. It is important to note that application of an MG relationship based on relatively homogenous and ductile base metal or weld metal data can be considered non-conservative. As weldments are susceptible to localized damage and low ductility.

$$t_f = 0.062 \cdot MCR^{-0.938} \tag{1}$$

where t_f in (hours) and MCR in $(1/hr)$
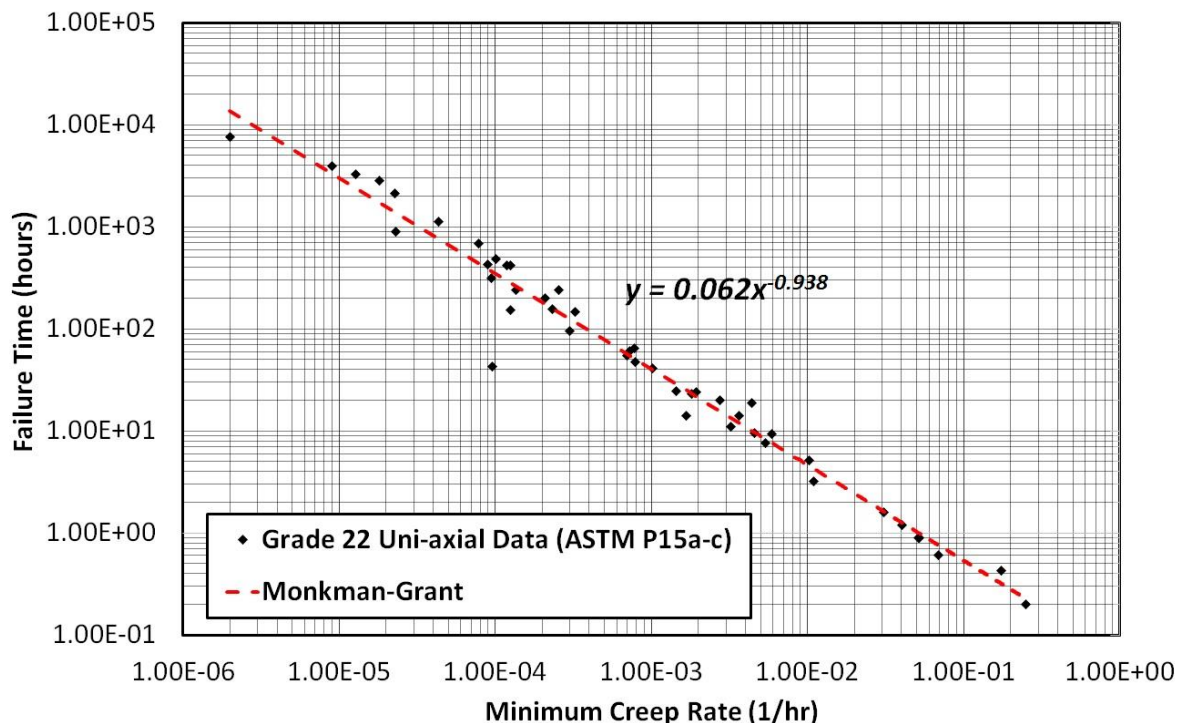
Figure 6. Monkman-Grant relationship using Grade 22 uni-axial creep data from Ref. [19].

4. Discussion

The impression creep test results were used in conjunction with uni-axial creep data to estimate the remaining useful life via two different methods. Previous literature was also reviewed to highlight the importance of creep mis-match, design, operation, fabrication and metallurgy of low alloy (CrMo) seam welds exposed to high temperatures and pressure. This discussion will review the following:

1. The useful remaining life of high-risk plug (3A) from iso-stress impression creep results for operating conditions of 45MPa (hoop stress) and 538°C (1000°F)
2. Assessment of experimental impression creep data using a Larson-Miller approach and use of published tools (EPRI, ECCC and API-579)
3. The effects of creep mis-match between zones (BM, WM, HAZ), design, operation, fabrication and metallurgy on long term performance of low alloy seam welds.

4.1. Calculation of remaining life for high-risk plug using iso-stress experimental impression creep data

The impression creep (IC)-derived strain rates for the iso-stress tests at applied loads for an equivalent uniaxial stress of 45 MPa (6.525 ksi) were plotted on a natural log of strain rate vs. the inverse of temperature, shown in Figure 7. The operating condition of 538°C (1000°F, 811°K) was then used as the input for Equation (2). The remaining life calculation is then made from the MG equation (1).
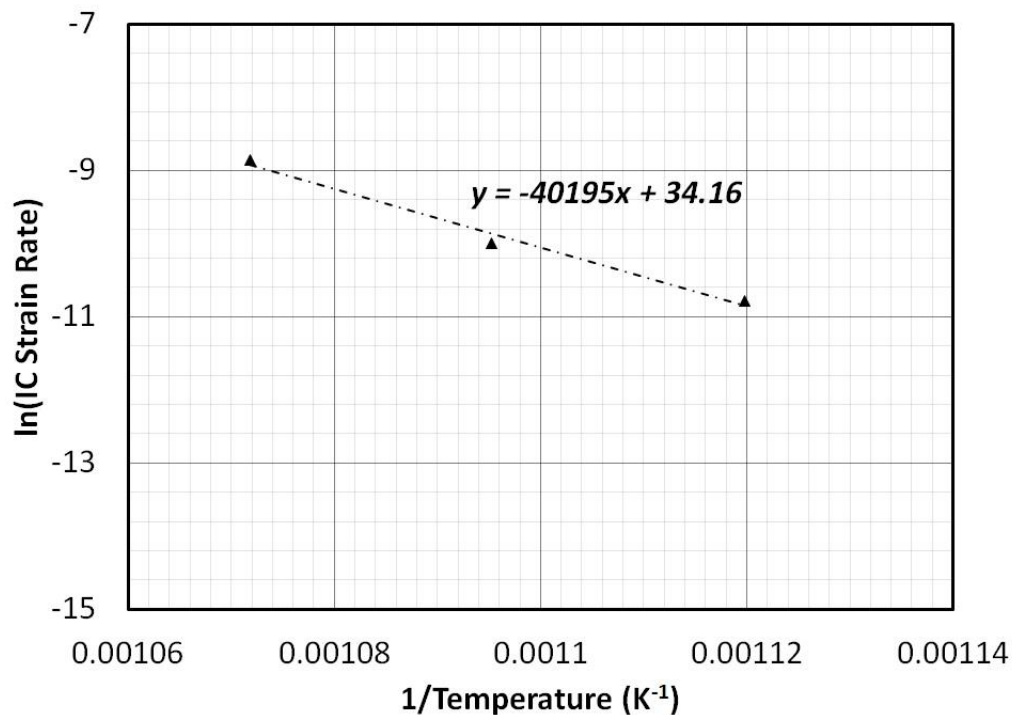

Figure 7. Natural log of Impression Creep (IC) Strain Rate vs. Inverse Temperature for iso-stress impression creep tests of weld metal at 45MPa on high-risk plug (3A).

$$\ln(IC\ strain_{rate}) = -40195\left(\frac{1}{T}\right) + 34.16 \qquad (2)$$

The various impression creep strain rates at different testing temperatures under the same loading conditions show the temperature dependence for creep. This is typically expressed as the activation energy and can be found using the slope from equation (3) multiplied by the universal gas constant (8.314 J/mol-k). Experimental results of the impression creep testing show that activation energy is very consistent between the testing temperature of 620 to 660°C (1148 to 1220°F). Assuming the activation energy is consistent at operating conditions of 538°C (1000°F) at a given stress of 45 MPa (6.53 ksi), the fit can be used to predict the minimum creep rate. It is important to note that the range of extrapolation from data at 660 to 620°C, down to 538°C, is significantly large. Thus, this may explain why life estimates were lower using this method compared to the Larson-Miller method shown in section 4.2. These experimental findings and calculations are shown in Table 4.

Table 4. Estimated Remaining Life using Iso-stress Data and MG Relationship.

Sample	Zone	Temperature (°C)	Stress (MPa)	MCR (1/hr)	MG Rupture Time (hrs)*
Plug 3A (high-risk)[1]	WM	620	45	2.07E-5	1535
Plug 3A (high-risk)[1]	WM	640	45	4.54E-5	735
Plug 3A (high-risk)[1]	WM	660	45	1.43E-4	250
Estimated Remaining Life	*-*	*538*	*45*	*2.05E-7**	*116404*

[1] Minimum Creep Rate from Stepped Temperature Test (same load)

*Estimated using MG Relationship in Equation (2)

For the test stress and corresponding pressure (if applied in future operation), the estimated remaining life of the high-risk plug (3A) was found to be over 116,000 hours, which is almost 20 years of operation at a 70% availability factor. The estimated remaining life appears lower than that in the preliminary EPRI study (≈231,000 h, 351,000 h, see Table 1 and related text) that used nominal conditions with a lower applied stress, albeit a more conservative rupture curve. Based on continued operation at nominal conditions (538°C, 4.17 MPa pressure), it appears reasonable that this segment of the HRH piping system could operate more than 20 years (at 60 to 80% availability factor) based upon impression creep estimates of life and supporting metallurgical results showing minimal damage at the cusp and weld toes. It should be noted that such estimates of remaining life do not include time expended in the progression of the cracking forms of damage, particularly relevant where creep damage occurs locally. In this regard, such estimates are conservative. On the other hand, estimates made based on tests of relatively homogenous material do not capture the effect of local weak and/or creep brittle zones and the effect of varying creep rates in adjacent zones of the weldment seen in an operating component, and may therefore not be conservative (see discussion later).

4.2. Assessment of experimental impression creep data using a Larson-Miller approach

The impression creep-derived rupture time results may also be presented and analyzed using the Larson-Miller time-temperature parameter. The approach allows for a comparison of data with established rupture strength curves representing the behavior of base metal. In recent years, several organizations have determined statistical data fits for Grade 22 uni-axial creep rupture data. These fits can be used for extrapolation of service-like conditions to estimate life of high temperature components in the creep regime. The Electric Power Research Institute (EPRI) [20], European Creep Collaborative Committee (ECCC) [21] and American Society of Mechanical Engineers (ASME) [22] statistical data fits are the basis for the assessment in this section. The Larson-Miller (LMP) temperature-time dependent parameter is used in conjunction with stress to represent a single curve for all creep rupture data. The representative rupture times for the experimental impression creep data were used to determine the corresponding LMP values. The results are shown in Figure 8.
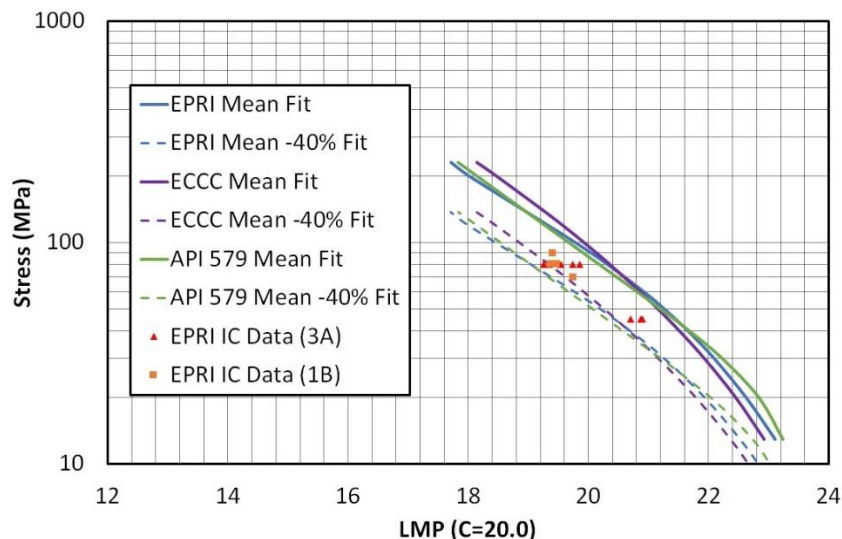

Figure 8. Larson-Miller vs Stress for Grade 22 Uni-axial and Impression Creep Data.

It is important to note that impression creep data at the base metal, heat-affected zone and weld metal are compared to average base metal curves, as shown in Figure 8. The impression creep-derived data suggest a qualitative difference between the predictions made for the low risk and the high-risk plug material, supporting the use of the test method in discriminating between materials with varying levels of creep strength. The experimental impression creep data fall below the average creep strength of base metal. The impression creep data points also appear to be just above the -40% of the mean strength for the three rupture strength curves (EPRI, ECCC and API-579). A calculation of remaining life using the -40% mean fit gave results summarized in Table 5. The LMP-based extrapolation of remaining life appears greater than that made with the MCR-MG method. A more rigorous comparison of impression creep test data and the MCR-MG relation with uniaxial data and the corresponding MG relationship is needed to better understand the potential reasons for the difference.

Again, lifetime estimates made from results on a weldment zone alone do not reflect the complex effect of mismatch, localized properties, concentration of damage, etc. that can produce reductions in lifetime from what is simply predicted from tests on a single zone of homogenous material.

Table 5. Estimated Remaining Life based on a 40% Reduction of Rupture Strength from Average Expected Behavior for Both Plug Samples using the LMP.

Fit Method	Temperature (°C)	Stress (MPa)	Remaining Life (hrs)
ECCC	538	45	174372
API 579	538	45	165542
EPRI	538	45	189984

4.3. The effects of creep mis-match between zones (BM, WM, HAZ), design, operation, fabrication and metallurgy on long term performance of low alloy seam welds

Creep mis-match, design, operation, fabrication and metallurgy have all been shown to have significant impacts on service life in high temperature structures and all influence the quality of welds. Creep mis-match over time leads to stress concentrations and can be exacerbated by weld geometries, such as weld width, weld preparation angle and the state of loading [5-8].

Unlike traditional uni-axial creep testing, the impression creep test can be used to test the individual zones (BM, WM, HAZ) of a weldment. Limited studies have shown that the impression creep minimum creep rates are directly relatable to uni-axial minimum creep rates when proper reference stresses are used [23,24]. Individual single stressed impression creep tests were performed at the BM, WM and HAZ (as shown in Figure 2 from methods section) for the low-risk plug sample using the same test conditions. Results are shown in Table 6 with the rupture time calculated using the same MCR-MG method applied to the high risk plug sample material test specimen data.

Table 6. Impression Creep Results for Low-risk Plug (1B) at BM, WM and HAZ.

Sample	Zone	Temperature (°C)	Stress (MPa)	MCR (1/hr)	MG Rupture Time (hrs)*
Plug 1B (low-risk)	BM	570	80	2.56E-5	1257
Plug 1B (low-risk)	WM	570	80	3.07E-5	1060
Plug 1B (low-risk)	HAZ	570	80	3.50E-5	938

*Estimated using MG Relationship in Equation (1)

The minimum creep rate in the different zones showed to be very similar, with minimal creep mis-match. The as-constructed weldment post-weld heat treat condition is not known. If the weldments were subcritically heat treated, as in the typical case for older seam-welded low alloy steel straight section piping (see Introduction), the effect of tempering due to extended elevated temperature service exposure (e.g., [25]) would be expected to significantly reduce the mismatch with exposure time. If the weldments were initially normalized and tempered, the starting mismatch would be lower than for the subcritical condition and there would be far less of an effect of service exposure on changes in mismatch during service.

The Holloman-Jaffee time-temperature parameter (a Larson-Miller representation) is often used to describe the effect of a heat treatment at a temperature for a specific time on the time-independent strength characterized by hardness [26]. To be clear, the time-independent strength or hardness does not represent the elevated temperature

time-dependent creep strength/resistance. Changes in hardness are nevertheless a measure of the extent of tempering which does affect the change in creep resistance and the mis-match in creep rates between various weldment zones. There is almost always a variation in hardness between the weld metal, heat-affected zone and base metal and the heat treatment following welding largely controls the initial hardness and its variation across a given weldment. Hardness results from the plug samples as presented in Figure 5 show that the heat-affected zone adjacent to weld metal exhibits a hardness level even lower than weld metal (15-20% difference), not generally seen in as-constructed weldments. The observation indicates that the weldment has been substantially tempered as would be expected from the extended elevated temperature operation. The hardness data are plotted on tempering curves for Grade 22 [25]. The LMP value is calculated for the operating period at 538°C (1000°F) without an equivalent time correction for any initial post-weld heat treatment (this is very small relative to the extended operating period LMP value). The apparent tempering effect of service is expected to reduce the weld metal-heat-affected zone creep rate mismatch (from the initial as-constructed) condition, and the impression creep results, albeit on material not immediately adjacent to the weld fusion line, are consistent with the expectation.
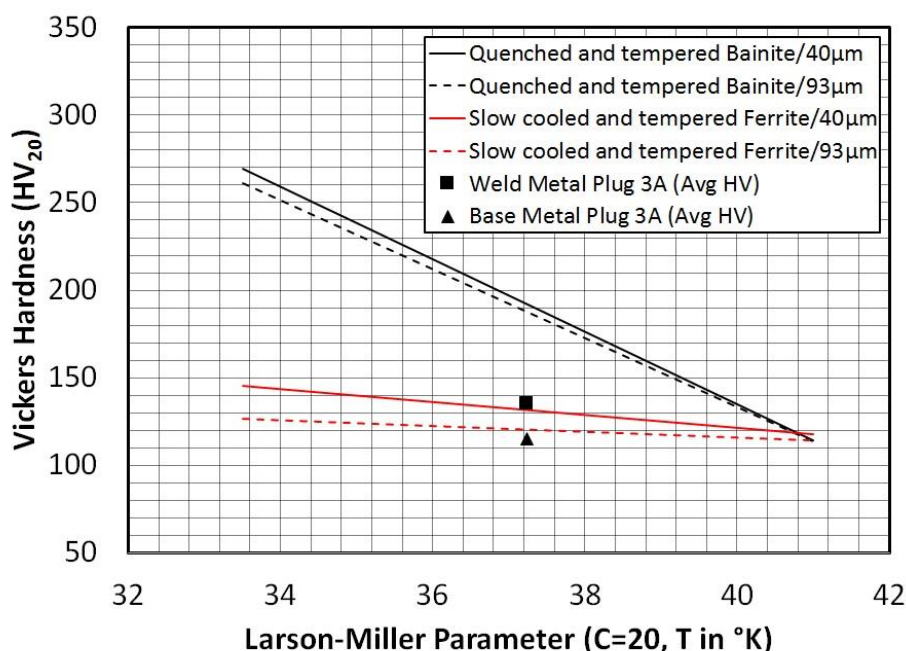

Figure 9. Reductions in Hardness as a Function of Time and Temperature for CrMo steels [25] with measured data on plug 3A material superimposed

It should be noted that in case the as-constructed weldments had been given a normalizing and tempering post-weld treatment, the creep rate mismatch would be expected to be low even before service exposure; i.e., the effect of in-service exposure would not be as significant. Regardless, for estimating the remaining life, what is of interest is the current condition, and the impression creep tests provide an indication of the creep mismatch going forward. Since the impression creep tests, although conducted on specific weldment zones, do not adequately characterize local, near-fusion line material properties that can be key to weldment lifetime, this limitation is recognized.

Impression creep testing provides valuable weldment zone-specific information that cannot be obtained from standard uniaxial test methods, in addition to allowing for the testing of in-service component material. In addition, as has been demonstrated for Grade 91 and CrMoV, the test is a tool that can discriminate between material of varying creep strength levels. With more research, the impression creep test could prove to be an asset when characterizing creep mismatch of service exposed welds, in addition to its application for remaining life estimation. Additional testing should be conducted on similar material of known behavior to compare findings. This will help in further exploring and validating the impression creep test method. It is also suggested that selected seam-welds be given a normalize and temper heat treatment, then re-evaluated by impression creep testing between the BM, WM and HAZ to assess mismatch conditions more representative of an as-constructed N&T condition. Uniaxial testing will also help validate suggested 'representative failure times' produced from impression creep test results.

5. Conclusions

Impression creep testing performed on service exposed seam welded hot-reheat piping material has been effective in discriminating between two material cases with expectedly different creep strength levels. The tests were also useful in indicating that the piping system material evaluated had useful remaining creep life. These findings are consistent with a previous preliminary study of the same service exposed system material. Two different evaluation methods of impression creep data were discussed, an LMP-based approach and MCR-MG method. The remaining life from extrapolation of the LMP-based approach showed slightly higher life predictions than that the MCR-MG method. Impression creep testing was also performed at various zones of the seam weld to show that there was nearly no creep mismatch between the base metal, weld metal and heat-affected zone. It is likely that observed minimal creep mismatch, proper design, operation and fabrication, combined with proper metallurgy are reasons this low-alloy seam-weld piping system has successfully seen over 300,000 hours of operation and still shows significant useful remaining life. It is recommended that additional impression creep be done on a reheat-treated (normalized and tempered) version of the same material in addition to uniaxial creep testing to examine the mismatch question and the most suitable means of test data interpretation for remaining lifetime estimation. Further metallurgical evaluation, including weld chemistry and oxygen content are planned to fully characterize the materials variables that can affect local damage rates.

References

1. "Philo 6 Steam-Electric Generating Unit." ASME.org. Accessed March 23, 2018.
2. Your Guide To Understanding Energy – Energy Information Administration. Accessed March 23, 2018. https://www.eia.gov/energyexplained/index.cfm?page=electricity_in_the_united_states.
3. "Coal & Electricity." World Coal Association. Accessed March 23, 2018. https://www.worldcoal.org/coal/uses-coal/coal-electricity.
4. *30-Plus Years of Long-seam Weld Failures in the Power Generation Industry –Perspective and Continuing Challenges with Life Management.* EPRI, Palo Alto, CA: 2017. 3002011587.
5. Samuelson, L.A.; Tu, S.-T.; Storesund, J., Life Reduction in High Temperature Structures Due to Mis-Match of Weld and Parent Material Creep Properties, Mis-Matching of Welds, ESIS 17, Edited by K.-H. Schwalbe and M. Kocak, Mechanical Engineering Publications, London, (1994) 845-860.
6. Segle, P.;. Tu, S.-T.; Storesund, J.; Samuelson, L.Å. Some issues in life assessment of longitudinal seam welds based on creep tests with cross-weld specimens, International Journal of Pressure Vessels and Piping, Volume 66, Issues 1–3, 1996, Pages 199-222
7. Storesund, J. Tu, S.-T.; Geometrical effect on creep in cross weld specimens, International Journal of Pressure Vessels and Piping, Volume 62, Issue 2, 1995, Pages 179-193
8. Segle, P. (2002). Numerical simulation of weldment creep response (PhD dissertation). Materialvetenskap, Stockholm.
9. Hyde, T. H.; Sun, W. (2001). Multi-step Load Impression Creep Tests for a 1/2Cr1/2Mo1/4V Steel at 565°C. Strain, 37(3), 99-103.
10. Brennan, K.; Brett, S.J.; Eaton-Mckay, J. Impression Creep Testing of Aberrant Grade 91 Material Removed from Piping in Service; 4th International ECCC Conference, 2017.
11. Barry, J.E.; Guilfoyle, C.J.; Rupinskas. R.L. "Sibley Station Life Extension Program." Life Extension and Assessment: Nuclear and Fossil Power-Plant Components 138 (June 19, 1988): 165-69.
12. Method for the Preliminary Assessment of a Seam-Welded Hot Reheat Piping System: Damage Estimation and Prioritization of Sections for Evaluation at Kansas City Power and Light Sibley Unit 3. EPRI, Palo Alto, CA: 2017. 3002011588.
13. ASTM E407-07(2015)e1, Standard Practice for Microetching Metals and Alloys, ASTM International, West Conshohocken, PA, 2015
14. ECCC Guidelines for Impression Creep Testing; Discussion at 3th International ECCC Conference, 2014.
15. ASME Code for Pressure Piping, B31, Power Piping B31.1-2016, ASME, New York, NY, 2016.

16. Foulds, J. R.; Viswanathan, R. (1995). Guidelines for Assessment of Seam-Welded High Energy Piping (III ed., Vol. 57). Chicago, IL: Proceedings of the American Power Conference.

17. Evans, M. (2006). A generalised Monkman-Grant relation for creep life prediction: An application to 1CrMoV rotor steel. Journal of Materials Science, 41(12), 3907-3915.

18. Povolo, F. (1985). Comments on the Monkman-Grant and the modified Monkman-Grant relationships. Journal of Materials Science, 20(6), 2005-2010.

19. ASTM Data series DS 6S2, "Supplemental report on the Elevated-Temperature Properties of Chromium-Molybdenum Steels (An evaluation of 2-1/4Cr 1Mo Steel)," ASTM, West Conshohocken, PA, 1971.

20. Recommendations for Weld Strength Reduction Factors. EPRI, Palo Alto, CA: 2010. 1019791.

21. Engineers, A. S. (2016). *API 579-1/ASME FFS-1 Fitness-For-Service*. American Society of Mechanical Engineers

22. ECCC Data Sheets 2005, European Creep Collaborative Committee, 2005.

23. Hyde, T.H.; Yehia, K.A.;. Becker, A.A Interpretation of impression creep data using a reference stress approach, International Journal of Mechanical Sciences, Volume 35, Issue 6, 1993, Pages 451-462.

24. Hyde, T.H.; Sun, W.; Becker, A.A. Analysis of the impression creep test method using a rectangular indenter for determining the creep properties in welds, International Journal of Mechanical Sciences, Volume 38, Issue 10, 1996, Pages 1089-1102.

25. Grade 22 Low Alloy Steel Handbook: 2-1/4Cr-1Mo, 10CrMo9 10, 622, STPA24. EPRI, Palo Alto, CA: 2005. 1012840.

26. Hollomon J.H.; Jaffe, L.D. "Time-Temperature Relations in Tempering Steel," Transactions, American Institute of Mining, Metallurgical Engineers, Volume 162, 1945, p. 223–249.

Technical Note: Experimental techniques for Impression Creep and Small Punch testing

J.H. Rantala [1,*]

[1] VTT Technical Research Centre of Finland Ltd

* Correspondence: juhani.rantala@vtt.fi; Tel.: +358400570386

Abstract: The test rig for Impression Creep testing was designed based on the application of resistance cable heating instead of a normal furnace. The thermal stability is crucial in Impression Creep testing because of small displacements, typically just some tens of micrometers. Good thermal stability was achieved by applying resistance heating cables with an integrated thermocouple inside. For frictionless displacement measurement, ceramic tube and rod are used, located inside the hollow loading bar, protected from direct heat radiation and thermal fluctuations, thus avoiding thermal strains. In an international Round Robin these innovative arrangements provided the best strain signal stability. For the Small Punch testing the aim was set to make the test rig gas tight in order to avoid ingress of oxygen. However, the combination of gas tightness and frictionless movement of the puncher are contradictory requirements. This was solved by using a metallic bellow. Only the spring load of the bellow needs to be compensated which is possible when the loading is provided by a servomechanical testing machine.

Keywords: Impression Creep, Small Punch, thermal stability, displacement measurement, frictionless

1. Introduction

Miniature test techniques are very useful for many material property characterisation applications, but the miniature test method will require some miniaturisation of the test rigs, which causes some technical challenges. In Impression Creep testing the biggest challenge is to achieve a good signal stability when so small displacements are measured, typically just some tens of micrometers. Many extensometer systems are capable of measuring these with sufficient accuracy as such, but the thermal fluctuation from a furnace will cause thermal expansion, which results in pseudo strain and scatter. In addition, friction in some extensometry systems will cause additional scatter.

In Small Punch creep testing the displacements are typically around two millimeters, so the accuracy in displacement measurement accuracy is not a problem. The fluctuation in temperature and frictional effects can cause some scatter in the creep rate of the test material. However, a serious problem in Small Punch creep testing is the oxidation of the small test specimen, which is just 0.5 mm thick. Argon flushing through the test rig with small tolerances will not protect the specimen from oxidation. Use of gaskets would give rise to friction, which is then impossible to compensate for.

2. Thermal stability

Using similar size furnaces for miniature testing as for traditional uniaxial creep testing is not an optimum solution because the test rigs are smaller and thus more sensitive to the inevitable thermal fluctuations caused by the furnace and a PID temperature controller. An on-off controller with a long idle time will certainly result in thermal fluctuations. Another problem especially in Impression Creep testing is that the contact surface between the specimens and the indenter is just 10 mm^2 and therefore it can easily occur that on one side (typically on the upper part of the rig) the tools are at higher temperature than on the other side because the thermal contact area is so small and as a result, the specimen temperature will be ambiguous. At VTT these problems were solved by using 250 W resistance heating cables wound around the test rig body with a 40 mm outer diameter. The heating arrangement is shown in Figure 1. Two coils are used which have their own PID temperature controllers. In this way the temperature of the upper and lower part of the test rig can be kept at the same temperature. The heating cables have a thermocouple integrated inside the metallic sheath, which was originally meant to work as overheating protection but has been used as the controlling thermocouple. In this way the temperature of the heating cable is constant and as a result the temperature measured from the test specimen is as constant as practically possible, most scatter coming from the inherent scatter of the measuring thermocouple itself. If the contact between the coil and the rig changes and the specimen temperature starts to drift away from the test temperature, small adjustments may be

needed in the temperature setting, especially when all parts are new. An example of the temperature stability is shown in Figure 2.

In Small Punch creep testing the thermal mass of the test specimen is very small compared with the much thicker surrounding parts of the test rig, so if there are large temperature gradients within the test rig, the temperature of the SP specimen can be ambiguous. Therefore, the same type of cable heating is used at VTT in the Small Punch test rig as for Impression Creep. During pilot testing phase the temperature can be measured from several different locations in the test rig and the location of the heating cable can be adjusted to reach the optimal temperature distribution.
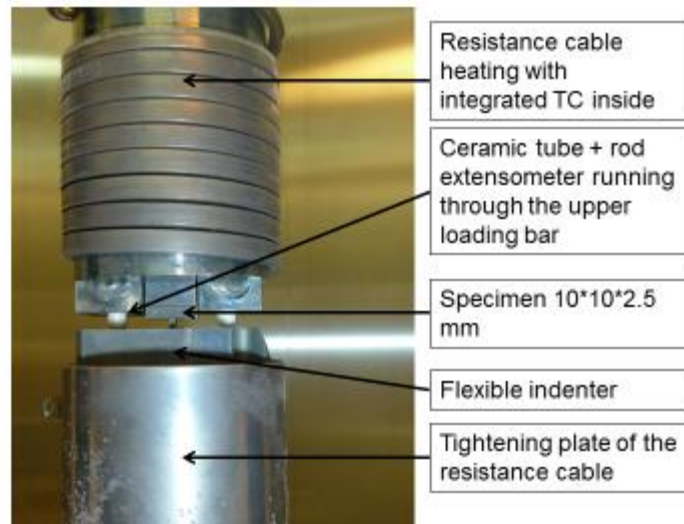

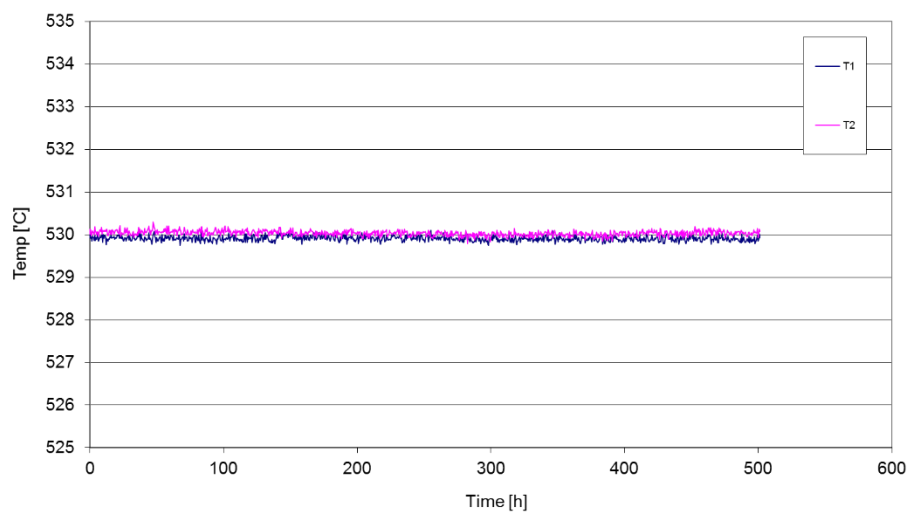**Figure 1.** Detail of the impression creep rig with the upper tightening plate removed.

Figure 2. An example of the specimen temperature in an Impression Creep test at 530°C.

3. Displacement measurement in Impression Creep

The basic idea in the displacement measurement system was to measure the indenter movement as close to the specimen as possible and to protect the extensometer from direct heat radiation and thermal fluctuations. This was achieved by using a tube and rod type of extensometer and placing it inside the hollow loading bar. Al_2O_3 tube with od 8 mm and id 5mm and a 4 mm rod are used as shown in Figure 2. Originally the tube and rod were run through the lower loading bar and the tube was held in place by pin loading which was not a very stable way of holding the tube in place. Later the whole system was reversed because then the tube is coming from above and is resting against a flat surface and the contact is better defined and stable. When the lower tip of the rod is centered so that it does not touch the tube and the upper tip is centered by the Heidenhain 12.5 mm digital displacement transducer with 10nm resolution, the extensometer is frictionless (disregarding the internal friction of the displacement transducer) which helps achieve very smooth displacement curves as shown in Figure 3. This in turn translates into steady strain rate curves as a function of time and a "constant" strain rate value calculated from the last 100h of the test data. To be precise, the strain rate does not become constant but is reducing continuously as a function of time.

During the setting up of a test the frictionless movement of the extensometer is verified at room temperature by doing a step-loading to 2000 N (or less if the test load is smaller) and recording the hysteresis loop of the load vs displacement curve. This could be a recommended practice to be introduced into a future standard for Impression Creep testing.
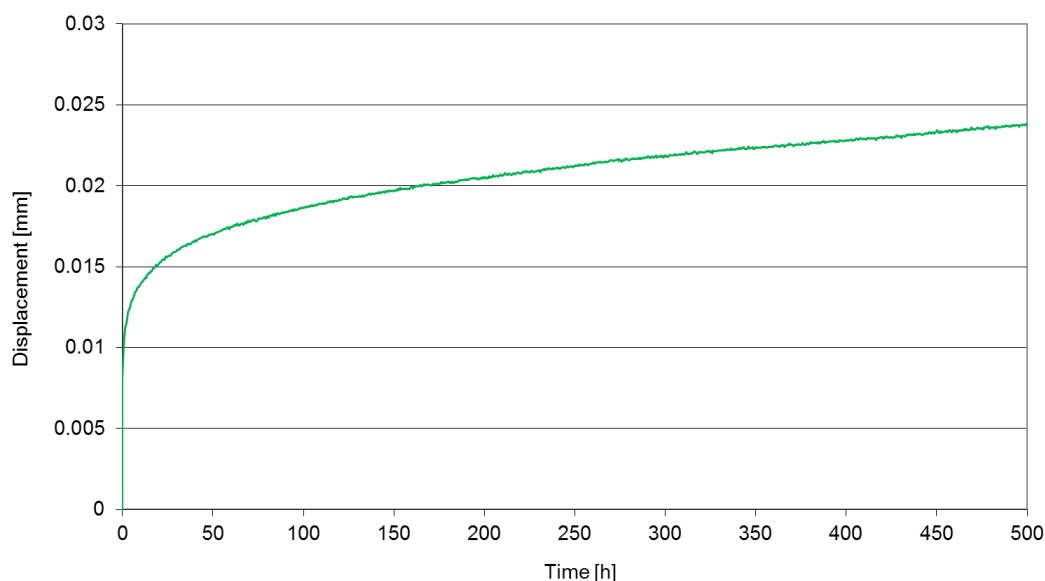

Figure 3. Impression Creep displacement curve for P91 at 89 MPa at 600°C.

4. Floating indenter

The loading bars illustrated in Figure 1 do not allow any flexibility to adjust the initial contact between the specimen and the indenter. Therefore, a flexible indenter was designed, which can tilt around the axis perpendicular to the indenter blade as shown in Figure 4. During setting up of the test the flexible indenter is moved sideways with a small load on (<10 N) until a good contact with the specimen is achieved. Flexibility around the second axis is of lesser importance as the indenter is just 1 mm wide and the initial plasticity will help achieve full contact of the indenter surface, as can be concluded from Figure 3 where the initial plasticity is several micrometers. The initial contact problem is valid only in the first test of step-loaded test series where the test load is increased after a "steady state" creep rate is achieved. A perfect contact is guaranteed in the subsequent tests.
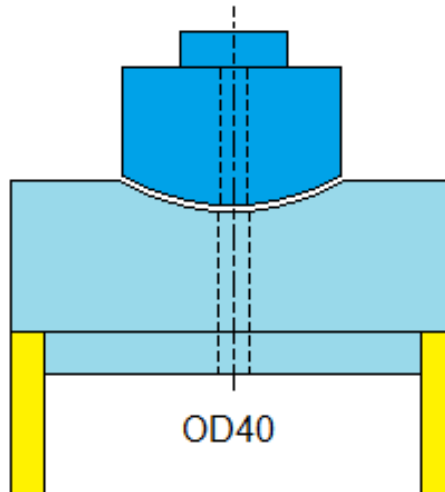
Figure 4. Schematic picture of the floating indenter with holes for the thermocouples

5. Gas tightness for Small Punch

Oxygen is a very aggressive element and will easily move against the gas flow and even against higher pressure. Therefore, oxygen ingress will be inevitable if the rig is not gas tight. For Small Punch testing at VTT a stainless steel tube is used instead of a ceramic tube because either this can be welded into the test rig body or as in our case a conical 45° part can be welded to one end of the tube and tightened against a counterpart in the test rig, allowing gas tightness and removal of the part. At the other end, a rubber bellow is used to prevent argon gas leak from between the tube and the 3 mm ceramic rod used for deflection measurement from below the SP specimen.

A much bigger challenge is to combine gas tightness with frictionless movement of the puncher. At VTT this has been achieved by using a metallic bellow which is welded into a stainless steel tube from both ends as shown in Figure 5. The puncher runs through the tube and is fitted by a flange connection. The wall thickness and the outer diameter of the bellow are 0.1 mm and 19 mm, respectively. Welding of such a thin wall proved to be painful when holes were burned and gas tightness lost. Finally, with orbital micro-TIG welding a sound joint was produced and gas tightness achieved. In hindsight, an easier option would have been to use factory made Swagelok corrugated tubes.

The metallic bellow will produce a spring load and this will reduce the load experienced by the specimen. The combined spring constant of the bellow and the displacement extensometers is 4.32N/mm and this has to be compensated for as a function of the puncher displacement. This is done either by increasing the load setting by hand or automatically by a computer controlled testing machine.

Figure 5. Metallic bellow welded into a stainless tube.

6. Combined thermocouple and extensometer rod for Small Punch

As the deflection of the SP specimen should be measured from below and the temperature should be measured preferably directly from the specimen a solution was introduced by combining these two functions by using a 3 mm ceramic rod with two holes inside for thermocouple wires. 0.5 mm S-type thermocouple wires were inserted through the holes and micro-TIG welded into a 0.5 mm thick Nimonic plate with 0.5 mm holes as shown in Figure 6. At the outer end, the thermocouple wire holes were sealed by epoxy glue. This arrangement then allows a direct measurement of the specimen temperature and the deflection measurement from below the specimen.
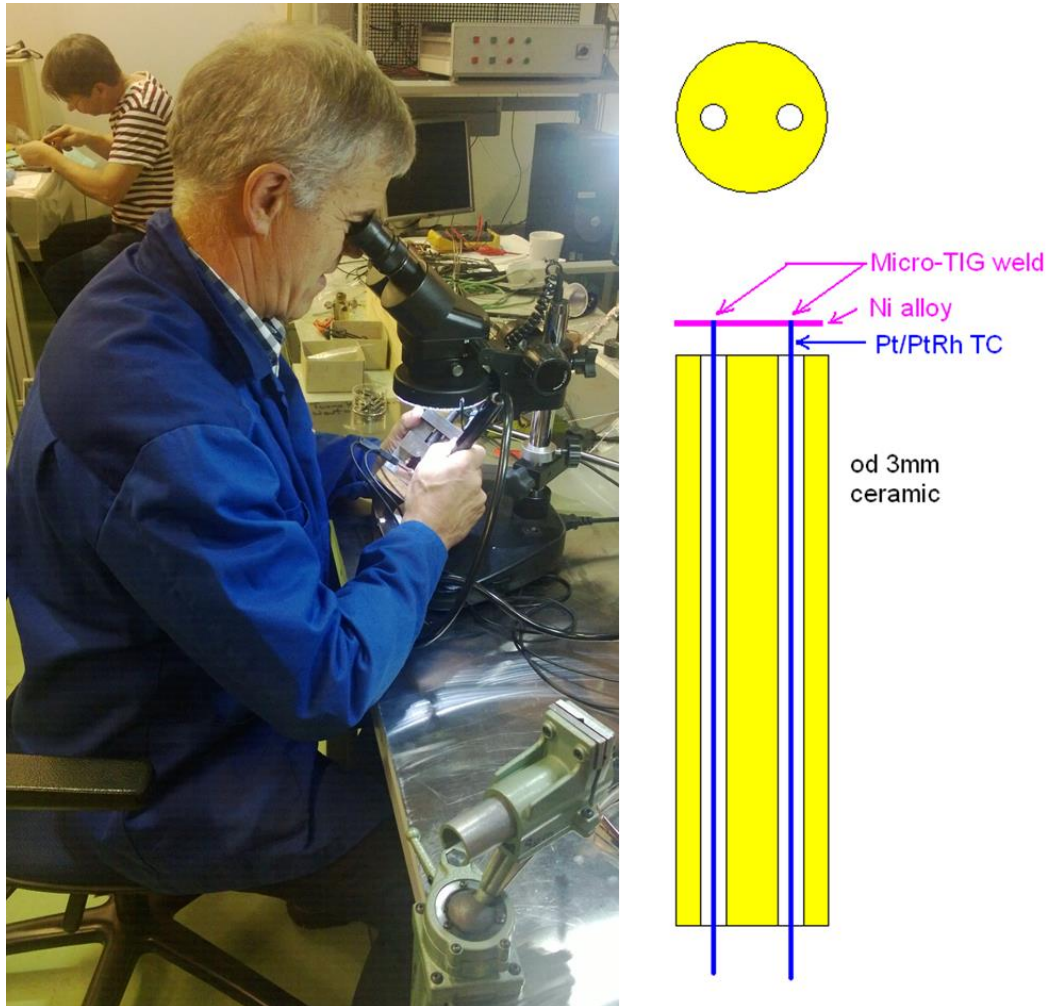

Figure 6. Welding of the thermocouple-extensometer combination by micro-TIG under microscope.

Development of a two-material miniature specimen testing technique and the associated inverse approach

W. Wen [1,*], W. Sun [1] and A.A. Becker [1]

[1]Faculty of Engineering, University of Nottingham, University Park, Nottingham NG7 2RD, UK

*Correspondence: wu.wen@nottingham.ac.uk; Tel.: +44-752-697-3730

Abstract: A miniature two-material test specimen has been developed for material property characterisation. A creep damage model has been applied for a semi-analytical computing model and a finite element (FE) model to simulate a miniature specimen for tensile or creep testing on a two-material system. An inverse optimisation algorithm has been developed, which can be used to extract the creep properties of the unknown material in the two-material system. Single material miniature specimen tensile tests have been performed for an aluminium alloy at room temperature and 400ºC and full stage creep tests have been performed for a P91 steel at 650ºC. The experimental results have been compared to the results from the corresponding conventional uniaxial tensile and creep tests on the same materials and under the same test conditions. Potentially, this miniature specimen testing technique and the developed inverse method could become an alternative approach for determining the elastic-plastic and creep properties for a two-material system at high temperature, e.g. a coating-substrate system.

Keywords: Tensile; Creep; Two-Material; Miniature Specimen; Inverse Method

---

Nomenclature

Symbol	Definition	Units
S_1, S_2	Cross-sectional areas	mm^2
$\sigma, \sigma_1, \sigma_2, \sigma_{eq}, \sigma_r$	Stresses	MPa
P	Loading force	N
L, L_0	Lengths	mm
u, u_1, u_2	Displacements	mm
$\varepsilon, \varepsilon_1, \varepsilon_2$	Strains	
E, E_1, E_2	Young's moduli	
A, B, n, χ, ϕ	Creep properties	MPa
η	Reference stress conversion factor	
β	Reference strain conversion factor	

1. Introduction

A high temperature environment is a common operating condition for many engineering applications, such as power plants, chemical plants, gas turbines and aero-engines. In many cases, it is desirable to assess the material behaviours and predict the future performance of certain components or structures for economic efficiency and risk management. For instance, creep strain and damage, which occur at elevated temperatures for extended periods of time, could lead to catastrophic failure of critical components or structures. A coating-substrate system is a typical case in the scenario of advanced high temperature applications. Usually the thickness of the coating is small and it is difficult to extract a large specimen for a conventional uniaxial creep test. Therefore, a small specimen testing technique is particularly desired in this case. Various types of small specimen testing technique have been used for mechanical and creep property characterisation [1, 2]. For example, the impression creep test (ICT) (e.g. [3, 4]), the small punch test (SPCT) (e.g. [5-7]), the small ring creep test (SRCT) (e.g. [8, 9]) and the small two bar creep test (STBCT) (e.g. [10, 11]). Figure 1 shows a schematic diagram of the small specimen loading arrangements. The ICT and the SRCT are suitable for determining minimum creep strain rate data,but are not able to provide the tertiary stage creep data. The STBCT provides full stage creep data, but it is difficult to determine which bar fails first. The SPCT can also provide full stage creep data, but the data is difficult to interpret due to the complex nature of the

physical deformation mechanism. The most challenging issue with the SPCT is the conversion or relation of the experimental data to the uniaxial creep test. A code of practice (CoP) was developed to convert the load and displacement data from SPCT to stress and strain data in 2006 [12]. Although this CoP has been accepted by many researchers, the relationships are empirical and developed for a particular testing geometry. It would be useful if an alternative small specimen testing method with more straightforward relation to the conventional creep test can be developed. The use of the inverse method could be an answer to the data conversion issue. Some inverse methods have been proposed to determine the elastic-plastic properties (e.g. [13-16]). Inverse methods have not been commonly used for the characterisation of creep properties (e.g. [7, 17]). The feasibility of extracting steady-state creep properties using an inverse method has been demonstrated, though the creep damage properties have not been included [7]. There are also studies on the creep behaviour analysis of two-material and multi-material systems (e.g. [18-22]). It has been shown that the creep damage properties can be determined numerically from the strain-time curves obtained from the uniaxial creep tests data based on certain assumptions.

The objective of the current study is to develop a miniature specimen testing technique and an inverse method to determine the elastic-plastic and creep damage properties of an unknown material from a two-material system. The proposed testing method can be directly related to the conventional uniaxial tests. Single material miniature specimen tensile tests and creep tests were carried out on an aluminium alloy and a P91 steel for the process of the methodology development. Future tests on the miniature coating-substrate specimen have been planned. The inverse method developed shows the potential to extract full stage creep damage properties of an unknown material from the compound creep testing results of a two material system based on theoretical experiments of the two-material system.
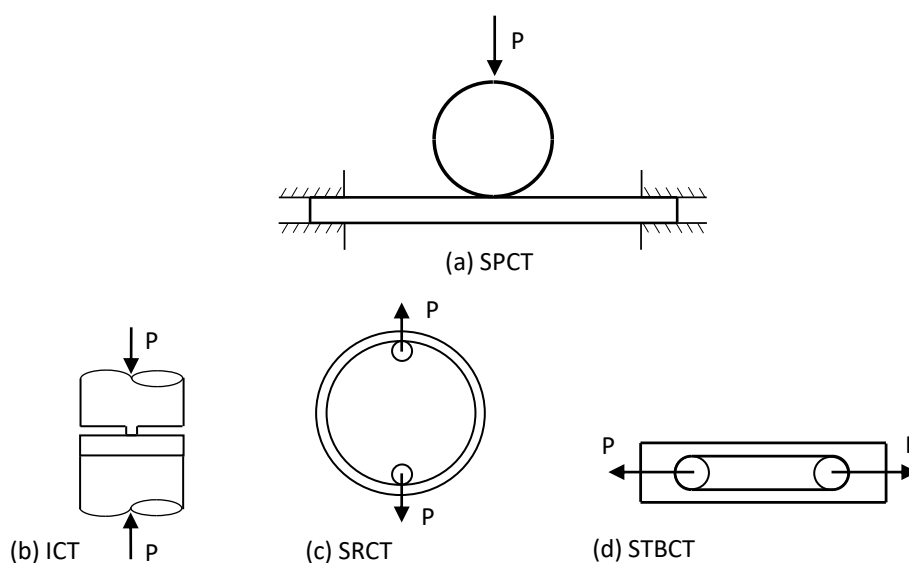

Figure 1. Schematic diagrams showing the small specimen types and loading arrangements: (a) SPT; (b) SIT; (c) SRT; and (d) STBT.

2. Two-Material System

The general methodology of the current study is 1) carrying out single-material tests for a substrate material and a coating material to obtain the single material responses; 2) carrying out two-material system (e.g. coating on substrate) tests to obtain the compound responses; 3) applying the developed inverse method to determine the unknown material properties; 4) using the determined material properties for semi-analytical computation or FE modelling of the single-material tests and comparing the predicted material behaviour to the experimental results to validate the reliability of the inverse method.

A two-material specimen in tension is shown in Figure 2. The two layers have equal length, L, equal width, d, and different thicknesses, h_1 and h_2, therefore, different cross-sectional areas, S_1 and S_2. It is assumed that the

properties of one of the materials are known in this study (e.g. the substrate material properties are known for a coated system).
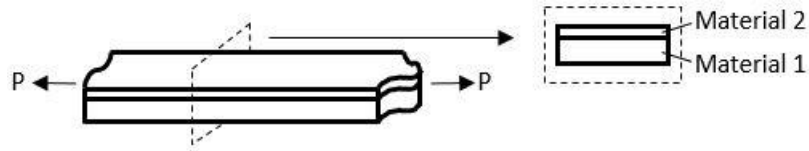

Figure 2. A two-material specimen in tension.

2.1. Tensile Behaviour

The equilibrium equation for the two-material system under tensile force, P, can be expressed as follows:

$$\sigma_1 S_1 + \sigma_2 S_2 = P \tag{1}$$

where σ_1, σ_2 are the stresses in materials 1 and 2, respectively. S_1 and S_2 are the cross-sectional areas of materials 1 and 2, respectively. The compatibility equation (the two layers have equal displacements) is:

$$u_1 = u_2 = u \tag{2}$$

or

$$\varepsilon_1 = \varepsilon_2 = \varepsilon \tag{3}$$

where u_1, u_2 and ε_1, ε_2 are the displacements and strains in materials 1 and 2, respectively. Assuming a power law hardening behaviour, the elastoplastic stress-strain relationships are expressed as follows:

$$\sigma = \begin{cases} E\varepsilon, & \varepsilon < \frac{\sigma_y}{E} \\ K\varepsilon^n, & \varepsilon \geq \frac{\sigma_y}{E} \end{cases} \tag{4}$$

where $K = E^n \sigma_y^{1-n}$. E, σ_y and *n* are the Young's modulus, yield stress and hardening exponent, respectively. The stress in the known material 1 can be determined as follows:

$$\sigma_1 = \begin{cases} E_1\varepsilon, & \varepsilon < \frac{\sigma_{y1}}{E_1} \\ E_1{}^{n_1}\sigma_{y1}{}^{1-n_1}\varepsilon^{n_1}, & \varepsilon \geq \frac{\sigma_{y1}}{E_1} \end{cases} \tag{5}$$

where E_1, σ_{y1} and n_1 are the Young's modulus, yield stress and hardening exponent of material 1, respectively. The stress in the unknown material 2 can be determined from Eqs (1) and (3):

$$\sigma_2 = \frac{P - \sigma_1 S_1}{S_2} \tag{6}$$

The constitutive equations for material 2 are as follows:

$$\sigma_2 = \begin{cases} E_2\varepsilon, & \varepsilon < \frac{\sigma_{y2}}{E_2} \\ E_2{}^{n_2}\sigma_{y2}{}^{1-n_2}\varepsilon^{n_2}, & \varepsilon \geq \frac{\sigma_{y2}}{E_2} \end{cases} \tag{7}$$

where E_2, σ_{y2} and n_2 are the Young's modulus, yield stress and hardening exponent of material 2, respectively. They can be determined numerically.

2.2. *Creep Behaviour*

2.2.1. Steady-State Creep

For steady-state creep, the creep strain rate, $\dot{\varepsilon}^c$, can be expressed as follows:

$$\dot{\varepsilon}^c = A\sigma^n \tag{8}$$

where σ is the stress and A and n are material constants. Assuming that the properties of material 1, i.e. A_1 and n_1, are known, the stress in material 1 can be determined with the measured strain rate $\dot{\varepsilon}^c$ using Eq (8) as follows:

$$\sigma_1 = \left(\frac{\dot{\varepsilon}^c}{A_1}\right)^{\frac{1}{n_1}} \tag{9}$$

with the equilibrium and compatibility equations (1)-(3), the stress in material 2 can be determined as follows:

$$\sigma_2 = \frac{P-\left(\frac{\dot{\varepsilon}^c}{A_1}\right)^{\frac{1}{n_1}} S_1}{S_2} \tag{10}$$

The creep properties of material 2, A_2 and n_2, can be determined numerically from the following constitutive equation:

$$\dot{\varepsilon}^c = A_2 {\sigma_2}^{n_2} = A_2 \left(\frac{P-\left(\frac{\dot{\varepsilon}^c}{A_1}\right)^{\frac{1}{n_1}} S_1}{S_2}\right)^{n_2} \tag{11}$$

2.2.2. Creep Damage

A Kachanov type creep damage model can be used to represent the creep behaviour (e.g. [23]). The formulations for the case of uniaxial stress state can be expressed as follows:

$$\dot{\varepsilon}^c = A\left(\frac{\sigma_{eq}}{1-\omega}\right)^n \tag{12a}$$

$$\dot{\omega} = B \frac{\sigma_r^\chi}{(1-\omega)^\phi} \tag{12b}$$

where σ_{eq} and σ_r are the equivalent and rupture stresses, respectively ($\sigma_{eq}=\sigma_r$ in the case of uniaxial stress); ω ($0 \leq \omega \leq 1$) is a damage variable; A, n, B, χ, and ϕ are material constants. For material 1 shown in Figure 1, the constitutive equations are:

$$\dot{\varepsilon}^c = A_1 \left(\frac{\sigma_1}{1-\omega_1}\right)^{n_1} \tag{13a}$$

$$\dot{\omega}_1 = B_1 \frac{\sigma_1^{\chi_1}}{(1-\omega_1)^{\phi_1}} \tag{13b}$$

Assuming the creep properties of material 1 (A_1, n_1, B_1, χ_1, and ϕ_1) are known, the stress σ_1 can be determined from Eq (13b) by applying the experimentally determined minimum strain rate (MSR), $\dot{\varepsilon}^c_{min}$, for the steady-state creep, during which there is no creep damage, i.e. $\omega_1 = 0$:

$$\sigma_1 = \left(\frac{\dot{\varepsilon}^c_{min}}{A_1}\right)^{\frac{1}{n_1}} \tag{14}$$

With the equilibrium and compatibility equations (1)-(3) and Eq (14), the stress in material 2 can be determined as follows:

$$\sigma_2 = \frac{P-\sigma_1 S_1}{S_2} = \frac{P-\left(\frac{\dot{\varepsilon}^c_{min}}{A_1}\right)^{\frac{1}{n_1}} S_1}{S_2} \tag{15}$$

The creep constitutive equations of material 2 are as follows:

$$\dot{\varepsilon}^c = A_2\left(\frac{P-(\frac{\dot{\varepsilon}^c_{min}}{A_1})^{\frac{1}{n_1}}S_1}{S_2(1-\omega_2)}\right)^{n_2} \tag{16a}$$

$$\dot{\omega}_2 = \frac{B_2}{(1-\omega_2)^{\phi_2}}\left(\frac{P-(\frac{\dot{\varepsilon}^c_{min}}{A_1})^{\frac{1}{n_1}}S_1}{S_2}\right)^{\chi_2} \tag{16b}$$

where A_2, n_2, B_2, χ_2, and ϕ_2 are the unknown creep constants of material 2, which can be determined numerically using Eq (15), (16a) and (16b).

2.3 Forward Analysis of the Two-Material System

Forward analysis can be performed for any two-material system with the known material properties based on the analysis presented in section 2.2. A demonstration of the forward analysis of a two-material system with fictional material properties is presented in this section. The elastoplastic behaviours were neglected for simplification since the elastic deformation was relatively small in these presented cases. Table 1 shows the creep damage properties of two fictional materials M1 and M2. The forward analysis was implemented through a semi-analytical computing script developed based on the Kachanov creep damage model as presented in section 2.2.2. Since the creep properties of the two materials are known, the compatibility condition (equal creep strain rate), the equilibrium condition and the Kachanov creep damage equations can be used for semi-analytical computations. To verify the computations, FE modelling has been carried out to simulate the creep responses under the same conditions and with the same material properties. Figure 3 shows the stress contour of the FE model, featuring the uniform stresses in the two layers of different materials as assumed for the semi-analytical computation.

The comparison between the semi-analytical computations and the FE modelling is shown in Figure 4. Figure 4(a) shows that the compound creep strains (the creep strains in the two material layers M1 and M2 are equal in both cases) obtained from semi-analytical computations and FE modelling agree very well. Figure 4(b) shows the creep damage evolutions of the two materials. The damage history of the two material layers are different: the MSR in material M1 is much higher than M2. The computation and the FE modelling show very close results again. Figure 4(c) shows the stress variations in the two materials. Again, the results from the semi-analytical computations and the FE modellings are very similar. For the semi-analytical computations, the instantaneous stresses in the two materials were obtained semi-analytically using the instantaneous damage values and creep strain rates obtained from the Kachanov creep damage model. The stresses in the two material layers show opposite trends: one increases and the other decreases. This is expected based on the equilibrium conditions since the total loading force is constant (44N). An instant change in the stresses can be seen at the beginning of the FE analysis which reflects the redistribution of the stress occurring at the transition point from elastic deformation to creep deformation. The slight differences found between the results from the semi-analytical computations and FE modelling might be mainly due to the fact that a uniaxial stress case was assumed for the computation while that was not exactly the case for the FE modelling. As a result, the equivalent stresses from the FE modelling were slightly lower than the computed stresses, as shown in Figure 4(c). This explains the fact that the creep strains and creep damage values from the FE modelling are slightly lower than the corresponding computed results, as shown in Figure 4(a) and (b).

Table 1. The creep damage properties of the fictional materials M1 and M2.

	A	n	B	χ	ϕ
M1	5×10^{-24}	11	2×10^{-22}	11	5
M2	5×10^{-25}	10	2×10^{-24}	10	4.5
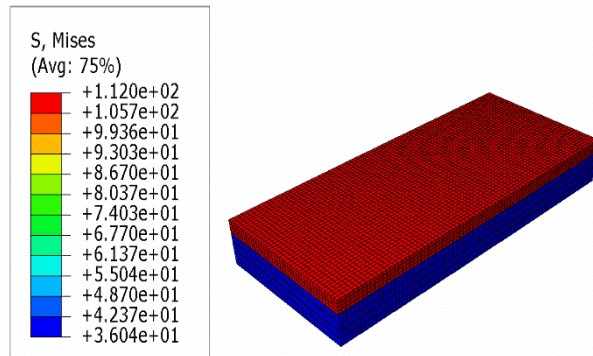
Figure 3. FE modelling Von Mises stress contour of the two-material system creep test.
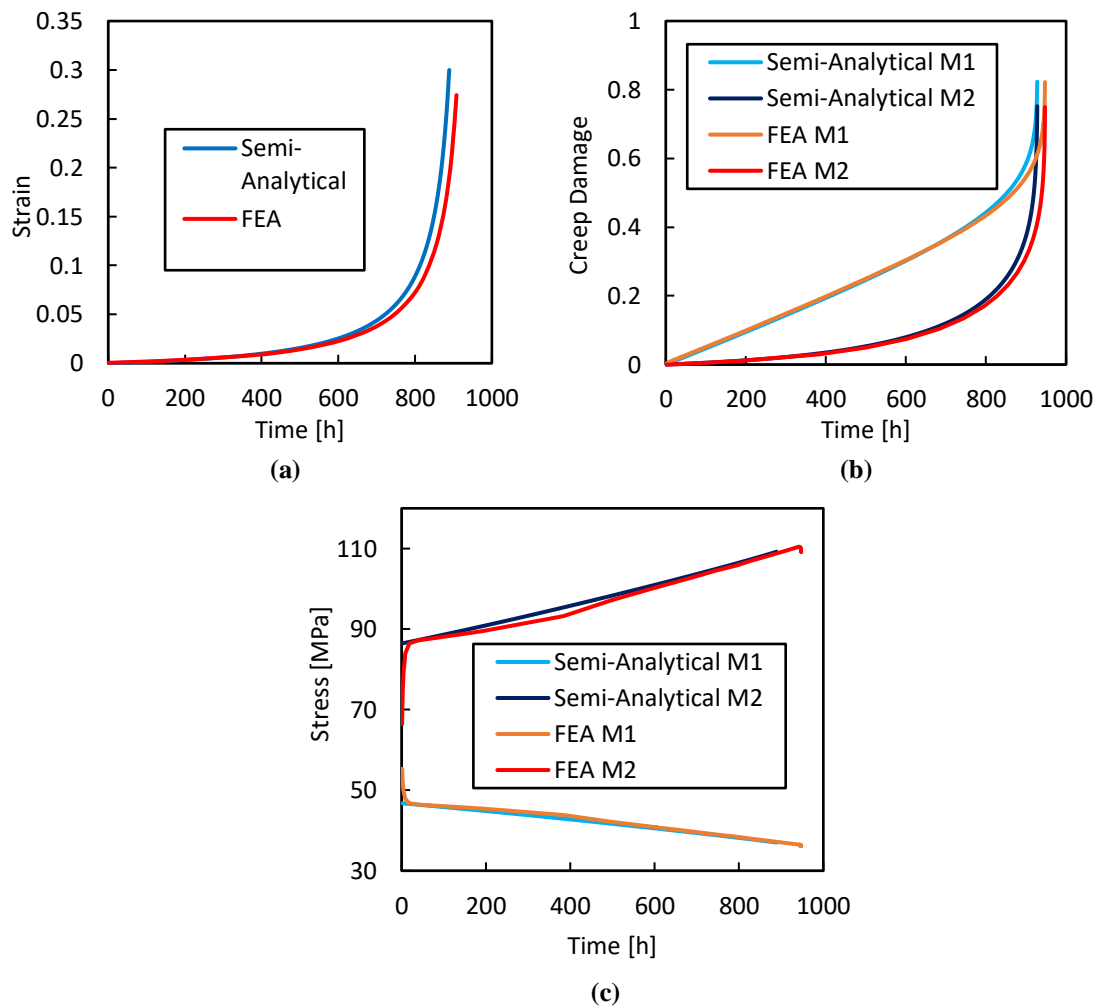

(a)

(b)

(c)

Figure 4. Forward creep analysis for the two-material system (M1 and M2) under the load of 44N: **(a)** creep strain **(b)** creep damage **(c)** stress.

3. Inverse Method and Application

3.1 The Inverse Method

An inverse method was developed based on the forward analysis method presented in section 2.3. FE modelling can be avoided to save computing time since the results of the semi-analytical computations have been proven to be very close to the FE modellings. Figure 5 shows a flowchart of the inverse algorithm. The experimental compound creep test results are supplied as the target values. The known material creep properties and an initial guess of the unknown material creep properties are supplied to the forward analysis method developed based on the Kachanov creep damage model (section 2.3). A nonlinear optimisation algorithm is used to minimise the differences

between the predicted compound creep responses and the experimental results until a set of optimised creep damage properties are obtained for the unknown material.
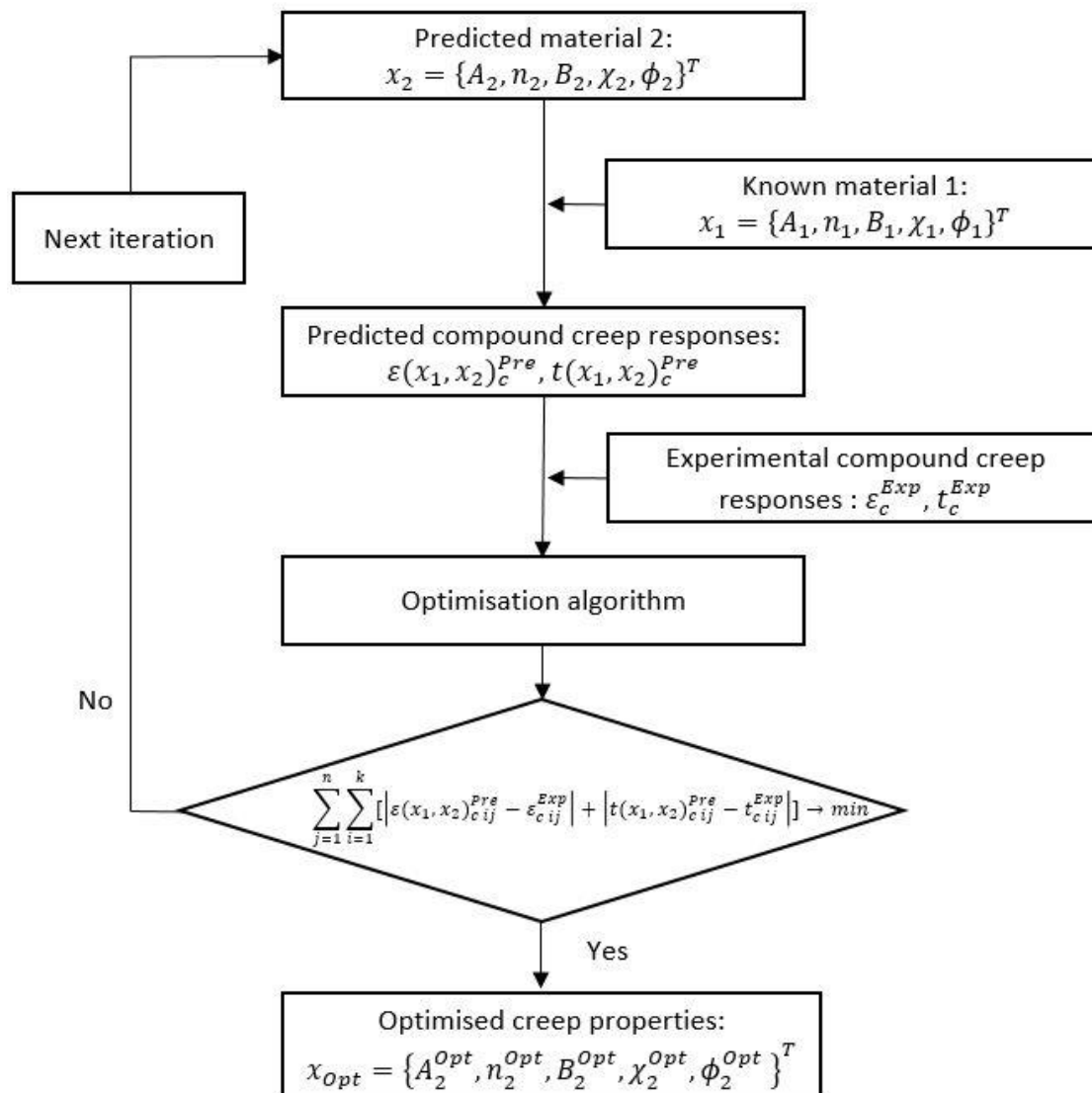

Figure 5. Flowchart of the inverse algorithm.

3.2 Application of the Inverse Method

To demonstrate the application of the proposed inverse method, it was applied to the two-material system used for the forward analysis presented in section 2.3, assuming that the properties for material M1 are known while the properties for material M2 are unknown. The objective was to determine the creep damage properties of M2 from the compound creep responses. Three different loads, 44N, 46N and 48N, were applied to the two-material system with the creep properties for materials M1 and M2 shown in Table 1 to produce three "theoretical" compound creep stress-strain curves (equivalent to the experimental compound creep responses shown in Figure 5) as the targets of the optimization. Figure 6 shows the strain-time curves obtained from the optimised creep damage properties compared to the theoretical experiment. It can be seen that the optimised results agree very well with the target curves for all three different loading forces regarding the creep strain rate and the time to failure. To evaluate the quality of the optimisation, the creep strain-time curves were also computed numerically using the creep properties of M2 and the optimised creep properties for a single-material model with three different loading forces: 75N, 80N and 85N. The comparison is shown in Figure 7. It can be seen that the agreement is still acceptable, i.e. the strains during the steady-state creep stage are very close for the material M2 (Table 1) and the optimised material at all three loading forces. Although the deviation increases as the creep develops near to failure. These results reveal that the optimised creep properties were close to the actual properties of the target material M2. It should be noted that the current inverse optimisation algorithm is still sensitive to the initial values of the unknown creep damage

properties (e.g. some initial values could lead to difficulty in convergence to the desired tolerance or extended computing time). This sensitivity to the initial conditions should be minimised in further development.
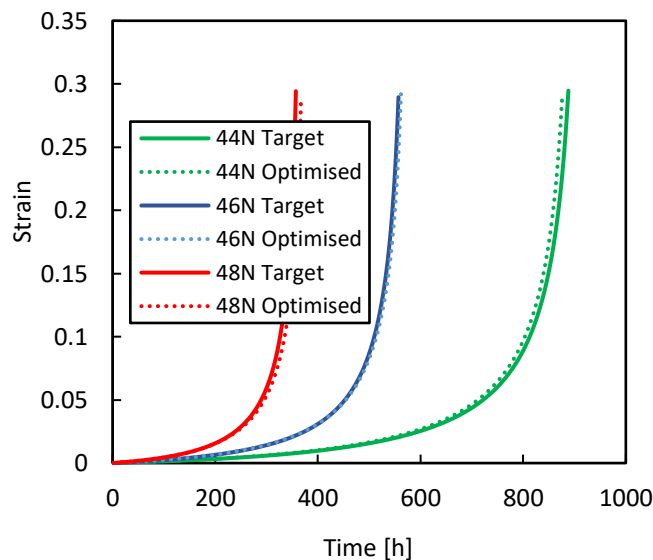

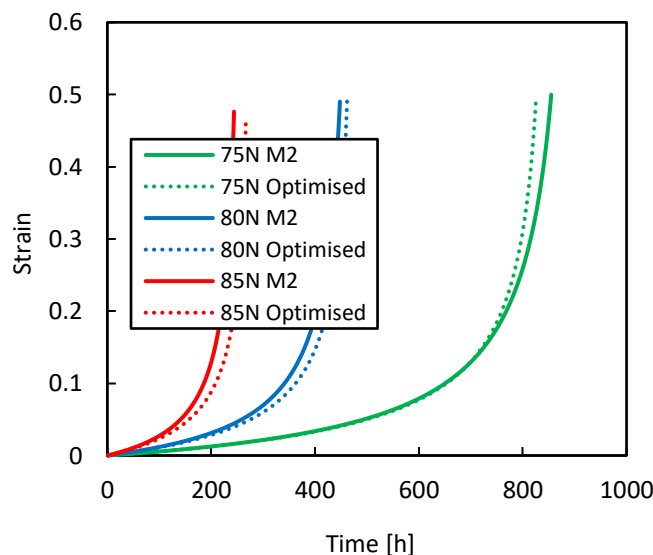**Figure 6.** The inverse optimised curves and the target curves.

Figure 7. The single-material model computations for material M2 (Table 1) and the optimised creep properties.

4. Experimental Testing using Single-Material Specimens

A miniature specimen tensile/creep testing technique has been developed. Tensile tests have been carried out for an aluminium alloy with both miniature specimens and large specimens. Creep tests have been performed at 650°C on a P91 steel at different stress levels: 100MPa, 93MPa, 87MPa, 82MPa and 70MPa for both the miniature and large specimens. These experiments are the foundation work for the objective of determining the high temperature properties of an unknown material from the compound responses of a two-material system, e.g. a coating on a substrate material. Figure 8 shows the geometry of the miniature specimen and the experimental set-up with the specimen mounted to clamps at both ends.
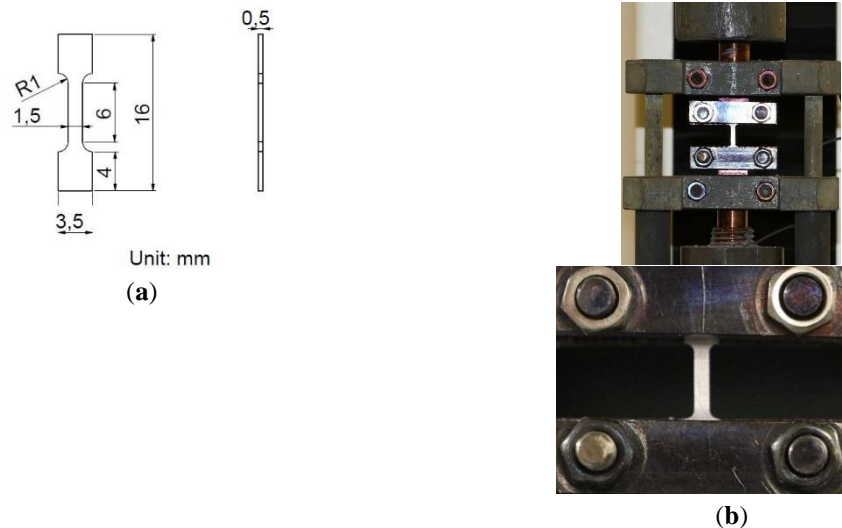
Figure 8. (**a**) Geometry of the miniature specimen; (**b**) The experimental set-up.

4.1. Miniature Specimen Tensile Tests on an Aluminium Alloy

Tensile tests were carried out on an aluminium alloy to be compared to the tensile testing results obtained from the large specimen to validate the developed miniature testing method. Figure 9 shows the comparison between the tensile testing results obtained from the miniature specimens and the large specimens at different temperatures. The results from the two types of tests are generally comparable. The differences in the strain measurement might be due to the random error in the clamping location, which is manually fixed. Also, the sensitivity of the detectors could be another factor of influence. The possible size effects, e.g. on the elastic modulus, yield stress and ultimate tensile stress, could be investigated in the future studies.
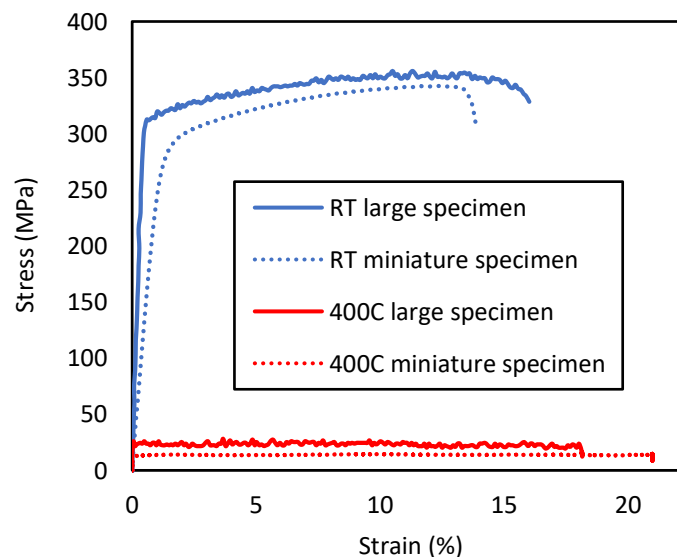

Figure 9. Miniature tensile test results on an aluminium alloy compared to the large specimen tensile test at different temperatures.

4.2 Miniature Specimen Creep Test

4.2.1 Data Conversion

It should be noted that the measurements were taken outside the gauge length region (at the clamped ends) for the miniature specimen tests because it is not feasible to fit a gauge into the very limited space. Therefore, the measured displacement was slightly different from the actual displacement of the gauge length area. In order to validate and interpret the data obtained from the miniature specimen creep test, it is important to ensure that the data can be accurately converted to the corresponding uniaxial creep test results. A reference stress method was applied

to determine the conversion relationships for stress and strain. The case of steady-state creep was applied for the demonstration.

Two conversion factors, η and β, were introduced to define the conversion relationships as follows:

$$\sigma_{ref} = \eta\sigma_{nom} \tag{17}$$

$$\dot{\varepsilon}_{ref} = \frac{\dot{\Delta}}{\beta L_0} \tag{18}$$

where σ_{ref}, $\dot{\varepsilon}_{ref}$, σ_{nom}, L_0 and $\dot{\Delta}$ are the reference stress, reference strain rate, nominal stress, the uniform section length, and the measured displacement rate, respectively. βL_0 is defined as the equivalent gauge length (EGL). The conversion factors are determined by carrying out a series of FE models of the miniature specimen creep test. A Norton power law is assumed to simulate the creep behaviours of the material, i.e. the steady state creep strain rate $\dot{\varepsilon}^c$ is expressed as follows:

$$\dot{\varepsilon}^c = A\sigma^n \tag{19}$$

where A and n are material constants. The conversion factor β can be expressed as follows:

$$\beta = \frac{\Delta}{A(\eta\sigma_{nom})^n L_0} \tag{20}$$

The conversion factors were assumed to depend solely on the geometry, so they should be material-independent. A series of FE models of the miniature specimen creep tests were carried out with different material constants A and n. The parameter n, with the range of 2 to 12, was used for FE modelling. The corresponding values of A were calculated assuming a constant creep displacement/strain rate, i.e. $A_0\sigma^{n_0} = A_i\sigma^{n_i}$. The steady-state creep displacement-time curves obtained from the FE models are shown in Figure 10. It can be seen that the displacement rates, or strain rates, are very close to each other for different cases, indicating that the assumption of an approximately constant strain rate is valid. The minimum displacement rate, $\dot{\Delta}_{ss}$, was calculated for each curve. The objective was to find the value of η with which the value of $\alpha = \frac{\dot{\Delta}}{A(\eta\sigma_{nom})^n L_0}$ becomes independent of A and n. Following the FE modelling, $\log(\alpha)$ was calculated for a range of values of η (0.5 to 1.2) and the results are shown in Figure 11. It can be seen that $\log(\alpha)$ is nearly constant for $\eta = 0.984$, independent of n and A. Therefore, the conversion factor β can be calculated, i.e. $\beta = 1.205$.
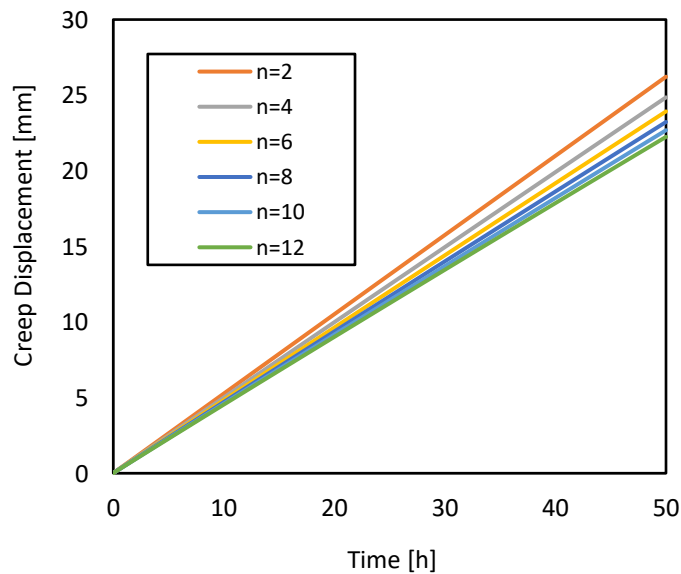

Figure 10. Steady-state creep displacement with variation of n and A.
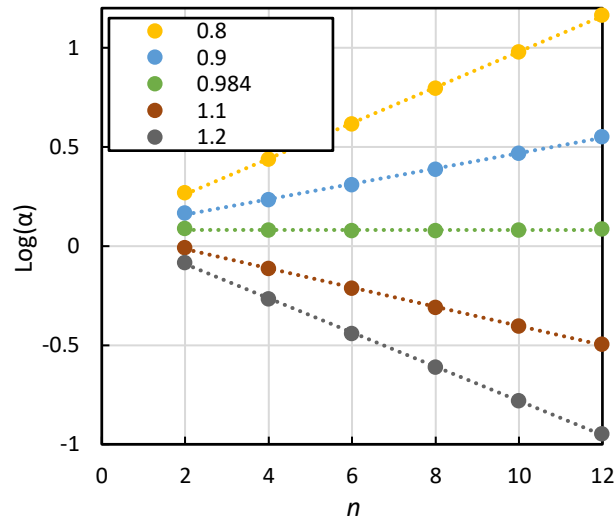
Figure 11. Variation of log(α) with *n* (and the corresponding *A*).

4.2.2 Miniature Specimen Creep Testing Results of P91 Steel

Preliminary creep tests were carried out on P91 steel at 650°C. The specimen geometry and the experimental set-up were the same as that as shown in Figure 6. Constant forces were applied to the specimen to achieve the stress levels of 100MPa, 93MPa, 87MPa and 70MPa. Figure 12 shows the creep testing results obtained from the miniature specimen and the uniaxial creep test. The creep strain rates during the steady state agree well for the miniature specimen test and the uniaxial test at the stress levels of 87MPa and 70MPa. The miniature specimen tests show a higher strain rate and a shorter time to failure compared to the uniaxial tests at higher stress level such as 93MPa and 100MPa. These differences might be due to the local stress concentration resulting from machining, e.g. near the clamp at the gauge length ends. Also, the testing results of the miniature specimen could be affected by the amount of clamping force applied to it, e.g. the pre-existing stress in the material before the creep test. The strain measurement could be affected by the sensitivity of the detectors. For example, the tertiary stage of the 70MPa miniature specimen creep curve is not smooth. Figure 13 shows the variation of the MSR and the time to failure versus stress level, plotted on logarithmic scales. The approximate linear trends indicate the general consistency of the miniature specimen creep tests at different loading levels.
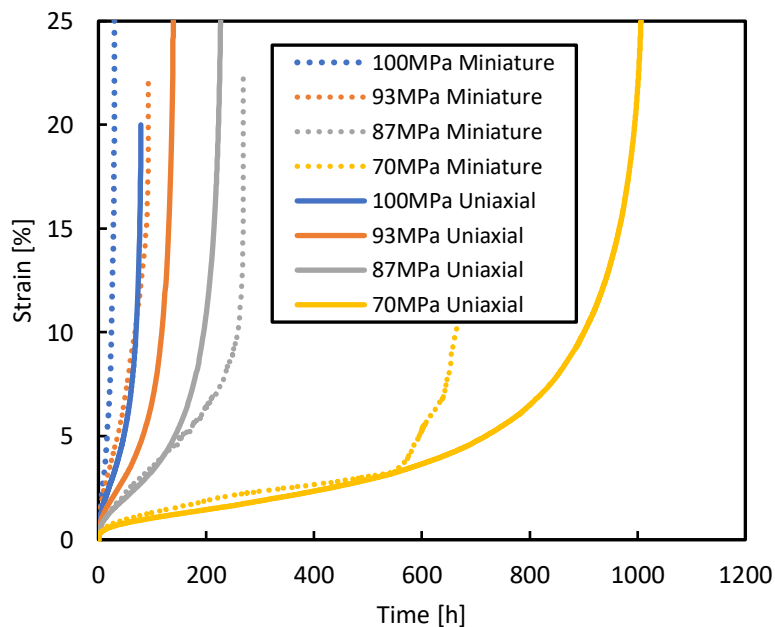

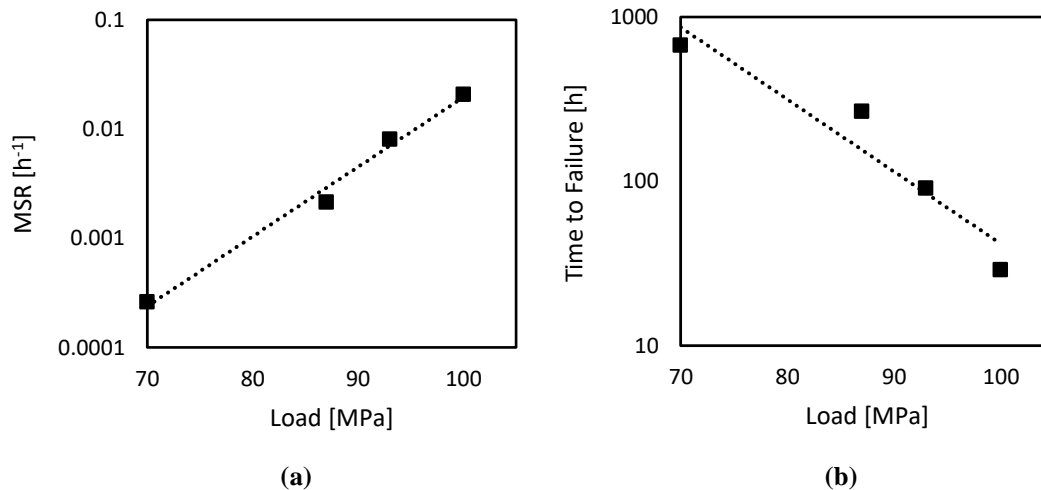**Figure 12.** Miniature specimen creep tests on P91 steel at 650°C.

Figure 13. Variation of **(a)** the MSR and **(b)** the time to failure versus stress level, plotted on logarithmic scales.

5. Discussion and Future Work

The methodology development of a miniature specimen testing technique and an inverse method to determine the creep properties of an unknown material from the compound creep behaviours of a two-material system has been presented. The forward analysis and the inverse method were demonstrated through a case study of a theoretical experiment. The semi-analytical computation and the FE modelling showed very good agreement. The optimised compound creep behaviours were close to the target results. It was verified by the single-material model computations that the optimised creep properties were close to the target material. The differences might be due to that the actual stress distribution in the two material layers was not evaluated by the inverse optimisation approach, since the stress was not a measurable quantity in experiment. As a result, the stresses in the two material layers acted as the extra 'variables' during the optimization process, leading to some random deviations.

Single-material miniature tensile tests and creep tests were carried out on an alunimium alloy and P91 steel, respectively. The experimental results were compared to the results from the large specimen uniaxial tests on the same materials. The results of the miniature specimen tests were generally comparable to the uniaxial tests while some differences were found. Those differences could be a result of the possible local stress concentration due to machining, the random errors in the manual handling procedures (e.g. the clamping locations), the pre-existing strains and the sensitivity of the displacement detectors. Also, the possible size effects will be investigated in future studies.

For future work, creep tests should be carried out on the coating-substrate system with the miniature specimen. The inverse method should be improved regarding the efficiency and the sensitivity to the initial estimation and validated by applying it to the experimental results obtained from single-material tests and coating-substrate miniature specimen tests. Full FE models, instead of only the gauge length part, will be used to simulate the realistic miniature specimen tensile/creep tests of the coated system.

References

1. Hyde T.H.; Sun W.; Williams J.A. The requirements for and the use of miniature test specimens to provide mechanical and creep properties of materials: - a review. *Int. Mater. Rev.* 2007, *52*, 213-55.
2. Morris A.; Cacciapuoti B.; Sun W. The role of small specimen creep testing within a life assessment framework for high temperature power plant. *Int. Mater. Rev.* 2018, *63*, 102-37.
3. Hyde T.H.; Sun W.; Becker A.A. Analysis of the impression creep test method using a rectangular indenter for determining the creep properties in welds, *Int. J. Mech. Sci.* 1996, 38, 1089-102.

4. Sun W.; Hyde T.H.; Brett S.J. Application of impression creep data in life assessment of power plant materials at high temperatures. *J. of Materials: Design and Applications* 2008, 222, 175-82.

5. Rouse J.P.; Cortellino F.; Sun W.; Hyde T.H.; Shingledecker J. Small punch creep testing: a review on modelling and data interpretation. *Mater. Sci. Technol.* 2013, 29, 1328-45.

6. Cortellino F.; Rouse, J.; Cacciapuoti B.; Sun W.; Hyde T. H. Experimental and numerical analysis of initial plasticity in P91 steel small punch creep samples. *Experimental Mechanics* 2017, 57, 1193–212.

7. Li Y.Z.; Stevens P.; Geng J.F.; Ma D.F.; Xu L. Determination of creep properties from small punch test with reverse algorithm. *Key Engineering Materials* 2017, *734*, 212-36.

8. Hyde T. H.; Sun W. A novel, high sensitivity, small specimen creep test. J. of Strain Anal. Eng. 2009, 44, 171-85.

9. Sun W.; Hyde T.H. Determination of secondary creep properties using a small ring creep test technique. *Metallurgical Journal* 2010, 63, 185-93.

10. Sun W.; Hyde T.H.; Ali B.S.M. Small tensile bar specimen creep tests for use in determining creep deformation and rupture properties. *3nd Proc. Int. Conf. SSTT*, ed. K. Matocha, R. Hurst, W. Sun. pp. 360-67. © OCELOT s.r.o. Ostrava, September 2014.

11. Balhassn A.; Hyde T.H.; Sun W.; Analysis and design of a small, two-bar creep test specimen. *Trans. ASME J. Eng. Mater. & Technol.* 2013, 135, 041006-1-041006-9.

12. CEN CWA 15627 Workshop Agreement: Small punch test method for metallic materials (Part A), *European Committee for Standardization*, Brussels, December 2006.

13. Kang J.J.; Becker A.A.; Wen W.; Sun W. Extracting elastic-plastic properties from experimental loading-unloading indentation curves using different optimization techniques. *Int. J. Mech Sci.* 2018 (accepted).

14. Iracheta O., Bennett C.J., Sun W. Characterisation of material property variation across an inertia friction welded CrMoV steel component using the inverse analysis of nano-indentation data. *Int. J. Mech. Sci.* 2016, 107, 253-63.

15. Kang J.; Becker A.A.; Sun W. A combined dimensional and optimization approach for determining elastic-plastic properties from indentation tests. *J. of Strain Anal. Eng.* 2011, 46, 749-59.

16. Kang J.; Becker A.A.; Sun W. Determining elastic-plastic properties from indentation data obtained from finite element simulations and experimental results. *Int. J. Mech. Sci.* 2012, 62, 34-46.

17. Lu J.; Campbell-Brown A.; Tu Shan-Tung; Sun W. Determination of creep damage properties from miniature thin beam bending using an inverse approach. *Key Eng. Mats.* 2017, 734, 260-72.

18. Hyde T.H.; Sun W. Determining creep properties for columnar and equiaxed regions of a 9CrMoNbV weld metal at 650°C using bulk uniaxial creep test data. *Proc. of 3rd Int. Conf. on Integrity of High Temp Welds IoM Communications,* London, April 2007, pp. 139-148.

19. Hyde T.H.; Sun W.; Tang A.; Budden P.J. An inductive procedure for determining the stresses in multi-material components under steady-state creep. *J. of Strain Anal. Eng.* 2000, 35, 347-58.

20. Hyde T.H.; Sun W.; Tang A.A general formulation of the steady-state creep deformation of multi-material components. *Proc. of the 4th Int. Conf. on Modern Practice in Stress and Vibration Analysis*, Nottingham, UK, Ed. A.A. Becker, September 2000, pp. 481-492.

21. Hyde T.H.; Yehia K.; Sun W. Observation on the creep of two-material structures. *J. of Strain Anal. Eng.* 1996, 31, 441-61.

22. Hyde T.H.; Sun W. Elastic-creep behaviour of a three-material plate subjected to a bi-axial stress state. *Materials Science and Engineering A* 2006, 417, 174-81.

23. Kachanov L. On rupture time under condition of creep. *Izvestia Akademi Naul USSR*, Otd. Techn. Nauk, Moskwa, 1958; Volume 8, pp. 26-31.

Application of micro-tensile test for material characterization of mild steel DC01

P. Konopik [1], P. Farahnak [1], M. Rund [1], R. Prochazka [1] and J. Dzugan [1,*]

[1] COMTES FHT a.s., Prumyslova 995, Dobrany, Czech Republic, 33441; pkonopik@comtesfht.cz

* pkonopik@comtesfht.cz; Tel.: +420-723-883-915

Abstract: During recent years, material characterization based on miniature tensile specimens has been investigated extensively. The Small Punch Test (SPT) is often used for determination of tensile properties but alternative miniature tensile specimen geometries have been suggested due to the limitations of the SPT specimen geometry. However, compared to SPT, the Micro-Tensile Test (M-TT) has a significant advantage since it does not need previous established correlations and enables direct results conversion into standard terms. In this paper, the applicability of the M-TT is investigated for material characterization including Lankford coefficients, hardening laws and stress-strain curves. For this purpose, mild steel DC01 M-TT samples were extracted from sheet in Rolling, Transverse and Diagonal Directions. Moreover, M-TT samples were machined to achieve different thicknesses for indicating thickness effects on strain path.

Keywords: Small Punch Test; Micro-Tensile Test; digital image correlation (DIC); Lankford coefficients; DC01 steel

1. Introduction

A substantial effort is currently devoted to the development of small specimens and corresponding test techniques from which useful information can be derived. A number of techniques have been developed to extract mechanical properties from sub-sized specimens [1-4]. These include specimens that are either miniaturized versions of their full-scale counterparts or specifically designed discs or coupon specimens of small dimensions. One of the most used methods is the Small Punch Test (SPT). SPT is widely used, but its application is traditionally bound with necessity of known correlation parameters valid for a specific material only and thus it is impossible to use it on a blind material [5]. Recently, there are assumptions to used trained neural networks for SPT evaluation [6] but again, neural networks can be trained for some material group but they are not generally valid.

Based on the SPT disc, which is typically 8 mm in diameter and 0.5 mm in thickness, a new specimen geometry for developing the testing procedure was suggested [7]. The target was to run a real tensile test, free of any necessary correlations, on specimens using the same material volume as SPT. After initial finite element modelling (FEM) calculations, a specimen with a thickness of 0.5 mm, width of 1.5 mm and parallel length of 3 mm was suggested. The newly proposed specimen size was very small in comparison to standard size or sub-size specimens and thus the new testing procedure was named the Micro-Tensile Test (M-TT).

The specimen did not fit into any kind of testing fixtures and thus the next step was to develop a new set of testing fixtures. Initially, a very simple test set up was used for the first M-TT trials and an actuator LVDT was used for strain measurement. The first results were very promising, since the stress levels obtained at M-TT were very close to those obtained for standard size specimens. A further step was then improvement of the strain measurement. Due to the miniature specimen size, it was not possible to attach a standard extensometer directly on the test piece. Alternatively, the extensometer was attached to the grips. At this stage, it was just slightly improved crosshead measurement. The obtained curves were very similar to the curves obtained for standard size samples, except the yielding part of the curve.

In the last stage of the testing procedure was the development of the strain measurement for M-TT, where Digital Image Correlation (DIC) system ARAMIS was used. The principle of the DIC method is based on the recognition of change in the sequence of images. A stochastic pattern is applied on the surface of the specimen prior to testing. The test itself is recorded by one (2D in-plane deflection measurement) or two (3D) cameras. Under the applied load, the specimen is deformed and so is the applied pattern. Comparing the images, changes in the pattern are registered and displacements and strains are calculated. Systems based on this method enable 3D strains measurements of either testing samples or real components to be recorded. Distribution of major or minor strain can be depicted in color maps (see Figure 1) but for M-TT, DIC was used as a very precise video extensometer.
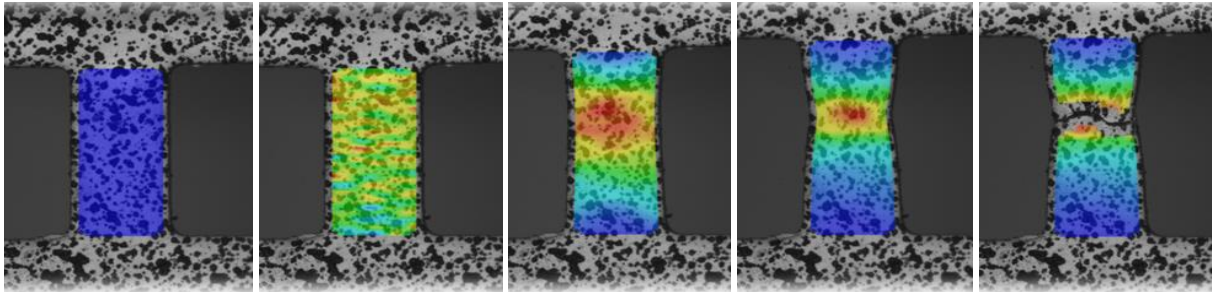
Figure 1. Color map of major strain of M-TT sample.

Tests were carried out on several various materials with a wide range of tensile properties. Namely, Al-alloy, Ni-alloy, Titanium Gr. 5, and several steels were compared while tested on standard size specimens and with the use of M-TT. Standard size samples were cylindrical with diameters ranging from 5 to 10mm. The resulting curves of these tests were almost identical and there can be found excellent agreement for all materials investigated between standard size specimens and M-TTs for a whole range of strength levels from about 250MPa up to 1250MPa [8].

Nowadays, M-TT is used for a wide range of applications (in addition to the standard tensile properties already mentioned):

- Local mechanical properties of steel weld [9]
- Tensile properties for high temperature (hot M-TT) [10]
- Strain rate sensitivity [11]
- High and low cycle fatigue [12–14]

In this paper, the application of M-TT for determination of Lankford coefficients and strain hardening determination is investigated. These parameters are crucial as input data for any reliable material model represent the material behaviour in the course of the processing. To demonstrate usability of the M-TT for the above mentioned purpose, metal sheet DC01was chosen as a very well known and widely used material for metal sheet forming. Metal sheets exhibit certain peculiarities in comparison to bulk materials, due to their crystallographic structure and the characteristics of the rolling process where sheet metals usually exhibit a certain degree of mechanical properties anisotropy. The properties variation has to be described together with strain hardening for precise material behaviour description. Moreover M-TT can be effectively applied for FEM models verification, e.g. by evaluation of local ductility of sheet in the processed component that can be confronted with FEM model prediction for the same location. During the sampling from components with very complex shapes, the M-TT specimen can be expected to obtain lower thickness than is initially used in sheet. Therefore, M-TT was machined to achieve different thicknesses for indicating thickness effects on strain path.

2. Standard and M-TT tests

Tensile tests were performed on flat samples made of DC01steel sheet according to standards [15,16]. The original sheet thickness was 1.5 mm. Standard size specimens with a thickness of 1.5 mm and the geometry according to Figure 2a were milled as a stock of 10 specimens. M-TT specimens, with the geometry according to Figure 2b and thicknesses of 0.2 mm and 0.5 mm, were machined from the middle part of the sheet by spark eroding of the specimen silhouette and grinding to the final thickness. M-TTs specimens with a thickness 1.5 mm were not grinded at all.
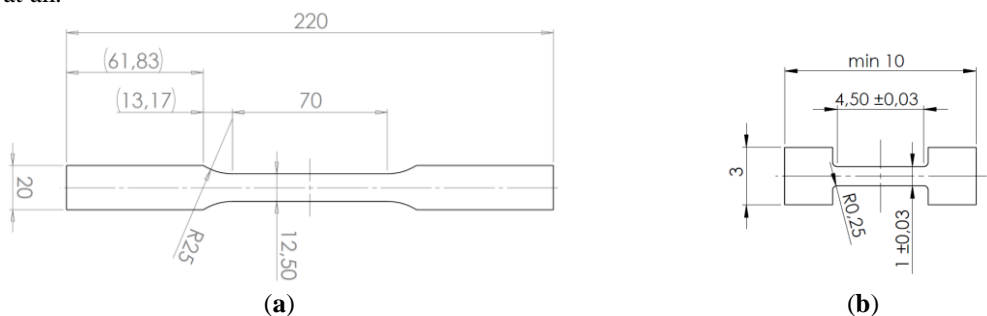

(**a**) (**b**)

Figure 2. Tensile test specimen geometry: (**a**) Standard geometry; (**b**) M-TT geometry.

Standard specimen orientations were considered for both specimen geometries: longitudinal direction 0°, diagonal direction 45° and transverse direction 90°, related to the rolling direction. Testing was carried out with the use of the MTS servo-hydraulic testing system with the capacity of 25 kN for standard sized specimens. M-TT specimens were tested on a small size testing system with a linear drive with the load capacity of 5 kN. All tests were executed at room temperature and the strain measurement was achieved with the use of a Mercury RT Digital Image Correlation system (DIC). Three specimens per condition were tested for all considered cases. Quasi-static tensile tests were carried out for both specimen geometries and all sampling directions for comparison of the results obtained from standard size and M-TT specimens. On the basis of these tests, strain hardening and plastic strain ratio were subsequently evaluated. Specimen designation consists of specimen geometry (Standard or M-TT), specimen orientation and the specimen thickness in mm. Representative tensile curves obtained for all tested conditions are shown in Figures 3-5.
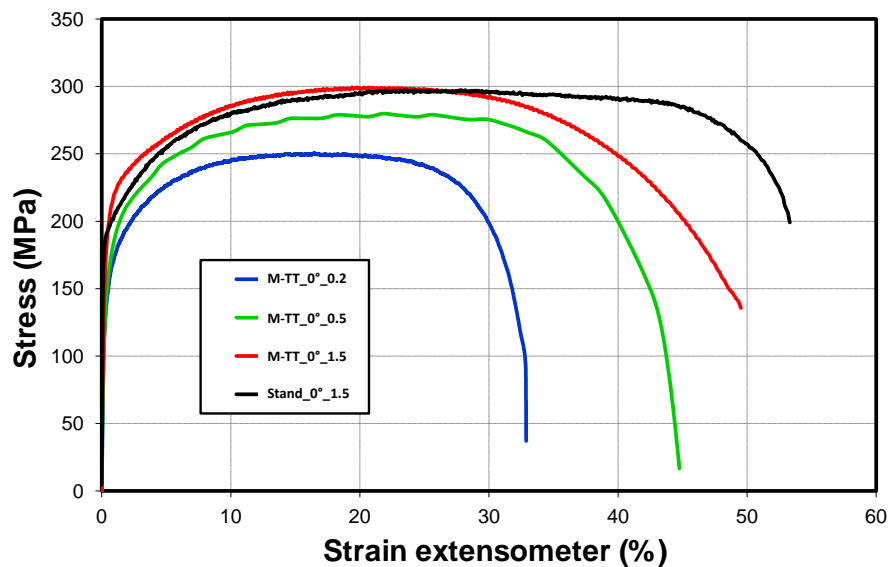

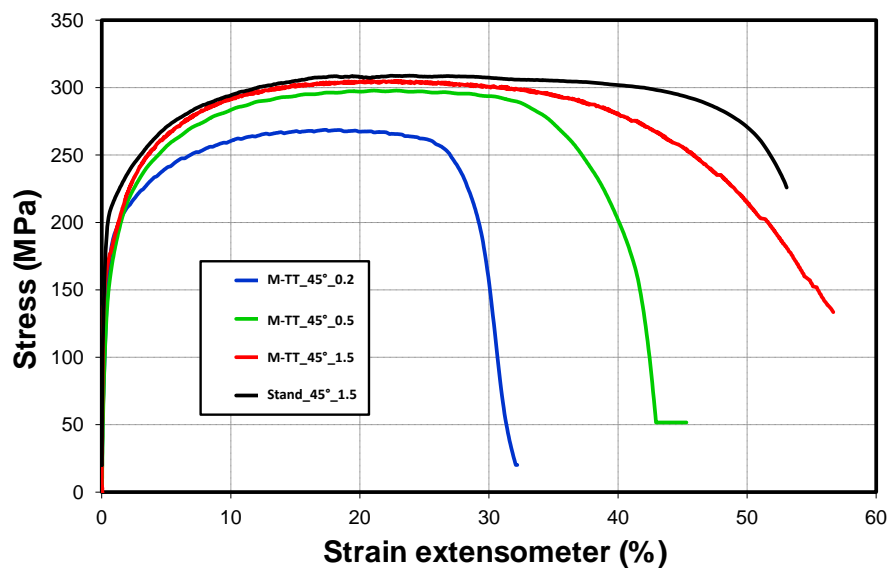**Figure 3.** Tensile curves of both specimen geometries in longitudinal direction.

Figure 4. Tensile curves of both specimen geometries in diagonal orientation.
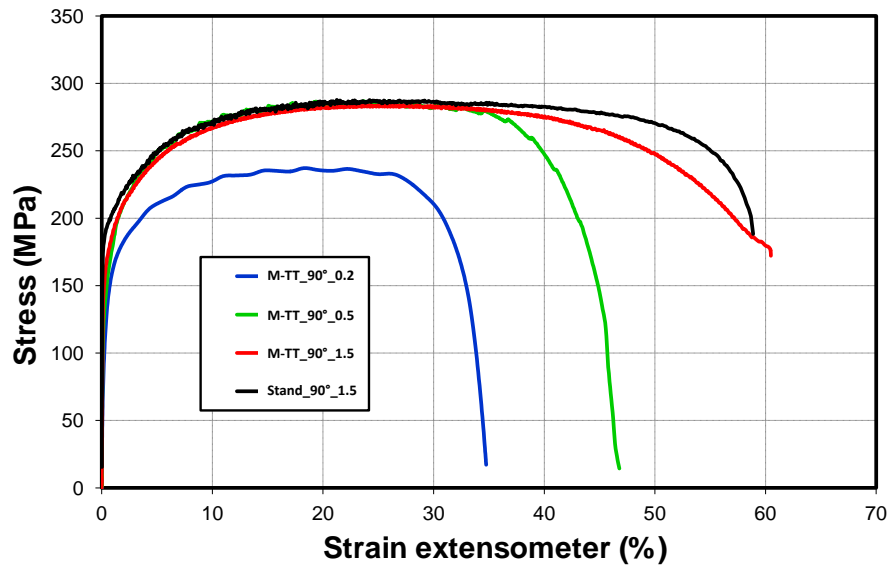
Figure 5. Tensile curves of both specimen geometries in transversal orientation.

3. Evaluation and Results

3.1. Tensile test

Tensile tests were evaluated based on ISO 6892-1 standard [15]. Results of averaged values from three tests per conditions are shown in Table. 1, where YS is Yield strength, UTS is Ultimate tensile strength, A_g is plastic extension at maximum force, A is permanent elongation of the gauge length after fracture (GL for standard geometry was 50 mm and for M-TT 4 mm) and Z is maximum change in cross-sectional area.

Table 1. Summary of tensile tests results.

Specimen	YS	UTS	A_g	A	Z
	MPa	MPa	%	%	%
M-TT_0°_0.2	151.4	238.8	15.8	34.8	58.4
M-TT_0°_0.5	179.8	283.7	17.9	50.2	78.2
M-TT_0°_1.5	182.0	292.1	20.9	56.6	81.6
Standard_0°_1.5	189.3	297.2	24.2	42.1	65.7
M-TT_45°_0.2	172.2	269.7	16.8	32.0	51.8
M-TT_45°_0.5	178.6	302.8	21.2	41.9	72.6
M-TT_45°_1.5	192.1	303.5	21.7	58.2	85.6
Standard_45°_1.5	199.8	310.8	23.2	42.3	41.8
M-TT_90°_0.2	147.5	228.4	17.9	36.4	54.8
M-TT_90°_0.5	161.1	287.0	22.8	50.9	81.5
M-TT_90°_1.5	166.9	284.1	26.0	60.4	85.9
Standard_90°_1.5	190.2	292.7	23.0	45.4	66.7

3.2. Strain hardening

The evaluation of strain hardening parameters was carried out based on Hollomons equation 1:

$$\sigma = C.\varepsilon^n. \tag{1}$$

Where the power law relationship between the stress and the amount of plastic strain is used. The fitting range considered for the Hollomons law parameters is between 2-A_g percent of the plastic strain. The example of the evaluation is shown in Figure 6. Results are summarized in Figures 7-8.
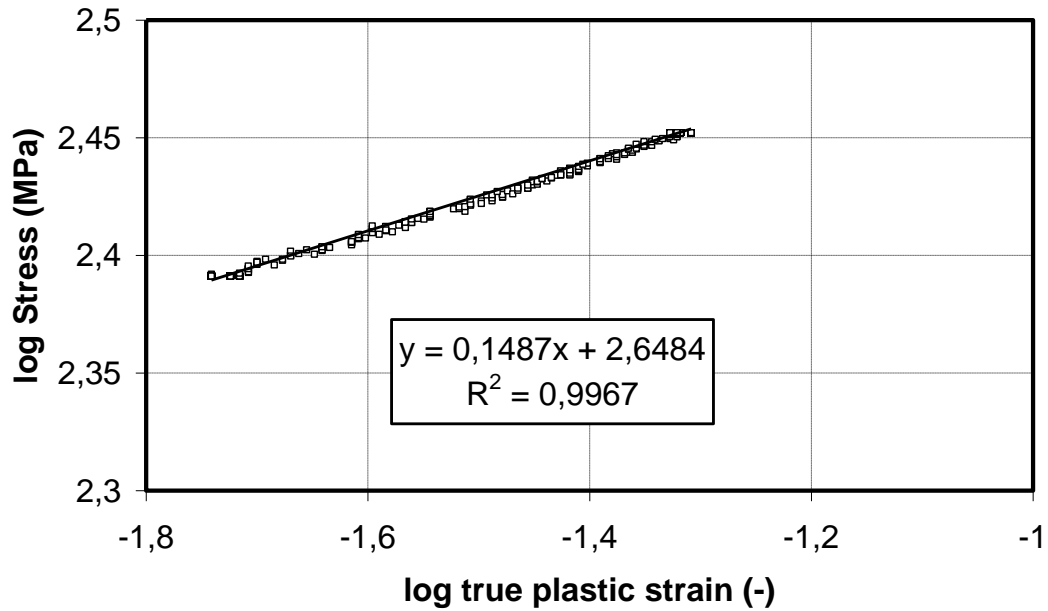

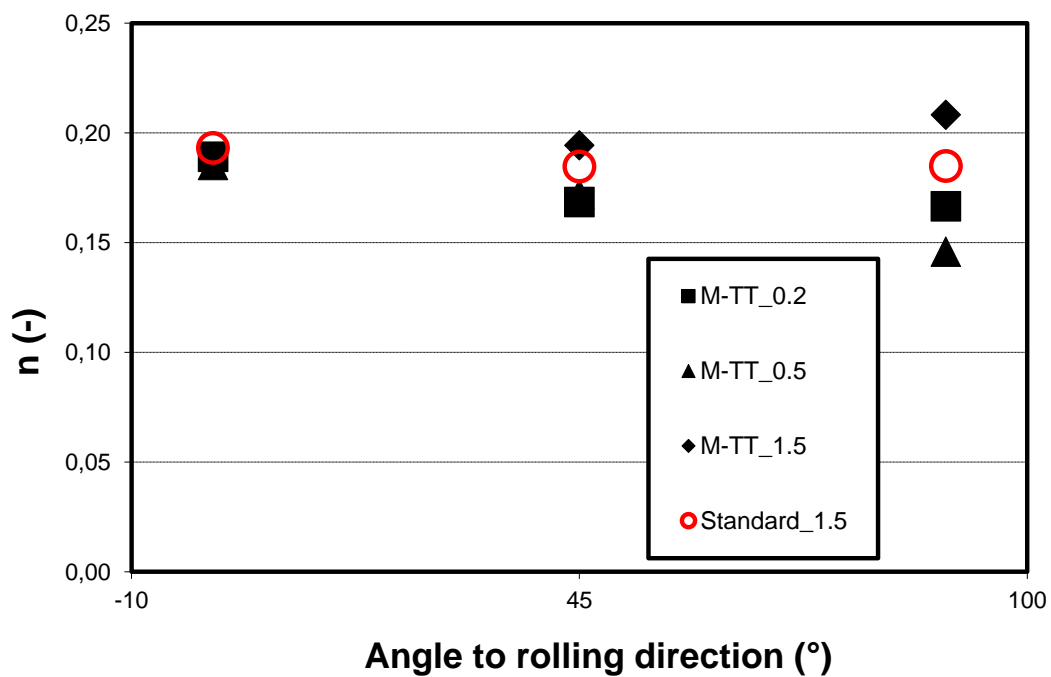**Figure 6.** Example of Hollomons law parameters fitting.

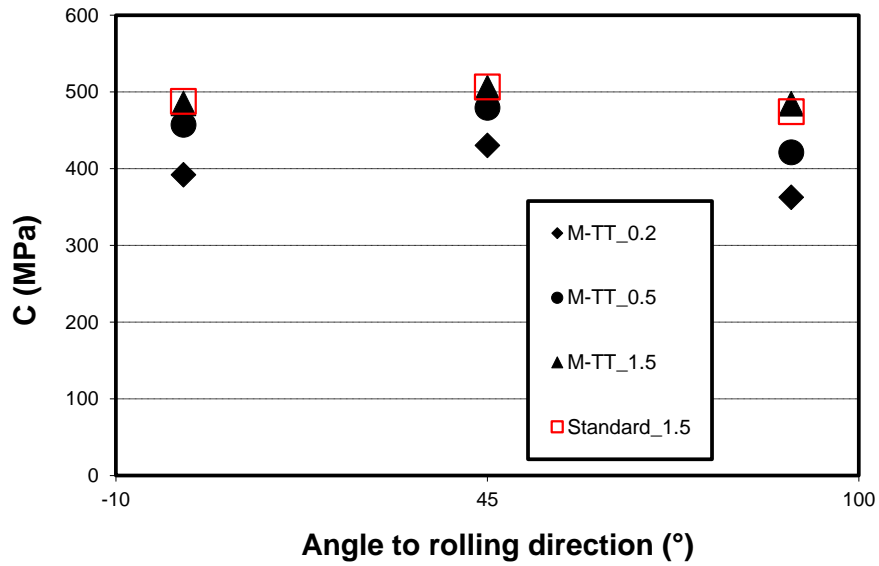**Figure 7.** Strain hardening exponent.

Figure 8. Strength coefficient.

3.3. Plastic strain ratio - Lankford coefficients

Lankford coefficients are one of the key parameters in the metal sheet forming process [17-21]. The measurement for the plastic strain ratio determination was performed with the use of continuous strain measurement by DIC system ARAMIS. The plastic strain ratio was determined from the measured data with the use of equation 2:

$$r = \frac{-m_r}{1 + m_r}$$

(2)

Where m_r is determined from the linear regression fit between the lower limit (2% plastic strain) and the upper limit (A_g value) through the origin [16].

Longitudinal (ε_l) and transverse (ε_b) true plastic strains are calculated according to equations 3 and 4:

$$\varepsilon_l = ln \left[\frac{L_e - \Delta L}{L_e} - \frac{F}{S_0 . m_E} \right]$$

(3)

$$\varepsilon_b = ln \left[\frac{b_0 - \Delta b + \frac{b_0 . v . F}{S_0 . m_E}}{b_0} \right]$$

(4)

Where:

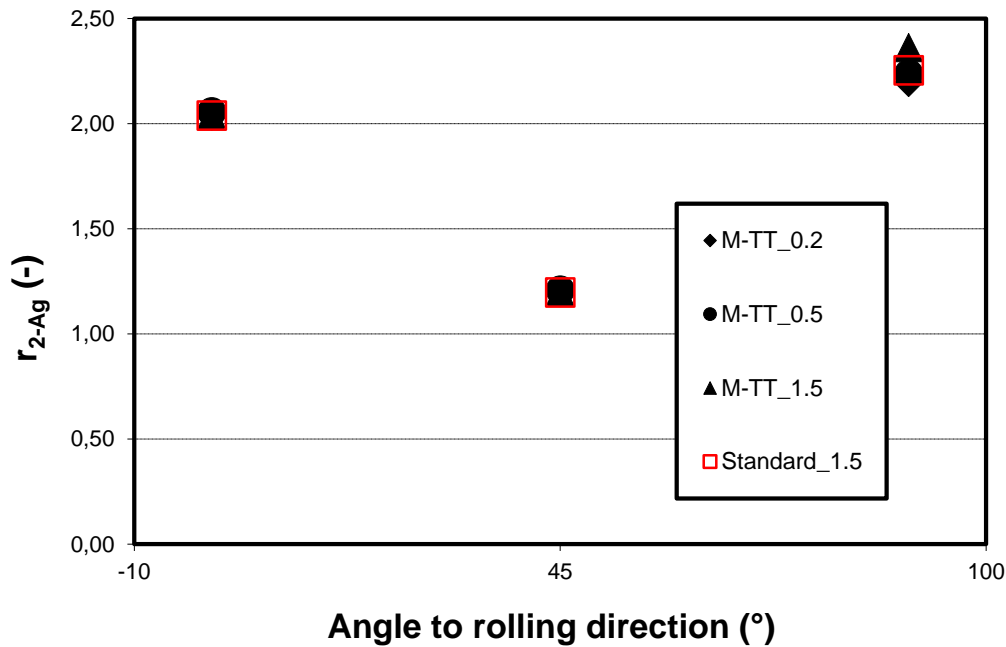|		
L_e	Extensometer gauge length	mm
b_0	Original gauge width	mm
ΔL	Instantaneous elongation/ extension of the measurement base	mm
Δb	Instantaneous width elongation	mm
F	Force	N
S_0	Original cross-section area	mm^2
v	Poisson constant	-
m_E	Young modulus	MPa

Results are summarized in Figure 9.

Figure 9. Plastic strain ratio for considered orientations.

4. Discussion

The results of the M-TT specimens were compared with standard size specimens for 0°, 45° and 90° sampling orientations. The investigation was performed at room temperature. The following parameters were compared: tensile technological parameters (YS, UTS, Ag, A, Z), strain hardening and plastic strain ratio. Overall, the agreement ranged from acceptable results to excellent results. The biggest differences were seen in the stress-strain curves obtained from M-TT 0.2 mm in thickness, where the most significant deviation was measured in respect of UTS and corresponding C values. This can have several causes. Firstly, machining and handling with a specimen 0.2 mm thick is challenging and surface finish could possibly have a big influence. Furthermore, the specimens were taken from the middle part of the sheet where the material can be softer than material near to the surface. On the other hand, excellent results were obtained for plastic strain ration for all tested M-TT thicknesses and all directions. Trends obtained here for this parameter are in agreement with those published in [18-20].

Except for the previously mentioned 0.2 mm M-TT specimens, assessment of strain hardening coefficients points out excellent agreement within a few MPa between *C* coefficients of standard sized specimens and M-TT specimens for 0.5 mm and 1.5 mm and angle direction 0 and 45°. For M-TT 0.5 mm and 90° direction, the deviation is about 50 MPa. This point was scrutinized, but there was not found to be any error in the measurement of evaluation and thus it was kept among the results population and was not discarded. In the case of the *n* parameter, a difference of about 0.03 can be found for the transverse direction, while the values in the other directions agree very well.

5. Conclusions

The paper presented here successfully shows possibility of metal sheet characterization for forming processes with the use of miniaturized tensile specimens. Generally, very good agreement was found for all considered parameters and conditions between the results attained with the use of standard and M-TT specimens. Slight discrepancies between results from M-TT and standard size specimens can be assigned to sampling location of the M-TT specimens in the middle of the sheet thickness, where small material behavior deviation from near surface properties can be expected. Further investigations are planned to assess the influence of the M-TT specimen localization within the sheet thickness.

References

1. Lucas, G.E.; Odette, G.R.; et al. The role of small specimen test technology in fusion materials development. *J NUCL MATER*. **2007**, *Volume 367–370*, p. 1549–1556, DOI 10.1016/j.jnucmat.2007.04.034.

2. Yuan, J.; Zhang Z.L.; et al. Influence of specimen thickness with rectangular cross-section on the tensile properties of structural steels. *MAT SCI ENG A-STRUCT* **2012**, *Volume 532*, p. 601–605, DOI 10.1016/j.msea.2011.11.021.

3. Olbricht, J.; Bismarck, M.; Skrotzki, B. Characterization of the creep properties of heat resistant 9–12% chromium steels by miniature specimen testing. *MAT SCI ENG A-STRUCT* **2013**. *Volume 585*, p. 335–342, DOI 10.1016/j.msea.2013.07.067.

4. Cao, L.; Bürger, D.; et al. Testing of Ni-base superalloy single crystals with circular notched miniature tensile creep (CNMTC) specimens. *MAT SCI ENG A-STRUCT* **2018**. *Volume 712,* p. 223–231, DOI 10.1016/j.msea.2017.11.102

5. Dzugan, J.; Konopik, P.; et al. Determination of local tensile and fatigue properties with the use of sub-sized specimens. ASME PRESSURE VESSELS AND PIPING CONFERENCE – 2015, VOL 1A, Boston, MA, USA, JUL 19-23, 2015, Edited by: Xu S.X., Hojo K., Cipolla, R.C.; Publisher: AMER SOC MECHANICAL ENGINEERS, THREE PARK AVENUE, NEW YORK, NY 10016-5990 USA, DOI: 10.1115/PVP2015-45958.

6. Abendroth, M.; Kuna, M. Determination of deformation and failure properties of ductile materials by means of the small punch test and neural networks. *COMP MATER SCI* **2003,** *Volume 28,* p. 633-644, DOI 10.1016/.j.commatsci.2003.08.031

7. Džugan, J.; Procházka R.; Konopík P. Micro-tensile test technique development and application to mechanical property determination. Small Specimen Test Techniques. 6th Volume. STP 1576. Mikhail A. Sokolov and Enrico Lucon. Eds.. s. 12–29. ASTM International. West Conshohocken. PA 2014, DOI 10.1520/STP157620140022.

8. Rund, M.; Džugan, J.; et al. Investigation of Sample-size Influence on Tensile Test Results at Different Strain Rates. *Procedia Eng* **2015**, *Volume* 114, p. 410-415. DOI org/10.1016/j.proeng.2015.08.086

9. Konopík, P.; Džugan, J.; Procházka, R. Evaluation of Local Mechanical Properties of Steel Weld by Miniature Testing Techniques. Materials Science and Technology Conference and Exhibition 2013, Montreal, QC, Canada. October 27–31 2013. Volume 4, 2014, p. 2404-2411

10. Konopík, P.; Džugan, J.; Rund. M.; Procházka. R. Determination of local mechanical properties of metal components by hot micro-tensile test. 25th international conference on metallurgy and materials metal 2016. May 25th - 27th 2016 / Brno. Czech Republic. p. 741-746

11. Konopik. P.; Rund. M.; et al. Investigation of the mechanical behaviour of zirconium alloy at different strain rates using sub-size tensile specimens. 6th International Conference on Mechanics and Materials in Design (M2D). Ponta Delgada, Azores, Portugal. July 26-30 2015, Edited by: Gomes, J.,S.; Meguid, S.A. Publisher: INEGI-FEUP, RUA DR ROBERTO FRIAS, PORTO, 4200-465, PORTUGAL

12. Dzugan. J.; Konopik. P.; Rund. M.; Prochazka. R. Determination of Local Tensile and Fatigue Properties with the Use of Sub-Sized Specimens. ASME 2015 Pressure Vessels and Piping Conference. JUL 19-23, 2015, Edited by: Xu, S.,X.; Hojo, K.; Cipolla, R.C. DOI: 10.1115/PVP2015-45958

13. Dzugan. J.; Prochazka. R.; Konopik. P. Low cycle fatigue tests with the use of miniaturized test specimens. Pressure Vessels and Piping (PVP-2017). PVP2017-66174. Waikoloa. Hawaii. USA. July 16-20. 2017, Edited by: Crane, R.; Hojo, K.; Xu, S.,X.; Cipolla, R.,C.

14. Yatomi, M; Bettinson, A.D.; et al. Modelling of damage development and failure in notched-bar multiaxial creep tests. *FATIGUE FRACT ENG M* **2004**, *Volume: 27 Issue: 4,* p. 283-295, DOI 10.1111/j.1460-2695.2004.00755.x

15. ISO 6892-1:2016: Metallic materials -- Tensile testing -- Part 1: Method of test at room temperature

16. ISO 10113:2006: Metallic materials Sheet and strip determination of plastic strain ratio.

17. Nasri, W.; Gavrus, A.; et al. Experimental and numerical study concerning the anisotropic behavior of an AA2024-T351 thick sheet using the uni-fied formalism, a multi-mechanism model and a polycrystalline approach, 22ème Con-grès Français de Mécanique, Lyon, August 24 to 28 2015

18. Gavrus, A.; Francillette, H. An Anisotropic Behaviour Analysis of AA2024 Aluminium Alloy Undergoing Large Plastic Deformations Aluminium Alloys, Theory and Applications, 2011, DOI: 10.5772/14729

19. Ramos, G.C; Stout, M.; et al: Study of a drawing-quality sheet steel. I: Stress/strain behaviors and Lankford coefficients by experiments and micromechanical simulations, *INT J SOLIDS STRUCT* **2010**; *Volume 47, Issue 17*, p. 2285-2293, DOI 10.1016/j.ijsolstr.2010.04.023

20. Banabic, D. Sheet metal forming process, Berlin, Heidelberg: Springer-Verlag Berlin Heidelberg, 2009., DOI 10.1007/978-3-540-88113-1

21. Danckert, J.; Nielsen, K.B. Determination of the plastic anisotropy r in sheet metal using automatic tensile test equipment, *J MATER PROCESS TECH* **1998**, *Volume 73, Issue 1-3,* p. 276-280, DOI 10.1016/S0924-0136(97)00238-0

The development of a novel small ring specimen tensile testing technique

J. Kazakeviciute [1,*], J.P. Rouse [1] and C.J Hyde [1]

[1] Gas Turbine and Transmission Research Centre (G2TRC), University of Nottingham, UK, NG7 2RD;

* Correspondence: Julija.Kazakeviciute@nottingham.ac.uk; Tel.: +44-115-748-3694

Abstract: The use of small specimens in routine testing would reduce resource requirements, however, limitations exist due to concerns over size effects, manufacturing difficulties, uncertainties related to the application of representative loading conditions, and complex interpretation procedures of non-standard data. Due to these limitations, small specimen testing techniques have been mostly applied for ranking exercises and to determine approximate or simple material parameters such as Young's modulus, creep minimum strain rate and fracture toughness. The small ring method is a novel, high sensitivity small specimen technique for creep testing and has been extended in the present work for the determination of tensile material properties. Wrought aluminium alloy 7175-T7153 was tested at room temperature at 5 different loading rates. Finite element analysis was completed to evaluate the equivalent gauge section and equivalent gauge length in order to compare uniaxial tensile testing results and small ring specimen tensile testing results. An analytical solution has also been derived in order to validate the finite element analysis. It was discovered that the finite element analysis model was suitable, validated by both experimental results and analytical solution as well as that small ring specimens can be used to acquire same stress/strain data as uniaxial specimens.

Keywords: small specimen; small ring specimen; tensile testing.

1. Introduction

Small specimen testing is a developing field as small specimens are used in situations where not enough material is available for repeat testing, such as when developing a new material, or if testing facilities are too small for full size specimens, such as when effects of irradiation are being investigated. Small specimens can be used to acquire tensile properties, fatigue properties [1], fracture properties [2], crack propagation properties [3] but most of the work has been done in acquiring creep properties from small specimen testing [4].

In general there are two main types of small specimens used for tensile testing – small punch specimen and miniaturized standard specimen. Small punch specimens are suitable for identifying yield strength and UTS [5], while miniaturized standard specimens are suitable for identifying the whole stress/strain curve including Young's modulus [1]. Small punch specimens are rather standard, with most being either square 10mm x 10mm x 0.5mm [5] or circular with a diameter between 3mm [6] and 10mm [7] and similar thickness to square specimens. The force/displacement curves of these are complicated, with many different regions representing different stages of deformation in the small punch specimen, making the data difficult to interpret. Miniaturized standard specimens vary in size from 0.5mm x 0.3mm x 0.3mm gauge section [8] to rather large but still smaller than standard. Their data is easier to understand, but they are small and difficult to handle when inserting into a testing machine and ensuring suitable alignment.

The small ring specimen was developed in 2009 by T. H. Hyde and W. Sun [9]. It was developed to obtain creep strain data and had several advantages over alternative methods, such as having a long equivalent gauge length, being self-aligning and being simple to manufacture. The main shortcoming of this specimen type is that it cannot be used to obtain tertiary creep data.

The current study was undertaken in order to discover if small ring specimens are suitable for tensile testing and if stress/strain data equivalent to uniaxial stress/strain data can be extracted from the results. The main conclusion was that for this aluminium alloy at room temperature and a wide range of loading rates, small ring specimens are suitable for tensile testing.

2. Materials and Methods

The finite element model that was used modelled $1/8^{th}$ of the small ring with two pins, taking advantage of 3 planes of symmetry with symmetry boundary conditions on each. The dimensions of the model match the dimensions of the experimental small ring setup: ring internal diameter is 9mm, external diameter is 11mm,

thickness is 2mm and diameter of the loading pin in 2.5mm. The pin was modelled as an analytical rigid body because in the experimental setup the material of the pin is significantly stiffer than the material of the ring being tested. ABAQUS FEA package was used for modelling. Geometric nonlinearity is on during the loading step, as large deformations happen.

A vertical displacement of 2mm (equivalent to displacement of 4mm during experimental testing) is applied to the reference point on the modelled pin (as show in Figure 1 (a)) in order for it to deform the small ring specimen. The displacement was chosen as it is approximately the deformation at which small rings tested under tensile loading definitely fail. The displacement rate used is 0.2mm/min, but it does not affect the results as the current model is rate independent, because the material modelled does not exhibit rate dependent behaviour.
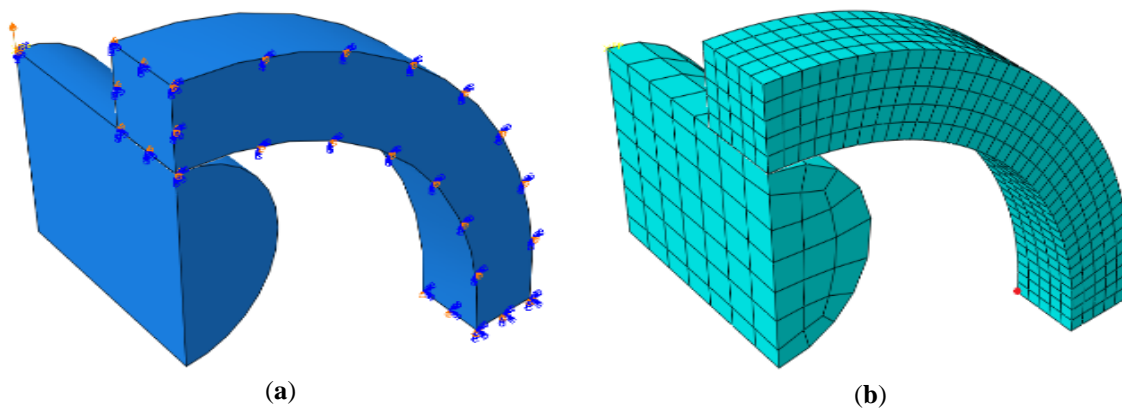

| (**a**) | (**b**) |

Figure 1. (**a**) Loads and boundary conditions in small ring FEA model; (**b**) Mesh in the small ring and the pin model, point from which stress and strain were extracted for equivalent gauge section and length calculations highlighted in red.

Contact is defined between the pin and the ring, with the pin surface acting as a master surface because it is rigid and the surface of the ring acting as a slave surface. ABAQUS surface-to-surface contact was used with Coulomb friction. As there was no way to evaluate the coefficient of friction before this study a coefficient of friction sensitivity study was performed. It was discovered that for deformations of interest (up to 2mm in FEA), the coefficient of friction had no effect on stress, strain or reaction force on the pin when varied between minimum and maximum values of metal on metal contact therefore the model was set up with frictionless contact.

In all cases ABAQUS C3D20R elements were used for meshing. Different element types were investigated, from linear to quadratic and from 2D to 3D, this element was discovered to produce the force/displacement response of the model, the most similar to the force displacement response of experimental work. Mesh sensitivity study was undertaken to see whether the mesh was sufficiently fine to show the correct force/displacement response, but not too fine that too much computation time is spent modelling. Mesh density was uniform in the small ring specimen, where an element size of 0.2mm was used. As for the pin, the element size is larger, but it does not have a significant effect on the model outputs of interest. Both meshes can be seen in Figure 1 (b).

In order to be able to compare stress/strain data from uniaxial tests and stress/strain data calculated from small ring tensile tests, an equivalent gauge length and gauge section had to be calculated. The process was as follows: stress and strain in the y direction were extracted from the corner of the ring model (highlighted in Figure 1 (b)), reaction force and displacement in y direction were extracted from the reference point of the pin. It was determined that the shape of the force/displacement curve is due to plasticity. The FEA model was run as elastic-only and elastic-plastic, the results of both analyses can be seen in Figure 2. The initial part of the curves were determined to be elastic because the response of both models match while the next part of the curves diverged because of plasticity in the model, as nothing else was changed between the two analyses.
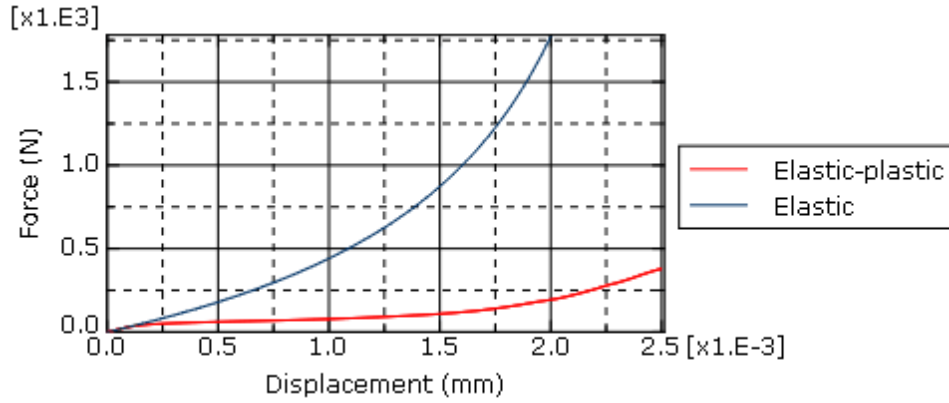
Figure 2. Comparison between elastic only material model and elastic-plastic material model response in ABAQUS.

Equivalent gauge section and length [9] were calculated using the following equations derived from the definition of strain and stress:

$$L_{gauge} = \frac{\Delta L}{\varepsilon}, \tag{1}$$

$$A_{gauge} = \frac{F}{\sigma}, \tag{2}$$

where L_{gauge} is the equivalent gauge length of the specimen, ΔL is the change in length, ε is strain, A_{gauge} is equivalent gauge section of the specimen, F is the force applied to the specimen and σ is the stress.

Material properties were acquired from uniaxial tests. As the pins are defined as analytical rigid bodies, their material properties did not need to be defined. Material was assumed to be isotropic, as previous studies show that [10].

In order to be able to use the uniaxial tensile data in ABAQUS FEA, the Ramberg-Osgood material model (deformation plasticity in ABAQUS) was fitted to it in the form of

$$\varepsilon = \frac{\sigma}{E} + \alpha \frac{\sigma}{E} \left(\frac{\sigma}{\sigma_y} \right)^{n-1}, \tag{3}$$

where E is Young's modulus, σ_y is the yield stress and α and n are constants. These model parameters were fitted to uniaxial data using Matlab Optimization toolbox. They are shown in Table 1. Poisson's ratio was determined only for one testing condition, therefore a sensitivity study was done in order to investigate the effect of Poisson's ratio on model outputs of interest. It was discovered that there is no significant effect and Poisson's ratio used was the same as experimentally determined for that one condition.

Table 1. Material parameters from Ramberg-Osgood material model.

Material	Temperature (C)	Loading rate (%/s)	E (GPa)	σ_y (MPa)	α	n
7175-T7153	RT	all	72.5	450	0.973	14.805

The material that was tested was aluminium alloy 7175-T7153, its composition can be seen in Table 2. The aluminium alloy is wrought and heat treated, specimens were machined from a hot rolled plate.

Table 2. Composition of aluminium alloy 7175-T7153 [10].

Name	Zn	Mg	Cu	Cr	Ti	Fe	Mn	Si	Other	Al
wt%	5.7	2.5	1.6	0.2	0.04	0.06	0.02	0.03	0.02	Bal

The loading rates used for uniaxial testing were 10mm/min, 1mm/min and 0.1mm/min. As the material exhibited no rate dependency at room temperature, arbitrary loading rates were chosen for small ring tensile testing. They were 60mm/min, 6mm/min, 2.04mm/min, 0.204mm/min and 0.0204mm/min.

Different machines were used to perform tensile tests. Uniaxial tests on the aluminium alloy at room temperature at 1mm/min loading rate were tested on an Instron testing machine, other loading rates were tested on a Mayes testing machine. Small ring specimens that were tested at 2.04mm/min, 0.204mm/min and 0.0204mm/min were tested on the Mayes testing machine, while others were tested on a Tinius Olsen testing machine, due to machine availability.

The analytical solution was based on a strain energy solution method. There were several assumptions made for it: the beam is slender and stress through the thickness of the ring is constant. This solution is valid for elastic behaviour only. The simplified loading situation and free-body diagram can be seen in Figure 3 (a) and (b).
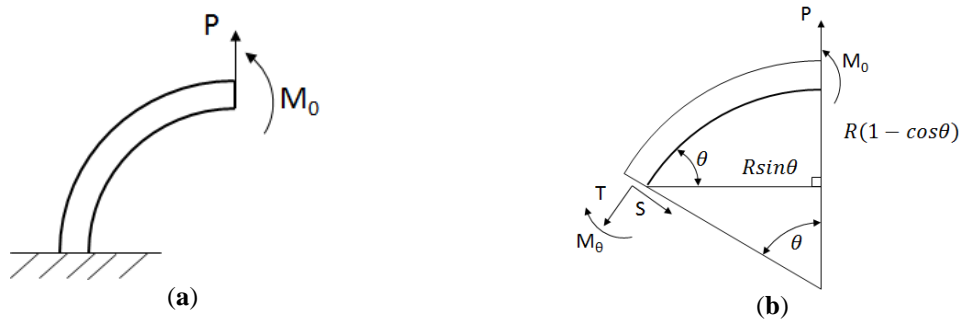

Figure 3. (**a**) Simplified loading for analytical solution; (**b**) Free-body diagram used for strain energy based analytical solution.

The moments were balanced, resulting in

$$M_\theta = M_0 + PR\sin\theta, \tag{4}$$

then, according to strain energy approach,

$$U_b = \int_0^L \frac{M_\theta^2}{2EI} \, dx = \int_0^{\frac{\pi}{2}} \frac{M_\theta^2}{2EI} \, Rd\theta. \tag{5}$$

As there is no rotation caused by moment M_0, then

$$\frac{\partial U_b}{\partial M_0} = \frac{R}{2EI} \left(2M_0 \frac{\pi}{2} - 2PR \right) = 0, \tag{6}$$

therefore

$$M_0 = \frac{2}{\pi} PR. \tag{7}$$

Deformation happens primarily because of bending, but there also is a tensile and shear contribution, so after balancing the force in the x and y directions and solving for T and S

$$T = P\sin\frac{\theta}{2}, \tag{8}$$

$$S = P\cos\frac{\theta}{2}. \tag{9}$$

Tensile complimentary strain energy is

$$U_t = \int_0^L \frac{T^2}{2AE} \, ds = \int_0^{\frac{\pi}{2}} \frac{T^2}{2AE} \, Rd\theta, \tag{10}$$

while shear complimentary strain energy is

$$U_s = \int_0^L \frac{S^2}{2AG} \, ds = \int_0^{\frac{\pi}{2}} \frac{S^2(1+\nu)}{AE} \, Rd\theta. \tag{11}$$

As the vertical displacement of interest and it is caused by load P it is equal to

$$u_v = \frac{\partial U_b}{\partial P} + \frac{\partial U_t}{\partial P} + \frac{\partial U_s}{\partial P}. \tag{12}$$

After integrating (5), (10) and (11), then differentiating them according to (12) vertical displacement is

$$u_v = \frac{PR^3}{EI}\left(\frac{\pi}{4} - \frac{2}{\pi}\right) + \frac{PR\pi}{4AE} + \frac{PR\pi}{2AE}(1 + v). \tag{13}$$

3. Results

Figure 4 (a) shows stress/strain results from uniaxial testing of the aluminium alloy of interest at room temperature. There is no noticeable rate dependency at these loading rates. The scatter for stress is about 50MPa. It can be seen that the Ramberg-Osgood material model does not fit very well around yield point but it fits well everywhere else. Figure 4 (b) shows the force/displacement results from small ring tensile testing of the aluminium alloy of interest at room temperature. As in uniaxial tensile testing, there is no noticeable rate dependency at these loading rates. The force scatter is about 50N. The force/displacement curves have steps in them (best seen in 60mm/min rep2).
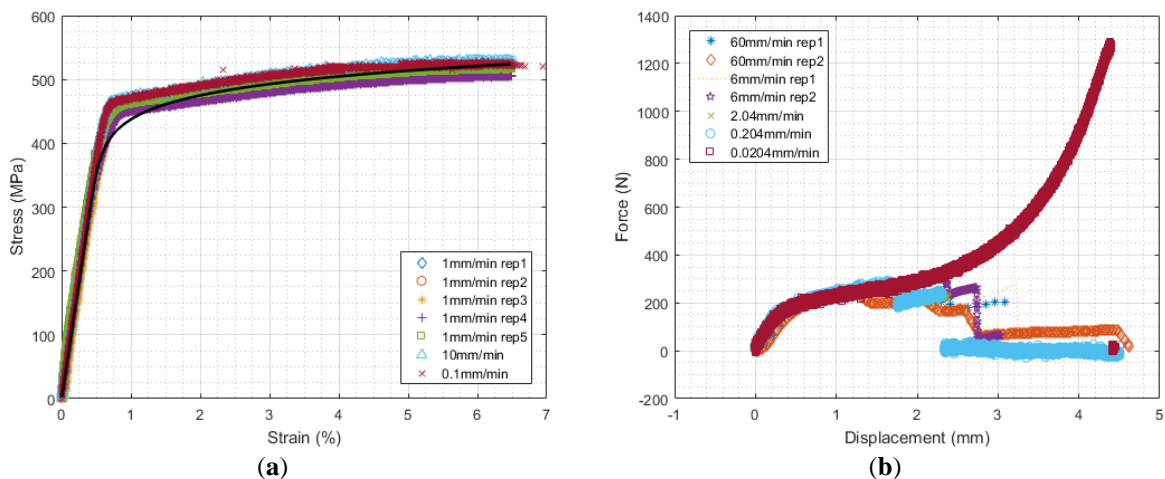

Figure 4. (**a**) Collated stress/strain curves from uniaxial testing aluminium alloy at room temperature; (**b**) Collated force/displacement curves from small ring tensile testing aluminium alloy at room temperature.

Figure 5 (a) shows the equivalent gauge section, plotted against reaction force on the loading pin. The plot can be approximated to two linear regions: a horizontal one and one with a constant slope, making it simple to implement in calculating stress data from small ring tensile tests in order to compare it to uniaxial stress data. Figure 5 (b) shows the equivalent gauge length, plotted against reaction force on the loading pin. The plot can be approximated to three linear regions: a horizontal one, one with constant slope and another horizontal one, however this approximation is less accurate than the one for equivalent gauge section. This can then be used to calculate strain from the small ring tensile test in order to compare it to uniaxial strain data.
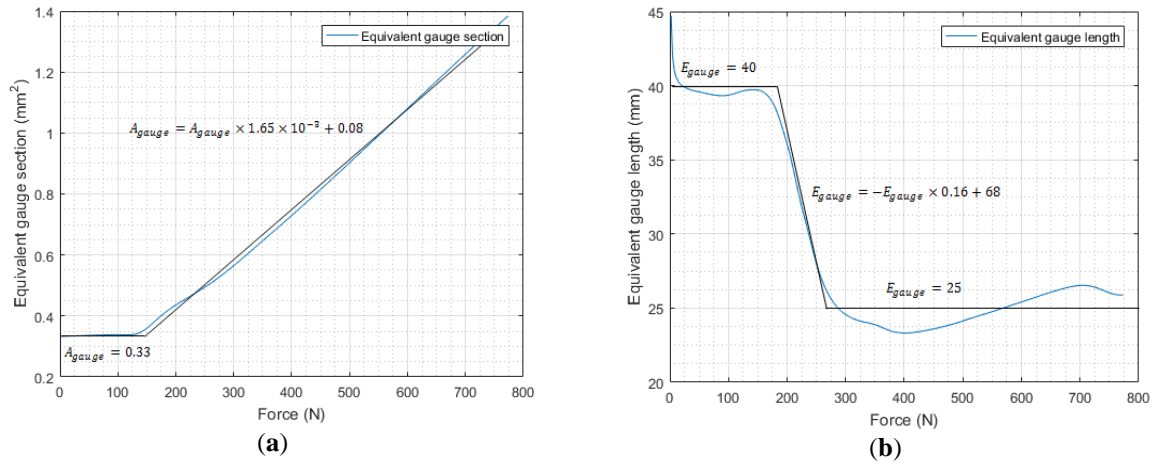
Figure 5. (**a**) Equivalent gauge section, calculated from FEA plotted against force, linear approximation in black; (**b**) Equivalent gauge length, calculated from FEA plotted against force, linear approximation in black.

Figure 6 (a) shows an example of the small ring tensile data sets plotted along with ABAQUS FEA simulation equivalent and analytical solution equivalent. It can be seen that analytical solution matches FEA and experimental data well at the elastic region of the force/displacement curve then diverges. The FEA solution matches experimental data very well up to 1mm of displacement and quite well up to the first crack in the experimental data. Figure 6 (b) shows an example of how well the data matches the uniaxial tensile test results plotted along with stress/strain data calculated from one of the small ring tensile tests. It can be seen that both uniaxial and calculated data match well, apart from the region around yield.
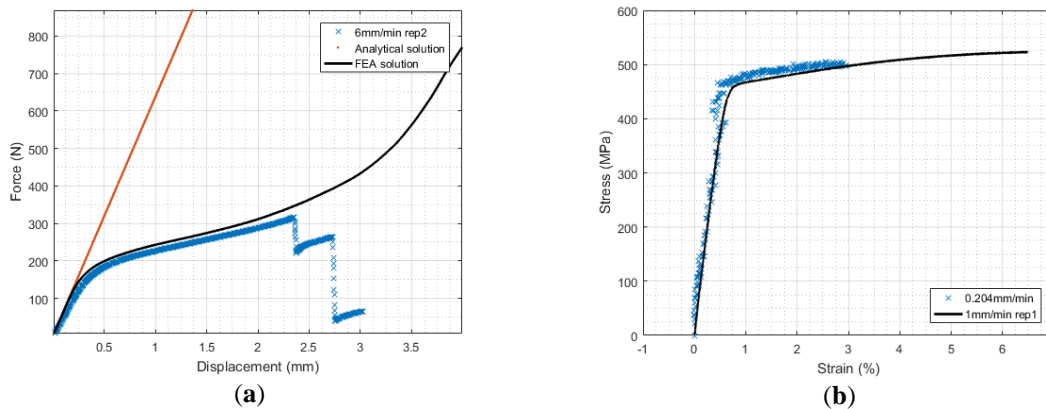

Figure 6. (**a**) Small ring tensile experimental data plotted against FEA solution data and analytical solution data; (**b**) Stress/strain data from uniaxial test plotted against stress/strain data calculated from small ring tensile test data and FEA solution.

4. Discussion and Conclusions

As seen in Figure 4 (a) uniaxial test results are repeatable, which means that the material is uniform and the testing machine and methodology are suitable for this test. The Ramberg-Osgood material model does not fit well around yield because the maximum strain to which it is fitted is too high. If it was lower the model would fit around yield better. The higher strain was selected for the material model because the small ring experiences large strains during tensile testing, so representing large strains is important.

Small ring tensile testing results are also repeatable as seen in Figure 4 (b) and the material does not exhibit rate dependency, like during uniaxial testing. This means that results from small ring tensile testing and uniaxial testing can be compared. The steps in the force displacement curves are there because when the ring fails it does not usually crack through the whole thickness of the ring but instead a crack forms, the ring deforms some more and the crack grows in steps until it finally fails.

Linear approximations of equivalent gauge section and length seen in Figure 5 (a) and (b) do not represent the region around yield very well. A constant equivalent gauge section in Figure 5 (a) is in the elastic region and steadily

increasing one is in the plastic region. The part which diverges from linear approximation is around where yield first happens and is most likely there because the ring geometry and loading is quite complicated in comparison with a uniaxial specimen. The first horizontal region in Figure 5 (b) is the elastic region, latter regions are plastic.

As seen in Figure 6 (a) the FEA solution was validated by the analytical solution in the elastic region of the force/displacement curve. The FEA solution also matches experimental data well, therefore the model in FEA is suitable for modelling this test. There does not seen to be a way to implement damage mechanics into this model and get any useful results because first crack initiates over a wide range of displacement values and the number of steps in the force/displacement data also does not seem to follow a trend.

Uniaxial test results match well with calculated test results seen in Figure 6 (b), apart from the region around yield, which could be improved by using a piecewise approximation with more pieces. Even with the current approximation small ring tensile test can be used to get the similar data to uniaxial tensile testing. Maybe if inverse analysis described in [11] was used, small ring tests could be used to get uniaxial stress/strain curves.

Overall small ring specimens appear to be suitable to perform tensile tests on this material as both material and ring are isotropic. The scatter in both uniaxial and small ring tensile testing is similar when compared after adjusting the force data with equivalent gauge section.

Regarding future research, there are three main follow-up investigations that will be happening. The first one is testing this same material at elevated temperatures and developing an FEA model that can produce comparable force/displacement curves. This will most likely require the introduction of rate dependency in the model as at elevated temperature this material exhibits noticeable rate dependency. The second investigation is testing different materials, such as a steel or a nickel superalloy at various temperatures and checking if FEA and experimental data matches. If both of those are successful the third follow-up investigation is to develop a method for cyclically loading the small ring specimen in order to get fatigue data from it.

References

1. Holländer, D.; Kulawinski, D. et al. Investigation of isothermal and thermo-mechanical fatigue behavior of the nickel-base superalloy IN738LC using standardized and advanced test methods. *Mater. Sci. Eng. A* **2016**, *67,* 314-324, 10.1016/j.msea.2016.05.114.
2. Han, W.; Yabuuchi, K. et al. Application of small specimen test technique to evaluate fracture toughness of reduced activation ferritic/martensitic steel. *Fusion Eng Des* (in press).
3. Shin, C.-S.; Lin, S.-W. Evaluating fatigue crack propagation properties using miniature specimens. *Int J Fatigue* **2012**, *43*, 105-110, 10.1016/j.ijfatigue.2012.02.018.
4. Hyde, T.H.; Hyde, C.J.; Sun, W. Theoretical basis and practical aspects of small specimen creep testing. *J Strain Anal Eng Des* **2013**, *48*, 112-125, 10.1177/0309324712463299.
5. García, T.E.; Arroyo, B. et al. Small punch test methodologies for the analysis of the hydrogen embrittlement of structural steels. *Theor. Appl. Fract. Mech.* **2016**, *86*, 89-100, 10.1016/j.tafmec.2016.09.005.
6. Kumar, K.; Pooleery, A. et al. Evaluation of ultimate tensile strength using Miniature Disk Bend Test. *J Nucl Mater* **2015**, *461*, 100-111, 10.1016/j.jnucmat.2015.02.029.
7. Song, M.; Guan, K. et al. Size effect criteria on the small punch test for AISI 316L austenitic stainless steel. *Mater. Sci. Eng. A* **2014**, *606*, 346-353, 10.1016/j.msea.2014.03.098.
8. Kumar, K.; Pooleery, A. et al. Optimisation of thickness of miniature tensile specimens for evaluation of mechanical properties. *Mater. Sci. Eng. A* **2016**, *675*, 32-43, 10.1016/j.msea.2016.08.032.
9. Hyde, T.H.; Sun, W. A novel, high-sensitivity, small specimen creep test. *J Strain Anal Eng Des* **2009**, *44*, 171-185, 10.1243/03093247JSA502
10. Wing Cheong, M. F. L. Experimental and Numerical Investigations into the Behaviour of a 7175-T7351 Aluminium Alloy for Aerospace Gearbox Housing Applications at Elevated Temperatures. PhD, University of Nottingham, Nottingham, UK, 2018.
11. Husain, A.; Sehgal, D.K.; Pandey, R.K. An inverse finite element procedure for the determination of constitutive tensile behavior of materials using miniature specimen. *Comput Mater Sci* **2004**, *31*, 84-92, 10.1016/j.commatsci.2004.01.039.

Localized damage analysis for high strength S960 steel using micro-tensile testing and digital image correlation

R.G. Dowding [1*], C. Pinna [2], H. Ghadbeigi [3] and D. Farrugia [4]

[1] The University of Sheffield; rdowding1@sheffield.ac.uk
[2] The University of Sheffield; c.pinna@sheffield.ac.uk
[3] The University of Sheffield; h.ghadbeigi@sheffield.ac.uk
[4] Tata Steel UK Limited didier.farrugia@tatasteel.com
* Correspondence: rdowding1@sheffield.ac.uk

Abstract: In-situ interrupted tensile tests combined with Digital Image Correlation (DIC) were performed on S960 hot rolled steel to identify damage initiation on the surface of the sample. Shear bands and damage initiation and evolution in the microstructure were observed during the test. It was found that shear bands are generated on the surface as plastic deformation occurs. Void nucleation was found to be initiated where a large plastic deformation gradient is observed.

Keywords: Steel; DIC; Damage; Microscale tensile

1. Introduction

High strength steels used in structural elements have a reduced bendability compared to lower strength steels, limiting manufacturing processes. Previous work has found shear bands to be prevalent on the outer, tensile stressed region of the bend [1]. This localization of strain is the source of failure in bending [2].

Work has been undertaken to identify the failure mechanism for 3 point bending in high strength S960 steel. To better understand damage initiation in bending, tensile tests have been performed inside a Scanning Electron Microscope (SEM) to identify failure mechanisms in the sample. These failure mechanisms can then be compared to those observed in bending tests.

Similar work has been used to determine the strain bands, localized strains in microstructures and damage initiation mechanism in Dual Phase (DP) steels, consisting of martensitic and ferritic phases [3], however the micro mechanisms of deformation and damage in S700, S960 and S1100 have not been studied before.

2. Materials and Methods

The material is an experimental lab produced hot rolled S960 grade steel with a thickness of 6mm that contains martensitic and bainitic microstructures. The sample geometry as developed by Ghadbeigi et. al. [3] was used in this study in order to ensure the deformation is localized within the field of view of the microscope at high magnifications. Fig. 1 shows the selected geometry and associated dimensions of the samples used.
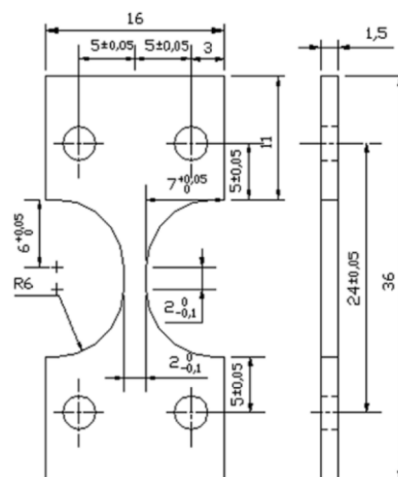

Figure 1. Tensile test sample dimensions for use within the SEM [3].

This sample was then ground and polished to remove material with residual stresses, deformations from machining and obtain a polished surface. Chemical etching using 2% nital solution was then used to reveal the microstructure of the steel. Lines were engraved onto the sample as shown in Fig. 2, to evaluate elongation of the gauge length optically. The tensile test was then carried out with regular interruptions to record images of the area of interest in the gauge length of the microstructure up to fracture of the specimen. The etched microstructure provides identifiable patterns that can be processed by the Davis DIC software [4] to produce strain maps as used by Al-Harbi et al [5].
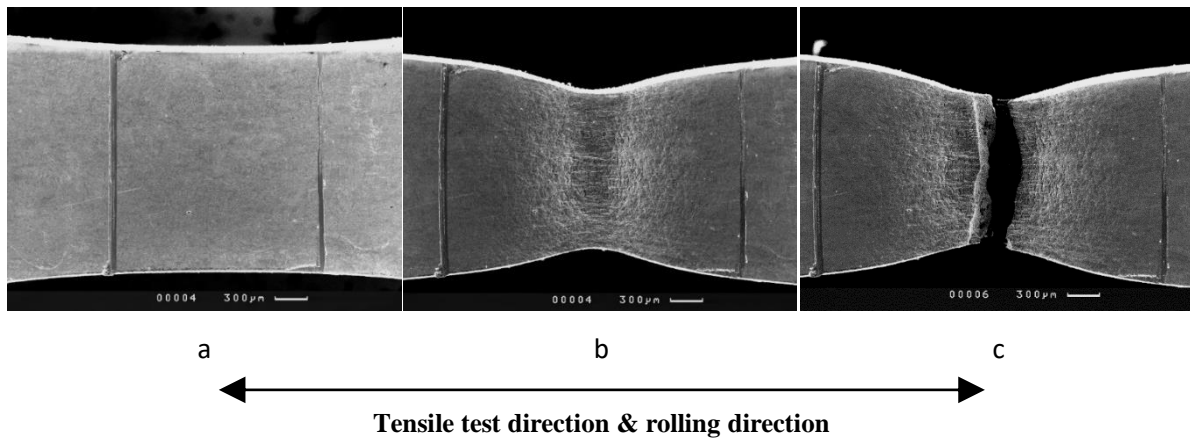

Figure 2. Images of the gauge length at 30x magnification during a tensile test. **a)** No deformation **b)** necking at 57% plastic strain and **c)** failure.

3. Results

Using these methods we can produce stress strain curves from the tensile test and identify void nucleation points and their localized strain using DIC. These are analyzed to understand the formation of damage leading to failure of the sample.

3.1. Plastic deformation curve

By performing a tensile test a stress strain curve was obtained. Since only the plastic region is of interest, the stress-plastic strain curve was created free of elastic effects as shown in Fig. 3.

The steel reaches its elastic limit at 976MPa and UTS at 1102MPa, maximum elongation reaches 58%. The elongation is exaggerated by the sample geometry and is reported to be of an order of 5 times greater than a standard tensile test [3]. This is due to the sample geometry extending the post uniform section of the stress strain curve due to the stress triaxiality state being different to a standard tensile test specimen. This extends the testing of the sample providing better conditions to study damage development in the microstructure.

3.2. SEM micrographs

Low magnification micrographs of the specimen are shown in Fig. 2. It can be seen that the sample undergoes a significant amount of necking and elongation in image Fig. 3b) with the surface becoming rough, therefore highlighting the very large plastic deformation experienced by the microstructure.
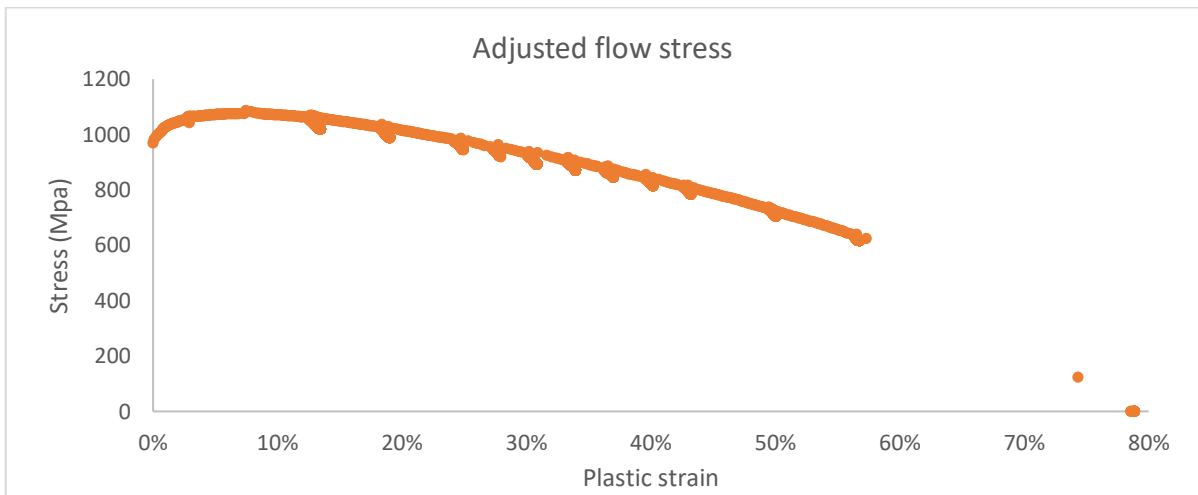
Figure 3. Stiffness adjusted stress vs strain curve for the tensile test parallel to the rolling direction for S960 steel.

3.3. Strain Maps

Micrographs from Fig. 4 were processed in Deben 8.4.0. This was using the sum of differences correlation mode, with a step size of 15 and subset of 35 pixels. The mapping is displaying strain parallel to the tensile test direction.
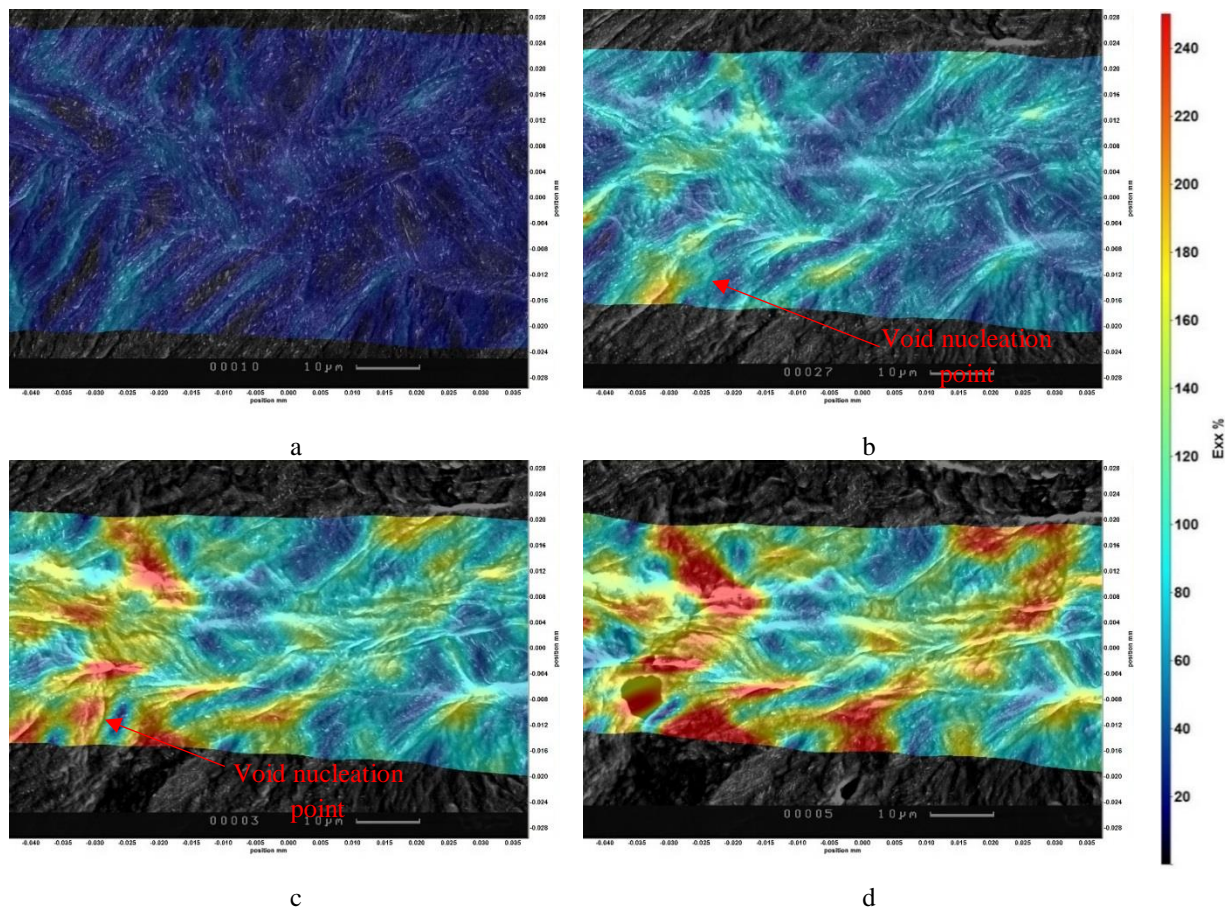

Figure 4. Tensile strain maps overlaid on the microstructure images produced using high magnification SEM images processed using Davis [4], **a)** 19% plastic strain **b)** 40% plastic strain, **c)** 50% plastic strain **d)** last image prior to failure, 57% plastic strain.

Once plastic deformation occurs within the sample, shear bands become visible at around 45 degrees to the tensile test direction in Fig4a) and b). Strain localizes in these bands which become very clearly defined by the end of the test due to the high strain gradient with the surrounding regions of the microstructure. As shown in Fig4 b) and c) the void nucleation point is found in a region straddling a shear band and a low strain point. It is found that the void is generated at 160% strain with the high strain region reaching values up to 240% and a lowest point of 8% strain. Due to the triaxiality of the sample, the failure begins at the center of the sample and the images are of the failure reaching the surface. The maximum and minimum strain values are found to be 5µm apart from one another. This high strain differential is enough to cause a failure that cracks proceed off leading to failure shortly after Fig4d) was acquired.

There is a second crack that formed off another void at the bottom of Fig4d). This crack follows another shear band showing the importance of shear bands in this steel's failure. These voids are nucleating from the subsurface and more instances of the damage are required to better understand how this steel fails. In bending, the failure occurs due to shear bands and this work highlights that the tensile test failure is also affected by shear bands. The procedure also shows that strain mapping can be obtained with good correlation even with high strains when imaging S960 high strength steels.

As shown in Fig. 5, a series of images are acquired until the sample failed from a-d. It can be seen how the surface becomes visibly rough through the tensile test. Eventually bright lines running parallel to the tensile test direction become prevalent as out of plane deformation occurs. Finally cracks and voids nucleate at the surface in image d. All images were then processed by DIC to produce stain maps for the analysis of damage development in relation to strain distributions. This presented difficulties for the operator, particularly maintaining the images in the same position, in focus and adjusting the brightness and contrast as beam contamination and out of plane deformation occurred on the sample. Doing this results in better correlation with DIC. Even with this deformation using Davis DIC software with sum of differential correlation mode a satisfactory strain map can be produced.
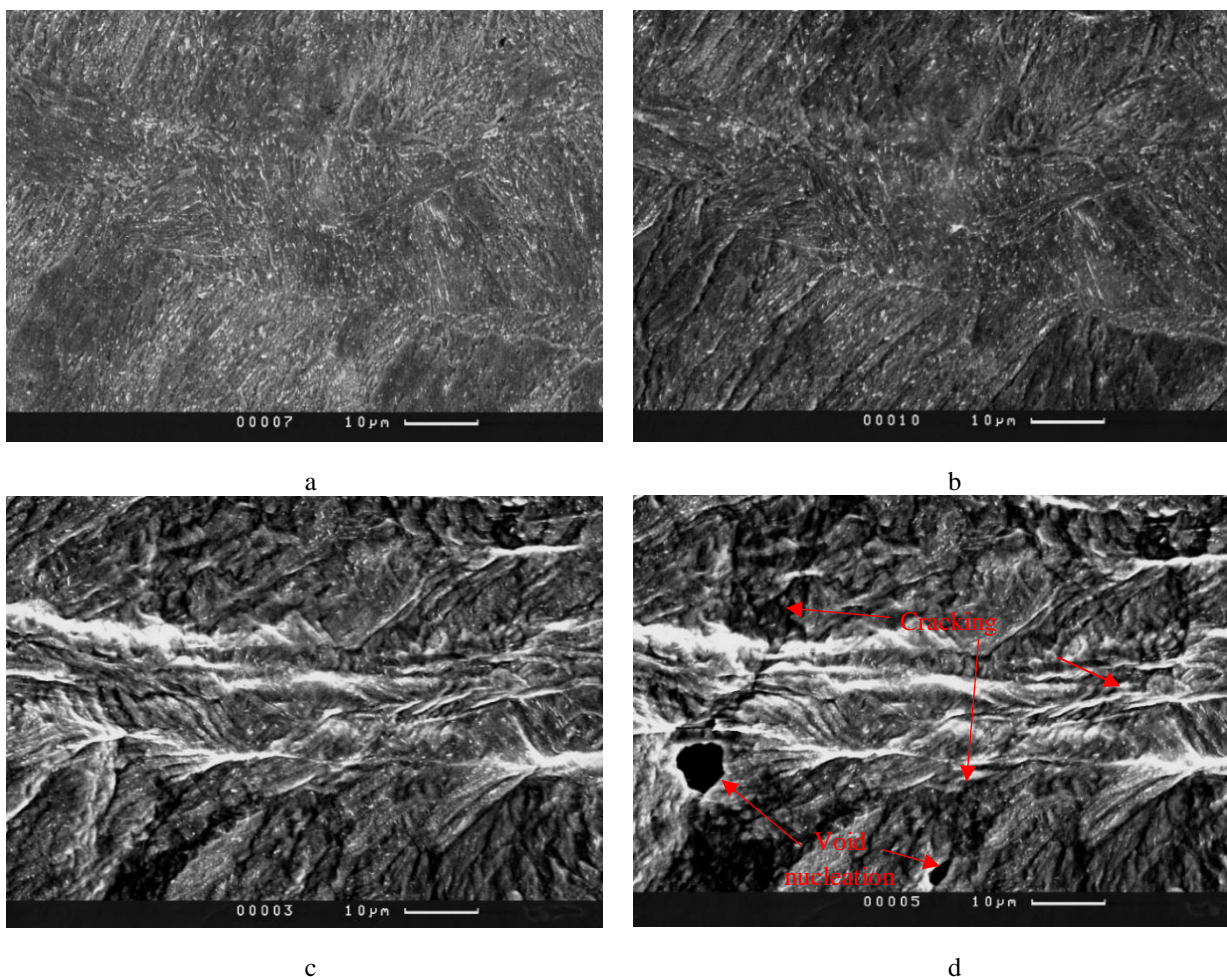

a

b

c

d

Figure 5. High magnification SEM images at 1400x of the tensile test sample, **a)** No deformation **b)** 19% plastic strain **c)** 50% plastic strain **d)** last image prior to failure; 57% plastic strain.

4. Conclusions

This work has demonstrated that the combination of small-scale tensile testing and DIC can be successfully applied to the study of damage formation in S960 steels in relation to large strain distributions up to failure. Tensile strain values up to 240% have been recorded in the microstructure with damage nucleating at local values of 160%. Results have shown that damage forms at the boundary between high-strain shear bands and low-strain regions.

References

1. Crowther, D.N.; Wen, S.; Wade, B.A. Shear band formation during bend testing of S960., Internal TATA steel presentation, 2015.
2. Kaijalainen, A.J.; Suikkanen, P.P.; Karjalainen, L.P.; Porter D.A. Influence of subsurface microstructure on the bendability of ultrahigh-strength strip steel. *Materials Science & Engineering A,* **2016**, *654,* 151-160.
3. Ghadbeigi, H.; Pinna, P.; Celotto, S.; Yates, J. R. Local plastic strain evolution in a high strength dual phase steel, *Materials Science & Engineering A,* **2010**, *527,* 5026-5032.
4. DaVis 8.4.0, LaVision GmbH.
5. Alharbi, K.; Ghadbeigi, H.; Efthymiadis, P.; Zanganeh, M.; Celotto, S.; Dashwood, R.; Pinna, C. Damage in dual phase steel DP1000 investigated using digital image correlation and microstructure simulation, *Modelling Simul. Mater. Sci. Eng.,* **2015**, *23,* 1-17.

Some considerations in using the small punch testing for thermally sprayed CoNiCrAlY coatings

H. Chen*

Department of Mechanical, Materials and Manufacturing Engineering, Faculty of Science and Engineering, University of Nottingham Ningbo China, Ningbo 315100, China
* Correspondence: Hao.Chen@nottingham.edu.cn; Tel.: +86-574-8818-0000

Abstract: Small punch testing shows great potential in mechanical characterisation of thin coatings. This testing method can be used to determine the mechanical performance of thermally sprayed coatings, especially to qualitatively characterise the effects of coating defects on the mechanical behaviour. In this work, some considerations in using the small punch testing for coatings are presented through a microstructure evolution analysis of a vacuum plasma sprayed CoNiCrAlY coating under small punch test. The CoNiCrAlY coating was characterised with a large number of un-melted particles as the coating defects. It is shown that the clamping in the small punch test rig can result in micro-cracking around the un-melted particles in the coating prior to testing. It is also found that the un-melted particles in the coating act as predominant cracking sites and fast failure occurred around the un-melted particles. Careful considerations need to be taken into account when using the small punch test for coatings to avoid any changes in the coating microstructure and plasticity during the clamping stage.

Keywords: Small punch test; Mechanical behaviour; CoNiCrAlY coatings; Un-melted particles; Cracking

1. Introduction

Since the first introduction of the small punch testing (SPT) technique in 1980s, this small specimen test method has been widely used to mechanically characterise the power plant steels, weldments and alloys [1-11]. A CEN Code of Practice was established to specify the geometrical set-up and test procedures of SPT [12]. Among the available small specimen test methods, the unique characteristic of the SPT is the disc-type specimen (8-10 mm in diameter, 0.25-0.5 mm in thickness), which allows the life assessment to be achieved from a small volume of materials. In recent decades, SPT has been developed into two categories, namely the small punch tensile test to investigate the fracture behaviour and the small punch creep test to examine the creep characteristics [13, 14]. Works concerned on the SPT for mechanical performance evaluation of various materials have been extensively reported, ranging from experimental studies to numerical simulations [15-24]. However, due to the complexity of biaxial loading in SPT, the data interpretation remains challenging since no universally accepted methodology has been developed yet. Nevertheless, SPT has been demonstrated to be a useful tool for mechanical characterisation of materials, even without the fully verified route for data interpretation [25].

More recently, the application of SPT has been expanded to other areas where the availability of materials is limited, such as coatings [26]. In general, coatings exhibit different mechanical and chemical properties when comparing to the bulk materials. It has been increasingly difficult to characterise the mechanical performance of coatings by conventional uniaxial testing due to the small coating thickness and the delamination between the coating and substrate [27]. The SPT appears to have the potential to evaluate the mechanical behaviour of coatings since it has the capability in testing disc specimens with thicknesses close to typical coating thicknesses (~0.5 mm). Kameda et al. used the SPT to evaluate the high temperature mechanical degradation of CoCrAlY coatings [28-30]. Eskner et al. employed the SPT to investigate the temperature dependent mechanical properties of NiCoCrAlY and NiAl coatings [31, 32]. Soltysiak et al. reported a study on using SPT to characterise a thermally sprayed IN625 coating [33]. Chen et al. applied SPT to evaluate the ductile-to-brittle transition and creep behaviour of CoNiCrAlY coatings [34-36]. These are the limited studies available on using the SPT for coatings, which have demonstrated the importance and suitability of using the SPT for mechanical characterisation of thermally sprayed coatings.

However, further considerations need to be taken into account when using the SPT for coatings. Coatings are usually obtained by spray deposition methods, such as high velocity oxy-fuel (HVOF) thermal spray or vacuum plasma spray (VPS) [37, 38]. Depending on the spray parameters, the splat-on-splat nature of thermally sprayed coatings can result in various defects, i.e. pores, oxide inclusions or un-melted particles [39, 40]. This means the coatings generally exhibit quite different structures and properties than the cast alloys of the same chemistry. The defects embedded in the coatings can have a significant influence on their mechanical response during the SPT.

Therefore, in this paper, the performance of a thermally sprayed CoNiCrAlY coating with some initial defects is assessed via SPT under constant load (small punch creep test). The CoNiCrAlY coating is deliberately prepared with a number of un-melted particles using vacuum plasma spray. The microstructure evolution of this CoNiCrAlY coating during SPT is investigated to identify the roles of un-melted particles on the mechanical response of this CoNiCrAlY coating in the SPT. Some general comments and considerations for future exploitation of the SPT on thermally sprayed coatings are also addressed.

2. Materials and Methods

The CoNiCrAlY coating was prepared by vacuum plasma spraying using a commercially available Amdry 9951 powder with a nominal composition Co-31.7%Ni-20.8%Cr-8.0%Al-0.4%Y (all in wt%). The size range of the powder particles is 5-38 µm, as characterised by a laser diffractometer. The detailed spray parameters and processes are given elsewhere [40]. Free-standing CoNiCrAlY coating alloys with an approximate thickness of 0.5 mm were obtained by debonding the coating from substrate. The as-sprayed coatings were subjected to an initial heat treatment of 2 h at 1100 °C to fully develop the microstructure and reduce the existing coating porosity. Disc specimens of 8 mm in diameter were cut from the heat treated coatings by wire electro-discharge machining and were carefully ground and polished to a final thickness of approximately 430 µm. Although the coating thickness does not comply with the CEN Code of Practice of 0.5 mm specimen thickness, it is still possible to evaluate the coating performance through microstructural analysis.

Tests were carried out in the E.ON test rig at 750 °C in air with a load range of 50-100 N. The lowest load, 50 N, was used to allow the long-term deformation of the specimen to study the failure mechanism of the material. The specimens were clamped between the upper and lower die under a clamping torque of ~40 Nm as measured a "Britool" torque wrench. The configuration of the rig set-up is detailed in previously reported work [34]. The microstructure of the coating specimens before and after testing was investigated via a FEI XL30 scanning electron microscope (SEM) using secondary electron and backscatter electron imaging.

3. Results and discussion

3.1. Microstructure of coatings prior to testing

The microstructure of the initially heat-treated CoNiCrAlY coatings is depicted in Figure 1. The coating shows a clear two phase structure, consisting of the dark contrast β-NiAl phase and the bright contrast γ-Ni phase. The volume fraction of the β phase is measured to be around 30% by image analysis. The coating exhibits an oxide-free structure, which agrees well with the nature of vacuum plasma spraying in limiting the oxidation of in-flight powder particles [41]. It is seen that the heat treated CoNiCrAlY coating exhibits very little porosity, showing a dense microstructure of the coating. Some spherical features are further noticed in Figure 1b and they are presumably the un-melted particles which retain their original shape during the spraying process. Figure 2 depicts the morphology of the coating surface. The un-melted particles are spherical in morphology and undergo limited plastic deformation, which is consistent with the cross-sectional microstructure of the coating in Figure 1b.

Prior to testing, the coating specimens were clamped in the test rig at room temperature with a clamping torque of 40 Nm (equivalent clamping stress ~250 MPa). This clamping torque was chosen based on the previous studies to prevent the sample slipping during the test [34, 35]. Since the un-melted particles can behave differently compared to the adjacent regions in the coating, the specimens after clamping were taken out from the rig to identify if any microstructural discrepancy occurred. Figure 3 shows the microstructure of coating specimen in the clamped region prior to testing. Some dark contrast features are developed in Figure 3a. These features are the micro-cracks seen in Figure 3b. The micro-cracks are mainly developed around the un-melted particles, indicating the mechanical property variations in the coating. No cracks are found in the unclamped regions of the specimen. It is evident that the initial coating exhibits a crack-free structure, as seen in Figure 1. Thus, it is believed the micro-cracks seen in Figure 3 are largely resulted from the clamping stage in the test rig. The initial cracking of the coating specimen can significantly affect the initial plasticity of the material prior to SPT. Though considerations have been thought to reduce the clamping force, it is essential to maintain sufficient specimen clamping to prevent the slipping of the specimen in the subsequent SPT.
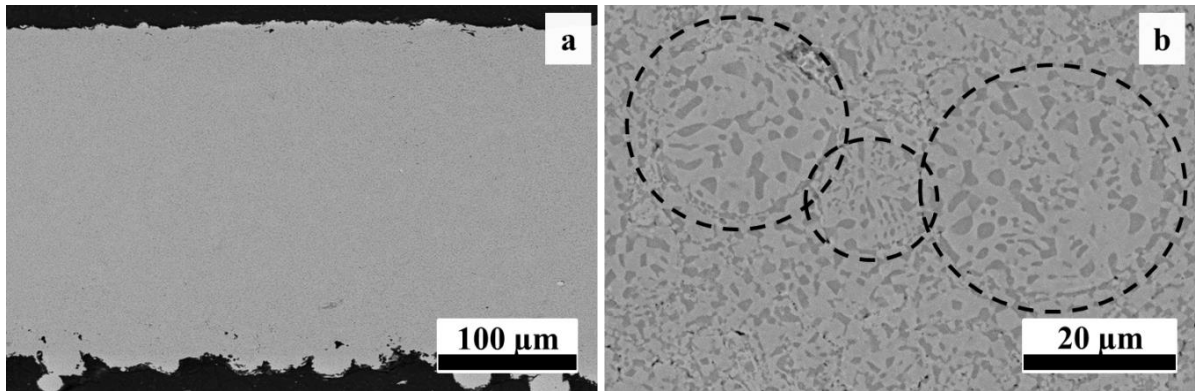
Figure 1. Microstructure of the heat treated VPS CoNiCrAlY coating at 1100 °C for 2 h: (a) the low magnification image showing the oxide-free and pore-free structure; (b) the high magnification image show the two phase structure with un-melted particles highlighted.
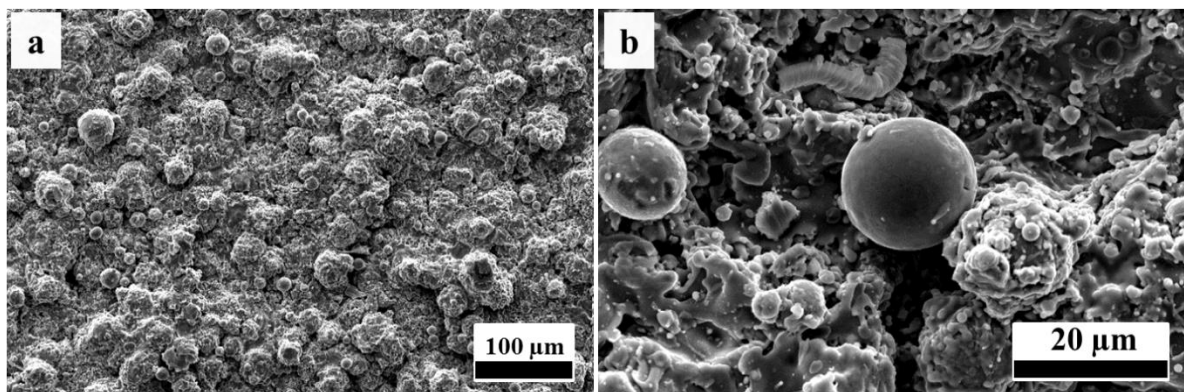

Figure 2. The morphology of the CoNiCrAlY coating surface: (a) the low magnification image showing the large number of un-melted particles; (b) the high magnification image showing the spherical shapes of un-melted particles.
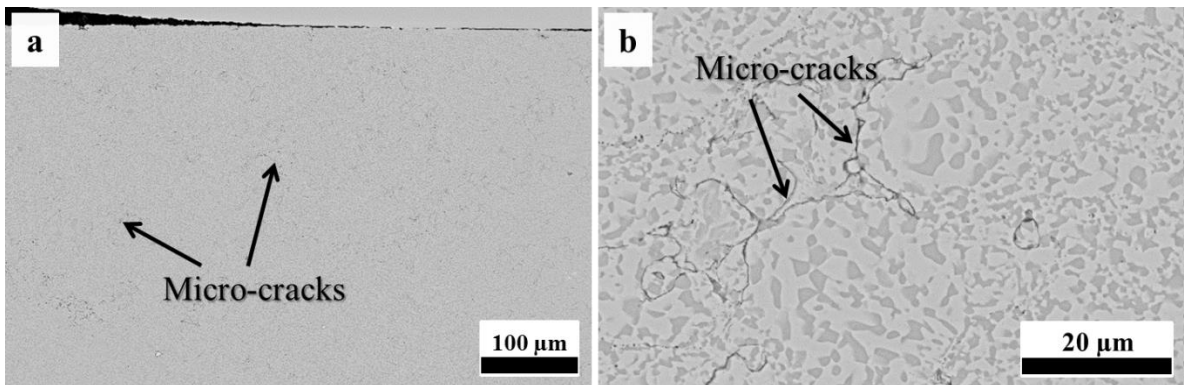

Figure 3. The microstructure of the VPS CoNiCrAlY coating in the clamped region prior to testing: (a) the low magnification image showing some dark contrast features; (b) the high magnification image showing micro-cracks along the un-melted particles.

3.2. Small punch creep test results

The SPT results under various constant loads at 750 °C are shown in Figure 4. It can be seen the coatings fail quite rapidly at loads between 94.4-100 N. The test curves reflect the large and instant plastic deformation upon loading in this range. At lower loads between 75-81.5 N, the results exhibit the typical creep displacement curves in SPT, with an initial primary region, a steady-state secondary region and a tertiary region leading to fracture. It should be noted that the total failure times at this load range are still quite small, varying between 4.5-14.5 h. Given the short period of the failure times, it is believed this CoNiCrAlY coating material mainly undergoes plastic deformation rather than creep. Previous work has demonstrated that the time to failure of the crack-free CoNiCrAlY

coating at the same composition ranges from 20-400 h at the similar load range [34]. Since the clamping torque is the same and the major difference is the amount of un-melted particles, it is indicated that the un-melted particles and the initial cracking can significantly influence the time to failure of this CoNiCrAlY coating during the SPT.
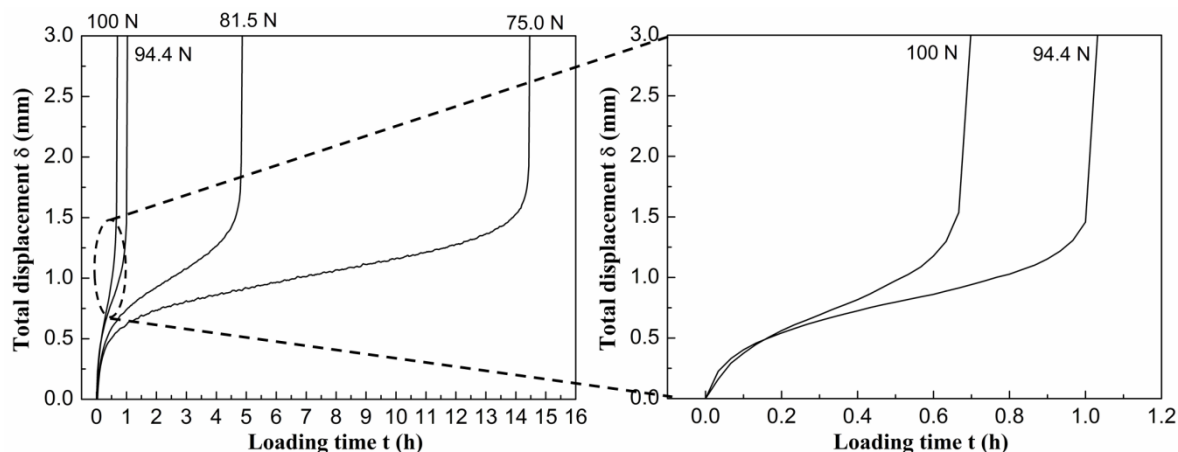

Figure 4. The SPT results for VPS CoNiCrAlY coating at 750 °C under a load range of 75-100 N.

Due to the initial cracking and the associated changes in the plasticity of the coating material, the SPT results can only reflect the mechanical response of the cracked sample. This means the derivation of the mechanical properties becomes less practical in this study. As discussed previously, the coatings have undergone an initial cracking stage prior to the SPT. The initial cracks which act as large defects have already changed the load-carrying capacity of the coating material. During the SPT, localised stretching occurs as the specimen deforms, whilst the resistance to the cavity nucleation depends on the bonding strength of the splats. The presence of micro-cracks in the coating, however, limits the effective bonding of the splats and weakens the mechanical strength of the coatings. Thus the initial micro-cracks act as fast fracture sites of the coating and short failure times are resulted in the SPT.

3.3. Post-test microstructural analysis

Figure 5 shows the fracture surfaces of the CoNiCrAlY coating after SPT. The domed shape of the failed specimen is seen in Figure 5a, indicating the deformation of the specimen during the test. The rough fracture surface indicates that extensive tearing has occurred. This is indeed seen in Figure 5b. It has been reported that the ductile-to-brittle transition of this CoNiCrAlY coating alloy is between 500-700 °C [35, 42]. The SPTs conducted in this study are at 750 °C, which falls into the ductile region of this material. As a result, the fracture surface exhibits the tearing behaviour. Since there are a large number of un-melted particles in the coating, the evidence of un-melted particles on the fracture surface can also be found, as shown in Figure 5c. It can be seen the limited bonding between the un-melted particles and the bulk material, which is likely resulted from the initial cracking around the un-melted particles.

The cross-sectional microstructure of the deformed specimen for 1000 h at 50 N prior to failure is shown in Figure 6. The deformed shape of the specimen agrees well with the dome-shaped specimen since the failure generally occurs at the edge of contact between the punch and specimen. The dark contrast macroscopic cavities are seen throughout the coating specimen in Figure 6a. The evidence of cracking around un-melted particles is still visible in Figure 6b. It is found that the initial micro-cracks have grown and propagated during the SPT. In comparison to the microstructure of the clamped specimen in Figure 3, it is seen that the void nucleation also occurred during the deformation in SPT. Such voids tend to link together to form large cavities, as seen in Figure 6b. The continuous linkage of large cavities and the propagation of the initial micro-cracks eventually lead to the failure of the coating specimen in SPT.
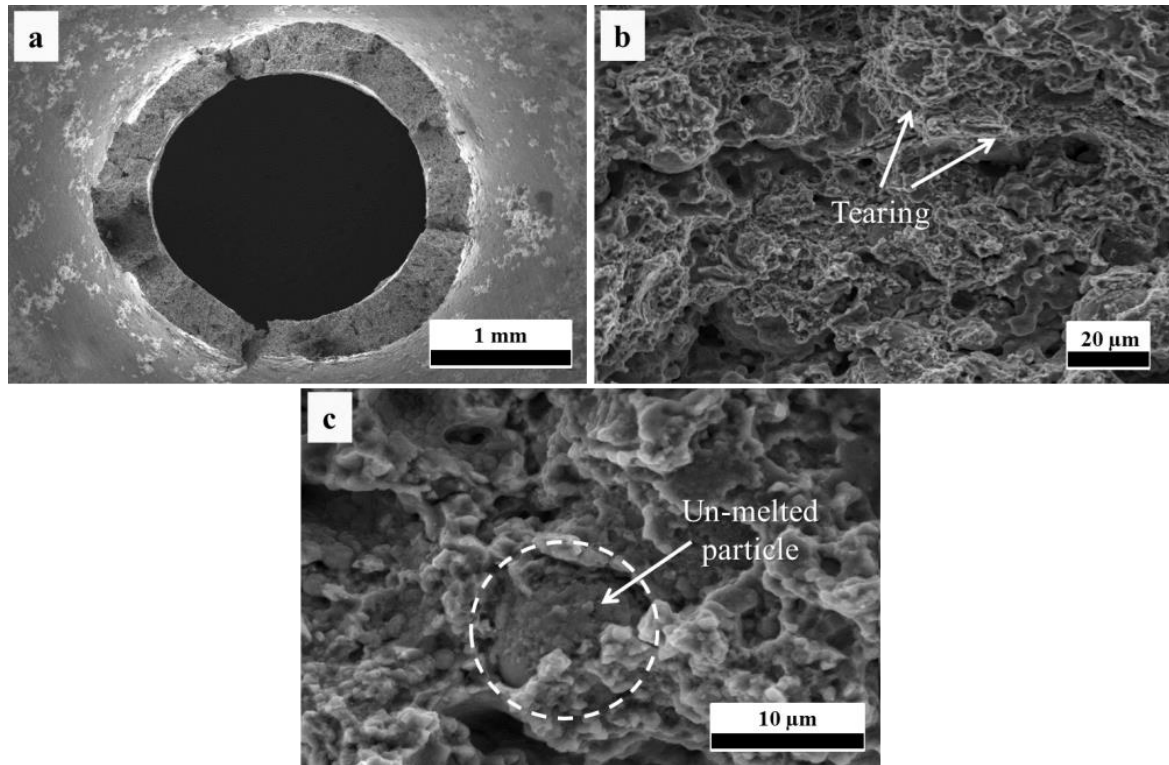
Figure 5. The fracture surface of the VPS CoNiCrAlY coating after the SPT at 75 N: (a) the dome-shaped fracture surface; (b) the evidence of tearing; (c) un-melted particle at the fracture surface.
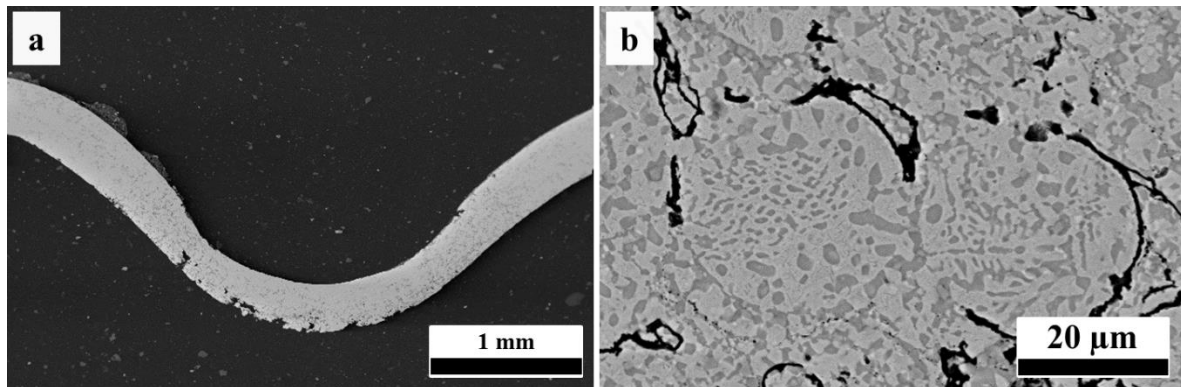

Figure 6. The cross-sectional microstructure of the deformed CoNiCrAlY coating but without final failure at 750 °C for 1000 h under a load of 50 N: (a) low magnification image show the shape of the deformed coating; (b) high magnification image showing the linkage of macro-cracks and cavities.

4. Concluding remarks

The small punch test technique, due to its suitability to test thin specimens, can be used to test the mechanical performance of thermally sprayed CoNiCrAlY coatings. But thermally sprayed coatings usually exhibit many defects, i.e. un-melted particles, which results in mechanical discrepancies within the coating. When such coatings with un-melted particles are subjected to SPT, initial cracking is likely to occur around the un-melted particles during the clamping stage of SPT due to the limited bonding between the un-melted particles and the bulk coating materials. The initial cracking can significantly affect the mechanical response of the CoNiCrAlY coating material in the subsequent SPT. Although the SPT results of such pre-cracked coatings are superficially similar to the conventional SPT curves in power plant steels, the rapid time to failure is obtained due to the initial micro-cracks, which only reflects the mechanical behaviour of the cracked coatings. Therefore, careful considerations need to be taken into account when using SPT for mechanical characterisation of such thermally sprayed coating since the initial plasticity of the coating has been changed in the clamping stage, especially when cracking has occurred due to the defects in the coating. Appropriate clamping force must be considered when testing thermally sprayed

coatings to avoid the large changes in the coating plasticity and, in the meantime, to provide sufficient clamping without specimen slipping.

References

1. Manahan, M.P. A new postirradiation mechanical behavior test-the miniaturized disk bend test, Nucl. Technol. 63 (1983) 295-315.
2. Manahan, M.P.; Argon, A.S.; Harling, O.K. The development of a miniaturized disk bend test for the determination of postirradiation mechanical-properties, J. Nucl. Mater. 103 (1982) 1545-1550.
3. Mao, X.; Shoji, T.; Takahashi, H.; Characterization of fracture behaviour in small punch test by combined recrystallization-etch method and rigid plastic analysis, J. Test. Eval. 15 (1987) 30-37.
4. Bulloch, J.H.; A review of the ESB small punch test data on various plant components with special emphasis on fractographic details, Eng. Failure Anal. 9 (2002) 511-534.
5. Hyde, T.H.; Sun, W.; Williams, J.A. Requirements for and use of miniature test specimens to provide mechanical and creep properties of materials: a review, Int. Mater. Rev. 52 (2007) 213-255.
6. Dobes, F.; Milicka, K. Application of creep small punch testing in assessment of creep lifetime, Mater. Sci. Eng. A 510 (2009) 440-443.
7. Ma, Y.W.; Shim, S.; Yoon, K.B. Assessment of power law creep constants of Gr91 steel using small punch creep tests, Fatigue Fract. Eng. Mater. Struct. 32 (2009) 951-960.
8. Dobeš, F.; Milička, K. Estimation of ductility of Fe–Al alloys by means of small punch test, Intermetallics 18 (2010) 1357-1359.
9. Hyde, T.H.; Stoyanov, M.; Sun, W.; Hyde, C.J. On the interpretation of results from small punch creep tests, J. Strain Anal. Eng. Des. 45 (2010) 141-164.
10. Rouse, J.P.; Cortellino, F.; Sun, W.; Hyde, T.H.; Shingledecker, J. Small punch creep testing: review on modelling and data interpretation, Mater. Sci. Technol. 29 (2013) 1328-1345.
11. Hurst, R.C.; Matocha, K.; A Renaissance in the Use of the Small Punch Testing Technique, In ASME Pressure Vessels and Piping Conference, (2015) PVP2015-45095.
12. CEN Workshop Agreement. CWA 15627:2006 E, "Small punch test method for metallic materials," CEN, European Committee for Standardization, Brussels Belgium, 2006.
13. Bruchhausen, M.; Holmström, S.; Simonovski, I.; Austin, T.; Lapetite, J.M.; Ripplinger, S.; de Haan, F. Recent developments in small punch testing: Tensile properties and DBTT, Theor. Appl. Fract. Mech. 86A (2016) 2-10.
14. Dymáček, P. Recent developments in small punch testing: Applications at elevated temperatures, Theor. Appl. Fract. Mech. 86A (2016) 25-33.
15. Bulloch, J.H. The small punch toughness test: some detailed fractographic information, Int. J. Pressure Vessels Piping 63 (1995) 177-194.
16. León, C.A.; Drew, R.A.L. Small punch testing for assessing the tensile strength of gradient Al/Ni–SiC composites, Mater. Lett. 56 (2002) 812-816.
17. Giddings, V.L.; Kurtz, S.M.; Jewett, C.W.; Foulds, J.R.; Edidin, A.A. A small punch test technique for characterizing the elastic modulus and fracture behavior of PMMA bone cement used in total joint replacement, Biomaterials 22 (2001) 1875-1881.
18. Evans, M.; Wang, D. The small punch creep test: some results from a numerical model, J. Mater. Sci. 43 (2008) 1825-1835.
19. Yang, Z.; Wang, Z. Relationship between strain and central deflection in small punch creep specimens, Int. J. Pressure Vessels Piping 80 (2003) 397-404.
20. Bulloch, J.H. A study concerning material fracture toughness and some small punch test data for low alloy steels, Eng. Failure Anal. 11 (2004) 635-653.
21. Rodríguez, C.; Cárdenas, E.; Belzunce, F.J.; Betegón, C. Fracture Characterization of Steels by Means of the Small Punch Test, Exp. Mech. 53 (2013) 385-392.

22. Li, Y.; Sturm, R.Determination of Creep Properties From Small Punch Test, Proc. ASME Pressure Vessels & Piping Division Conference, Chicago, USA, (2008) 739-750.

23. Wen, C.; Xu, T.; Guan, K. Correlation Factor Study of Small Punch Creep Test and Its Life Prediction, Materials 9 (2016) 796.

24. García, T.E.; Rodríguez, C.; Belzunce, F.J.; Suárez, C. Estimation of the mechanical properties of metallic materials by means of the small punch test, J. Alloys Compd. 582 (2014) 708-717.

25. Hyde, T.H.; Sun, W. Some considerations on specimen types for small sample creep tests, Mater. High Temp. 27 (2010) 157-165.

26. Chen, H.; Jackson, G.A.; Sun, W. An Overview of Using Small Punch Testing for Mechanical Characterization of MCrAlY Bond Coats, J. Therm. Spray Technol. 26 (2017) 1222-1238.

27. Taylor, M.P.; Evans, H.E.; Busso, E.P.; Qian, Z.Q. Creep properties of a Pt-aluminide coating, Acta Mater. 54 (2006) 3241-3252.

28. Kameda, J.; Bloomer, T.E.; Sugita, Y.; Ito, A.; Sakurai, S. Mechanical properties of aluminized CoCrAlY coatings in advanced gas turbine blades, Mater. Sci. Eng. A 234-236 (1997) 489-492.

29. Kameda, J.; Bloomer, T.E.; Sugita, Y.; Ito, A.; Sakurai, S. High temperature environmental attack and mechanical degradation of coatings in gas turbine blades, Mater. Sci. Eng. A 229 (1997) 42-54.

30. Kameda, J.; Bloomer, T.; Sakurai, S. Oxidation/carbonization/nitridation and in-service mechanical property degradation of CoCrAlY coatings in land-based gas turbine blades, J. Therm. Spray Technol. 8 (1999) 440-446.

31. Eskner, M.; Sandström, R. Measurement of the ductile-to-brittle transition temperature in a nickel aluminide coating by a miniaturised disc bending test technique, Surf. Coat. Technol. 165 (2003) 71-80.

32. Eskner, M.; Sandström, R. Mechanical properties and temperature dependence of an air plasma-sprayed NiCoCrAlY bondcoat, Surf. Coat. Technol. 200 (2006) 2695-2703.

33. Soltysiak, S.; Selent, M.; Roth, S.; Abendroth, M.; Hoffmann, M.; Biermann, H.; Kuna, M. High-temperature small punch test for mechanical characterization of a nickel-base super alloy, Mater. Sci. Eng. A 613 (2014) 259-263.

34. Chen, H.; Hyde, T.H.; Voisey, K.T.; McCartney, D.G.; Application of small punch creep testing to a thermally sprayed CoNiCrAlY bond coat, Mater. Sci. Eng. A 585 (2013) 205-213.

35. Chen, H.; Hyde, T.H. Use of multi-step loading small punch test to investigate the ductile-to-brittle transition behaviour of a thermally sprayed CoNiCrAlY coating, Mater. Sci. Eng. A 680 (2017) 203-209.

36. Jackson, G.A.; Chen, H.; Sun, W.; Mccartney, D.G. The high temperature creep properties of a thermally sprayed CoNiCrAlY coating via small punch creep testing, Key Eng. Mater. 734 (2017) 37-48.

37. Saeidi, S.; Voisey, K.T.; McCartney, D.G. The Effect of Heat Treatment on the Oxidation Behavior of HVOF and VPS CoNiCrAlY Coatings, J. Therm. Spray Technol. 18 (2009) 209-216.

38. Saeidi, S.; Voisey, K.T.; McCartney, D.G. Mechanical Properties and Microstructure of VPS and HVOF CoNiCrAlY Coatings, J. Therm. Spray Technol. 20 (2011) 1231–1243.

39. Chen, H.; Jackson, G.A.; Voisey, K.T.; McCartney, D.G. Modelling and experimental study on β-phase depletion behaviour of HVOF sprayed free-standing CoNiCrAlY coatings during oxidation, Surf. Coat. Technol. 291 (2016) 34-42.

40. Chen, H. Microstructure characterisation of un-melted particles in a plasma sprayed CoNiCrAlY coating, Mater. Charact. 136 (2018) 444-451.

41. Richer, P.; Yandouzi, M.; Beauvais, L.; Jodoin, B. Oxidation behaviour of CoNiCrAlY bond coats produced by plasma, HVOF and cold gas dynamic spraying, Surf. Coat. Technol. 204 (2010) 3962-3974.

42. Jackson, G.A.; Sun, W.; Mccartney, D.G. The Application of the Small Punch Tensile Test to Evaluate the Ductile to Brittle Transition of a Thermally Sprayed CoNiCrAlY Coating, Key Eng. Mater. 734 (2017) 144-155.

Application of the small punch test to evaluate the integrity of a cold spray titanium coating

A. Wong [1], Y.L. Tan [1], M. Pilot [1], R.J. Lancaster [1], S.P. Jeffs [1], F. Li [2], A.W.Y. Tan [3], W. Sun [3], E. Liu [3], I. Mitchell [4]

[1] Institute of Structural Materials, Swansea University, Bay Campus, Swansea, UK, SA1 8EN
[2] Rolls-Royce Singapore, 1 Seletar Aerospace Crescent, 797565 Singapore
[3] Nanyang Technological University, 50 Nanyang Ave, Singapore
[4] Rolls-Royce plc., P.O. Box 31, Derby, UK, DE24 8BJ
* Correspondence: r.j.lancaster@swansea.ac.uk; Tel.: +44-1792-295965

Abstract: Metal Cold Spray (MCS) is currently under evaluation for its suitability for aerospace applications. However, before this technology can be implemented into the jet engine, the mechanical performance and structural integrity of this novel process must be fully understood. Limited data is currently available to determine key materials properties given the discrete and transient nature of a MCS component. Furthermore, it is extremely challenging to produce uniaxial test coupons that are truly representative of the in-service geometry. As such, the small punch (SP) test offers an attractive alternative, since miniature disc SP specimens can be extracted from localised discrete locations. This paper will report the findings from an experimental collaborative programme of work currently being undertaken by Swansea University, Rolls-Royce Singapore and Nanyang Technological University Corp Lab to understand the contrasting modes of failure in a Ti-6Al-4V coating sprayed on to a Ti-6Al-4V substrate, which is expected to have properties akin to a forged variant. This will include a series of SP tests to assess the integrity and performance across the substrate, bond line and coating. Results will be supported by additional microstructural and fractographic investigations.

Keywords: Small Punch Test, Tensile, Cold Spray, Ti-6Al-4V

---

1. Introduction

Performance, cost and time are among the main drivers of material technology in the aerospace industry. As novel materials and processes are developed and incorporated in gas turbine engines, repair technologies are evolving simultaneously to ensure that aerospace components can still operate in optimal condition during service in a cost-effective approach. Traditional repair methods such as welding or hot spraying can lead to a number of deleterious effects on the component being repaired. These include the formation of heat affected zones, residual stresses, oxidation and porosity [1]. Furthermore, the deposition of sufficiently thick coatings is prohibited by thermal stresses generated within the component [2]. These effects can potentially reduce the service life of components and lead to premature failure.

In light of these issues, cold gas dynamic spray (or cold spray) offers a promising alternative that could alleviate the shortcomings caused by high temperature repair processes. Cold spray is a solid-state material deposition process where micron-sized particles are sprayed onto substrates at temperatures below the melting point of the metallic particles and under supersonic velocities [3]. Particle-substrate and particle-particle bonds are formed via mechanisms pertaining to adiabatic shear instabilities of particles upon impact rather than high temperatures [1, 3]. The name of this process is derived from the fact that the feedstock powder material remains solid during the process, which is different from conventional thermal spraying methods, where particles are partially or entirely molten as they impinge on the substrate [3]. Besides avoiding the aforementioned drawbacks, cold spray is cost effective as it offers short processing times [4]. Detailed explanations of the cold spray process can be found in [1, 3].

In order to evaluate the quality of repair methods, mechanical test techniques for assessing the structural integrity of materials are a critical aspect to consider. Although conventional approaches such as the uniaxial tensile test, Charpy impact test and fatigue test are well standardised, they still contain a number of inherent limitations. For instance, they require a sufficiently large volumes of material for the specimens to be machined to certain specifications, which can pose a problem if there is limited material availability. They also sometimes fail to capture the local microstructural effects during testing due to geometric constraints in the component [5]. Therefore, miniaturised test techniques such as the small punch (SP) test have been developed to address these issues. This

technique is a research topic of great interest to the scientific community, due to its ability to assess the mechanical behaviour of materials in small volumes. However, there is very little published literature describing the use of SP test as a means to assess the mechanical properties of cold-sprayed metal specimens. This paper aims to report results from the characterisation of mechanically tested Ti-6Al-4V MCS samples using SP testing. Of particular interest are the contrasting failure modes of samples when they are tested at different loads, times and temperatures, and the microstructural evolution across the bondline and into the coating. Experimental results from mechanical tests are further elucidated with the use of optical and scanning electron microscopy to identify important fractographic features such as the crack origin and propagation route. Characterisation results will also be compared for different test parameters.

2. Materials and Methods

2.1. Material

The material used in in this study originated from rectangular blanks with a Ti-6Al-4V coating thickness of 1.5mm and a Ti-6Al-4V substrate thickness of 4.2mm. A schematic illustration of the cold spray apparatus is shown in Figure 1. In the following step, cylindrical rods with a 9.5mm diameter were extracted from these blanks. These specimens were then sectioned into slices with a thickness of approximately 0.7-0.8mm. In order to prepare specimens according to guidelines provided in the European Code of Practice (EUCoP) for Small Punch Testing [6], the slices were ground and polished to a specimen thickness of 0.5mm ± 0.005mm with progressively finer grades of silicon carbide (SiC) abrasive paper. A final grade of 1200-grit was used to achieve a polished surface finish. Additionally, as-sprayed samples were sectioned from the remnants of the rectangular blanks for material characterisation.
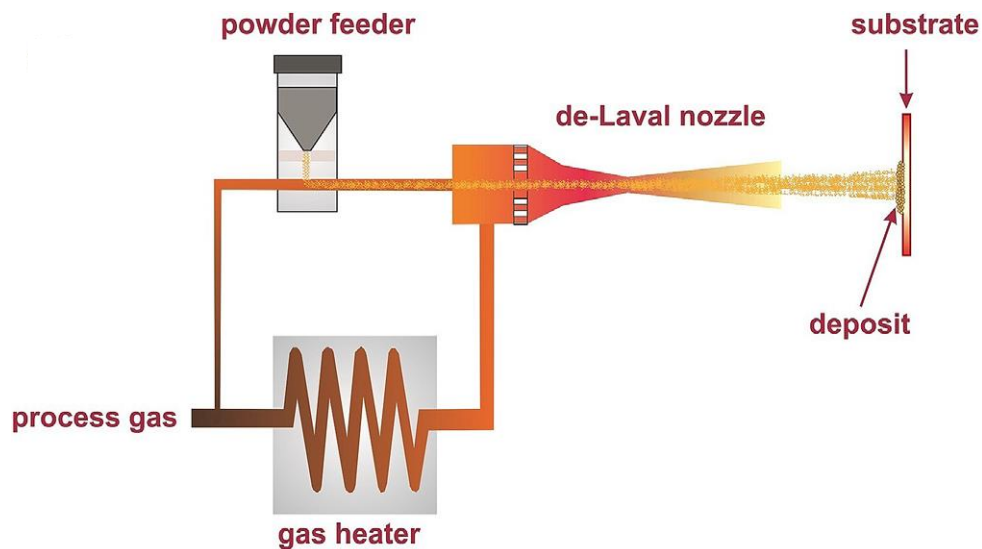

Figure 1. Schematic diagram of cold spraying apparatus [3].

2.2. Small Punch Tensile Testing

SP tensile tests were conducted using a bespoke test jig manufactured from Nimonic-90, housing both the SP disc specimen and the hemispherical indenter punch, as shown in Figure 2. The tensile test jig consists of an upper and lower die with a receiving hole of 4mm diameter, designed to clamp the miniature disc specimen in place. The specimen is punched from above by an indenter with a hemispherical tip of 2.5mm diameter aligned perpendicular to the flat upper surface of the specimen. SP tensile tests were conducted at constant displacement rates of 0.5mm·min^{-1}, all of which are within the EUCoP recommended range of 0.2mm·min^{-1} to 2mm·min^{-1} [6]. The specimens used for SP tensile test are classified according to their microstructure. Samples C, C2 and C3 are those with the coating layer only, while samples S, S2 and S3 consist of the substrate layer only. Samples B, B2 and B3 are taken from across the bondline, where the coating and substrate content is approximately equal. For convenience, samples denoted by B (i.e. B, B2 and B3) will be referred to as bondline samples, those denoted by S referred to as substrate and those denoted by C referred to as coating. Substrate and coating sample were tested only at 600 K,

whereas bondline samples were tested at 3 different temperatures: room temperature, 600 K and 650 K. All bondline specimens were tested with the punch in contact with substrate surface. The room temperature tests were carried out in a controlled laboratory environment at 20°C ± 2°C. During the elevated temperature tests, temperature was monitored using a Type N thermocouple, which was inserted into the jig from below through a hollow quartz rod in contact with the specimen. The deflection of the specimen was measured using a linear variable displacement transducer (LVDT). The LVDT was located directly below the underneath of the disc and maintained contact with the specimen via the quartz rod [7].
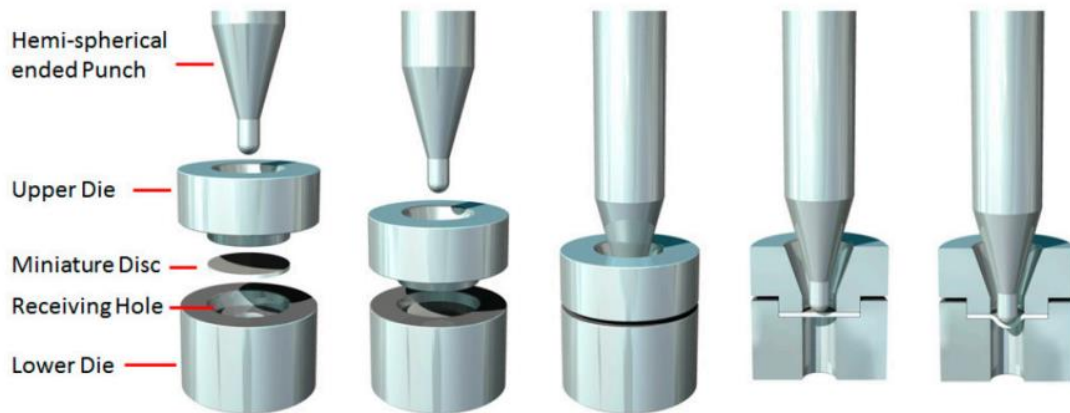

Figure 2. Small punch tensile test apparatus.

2.3. Microscopy

Microstructural characterisation of the SP and as-sprayed samples were performed using a Keyence VHX-700FE digital microscope and a Hitachi SU3500 scanning electron microscope (SEM). In the first instance, the Keyence was used to obtain plan view micrographs from the top, side and bottom surfaces of the SP samples. Secondary electron (SE) imaging mode in the SEM was used to analyse the failure modes, volume fraction and general microstructure of samples used in this study. Furthermore, the porosity in the as-sprayed samples were studied using a Zeiss Smartzoom 5 digital microscope, and post-analysis was performed using ImageJ.

3. Results and Discussion

3.1. Small Punch Tensile Testing

SP test results at 600 K are provided in Figure 3. The pure substrate samples showed the highest average maximum load of 1.44 kN. The bondline samples showed moderate strength with an average maximum load at 0.99 kN, whereas the coating samples showed the lowest average of 0.36 kN. A potential cause for the reduced performance in the coating samples is the population of porosity found in this variant. The presence of porosity tends to allow cracks to propagate more easily across the powder particles and can act as internal stress raisers, reducing the integrity of the material. In contrast, substrate samples can sustain a higher load as the number of porosity sites are expected to be minimal. A more detailed investigation on the levels of the porosity in each of the specimens will be discussed later in the paper. Since bondline samples consist of coating and substrate layer, they have moderate strength as compared to pure substrate or pure coating samples.

The displacement at failure values shown on each graph give an estimation of the ductility across the three locations. The results suggest that the coating samples showed the most brittle behaviour, while the substrate samples showed reasonable ductility. Bondline samples displayed the most ductile behaviour, as evidenced by the significant amounts of deflection achieved prior to failure.
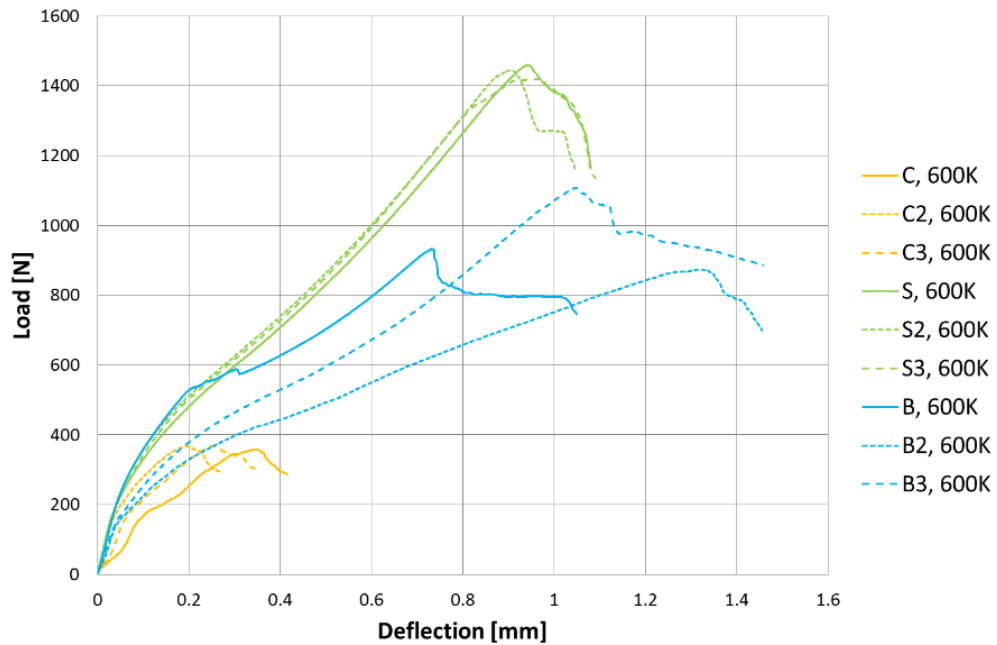
Figure 3. Collation of SP test load-displacement data for coating, substrate and bondline specimens at 600K with a displacement rate of 0.5mm·min^{-1}.

SP test results for bondline samples are shown in Figure 4. Although the bondline samples were all tested under the same conditions, the corresponding load-displacement curves showed considerable differences. The variation in the results can be attributed to the differing fractions of substrate and coating layers in these samples. For example, the peak load for sample B3 is significantly higher than that for samples B and B2 when they were tested at 600 K (see black arrows in Figure 4). According to Table 1, the percentage of substrate thickness for sample B3 (i.e. 90%) is much higher than that for the percentage of coating thickness (i.e. 10%). In contrast, the percentage of substrate thickness for sample B2 (i.e. 60.2%) is only slightly higher than the percentage of coating thickness (i.e. 39.8%). Therefore, a higher proportion of substrate will confer more strength to the bondline samples. Another important observation can be made when the test temperature is varied. The bondline sample tested at 650 K (i.e. B3) gave a peak load of 0.89 kN, whereas sample B2 tested at 600 K had a slightly lower peak load of 0.87 kN. However, when tested at room temperature, the bondline sample (i.e. B3) achieved a much lower peak load of 0.72 kN. These observations suggest that the ductility of bondline samples increase with temperature, hence they are able to deflect more and bear higher loads.
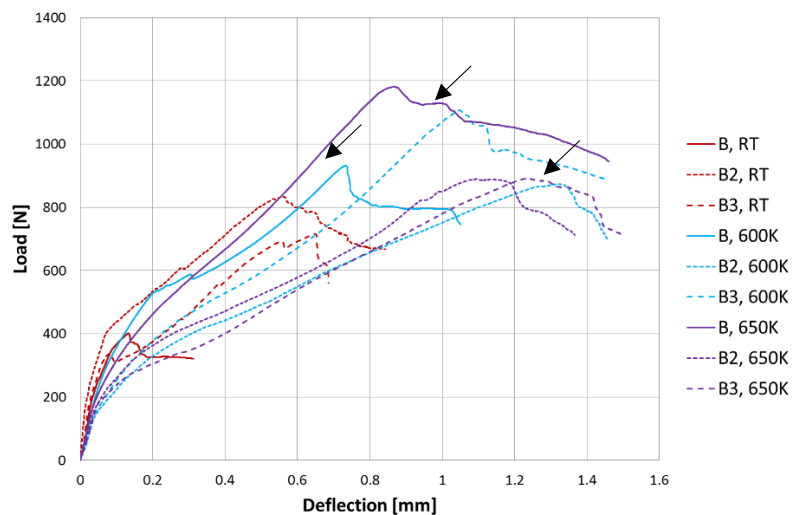

Figure 4. Collation of SP test load-displacement data for bondline specimens at room temperature, 600 K and 650 K with a displacement rate of 0.5mm·min^{-1}.

Table 1. Volume fraction calculation of bondline specimen.

Sample number	Percentage Thickness (%)	
	Coating	Substrate
BONDLINE RT		
B (10)	100.0	0
B2 (29)	37.6	62.4
	37.0	63.0
*B3 (12)	48.8	51.2
	44.2	55.8
BONDLINE 600K		
B (13)	55.0	45.0
	44.0	56.0
*B2 (14)	51.4	48.6
	39.8	60.2
B3 (15)	10.0	90.0
	20.2	79.8
BONDLINE 650K		
B (25)	31.4	68.6
	17.0	83.0
B2 (26)	39.0	61.0
	52.8	47.2
*B3 (27)	46.8	53.2
	45.8	54.2

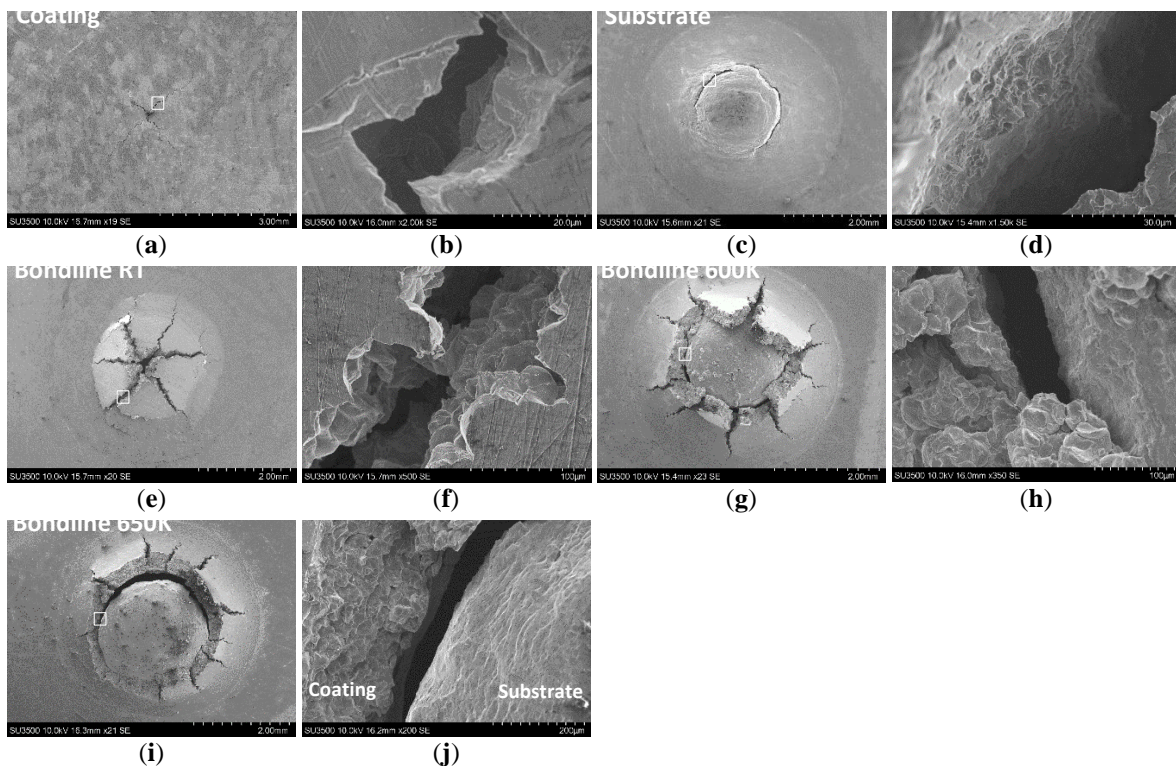*Samples B3(12), B2(14) and B3(27) were selected for further investigation*

Figure 5. Macroscopic and microscopic micrographs of disc fracture surfaces from SP tests: (**a,b**) coating specimen at 600K, C3; (**c,d**) substrate specimen at 600K, S; (**e,f**) bondline specimen at RT, B3; (**g,h**) bondline specimen at 600K, B2; (**i,j**) bondline specimen at 650K, B3.

The fracture surfaces of coating C3(2), substrate S(5), and bondline samples B3(12), B2(14) and B3(27) are shown in Figure 5. Based on their appearance, these samples showed distinct differences in their deformation behaviour. The coating sample (Figure 5a,b) shows a flat crack surface without much evidence of plastic deformation. When viewed at a higher magnification, facets can be observed on the crack surface, which suggests

that it failed in a brittle manner. In contrast, the dominant circumferential crack on the substrate sample (Figure 5c,d) is evidence of a typically ductile failure. A dimple fracture is observed due to the formation of micro-voids which then grow and coalesce, suggesting the occurrence of ductile tearing during disc rupture [8, 9].

For the bondline samples, images were taken on the underneath of the sample, capturing the deformation of the coating since the punch was imparted onto the substrate layer of the disc. On the macro scale, a star-shape crack is observed in the bondline specimens across all three temperatures (Figure 5e,g,i). As the temperature increases, the coating layer tends to detach from the sample. This could be due to the fact that at a higher temperature, the substrate layer tends to be more ductile which creates more deflection towards to the coating layer. Furthermore, at higher temperatures, the coating layer is expected to be more rigid and the powder particles are packed more closely together as the number of porosity sites may be reduced, thereby increasing the strength of the material.

3.2 Microstructural characterisation

3.2.1 SEM characterisation of as-sprayed samples

This section presents results obtained from the microstructural characterisation of as-sprayed samples using the SE imaging mode in the SEM. Figure 6 shows the SEM micrographs of as-sprayed MCS samples. The red arrow in Figure 6 (a) represents a view perpendicular to the surface of the coating layer, whereas the green arrow represents a view perpendicular to the cross-section of the sample. The microstructures in Figures 6(b-e) are viewed according to the direction of the green arrow, whereas Figure 6(f) is viewed according to the direction of the red arrow. The morphology of constituent layers of as-sprayed samples is shown in Figure 6(b), which depicts the deformed appearance of powder particles. Individual particles are clearly separated by boundaries. According to Figure 6(c), the substrate layer shows a typical duplex microstructure in Ti-6Al-4V, which contains near equiaxed primary α grains and lamellar secondary α within β matrix. The duplex microstructure gives the alloy well-balanced mechanical properties. This is because equiaxed microstructures usually provide good ductility and fatigue strength, whereas lamellar microstructures enhance the fracture toughness, resistance to fatigue crack growth and creep of the alloy. An interesting feature in Figure 6(d) is shown by the appearance of small, irregular-shaped particles surrounded by larger particles in the microstructure (see yellow arrow). Identical observations have also been made at other regions in the coating layer of the sample. While the exact reasons for these observations are unknown, a possible explanation is that particles have broken into smaller fragments during impact on the substrate surface, which then compacted tightly together as successive layers of particles were sprayed. According to Assadi et al. [3], particle impact during the deposition process is related to the viscoplastic deformation of feedstock powder particles, which leads to two phenomena. The first is the compaction of particles into a deposit, and the second is the formation of bonds between particles themselves. These processes will influence the density and strength of the deposit. An in-depth explanation about the underlying physics of the particle impact and deformation is described in published literature by Assadi et al. [3]; the same author(s) also explored the optimisation of the cold spray process based on different parameters using an integrated experimental-numerical approach in [10]. Another notable feature of the coating surface are crevices such as those in Figures 6(d) and (e), where the spherical outline of powder particles can be seen (see black arrows) inside the crevices. As mentioned earlier, particles are sprayed onto the substrate surface at a temperature below their melting point in the cold spray process, and they bond due to plastic deformation. Hence, they are still visible in the microstructure as they have not melted. In Figure 6(f), an acicular morphology can be observed in the particle, which is in good agreement with findings published in [11]. Micro-porosities (see black arrows) are also located along the boundaries between particles.
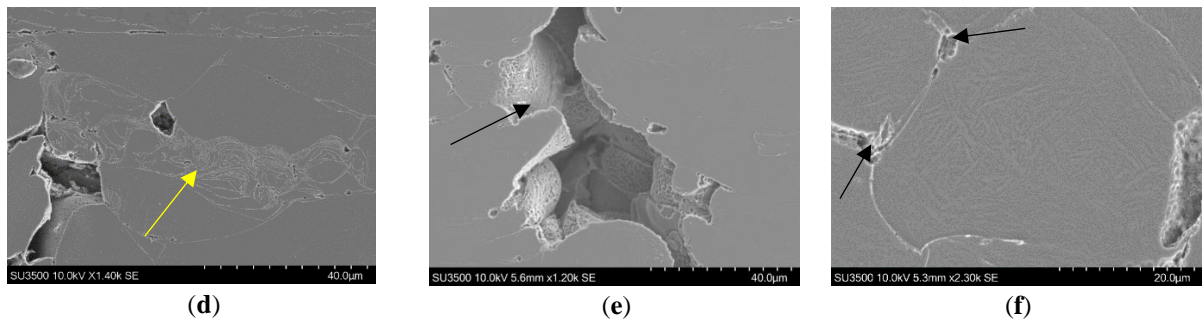

(a)   **(b)**   **(c)**

(**d**)　　　　　　　　　(**e**)　　　　　　　　　(**f**)
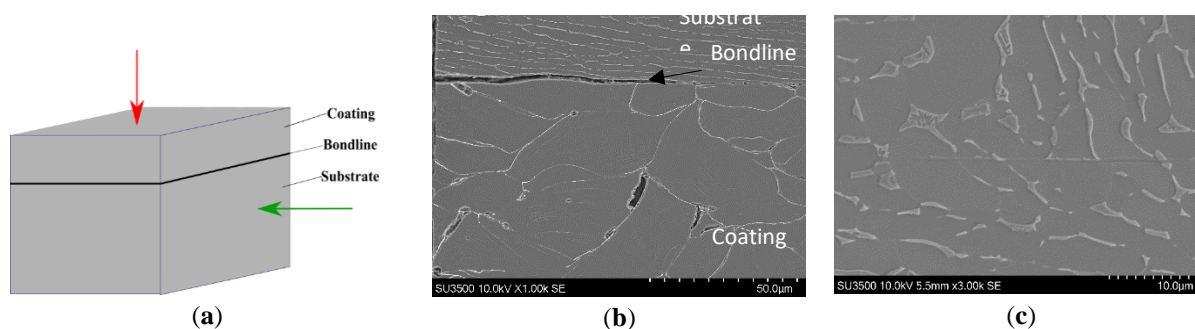
Figure 6. SEM micrographs of as-sprayed samples; (**a**) Schematic of viewing directions on samples, (**b**) Region showing the substrate, bondline and coating layers, (**c**) Substrate layer, (**d**) Coating layer, (**e**) Cavity in coating layer, (**f**) Acicular morphology and porosities in coating layer.

3.2.2 Porosity analysis of as-sprayed samples

This section presents results from the porosity analysis of as-sprayed samples. The analysis is performed by obtaining optical micrographs of samples in the unetched condition, followed by image processing of the micrographs using ImageJ. Samples were analysed in the unetched condition so that porosities can be clearly detected without being masked by features revealed from etching such as grain boundaries. The faint bands observed in Figure 7(a) are scan marks from the image stitching process in the Smartzoom microscope that do not affect the porosity analysis of the sample. In ImageJ, the first step for image processing is converting the optical micrographs into binary images. Statistical tools in the software are then used to measure the area of porosities [12]. In order to distinguish real porosities from other features in the microstructure, the software is set to detect objects with a circularity of 0.2-1, where values of 0 and 1 represent a perfect line and a perfect sphere respectively. The outlines of detected objects are displayed. An example is given in Figure 7(b), which shows the magnified image of the region highlighted (see red square) in Figure 7(a). The same procedures were repeated when analysing the porosities in sample 4. However, only the coating layer is analysed as the substrate layer contains a negligible amount of porosities. In Figure 7(c), the area highlighted by the red square is magnified and shown in Figure 7(d).
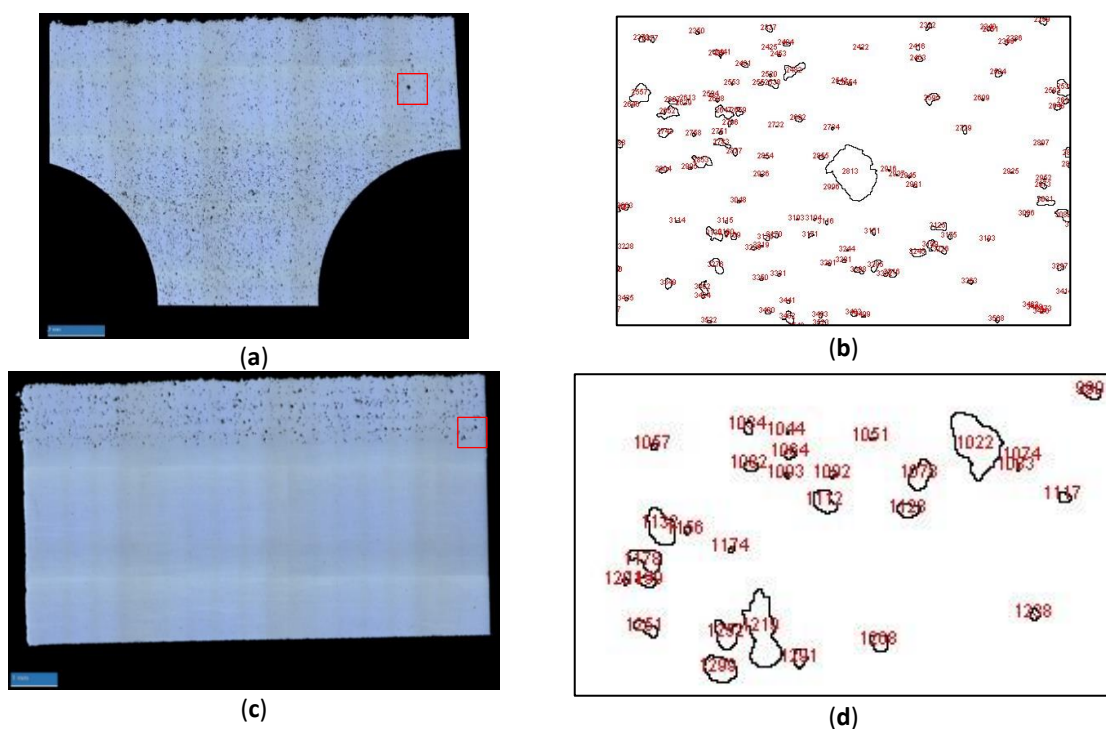

Figure 7. Optical micrographs for porosity analysis in as-sprayed samples; (**a**) Micrograph of sample 8b in unetched condition (viewed perpendicular to coating layer), (**b**) Processed image of sample 8b on ImageJ, (**c**) Micrograph of sample 4 in unetched condition (viewed perpendicular to cross-section of sample), (**d**) Processed image of sample 4 on ImageJ.

Quantifiable data associated with the porosity analysis of as-sprayed samples is presented in Table 2. Samples 1 and 8b are those that are viewed perpendicular to the coating layer, whereas samples 4 and 7 are viewed perpendicular to the cross-section of the sample. Several trends in the size of porosities can be drawn from Table 2. For instance, the average area analysed is approximately 10-4 mm2; the maximum area is approximately between 10-3 -10-2 mm2; and the minimum area is approximately 10-6 mm2. It is clear that the sizes of porosities can vary quite significantly, which correlates to Figure 15(b). The percentage porosity is calculated using the following formula:

$$Percentage\ porosity = \frac{Total\ area\ occupied\ by\ porosities}{Area\ of\ region\ analysed\ on\ the\ image} \times 100\%. \qquad (1)$$

The percentage porosity of all samples were found to be below 10%. A primary reason for the formation of pores in the coating layer is due to the entrapment of air as a result of the high surface reactivity between titanium powder particles and oxygen [13]. A highly porous structure may also form if there is inadequate deformation between interacting particles as a result of low deposition velocity [3, 14]. Although the process parameters affecting porosity are not studied in detail in this paper, it is vital to understand their relationship as it influences the mechanical properties of cold spray samples. For example, it has previously been found that coating microhardness can be enhanced when porosity levels are reduced via an increase in deposition velocity [11, 15-16]. The effect of powder morphology on porosity was investigated by Wong et al. [15]. The type of deposition gas also affects the porosity level, where Zahiri and co-workers [16] discovered that the use of helium gas greatly reduces the volume fraction of porosities. Other important factors that affect porosity include powder flight distance, powder sizes, gas pressure and temperature [16]. It should be noted that the porosity analysis method used in this study gives a relatively simple representation of the porosity levels in as-sprayed samples. The accuracy of the data can be improved by using methods such as the ASTM C20:2000 standard, which was implemented to measure the porosity levels in commercially pure titanium cold spray samples in [16].

Lastly, the substrate layer in Figure 16(c) shows virtually no evidence of porosity. Based on this observation, results from the porosity analysis are in good agreement with those presented in Figure 3, where the peak loads of bondline samples are higher than those of coating samples. The coating layer is brittle due to high amounts of porosity. Therefore, the presence of the substrate layer will engender more strength to the cold spray sample.

Table 2. Porosity analysis data.

Item	Sample 1	Sample 8b	Sample 4	Sample 7
Number of porosities	38894	13334	1418	9121
Area of sample (mm^2)	138.19	104.43	53.70	89.99
Average area of porosity (mm^2)	3.45×10^{-4}	3.28×10^{-4}	2.95×10^{-4}	2.40×10^{-4}
Maximum area of porosity (mm^2)	1.30×10^{-2}	1.30×10^{-2}	3.00×10^{-3}	7.00×10^{-3}
Minimum area of porosity (mm^2)	4.80×10^{-6}	4.84×10^{-6}	4.79×10^{-6}	4.81×10^{-6}
Area of region analysed on the image (mm^2)	138.19	104.43	14.20*	22.74*
Total area occupied by porosities (mm^2)	13.42	4.37	0.42	2.19
Percentage porosity (%)	9.71	4.18	2.96	9.63

Since samples 4 and 7 are viewed perpendicular to the cross-section (i.e. showing the coating, bondline and substrate layers), the area of analysis is restricted only to the coating layer so that the porosity analysis is performed consistently with samples 1 and 8b (i.e. which are viewed perpendicular to the coating layer).

4. Conclusions

The failure modes of cold spray Ti-6Al-4V coating on a TI-6Al-4V substrate has been studied and elucidated in this paper. A series of SP tests have been performed, followed by fractographic investigations. Additional material characterisation has also been performed to gain a better understanding of the cold-sprayed microstructure. The following conclusions can be drawn from this study:

1. SP tests have shown that coating samples displayed a brittle behaviour and could withstand the least peak load, whereas substrate samples showed reasonable ductility and were able to withstand the highest peak load among all samples. Bondline specimens displayed the most ductile behaviour and could sustain a moderate peak load.

2. At different temperature, the bondline samples tend to show a variance in ductility. Ductility was found to increase with temperature, which enabled them to plastically deform to a greater extent and withstand higher load.

3. SEM characterisation of SP specimens has shown that coating samples failed in a brittle manner since they display a flat crack surface with facets while substrate samples exhibit a more ductile, dimple type fracture due to the formation of microvoids which eventually grow and coalesce. Bondline samples exhibit both ductile and brittle fracture surfaces. The increase in temperature was found to cause the detachment of the coating layer from the sample.

4. The deformed morphology of powder particles in as-sprayed samples are in good agreement with plastic deformation mechanisms for particle-particle and particle-substrate bonding as reported in published literature.

5. The size of porosities in as-sprayed samples followed a certain trend: (i) The maximum area of porosities were approximately 10^{-3}-10^{-2} mm^2, (ii) the minimum area of porosities were approximately 10^{-6} mm^2, and (iii) the average area of porosities were approximately 10^{-4} mm^2. Additionally, the level of porosity in the coating of as-sprayed Ti-6Al-4V material was found to be consistently above approximately 3% and is expected to have a strong influence on the mechanical performance of such materials.

References

1. Singh, H.; Sidhu, T.S.; Kalsi, S.B.S. Cold spray technology: future of coating deposition processes, *Frattura ed Integrità Strutturale* **2012**, *6*, 69-84, DOI: 10.3221/IGF-ESIS.22.08.

2. Khun, N.W.; Tan, A.W.Y.; Liu, E. Mechanical and tribological properties of cold-sprayed Ti coatings on Ti-6Al-4V substrates, *J. Therm. Spray Tech.* **2016**, *25*, 715-724, DOI: 10.1007/s11666-016-0396-6.

3. Assadi, H.; Kreye, H.; Gärtner; F.; Klassen. T. Cold spraying – A materials perspective, *A. Materialia* **2016**, *116*, 382-407, DOI: 10.1016/j.actamat.2016.06.034.

4. Henao, J.; Sharma. M.M. Characterization, Deposition Mechanisms, and Modeling of Metallic Glass Powders for Cold Spray. In *Cold-Spray Coatings: Recent trends and future perspectives*, 1st ed.; Cavaliere, P., Ed.; Springer: Cham, Switzerland, **2018**; pp. 251-272, ISBN: 978-3-319-67183-3.

5. IIIsley, H.; Lancaster, R.J; Hurst, R.C.; Jeffs, S.P.; Baxter. G. Mechanical property characterisation of electron beam melted (EBM) Ti-6Al-4V via small punch tensile testing, Proceedings of the 4th International Conference on Small Scale Test Techniques, Shanghai, China, Oct 12-14; Guan, K., Matocha, K., Xu, T., Eds.; Trans Tech Publications: Zurich, Switzerland, 2016.

6. CEN Workshop Agreement CWA 15627, European Code of Practise: Small Punch Test Method for Metallic Materials. (2007).

7. Davies, S.; Lancaster, R.; Jeffs, S.; Baxter. G. Small Punch Testing of Powder Bed Direct Laser Deposits, Proceedings of the 4th International Conference on Small Scale Test Techniques, Shanghai, China, Oct 12-14; Guan, K., Matocha, K., Xu, T., Eds.; Trans Tech Publications: Zurich, Switzerland, 2016.

8. Parrington, R.J. Fractographic Features in Metals and Plastics. *Adv. Mater. Process* **2003**, 161, 37–40.

9. Becker, W.T.; Lampman, S. Fracture Appearance and Mechanisms of Deformation and Fracture. *ASM Handb.*, **2012**, 11, 559–586.

10. Assadi, H.; Schmidt, T.; Richter, H.; Kliemann, J.O.; Binder, K.; Gärtner, F.; Klassen, T.; Kreye, H.; On Parameter Selection in Cold Spraying, *J. Therm. Spray Tech.*, **2011**, *20*, 1161-1176, DOI: 10.1007/s11666-011-9662-9.

11. Ajaja, J.; Goldbaum, D.; Chromik, R.R. Characterisation of Ti cold spray coatings by indentation methods, *A. Astronautica.*, **2011**, *69*, 923-928, DOI: 10.1016/j.actaastro.2011.06.012.

12. Moy, C.K.S.; Cairney, J.; Ranzi, G.; Jahedi, M.; Ringer. S.P. Investigating the microstructure and composition of cold gas-dynamic spray (CGDS) Ti powder deposited on Al 6063 substrate, *Surface and Coatings Technology*, **2010**, *204*, 3739-3749, DOI: 10.1016/j.surfcoat.2010.04.016.

13. Li, W.Y.; Zhang, C.; Wang, H.T.; Guo, X.P.; Liao, H.L.; Li, C.J.; Coddet, C. Significant influences of metal reactivity and oxide films at particle surfaces on coating microstructure in cold spraying, *Applied Surface Science*, **2007**, *253*, 3557-3562, DOI: 10.1016/j.apsusc.2006.07.063.

14. Ogawa, K.; Seo, D. Repair of Turbine Blades Using Cold Spray Technique. In *Advances in Gas Turbine Technology*, 1st ed.; Benini, E. Ed.; InTech: London, United Kingdom, 2011; pp. 499-526, ISBN: 978-953-307-611-9.

15. Wong, W.; Rezaeian, A.; Irissou, E.; Legoux, J.G.; Yue. S. Cold spray characteristics of commercially pure Ti and Ti-6Al-4V, *Adv. Mater. Research*, **2010**, *89-91*, pp 639-644, DOI: 10.4028/www.scientific.net/AMR.89-91.639.

16. Zahiri, S.H.; Antonio, C.I.; Jahedi. M. Elimination of porosity in directly fabricated titanium via cold gas dynamic spraying, *Journal of Materials Processing Technology*, **2009**, *209*, 922-929, DOI: 10.1016/j.jmatprotec.2008.03.005.

Experimental investigations on the failure of a coating-substrate compound by means of the C-specimen concept and the small punch test

M. Selent [1], M. Abendroth [1], M. Kuna [1], and B. Kiefer [1,*]

[1] TU Bergakademie Freiberg, Institute of Mechanics and Fluid Dynamics, Lampadiusstraße 4, D-09596 Freiberg, Germany

* Correspondence: Marcel.Selent@imfd.tu-freiberg.de; Tel.: +49-3731-39-3356

Abstract: In previous work at the Institute of Mechanics and Fluid Dynamics of the TU Bergakademie Freiberg the thermomechanical fatigue of corrosion protection coatings was investigated, which had been manufactured by high velocity oxygen fuel spraying (HVOF) of a nickel-base superalloy. The failure behaviour of this coating-substrate compound under thermomechanical cyclic service loading is characterised by the combination of multiple damage mechanisms. During the course of the project, two dominant damage mechanisms were identified, that result in a functional failure of the coating. The first significant damage mechanism is the formation of delamination areas between coating and substrate, which result in local coating spallings, if they reach a critical size. The second important damage mechanism is the initiation and the propagation of inter-particle cracks in the coating. Regarding the functionality of the corrosion-preventive coating, these cracks become critical if they extend across the whole layer thickness up to the substrate. In order to further investigate the interface delamination between coating and substrate, the so-called C-specimen concept (CSC) has been developed. The characterisation of the inter-particle failure of the pure coating on the other hand is realised by the small punch test (SPT). In this contribution, both possible sources of the coating-substrate compound failure behaviour are addressed and have been experimentally examined by the use of the CSC and the SPT. These tests were conducted with the purpose of building a sufficiently detailed experimental data base suitable for the parameter identification of cyclic cohesive zone-based failure models.

Keywords: C-specimen concept, small punch test, high velocity oxygen fuel spraying, coating-substrate compound, nickel-base superalloy

1. Introduction

The standard DIN 50903 [1] aims at a unification of the terminology for pores, inclusions, bubbles, and cracks in metallic coatings. Pores, inclusions, bubbles, and cracks are localised discontinuities of the coating material. Figure 1 shows possible crack characteristics in coating-substrate compounds.
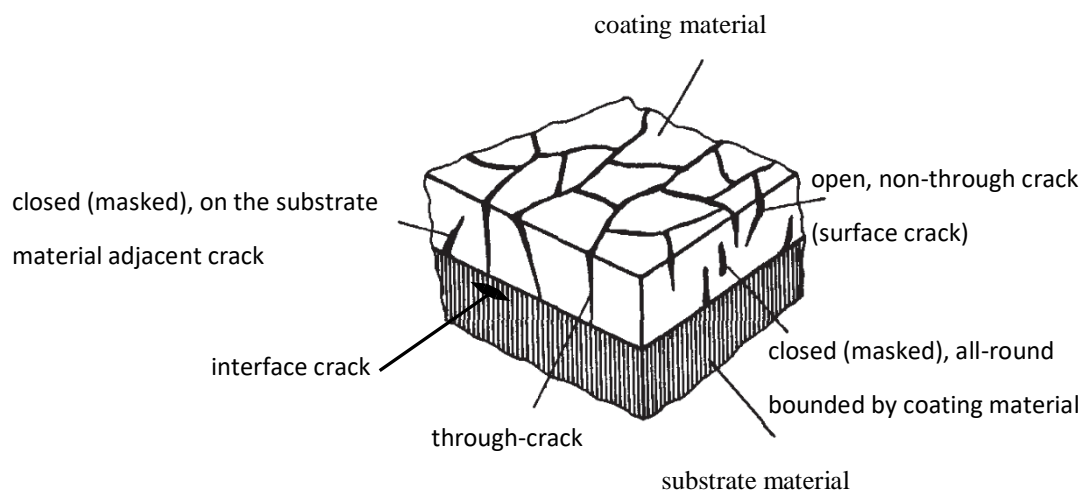

Figure 1. Classification of cracks in coating-substrate compounds (in accordance to [1]).

The investigated coating-substrate compound consisting of a modified variant of IN-625 (coating material) and vessel steel 16Mo3 (substrate material) is subjected to thermomechanical fatigue at service loading (e.g. at superheater tubes and heat exchangers of waste-fired boiler plants). The first significant damage mechanism is the formation of delamination areas between coating and substrate, which result in local coating spallings, if they reach a critical size. The second important damage mechanism is the initiation and the propagation of inter-particle cracks in the coating. Regarding the functionality of the corrosion-preventive coating, these cracks become critical if they extend across the whole layer thickness up to the substrate material (compare Figure 2).
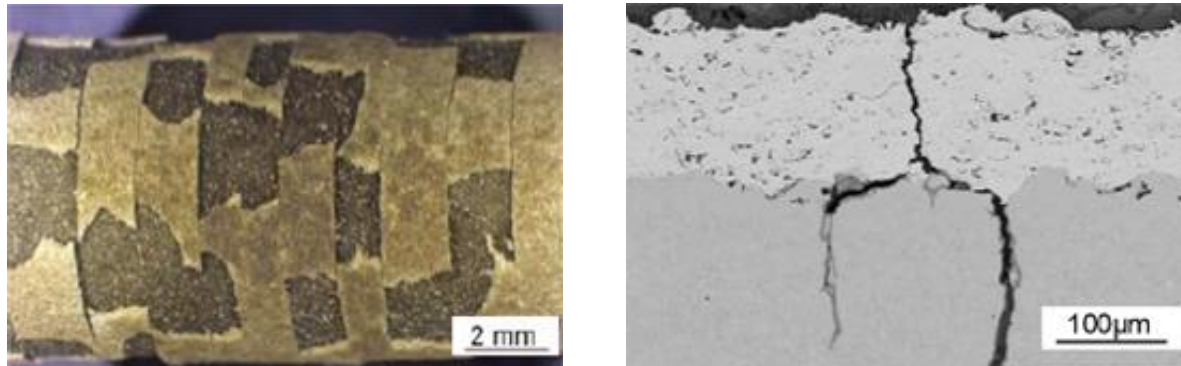

Figure 2. Interface delamination between coating and substrate (left) and interparticle failure of pure coating (right) [2].

2. Coating-substrate compound

The coating is applied onto the substrate by a HVOF spraying process under conditions of use, which are protected intellectual property of the coating company. The thermal spray powder produces a dense, self-bonding coating which is oxidation- and corrosion-resistant at elevated temperatures. Table 1 comprises the main chemical composition of the used thermal spray powder.

Table 1. Chemical composition of the thermal spray powder.

Element	Ni	Cr	Fe	Mo	Nb+Ta
[nominal wt. %]	Bal.	21.5	2.5	9.0	3.7

Due to the manufacturing process the coating is relatively coarsely textured, since the particle size of the spheroidal spray powder is about 45 to 90 µm. The particle size of the coating after the flame spraying process is analysed using confocal microscopy. The surface profile of the coating is measured on a straight line. The entire measuring length l_n is 2.3335 mm. A cut-off wavelength λ_c of 80 µm is used. The resulting primary profile is separated into a waviness and a roughness profile by this cut-off wavelength, see Figure 3 (left). For the purpose of better visualisation the profiles are plotted up to a measuring distance of 400 µm. Whereas the waviness profile provides conclusions about the macroscopic surface planarity, the roughness profile characterises the microscopic surface topography.
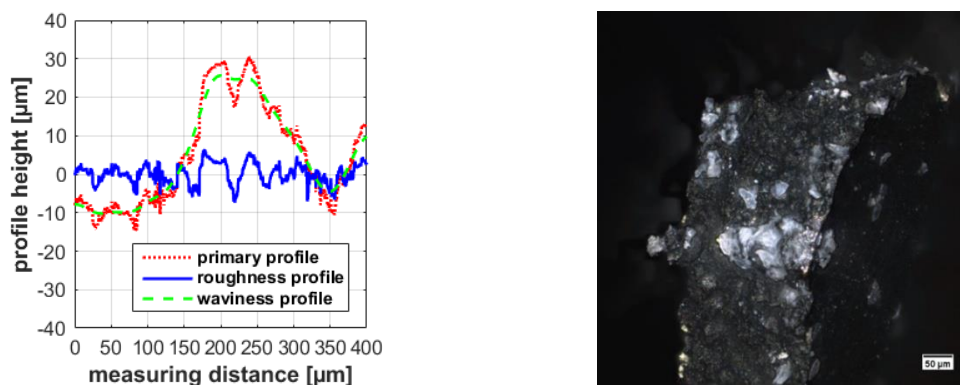

Figure 3. Investigation of coating particle size employing confocal microscopy.

The roughness profile contains information about the particle size of the coating after the HVOF spraying process. The original particle size of the spheroidal spray powder was about 45 to 90 µm. Particles of this size range can also be found in the roughness profile. Figure 3 (right) shows the fracture surface of a SPT-specimen of pure coating material tested at 500 °C. A demarcation of original particles of the spheroidal spray powder is observable. This indicates a low ductility of the particles and a crack growth along the particle interfaces (inter-particle failure).

3. C-specimen concept (CSC)

3.1. Test conception

The main demand on the test conception consists in the performance of fatigue tests under reverse bending loading of sprayed metallic corrosion-preventive coating-substrate compounds. The aim of the experiment is the investigation of the cyclic interface delamination behaviour between coating and substrate. For generating a bending stress distribution in the observed sample cross-section, two realisation variants of the test set-up have been taken into account to meet the requirements. The standardised cyclic 4-point-bending-test (technical designation in materials testing: 8-point-bending-test [3]) and the non-standardised CSC, developed in-house. The cyclic delamination test was realised by CSC. The advantages of the CSC compared to the cyclic 4-point-bending-test are emphasised in section 3.5.

3.2. Basic C-specimen geometry

Figure 4 contains the basic geometric design features of the designed C-specimen (left) and defines the meaning of the respective geometry parameters (right).
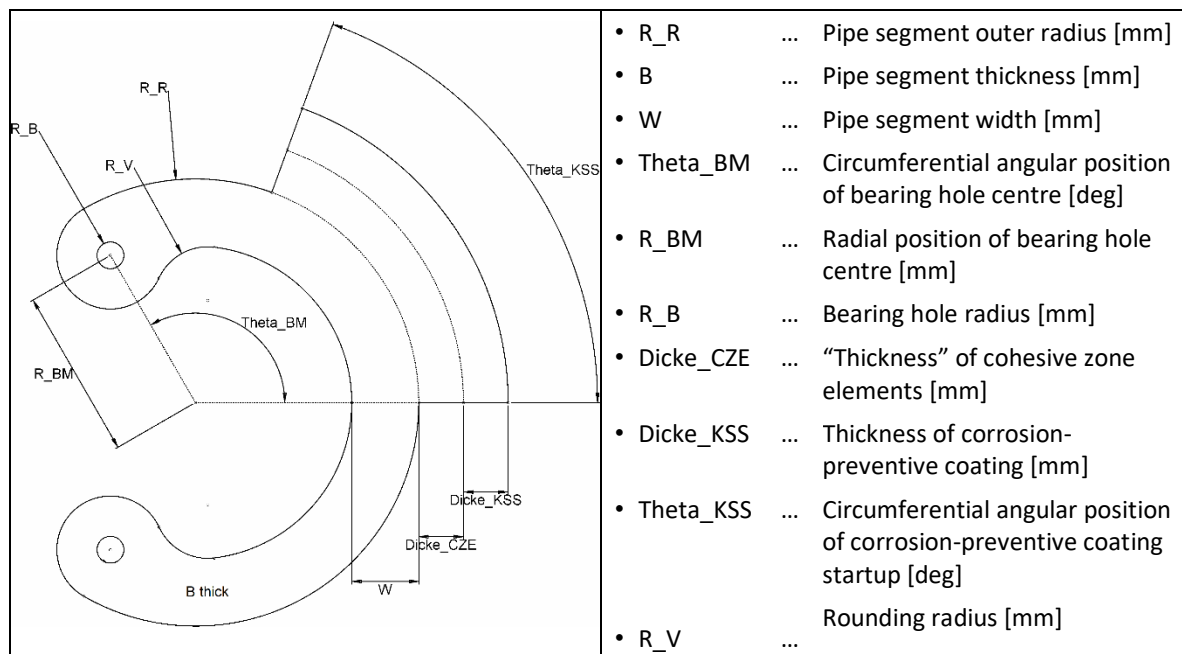

• R_R	...	Pipe segment outer radius [mm]
• B	...	Pipe segment thickness [mm]
• W	...	Pipe segment width [mm]
• Theta_BM	...	Circumferential angular position of bearing hole centre [deg]
• R_BM	...	Radial position of bearing hole centre [mm]
• R_B	...	Bearing hole radius [mm]
• Dicke_CZE	...	"Thickness" of cohesive zone elements [mm]
• Dicke_KSS	...	Thickness of corrosion-preventive coating [mm]
• Theta_KSS	...	Circumferential angular position of corrosion-preventive coating startup [deg]
• R_V	...	Rounding radius [mm]

Figure 4. Conceptual C-specimen geometry.

3.3. Technical drawing of the optimised specimen geometry

On the basis of this geometric specification, parameter studies have been conducted employing the finite element method (FEM) to obtain an optimal set of geometric parameters suitable for the experimental requirements and boundary conditions. Figure 5 depicts the result of these FE-computations by means of a technical drawing of the optimised specimen geometry.
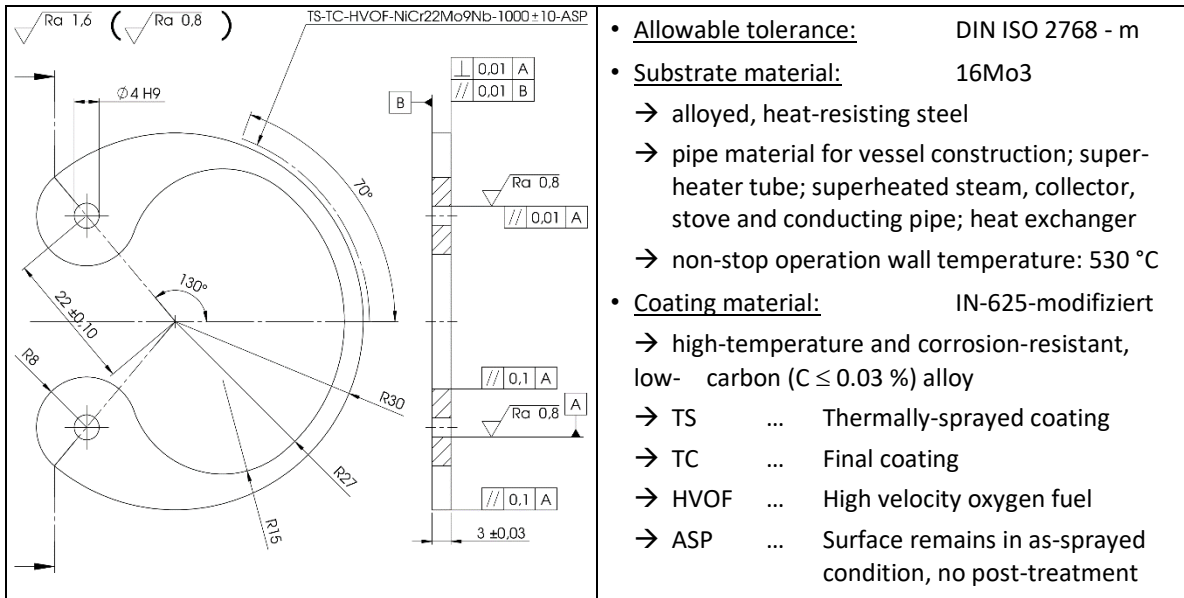
Figure 5. Technical drawing of the optimised specimen geometry (all dimensions in mm).

3.4. Analytical distribution of internal forces

In Figure 6 the normalised analytical distribution of the internal normal force F_N, shear force F_Q and bending moment M_b are shown as a function of the circumferential angle θ ($0° \leq \theta \leq +130°$). For the bottom sample half ($0° \geq \theta \geq -130°$) result equivalent distributions due to the symmetry in geometry and loading.
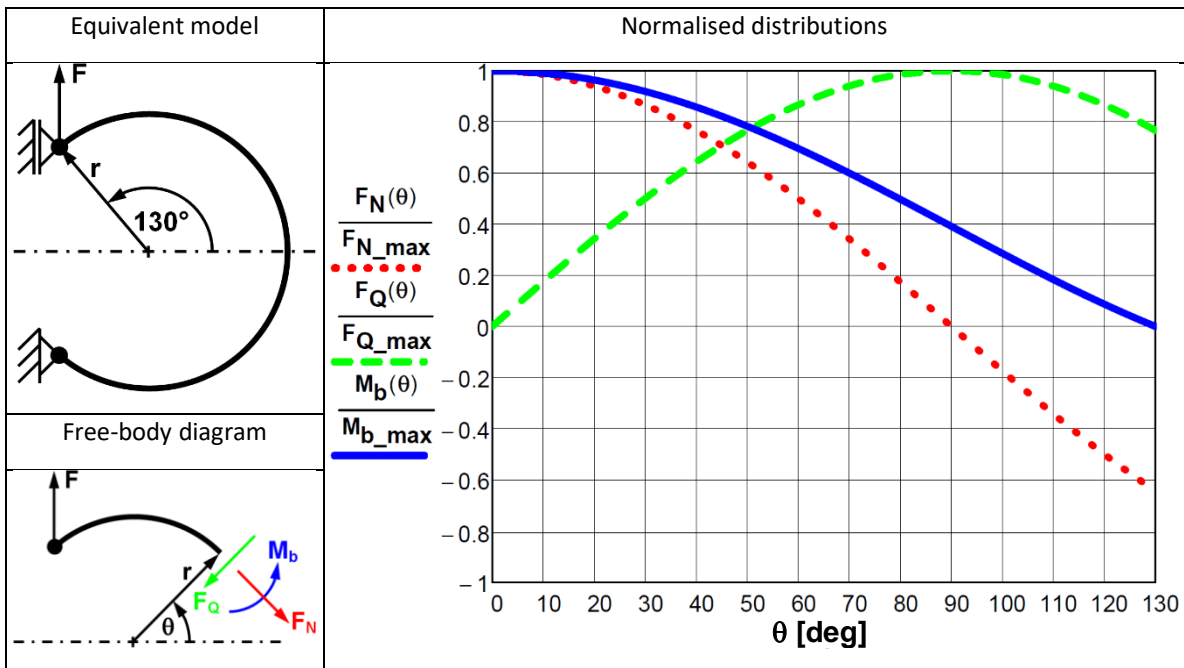
Figure 6. Analytical distribution of internal forces and bending moment.

The normal force and the bending moment have their maxima at the C-specimen vertex ($\theta = 0°$) and both decrease with increasing circumferential angle. The normal force vanishes at $\theta = 90°$ and reaches its minimum at $\theta = 130°$. The bending moment becomes zero at $\theta = 130°$. The shear force vanishes at the C-specimen vertex ($\theta = 0°$), increases with increasing circumferential angle up to its maximum at $\theta = 90°$, and then again decreases in the range between $90° \leq \theta \leq 130°$.

3.5. Conceptual advantages

From the design point of view, the eight bearing rollers of the cyclic 4-point-bending-test are eliminated in the CSC. Thereby no expensive bearings (roller/slide bearings) with backlash are required. A prestressing for the elimination of backlash is unnecessary. In addition, line loadings in the contact area of the bearing rollers and the accompanying local spalling of the sensitive coating are avoided.

From the experimental view, the CSC is characterised by a simple jig assembly, specimen carrier, and general experimental set-up. With the used jig, samples of different dimensions can be tested. It features a high flexibility regarding the tested specimen geometry and it is less sensitive to thermal expansion.

The key advantage of the CSC compared to the cyclic 4-point-bending-test is the stress distribution in the loaded sample. In the C-specimen there exists only one sample cross-section with maximal bending moment (confer Figure 6). In contrast, the maximum bending moment in the cyclic 4-point-bending-specimen is located along the entire span width between the two inner bearings. Thus, the CSC ensures a localisation of the damage zone and the potential initiation point for the delamination of the coating from the substrate is known a priori. Moreover, the better optical access enables an in-situ observation of the damage zone and its evolution during the experiment with a pulsed reflection microscope.

3.6. Experimental set-up

Figure 7 (left) displays three main components of the realised test rig construction: testing machine (TM), temperature chamber (TC), and loading device (LD). Essential component properties can be found on the right-hand side of Figure 7. Two further main components are a pulsed reflection microscope (PRM) [4] and the C-specimen (see Figure 8).
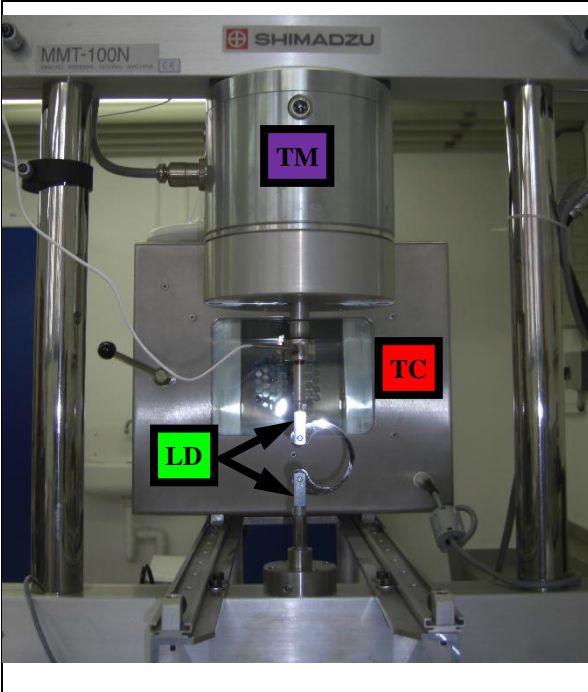

- **Testing Machine (TM):** **MMT-100NB-10**
  - → force F [N]: $-100 \leq F \leq +100$
  - → displacement u [mm]: $-10 \leq u \leq +10$
  - → test frequency f [Hz]: $0.1 \leq f \leq 60$
  - → cycle counter [-]: maximal 10^9
- **Temperature Chamber (TC):** **TH 2700**
  - → temperature range [°C]: $-70 \leq \vartheta \leq +280$
  - → control accuracy [°C]: 0.1
  - → interior dimensions [mm]: 200 x 300 x 220
  - → window dimensions [mm]: 100 x 100
- **Loading Device (LD):**
  - → 2 clevises G 5x20 M5 QB⌀4 white galvanised
  - → 2 folding spring bolts FKB 5x20 B⌀4 white galvanised
  - → several shim rings for axial backlash compensation DIN 988 - 4x8x(0.1, 0.2, 0.3, 0.5, 1.0) - St (test of different specimen thicknesses B with one device)
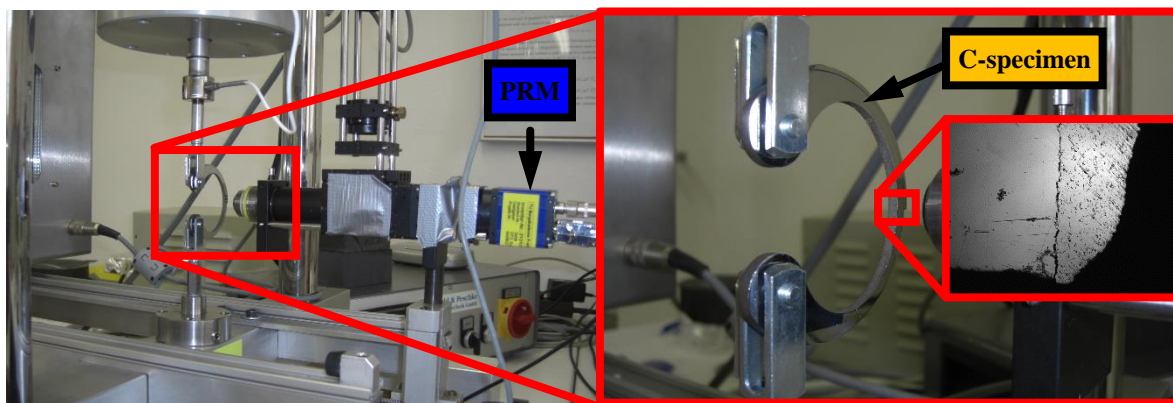
Figure 7. Components of the test rig set-up 1.

Figure 8. Components of the test rig set-up 2.

The particular C-specimen used in this study features a HVOF coating on a partial circular arc of the sample outer radius in accordance with the technical drawing of Figure 5. The objective is to ensure the development of a single crack front during the delamination tests, starting from the local main damage zone at the C-specimen vertex ($\theta = 0°$). The PRM serves the in-situ observation of the damage zone evolution during the cyclic delamination experiments. In Figure 8 the PRM focuses on the interface between coating and substrate at the C-specimen vertex. The enlarged image detail on the right shows a clear demarcation between the substrate material (left), the coating material (right), and the dividing interface with already advanced delamination.

3.7. Experimental result

After sample preparation, five C-specimens with 200 µm, six C-specimens with 500 µm, and six C-specimens with 1000 µm coating thickness were available for delamination tests. It was possible to infer from FE-simulations for test optimisation that the delamination theoretically proceeds faster for the C-specimens with 1000 µm layer thickness than for the samples with thinner coatings. Therefore the first test was performed on a C-specimen with 1000 µm layer thickness. The experimental conditions were defined as follows: isothermal, displacement controlled, and cyclic fatigue test under reverse loading ($R = -1$) at room temperature. The amplitude of the sinusoidal displacement control at the top floating bearing was increased stepwise up to a maximum of $u_a = \pm 1.0$ mm in order to avoid global plastic cyclic deformations inside the C-specimen. A stepwise increase in test frequency up to maximally $f = 1.5$ Hz was also realised. This maximum frequency represents a reasonable compromise between PRM image sharpness, repeatability of the recordings concerning the position on the polished sample surface, and test duration. The PRM images, displacement u, force F, and number of cycles N were captured cyclewise during the test in the turning points of the floating bearing displacement control signal. Figure 9 exemplarily shows the development of the cyclic interface delamination between coating and substrate during the test.
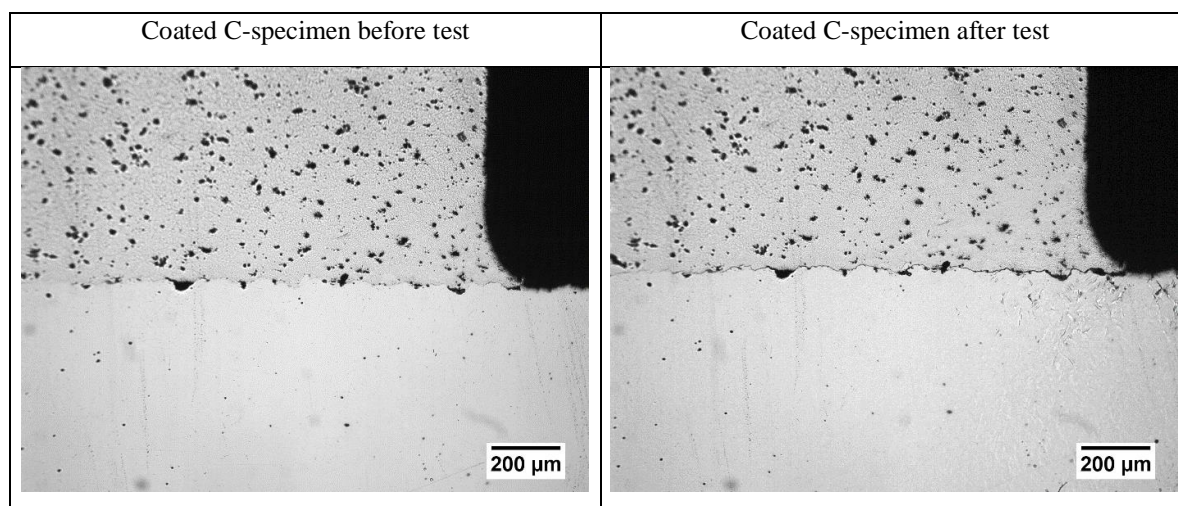

Figure 9. Development of cyclic interface delamination between coating (above) and substrate (below) during the test.

The left PRM image depicts the coating-substrate compound in the original state before testing with no interface damage. The right PRM image shows the interface damage in the final state after testing. Due to a lack of experimental reference results prior to the test concerning the delamination velocity, it was necessary to proceed in a stepwise manner while conducting the experiment, to carefully approach suitable maximum values for the amplitude of the sinusoidal displacement control and the testing frequency. Thus, the interface damage state at the end of the experiment is not the result of a single-stage test with a constant test frequency, but rather of multiple single-stage tests with variable test frequency.

4. Small punch test (SPT)

4.1. Experimental set-up

Figure 10 displays on the left-hand side the basic SPT-set-up and on the right-hand side the detailed components of the SPT-apparatus.
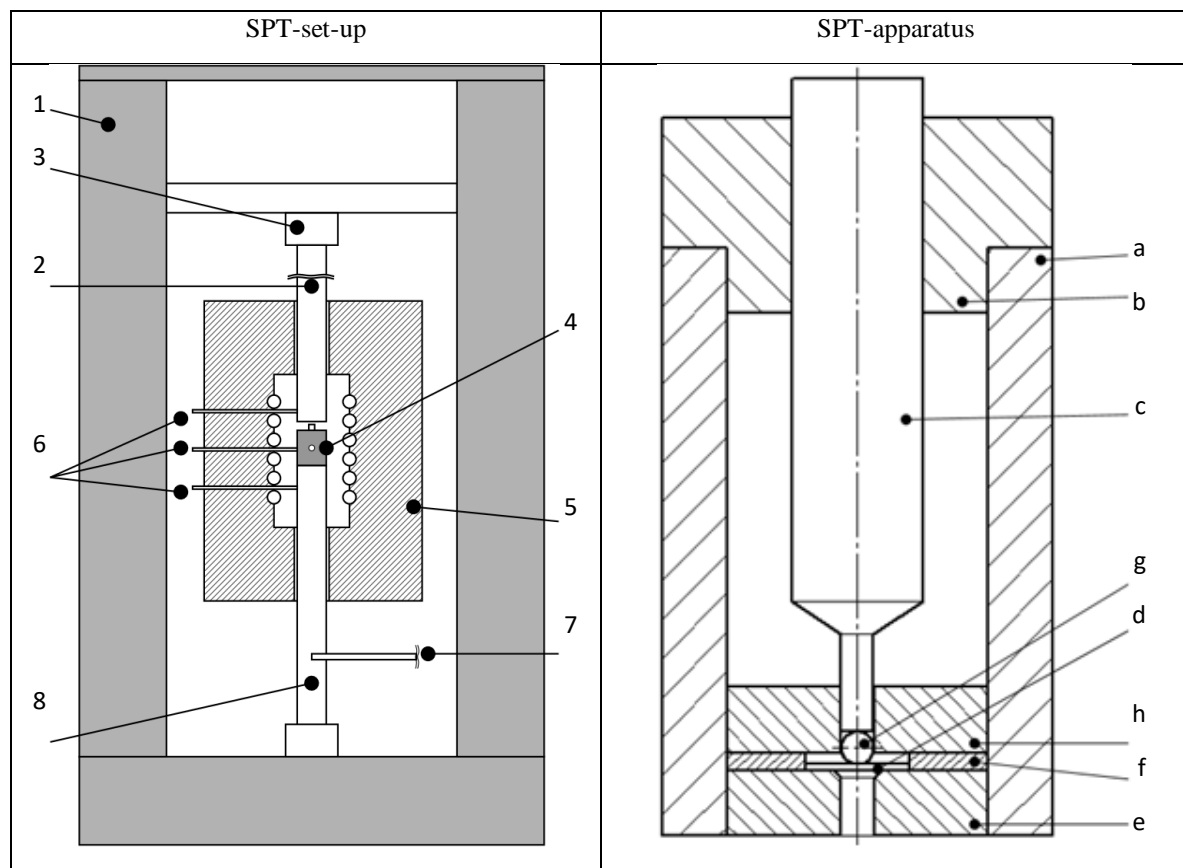

Figure 10. Scheme of SPT-set-up and SPT-apparatus.

The SPT experiments are performed under displacement control (0.05 mm/min) with the universal testing machine (1) *inspect table 10* from HEGEWALD & PESCHKE [5]. The upper push-rod (2) is attached to a 1 kN load cell (3). The SPT-apparatus (4) is enclosed by the electrical furnace (5). The electrical furnace has a maximal operating temperature of 1200 °C and is controlled by three thermocouples (6) in three different heating zones. With a fourth thermocouple, which is placed inside the SPT-apparatus at the height of the sample location, the specimen temperature is monitored. In order to avoid high temperature corrosion, argon is injected through the supply pin (7) into the lower push-rod (8) and arrives preheated in the SPT-apparatus.

The housing (a), the housing cover (b), and the punch (c) are manufactured of the heat-resistant, austenitic steel X15CrNiSi25-21. The purpose of the housing cover is to guide the punch and to seal the upper part of the housing, maintaining a protective argon atmosphere. The SPT-specimen (d) is supported by the die (e). A concentric alignment of the sample relative to the punch and the die is assured by the centring ring (f). The punch tip and the loading-ball (g) are directed by the guide-way (h). The die, the centring ring, the loading-ball, and the guide-way

are made of high-density Al_2O_3. In this case, the SPT-experiments are performed without down-holding force, meaning without axial clamping of the SPT-specimen.

4.2. Experimental result

The SPT was used to examine the inter-particle fracture behaviour of the thermally-sprayed corrosion-preventive coating. 45 SPT-samples (diameter $d = 8$ mm) with different thicknesses ($t = [200, 500, 1000]$ µm) were tested under quasistatic, isothermal, and displacement controlled conditions at three temperature levels ($\vartheta = [RT, 300, 500]$ °C). This corresponds to five specimens of each thickness per test temperature.

The brittle-ductile transition temperature of IN-625-modified had been identified to about 600 °C in [6]. Thus, the performed experiments characterise the fracture behaviour in the lower shelf. In this temperature range, the samples fail by pure brittle fracture. The fracture behaviour of IN-625-modified in the upper shelf had previously also been investigated, see [6].

In the case of pure brittle material failure, the concepts of the linear-elastic fracture mechanics can be applied. Consistent with GRIFFITH's theory of the global energy equilibrium at fracture [7], the specific surface energy results in:

$$\gamma = \frac{G_c}{2} = \frac{E^{SP}}{2at}, \tag{1}$$

and the SPT fracture toughness is given by:

$$K_c = \sqrt{G_c E} = \sqrt{\frac{E^{SP} E}{at}}, \tag{2}$$

both in the case of plane stress. Here, G_c is the critical energy release rate, E^{SP} is the small punch energy (area under the force-displacement curve), a is the crack length after fracture, t is the specimen thickness, and E is the modulus of elasticity.

Figure 11 comprises the maximum, minimum, and mean values of γ and K_c for the coating IN-625-modified as a function of layer thickness and test temperature. The scatter of γ and K_c increases with increasing sample thickness because of the higher imperfection occurrence probability with increasing stressed material volume. Note that there is no temperature dependence observable in the fracture-mechanical parameters, since the experiments have been performed in the lower shelf.
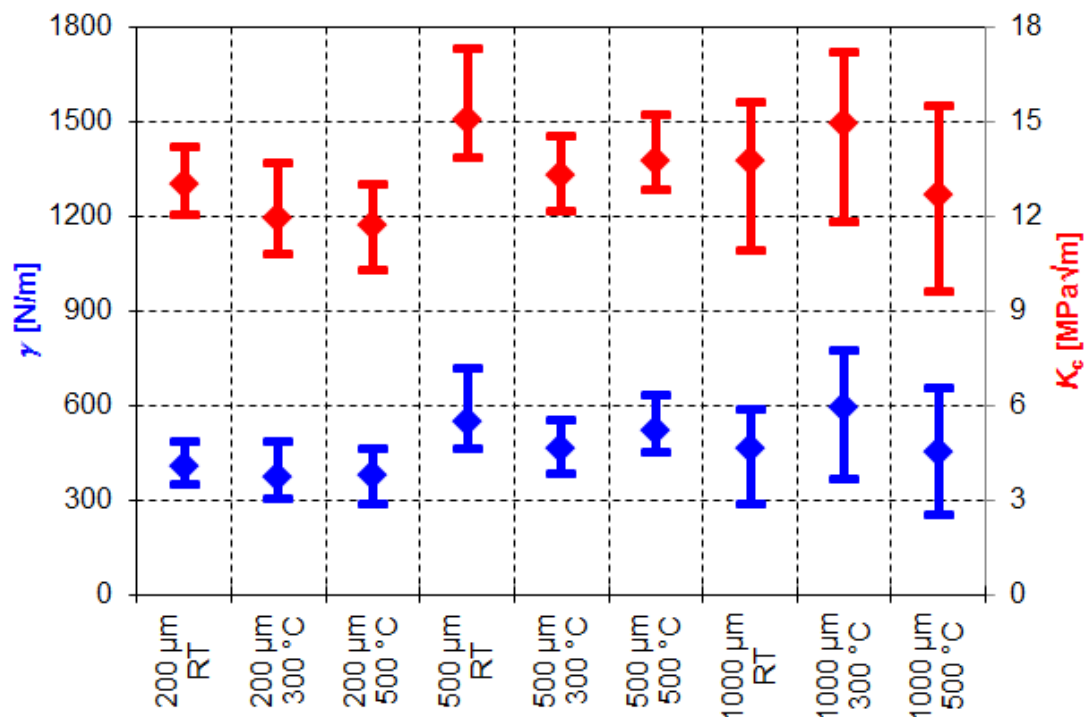

Figure 11. Specific surface energy γ and SPT fracture toughness K_c.

5. Conclusions and outlook

It was demonstrated that with the presented C-specimen concept, an investigation of the cyclic interface delamination between the thermally-sprayed corrosion-preventive coating (IN-625-modified) and the substrate (16Mo3) is possible. For the coated C-specimen, a delamination of the coating from the substrate can be observed in-situ with a pulsed reflection microscope. The initiation point of the delamination coincides with the main local damage zone at the C-specimen vertex ($\theta = 0°$). The aim of further experiments is to expand these qualitative results by quantitative statements regarding the delamination length development as a function of the cycle number under single-stage loading.

In the case of pure brittle material failure in the lower shelf, a fracture-mechanical characterisation of the coating material (IN-625-modified) has been realised via the small punch test. Considering the mean values of all temperature levels for each sample thickness, the SPT fracture toughness K_c falls in the range [12.23 … 14.03] MPa√m. Hence, it is larger than that of technical ceramics ([2 … 5] MPa√m), but significant smaller than that of classical steels (> 40 MPa√m). It was found that the characteristic damage mechanism of the coating material is inter-particle crack growth, independent of test temperature and layer thickness.

References

1. Standard DIN 50903:1967. Metallic coatings – pores, inclusions, blisters, and cracks – definitions. German Institute for Standardisation (registered association), Berlin
2. Biermann, H.; Kuna, M.; Brücker, C.: Thermomechanical fatigue and process analysis of HVOF-coated heat exchangers and TiAl-alloys. - 2014. - 56 pp. - Freiberg, Technische Universität Bergakademie Freiberg, final report of ADDE-sub-project 15 (SAB-project-number: 100111101), 2014
3. Standard ISO 12108:2012. Metallic materials – Fatigue testing – Fatigue crack growth method. International Organisation for Standardisation, Geneva
4. Zybell, L.; Chaves, H.; Kuna, M.; Mottitschka, T.; Pusch, G.; Biermann, H.: Optical in situ investigations of overload effects during fatigue crack growth in nodular cast iron. Eng Fract Mech 2012, 95, pp. 45-56, DOI: 10.1016/j.engfracmech.2012.01.006
5. Hegewald & Peschke Meß- und Prüftechnik GmbH: Downloads universal testing machines – Static testing machines. Available online: https://www.hegewald-peschke.com/fileadmin/_migrated/content_uploads/10-030-X0X_inspekt_ table_5_-_50kN__standard_eng.pdf (accessed on 14.05.2018)
6. Selent, M.; Soltysiak, S.; Roth, S.; Abendroth, M.; Hoffmann, M.; Kuna, M.: Mechanical Characterisation of a Thermally Sprayed Nickel-base Superalloy by Means of the High Temperature Small Punch Test. 3rd International Conference SSTT (Small Sample Test Techniques) 2014, 23.09.-25.09.2014, Austria. Conference Proceedings, pp. 98-111, ISBN 978-80-260-6722-1
7. Griffith, A.A.: The Phenomena of Rupture and Flow in Solids. Philosophical Transactions of the Royal Society of London, Series A, Containing Papers of a Mathematical or Physical Character 1921, 221, pp. 163-198, DOI: 10.1098/rsta.1921.0006

High temperature mechanical deformation of an additive manufactured nickel based superalloy using small scale test methods

H. Hilal [1], R.J. Lancaster [1], S.P. Jeffs [1], L. Ednie [1], J. Boswell [2], D. Stapleton [2], G. Baxter [2]

1 Institute of Structural Materials, Bay Campus, Swansea University, Swansea, UK, SA1 8EN
2 Rolls-Royce plc., P.O. Box 31, Derby, UK, DE24 8BJ

[1] 710170@Swansea.ac.uk, S.P.Jeffs@Swansea.ac.uk, R.J.Lancaster@Swansea.ac.uk, 826065@Swansea.ac.uk
[2] John.Boswell@Rolls-Royce.com, David.Stapleton2@Rolls-Royce.com,
[2] Grant.Gibson@Rolls-Royce.com, Gavin.Baxter@Rolls-Royce.com.

Abstract: Nickel based superalloys have been utilised within numerous industrial sectors from power generation to chemical processing plants for over four decades as a result of their ability to retain mechanical properties at arduous temperatures alongside excellent oxidation and corrosion resistance. Within the aerospace industry, they have been primarily used within regions of the gas turbine engine where metal temperatures can often exceed 1000ºC and high temperature deformation mechanics are prominent. Although typically manufactured using traditional wrought and casting methodologies, the aerospace industry has become increasingly interested in the use of Additive Layer Manufacturing (ALM) as a means of fabrication to take advantage of the numerous benefits that ALM has to offer. Detailed characterisation of the structural integrity of components processed via additive processes is a key requirement of the understanding. In this paper, the small punch creep (SPC) test has been applied to samples of a high gamma prime containing nickel-based superalloy manufactured using the laser powder bed fusion (LPBF) process. Several different builds are investigated and ranked, with ALM builds provided in different epitaxial orientations and with contrasting process parameters to help determine the optimal process parameters.

Keywords: nickel superalloy; additive layer manufacturing; small punch testing; creep; process parameters.

1. Introduction

Nickel based superalloys display an impressive range of mechanical properties from high temperature strength and toughness to excellent oxidation/corrosion resistance. It is these physical and mechanical properties that have led to its incorporation within numerous industrial sectors, in particular the aerospace industry where nickel is utilised in up to 40% of the gas turbine engine, primarily in the latter region [1].

Nickel based superalloys comprise of two major phases, namely gamma (γ) and gamma prime (γ') with additional secondary phases such as carbides and borides typically present. Although γ, a continuous matrix of face centered cubic (FCC) structured nickel, is the primary constituent in which additional phases reside, γ' typically acts as the key strengthening phase. This occurs as a result of several mechanisms, the main of which being its ordered $L1_2$ crystal structure of alternating Ni and Al. Given their similarity in terms of stoichiometry, there is a significant degree of directional covalent bonding, giving rise to a strong degree of 'chemical order' [2]. In addition to this strengthening mechanism, γ' precipitates can lead to a mechanism known as precipitation hardening, where hard intermetallic particles present within the disordered FCC matrix impede dislocation movement [3].

Despite the association of γ' with strengthening and therefore, increased high temperature capabilities, there is a trade off in regards to fabricability and weldability. This occurs due to a phenomenon known as ductility dip cracking (DCC), where a drop in ductility is observed at intermediate temperatures. Given this, the development of manufacturing methodologies both pre and post fabrication that can alleviate defect forming mechanisms has become precedent. Although nickel superalloys have been traditionally fabricated using wrought and casting methodologies [4], the aerospace industry has become increasingly interested in the use of alternative manufacturing routes such as powder processing, giving the potential scope for more complex alloy design of alloys containing >44% γ' content.

Additive layer manufacture (ALM) is a novel near-net shape manufacturing technique that utilises high energy heat sources in order to fabricate 2D slices of computer aided design (CAD) data, layer by layer until a full 3D component is produced. Although the innovation for this technology occurred in the late 1980s with stereolithography, it was the medical industry that drove its major development throughout the 1990s and 2000s

with the fabrication of numerous functional medical devices [5]. Despite the various forms of additive manufacturing (AM) utilised within the aerospace industry today for both component repair and manufacture, direct layer deposition (DLD) processes such as laser powder bed fusion (LPBF) have become prominent. LPBF is a multi-weld process that incorporates high-energy lasers in order to melt and fuse powders in a desired 3D geometry as illustrated in Figure 1. This leads to numerous advantageous characteristics and capabilities such as the formation of components with highly complex and intricate design geometries [6].
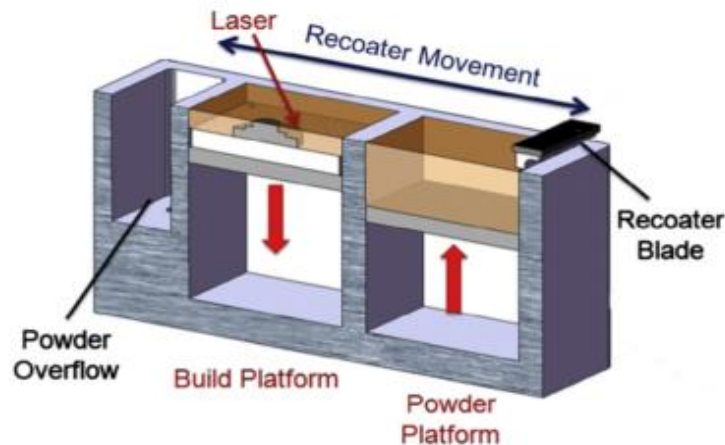

Figure 1. Schematic of LPBF and the Concept Laser M2 recoating system [6].

Regardless of the major advantages of AM in comparison to traditional cast and wrought processing, it has been observed that the frequent presence of material discontinuities needs to be considered, since questions arise regarding structural integrity. As a result of this, there has become an ever increasing importance in gauging a better understanding of how process parameters such as beam speed, power and hatch spacing influence the associated defect forming mechanisms. In addition to these parameters, alternative variables such as build orientation have also been shown to majorly influence mechanical properties as highlighted in numerous papers [7]. It has been hypothesised that a significant enhancement of mechanical properties can be seen when components have build orientations perpendicular to the loading axis. Previous work found that the individual influence of these parameters can be normalized and plotted onto a process map with diagonal isopleths indicating varying degrees of energy density [8]. It has been established that low energy densities are not substantial enough to melt the bulk of powder, leading to high frequencies of void formation. In contrast, higher energy densities are hypothesised to give rise to crack formation mechanisms such as ductility dip cracking (DDC), where a drop in ductility is noticed at intermediate temperatures [9].

In order to characterise builds which will exhibit evolving microstructures throughout, localised mechanical testing methodologies such as small punch testing (SPT) will prove useful. Originally developed within the nuclear industry in the early 1980s, SPT was utilised in order to obtain mechanical property data from small volumes of materials [10]. Given the cost saving implications associated with this alongside localised testing, numerous industrial sectors began to implement this methodology into their arsenal, leading to the resurgence of SPT during the late 1990s and early 2000s when it was successfully utilised to generate creep data [11]. Given the small volume of material required, the aerospace industry has begun to incorporate the use of SPT for the assessment and characterisation of advanced materials such as additively manufactured components, where traditional methodologies such as uniaxial testing may not be possible given design geometries [7].

In SPT, small cylindrical discs of 8-9.5mm diameter and 0.5mm +-0.005mm thickness are subjected to a load via a 2-2.5mm diameter hemi-spherical punch head or ball, either under constant displacement rate or constant load. The selection of which methodology is dependent on what mechanical data is desired. However, given the nature of nickel superalloy usage within the gas turbine engine, high temperature deformation mechanisms such as creep is prominent. As such, small punch creep (SPC) testing is conducted, where the indenter is imparted upon the specimen at a constant load. SPC testing is performed in a 'dead-weight' testing arrangement. The specimen is circumferentially clamped and restrained between the upper and lower die, otherwise referred to as 'bulge' testing. Within this setup, the upper die contains an aperture allowing the puncher to pass through and impose force upon the specimen. Upon plastic deformation which will be onset during primary creep, the specimen will pass and

emerge through the circular 4mm diameter aperture present within the lower die. Heating is then applied through the use of a standard three zone radiant furnace. However, given the high temperatures present, oxidation and corrosion can become prominent. Therefore, it is evident that these tests need to be performed in an inert environment such as argon.

Utilising SPC testing as a means for mechanical characterisation, this paper will explore the influence of process parameters on the microstructural integrity of γ' rich nickel superalloys. Furthermore, the adverse effect of various material discontinuities on mechanical properties will be compared and evaluated.

2. Materials and Methodology

2.1 High Gamma Prime Nickel Superalloys

The alloys of particular interest in this work are polycrystalline high gamma prime nickel superalloys. Although originally intended for utilisiation within directionally solidified blade and vane castings given its exceptional resistance to grand boundary cracking, properties attributed with their coarse grain size [12]. Given its desired application, these alloys coarse grain structure acts as a means of creep enhancement given that grain boundaries are typically susceptible to high temperature creep deformation. This can be achieved through its chemical composition, with the addition of high concentrations of γ' formers, specifically Al + Ti Given the high addition of Al and Ti, high gamma prime alloys contain 50-60% γ' and as a result are sensitive to defect forming mechanisms in AM processing. Figures 2a and 2b showcase both the frequency and distribution of this phase within high volume fractions of γ'. The variation in γ' sizing known as primary, secondary and tertiary γ' can be seen in Figure 2a whilst the distribution of γ', specifically along grain boundaries can be seen in Figure 2b. The presence of γ' along grain boundaries aids a mechanism known as grain boundary pinning, preventing dislocation movement and giving rise to a strengthening effect at a cost for ductility.
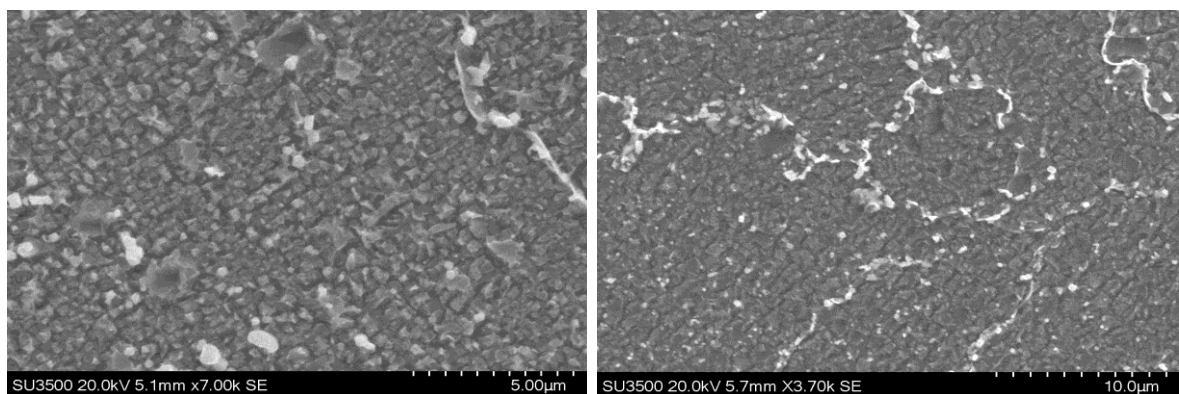

Figure 2. a) CM247LC's high volume fraction of gamma prime (primary, secondary and tertiary), **b)** gamma prime formation and distribution along grain boundaries.

Given the potential scope of high γ' nickel superalloys, there has been on-going work regarding the fabrication of high gamma prime nickel superalloys and as to whether the selection of manufacturing parameters can alleviate the presence of material discontinuities to what is considered a tolerable level. It has been showcased that low energy densities lead to the formation of voids as seen in Figure 3a. It is hypothesised that this occurs as a result of a lack of powder consolidation and therefore lack of complete melting. Conversely, it has been displayed that high energy densities leads to the formation of crack development as seen in Figure 3b. As previously mentioned, this has been attributed to DCC, a phenomenon that occurs as a combination of two mechanisms. These include micro stressing as a result of incoherent grain boundary carbides interrupting stoichiometry alongside macro residual stresses induced through welding.
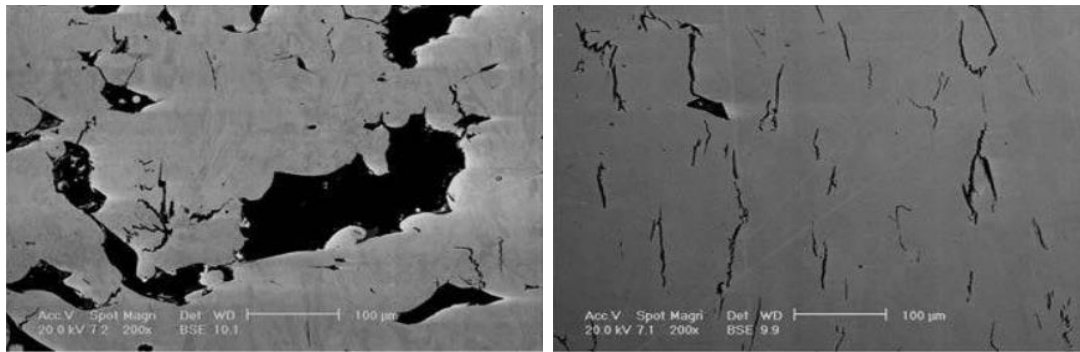
Figure 3. a) Large evidence of voids attributed to a lack of powder consolidation at low energy densities**, b)** high microcracking attributed to DCC witnessed at high energy densities [9].

As previously mentioned, the University of Sheffield developed the Normalised Process Parameters map over a range of alloying systems including nickel, titanium and steel alloys in order to illustrate the influence of combined parameters as depicted in Figure 4. It is worth noting that within this process map, high gamma prime nickel superalloys showxase an extremely limited process window, which is mainly accredited to its poor fabricability as discussed. Energy Density (*E**), as indicated by the diagonal isopleths, is quantified through the following equations:

$$E* = \frac{q*}{v*l*} = \left[\frac{Aq}{2vlrB}\right]\left[\frac{1}{\rho Cp(Tm-T0)}\right] \qquad\qquad \frac{1}{h*} = \frac{rB}{h}$$

Where *q** = normalized power, *v** = normalized beam velocity, *l** = layer height, *a* = surface absorptivity, *q* = power (W), *v* = beam velocity (ms^{-1}), *l* = layer height (m), *rB* = beam radius (m), *ρ* = density (kgm-3), C_p = specific heat capacity (J Kg K^{-1}), T_m = melting temperature (K), T_0 = initial powder bed temperature (K), *h** = normalised hatch spacing and *h* = hatch spacing (m).
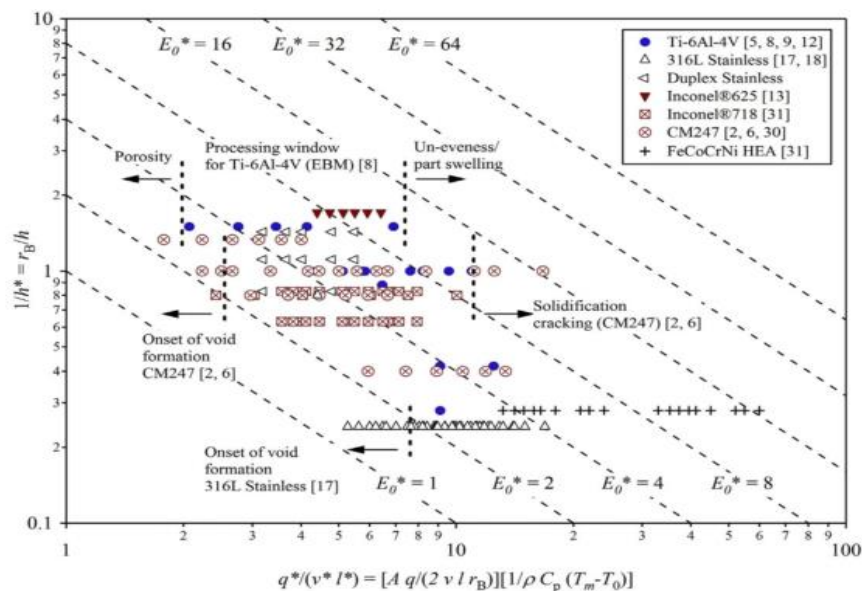

Figure 4. Normalised process parameters map with dimensionless beam power over beam velocity and layer height in comparison to normalized hatch spacing [13].

Given the limited window for processability, samples from the extremities of the window were additively manufactured and mechanically tested in order to gauge an understanding of energy density on mechanical properties. When considering the diagonal isopleths, as can be seen in Figure 4, the top right represents a high energy density with the bottom left being low. The labelling system for the specimens is explained below with the following example:

90-DOE-3-2 Position 1

Where 90 refers to the build orientation (90°), 3 refers to the parameter set (low energy density), 2 refers to the build number and position 1 refers to post processing conditions (1 HIPed, 2 as built). It is worth noting that for build orientation, samples were extracted from thin plates rather than rods as shown in Figure 5.
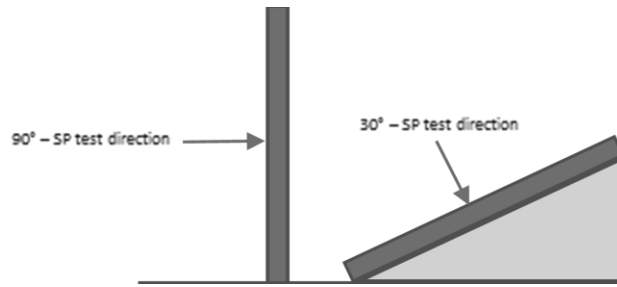

Figure 5. 30 and 90° orientation build schematics.

Post manufacturing processing such as heat treatments (HT) and hot isostatic pressing (HIPing) have been shown to have an adverse effect on both microstructure and discontinuities such as porosity and cracking [14]. Heat treatments, in particular can leave cracks and pores in the microstructure. However, when combined with HIPing the microstructure can internally heal cracking as shown below in Figures 6a and 6b. The extended heat treatment has also been shown to develop a coarser grain structure. This paper will compare several additively manufactured builds in as built and HIPed conditions in order to assess whether these processes aid mechanical performance.
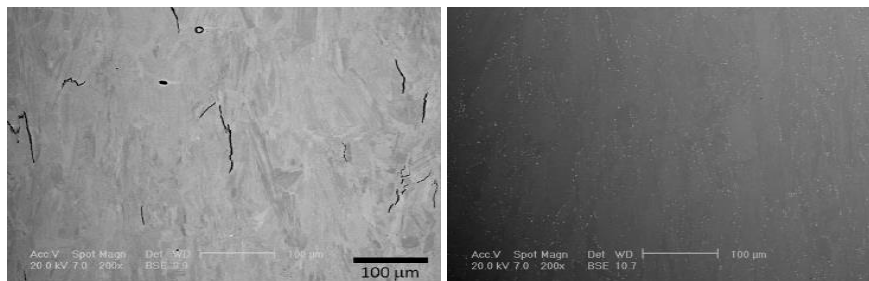

Figure 6. Additive Layer Manufactured nickel superalloys solidification cracks internally 'healed', **a)** before and **b)** after HIPing [14].

2.2 Small Punch Creep Testing

Using a series of grinding papers, samples of 9.5mm diameter, 2.2mm thickness were reduced to 1mm thickness using a 60# paper. From here, the sample was ground down to 0.6mm using a 500# paper, and finally reduced to 0.500mm with tolerances of +- 0.005mm using a 1200# paper. The edges of the sample were also rounded and both sides equally ground down in order to ensure uniformity and prevent beveling. Multiple SPC tests were performed on a modified high temperature SPC frame developed at Swansea University as illustrated in Figure 7a.
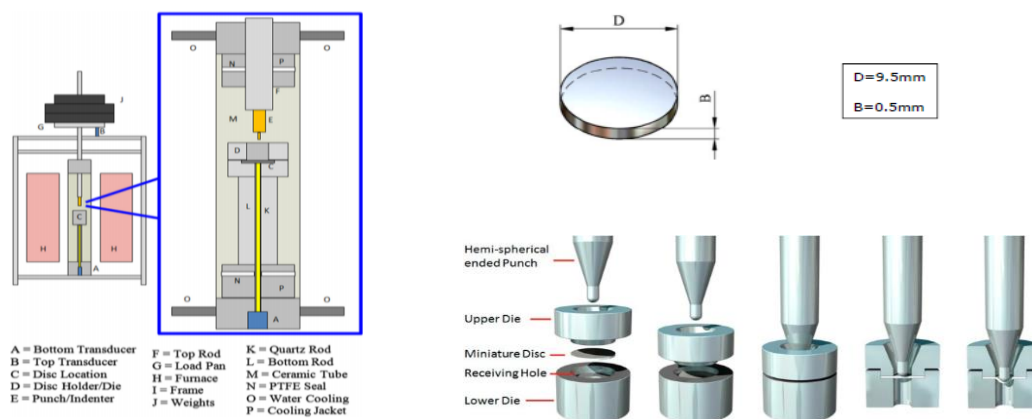

A = Bottom Transducer
B = Top Transducer
C = Disc Location
D = Disc Holder/Die
E = Punch/Indenter

F = Top Rod
G = Load Pan
H = Furnace
I = Frame
J = Weights

K = Quartz Rod
L = Bottom Rod
M = Ceramic Tube
N = PTFE Seal
O = Water Cooling
P = Cooling Jacket

Figure 7. a) SPCT frame developed at Swansea University [15], **b)** SP disc diameters matching the European CoP specifications, **c)** lower and upper die clamping system [16].

The small cylindrical specimens, as shown in Figure 7, match the specifications set forth by the European Code of Practice for Small Punch Testing [17] and were circumferentially clamped within the threaded upper and lower die, with the top rod being aligned centrally to the disc from the above loading pan. Below the top rod, a ceramic indenter with a cylindrical head of 2mm diameter is utilised in order to deform the material under a total constant load of 150N. LVDTs located both underneath the loading pan and the underside of the disc measures and records the displacement/deflection that occurs during the test with the 'dead-weight' testing frame. All tests were performed at 950°C.

Once ruptured, macroscopic images of the fractured specimens were taken. The discs were then mounted on a stub and stage using a carbon sticker and imaged using a scanning electron microscope (SEM), both from a macro and microstructural point of view. Fracture surfaces in particular were imaged at high magnifications in order to help gauge an understanding of the failure modes involved.

3. Results & Discussion

As previously mentioned, parameter selection is a vital staple within ALM which consequently influences microstructure and the presence, frequency and type of material discontinuities present. Mechanical property assessment utilising SPC testing was used in order to determine whether low, medium or high energy densities are optimal for creep performance. Figure 8 indicates that medium energy density (90-DOE, etc.) offers optimal performance with time to rupture being 21.5 hours as displayed in Table 2. In addition to this, 90-DOE-1-1 (low) exhibits the highest displacement before rupture. This, alongside the highest minimum displacement rate achieved of all tests (0.045mm.hr^{-1}) suggests that it behaves as the most ductile of the 3 samples. It is these mechanisms together with the minimal frequency of material abnormalities in 90-DOE-1-1 that has led to this variant's superior resistance to creep deformation.

The comparison of various types of abnormalities and their detriment to mechanical properties can also be observed in Figure 9. High energy samples containing various forms of microcracking such as solidification and ductility dip cracking (90-DOE-2-1) can be compared and contrasted with low energy samples containing frequent voidage and porosity (90-DOE-3-1). Such a comparison indicates the influence of energy density on mechanical performance. As can be seen in Table 1, low energy densities tend to have a far more detrimental effect on creep performance than high energy densities, 16.1 hours in comparison to 2.8 hours. The most plausible explanation for this would be the one previously alluded to in the Materials and Methodology section. 90-DOE-3-1, despite being located within the processing window, contains frequent porosity and voidage in comparison to its higher energy counterpart. This occurs as a result of the energy input per unit area not being sufficient enough to melt all the powder, leading to lack of powder consolidation. Subsequently, there is a deficit in performance as the presence of porosity and voidage act as both initiation sites and stress concentrations. On the other hand, 90-DOE-2-1 contains frequent microcracking which although do act as a detriment to mechanical properties as can be seen, is nowhere near as substantial. As previously mentioned, macro images were taken using an optical microscope, where Figures 10a, b and c showcase the increasing severity of cracking and rupture.

Table 1. Mechanical property data gathered from SPC testing for low, medium and high energy densities.

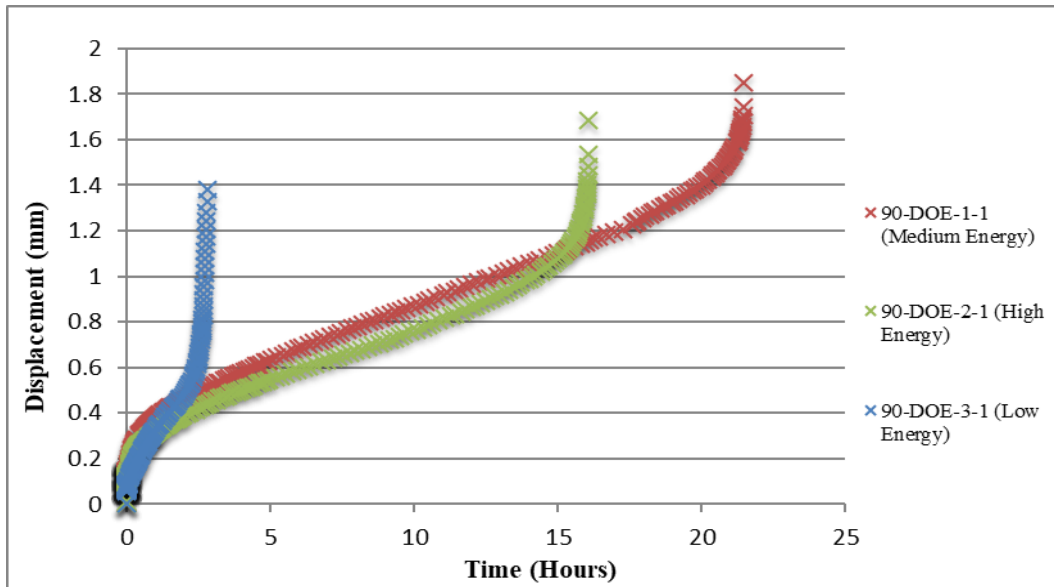| Sample ID	Load [N]	Temperature [°C]	Time to Rupture [hours]	Minimum displacement rate [mm.hr^{-1}]
90-DOE-1-1	150	950	21.5	0.045
90-DOE-2-1	150	950	16.1	0.041
90-DOE-3-1	150	950	2.8	0.147

Figure 8. A direct contrast of parameter sets (low, medium and high energy densities) influence on creep performance.
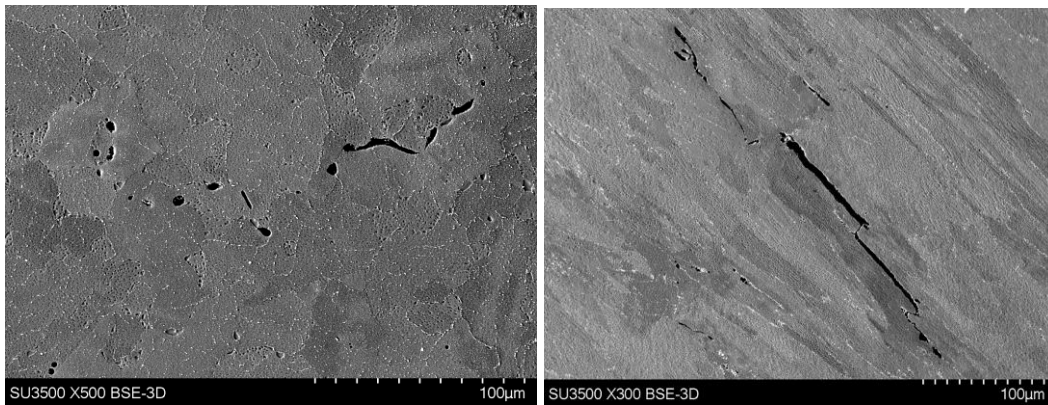

Figure 9. Back-scattered electron imaging of 90-DOE-3-1 (left) and 90-DOE-2-1 (right).
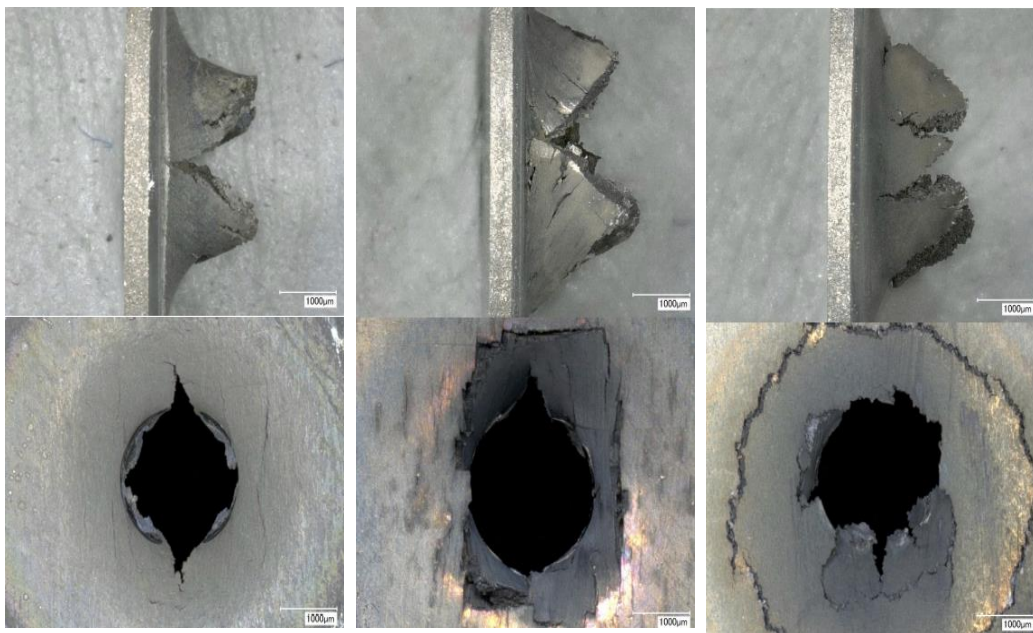

Figure 10. Optimal microscopy of samples **a)** 90-DOE-1-1, **b)** 90-DOE-2-1, **c)** 90-DOE-3-1.

In addition to parameter selection, Figure 11 emphasises and highlights the range of scatter that can be seen in separate builds, despite the same parameter set being used. Table 2 indicates that this scatter is as much as 3-fold, with the minimum time to rupture being 21.5 hours seen in 90-DOE-1-1 and the maximum being 59.2 hours for 90-DOE-1-3. Regardless of the same parameters and post manufacture processing utilised, the most plausible explanation for this would be down to the elastic heterogeneity of the microstructure. SPC testing utilises a small volume of material for its specimens, specifically 9.5mm diameter and 0.5mm thickness. As a result of this, the methodology is specifically sensitive in picking up these variations within localised regions of microstructure. Despite the similarity in columnar grain structures, Table 3 showcases the 90-DOE-1-1 sample picking up a higher volume of clustered fine columnar grains, giving rise to creep detrimental qualities giving the increased volume of grain boundaries. Conversely, 90-DOE-1-3s grains are indicated as being generally coarser. In addition to this, Figure 12 indicates that the 90-DOE-1-1's specimen has picked up a higher occurrence of porosity, in larger sizes, which in some cases are located at grain boundaries. This is in direct contrast to 90-DOE-1-3, where the lower volumes of smaller porosity are located within the grains. Given the small volume of material and heterogeneity of the sample, specimens may pick up differing volumes of extremely detrimental material defects that could act as stress raisers, inhibiting creep resistance and as a result leading to high scatter in data. Table 2 supports this proposed mechanism as being a major influencer in the particularly high minimum displacement rate seen in 90-DOE-1-1 suggesting that the porosity found has accelerated plastic deformation.

Table 2. Mechanical property data gathered from SPCT for varying build numbers at 90°, parameter set 1.

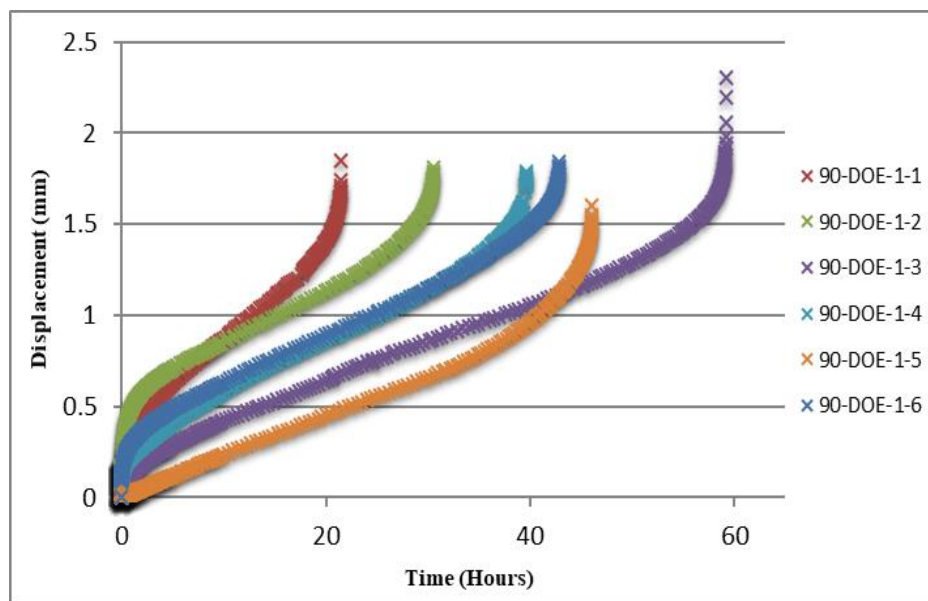| Sample ID	Load [N]	Temperature [°C]	Time to Rupture [hours]	Minimum Displacement Rate [mm.hr-1]
90-DOE-1-1	150	950	21.5	0.045
90-DOE-1-2	150	950	30.5	0.027
90-DOE-1-3	150	950	59.2	0.019
90-DOE-1-4	150	950	39.7	0.026
90-DOE-1-5	150	950	46.0	0.020
90-DOE-1-6	150	950	42.8	0.024

Figure 11. A comparison of the effect of build number on creep life for a 90º build parameter set 1.

Table 3: Grain size measurements of 90-DOE-1-1 in comparison to 90-DOE-1-3.

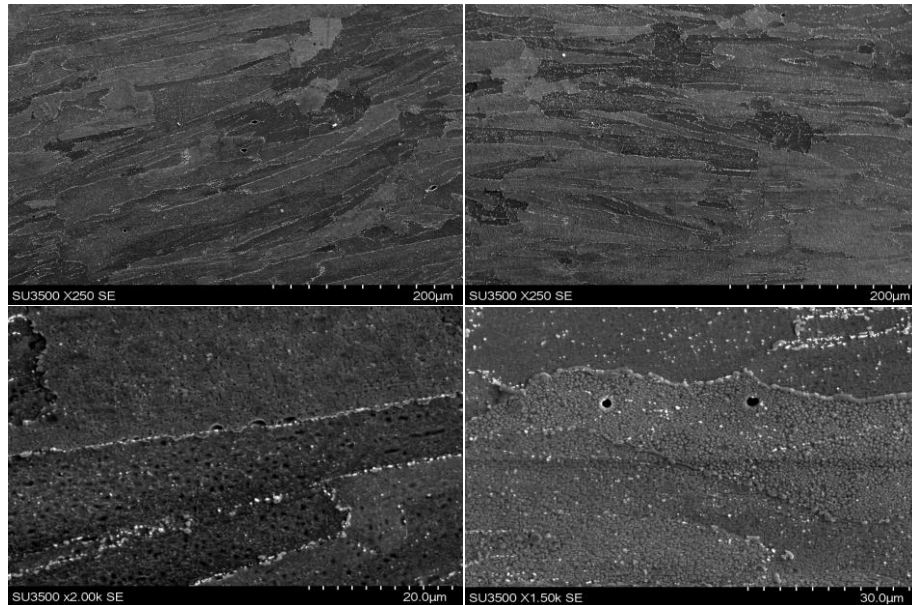| Sample	Average Grain Length (µm)	Average Grain Width (µm)
90-DOE-1-1	208.81	24.90
90-DOE-1-3	294.47	30.19

Figure 12. 90-DOE-1-1at low and high magnification (left), 90-DOE-1-3 at low and high magnification (right).

Moreover, post rupture fractography as shown in Figure 13 highlights the distinctly different fracture surfaces and as a result, the contrasting failure mechanisms. 90-DOE-1-1's fracture surface displays faceted features, suggesting that a brittle transgranular failure has taken place. This further supports its relatively high minimum displacement rate as brittle failures are known to be more instantaneous and as a result catastrophic.

90-DOE-1-3s failure could not be distinguished as to whether it was intergranular or transgranular as a result of oxycarbide formation along the fracture surface. Given the improved lifetime of 90-DOE-1-3, it is hypothesised that these oxycarbides can further aid grain boundary pinning, further aiding an enhancement in creep life and as a result explaining both the slow onset of minimum displacement rate and high final displacement value before rupture.
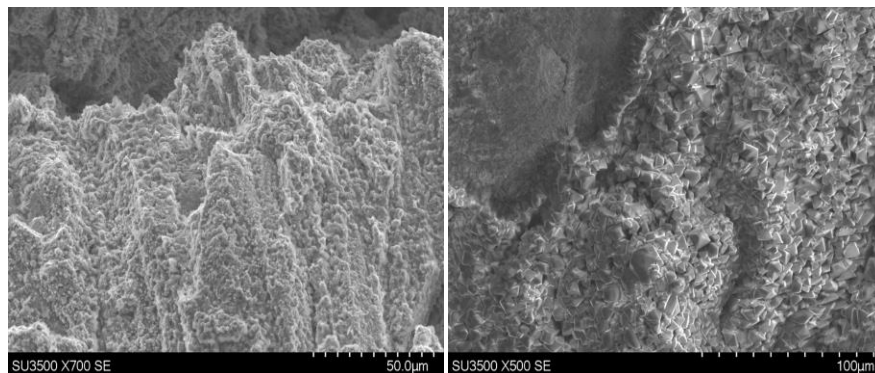

Figure 13. 90-DOE-1-1s brittle faceted fracture surface (left), 90-DOE-1-3s ductile dimpled fracture surface (right).

In addition to parameter sets and build variations, build orientation is shown to have a major influence in the mechanical performance of these samples, where Figure 14 highlights a major drop in time to rupture between 30° and 90° builds, irrespective to build number variation. Table 4 highlights this remarkable drop of 18.2 hours in lifetime between 90-DOE-1-1 & 30-DOE-1-1, alongside a staggering 56.2 hour drop between 90-DOE-1-3 and 30-DOE-1-3. This can be explained from a microstructural perspective, where under stress and specifically creep

deformation, cavities form at boundaries. Within the 30° builds, the microstructure is equiaxed in relation to the transverse direction as seen in Figure 15 and subsequently grain boundaries are typically located parallel to the stress orientation induced during SPC testing. As a result of this, these boundaries are subject to more load given both the higher volume of grain boundaries and the fact that grain boundary sliding is encouraged. Therefore, cavitations are set to coalesce quicker, resulting in lower rupture times and higher minimum displacement rates as shown. Given the higher minimum displacement rate, it would be expected that the 30° build displays a severely faceted fracture surface which can be validated in Figure 16.
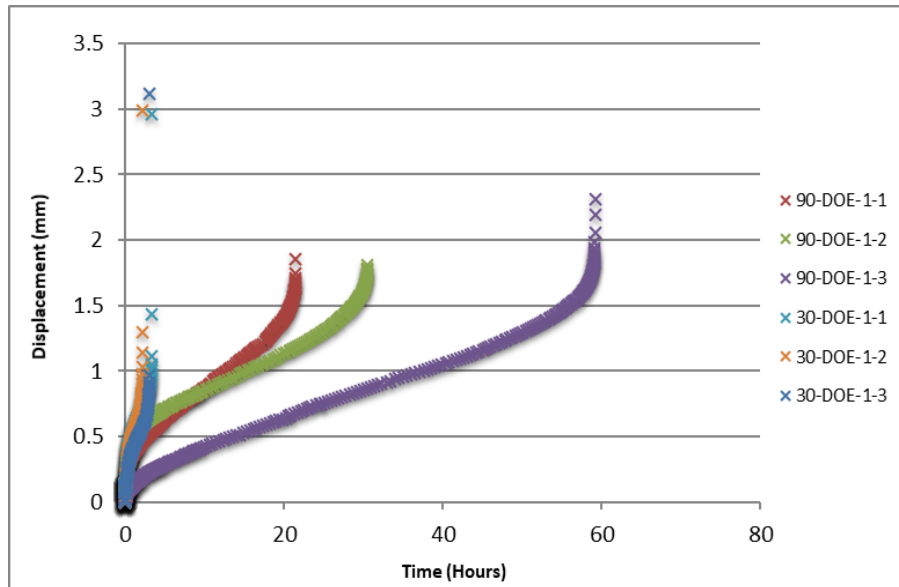

Figure 14. Effect of build orientation on creep properties for parameter set 1, build numbers 1-3.

Table 4. Mechanical property data gathered from SPCT for 30 and 90° builds orientations.

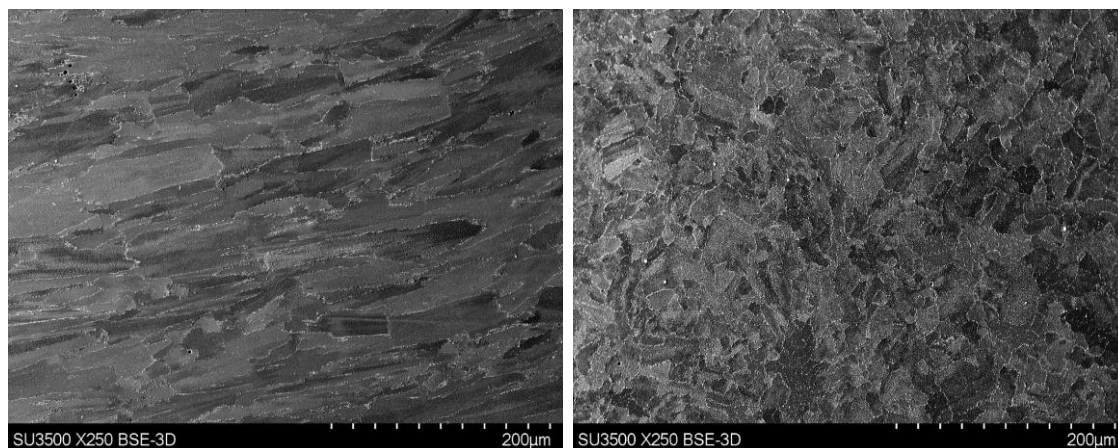| Sample ID	Load [N]	Temperature [°C]	Time to Rupture [Hours]	Minimum displacement rate [mm.hr⁻¹]
90-DOE-1-1	150	950	21.5	0.045
90-DOE-1-2	150	950	30.5	0.027
90-DOE-1-3	150	950	59.2	0.019
30-DOE-1-1	150	950	3.3	0.135
30-DOE-1-2	150	950	2.2	0.169
30-DOE-1-3	150	950	3.0	0.128

Figure 15. 90-DOE-1-1s columnar grain structure (left) and 30-DOE-1-1s equiaxed grain structure. (right).
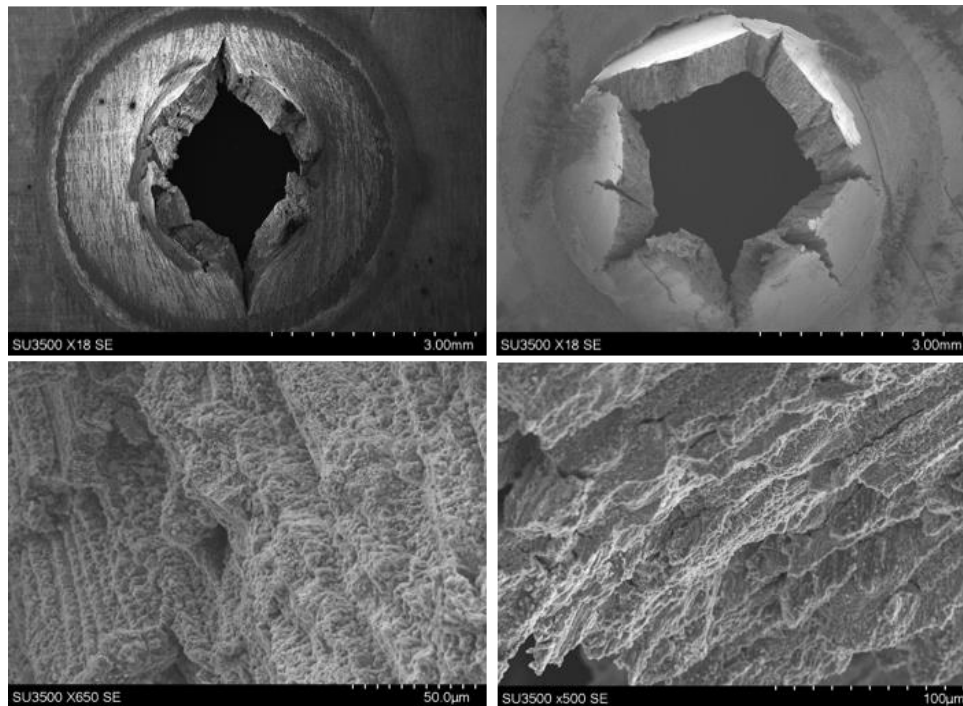
Figure 16. Fracture surface images of 90-DOE-1-1 at low and high magnifications (left side). Fracture surface images of 30-DOE-1-1 at low and high magnifications (right side).

4. Conclusions

The investigation of additively manufactured high gamma prime nickel superalloys with various process parameters and variables were investigated both microstructurally and mechanically utilising the small punch creep test. It has been shown that energy density has a considerable impact on both the type and size of microstructural discontinuities present through differing mechanisms. Porosity and voids attributed to low energy densities in particular have been shown to be severely more detrimental to mechanical properties than microcracking mechanisms accredited to high energy densities.

In addition to the differing parameter sets, the inconsistency of mechanical properties and microstructures between builds fabricated using the same processing variables has also been picked up utilising small punch creep testing. It is believed that this occurs due to the elastic heterogeneity of the samples microsctructure, where localised regions of differing microstructure have been picked up. In addition to this, given the small volume of material used in this methodology, results are subject to the sensitivity of material abnormalities such as porosity picked up within the specimens, giving rise to scatter. Fractography displayed contrasting failure modes between the best and worst performing build numbers, with 90-DOE-1-1 showcasing a brittle transgranular fracture and 90-DOE-1-3s failure displaying oxycarbides which indicated a grain boundary pinning/strengthening mechanism.

Finally, a comparison of samples fabricated at $30°$ and $90°$ build orientation was conducted. The creep resistance of $30°$ builds were significantly degraded as a result of their grain boundaries being oriented parallel to the loading axis induced during SPC testing. This gives rise to accelerated coalescence of cavitations and consequently faster creep deformation at an accelerated minimum displacement rate of $0.135 mm.hr^{-1}$ in comparison to $0.045 mm.hr^{-1}$. Fractography of these samples indicated that the $30°$ builds displayed more severe brittle transgranular fracture.

References

1. Pollock, T.R.; Tin, S. "Nickel based superalloys for advanced turbine engines: chemistry, microstructure and properties," J. Propuls. power, vol. 22, no. 2, pp. 361–374, 2006.
2. Reed, R.C. The Superalloys, Fundamentals and Applications, vol. 53, no. 9. 2006.
3. Kozar, R.W.; Suzuki, A.; Milligan, W.W.; Schirra, J.J.; Savage, M.F. "Strengthening Mechanisms in Polycrystalline Multimodal Nickel-Base Superalloys," 2009.
4. Donachie, M.; Donachie, S. Superalloys: A Technical Guide, 2nd Edition. ASM International, 2002.
5. Gokhare, V.G. "A review paper on 3D-Printing aspects and various processes used in the 3D-Printing," vol. 6, no. 6, pp. 953–959, 2017.
6. Carter, L.N.; Martin, C.; Withers, P.J.; Attallah, M.M. "The influence of the laser scan strategy on grain structure and cracking behaviour in SLM powder-bed fabricated nickel superalloy," J. Alloys Compd., vol. 615, pp. 338–347, 2014.
7. Jeffs, S.; Lancaster, R.; Davies, S. "Effect of Build Orientation and Post Processing of a Direct Laser Deposited Nickel Superalloy as Determined by the Small Punch Creep Test," Key Eng. Mater., vol. 734, no. April, pp. 128–136, 2017.
8. Thomas, M.; Baxter, G.J.; Todd, I. "Normalised model-based processing diagrams for additive layer manufacture of engineering alloys," Acta Mater., vol. 108, pp. 26–35, 2016.
9. Carter, L.N.; Essa, K.; Attallah, M.M. "Optimisation of Selective Laser Melting for a High Temperature Ni-Superalloy" Rapid Prototyping Journal 21, 1-8, 2015.
10. Manahan, M.P.; Argon, A.S.; Harling, O.K. "The development of a miniaturizsed disk bend test for determination of post irradiation mechanical properties," J. Nucl. Mater., vol. 104, pp. 1545–1550, 1981.
11. Parker, J.D.; James, J.D. "Disc-bend creep deformation behaviour of 1/2Cr1/2Mo1/4V low alloy steel," in creep and fracture of engineering materials and structures, 1993, pp. 651–660.
12. Harris, K.; Erickson, G.L.; Schwer, R.E. "MAR M 247 Derivations - CM247LC Directionally Solidified Alloy - Properties and Performance," pp. 221–230.
13. Thomas, M.; Baxter, G.J.; Todd, I. "Normalised model-based processing diagrams for additive layer manufacture of engineering alloys," Acta Mater., vol. 108, pp. 26–35, 2016.
14. Carter, L.N.; Attallah, M.M., Reed, R. C. "Laser Powder Bed Fabrication of Nickel-Base Superalloys: Influence of Parameters; Characterisation, Quantification and Mitigation of Cracking," in 12th International Symposium on Superalloys, 2012, pp. 577–586.
15. Hurst, R.C.; Lancaster; R.J.; Jeffs, S.; Bache, M.R. "The contribution of small punch testing towards the development of materials for aero-engine applications," Theor. Appl. Fract. Mech., vol. 86, pp. 69–77, 2016.
16. Lancaster, R.J.; Davies, G.; Illsley, H.; Jeffs, S.; Baxter, G. Structural Integrity of an Electron Beam Melted Titanium Alloy, Article Materials 2016, 9(6), 470.
17. CEN Workshop Agreement CWA 15267, "European Code of Practise: Small Punch Test Method for Metallic Materials." 2007.

Investigations into Taylor-Quinney coefficient determination for a 7000 series aluminium alloy using a novel small specimen test technique

J. P. Rouse [1]*, C. J. Hyde [1] and J. Kazakeviciute [1]

[1]Gas Turbine and Transmission Research Centre (G2TRC), University of Nottingham, UK, NG7 2RD
***Correspondence: james.rouse@nottingham.ac.uk; Tel.: +44-115-8467-683

Abstract: Thermo-mechanical coupling is a critical component in the thermodynamics of irreversible processes and is related to the dissipation of thermal energy during plastic straining. The Taylor-Quinney coefficient may be thought of as a ratio between thermally dissipated energy and plastic work, thereby giving insight into the thermo-mechanical coupling term. The inclusion of this parameter in a meaningful way is complicated by the various dependencies that the Taylor-Quinney coefficient may be subject to (e.g. loading rate and temperature). Determination of these dependencies is usually achieved through extensive experimentation, wherein temperature variations are monitored (with reference to an unloaded control sample) in a test piece during mechanical loading. There are practical limitations in full size testing methods however, not least relating to the location of full sized control and loaded samples in an environment chamber/furnace while simultaneously maintaining (control sample) temperature uniformity and high resolution temperature measurement (in the loaded sample). The present work details a method based on a novel small specimen testing technique that is currently under development at the University of Nottingham. A small ring of 7175-T7351 aluminum alloy (approximately 10mm in diameter and 2mm in thickness) is loaded between two pins at room temperature, with the local specimen temperature field monitored during monotonic deformation using an infra-red thermal camera. Experimental results are compared for different pin loading rates (namely 0.1mm/s, 1mm/s, and 10mm/s), with particular emphasis placed on localised temperature variations in areas of expected high plasticity. Differences of approximately 0.6°C were observed between 0.1mm/s and 1mm/s tests, with higher temperatures recorded in the latter. Higher temperatures were also noted at small specimen locations associated with localised plasticity. Fundamental thermal material properties are reported for the 7175 alloy in order to facilitate future analysis and heat equation solution efforts (working towards Taylor-Quinney coefficient determination).

Keywords: Small Ring, Taylor-Quinney, Aluminium 7175, Thermoplasticity

1. Introduction

In order to provide a thermodynamic justification for material deformation and damage accumulation models rigorous experimental methods are required which can inform fundamental energy balances. It is well known that, after yield, a potentially large fraction of energy is dissipated as heat. In sufficient circumstances (highly localised high strain rate loadings, for example) this dissipated energy can be observed as a significant change in temperature. The Taylor-Quinney coefficient may be defined as the ratio of energy dissipated as heat during plastic straining to the total plastic work done on the material element. It is the most fundamental material parameter associated with thermoplastic effects, however values are often assumed in the literature without proper experimental justification [1]. In addition to allowing for the more robust thermodynamic formulations of material constitutive equations, representative Taylor-Quinney values (or more aptly, Taylor-Quinney relationships, as multiple dependencies have been experimentally demonstrated in the literature, see section 2) may be used to evaluate plastic dissipation fractions in sophisticated energetic failure criterion (for example, see the work of Daily and Klingbeil in relation to low cycle fatigue crack growth [2] or see Einav et al. [3]). The present work details the use of a small specimen testing technique for the study of the Taylor-Quinney coefficient. An aluminium alloy is used in the present work, however it is expected by the authors that similar techniques could be applied to any material for which the representative volume element is smaller than the small ring geometry. For reference, small rings used in the present work have internal and external radii of 10mm and 11mm, respectively, with a ring thickness of 2mm.

Due to attractive combinations of (relatively) high strength and low density, 7000 series aluminium alloys (such as the 7175-T7351 alloy considered in the present work) have numerous naval, aerospace, and military applications [4–6] and have consequently received a great deal of attention in the literature. In the work of Benoit et al., for example, the microstructure of two 7000 series alloys was analysed, in addition to fundamental mechanical

response parameters such as yield stress, ultimate tensile strength, elongation at fracture, and fracture initiation energy [4]. The orientation of sample forgings and grain size demonstrated no significant influence on yield stress. For 7175 alloys yield strength values of approximately 338+/-8.5MPa were determined. Of particular note was the identification of Zn, Mg, and Cu precipitates, which may act as a hindrances to dislocation motion (thereby providing an important strengthening mechanism). Zn and Mg precipitates were particularly noted for promoting solution strengthening, precipitate strengthening, and stacking fault strengthening mechanisms. 7175-T735 alloys were also studied in the work of Jaya Rao et al. using nonlinear ultrasonic non-destructive methods [7]. Samples with prior plastic straining were analysed, with resulting NLU parameter variations suggesting two stage dislocation process in the material's deformation behaviour. Wen et al.'s work focused on the effects of various ageing treatments on the texture/microstructure of high Zn content aluminium alloys, particularly through the determination of hardness, electrical conductivity, and basic mechanical material properties [5]. Transmission electron microscopy (TEM) was also used to investigate precipitates geometric characteristics and mismatches with the matrix material. Rapid reductions in yield stress, ultimate tensile strength, and hardness were observed with exposure time for ageing processes at 160°C, with approximate values for high Zn content precipitate size and spacings in the range of 2-7nm and 7-13nm, respectively. Similar results, along with phenomenological model developments, are reported in the work of Lam Wing Cheong et al. for 7175-T7351 alloys [8].

The influence of Cu rich precipitates on extrusion characteristics of aluminium alloys was investigated by Paulisch and co-workers through examination of 7108 (which is Cu free) and 7175 [9]. Extrusions performed with 7108 could be made with a wide range of parameters and resulting strands were crack free (the ultimate tensile strength after ageing was estimated as 426MPa). Conversely, 7175 extrusions speeds were limited as frictional heating (potentially generating temperatures of 525°C) led to the formation of eutectic AlMgZnCu phase. 7175 extrusion strands displayed hot cracks, however great improvements in ductility were noted through reductions in dislocation density and enhanced dynamic recovery. Ultimate tensile strength values of 636MPa were determined. Paulisch and co-workers also investigated natural ageing in 7020 and 7175 alloys by monitoring samples at room temperature over an 18 month period. Two phases, namely Al2CuMg and Al12Mg2Cr2, were identified in 7175 as being potentially hazardous due to the capacity for remelting. Fe rich particles in 7020 were not influenced by repeat annealing. Langille et al. noted a break down in the commonly assumed linear relationship between fracture strain and yield stress in AA6063 for samples which were plastically pre-strained prior to ageing [10]. Linear relationships could however be recovered when dislocation spacing is considered in formulations. Goueffon and co-workers examined coefficients of thermal expansion in anodised 7175 films for space applications using 10mm thick beam bending experiments (values of $13.0+/-1.0 \times 10^{-6}K^{-1}$ were suggested [6]), with values being relatively independent of the porosity of the film [11].

The present work describes a small specimen method which is suitable for the investigation of the Taylor-Quinney coefficient. The small ring test was originally proposed by Hyde and Sun as a high sensitivity method for the study of primary and steady state creep [12]. Large (by small specimen standards) gauge lengths of approximately 50mm were noted for modest levels of total deformation, however it must be noted that gauge length is a function of total ring deflection. For nominally constant load creep tests (equivalent to traditional full sized uniaxial tests) adaptive loading must be implemented to account for this [13]. The small ring test set-up is summarised in figure 1 (showing both undeformed and deformed specimen states). A ring is loaded by two pins (allowing for self-alignment and a minimal influence of friction on the specimen response) such that it may elongate. In creep tests, a constant load P is applied and deflection of the pins is monitored. Tensile (imposed constant deflection rate) small ring tests are performed in the present work at room temperature, with specimen surface temperatures monitored in order to observe thermoplastic effects. P is recorded for changes in pin displacement (Δ-Δ_0). To the authors' knowledge, this is the first instance of a small specimen being used for this type of study.
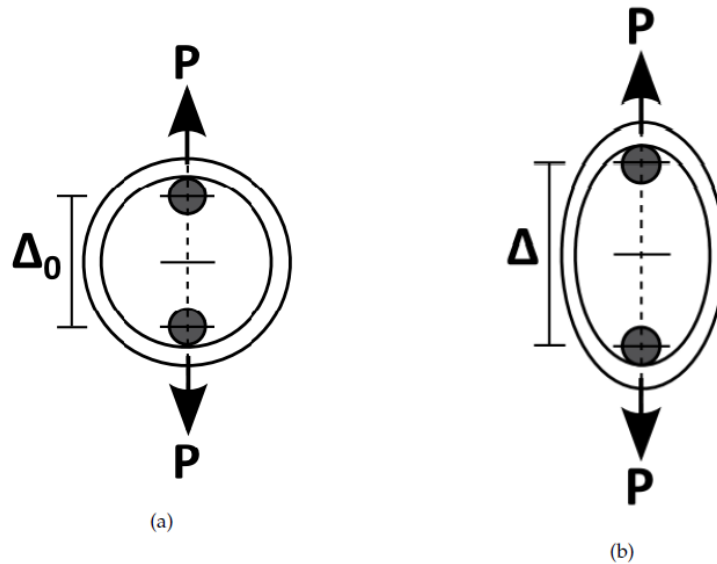
Figure 1. A schematic of the small ring testing method, showing (a) undeformed and (b) deformed specimens.

2. An Overview of Thermoelastic and Thermoplastic Phenomenon

Heat transfer associated with material straining has received a good deal of attention in the literature, however Rittel has noted that the Taylor-Quinney coefficient (the most fundamental parameter associated with thermoplastic effect, which is particularly important in impact analyses [14]) values are often assumed to be 0.9 [1]. Dependencies on factors such as loading rate have been experimentally demonstrated, yet resulting relationships are often neglected in otherwise detailed simulations. The Taylor-Quinney coefficient (β) may be expressed by equation (1), where $\dot{q}_P$ is the (specific) power dissipated as heat (due to irreversibilities associated with plasticity or damage, for example) and $\dot{w}_P$ is the (specific) plastic power [15]. Note lower case terms used in this section relate to specific quantities. It is of course easy to show that the fraction of stored energy, η, is related to β by $\eta=1-\beta$ [16]. Care must however be taken when defining β. As pointed out by Rittel [17], power quantities are considered in equation (1) (rate terms, such as those related to the heat and work quantities q_P and w_P, are here denoted by a dot). The "integral" form of β (here defined at β_{int} and related to a time period t) can be expressed as equation (2), allowing for the relationship between β and β_{int} given in equation (3) to be developed [18].

$$\beta = \frac{\dot{q}_P}{\dot{w}_P} \tag{1}$$

$$\beta_{int} = \frac{q_P}{w_P} = \frac{1}{w_P}\int_0^t \beta \dot{w}_P d\tau \tag{2}$$

$$\beta = \beta_{int} + \frac{w_P}{\dot{w}_P}\dot{\beta}_{int} \tag{3}$$

The determination of β for polymer materials has received particular attention in the literature. Shao et al. considered the glassy polymers polycarbonate (PC) and polymethyl methacrylate (PMMA) and showed, using material models which accounted for strain hardening and softening, that β can vary between approximately 0.5 and 0.8 (based on plastic strain magnitude and loading rate) [14]. Maurel-Pantel and co-workers investigated semi-crystalline polyamide 66 (PA66) using digital image correlation (DIC) and infra-red imaging techniques (to evaluate total strain and thermal field parameters, respectively) at multiple tensile strain rates, namely 0.1/s, 0.01/s, and 0.001/s [19]. A difference in peak temperature of 15°C was noted between different loading rate results, with similar observations for shear tests. Constitutive relations used in this work were based on Billon [20]. PA66 was also studied by Benaarbia et al. for low cycle fatigue conditions [21]. Cycle by cycle evaluations of β highlighted hot spots in dissipation fields and a range of values (from 0.4 to 0.8) were noted (over approximately 7000 loading cycles). Due to the importance of β in high strain rate problems (such as impact), split-Hopkinson (or Kolsky) bars have been used in several experimental studies. The dependence of dynamic loading mode on β was studied by Rittel, for example, and potentially large fluctuations correlated with loading mode for certain materials (e.g.

annealed commercially pure Titanium, grade 2) [1]. Similar work was conducted by Galán et al. for Ti6Al4V [22] and Jovic et al. for 304L stainless steel and 5754 aluminium alloy [23]. A strong dependence on strain rate was noted in the work of Fekete for 15Ch2MFA (bainitic structure with fine grains) reactor steel, although 08Ch18N10T (austenitic structure with coarse grains) showed negligible levels of loading rate dependency [16]. Multi-phase (Martensite and Austenite) 304 stainless steel materials were analysed by Zaera [24]. This work highlighted that phase transformation mechanisms can release latent heat, leading to experimental observations where β takes a value greater than unity. Polycrystalline aluminium was investigated by Badulescu, with a relationship between β and grain orientation suggested [25].

It is worth noting here (in order to assist discussion later in the present work) that the measurement small temperature changes on the surface of components/specimens has been used for many years to evaluate stress fields. Such techniques are generally known as thermoelastic stress analysis methods and commonly require that material samples are cycled at such a rate that conduction can be neglected [26]. A general expression for the temperature change associated with thermoelastic mechanisms is given in equation (4), where T is the observed temperature, ρ is the material density, C_ϵ is the specific heat capacity at constant strain, σ_{ij} is a component of the symmetric stress tensor, ϵ_{ij} is a component of the symmetric total strain tensor, and Q is an input heat. If conduction is neglected, plane stress conditions assumed, and it is reasonable to consider parameters such as Young's modulus and Poisson's ratio (E and υ, respectively) independent of temperature, equation (4) may be simplified and rearranged to give equation (5), which can relate measured temperature fluctuations to stress state. Note that C_ϵ may be related to the specific heat capacity at constant pressure (C_P) by equation (6) (where α is the coefficient of thermal expansion) and that $\alpha/\rho C_P$ is often referred to as the thermoelastic constant. Thermodynamic justification for thermoelastic effects (and importantly equation (4)) is based on the assumption of reversibility in elastic deformation [27]. The Helmholtz free energy (φ) may be defined as the internal energy (u, a function of temperature and total strain) less the product of temperature (T) and entropy (s), or φ=u-Ts. Recalling the first and second laws of thermodynamics and evaluating specific heat and work contributions, an expression for the increment in entropy may be found such that equation (4) can be derived [27].

$$\Delta T = \frac{T}{\rho C_\epsilon} \Sigma \frac{\partial \sigma_{ij}}{\partial T} \epsilon_{ij} + \frac{Q}{\rho C_\epsilon} \text{ for } i,j = 1,2,3 \tag{4}$$

$$\Delta T = -\frac{\alpha}{\rho C_P} T \sum_{i=1,2} \sigma_{ii} \tag{5}$$

$$C_\epsilon = C_P - \frac{2E\alpha^2 T}{\rho(1-\nu)} \tag{6}$$

In irreversible processes, such as plastic deformation, there is always an increase in entropy [27]. The definition of Helmholtz free energy presented above (φ=u-Ts) is still valid, however it is important to note that in the elastic-plastic case internal energy is a function of state variables related to, for example, kinematic and isotropic hardening (allowing for the quantification of plastic strain) in addition to the elastic strain component and temperature (as was assumed in the thermoelastic case). The Clausius-Duhem inequality expresses the second law of thermodynamics in a way which is convenient for continuum mechanics study and may be represented by equation (7), where $\dot{\sigma}$ and $\dot{\epsilon}$ are the stress and strain rate tensors, respectively, and $\dot{q}$ is a heat flux. Equation (7) quantifies a total dissipation (d), which may be decomposed into a mechanical (also known as intrinsic) component (d_m, see equation (8), which is equivalent to the quantity $\dot{q}_P$ referenced in equation (1)) and a thermal component (d_{th}, see equation (9)), such that $d=d_m+d_{th}$ [28]. Note that the former is related to irreversibilities which cause a change in the material's microstructure (plasticity, for example) and the latter is related to the existence of a temperature gradient across the material. In order to experimentally evaluate d_m (=$\dot{q}_P$) the heat equation must be solved (equation (10)). Note that mechanical dissipation may be decomposed into thermomechanical coupling and dissipative components. Thermomechanical contributions have been neglected in some studies [21], however evaluation may be related in some cases to thermoelastic power [15].

$$d = \dot{\psi} + s\dot{T} - \frac{1}{\rho}\sigma : \dot{\epsilon} + \frac{\dot{q}.\nabla T}{\rho T} \leq 0 \tag{7}$$

$$\delta_m = \dot{q}_P = \frac{1}{\rho}\sigma : \dot{\epsilon} - \dot{\psi} - s\dot{T} \tag{8}$$

$$\delta_{th} = -\frac{\dot{q}.\nabla T}{\rho T} \tag{9}$$

$$\rho C_P \frac{\partial T}{\partial t} - \nabla.(k\nabla T) = \delta_m = \dot{q}_P \tag{10}$$

Multiple excellent review articles have been published on thermoplastic effects from both theoretical and experimental perspectives. Interested readers are directed to the work of Bertram and Krawietz [28], Knysh and Korkolis [18], Einav et al. [3], and Pottier et al. [15].

3. Experimental Setup

Small ring testing is completed here using a Tinius-Olsen H25KS test rig (see figure 2 (a)). Load is transferred from the machine end grips to the small ring sample through a modified Nimonic alloy test specimen (see figure 2 (b)) which also locates Nimonic loading pins. Pin displacement is recorded through LVDTs connected to knife edge ridges on the modified Nimonic test specimen. The Young's modulus of Nimonic is approximately three times greater than that of aluminium. Consequently, the stiffness of the ring test specimen is assumed to be significantly less than the stiffness of the modified "grip" sample, suggesting that LVDT measurements are approximately equivalent the to the pin displacements. Three loading rates (namely 0.1mm/s, 1mm/s, and 10mm/s) are applied here in order to indicate any rate dependencies for the 7175 material and alter the time scales for heat transfer.

Temperature fields are monitored using a FLIR SC7200 infra-red thermal camera. A thermal calibration curve for the high magnification camera lens used in the present work was established by relating thermocouple readings to measured digital levels. Diurnal variations in laboratory ambient temperature were used to generate a range of data points (see figure 3). A linear correlation is used in the present work, allowing for the evaluation of temperatures (T) based on camera digital level (X) using the function $T = 6.745 \times 10^{-3}X - 11.480$. Note that two independent tests were performed for each loading rate, thereby allowing temperature fields to be monitored during deformation on "front" (as shown in figure 1) and "side" projections of the small ring sample. Example temperature field plots for both of these projections and all loading rates are given in figure 4. Temperature fields were sampled at 100Hz in the 0.1mm/s and 1mm/s tests and at 200Hz in the 10mm/s tests.
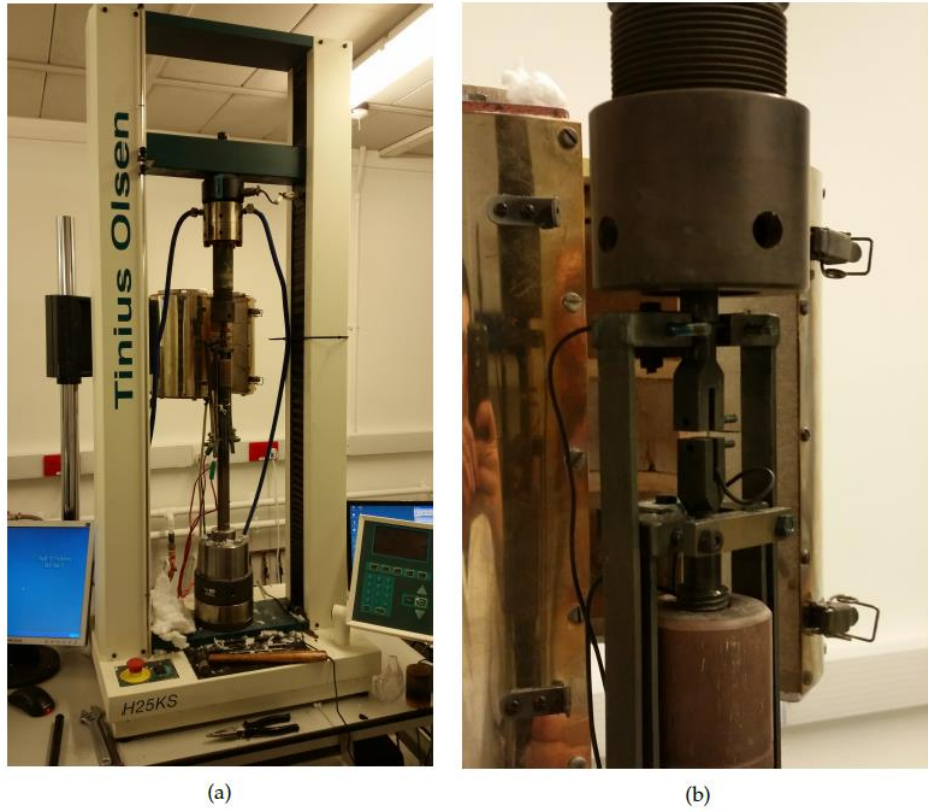
Figure 2. The Tinius-Olsen H25KS test rig used for small ring testing in the present work, showing **(a)** the general experimental setup and **(b)** a close up of the modified small ring specimen grips.
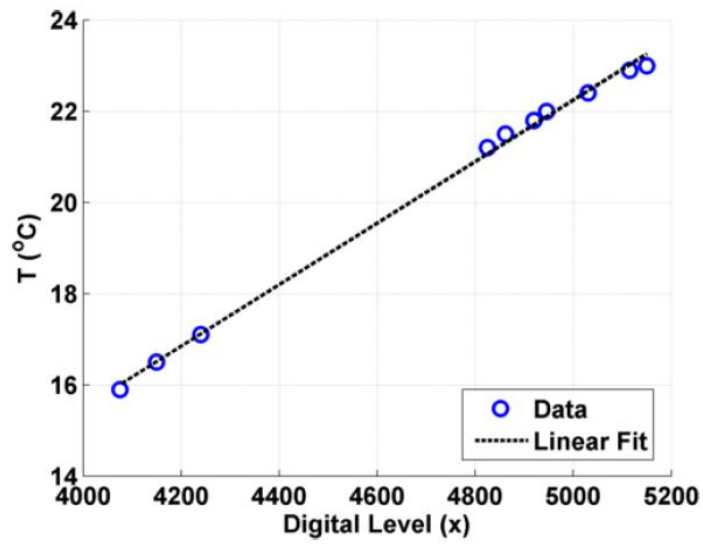

Figure 3. The thermal calibration curve used in the present work, used to correlate thermal camera digital levels and temperature.
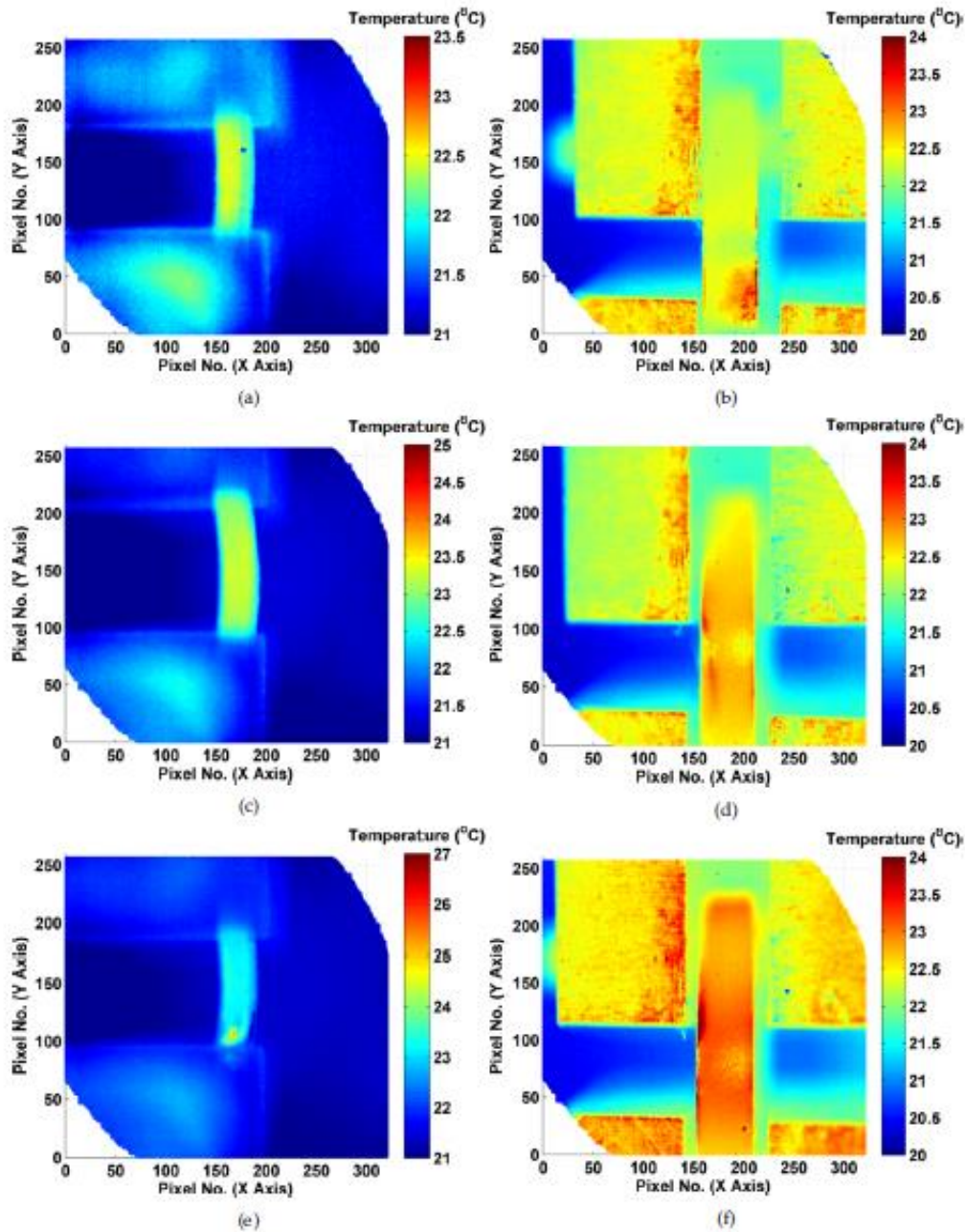
Figure 4. Example temperature field plots, shown for 'front' and 'side' projections for 0.1mm/s ((a) and (b)), 1mm/s ((c) and (d)) and 10mm/s ((e) and (f)) loading rates.

4. Thermal Parameter Determination

In order to investigate thermoplastic effects (and consequently estimate Taylor-Quinney coefficients) it is necessary to solve the heat equation. Thermal source terms related to plastic straining must be balanced with losses to the testing environment (by natural convection, for example) in order to approximate the dynamic temperature field. Fundamental thermal properties of 7175-T7351 aluminium are explored here in order to facilitate future heat transfer analyses. Specific heat capacity was estimated using a Netzsch DSC 204 HP Differential Scanning Calorimeter. Tests were performed at ambient conditions. Variations in specific heat capacity were observed over a 5 hour period in order to determine the stability of the results. Only minor variations were observed over this sampling period. A mean value of 864.40J.kg^{-1}.K^{-1} is suggested here.
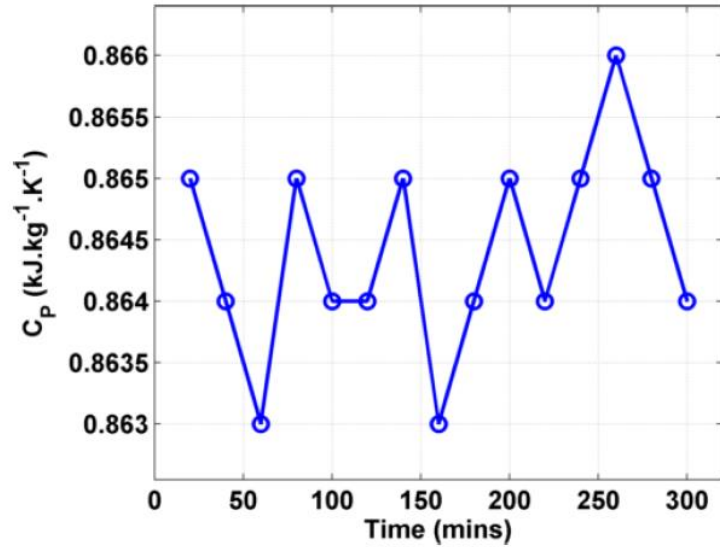
Figure 5. Variations in specific heat capacity (C_p) recorded over 5 hours.

The Wiedemann-Franz law is used in the present work in order to estimate thermal conductivity based on electrical conductivity measurements. The Wiedemann-Franz law may be expressed in the form shown in equation (11), where κ is thermal conductivity, σ_E is electrical conductivity, T is instantaneous temperature (here assumed to be 273K, representative of typical laboratory ambient temperatures), and L is the Lorenz number (here taken to be 2.44×10^{-8}W.Ω.K^{-2}) [29]. Four point direct current potential drop tests were performed using 4 injection current levels on a 0.03m by 0.072m by 0.6m bar of the 7175 material. Results are presented in table 1. Difficulties in reading small potential drops are suggested for the apparent dependency of thermal conductivity on injection current observed in table 1, therefore a value of 190.04W.m^{-1}.K^{-1} is recommended here (being the average of the "stabilised" 2.5A and 3A results).

$$\frac{K}{\sigma_E} = LT \tag{11}$$

Table 1. A summary of four point potential drop test results performed on 7175 and resulting thermal conductivity estimations (based on the Wiedemann-Franz law, see equation (11)).

Current (A)	Potential Drop (μV)	Resistance ($\mu \Omega$)	Electrical Resistivity ($\Omega.m$)	Electrical Conductivity ($S.m^{-1}$)	Thermal Conductivity ($W.m^{-1}.K^{-1}$)
1	9.5	9.5	3.42×10^{-8}	29.24×10^6	209.04
2	20	10	3.60×10^{-8}	27.78×10^6	198.59
2.5	26	10.4	3.74×10^{-8}	26.71×10^6	190.95
3	31.5	10.5	3.78×10^{-8}	26.46×10^6	189.13

Density for the 7175 material was estimated using a MicroMetrics Accupyc 1330 pycnometer. 10 successive runs (purges) were performed on a 19.1867g sample. A mean density value of 2.7581g.cm^{-3} was found, with a peak deviation from mean of 0.0487%.

5. Results

Conventional (full size) monotonic testing of 7175 at room temperature has suggested minimal time dependency in the constitutive behaviour. Results presented in figure 6, which show the relationship between pin load and displacement, support this observation for the 0.1mm/s and 1mm/s results. A remarkable level of repeatability (in terms of initial linear and non-linear material behaviour) should be noted in all observations made here; this directly follows from the self-aligning nature of the small ring specimen and the negligible influence of friction on the recorded specimen response. Further evidence of specimen response repeatability can be seen in the time series plots shown in figure 7. A clear deviation in the specimen response is observed in the 10mm/s data sets

(see figures 6 and 7). Possible explanations for the alternative specimen behaviours are discussed in section 6. At presents, readers are requested to note that, in the 0.1mm/s and 1mm/s results, non-linearity appears to commence at pin loads of approximately 150N. From figure 7, this pin load can be related to test times of 3.5s and 0.4s for the 0.1mm/s and 1mm/s cases, respectively.
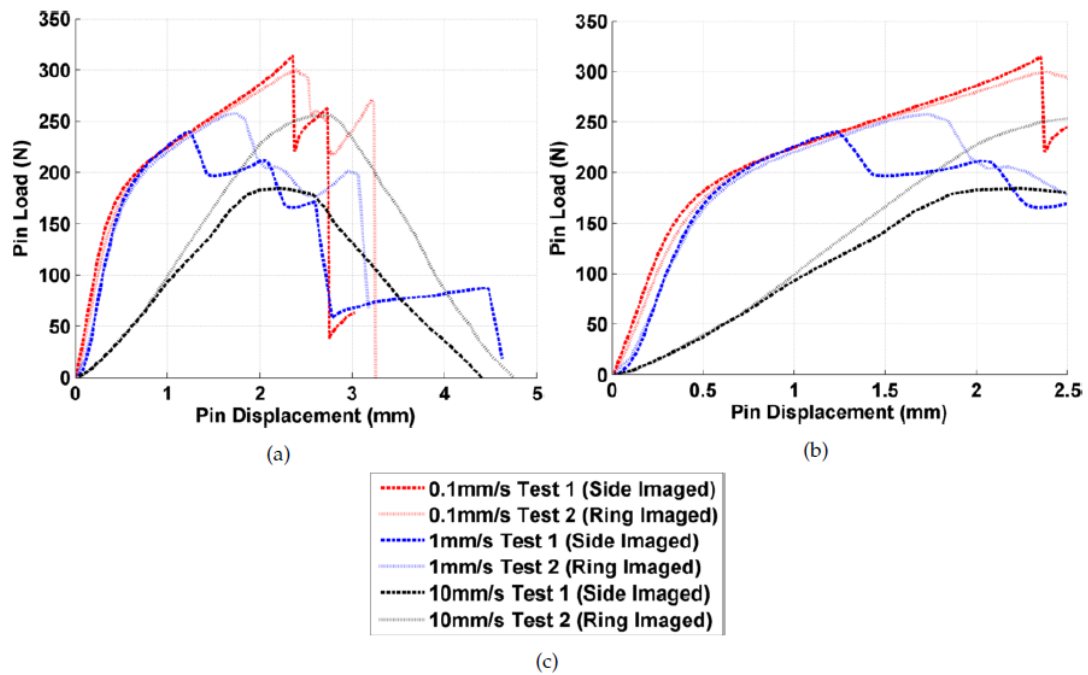

(a)

(b)

(c)

Figure 6. Pin load /displacement relationships observed for the three loading rates (0.1mm/s, 1mm/s and 10mm/s) used in the present work (note that repeat results are denoted by the temperature field imaging orientation, namely 'front' and 'side'). Full load/displacement curves are shown in **(a)** with elastic/plastic behaviour highlighted in **(b)** (a figure legend is presented in **(c)**).
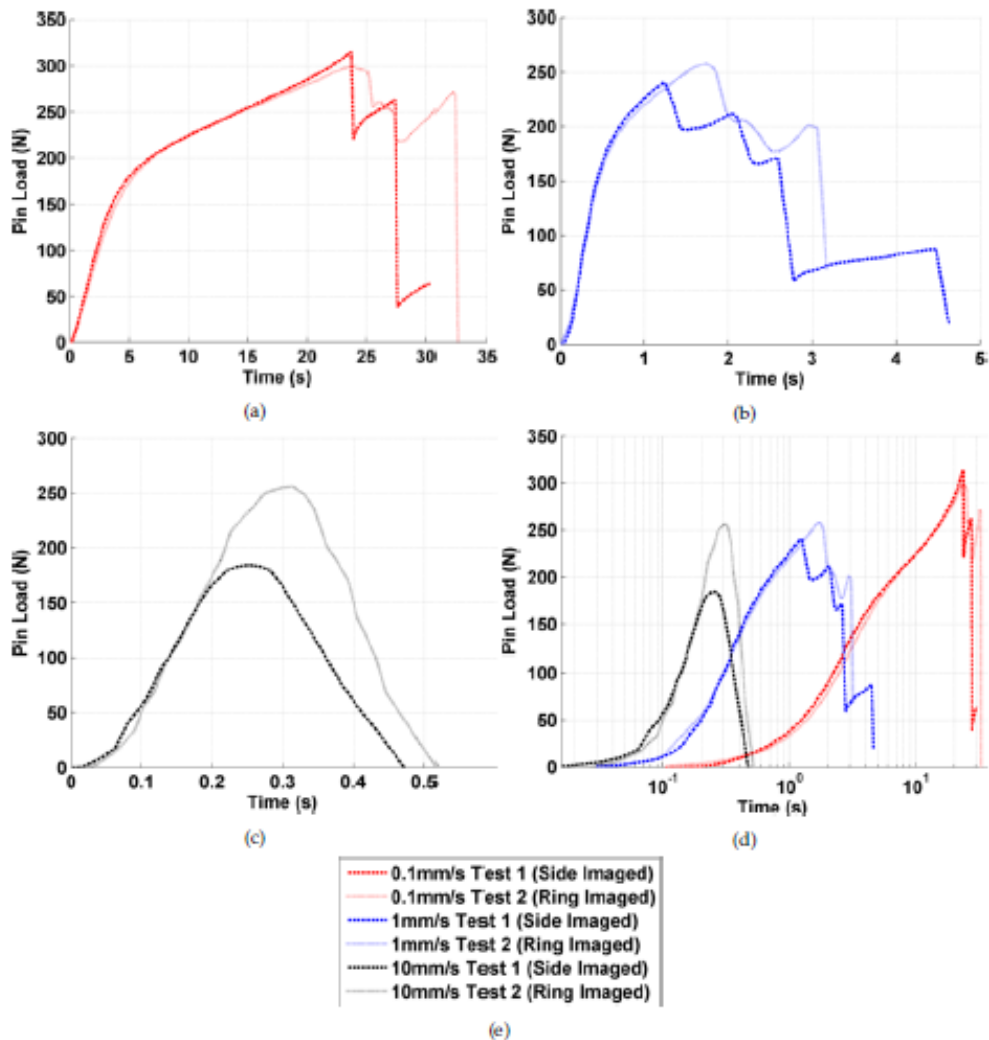
Figure 7. Pin load /time relationships observed for the three loading rates (0.1mm/s, 1mm/s and 10mm/s) used in the present work (note that repeat results are denoted by the temperature field imaging orientation, namely 'front' and 'side'). Full load/time curves are shown in **(a), (b),** and **(c)** (relating to loading rates 0.1mm/s, 1mm/s and 10mm/s respectively). Logarithmic time series are used in **(d)** to compare the three loading rate results. A figure legend is presented in **(e)**.

Temperature variations for various time instants in the small ring tests are presented in figures 9 to 11 (for the 0.1mm/s, 1mm/s, and 10mm/s, respectively). Figure 8 indicates the locations of sampling paths for front and side projections of the ring. In both cases, sampling is conducted from left to right (as shown in figure 8). Bespoke Matlab scripts have been developed to allow the user to track the ring as it deforms. Consequently, the paths presented in figure 8 are assumed to translate with the deforming small ring specimen. It is however important to note that, as the sampling paths are located on planes of symmetry in the specimen, they are assumed to remain planar. Generally speaking, uniform temperature profile are observed through the specimen thickness (side projections, or (b) sub-figures below), with the magnitude of this temperature increasing with test time. For front projections, higher temperatures are noted at the internal ring surface. Anomalies such as the large increase in temperature observed to the right hand side of figure 9 (b) associated here with the onset of failure and non-uniform contact (finite element simulation of the small ring has indicated a relaxation of contact pressure at the edges of the sample during loading). Future work will look to investigate this further.
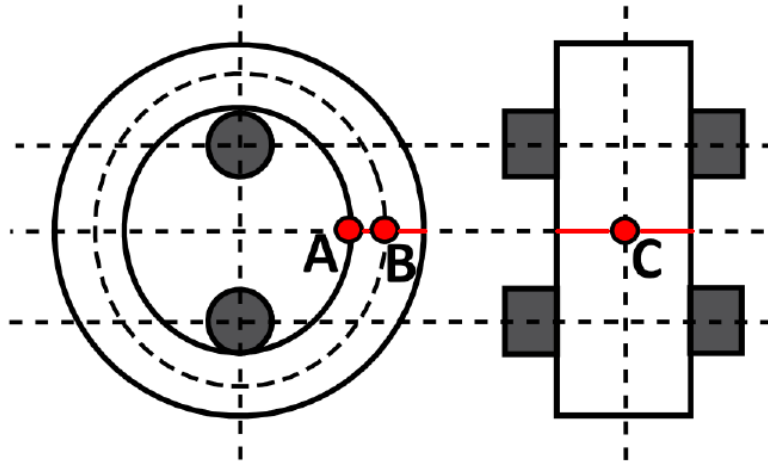
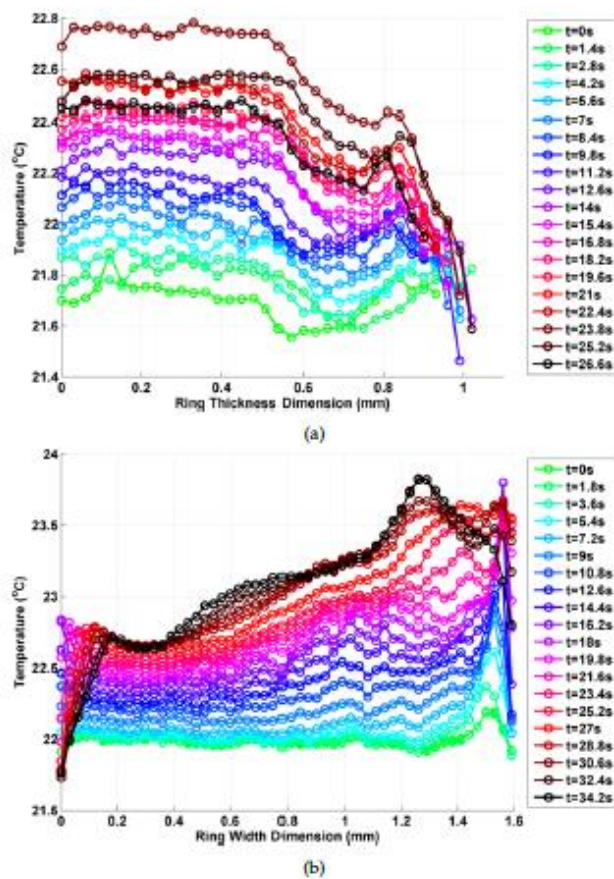**Figure 8.** Sampling paths and points used for examination of temperature fields in the small ring samples.

Figure 9. Temperature distribution variations (with test time) along the paths defined in figure 8, showing **(a)** front and **(b)** side projections for the 0.1mm/s loading case.

Figure 10. Temperature distribution variations (with test time) along the paths defined in figure 8, showing **(a)** front and **(b)** side projections for the 1mm/s loading case.
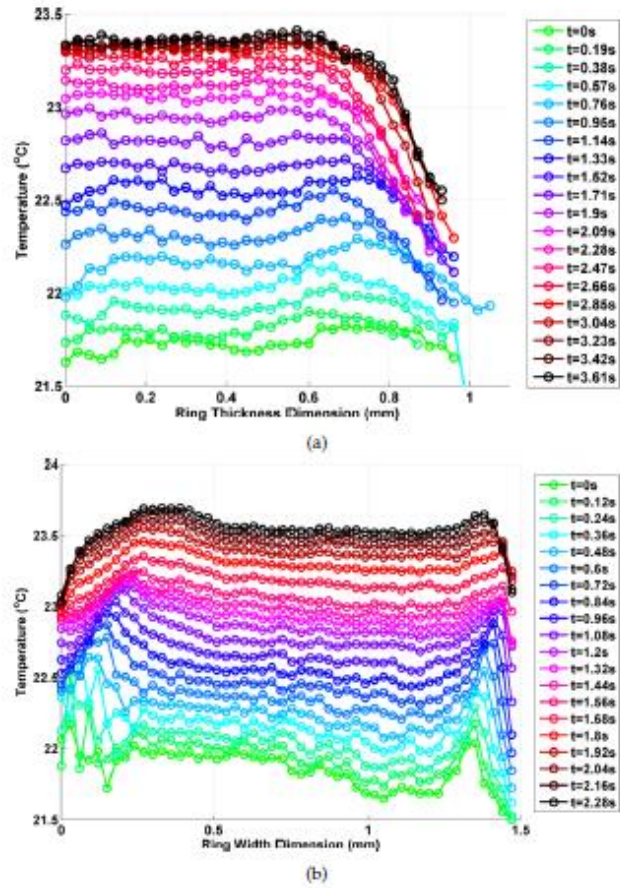
Figure 11. Temperature distribution variations (with test time) along the paths defined in figure 8, showing **(a)** front and **(b)** side projections for the 10mm/s loading case.
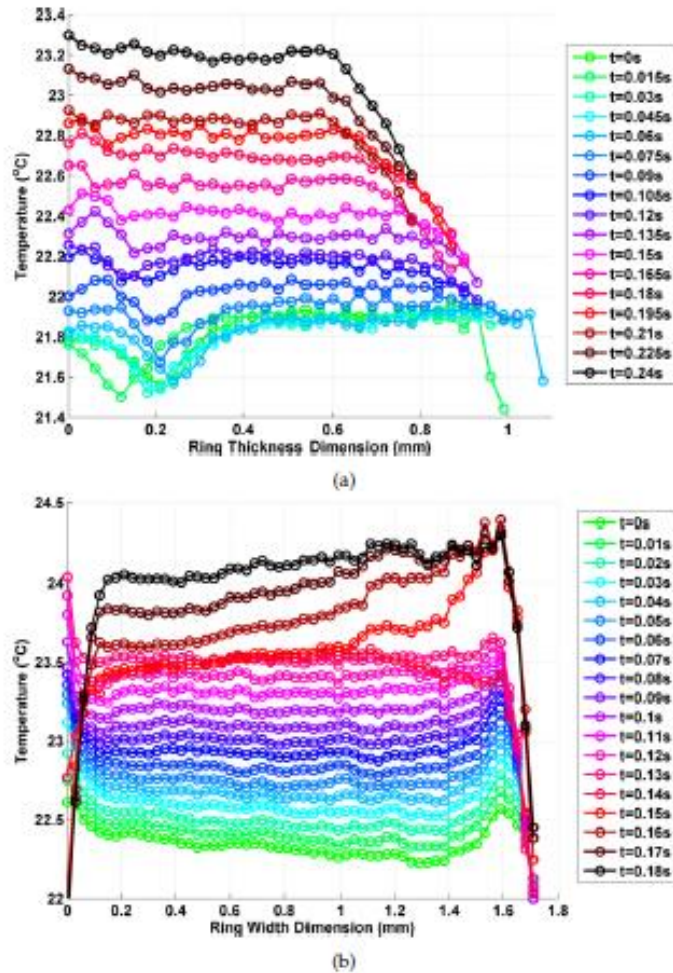
6. Discussion and Conclusions

A small ring tensile testing technique has been employed in order to investigate thermoplastic effects in 7175-T7351 aluminium alloy. Highly localised regions on plasticity (at the inside ring surface perpendicular to the loading direction) combined with very small volumes of material in the specimen were expected to develop characteristic temperature fields, thereby resulting in a sensitive testing method suitable for the study of the Taylor-Quinney coefficient. Indeed, front projections in figures 9 to 11 indicate higher temperature profiles at the internal ring surface, as expected. Figure 12 displays temperature changes associated with the sampling locations identified in figure 8 (A, B, and C) and, in the case of the 0.1mm/s and 1mm/s data, 1mm/s temperature profiles are approximately 0.6°C greater than 0.1mm/s profiles prior to failure. It is important to note that, in figure 11, temperature changes have been corrected for variations in ambient temperature by monitoring grip temperature fields (which are almost entirely uniform) throughout the test. Temperature changes associated with the 10mm/s data do not confirm with the expected trend. Even if no rate dependency in the Taylor-Quinney coefficient is assumed for 7175, a reduction in time scales over which heat transfer may take place (resulting from the faster loading rate) would suggest more localised and higher magnitude temperature fields. The thermal parameters determined in section 4 may be used to explore this point further through evaluation of 7175's thermal diffusivity ($7.97 \times 10^{-5} \mathrm{m}^2.\mathrm{s}^{-1}$). Taking a characteristic length of 1mm (the thickness of the small ring specimen), a diffusive characteristic time of 79.71s may be determined. Given that all test durations are less that this value (see figure 7), local temperature field features are justifiably expected. As noted previously, the linear and non-linear regions observed in force/displacement plots (see figure 6) for the 0.1mm/s and 1mm/s tests are not observed in the 10mm/s tests. A potential explanation for this can be derived by observing the initial non-linearity in the 1mm/s force/displacement curve (figure 6 (b)). The small ring specimen is in contact with two loading pins. It is assumed that local deformation around these pins does not

significantly contribute to the overall deformation of the specimen (the ring being intrinsically flexible upon first loading). At high strain rates however, it is suspected that this is not the case. Note that, based on a representative gauge length of 50mm, the strain rates associated with loading rates of 0.1mm/s, 1mm/s, and 10mm/s are 0.2%/s, 2%/s, and 20%/s, respectively. The latter of these is noted as being particularity high and may represent a limit for the small ring test in its current form. Future work will look to test intermediate strain rates in order to support this claim.

Some evidence of thermoelastic effects may be observed in the results presented here. Temperature changes associated with the linear region of the specimen force/displacement response are generally small (note that profiles in figures 9 and 10 are of similar magnitude before 3.5s and 0.4s for the 0.1mm/s and 1mm/s results, respectively). Furthermore, drops in temperature may be observed at the beginning of the tests in figure 12. The non-cyclic nature of the tensile small ring test makes further examination of these effects difficult (conditions close to adiabatic have clearly not been achieved), however the results discussed here indicate a potential focus for future work.

The experimental technique employed here appears to β suitable for the determination of the Taylor- Quinney coefficient at modest strain rates. Very good levels of repeatability and the small amounts of source material used have the potential to make small ring tensile tests an effective and efficient to study some of the various dependencies associated with β. As with full sized samples failure is less repeatable (see figure 6) and it is unclear at present how sensitive these results are to tolerances in the specimen design. Localised plasticity has allowed for temperature changes to 1.7°C to be observed, resulting from intrinsic material dissipation. Small specimens hold a further advantage over full sized equivalents in this field of study. It is reasonably easy to mount several in a furnace simultaneously, allowing for the investigation of β at temperature (with one unloaded sample acting as a reference for environmental temperature control). The isolation of noise in results of this type is a problem that plagues all testing (full sized or small), however the highly localised nature of plasticity in the small ring specimen may offer a solution to this in the future.
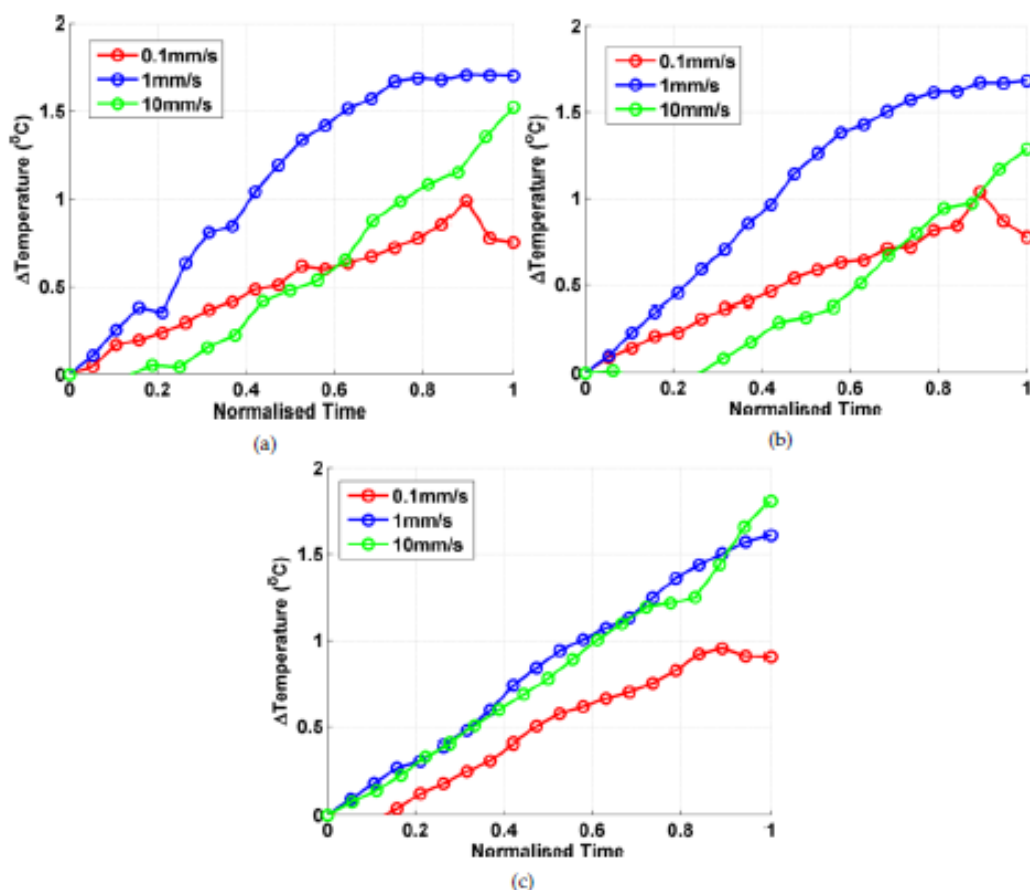

Figure 12. Observed temperature changes in sampling locations **(a)** A, **(b)** B and **(c)** C (see figure 8) for the three loading rates applied in the present work.

References

1. Rittel D.; Zhang L.H.; Osovski S. The dependence of the Taylor-Quinney coefficient on the dynamic loading mode. Journal of the Mechanics and Physics of Solids. 2017;107:96–114.
2. Daily J.S.; Klingbeil N,W. Plastic dissipation in fatigue crack growth under mixed-mode loading. International Journal of Fatigue. 2004;26:727–738.
3. Einav I.; Houlsby G.T.; Nguyen G.D. Coupled damage and plasticity models derived from energy and dissipation potentials. International Journal of Solids and Structures. 2007;44:2487–2508.
4. Benoit S.G.; Chalivendra V.B.; Rice M.A.; Doleski R.F. Characterisation of the microstructure, fracture, and mechanical properties of aluminium alloys 7085-O and 7175-T7452 hollow cylinder extrusions. Metallurgical and Materials Transactions A. 2016;47A:4476–4483.
5. Wen J.; Fan Y.; Wang G.; Jin L.; Li X.; Li Z.; et al. Aging behavior and precipitate characterization of a high Zn-containing Al-Zn-Mg-Cu alloy with various tempers. Materials & Design. 2016;101:16–23.
6. Goueffon Y.; Mabru C.; Labarrére M.; Arurault L.; Tonon C.; Guigue P. Mechanical behaviour of black anodic films on 7175 aluminium alloy for space applications. Metal Finishing. 2010;108:22–27.
7. Jaya Rao V.V.S.; Kannan E.; Prakash K.R.; Balasubramaniam. V. Observation of two stage dislocation dynamics from nonlinear ultrasonic response during the plastic deformation of AA7175-T7351 aluminium alloy. Materials Science and Engineering: A. 2009;512:92–99.
8. Lam W.; Cheong M.F.; Rouse J.P.; Hyde C.J.; Kennedy A.R. The prediction of isothermal cyclic plasticity in 7175-T7351 Aluminium alloy with particular emphasis on thermal ageing effects. International Journal of Fatigue, https://doi.org/10.1016/j.ijfatigue.2018.05.010.
9. Paulisch M.C.; Lentz M.; Wemme H.; Andrich A.; Driehorst I.; Reimers W. The different dependencies of the mechanical properties and microstructures on hot extrusion and artificial aging processing in case of the alloys Al 7108 and Al 7175. Journal of Materials Processing Technology. 2016;233:68–78.
10. Langille M.R.; Diak B.J.; Saimoto S. Re-examining the relation between fracture strain and yield stress in Al-Mg-Si alloys. Materials Science and Engineering: A. 2017;705:196–199.
11. Goueffon Y.; Mabru C.; Labarrére M.; Arurault L.; Tonon C.; Guigue P. Investigations into the coefficient of thermal expansion of porous films prepared on AA7175 T7351 by anodizing in sulphuric acid electrolyte. Surface and Coatings Technology. 2010;205:2643–2648.
12. Hyde T.H.; Sun W. A novel, high-sensitivity, small specimen creep test. Journal of Strain Analysis for Engineering Design. 2009;44:171–185.
13. Hyde C.J.; Hyde T.H.; Sun W. Small ring testing of high temperature materials. Key Engineering Materials. 2017;734:168–175.
14. Shao G.; Zhu S.; Wang Y.; Zhao Q. An internal state variable thermodynamic model for determining the Taylor-Quinney coefficient of glassy polymers. International Journal of Mechanical Sciences. 2017;126:261–269.
15. Pottier T.; Toussaint F.; Louche H.; Vacher P. Inelastic heat fraction estimation from two successive mechanical and thermal analyses and full-field measurements. European Journal of Mechanics - A/Solids. 2013;38:1–11.
16. Fekete B.; Szekeres A. Investigation on partition of plastic work converted to heat during plastic deformation for reactor steels based on inverse experimental-computational method. European Journal of Mechanics - A/Solids. 2015;53:175–186.
17. Rittel D. On the conversion of plastic work to heat during high strain rate deformation of glassy polymers. Mechanics of Materials. 1999;31:131–139.
18. Knysh P.; Korkolis Y.P. Determination of the fraction of plastic work converted into heat in metals. Mechanics of Materials. 2015;86:71–80.
19. Maurel-Pantel A.; Baquet E.; Bikard J.; Bouvard J.L.; Billon N. A thermo-mechanical large deformation constitutive model for polymers based on material network description: Application to a semicrystalline polyamide 66. International Journal of Plasticity. 2015;67:102–126.
20. Billon N. New constitutive modelling for time-dependent mechanical behaviour of polymers close to glass transition: Fundamentals and experimental validation. Journal of Applied Polymer Science. 2012;125:4390–4401.
21. Benaarbia A.; Chrysochoos A.; Robert G. Kinetics of stored and dissipated energies associated with cyclic loadings of dry polyamide 6.6 specimens. Polymer Testing. 2014;34:155–167.

22. Galán J.; Verleysen P.; Degrieck J. Thermal Effects During Tensile Deformation of Ti-6Al-4V at Different Strain Rates. Strain. 2013;49:354–365.

23. Jovic C.; Wagner D.; Herve P.; Gary G.; Lazzarotto L. Mechanical behaviour and temperature measurement during dynamic deformation on split Hopkinson bar of 304L stainless steel and 5754 aluminium alloy. Journal de Physique IV. 2006;134:1279–1285.

24. Zaera R.; Rodríguez-Martínez J.A.; Rittel D. On the Taylor-Quinney coefficient in dynamically phase transforming materials. Application to 304 stainless steel. International Journal of Plasticity. 2013;40:185–201.

25. Badulescu C.; Grédiac M.; Haddadi H.; Mathias J.D.; Balandraud X.; Tran H.S. Applying the grid method and infrared thermography to investigate plastic deformation in aluminium multicrystal. Mechanics of Materials. 2011;43:36–53.

26. Dulieu-Barton J.M. Introduction to thermoelastic stress analysis. Strain. 1999;35:35–39.

27. Pitarresi G.; Patterson E.A. A review of the general theory of thermoelastic stress analysis. The Journal of Strain Analysis for Engineering Design. 2003;38:405– 417.

28. Bertram A.; Krawietz A. On the introduction of thermoplasticity. Acta Mechanica. 2012;223:2257–2268.

29. Jones W.; March N.H. Theoretical Solid State Physics. Dover Publishing; 1986.

Determination of creep properties from small punch test using experimental correlation

P. Dymáček [1,2]*, F. Dobeš [1], Y. Li [3], S. Holmström [4] and P. Stevens [5]

[1] Institute of Physics of Materials, ASCR, Žižkova 22, 616 62 Brno, Czech Republic; pdymacek@ipm.cz
[2] CEITEC IPM, Žižkova 22, 616 62 Brno, Czech Republic; pdymacek@ipm.cz
[3] retired from DNV-GL, Arnhem, the Netherlands; yingzhili1943@hotmail.com
[4] European Commission, JRC, 1755 LE Petten, The Netherlands; stefan.holmstrom@ec.europa.eu
[5] DEKRA, Material Testing & Inspection, Utrecht, The Netherlands; Paul.Stevens@dekra.com
* Correspondence: pdymacek@ipm.cz; Tel.: +420-532-290-411

Abstract: The correlation of the small punch creep (SPC) test results with uniaxial creep test results is challenging due to several factors. The stress state is equibiaxial in the SPC test and the equivalent stress is not constant as the punch is advancing into the disc. The classical use of Chakrabarty membrane theory, with a constant F/σ ratio, is useful for rough estimates of equivalent stress but for more accurate estimations the strain hardening effect has to be accounted for. A new advanced method is introduced in this paper clearly showing robustness and good predictability in estimating short term uniaxial creep strength from SPC results. The equivalent stress in SPC can be estimated using equal rupture time as a base or by converting SPC deflection rate to equivalent uniaxial creep strain rate. The current study is using a large test data pool and the obtained empirical formulas are shown to reliably estimate equivalent stress for time to rupture predictions and the parameters for the Norton minimum creep rate law.

Keywords: creep; uniaxial; small punch; heat resistant steels

1. Background

In the early 1980's, the small punch test technique was developed in USA and Japan [1, 2]. This technique has been applied to nuclear reactors, electric power plants for safety assessments. European researchers have carried out the pioneering work on small punch creep testing (SPC), i.e. testing at constant force, in the 1990's [3-4]. The European Code of Practice (CoP) document has become available in 2006 [5], which provides a guide line to perform small punch tests for metallic materials, and introduces methods for estimation of tensile properties, fracture toughness and creep properties. At present, small punch testing is used for various applications to a broad range of materials including developed lightweight materials [6-20].

The application of the small punch test in practice is critically sensitive to the existence of a reliable procedure for comparison with the results of conventional creep tests. In the European Code of Practice, a rough estimate of the conversion between force F in small punch test and stress σ in conventional test was made using the Chakrabarty membrane stretch model [21] giving a constant ratio of $\Psi = F/\sigma$. The Chakrabarty ratio for the standard SP specimen geometry (initial specimen thickness $h_0 = 0.5$ mm) is $\Psi = 1.8908$ N/MPa [22, 23]. The ratio can be used for planning test load but it is not suitable for creep property assessment. If Chakrabarty model is used to predict the creep properties, the difference between the prediction and the uniaxial tests are commonly reported [23-28]. It has been shown that the Ψ ratio is not a constant but depends on both stress and temperature. The temperature and force dependence mainly originates from the effective area under the punch during the test.

The complexity of the SPC test consists in the inclusion of several non-linear problems: the geometrical non-linearity due to large deformation, the physical nonlinearity due to plasticity and creep and the contact nonlinearity due to the contact area between the punch and the specimen. Recently it has been found that the creep behaviour in SPC is also influenced by excessive plasticity during the loading [29].

In order to solve these problems, efforts have been made to improve the interpreting approach for SPC, and several conferences and symposia have been held to exchange ideas and experiences. Due to the complexity of the SPC test itself and a lack of systematic test data for verification, up to now there is no generally accepted method to estimate uniaxial creep properties from it. Now we may wish to review these thoughts, perhaps to obtain some benefits. Finally, we would like to propose a new simple procedure based on a detailed analysis of deflection *vs.* time curves available in parallel with the uniaxial creep data.

1.1 Formula of European Code of Practice

In the European code of practice (CoP) [5], a formula was put forward to estimate the membrane stress σ based on the Chakrabarty membrane stretch model

$$F / \sigma = 3.332\, k_{SP}\, a^{-0.2} R^{1.2} h_0 \quad \text{(for } u > 0.8 \text{ mm)} \tag{1}$$

where a is radius of lower die, R is punch radius and u is deflection (in mm). k_{SP} is a correlation factor introduced to adjust the theoretical model to the experimental results. A question is raised, how to estimate the value of k_{SP}?

Blagoeva in her Ph. D. thesis carried out an investigation on new P91 base metal and service exposed metal, where both SPC and conventional uniaxial tests were performed [24]. By using the test results provided by JRC [24] and IMT Slovenia [23], the equivalent stresses can be derived from the rupture time in SPC with the uniaxial data. By substitution of the obtained equivalent stress into Eq. (1), the k_{SP} is found to be 1.1 to 1.5, see Fig.1 for details. In the figure, the additional data obtained on various heats of P91 steel are presented [30]. The ductility factor k_{SP} is obviously increasing with the increasing force and it is probably also dependent on the test temperature. Two effects, the large deformation effect and the strain hardening effect, can be suggested to explain why k_{SP} is higher than 1.
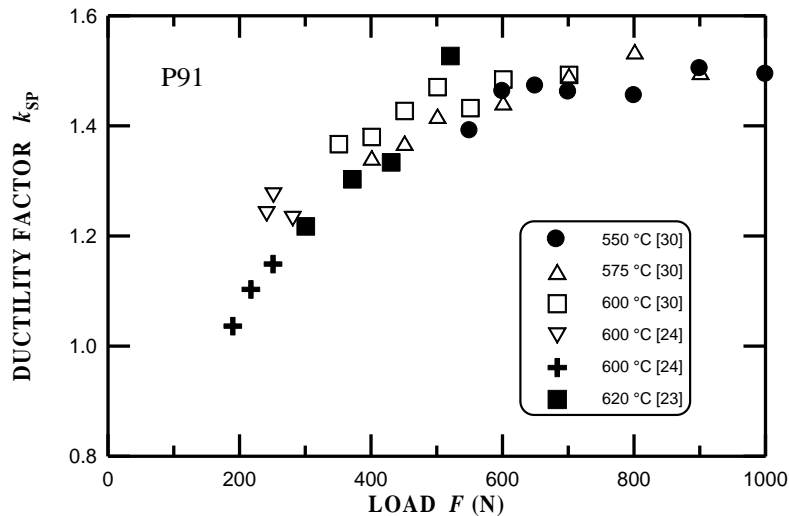

Figure 1. Load dependence of the factor k_{SP} for P91 steel determined from LICON and INTEGRITY projects [24] and IMT Slovenia [23] and IPM Brno creep results [30].

1.2 Large deformation effect

Hyde and Sun pointed out that the stationary stage of the SP creep curve is at the tertiary creep stage, rather than at the secondary creep stage. The reason is that the strain already reaches a level of 10-15% at such deflections [26]. Analysis of large deformation of a uniaxial specimen, in which strain rate $\dot{\varepsilon}$ at small strains is governed by the Norton equation, results in

$$\dot{\varepsilon} = A\left[(1+\varepsilon)\sigma\right]^n , \tag{2}$$

where ε and σ are engineering strain and engineering stress, respectively, A is a temperature-dependent factor and n is an exponent dependent on deformation mechanism.

An idea was put forward that the stress and strain entering into Chakrabarty analysis of membrane stretching are true stress σ_T and true strain ε_T, whilst these are engineering stress (i.e. the initial stress in constant load creep test) σ and engineering strain ε in the uniaxial test. Therefore when we compare the creep properties derived from the SPC test and the uniaxial test, the true stress and true strain in small punch test should be converted back to

engineering stress and engineering strain. According to the relation between true stress-strain and engineering stress-strain, we have:

$$\sigma = \sigma_T \exp(-\varepsilon_T). \tag{3}$$

The large deformation effect will give significant influence on the stress dependence of the rupture time. Assuming that for the CoP formula (1) is expressed in terms of the true stress no correction regarding experimental data is necessary. Substitution of the engineering stress σ into the left-hand side of Eq. (1) clearly reveals that:

$$k_{SP} = \exp(\varepsilon_T) = 1 + \varepsilon. \tag{4}$$

That is the reason why k_{SP} is always greater than 1, and its value depends on the strain ε at the minimum strain rate. The bigger the strain ε, the larger the value of k_{SP}. The large deformation effect can partially explain the difference between the theoretical and the experimental results, however, when the strain ε is too big due to large load deflection, Eq. (4) will give over correction.

The Norton constants A and n can be determined using the true stress σ_T and the true strain rate $\dot{\varepsilon}_T$, or using the engineering stress σ and the engineering strain rate $\dot{\varepsilon}$. The obtained results are quite close, but they are not exactly the same. Therefore, the large deformation effect gives a negligible influence on Norton constants.

1.3 Strain hardening effect

The effect of strain hardening should also be considered in creep analysis. For FEM analysis, the elastic plastic properties are part of the input data; therefore the strain hardening effect is already included automatically in the creep analysis. However, when the Chakrabarty model is used to derive the stress, the strain hardening effect should be considered, i.e., the stress given by the Chakrabarty model cannot be higher than those resulting from strain hardening law, e.g. given by combination of Hooke and Ramberg-Osgood equation:

$$\sigma = E\varepsilon \quad (\sigma \leq \sigma_y), \tag{5}$$

$$\sigma = K\varepsilon^p \quad (\sigma > \sigma_y), \tag{6}$$

where E is the elastic modulus and K and p are constants. In order to reduce the influence from excessive plastic deformation, Li suggested [31] that the maximum applied load in SPC should be limited: the maximum load F should not be higher than $1.891 \times \sigma_y$ for punch radius $r = 1.25$ mm in order to keep the membrane stress below the yield strength σ_y. This is because, for a uniaxial creep test, the applied stress is never higher than the yield strength.

1.4 Pre-strain effect

Hyde and Sun [26] insist that the excessive initial plastic deformation certainly influences the creep behavior. The evidence is that, even using the uniaxial data as input to the finite element analysis, the calculated deflection vs. time curve still does not coincide with the measured SPC curve. The importance of the effect drew the attention of Ule et al. [32]. They proposed and realized testing small punch specimens of a sombrero shape to avoid initial deformation after loading flat disc specimens. Recently, Cortellino et al. [29] have published their experimental and numerical results and prove that, the effect of pre-straining really exists and should be considered in the interpretation of creep properties.

2. Correlation of small punch and uniaxial data

The formula in the CoP is based on the Chakrabarty model. Although it is quite simple, it is obviously not sufficient to predict the creep behavior correctly. On the other hand, the large deformation effect, the strain hardening effect and the pre-strain effect are too complicated for engineering practice. A concept of "Fracture-based correlation" was put forward by Dobeš and Dymáček [33,34], the equivalent stress σ is derived using the rupture

time in SPC with the uni-axial data. In this paper, the "Fracture-based correlation" is further improved, not only to estimate the rupture time, but also to estimate the minimum strain rate. This new methodology is called the "SPC-curve-based approach". This approach is fully based on experimental tests data, no model or assumption is adopted. Thus all the effects mentioned above are already included. In addition, this approach delivers better prediction than the formula in CoP or the Chakrabarty model. Furthermore, it is very simple and user-friendly.

2.1 The "SPC-curve-based approach"

In order to predict the yield strength and the ultimate tensile stress from small punch tests at constant deflection rate, Purmenský and Matocha [35] proposed a correlation approach. They built up a data pool that includes both small punch and uniaxial tests data, and found an optimal parameter in small punch tests relative to the uniaxial quantities.

A similar approach can be applied to SPC analysis. However, the SPC analysis is more complicated than that in a constant deflection rate test. As in SPC, both the creep rupture time and the Norton creep law should be dealt with.

The basic idea of the "SPC-curve-based approach" is that the equivalent stress σ in SPC test can be estimated using the rupture time comparable with the uniaxial data, thus the ratio $\Psi = F/\sigma$ is obtained. Using the obtained equivalent stress σ the minimum strain rate can be also derived from the uniaxial data. The resulting ratio Ψ and the minimum strain rate are summarized in a sufficiently large data pool, from which empirical formulas of the ratio Ψ and the relation between the minimum deflection rate $\dot{u}_{min}$ and the minimum strain rate can be established with an optimal parameter.

2.2 The data pool

The test data pool contains 97 uni-axial tests and 159 SPC tests, covering temperatures from 550 °C to 700 °C, loads from 300 N to 900 N. The current materials, both new and exposed, are mainly low alloy steels and 9Cr steels, such as 14MoV63, X20CrMoV121, P91, P92 and Eurofer'97. A single example of austenitic steels, namely 316 L steel, is also included in the data pool. The contents and the data sources of the data pool are listed in Table 1. The test data were treated by Matlab procedure described in [38].

Table 1. The contents and data sources of the data pool.

No.	Material name	Temperature (°C)	Number of uni-axial tests	Number of SPC tests	Data source
1	14MoV63	550	4	2	IPM, IMT [4]
2	14MoV63	600	4	37	IPM,IMT [4]
3	14MoV63	650	4	2	IPM,IMT [4]
4	316L	700	4	5	JRC to be published
5	Eurofer'97	550	3	6	IPM [33]
6	Eurofer'97	600	4	7	IPM [33]
7	Eurofer'97	650	5	7	IPM [33]
8	MARBN-NPM1	600	5	4	IPM to be published
9	P22	600	7	15	IPM [36]
10	P91	620	4	8	IMT [23]
11	P91	550	5	6	IPM [30]
12	P91	575	6	6	IPM [30]
13	P91	600	6	7	IPM [30]
14	P92NT	600	5	7	IPM [34]
15	P92	600	4	5	JRC, IPM [34]
16	P92	600	4	5	IPM [34]
17	P92	625	3	5	JRC, IPM [34]
18	P92	650	2	5	JRC, IPM [34]
19	P92	650	4	5	IPM [34]
20	X20CrMoV121	550	4	3	IPM, IMT [37]
21	X20CrMoV121	600	4	6	IPM, IMT [37]
23	12.5Cr-4Ni-Mo	600	6	6	IPM (to be published)

2.3 Determination of equivalent stress

The deflection $u_{\min}$ at the minimum deflection rate $\dot{u}_{\min}$ is found to be the optimal parameter for the ratio Ψ. The acquired data pairs (F/σ, $u_{\min}$) are then fitted to the following empirical formula (Fig. 2)

$$\Psi = \frac{F}{\sigma} = B \cdot u_{\min}^{m} \quad \text{(N/MPa).}$$

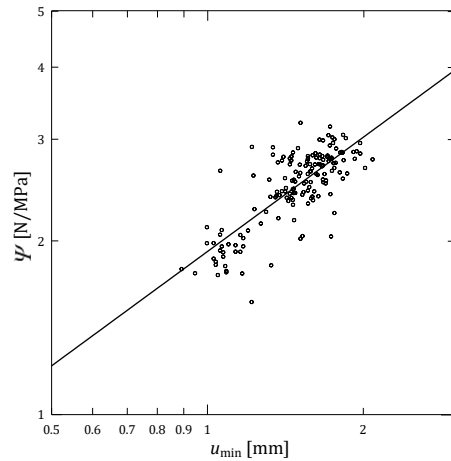(7)

The best fit is found at $B = 1.9204$ and $m = 0.6530$.

Figure 2. Relation between Ψ and the deflection $u_{\min}$ at the minimum deflection rate $\dot{u}_{\min}$.

2.4 Determination of the minimum strain rate

The derived minimum strain rates are also summarized in the same data pool. An empirical relation between the minimum deflection rate $\dot{u}_{\min}$ and the minimum strain rate is established and expressed as follows (see Fig. 3).

$$\dot{\varepsilon}_{\min} = C \cdot \dot{u}_{\min}^{q} \quad \text{(1/h),}$$

(8)

where the constants $C = 3.9220$ and $q = 1.1907$.
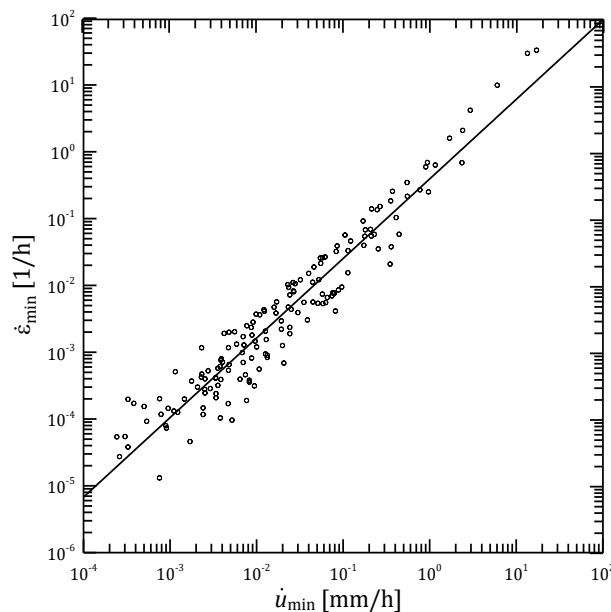
Figure. 3 Relation between the minimum deflection rate $\dot{u}_{\min}$ and the minimum strain rate $\dot{\varepsilon}_{\min}$.

3. Prediction of creep properties using "SPC-curve-based approach"

The procedure using the "SPC-curve-based approach" is described as follows. Carry out SPC test. For given load F, measure the rupture time t_r, the minimum deflection rate $\dot{u}_{min}$, and the deflection u_{min} at the minimum deflection rate $\dot{u}_{min}$. Using the deflection u_{min} at the minimum deflection rate $\dot{u}_{min}$, determine the ratio $\Psi = F/\sigma$ from Eq. (7), and consequently the equivalent stress σ is also obtained. Using the minimum deflection rate $\dot{u}_{min}$, determine the minimum strain rate $\dot{\varepsilon}_{min}$ from Eq. (8). With the equivalent stress σ, the rupture time t_r, and the minimum strain rate $\dot{\varepsilon}_{min}$ known, the rupture time vs. stress dependence and the Norton creep law are obtained.

4. Verification and examples

The best method for verification is to compare the prediction results directly with the uni-axial tests. The verification has been carried out for each test set during building up the data pool. Herewith some examples are shown below for predictions of the rupture time and the minimum strain rate. The prediction of Chakrabarty model is also attached. Obviously, the present approach gives much better prediction than the Chakrabarty model.

In Figs. 4-9, the open circles and the fit are the uniaxial data; for the black points and the fit, the equivalent stress σ are estimated using the rupture time in SPC test to compare the uniaxial data, then using the obtained equivalent stress σ to calculate the minimum strain rate in SPC from the uniaxial data, thus the two fits always overlap; the open triangles are derived from the empirical formulas Eqs. (7) or (8); the open squares are derived from Chakrabarty model.
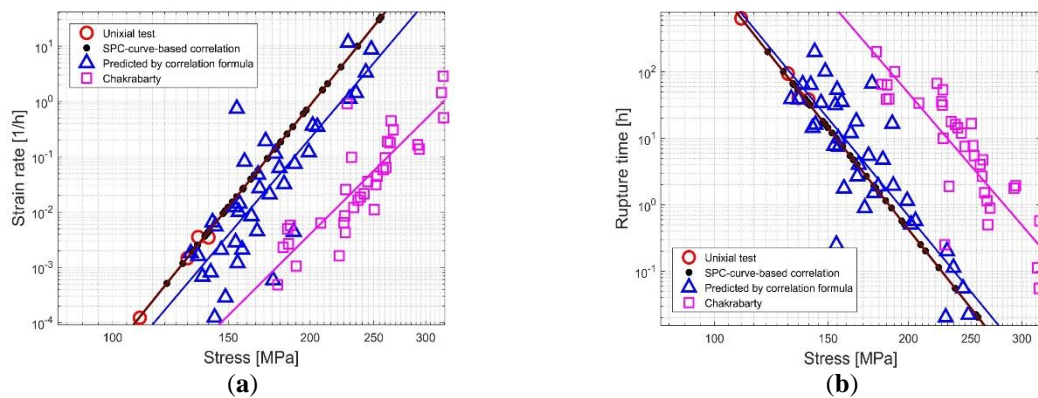

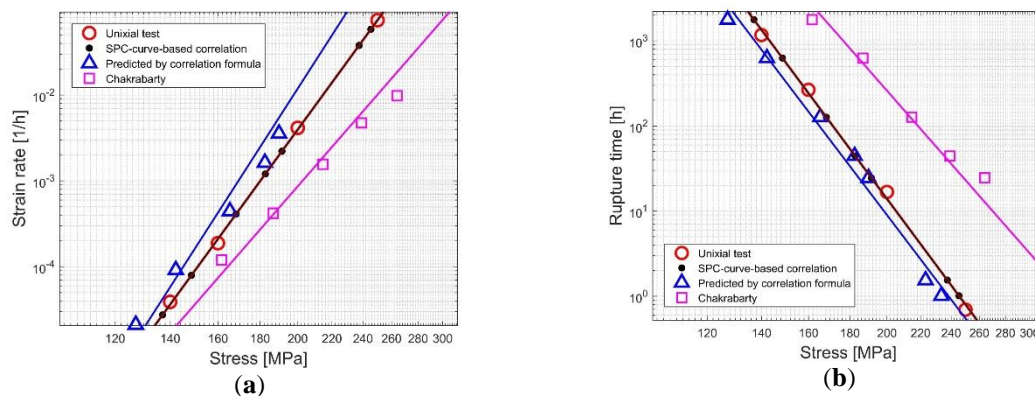**Figure 4**. Comparison of 14MoV63 at 600 $^\circ$C uni-axial data with prediction methods (**a**) Norton creep law; (**b**) Rupture time.

Figure 5. Comparison of Eurofer'97 at 600 $^\circ$C uni-axial data with prediction methods (**a**) Norton creep law; (**b**) Rupture time.
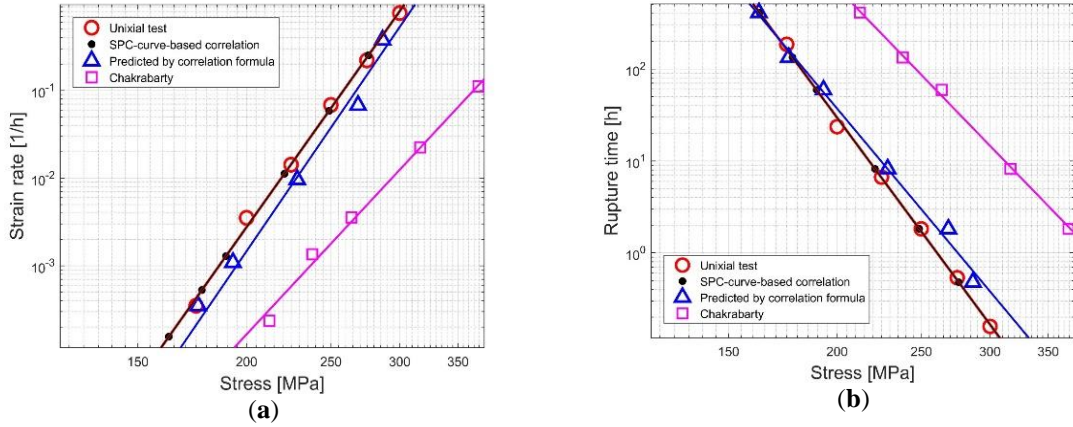
Figure 6. Comparison of P91 at 575 °C uniaxial data with prediction methods (**a**) Norton creep law; (**b**) Rupture time.
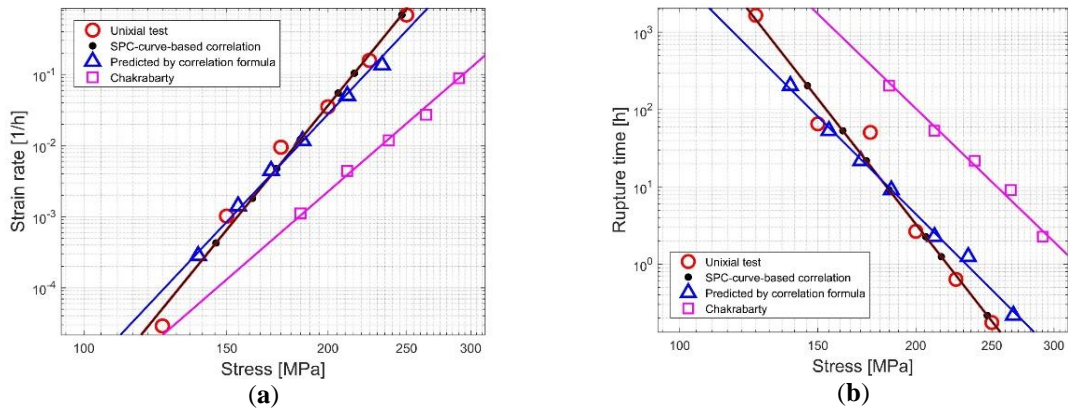

Figure 7. Comparison of P91 at 600 °C uniaxial data with prediction methods (**a**) Norton creep law; (**b**) Rupture time.
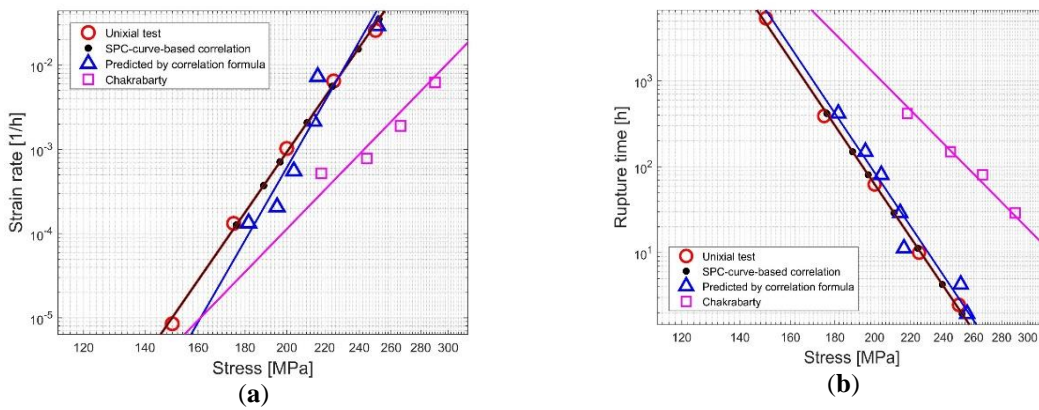

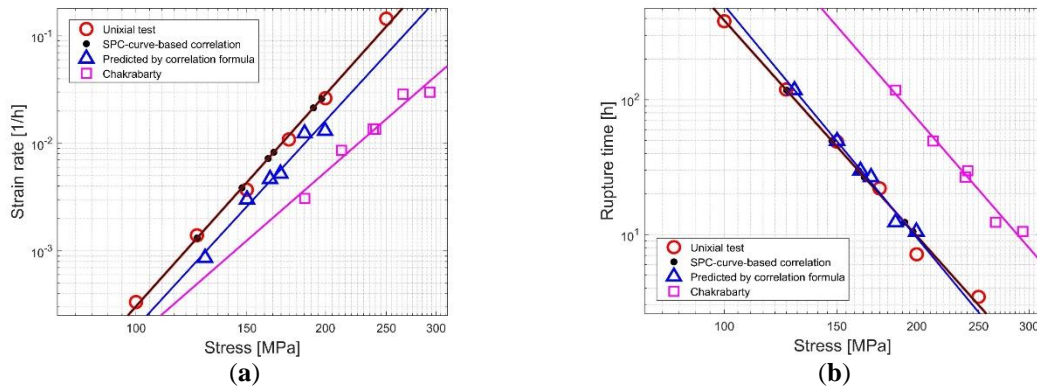**Figure 8.** Comparison of P92NT at 600 °C uniaxial data with prediction methods (**a**) Norton creep law; (**b**) Rupture time.

Figure 9. Comparison of 12.5Cr-4Ni-Mo steel at 600 °C uni-axial data with prediction methods (**a**) Norton creep law; (**b**) Rupture time.

5. Conclusions

The Chakrabarty model [21, 23] has been introduced in the European CoP to estimate the creep load setting. However, it is not sufficient for the prediction of creep properties from SPC tests. This is because the complicity of the SPC problem, as too many non-linearities are involved. Efforts have been made by considering different effects; however none of them is commonly accepted yet.

This paper puts forward a new methodology directly using experimental data. This is because the experimental data contains all effects, no theoretical assumption is needed.

Empirical formulas are given to estimate the equivalent stress and the minimum strain rate, thus creep properties can be predicted using the measured SPC data.

Verification has been carried out and shows that the predictions by the empirical formulas are in good agreement with the uniaxial data, and much better than those predicted by Chakrabarty model.

References

1. Manahan, M.P.; Argon, A.S.; Harling O.K., The development of a miniaturized disk bend test for the determination postirradiation mechanical properties. *J Nucl Mater* **1981**, 103&104, pp.1545-1550, DOI: 10.1016/0022-3115(82)90820-0.

2. Baik J.M.; Kameda J.; Buck O. Small punch test evaluation of intergranular embrittlement of an alloy steel. *Scripta Metall* **1983**, 17, pp. 1443-1447, DOI: 10.1016/0036-9748(83)90373-3.

3. Parker J.D.; James J.D. Disc-bend Creep Deformation Behaviour of 1/2Cr1/2Mo1/4V Low Alloy Steel. Proceedings of the Fifth International Conference on the Creep and Fracture of Engineering Materials and Structures, The Institute of Metals, London, 1993, pp. 651-660.

4. Ule B.; Šustar T.; Dobeš F.; Milička K.; Bicego V.; Tettamanti S.; Maile K.; Schwarzkopf C.; Whelan M.P.; Kozlowski R.H.; Klaput J. Small punch test method assessment for the determination of the residual creep life of service exposed components: outcomes from an interlaboratory exercise. *Nucl Eng Des* **1999**, 192, pp. 1–11, DOI: 10.1016/S0029-5493(99)00039-4.

5. CEN/WS CWA 15627 Workshop agreement: Small Punch Test Method for Metallic Materials. Part 1: A Code of Practice for Small Punch Testing at Elevated Temperatures. Report No. CEN/WS 21, European Committee for Standardization, 2007 Brussels

6. Ma Y.W.; Shim S.; Yoon K.B. Assessment of power law creep constants of Gr91 steel using small punch creep tests. *Fatigue Fract Eng M* **2009**, 32, pp. 951–960, DOI: 10.1111/j.1460-2695.2009.01394.x.

7. Rouse J.P.; Cortellino F.; Sun W.; Hyde T.H.; Shingledecker J. Small punch creep testing: review on modelling and data interpretation. *Mater Sci Tech-Lond* **2013**, 29: 1328-1345, DOI: 10.1179/1743284713Y.0000000278.

8. Rodríguez C.; Cárdenas E.; Belzunce F.J.; Betegón C. Fracture characterization of steels by means of the small punch test. *Exp Mech* **2013**, 53, pp. 385–392, DOI: 10.1007/s11340-012-9637-x.

9. Alegre J.M.; Cuesta I.I.; Lorenzo M. An extension of the Monkman-Grant model for the prediction of the creep rupture time using small punch tests. *Exp Mech* **2014** 54, pp.1441–1451, DOI: 10.1007/s11340-014-9927-6.

10. Lee T.; Ibupoto F.A.; Lee J.H.; Kim B.J.; Kim M.K. A direct methodology for small punch creep test. *Exp Mech* **2016**, 56, pp. 395–405, DOI: 10.1007/s11340-015-0108-z.

11. Nakata T.; Komazaki S.; Kohno Y.; Tanigawa H. Effects of geometry and dimension of specimen and rig on small punch creep property. *Exp Mech* **2017**, 57, pp. 487–494, DOI: 10.1007/s11340-016-0250-2.

12. Andrés D.; Lacalle R., Álvarez J.A. Creep property evaluation of light alloys by means of the Small Punch test: creep master curves. *Mater Des* **2016**, 96, pp.122–130, DOI: 10.1016/j.matdes.2016.02.023.

13. Holmstrőm S.; Auerkari P.; Hurst R.; Blagoeva D. Using small punch test data to determine creep strain and strength reduction properties for heat affected zones. *Mater Sci Tech-Lond* **2014**, 30, pp. 63-66, DOI: 10.1179/1743284713Y.0000000311.

14. García T.E.; Rodríguez C.; Belzunce F.J.; Suárez C. Estimation of the mechanical properties of metallic materials by means of the small punch test. *J Alloy Compd* **2014**, 582, pp. 708–717, DOI: 10.1016/j.jallcom.2013.08.009.

15. Geng J.F.; Cai H.S.; Ma D.F.; Feng X.S.; Guan K.S. Identification of creep parameters of P91 by small punch test. *Appl Mech Mater* **2014**, 529, pp. 439-443, DOI: 10.4028/www.scientific.net/AMM.529.439.

16. Naveena; Komazaki S. Evaluation of creep rupture strength of high nitrogen ferritic heat-resistant steels using small punch creep testing technique. *Mater Sci Eng A* **2016**, 676, pp. 100-108, DOI: 10.1016/j.msea.2016.08.102.

17. Hurst R.C.; Lancaster R.J.; Jeffs S.P.; Bache M.R. The contribution of small punch testing towards the development of materials for aero-engine applications. *Theor Appl Fract Mec* **2016**, 86, pp. 69-77, DOI: 10.1016/j.tafmec.2016.07.013.

18. Dyson C.C.; Sun W.; Hyde C.J.; Brett S.J.; Hyde T.H. Use of small specimen creep data in component life management: a review. *Mater Sci Tech-Lond* **2016**, 32, pp. 1567-1581, DOI: 10.1080/02670836.2015.1132536.

19. Nakata T.; Komazaki S.; Kohno Y.; Tanigawa H. Development of a small punch testing method to evaluate the creep property of high Cr ferritic steel: Part I – effect of atmosphere on creep deformation behaviour. *Mater Sci Eng A* **2016**, 666. pp. 54–60, DOI: 10.1016/j.msea.2016.03.100.

20. Ortiz-Mariscal A.; Saucedo-Muñoz M.L.; Naveena; Komazaki S. Application of small punch creep testing for evaluation of creep properties of as received and artificially aged 5Cr-0.5Mo steel. *Mater Sci Eng A* **2018**, 709, pp. 322-329, DOI: 10.1016/j.msea.2017.10.060.

21. Chakrabarty J. A theory of stretch forming over hemispherical punch heads. *Int J Mech Sci* **1970**, 12, pp. 315-325, DOI: 10.1016/0020-7403(70)90085-8.

22. Yang Z.; Wang Z. Relationship between strain and central deflection in small punch creep specimens. *Int J Pres Ves Pip* **2003**, 80, pp. 397-404, DOI: 10.1016/S0308-0161(03)00069-3.

23. Li Y.; Sturm R. Determination of creep properties from small punch test. In: Proceedings of the ASME Pressure Vessels & Piping Conference PVP 2008, Chicago, **2008**, Vol. 3, pp. 739-750, DOI: 10.1115/PVP2008-61437.

24. Blagoeva D. Development of a residual lifetime prediction methodology for creep and fracture behaviour of ferritic-martensitic steels using small punch testing technique. Dissertation, Universita di Pisa, Pisa, **2009**.

25. Nonaka I.; Kanaya A.; Komazaki S.; Kobayashi K. Standardization of test method for small punch creep testing in Japan. *Metallurgical J* **2010**, 63, pp.12-18.

26. Hyde T.; Sun W. Interpretation of small punch creep test data for ductile materials. *Metallurgical J* **2010**, 63, pp. 25-33

27. Wen Ch.; Xu T.; Guan K. Correlation factor study of small punch creep test and its life prediction. *Materials* **2016**, 9, 796, DOI: 10.3390/ma9100796.

28. Yang S.; Ling X.; Zheng Y. Creep behaviors evaluation of Incoloy800H by small punch creep test. *Mater. Sci. Eng. A* **2017**, 685, pp. 1–6, DOI: 10.1016/j.msea.2016.12.092.

29. Cortellino F.; Rouse J.P.; Cacciapuoti B.; Sun W.; Hyde T.H. Experimental and numerical analysis of initial plasticity in P91 steel small punch creep samples. *Mater Sci Tech-Lond* **2017**, 57, pp. 1193–1212, DOI: 10.1007/s11340-017-0296-9.

30. Milička K.; Dobeš F. Small punch testing of P91 steel. *Int J Pres Ves Pip*, **2006**, 83, pp. 625–634, DOI: 10.1016/j.ijpvp.2006.07.009.

31. Li Y.; Stevens P.; Geng J.; Ma D.; Xu L. Determination of creep properties from small punch test with reverse algorithm. *Key Eng Mat*, **2017**, 734, pp. 212-236, DOI: 10.4028/www.scientific.net/kem.734.212.

32. Ule B.; Šuštar T. The effect of initial hot plastic deformation on creep behaviour of 12 Cr steel specimens in small punch tests. *Mater High Temp* **2001**, 18, pp. 163-170.

33. Dobeš F.; Dymáček P. Fracture-based correlation of uniaxial and small punch creep data. *Theor Appl Fract Mec* **2016**, 86, pp. 34-38, DOI: 10.1016/j.tafmec.2016.08.020.

34. Dymáček P. Recent developments in small punch testing: Applications at elevated temperatures. *Theor Appl Fract Mec* **2016**, 86, pp. 25-33, DOI: 10.1016/j.tafmec.2016.09.013.

35. Purmenský J.; Matocha K. Testing of small specimens in physical metallurgy. In: Prnka T (ed) Proceedings of the 10th International Metalurgical Conference METAL 2001, TANGER, Ostrava, Czech Republic, 2001 pp. 70/1–70/13.

36. Dymáček P.; Milička K. Small punch testing and its numerical simulations under constant deflection force conditions. *Strength Mater* **2008**, 40, pp. 24-27, DOI: 10.1007/s11223-008-0007-y.

37. Dobeš F.; Milička K.; Ule B.; Šustar T.; Bicego V.; Tettamanti S.; Kozlowski R.H.; Klaput J.; Whelan M.P.; Maile K.; Schwarzkopf C. Miniaturized disk-bend creep test of heat-resistant steels at elevated temperatures. *Eng Mech* **1998**, 5, pp. 157-160.

38. Li Y.; Stevens P.; Dymáček P.; Dobeš F. Procedure of SPC data treatment for correlation with uniaxial tests SSTT2018, Swansea 2018 (submitted).

The effect of testing environment on small punch creep

H. Dawson [1,*], M. Richardson [1], M. Gorley [1], E. Surrey [1]

[1] UKAEA, Technology Department, Culham Science Centre, Abingdon, Oxfordshire, OX14 3DB, UK.

[*] Correspondence: huw.dawson@ukaea.uk; Tel.: +44 (0)1235466854

Abstract: Small punch creep testing (SPCT) is currently experiencing a resurgence of interest as a small-scale testing technique (SSTT) for a wide range of uses, including testing in-service components and materials with limited availability. SPCT is particularly pertinent for the fusion community since it is difficult to irradiate large volumes of material due to the high damage levels required and relatively low number of available facilities. An important aspect of the SPCT development that still requires investigation is the effect of the testing environment, which has been shown to impact the creep properties of materials when using standard testing techniques. This paper investigates the effect of using an air or an argon environment on the SPCT behaviour of the leading European fusion reactor material Eurofer97 at 550°C. The test environment was found to impact on the small punch creep behaviour: testing in an argon environment significantly increased time to failure and deflection at failure by a factor of approximately 30 and 7%, respectively. The test environment also appeared to affect the behaviour of the test via oxidation of the punch head which should be an important consideration in future testing.

1. Introduction

Nuclear reactors pose extremely demanding environments for structural materials. Therefore, comprehensive and rigorous testing is required of nuclear structural materials before they can be considered fit and safe for service. For the new generation of fission reactors and fusion reactors, a new generation of materials is being developed to withstand even harsher environments. They will require a large amount of testing; but new materials are often not mass-produced by industry and so are often in short supply. This places great pressure on the amount of destructive testing that can be carried out. Expensive and long irradiation times also restrict the volume of irradiated material that research groups can achieve. This is of even greater significance for the fusion community. Materials for fusion reactors will require experimental neutron irradiations with a 14.1 MeV peak to simulate the high energy neutrons that are produced by the deuterium-tritium (D-T) reactions which will be the dominant reaction in future commercial fusion reactors. There is currently no facility capable of producing such high energy neutrons in any significant volume.

One testing facility planned to be capable of producing high-energy, D-T fusion-like spectra of neutrons is the International Fusion Materials Irradiation Facility (IFMIF). The target is only planned to be able to irradiate a volume of ~0.5 litres, within the high flux region (>20dpa$_{(fpy)}$/year), with irradiation campaigns planned to run for upwards of 1 year [1-4]. This represents an extreme, but very real, example of the amount of testing material available being a critical problem. Therefore, the nuclear community is particularly interested in developing novel testing techniques that are able to properly assess material properties while using a much smaller volume of material.

Small punch testing (SPT) is a small-scale testing technique receiving significant interest as a potentially powerful method for measuring the mechanical properties of nuclear grade materials, including irradiated material. Small punch testing may be invaluable as a testing technique in many other fields too, where saving material is sought after. Small punch testing may also be used to measure in-service components; the small volume of material removed should mean that the components can continue service. In such a case SPT is considered a quasi-non-destructive test.

In SPT, a small, hard ball or hemispherical tip (punch) is driven through a small, thin cylindrical disc which is clamped between two dies. The resultant force-displacement or time-displacement curves can be used to derive analogous values of corresponding mechanical properties derived from standard uniaxial mechanical testing. The data is predominantly used on a relative scale though significant work is being conducted to achieve reliably derivable mechanical quantities. However, this is proving difficult; largely due to the tri-axial stress state present during SPT [5].

In this work, the SPT will be operated as a uniaxial creep equivalent – with the load on the specimen held constant and the curve of interest being displacement-time. There is not yet an established nomenclature for this, but it will be referred to in this work as Small Punch Creep Testing (SPCT). However, with the failure times seen in this study the test may be more relatable to traditional stress-rupture. It is also possible to test as uniaxial tensile equivalent by running in displacement control, or, utilising a slightly different experimental set-up, Small Punch Shear Testing.

It has been demonstrated that the testing environment can have significant effect on the creep behaviour of materials in uniaxial creep testing [6-9]. These mechanisms may well also be active in SPCT. Currently, limited literature on the effect of testing environment on SPCT has been conducted [10-12]. Though limited, the evidence seems to suggest that the testing environment can cause a significant effect, with tests in air rupturing after shorter test times. Further investigations are still required to validate the results and also to cast greater light on the scale of the environment's impact and the mechanisms involved; both of which are likely to be material dependent. These are important concerns for the technique if it is to become a fully standardized process and is of particular interest for the purposes of testing nuclear fusion structural materials as the components will be operating in an [ultra-high] vacuum vessel (VV).

This study will investigate the effect of testing environment on the Reduced Activation Ferritic-Martensitic (RAFM) steel Eurofer97 at a test temperature of 550°C. Eurofer97 is the prime candidate structural material and 550°C is the accepted operational temperature for present He cooled breeding blanket designs in the future DEMO fusion reactor.

2. Materials and Methods

2.1. Eurofer97

Eurofer97 is a 9%Cr Reduced Activation Ferritic-Martensitic (RAFM) steel. It contains very low concentrations of long-term activated elements, which significantly reduces any long-term activation of materials from future fusion reactors. The full elemental composition is given in Table 1. It was provided in the form of a fully martensitic, 6.5 mm thick, rolled plate and was tested in the as-received condition.

Table 1. Elemental composition of Eurofer97, in wt.% [13].

	Cr	W	Mn	V	Ta	C	N	Si	Al
Min	8.5	1	0.2	0.15	0.1	0.09	0.015	-	-
Max	9.5	1.2	0.6	0.25	0.14	0.12	0.045	0.05	0.01
	Mo	S	P	Ni	Cu	Co	Nb	B	Fe
Min	-	-	-	-	-	-	-	-	Bal.
Max	0.005	0.005	0.005	0.005	0.005	0.005	0.001	0.001	Bal.

2.2. Optical and electron microscopy

The as-received microstructure was characterised with a TESCAN Field Emission Gun Scanning Electron Microscope. An Electron Backscatter Diffraction (EBSD) map was created using an accelerating voltage of 20 keV with a step size of 0.11 µm. Data acquisition used Oxford Instruments AZtecHKL software and post-processing was carried out with Oxford Instruments HKL CHANNEL5 software. Optical macrographs of the tested specimens were taken on an Olympus SZX7 stereomicroscope.

2.3. Small punch testing

2.3.1. Small punch test rig and set-up

Testing was carried out on UKAEA's ODIN high temperature-test rig manufactured by Phoenix Materials Testing Ltd, Dudley; with a 20 kN actuator and 17-litre capacity chamber, see Fig. 1(a). Heating of the specimen was performed using an infra-red (IR) heating system that surrounds the dies. The temperature was measured via type N thermocouples that are inserted into holes in the upper die, resting close to the specimen and held in place with high-temperature wire tied around the die. The dies are made from H39 WM steel alloy.

2.3.2. Small punch creep testing of Eurofer97

Cylindrical discs of Eurofer97 with 8 mm diameter were cut by Electrical Discharge Machining (EDM), initially to a thickness of approximately 0.75 mm, with the longitudinal axis of the disc parallel to the short-transverse direction of the plate. The discs were then mechanically thinned to 0.5 ± 0.05 mm with a finish of P1200 grit from SiC paper, as in accordance with the CEN Workshop Agreement CWA 15627 [14]. Specimens were comprised from only material within the central 3 mm region of the 6.5 mm thick Eurofer97 plate to maximise microstructural homogeneity between specimens.

The upper die was tightened to a torque of 10 Nm, also in accordance with CWA 15627. All testing was carried out at 550°C and using a load of 675 N, after initial ramp up from 0 N at 2.5 N/s. However, specimens were tested in an air or inert-argon gas environment. The punch used was Ni-based Nimonic 90 alloy (Special Metals, UK) [15], with a hemispherical tip of 2.5 mm diameter, Fig. 1(b). The dies were machined with additional holes to allow the flow of air and argon to and from the region within the die and around the specimen, see Fig. 1(c). A different punch head was used for each environment, though both were ostensibly identical Nimonic punches.

For testing in the argon environment, the sealed chamber was purged with argon gas at a rate of 5 litres per minute (lpm) for 20 minutes at room temperature. The rate was then held at 1 lpm while the system heated up to 550°C. Then reduced to a low and steady flow rate <0.5 lpm. The argon testing also included four getters, small high-purity discs of titanium, placed in the chamber to react with oxygen remaining in the chamber.

After the test temperature was reached, all testing, regardless of environment was held at temperature for an hour before testing started, to allow the components of the testing rig to thermally equilibrate. The measuring apparatus was zeroed after this period before the test started.
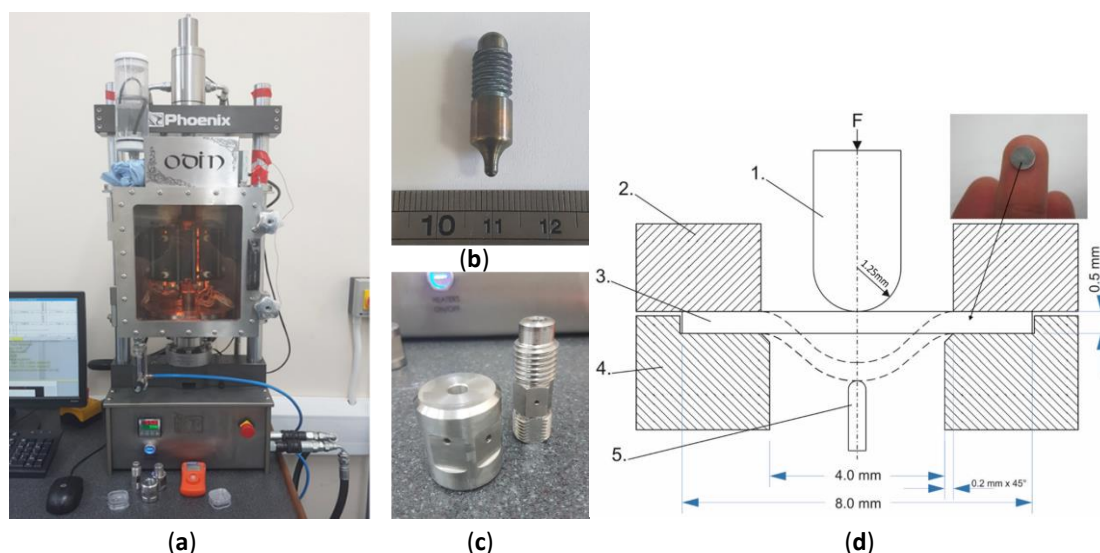

Figure. 1. (a) ODIN small punch test rig; **(b)** Nimonic punch head used for testing. **(c)** H39 WM steel dies used for testing. The holes used for gas circulation and for housing the thermocouples can be seen. The upper die is on the left; **(d)** Schematic diagram of the test set-up. 1. Punch head, 2. Upper die, 3. Specimen, 4. Lower die, 5. Extensometer [14].

3. Results

3.1. Microstructural characterisation

A representative EBSD map of the as-received microstructure of Eurofer97, along the Rolling Direction–Long-Transvere (RD-LT) plane, is given in Fig. 2. This is the same face as is the circular face of the thin disk specimens. Thick black lines represent high-angle (>10°) grain boundaries and thin lines represent low-angle (>2°) grain boundaries. Noise reduction was applied in order to allow delineation of these boundaries. Zero solutions were replaced with the most common orientation found amongst their four nearest neighbours [16]. Eurofer97 contains a range of grain sizes typically 1-5 µm with no strong preference for orientation. The plane perpendicular to this map would be parallel to the 500 µm longitudinal axis of the specimen. Since this is perpendicular to the RD, we would

expect grains to be no larger than those in Fig. 2. Therefore, the through specimen thickness should contain at least 100 grains and constitute a representative testing volume.
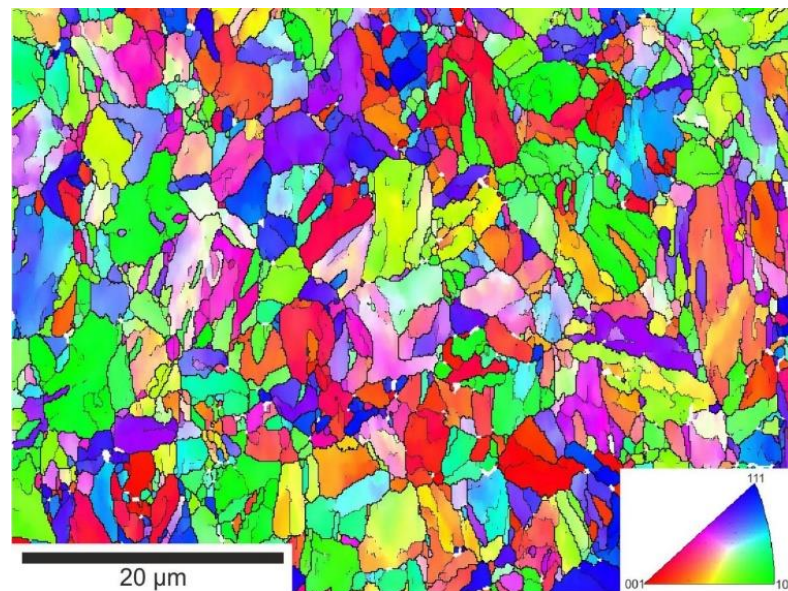

Figure 2. EBSD map of the Eurofer97 (RD-LT) and the associated Inverse Pole Figure (IPF). The map is of the RD-LT plane i.e. parallel to the top face of the plate. The reference axis (001) for the IPF is out of the plane of the page.

3.2. Small punch creep behaviour

The small punch creep behaviour was investigated by assessing three criteria: time to failure, deflection at failure and the minimum deflection rate. Deflection (δ) is defined as the change in position of the extensometer against the base of the sample as the specimen is deformed. Selecting start and end points of the secondary creep phase is somewhat arbitrary and therefore determining a reliable average creep rate is difficult. The minimum creep rate is a useful alternative; and was calculated using the following method. Utilising OriginPro software, the data range was set to exclude the majority of the primary and tertiary creep phases. A high order (9th) polynomial was then fitted to this data range. The differential ($d\delta/dt$) of this polynomial was calculated and plotted. The y-axis now represents the deflection rate and it follows that the minimum value is the minimum deflection rate. Fig. 3(d)-(f), illustrates the process used to derive the minimum deflection rates from the SPCT curves. Representative SPCT curves from both air and argon tests are also given, Fig. 3(a), along with the macrographs of the associated tested specimens, Fig. 3(b) and (c), respectively.
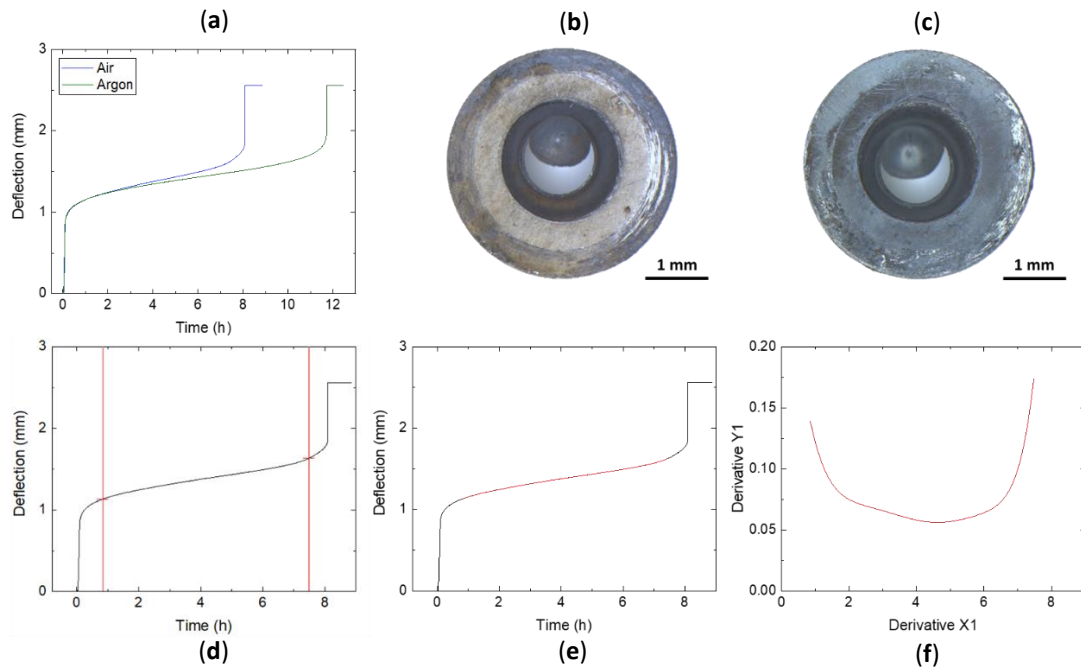
Figure 3. (a) Representative SPCT curves for the air and argon test environments; **(b)** Associated air tested specimen; **(c)** Associated argon tested specimen; **(d)** Representative example of the data range over which a polynomial was fitted in order to attain the minimum deflection rate; **(e)** The fitted polynomial, shown in red; **(f)** graph of the first order differential of the fitted polynomial. The minimum of this curve represents the minimum deflection rate; **(d)-(f)** are from the same air test data.

The results of the times to failure, minimum creep rate and deflection at failure are shown in Fig. 4 and Table 2. The results indicate that there is an effect of test environment on the small punch creep behaviour. The mean values for the time to failure and deflection at failure are larger for the argon test environment, while smaller for the minimum deflection rate. The error bars for the two environments do not overlap, implying that these differences in mean values are significant and therefore due to the environment rather than chance arising from scatter in the data. The error bars in the graphs represent the standard error of the mean.
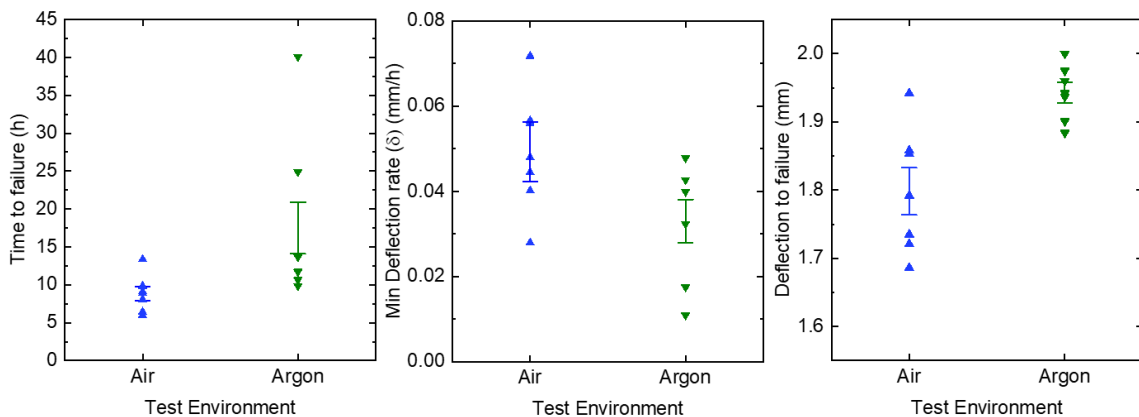
Figure 4. Graphs of results of the effect of test environment on **(a)** Time to failure; **(b)** Minimum deflection rate; **(c)** Deflection at failure. The error bar shown in each graph is the standard error of the mean.

Table 2. Summary of the SPCT results for air and argon test environments. The uncertainty is the standard error on the mean.

Environment	Time to failure (h)	Minimum deflection rate (mm/h)	Deflection to failure (mm)
Air	8.8±0.93	0.049±0.0070	1.80±0.034
Argon	18±3.4	0.033±0.0051	1.940±0.015

The results as a function of test number were plotted in order to help discern whether other factors may be influencing the results along with the different test environments; particularly since there appeared to be a relatively large range in the times to failure. See Fig. 5.
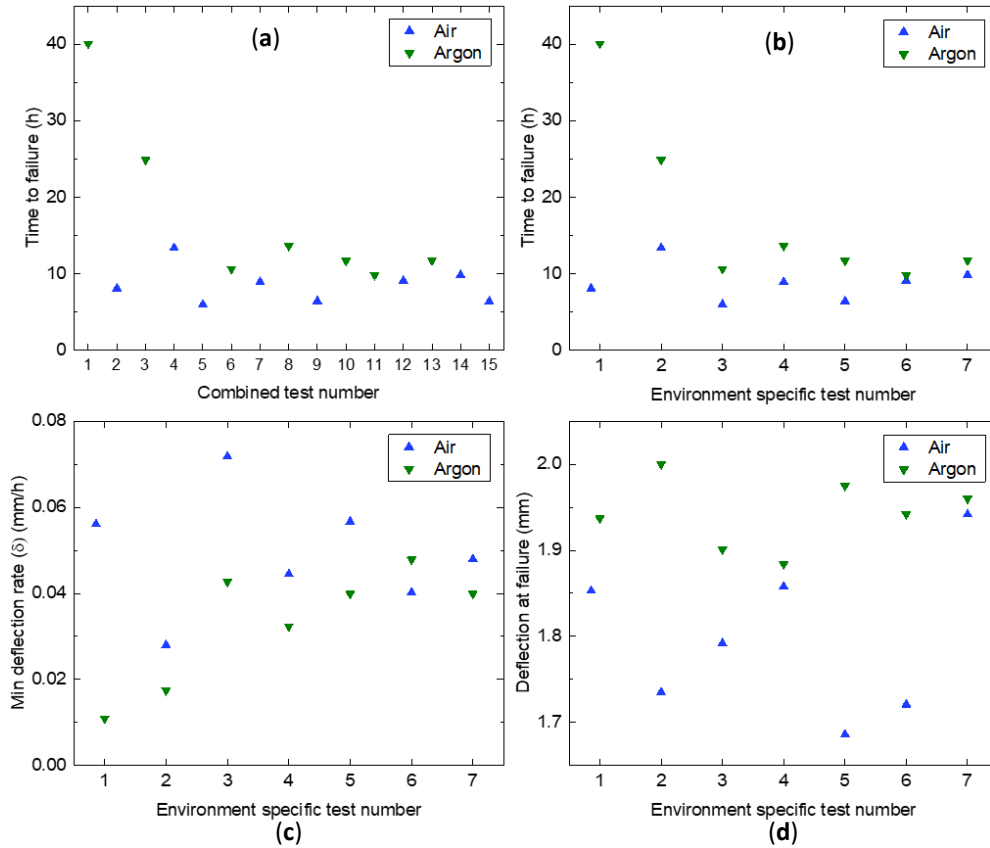
Figure 5. SPCT results as a function of their test number: **(a)** Time to failure as a function of combined test number, i.e. order the testing was carried out regardless of test environment; **(b)-(d)** as a function of the environment test number, i.e. counting only tests from the specific test environment; **(b)** Time to failure; **(c)** Minimum deflection rate; **(d)** Deflection at failure.

Fig. 5 does reveal a seemingly non-random evolution in the time to failure and minimum deflection with progressive test number for the argon environment. The first two argon tests have a time to failure that is much greater than the subsequent majority, with the first test being again significantly greater than the second. This effect is mirrored in the minimum deflection rate – with lower rather than higher values. The deflection at failure appears to be largely independent from this probable effect. The tests in air either do not share this time to failure evolution, or may do, but to a much lesser extent that one cannot discern from natural variation in the data. It is important to consider, however, that for the first two 'anomalous' argon tests, statistical variation cannot be ruled out and any systematic cause may simply be an illusion. Though due to the scale of this difference it seems unlikely.

The tests were deliberately run approximately alternately between argon and air. Therefore, any systematic change to the hydraulics, measuring equipment etc. of the rig seems unlikely. Likewise, the same dies were used in both environments and so any systematic change to the dies, either by oxidation, mechanical or dimensional changes seems implausible to be the cause – at least as the dominant cause.

Separate punch heads were used for each of the environments and therefore this is likely to have played a dominant role in the large decrease in time to failure observed in argon with successive testing. It is possible that a progressive change in oxidation could have caused a change in the observed mechanical behaviour, most likely due to a change in the coefficient of friction between the punch and the test specimen [12,17-19]. Nimonic 90 is an oxidation resistant alloy, so more specifically the bulk of the punch would not be oxidised but a chromate (Cr_2O_3) scale [20,21] would form on the surface. Therefore, the punch head should not experience significant softening, but the coefficient of friction would presumably change. Fig. 6 shows images of an unused punch (a) and the punch after a certain number of tests in argon (b)-(c). It is clear from the surface colour of the punch that it has oxidised despite the inert atmosphere. It should be noted that the chamber remained sealed and argon remained flowing until the chamber had cooled to [near] room temperature. Therefore, a post-test influx of air into the hot chamber with the still hot punch, is not the cause of the oxidation, but rather due to a small quantity of oxygen in the chamber despite the argon purge. It should also be noted that one preliminary test in argon was conducted using the same punch head, but the test used a different set of dies and therefore this test was not included in the data or in the test number counting.
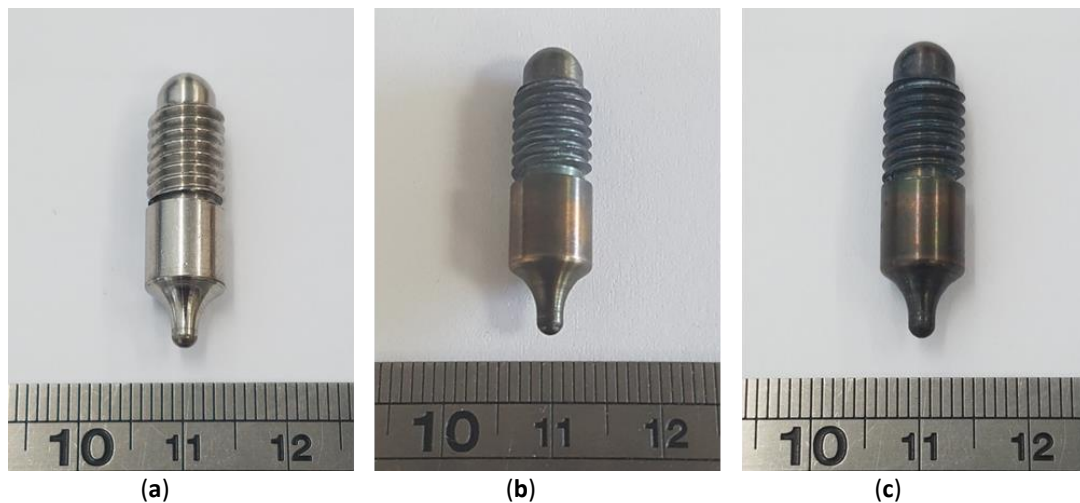

Figure 6. Nimonic 90 punch head: **(a)** Before testing; **(b)** After argon test no. 3; **(c)** After argon test no. 7.

Again, assuming that the sharp decrease in the argon time to failure is not down to natural variance in the data, a plausible explanation is that the relatively non-oxidised punch head in the first two argon tests, more notably for the first, has a different creep mechanism and significantly slower affiliated deflection rate. While testing in air, at high temperature, oxidation could happen quickly, and we would expect the punch to be near fully oxidised in the first test or perhaps before the test could begin during the equilibration stage. This would explain why the air test results were much more stable with successive testing. By test no. 3 for argon, the data suggests that the effect of changes to the punch head has stabilised. Therefore, the data has been re-represented with the first two argon tests omitted. This represents the results were the air and argon punch heads would be in a similar and pseudo-stable oxidation state, in which a comparison of the test environment's effect on tested specimens only can be investigated: see Fig. 7 and Table 3.
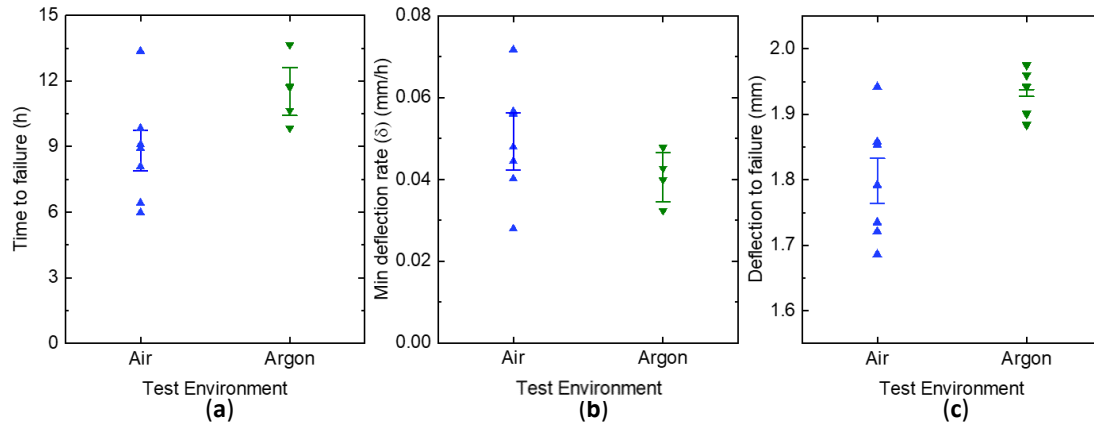
Figure 7. With the first data for the first two argon tests removed - graphs of results of the effect of test temperature on **(a)** Time to failure; **(b)** Minimum deflection rate; **(c)** Deflection at failure. The error bar shown in each graph is the standard error about the mean.

Table 3. Summary of the SPCT results for air and argon test environments after first two argon tests excluded. Again, the uncertainty is the standard error on the mean.

Environment	Time to failure (h)	Minimum deflection rate (mm/h)	Deflection at failure (mm)
Air	8.8±0.93	0.049±0.0070	1.80±0.034
Argon	12±1.1	0.041±0.0060	1.932±0.0053

The results now show that the test environment still has a significant effect on the small punch creep behaviour. The time to failure and the deflection at failure are significantly greater when Eurofer97 was tested in the argon atmosphere. The minimum deflection rate was slightly greater in air but not above the margin of error.

4. Discussion

Literature available to compare the results with is limited. Kobayashi et al. did not compare air with argon environments for SPCT, but rather air with vacuum and observed a significantly greater time to failure when the specimens were tested in vacuum [11]. This was attributed to the formation of an oxide scale that formed which for air i) introduced a significantly larger volume of the sample that was softened by oxidation and ii) lowered the coefficient of friction with the punch head. Modelling has shown that friction can play a significant role in determining behaviour of SPCT [17-19] with time to failure increasing with increasing coefficient of friction. It is possible that the lack of gas in the chamber may have also influenced the results due to the lubricating effect of the gas also affecting the coefficient of friction. Nishioka et. al observed that SPCT with a low argon flow experienced shorter times to failure than when a high flow rate was used [12]. It was also observed that different oxide films were formed under these conditions: an Fe-rich oxide for the low flow rate and a Cr-rich oxide film for the high flow rate. These reduced and increased the coefficient of friction of the specimen, respectively, which caused the difference in rupture times. Both aforementioned studies used 2.25Cr-Mo low alloy steel. While these are not too similar to the Eurofer97 of this study, similar mechanisms appear to be occurring. Auger et. al [22], working on 9% Cr T91 steel, also observed that a "low oxidised" condition produced a Cr_2O_3 surface oxide, while those that were "air-oxidised" produced Fe_2O_3 on the surface.

Optical macrographs of the tested specimens showed that the specimens tended to have a different appearance depending on which test environment was used. The optical macrographs are shown in Fig. 3(b)-(c) and Fig. 8. The air tested specimens tended to have a 'flaky' grey scale while the argon tested specimens tended to be more dominated by a better adhered blue coloured scale. The air tested specimen in Fig. 3(b) may be misleading in its relatively smooth appearance and probably represents a specimen where most of the scale has flaked off. Further macrographs are provided in Fig. 8. The grey flaky scale is presumably iron oxide while the bluer scale is chromium oxide scale. Future investigations will aim to confirm this and also investigate the through specimen thickness of

the oxidation layers created during testing. The oxidation resistant Nimonic 90 punch has high Cr% and low Fe% composition and so it is unlikely that a different oxide layer would form for the different test conditions on the punch [15,20,21]. The similar hue of the punches after exposure to each of the high temperature environments supports this assumption.
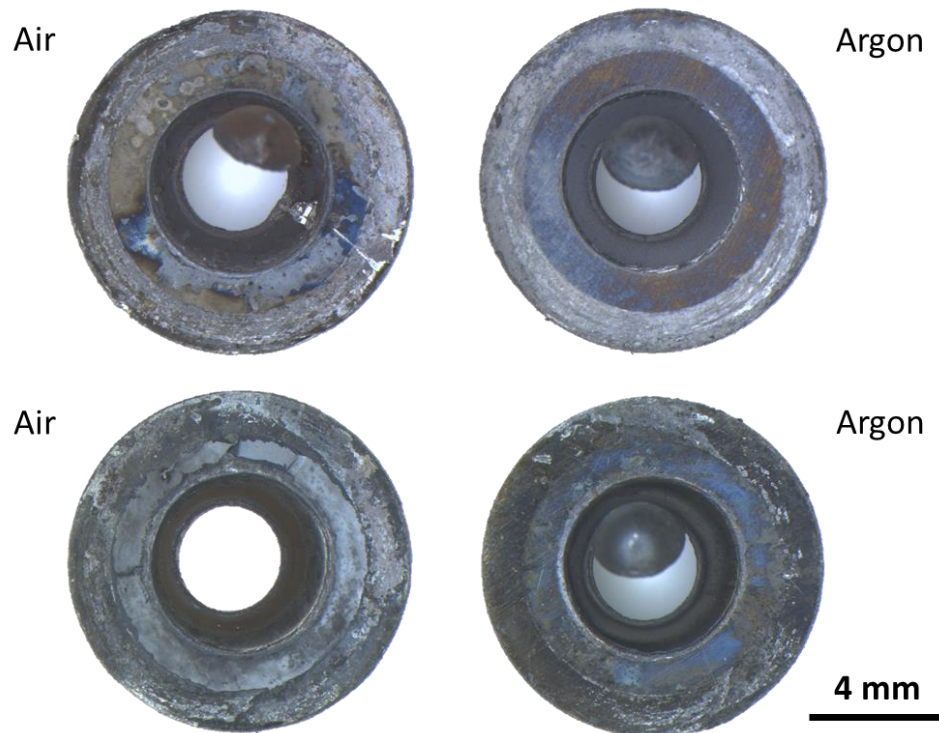

Figure 8. Optical macrographs of specimens tested in air (left) and argon (right).

It is therefore presumed that the difference observed in SPCT behaviour when using an air or argon environment can be largely attributed to differences in surface oxides formed on the specimens during high temperature testing, which alter the coefficient of friction between the punch head and the specimen. The influence of the oxidised material, with presumably degraded mechanical properties, has not been investigated yet in this study, but this might also play a significant role. Progressive change to the observed time to failure and minimum deflection rate is attributed to evolution of an oxidised surface on the punch head, which also affects the coefficient of friction between punch and sample. However, this effect appears to stabilise. The results of Fig. 7 and Table 3 are therefore considered much more representative of the true SPCT behaviour and of the scale of the difference between measured parameters from argon and air testing.

The failure mechanisms may also be influenced by the testing environment, which in turn could contribute to the differences in parameters measured in this study. Although relatively little work has investigated the failures involved in SPCT [23,24], particularly with regard to the influence of oxidation, it seems plausible that micro-cracks in the brittle oxidised material near the surface would be created and propagated much more easily than the more ductile un-oxidised steel during bending and the membrane-stretching of the material around the punch. The more brittle nature could in part contribute to the reduced time to failure and deflection to failure, and also the significantly greater scatter seen in the air-tested data. Oxidation of the fracture surfaces themselves, likely occurs too slowly to significantly influence the behaviour [24]. Further investigations, primarily scanning electron micrography, are required to make any conclusions on the differences and causes of the failure mechanisms. The scatter in both environments is significant but this is also a common feature of uniaxial creep and stress-rupture testing.

The results do have significant implications for high temperature SPCT. The test environment, and control of the test environment as Nishioka et. al demonstrated [12], must be considered for standardisation of the technique. SPCT data, especially at relatively high temperatures, will be difficult to compare when a different environment is used or when the same environment is used but at a range of different temperatures. A drop in mechanical performance with temperature may be partly an illusion due to oxidation. Testing in air, where the percentage of the

sample that becomes oxidised may become relatively high, may also confuse interpretation of the data particularly as different materials will oxidise differently and at different rates. In this regard, testing in argon may be superior to air at high temperature. The argon data also appears to produce a lower scatter in the data – allowing more reliable interpretation and less test material to be required.

The punch head selection and condition are also important considerations for standardisation and comparative analysis in SPCT. Regardless of test environment, different punch materials will exhibit different coefficients of friction which have been shown to impact time to failure in models. If changes to the punch with progressive testing can impact the results, as is suggested in this study, this must be taken into consideration as part of any study involving SPCT, and likely SPT [25,26]. Either by stabilising changes to the punch by forming a scale on the punch before testing by heating in air or selecting a different material for the punch that is hard, creep resistant, and oxidation resistant without the formation of a scale, such as diamond.

Along with investigations into the bulk and surface oxidation of the tested samples, future investigations will include fractography to analyse failure modes and further testing to ascertain whether the change in minimum deflection rate with test environment was significant. Much of the future testing will be conducted in vacuum. This will allow the further study of a different test environment, but also an opportunity to observe whether the progressive change in SPCT behaviour will be replicated in a different low oxygen environment.

5. Conclusions

The results show that the testing environment can have a significant effect on the small punch creep behaviour. Both time to failure and deflection at failure increased when testing in the argon environment compared to the air environment by a factor of approximately 30 and 7%, respectively. These values are calculated from the data with the initial two argon tests omitted. The minimum deflection rate also decreased in the argon environment compared to testing in air, but not to a significant degree. The investigations also strongly imply that the testing environment can affect the punch head which in turn can influence the outcomes of the testing.

References

1. Jednorog, S.; Laszynska, E.; Batistoni, P.; Bienkowska, B.; Cufar, A.; Ghani, Z.; Giacomelli, L.; Klix, A.; Loreti, S.; Mikszuta, K. and Packer, L. Activation measurements in support of the 14MeV neutron calibration of JET neutron monitors. *FusEngDes* **2017**, 125, 50-506, https://doi.org/10.1016/j.fusengdes. 2017.10.024.
2. IFMIF. Available online: http://www.ifmif.org/?page_id=114 (accessed on 30 01 2018).
3. Knaster, J.; Garin, P.; Matsumoto, H.; Okumura, Y.; Sugimoto, M.; Arbeiter, F.; Cara, P.; Chel, S.; Facco, A.; Favuzza, P. and Furukawa, T. Overview of the IFMIF/EVEDA project. *Nucl. Fusion* **2017**, 57(10), 102016, https://doi.org/10.1088/1741-4326/a6a6a.
4. Arbeiter, F.; Abou-Sena, A.; Averhals, J.; Böttcher, T.; Chen, Y.; Dolensky, B.; Fischer, U.; Heinzel, A.; Heinzel, V.; Heupel, T. and Jacquet, P. Design description and validation results for the IFMIF High Flux Test Module as outcome of the EVEDA phase. *Nucl. Mater. Energy* **2016**, 9, 59-65, https://doi.org/10.1016/j.nme.2016.04.013.
5. Bruchhausen, M.; Holmström, S.; Simonovski, I.; Austin, T.; Lapetite, J.M.; Ripplinger, S. and de Haan, F. Recent developments in small punch testing: Tensile properties and DBTT. *Theoretical and Applied Fracture Mechanics* **2016**, 86, 2-10, https://doi.org/10.1016/j.tafmec.2016.09.012.
6. Bueno, L.D.O.; Sordi, V.L. and Marino, L. Constant load creep data in air and vacuum on 2.25 Cr-1Mo steel from 600° C to 700° C. *Mat. Res.* **2005**, 8(4), 401-408, http://dx.doi.org/10.1590/S1516-14392005000400008.
7. Abduluyahed, A.A. and Kurzydłowski, K.J. Tensile properties of a type 316 stainless steel strained in air and vacuum. *Mater. Sci. Eng., A.* **1998**, 256(1-2), 34-38, https://doi.org/10.1016/S0921-5093(98)00841-7.
8. Aning, K. and Tien, J.K. Creep and stress rupture behavior of a wrought nickel-base superalloy in air and vacuum. *Mater. Sci. Eng.* **1980**, 43(1), 23-33, https://doi.org/10.1016/0025-5416(80)90203-7.

9. Kim, W.G.; Lee, G.G.; Park, J.Y.; Hong, S.D. and Kim, Y.W. Creep and Oxidation Behaviors of Alloy 617 in Air and Helium Environments at 1173 K. *Procedia Eng.* **2013**, 55, 819-822, https://doi.org/10.1016/j.proeng.2013.03.337.

10. Nakata, T.; Komazaki, S.I.; Kohno, Y. and Tanigawa. H. Development of a small punch testing method to evaluate the creep property of high Cr ferritic steel: part I—effect of atmosphere on creep deformation behavior. *Mater. Sci. Eng., A.* **2016**, 666, 54-60. https://doi.org/10.1016/j.msea.2016.03.100.

11. Kobayashi, K.I.; Kaneko, M.; Koyama, H.; Stratford, G.C. and Tabuchi, M. The influence of both testing environment and fillet radius of the die holder on the rupture life of small punch creep tests. *Journal of Solid Mechanics and Materials*

12. Nishioka, T.; Uemura, H.; Ohsawa, T. and Sawaragi, Y. Effects of specimen surface condition and atmosphere on small punch creep property of low alloy steel. *Journal of the Society of Materials Science* **2011**, 60(2), 146-152, https://doi.org/10.2472/jsms.60.146.

13. Möslang, A.; Diegele, E.; Klimiankou, M.; Lässer, R.; Lindau, R.; Lucon, E.; Materna-Morris, E.; Petersen, C.; Pippan, R.; Rensman, J.W. and Rieth, M. Towards reduced activation structural materials data for fusion DEMO reactors. *Nucl. Fusion* **2005**, 45(7), 649, https://doi.org/10.1088/0029-5515/45/7/013.

14. CWA 15627: Small Punch Test Method for Metallic Materials; CEN, Brussels, 2007.

15. Special Metals NIMONIC alloy 90. Available online: http://www.specialmetalswiggin.co.uk/products/nimonic-alloy-90 (accessed on 24 04 2018).

16. *Oxford Instruments CHANNEL 5 User Manual;* Oxford Instruments, Oxford, 2010, pp. 297.

17. Nakata, T.; Komazaki, S.I.; Kohno, Y. and Tanigawa, H. Development of a small punch testing method to evaluate the creep property of high Cr ferritic steel: Part II–Stress analysis of small punch test specimen by finite element method. Mater. Sci. Eng., A. 2016, 666, pp.80-87, https://doi.org/10.1016/j.msea.2016.03.102.

18. Cortellino, F.; Sun, W. and Hyde, T. On the effects of friction modelling on small punch creep test responses: a numerical investigation. J. Strain. Anal. Eng. Des 2016., 51(7), 493-506, https://doi.org/10.1177/0309324716655661.

19. Dymáček, P.; Seitl, S.; Milička, K. and Dobeš, F. Influence of Friction on Stress and Strain Distributions in Small Punch Creep Test Models. *Key Eng. Mater.* **2010**, 417, 561-564, https://doi.org/10.4028/www.scientific.net/KEM.417-418.561.

20. Sinharoy, S. and Narasimhan, S.L. Oxidation behavior of two nickel-base superalloys used as elevated temperature valves in spark ignited engines and diesel exhaust recirculation (EGR) applications. *Superalloys* **2004**, 623-626.

21. Sato, A.; Chiu, Y.L. and Reed, R.C. Oxidation of nickel-based single-crystal superalloys for industrial gas turbine applications. *Acta Mater.*, **2011,** 59(1), 225-240, https://doi.org/10.1016/j.actamat.2010.09.027.

22. Auger, T.; Serre, I.; Lorang, G.; Hamouche, Z.; Gorse, D. and Vogt, J.B. Role of oxidation on LME of T91 steel studied by small punch test. *J. Nucl. Mater* **2008**, 376(3), 336-340, https://doi.org/10.1016/j.jnucmat.2008.02.076.

23. Nakata, T.; Komazaki, S.I.; Kohno, Y. and Tanigawa, H. Development of a small punch testing method to evaluate the creep property of high Cr ferritic steel: part I—effect of atmosphere on creep deformation behavior. *Mater. Sci. Eng., A.* **2016**, 666, 54-60, https://doi.org/10.1016/j.msea.2016.03.100.

24. Cortellino, F. Experimental and numerical investigation of small punch creep test, University of Nottingham, UK, November 2015.

25. Prakash, R.V. and Arunkumar, S. Influence of Friction on the Response of Small Punch Test. *Transactions of the Indian Institute of Metals* **2016**, 69(2), 617-622, https://doi.org/10.1007/s12666-015-0769-4.

26. Pathak, K.K.; Dwivedi, K.K.; Shukla, M. and Ramadasan, E. Influence of key test parameters on SPT results. *Indian journal of engineering and material sciences* **2009**, 16, 385-389.

SP creep properties of Gr.91 boiler pipings service-exposed in different USC power plants

S. Komazaki [1],*, K. Obata [1], M. Tomobe [2], M. Yaguchi [2] and A. Kumada [3]

[1] Kagoshima University
[2] Central Research Institute of Electric Power Industry
[3] Kobe Material Testing Laboratory Co., Ltd.
* Correspondence: komazaki@mech.kagoshima-u.ac.jp; Tel.: +81-99-285-8245

Abstract: The small punch (SP) testing technique was applied to five heats of Gr.91 steel, which had been actually used for boiler pipings in different USC power plants for long periods of time to investigate the applicability of this technique to the assessment of heat-to-heat variation of creep property. The experimental results revealed that the SP creep rupture strength and deformation behavior were quite different depending on the heat. Those differences in SP creep property, which could not be evaluated by hardness measurement, were qualitatively similar to those in standard uniaxial creep one. It was expected that the SP creep testing technique was applicable to the assessment of heat-to-heat variation for in-service boiler pipings.

Keywords: small punch creep test; USC power plant; boiler pipings; heat-to-heat variation; Gr.91 steel

1. Introduction

9-12%Cr heat resistant ferritic steels, such as Gr.91, Gr.92 and Gr.122 steels, have been widely used in ultra-super critical (USC) power plants, because of their superior high temperature strength and resistance to corrosion/oxidation. But, premature failures at their welded joint have been a worldwide issue in recent years. This failure occurs at the outer edge of the heat affected zone (HAZ), and it is well known as "Type IV creep damage". It has been recently revealed by the co-author that the creep strength of welded joint is closely associated with that of base metal. That is to say, when the base metal has an insufficient strength, the strength of its welded joint is also low leading to unexpected premature failure. Figure 1 [1] shows the comparison of creep rupture lives of two different heats of Gr.91 steel (base metal and welded joint), which had been actually used for a long period of time in USC plants A and B. As can be clearly seen in this figure, the Gr.91 steel of B plant has much lower creep rupture strength than that of A plant for both of base metal and welded joint. The creep rupture life of welded joint removed from B plant is only a fifth of that removed from A plant, and the difference is more pronounced for the base metal. This result indicates that it is very important to assess variation in creep strength of in-service pipings, i.e., heat-to-heat variation, and the creep strength of welded joint may be roughly estimated if that of base metal is available.

In the late 1970s and early 1980s, the small punch (SP) testing technique using a miniaturized disk-type specimen was developed for determining post-irradiation mechanical properties. This technique has been widely used for evaluating various material properties, such as tensile property, ductile-brittle transition behavior, fracture
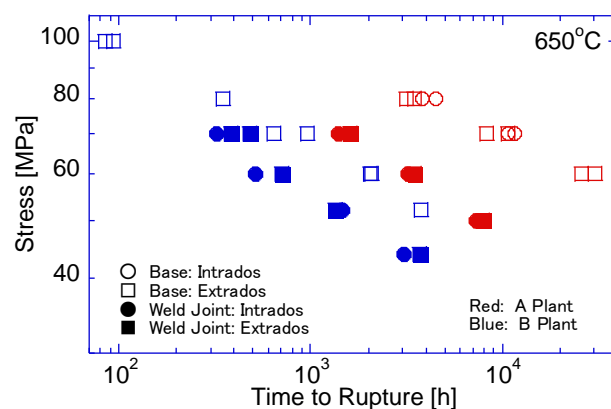

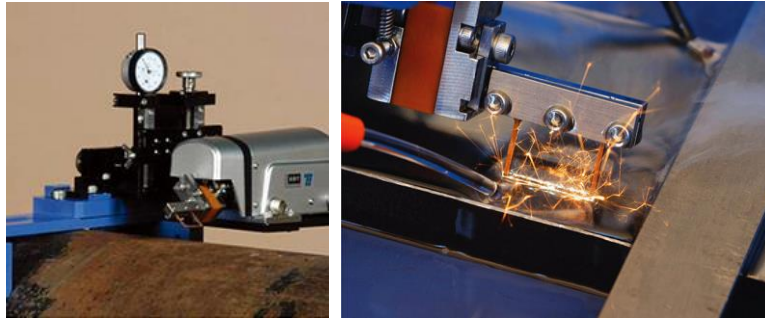**Figure 1**. Comparison of creep test data of long-term used Gr.91 steels [1].

Figure 2. On-site electric discharge sampling equipment with copying mechanism.

toughness, hydrogen embrittlement, and stress corrosion cracking. It has also been successfully employed in evaluating high temperature creep property. Since this SP creep test requires only a small amount of sample, the damage caused by removing the sample from components can be minimized. In recent years, a novel on-site electric discharge sampling equipment with copying mechanism has been also developed for this purpose (Figure 2 [2]). This equipment is capable of taking a small plate-type sample as thin as 1 mm from the component's surface.

In this study, the creep property of Gr.91 steel was measured by the SP testing technique for investigating the applicability of this technique to the assessment of heat-to-heat variation of creep strength. The SP creep test was carried out at the temperature of 650°C and under the loads of 190, 230, 300 N using the Gr.91 steel base metals removed from five different boiler pipings, which had been actually used in the USC power plants for a long period of time.

2. Materials and Experimental Procedures

Table 1. Nominal dimensions and operating conditions of Gr.91 boiler pipings.

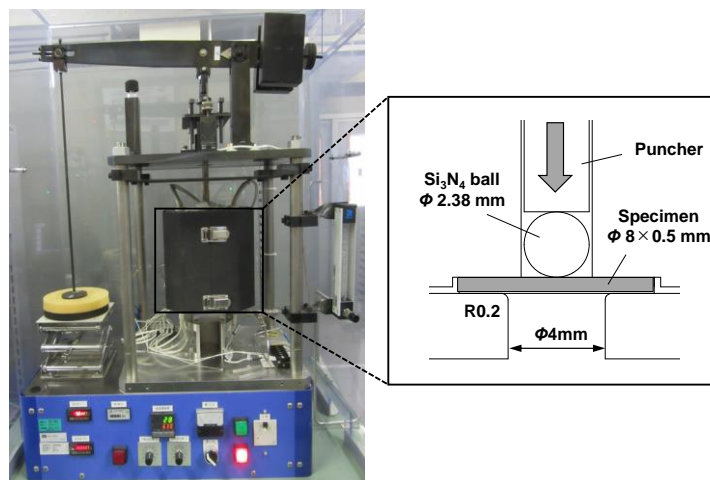|	Nominal dimensions	Operating conditions
Plant A	Elbow pipe (Plate) $\Phi 711 \times t 39$ mm	
Plant B	Elbow pipe (Plate) $\Phi 457 \times t 22$ mm	Temp.: 593～608 ℃
Plant M	Straight pipe (Plate) $\Phi 864 \times t 43$ mm	Pressure: 3.9～4.7 MPa
Plant N	Elbow pipe (Plate) $\Phi 610 \times t 29$ mm	Time: 54000～142000 h
Plant T	Straight pipe (Plate) $\Phi 864 \times t 51$ mm	

Figure 3. SP creep test apparatus and loading and specimen support configuration for SP creep test.
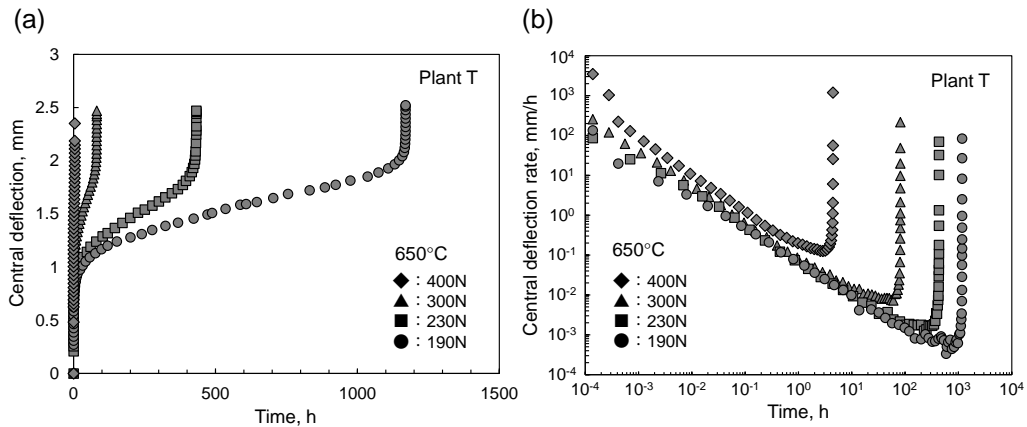
Figure 4. SP creep test results obtained from heat N: (a) Time-central deflection curve; (b) Time-central deflection rate curve.

The materials used in this study were five different heats of Gr.91 steel (base metal), which had been actually used for boiler piping in different USC power plants (plants A, B, M, N, T) for a long period of time. Their nominal dimensions and operating conditions are summarized in Table 1. There was almost no difference in hardness between them in spite of significant difference in creep property.

The small disk-type specimen (8 mm in diameter) was prepared for the SP creep test. Both sides of the specimen were carefully ground to a thickness of 0.5 mm with a thickness tolerance of 0.005 mm. The specimen surfaces were finally polished using 0.3 μm Al$_2$O$_3$ solution. As schematically illustrated in Figure 3, the specimen was tightly clumped between the upper and lower dies, and a certain constant load was applied on the center of specimen through a puncher and Si$_3$N$_4$ ball (2.38 mm in diameter). The central deflection was continuously measured by recording the displacement of compression rod using a linear variable differential transformer (LVDT). The SP creep test was carried out at the temperature of 650°C and under the loads of 190, 230, 300, 400 N. In order to avoid severe oxidation of the specimen, the test was performed in an argon gas atmosphere and the gas was continuously passed through during the test.

3. Results and Discussion

As examples of SP creep test result, the time-central deflection curves and the time-central deflection rate curves measured on the heat T (Gr.91 steel taken from the plant T) are given in Figure 4. As reported in the previous studies [3-5], the overall shape of curve is qualitatively similar to that obtained from standard uniaxial creep test, although the instantaneous deflection is significant at the time of initial load application in the SP creep test (Figure 4 (a)). This enormous deflection is attributable to the plastic bending deformation rather than the creep one. After the initial load application, the specimen experiences an instantaneous high stress due to small initial contact area
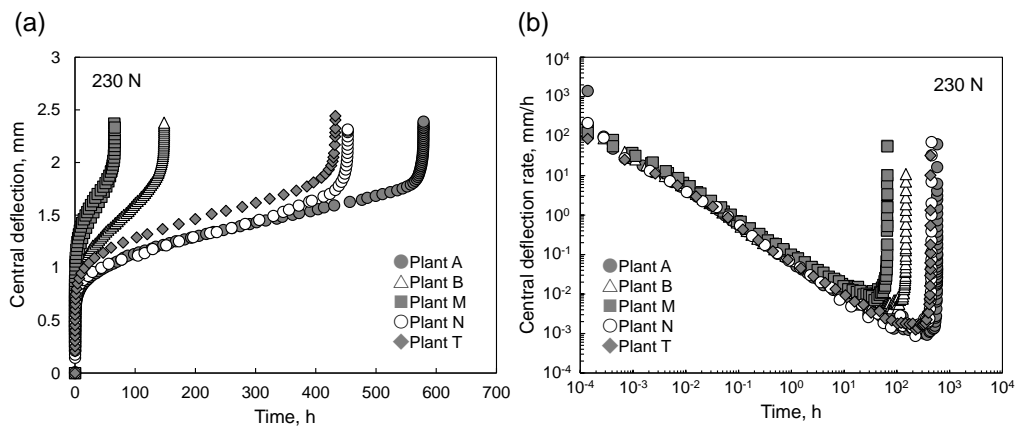

Figure 5. SP creep test results of heats A, B, M, N and T: (a) Time-central deflection curve; (b) Time-central deflection rate curve.
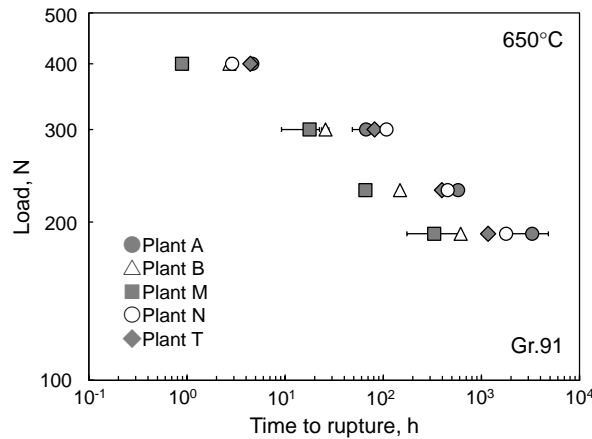
Figure 6. SP creep rupture test results of heats A, B, M, N and T.
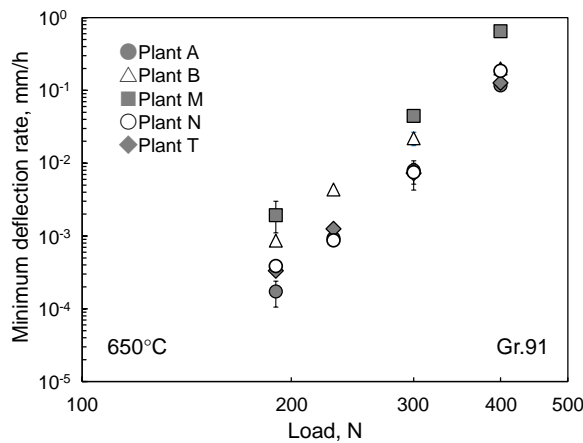

Figure 7. Minimum deflection rate measured on heats A, B, M, N and T.

between the specimen and ball. This high stress causes higher plastic deformation and thereby large bending deflection. It can be seen from the time-central deflection rate curves (Figure 4 (b)) that the deflection rate in the transient region shows no difference irrespective of test condition. This result means that the SP creep proceeds under similar deformation mechanism. However, the minimum deflection rate decreases with decreasing applied load, resulting in longer time to rupture. There is no significant difference in the central deflection to rupture, and it is around 2.5 mm irrespective of test conditions.

Figure 5 shows the time-central deflection curves and the time-central deflection rate curves of five heats measured at 650°C/230 N. As can be clearly seen, the rupture life is obviously different depending on the heat. The rupture lives of heats A and M were 579 and 65 h respectively, and the former was almost ten times as long as the latter. The rupture life of heat B is also relatively short compared with the heats A, N and T. Figure 6 shows the results of SP creep rupture tests, where the time to rupture is plotted against the applied load. The rupture lives of heats A, N and T are as a whole longer than those of heats B and M, and this difference seems to be more pronounced with decreasing applied load although some scattering results can be seen. At the lowest applied load of 190 N, the time to rupture of heat B is almost one order of magnitude shorter than that of heat A. The minimum deflection rate measured by the SP creep test is plotted against the applied load in Figure 7. The minimum deflection rate is different depending on heat, and, according to the time to rupture, the rate is also decreased in approximately the following ascending order: heats A, N, T, B and M. Figure 8 shows the relationship between the minimum deflection rate and the time to rupture. There is a unique correlation between those quantities irrespective of heats and test conditions, which is well known as Monkman-Grant correlation in uniaxial creep.

Figure 9 shows the SEM micrographs of specimens ruptured at 650°C/230 N. In all the specimens, the fracture occurred at a distance away from the center of specimen along the circumference, where the stress and strain had
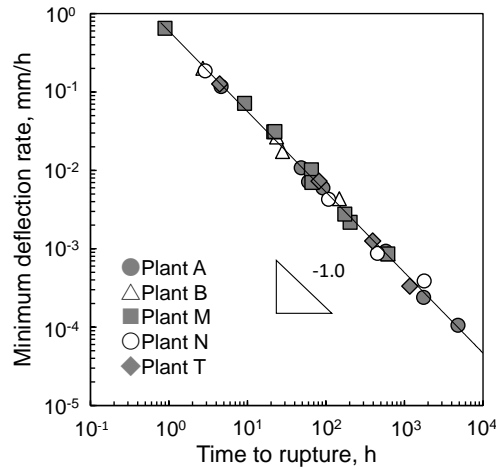
Figure 8. Relationship between minimum deflection rate and time to rupture.

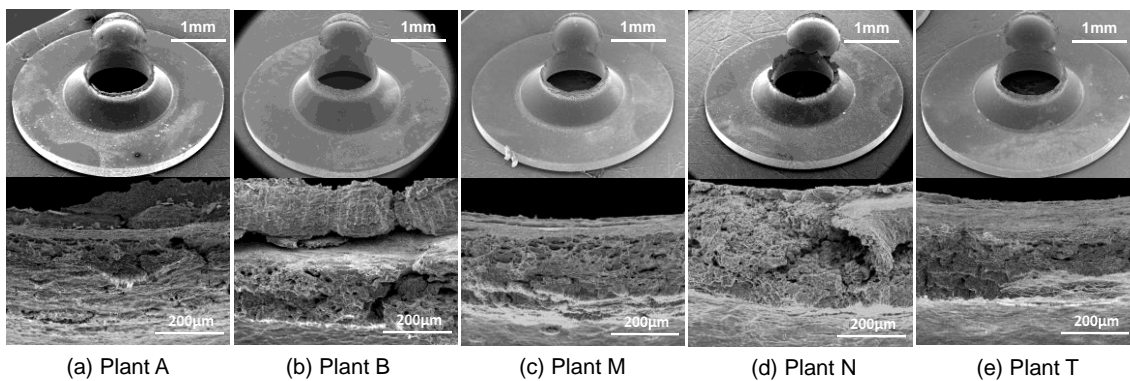| (a) Plant A | (b) Plant B | (c) Plant M | (d) Plant N | (e) Plant T |

Figure 9. SEM micrographs of SP creep specimens ruptured at 650°C/230 N.

maximum values. A cap-like part remained on the specimen without dropping out even after complete fracture. This macroscopic fracture morphology is a typical characteristic of ductile materials. No brittle fracture surface like an intergranular cracking was observed in all of the heats under the present test conditions. The fracture modes of all the specimens were a typical ductile transgranular with dimples, and there was no large difference in fracture irrespective of the steels and test conditions.

Those differences in SP creep strength and deformation properties between the five different heats are qualitatively similar to those in standard uniaxial creep ones [1, 6]. The results obtained in this study indicated that the SP creep testing technique was applicable to the assessment of heat-to-heat variation of creep property for in-service boiler pipings.

4. Summary

The small punch (SP) testing technique was applied to five heats of Gr.91 steel, which had been actually used for boiler pipings in different USC power plants (A, B, M, N, T) for long periods of time, to investigate the applicability of this technique to the assessment of heat-to-heat variation of creep property. The experimental results revealed that the SP creep rupture lives of heats A, N and T as a whole were longer than those of heats B and M. Additionally, according to the creep rupture strength, the minimum deformation rates were also decreased in approximately the following ascending order: heats A, N, T, B and M. Those differences in creep property, i.e., heat-to-heat variation were also measured by the standard uniaxial creep test, and there was a qualitatively good correlation between the results of SP and uniaxial tests. The results obtained in this study indicated that the SP creep testing technique was a strong tool for the assessment of heat-to-heat variation of creep property for in-service boiler pipings.

References

1. Yaguchi, M.; Nagai, S.; Sawada, K. and Kimura, K. "Microstructure and Creep Strength of Grade 91 Steel Used in USC Plants", Proc. 8th International Conference on Advances in Materials Technology, 2016, pp. 447-458.

2. Okamoto, K.; Kitagawa, H.; Kusumoto, J.; Kanaya A. and Kobayashi, T. "Development of Electric Discharge Equipment for Small Specimen Sampling", Int. Journal of Pressure Vessels and Piping, Vol. 86, 2009, pp. 633-636.

3. Parker, J.D.; and James, J.D. "Disk-Bend Creep Deformation Behaviour of 1/2Cr-1/2Mo1/4V Low Alloy Steel", Proc. Fifth Int. Conf. on Creep and Fracture Engineering Materials and Structures, Institute of Materials, 1993, pp. 651-660.

4. Milička, K.; Dobeš, F.; Ule, B. and Šustar, T. "Comparison of Time to Fracture in Small Punch and Conventional Creep Tests of 14MoV 6 3 Steel", Proc. Int. Conf. FRACTOGRAPHY '97, 1997, pp. 459-462.

5. Komazaki, S.; Hashida, T.; Shoji, T. and Suzuki, K. "Development of Small Punch Tests for Creep Property Measurement of Tungsten-Alloyed 9%Cr Ferritic Steels" Journal of Testing and Evaluation, 28, 2000, pp. 249-256.

6. Yaguchi, M.; Nakahashi, S. and Tamura, K. "Estimation of Creep Strength of Grade 91 Steel Welded Joint in Time Region over 100000 Hours", Proc. of the 2018 ASME on Elevated Temperature Applications of Materials for Fossil, Nuclear, and Petrochemical Industries, ETAM2018-6720, 2018.

FE modelling of small punch creep test using Kocks-Mecking-Estrin model

H.K. Al-Abedy*, I.A. Jones and W. Sun

Faculty of Engineering, University of Nottingham, Nottingham NG7 2RD, UK
* Corresponding Author: E-mail address: Hiydar.Al-Abedy@nottingham.ac.uk

Abstract: Small punch creep testing (SPCT) of thin disc specimens can be considered as a useful technique for determination of creep properties of exposed components of power generation. In this work, the Kocks-Mecking-Estrin (KME) constitutive model is used to simulate the small punch creep behaviour of the P91 steel at 600℃ based on a full set of experimental results. An implicit computational algorithm is developed based on the radial return mapping approach. Finite element analyses of a small punch creep test is carried out using ABAQUS software coupled with a UMAT material subroutine which has been developed by the authors. The small punch creep test results are compared with the corresponding results from modelling using the UMAT code. In addition, a comparison of results of the uniaxial tensile test for the P91 steel at 600℃ with the corresponding modelling results is also presented. The numerical results obtained have shown the model's versatility and good predictive capability for the P91 steel at 600℃.

Keywords: Small Punch Creep Test; Visco-Plasticity; Kocks-Mecking-Estrin Model; Finite Element Method

Nomenclature

b	The magnitude of dislocation Burgers vector	t	Time
C_{ijkl}	Stiffness matrix tensor	t_s	The thickness of small punch specimen
d	Punch diameter	T	Temperature
D	Receiving hole diameter	α	Constant
G	Shear modulus	μ	Friction coefficient
k	Boltzmann constant	$\varepsilon^p, \dot{\varepsilon}^p, \dot{\varepsilon}^c$	Plastic strain, plastic and creep strain rates
k_1	Dislocation storage constant	$\dot{\bar{\varepsilon}}^p$	Effective plastic strain rate
k_2	Recovery coefficient	$\dot{\varepsilon}_o$	Reference strain rate
k_{20}	Constant	$\dot{\varepsilon}_{ij}, \dot{\varepsilon}_{ij}^e, \dot{\varepsilon}_{ij}^c$	Total, elastic and creep strain rate tensors
m	The exponent of stress sensitivity	$\dot{\bar{\varepsilon}}^c$	Effective creep strain rate
M	Taylor factor	ρ	Dislocation density
n	Dynamic recovery exponent	σ_s	Saturation stress
$\mathbb{N}_{ij}$	Flow direction tensor	$\hat{\sigma}$	Flow stress
p	Creep exponent	$\tilde{\sigma}$	Effective stress
$P1$	Punch load magnitude	σ_{ij}	Stress Tensor
$P2$	Punch clamp magnitude	$\hat{\sigma}_{so}$	The saturation stress value properties
r	Corner radius of holder and support	θ_o	The initial strain hardening at the second stage.
S	The diameter of small punch specimen	ω	Time interpolation parameter
S_{ij}	Deviatoric stress tensor	Λ	Strain hardening constant

1. Introduction

In the last ten years, testing techniques using miniature samples have received increasing attention from the electricity generation industry companies for situations where the amount of material used in the test is limited. Published reviews for small specimen techniques have focused on their applications to conventional and nuclear plants [1, 2]. The removal of small amounts of material that are required for miniature specimen testing may not affect the structural integrity of in-service components. FE analysis of small specimen tests has the potential to make them more acceptable as a means of in-service testing of power plant materials [3, 4]. The ease of manufacture and testing of SPCT samples is one of the most important characteristics that distinguish it from other miniature testing

techniques. SPCT has one more advantage over other miniature testing techniques, namely that the SPCT can evaluate creep rupture [5].

Historically, more viscoplasticity models have been obtained and used to model the creep of materials. One of the most popular and well-received models is the Kocks–Mecking–Estrin (KME) model for secondary creep which has been developed for a wide range of materials [6]. The constitutive equation describes the viscoplasticity law relating to von Mises equivalent stress and plastic strain rate quantities for a given microstructure [7, 8].

Many numerical types of research have used constitutive models such as that proposed by Kachanov [9], which take account of the typical creep curve. Abendroth [10] used an FE approach but focused on the modelling guidelines: the geometry of the SPT, the convergence of the chosen mesh and the influence of friction coefficient on a load-deflection curve. Manahan et al. [11] developed a modified plasticity approach to simulate creep curves and compare them with the corresponding experimental data by minimising the sum of the squares to determine the parameters of the model. FE modelling of small punch specimens was also proposed by Shibli et al. to justify the conception of the creep behaviour [12]. Evans and Evans have made use of an extended visco-plasticity model of SPCT to take into account the effect of surface morphology [13].

In the present work, in an attempt to overcome some of the repeatability issues, the KME viscoplastic model is implemented without the need to carry out a uniaxial creep test. The results of the FE analysis for uniaxial tensile, small punch creep tests using the KME model are compared with experimental results to investigate the capability of the numerical model to provide creep behaviour for the small punch creep test.

This paper is structured as follows: the second section presents a brief reminder of the constitutive equations of the Kocks-Mecking-Estrin (KME) model which are based on macrostructure properties. The development of the user material subroutine (UMAT) is widely detailed in this section. The implementation of the constitutive model, in the implicit finite element code ABAQUS/Standard, is also presented. The third section details the material and microstructure of the P91 steel. The uniaxial tensile and small punch creep tests for the P91 steel at 600⁰C for several loads are presented as well. The fourth section of this paper is devoted to the application of the model by characterising the material using uniaxial tensile and small punch creep cases. These simulations are used to validate the accuracy of the UMAT by comparing numerical modelling and corresponding experimental tests. Finally, conclusions are discussed in the last section.

2. The Kocks-Mecking-Estrin Model and UMAT Development

2.1 The Kocks-Mecking-Estrin Model

The Kocks-Mecking-Estrin form is a unified elasto-viscoplastic constitutive model which is highly nonlinear and referred to as the kinetic equation by Kocks [6] and Mecking [14]. An appropriate mathematical formulation has been suggested by Kocks [6]:

$$\dot{\varepsilon}^p = \dot{\varepsilon}_o \left(\frac{\widetilde{\sigma}}{\widehat{\sigma}}\right)^m \tag{1}$$

where $\dot{\varepsilon}^p$ is effective plastic strain rate, $\dot{\varepsilon}_o$ is a reference strain rate which is proportional to the mobile dislocation density, $\widetilde{\sigma}$ is effective stress, and m is an exponent of stress sensitivity. The quantity of flow stress, an internal state variable, $\widehat{\sigma}$, represents the microstructural state of a material which is related to the total dislocation density ρ [15]:

$$\widehat{\sigma} = \alpha bGM\sqrt{\rho} \tag{2}$$

Here α is a constant, b is the magnitude of dislocation Burgers vector, G is the shear modulus, and M is the Taylor factor. The model assumes that the micromechanical strength of the material is due to piling up of dislocation-dislocation interactions.

The evolution of the dislocation density takes into account the athermal process as well as the dynamic recovery process of dislocations in the uniaxial loading [16].

$$d\rho = M\left[k_1\rho^{1/2} - k_2\rho\right]d\varepsilon^p \tag{3}$$

Here k_1 is a constant accounting for the dislocation storage and k_2 is the recovery coefficient which represents the thermal process for the low temperature or high-temperature case. In both cases, it can be written as [16]:

$$k_2 = k_{20}\left(\frac{\dot{\varepsilon}^p}{\dot{\varepsilon}_o}\right)^{-1/n} \tag{4}$$

where k_{20} is a constant. In the above formulation, the dynamic recovery exponent n can be written as

$$n = \frac{\Lambda}{kT} \tag{5}$$

Equation (5) shows that n is inversely proportional to absolute temperature T, where k is the Boltzmann constant and Λ is the work hardening parameter [6].

The constitutive equations of this model can be integrated with the case of constant plastic strain rate [14] and with constant stress creep [15].

$$\frac{d\sigma}{d\varepsilon} = (\sigma/m)\frac{d\ln\dot{\varepsilon}}{d\varepsilon} + \left(\sigma/\hat{\sigma}\right)\frac{d\hat{\sigma}}{d\varepsilon} \tag{6}$$

At the steady state, the evolution of $\hat{\sigma}$ does not change with the strain $\left(\frac{d\hat{\sigma}}{d\varepsilon} = 0\right)$, the Equation (6) may provide a simple discerption of deformation in a creep. Substituting Equation (1) into Equation (6) gives

$$\frac{d\ln\left(\frac{\dot{\varepsilon}}{\dot{\varepsilon}_s}\right)}{d\varepsilon} = \left(\frac{\theta_o m}{\hat{\sigma}}\right)\left[\left(\frac{\dot{\varepsilon}}{\dot{\varepsilon}_s}\right)^{-1/n-1/m} - 1\right] \tag{7}$$

where θ_o is the initial strain hardening within the second stage and $\dot{\varepsilon}_s$ is steady state strain rate.

One of the essential goals of this work is to utilise the strain rate as a function of strain in creep tests at constant stress. The steady state strain rate $\dot{\varepsilon}_s$ corresponding to $\frac{d\dot{\varepsilon}}{d\varepsilon} = 0$ is given

$$\dot{\varepsilon}_s = \dot{\varepsilon}_o^{m/(m+n)}\dot{\varepsilon}_o^{n/(m+n)}\left(\frac{\sigma}{\alpha b G M\left(\frac{k_1}{k_{20}}\right)}\right)^{mn/(m+n)} \tag{8}$$

One can simplify Equation (8) to give

$$\dot{\varepsilon}_s = \dot{\varepsilon}_o\left(\frac{\sigma}{\hat{\sigma}_{so}}\right)^p \tag{9}$$

where $\frac{m}{(m+n)} + \frac{n}{(m+n)} = 1$ and $\frac{1}{p} = \frac{1}{m} + \frac{1}{n}$

2.2 The Multi-Axial Formulation

The one-dimensional constitutive equations for the Kocks-Mecking model have been derived by Estrin [17]. In this section, the significant aspects of the 3-dimensional version are discussed.

Since in most cases of experimental tests, the materials have shown nonlinear behaviour, the stress state, σ_{ij}, is assumed to be a nonlinear function of the strain state, ε_{ij}. Thus, using Hooke's law in chain rule form, these can be re-expressed as a direct notation to gives

$$\dot{\sigma}_{ij} = C_{ijkl}\dot{\varepsilon}_{kl}^e \tag{10}$$

where $\dot{\sigma}_{ij}$, $\dot{\varepsilon}_{kl}^e$ are the Cauchy stress rate and elastic strain rate tensor respectively (a superposed dot refers to the time derivative) while C_{ijkl} is the fourth order elastic stiffness matrix tensor which depends on the strain, but not on the strain rate.

$$C_{ijkl} \equiv \frac{\partial\sigma_{ij}}{\partial\varepsilon_{kl}} \tag{11}$$

In elasto-viscoplasticity, it is usual to split the total strain rate tensor, $\dot{\varepsilon}_{ij}$, into two parts, namely an elastic strain rate, $\dot{\varepsilon}_{ij}^e$ and a creep strain rate tensor, $\dot{\varepsilon}_{ij}^c$, i.e.

$$\dot{\varepsilon}_{ij} = \dot{\varepsilon}_{ij}^e + \dot{\varepsilon}_{ij}^c \tag{12}$$

The update of $\dot{\varepsilon}_{ij}^e$ is given by

$$\dot{\varepsilon}_{ij}^e\big|_{n+1} = \dot{\varepsilon}_{ij}^e\big|_n + \left(\Delta\varepsilon_{ij} - \Delta\varepsilon_{ij}^c\right) \tag{13}$$

The elastic strain rate tensor can be connected with the rate form of Hooke's law, Equation (12), to give:

$$\dot{\sigma}_{ij}\big|_{n+1} = C_{ijkl} : \left(\dot{\varepsilon}^e_{ij}\big|_n + \Delta\varepsilon_{ij} - \Delta\varepsilon^c_{ij} \right) \tag{14}$$

To derive the incremental constitutive relationship, let us consider an integration over one step, Δt, from $t|_n$ to $t|_{n+1}$.

$$\sigma_{ij}\big|_{n+1} = \sigma_{ij}\big|_n + C_{ijkl} : \Delta\varepsilon_{ij} - C_{ijkl} : \Delta\varepsilon^c_{ij}\big|_{n+1} \tag{15}$$

$$\sigma_{ij}\big|_{n+1} = \sigma^{tr}_{ij} - C_{ijkl} : \Delta\varepsilon^c_{ij}\big|_{n+1} \tag{16}$$

where σ^{tr}_{ij} is an elastic predictor which is known and obtained by assuming the increment is entirely elastic, while $\Delta\varepsilon^c_{ij}$ are the creep strain increments [18].

In the following, we assume that the creep strain rate $\dot{\varepsilon}^c_{ij}$ is expressed using the Levy-von Mises equation as [19]:

$$\dot{\varepsilon}^c_{ij} = \dot{\tilde{\varepsilon}}^c \, \mathbb{N}_{ij} \;,\; \mathbb{N}_{ij} = \frac{3}{2}\frac{S_{ij}}{\tilde{\sigma}} \tag{17}$$

where $\dot{\tilde{\varepsilon}}^c$ is the effective creep strain rate, $\mathbb{N}_{ij}$ is the flow direction tensor, and S_{ij} denotes the deviatoric stress tensor, while the quantities in Equation (18) indicate the equivalent stress and equivalent creep strain rate respectively.

$$\tilde{\sigma} = \sqrt{\frac{3}{2}S_{ij} : S_{ij}} \text{, and } \dot{\tilde{\varepsilon}}^c = \sqrt{\frac{2}{3}\dot{\varepsilon}^c_{ij} : \dot{\varepsilon}^c_{ij}} \,, \tag{18}$$

2.3   The UMAT Coding and Implementation

The FE software ABAQUS permits the addition and implementation of various constitutive models into the ABAQUS library by using user material subroutines (UMATs) [20]. In the present study, the Kocks-Mecking-Estrin constitutive model described above for constant stress creep is implemented into ABAQUS by UMAT for the P91 steel at 600°C.

We here presented the implicit backward Euler integration for the multiaxial case of equations in the previous section. According to Equation (9), the rate form of the constitutive equation may be written in an incremental form as

$$\Delta\tilde{\varepsilon}^c = \Delta t \, \phi(\mathcal{F})^p \tag{19}$$

and thus may be expressed in a form suitable for Newton-Raphson iterative solution as [21]

$$\mathcal{R}(\Delta\tilde{\varepsilon}^c) = \Delta t \, \phi(\mathcal{F})^p - \Delta\tilde{\varepsilon}^c = 0 \tag{20}$$

Using Newton's method, one has

$$\mathcal{R} + \frac{\partial\mathcal{R}}{\partial\tilde{\varepsilon}^c} \, \delta\varepsilon^c = 0 \tag{21}$$

In this method, an additional iteration step i is introduced to calculate the increment in accumulated creep strain that gives $\mathcal{R}(\Delta\tilde{\varepsilon}^c) = 0$
The first step, $i = 0$ (initial) $\Delta\tilde{\varepsilon}^c_0 = 0$

$$\mathcal{R}_0 = \mathcal{R}(\Delta\tilde{\varepsilon}^c_0) \tag{22}$$

at the next step, (i) is replaced with $(i+1)$, so Equation (21) becomes [21]:

$$\delta\tilde{\varepsilon}^c\big|_{i+1} = -\frac{\mathcal{R}\big|_i}{\frac{\partial\mathcal{R}}{\partial\tilde{\varepsilon}^c}\big|_{\Delta\tilde{\varepsilon}^c_i}} \tag{23}$$

Now, the effective creep strain increment is updated by

$$\Delta\tilde{\varepsilon}^c_{n+1} = \Delta\tilde{\varepsilon}^c_n + \delta\tilde{\varepsilon}^c \tag{24}$$

The final step is to update the stress by

$$\sigma_{ij}\big|_{n+1} = \sigma_{ij}\big|_{n} + C_{ijkl} : \Delta\varepsilon_{ij}^{e}\big|_{n+1} \tag{25}$$

The flow chart of the implementation of the UMAT for the Kocks-Mecking-Estrin (KME) model is shown in Figure 1.
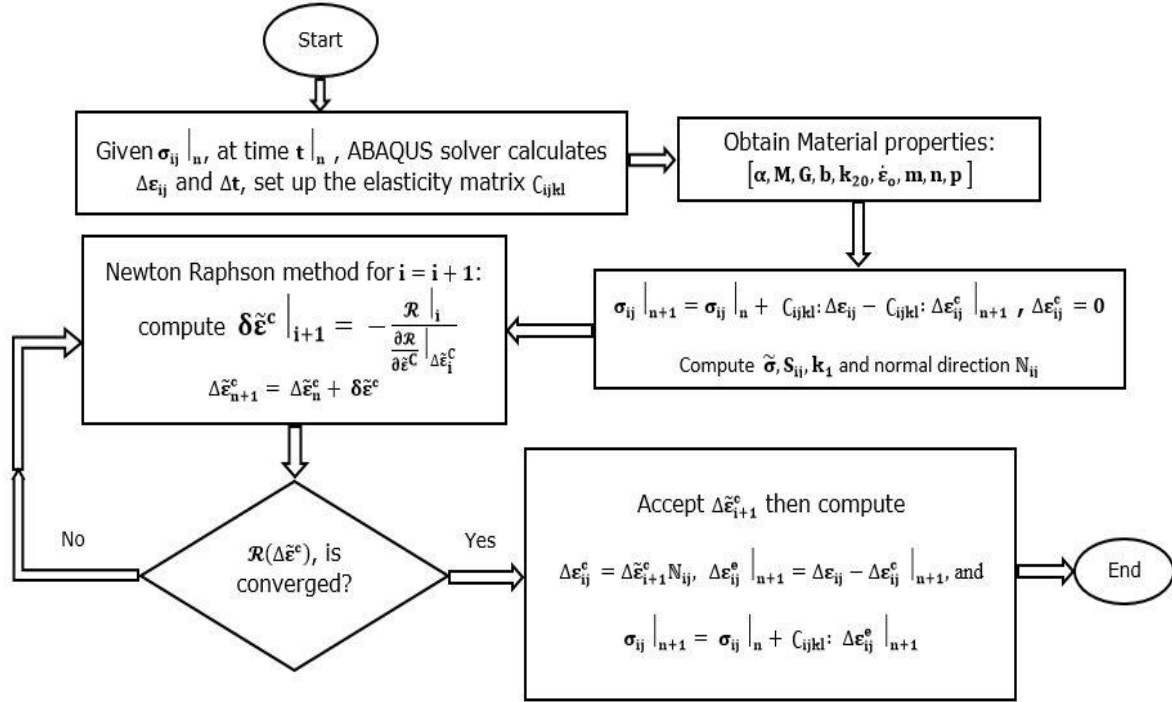

Figure 1. Flowchart of the implementation of the UMAT for KME model.

2.4   Material Jacobian Matrix

The material Jacobian can be described as a partial derivative

$$C_{ijkl} \equiv \frac{\partial\sigma_{ij}}{\partial\varepsilon_{kl}} = C_{ijkl}^{e} + C_{ijkl}^{cr} \tag{26}$$

A closed-form solution to C_{ijkl}^{e} the elastic stiffness matrix always knows. A closed-form solution to C_{ijkl}^{cr} the creep stiffness matrix may or may not know. Reversing the creep stiffness matrix, C_{ijkl}^{cr}, will furnish the creep compliance matrix, S_{ijkl}^{cr}, as given

$$S_{ijkl}^{cr} = \left(C_{ijkl}^{cr}\right)^{-1} = \frac{\partial\Delta\varepsilon_{ij}^{cr}}{\partial\Delta\sigma_{kl}} \tag{27}$$

The matrix was simplified to the following

$$S_{ijkl}^{cr} = \frac{\partial\Delta\varepsilon_{ij}^{cr}}{\partial\Delta\sigma_{kl}} = \frac{3}{2}\dot{\varepsilon}_{o}\,\hat{\sigma}_{so}^{-p}\Delta t\left[(p-1)\tilde{\sigma}^{p-2}\frac{\partial\tilde{\sigma}}{\partial S_{pq}}S_{ij} + \tilde{\sigma}^{p-1}\delta_{ip}\delta_{jq}\right]\frac{\partial S_{pq}}{\partial\Delta\sigma_{kl}}. \tag{28}$$

To obtain the stiffness matrix the compliance tensor must be inverted

$$C_{ijkl}^{cr} = \left(S_{ijkl}^{cr}\right)^{-1} \tag{29}$$

3. Experimental Work on P91 Steel at 600ºC

3.1 The P91 Material and Microstructure

Experimental tensile and small punch creep tests were presented for the P91 steel at 600ºC. The material chemical composition of the P91 steel used in the current work exhibits in Table 1. Figure 2a shows EBSD image of the virgin material microstructure.

Table 1. The chemical composition of the P91 steel [3].

Cr	Mo	C	Si	S	P	Al	V	Nb	N	W	Fe
8.60	1.02	0.12	0.34	0.002	0.017	0.007	0.24	0.070	0.060	0.030	Bal

3.2 Uniaxial Tensile Test

The conventional uniaxial tensile specimen is manufactured from a P91 pipe. The gauge length of the sample is 50mm, and the diameter of the gauge length is 10mm. The dimensions of the tensile specimen are shown in Figure 2b. The complete stress-strain curve obtained from the uniaxial tensile test at 600ºC. The Young's modulus of P91 steel is determined to be 145GPa at 600ºC, while the elongation of the specimen is 18% at the fracture.
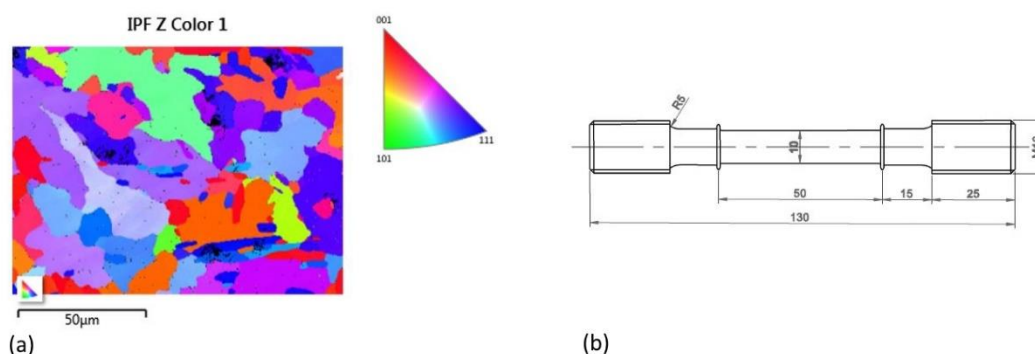
Figure 2. (**a**) EBSD texture of the virgin P91 steel used for the tests. (**b**) A uniaxial tensile test specimen, all dimensions in mm.

4. Modelling the Uniaxial Tensile and SPC Tests Using the Kocks-Mecking-Estrin Equations.

4.1 Modelling of Uniaxial Tensile Test

FE modelling of the uniaxial tensile test of the P91 steel at 600ºC was carried out using the UMAT coding via ABAQUS standard. The mesh of specimen consists of 673 axisymmetric quadrilateral elements. Only a quarter section was modelled due to symmetry. By including the geometrically non-linear effect, the uniaxial tensile specimen can induce significant deformation and neck with large localised strains. Figure 3 is a contour plot of the von-Mises stress at failure for a strain rate of $0.0005s^{-1}$, while Figure 4 shows the stress/strain curves obtained using the UMAT with the KME model and the corresponding tensile test carried out for the P91 steel at 600ºC. The material constant α, the magnitude of dislocation Burgers vector b, and Taylor factor M were taken from [22], these and other previous material constants used in calculations for the P91 steel are listed in Table 2.
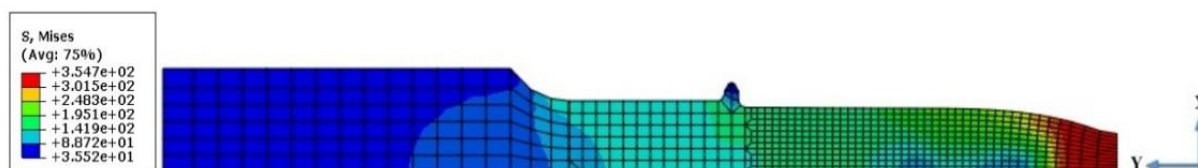

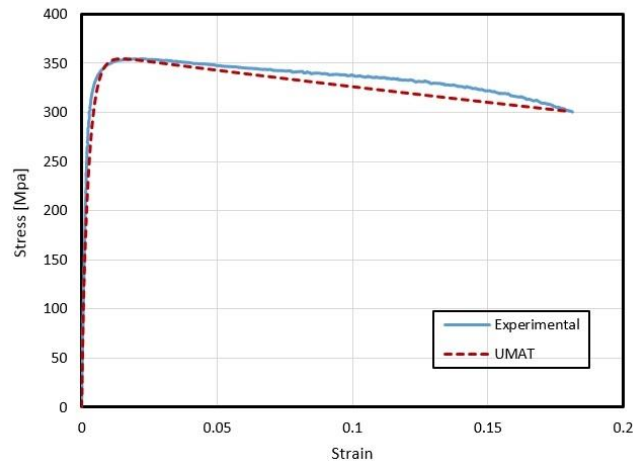**Figure 3.** Contour plot of the von-Mises stress at failure for the P91 steel at 600ºC.

Figure 4. Experimental and numerical FE stress-strain curves for the P91 steel at 600ºC.

Table 2. Notation and material constants used in numerical FE for the P91 steel at 600ºC [22].

Parameter	Name	Value
ρ_i	Initial Dislocation Density	1×10^{14} m^{-2}
v	Poisson's ratio	0.3
b	The magnitude of Burgers vector	2.5×10^{-10} m
m	The exponent of stress sensitivity	55.89
$\dot{\varepsilon}_o$	Reference strain rate	1 s^{-1}
k_{20}	Dynamic recovery	55
α	Constant	0.8
M	Taylor factor	3.06

4.2 Modelling of Small Punch Creep Tests

i. FE Model

Finite element modelling of small punch creep for P91 steel at 600℃ was carried for five levels of punch loads P1= 25, 28, 30, 34 and 40 kg using the UMAT code and the material properties given in Table 2. Figure 5 shows the geometry of the FE model where the punch radius (d/2) is 1.04mm, the holder and the support radius (r) is 0.25mm, the thickness (t$_s$), and radius of the specimen (S/2) are 0.5 and 4mm, respectively, the receiving hole radius (D/2) is 2mm. The punch, the holder, and the support were modelled as rigid bodies. Approximately half of the surface of the bottom of the specimen is constrained by a support to simulate being clamped between surfaces. The friction coefficient between these surfaces is assumed to be 0.8 [23]. The sample was implemented as a deformable body modelled using two different type of elements: the majority of the elements (1480) are 4-noded bilinear axisymmetric quadrilaterals with reduced integration (CAX4R), with transitions to zones of refined mesh involving ten 3-noded axisymmetric triangle elements (CAX3). The specimen was refined along the contact region between the punch and the sample. Figure 6 shows the mesh used for the SPCT analysis and the minimum element size, in the refined zone, is 0.025mm. The contacting interfaces between the top surface of the sample with rigid punch were assigned as a surface to surface contacts with a coefficient of friction assumed to have a value of 0.2 thus value being chosen from a parametric study described later in this section. The simulation was carried out with three types of boundary conditions. Firstly, the axial movement and rotation around the axis of symmetry of the support were constrained entirely. Secondly, the horizontal movement and rotation of punch and holder were also restricted to zero. The complete displacement and rotation constraints were applied on the left side of the specimen in the X-direction for all nodes located on the Y-axis. The loads are directed in the Y direction and are applied to the reference point of rigid punch that can represent the whole stiff punch, while a clamping load, 500N, is used on to the reference point of the holder die.
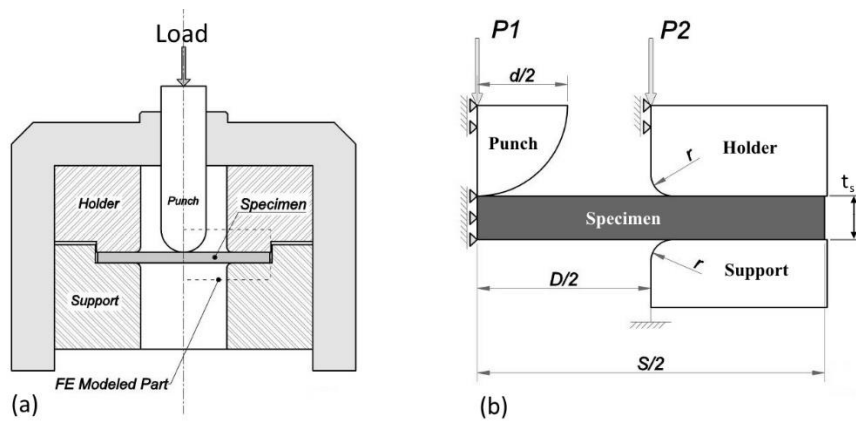
Figure 5. Schematic representation of a FE model for small punch creep testing analysis (D=4mm, S=8mm, d=2.08mm, r=0.25mm, t_s=0.5mm). (**a**) Schematic two-dimensional of rig for small punch creep testing. (**b**) Representation loads and boundary conditions of finite element modelled part.
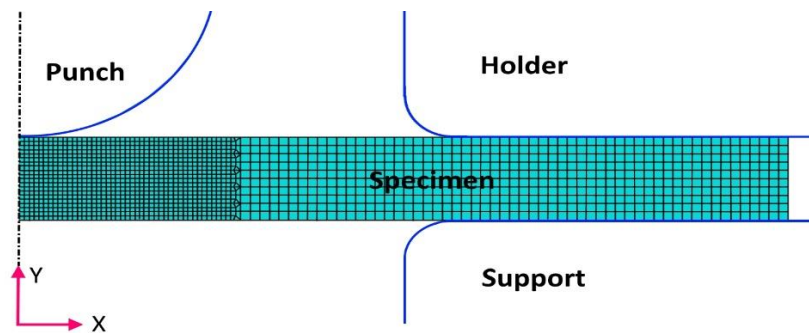

Figure 6. FE mesh used for SPCT specimen.

ii. Displacement-Time Curves

The parametric study of the different friction coefficients between the specimen and punch is carried out. The contact between the sample and punch was modelled using a surface to surface contact with various friction coefficients. Figure 7 shows the effect of friction coefficient for three values ($\mu = 0.2, 0.3$ and, 0.4) with two cases of loads 34 and 40kg, respectively. It can be observed clearly that the effect of the coefficient of friction on the FE outputs is significant and the value of the friction coefficient of $\mu = 0.2$ that gives the best approximation between modelling and practical data. The relationship between the coefficient of friction and the magnitude of the friction forces is directly proportional. For a given load levels, when the friction coefficient increases, the minimum deflection rate will drop and the failure time will increase.
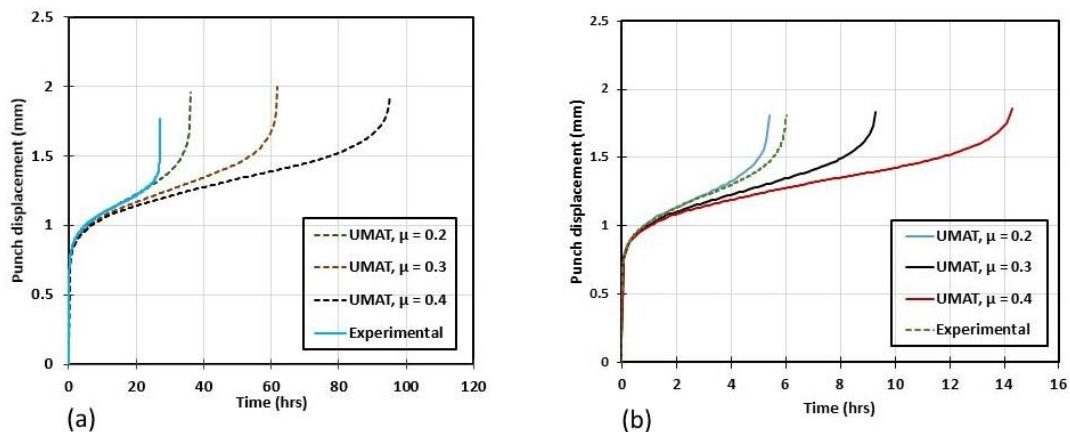
Figure 7. Calculated SPCT curve at the variation of the friction coefficient for punch load (**a**) 34Kg and, (**b**) 40Kg.

The experimental SPCT curves at five different load levels and the corresponding predicted curves are compared in Figure 8. The FE simulations using the proposed model show good agreement with the corresponding experimental results. The coefficient of friction between punch and specimen is assumed to be constant ($\mu = 0.2$) for all applied loads. During the first SPCT regime, the sample undergoes a severe change in shape. Change of the structure causes a decrease in the specimen's stiffness and a change in the deformation mechanism, from bending dominated to 'membrane stretching' dominated. In the second SPCT regime, the controlling mechanism is tensile stretching of the annular region around the contact edge between the punch and the specimen. Material creep damage is still acceptable to occur in the secondary SPCT region. The third SPCT region, symbolised by developing deformity rate, is governed by creep material degradation and specimen necking.
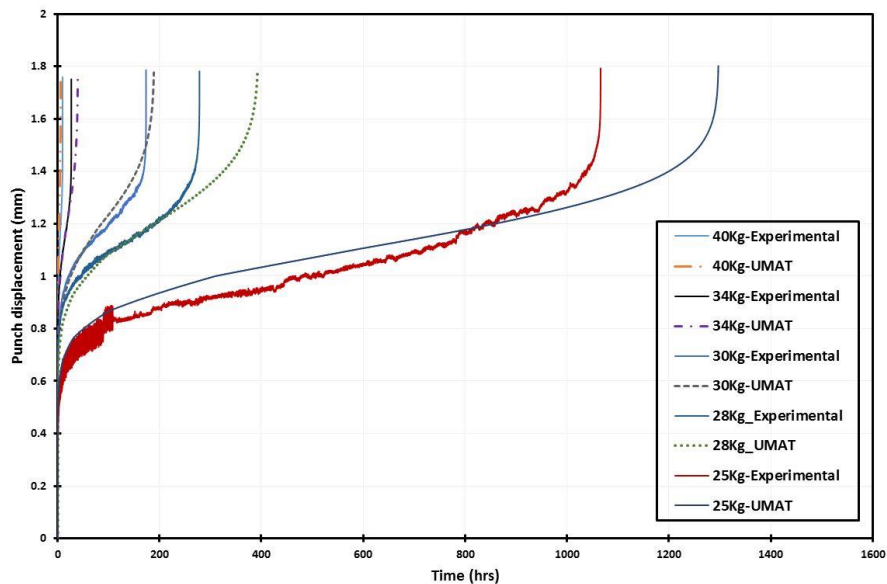
Figure 8. The experimental and calculated SPCT curves at punch load of 25, 28, 30, 34, and 40Kg [3].

iii. Contours of Displacement, von Mises Stress and Strain

The FE analysis of SPCTs was carried out using UMAT code through the ABAQUS package. Figure 9a shows the results of punch deformation at load 34Kg. The displacement of the punch is about 1.403mm after a time of 19 hours. Figure 9b shows the distribution of stress at the cross-section of the specimen after 19 hours under a constant punch load of 34Kg. The highest equivalent stress value is observed at the zone is located over a distance of 0.9mm, for the whole specimen thickness, from the centre of the initial specimen at the start of SPC test (see Figure 5b). Increasing stress is also observed at the top of sample surface located at distance of 2.0mm from the centre of the sample as a result of the tension in that region. Figure 9c shows the variations of equivalent strain under applied loads of 34Kg. Equivalent strains show a sharp rise in the area located on the bottom surface of the specimen at distance of 0.55mm from the centre of the sample. This deformation may be due to severe bending of the specimen from continuous of punch movement towards down which may ultimately lead to failure. Except for this region, the maximum equivalent strains occur identically to the rest of specimen.
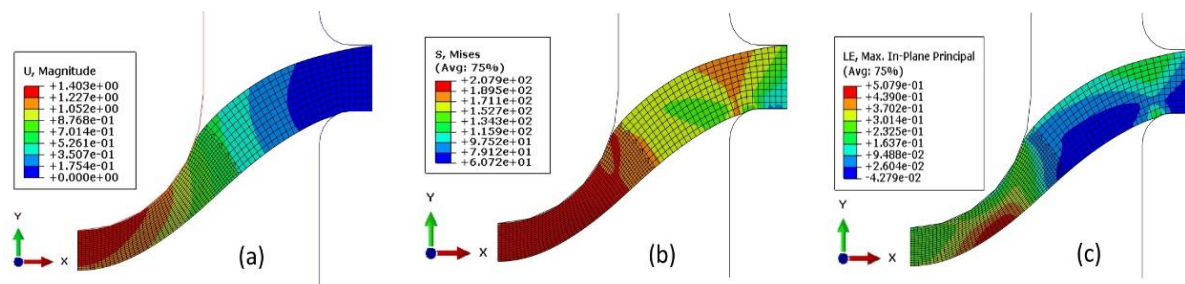
Figure 9. Contour plot of the SPCT at a punching load of 34Kg for (**a**) Punch direction deformation, (**b**) The equivalent stress and (**c**) The equivalent strains

Figure 10 shows SEM image of experimental SPC tests for punch load of P1= 25 kg which is postponed after 669 hours and the corresponding effective strain contour plots. The regions of local deformity were nearly identical to those of the experimental specimen tested. The directions and locations of the strain data are identified in Figures 9c and 10 where the effective strains at the weakest position do not change despite loading times increase.
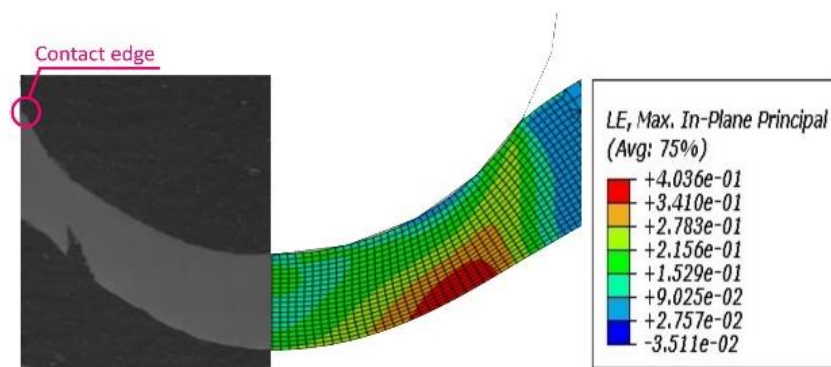
Figure 10. Contour plot of strain and SEM images of SPCT at punch load 25Kg for P91 steel at 600ºC.

5. Conclusions

The constitutive equations of KME model rely on the basic physical microstructure which was implemented by the finite element modelling through the user material subroutine (UMAT) and evaluated by the experimental results. The testing procedure involved SPCT, uniaxial tensile tests on the P91 steel at 600ºC.

For viscoplastic numerical simulations of SPC and uniaxial tensile tests under high forces, the KME modelling provides more accurate results with the experimental data at elevated temperatures.

The additional advantage of using the current model is the capability to determine the creep model parameters from utilizing microstructure information than uniaxial creep testing.

The influence of friction behaviour of the contact between punch and specimen was considered for SPCTs at different levels of load. The failure time gradually increases with an increase of the friction coefficient.

The maximum equivalent strain was observed within an annular zone on the underside of the specimen and this weakest location did not change even though loading time elapsed during SP creep testing analysis.

In the future work, the KME model will be extended to include material damage taking into account the effect of grain size. The determination of material parameters will be identified using a suitable optimisation strategy based on physical measurements.

References

1. Hyde, T.H.; Sun, W. and Williams, J.A. Requirements for and Use of Miniature Test Specimens to Provide Mechanical and Creep Properties of Materials: A Review. *Int Mater Rev.* **2007**, *52,* 213-255.
2. Morris, A.; Cacciapuoti, B. and Sun, W. The Role of Small Specimen Creep Testing within a Life Assessment Framework for High Temperature Power Plant. *Int Mater Rev.* **2018**, *63,* 102-137.

3. Cortellino, F.; Rouse, J.; Cacciapuoti, B.; Sun, W. and Hyde, T.H. Experimental and Numerical Analysis of Initial Plasticity in P91 Steel Small Punch Creep Samples. *Exp Mech.* **2017***,* 1-20.

4. Rouse, J.; Cortellino, F.; Sun, W.; Hyde, T.H. and Shingledecker, J. Small Punch Creep Testing: Review on Modelling and Data Interpretation. *Mater Sci Tech.* **2013***, 29,* 1328-1345.

5. Dymáček, P. and Milička, K. Small Punch Testing and Its Numerical Simulations under Constant Deflection Force Conditions. *Strength Mater+* **2008***, 40,* 24-27.

6. Kocks, U. Laws for Work-Hardening and Low-Temperature Creep. *J Eng Mater Tech.* **1976***, 98,* 76-85.

7. Wu, Y.; Zhou, J.; Dong, S.; Hu, A.; Wang, L. and Pang, X. Constitutive Modeling for Strain Rate-Dependent Behaviors of Nanocrystalline Materials Based on Dislocation Density Evolution and Strain Gradient. *J Mater Res* **2014***, 29,* 2982-2993.

8. Barlat, F.; Glazov, M.; Brem, J. and Lege, D. A Simple Model for Dislocation Behavior, Strain and Strain Rate Hardening Evolution in Deforming Aluminum Alloys. *Int J Plasticity* **2002***, 18,* 919-939.

9. Kachanov, L. *Introduction to Continuum Damage Mechanics*; Springer Science & Business Media: USA, 2013.

10. Abendroth, M. FEM Analysis of Small Punch Tests. *Key Eng Mat.* **2017***, 734,* 23-36.

11. Manahan, M.; Browning, A.; Argon, A. and Harling, O. Miniaturized Disk Bend Test Technique Development and Application. In The Use of Small-Scale Specimens for Testing Irradiated Material, ASTM International, New Mexico, 1986.

12. Shibli, I.; Holdsworth, S. and Merckling, G. Creep and Fracture in High Temperature Components: Design and Life Assessment Issues. In ECCC Creep Conference, London, UK, 2005.

13. Evans, R. and Evans, M. Numerical Modelling of Small Disc Creep Test. *Mater Sci Tech.* **2006***, 22,* 1155-1162.

14. Mecking, H. and Kocks, U. Kinetics of Flow and Strain-Hardening. *Acta Metall Mater.* **1981***, 29,* 1865-1875.

15. Estrin, Y. and Mecking, H. A Unified Phenomenological Description of Work Hardening and Creep Based on One-Parameter Models. *Acta Metall Mater.* **1984***, 32,* 57-70.

16. Estrin, Y. Dislocation Theory Based Constitutive Modelling: Foundations and Applications. *J Mater Process Tech.* **1998***, 80,* 33-39.

17. Estrin, Y., Dislocation-Density-Related Constitutive Modelling, in *Unified Plastic Constitutive Laws of Deformation*, KRAUSZ, A.S. and KRAUSZ, K., Academic Press limited: London. 1996. 69-106, 0-12-425970.

18. Rezania, M.; Taiebat, M. and Poletti, E. A Viscoplastic Saniclay Model for Natural Soft Soils. *Comput Geotech* **2016***, 73,* 128-141.

19. Chaboche, J. A Review of Some Plasticity and Viscoplasticity Constitutive Theories. *Int J Plasticity* **2008***, 24,* 1642-1693.

20. ABAQUS, Analysis User's Manual Version 6.8. Hibbitt, Karlsson and Sorensen, Inc.: Pawtucket, USA, **2010**.

21. Dunne, F. and Petrinic, N. *Introduction to Computational Plasticity*, 2nd ed.; Oxford University Press: New York, USA, 2005.

22. Domkin, K. Constitutive Models Based on Dislocation Density: Formulation and Implementation into Finite Element Codes. PhD thesis, Luleå University of Technology, Sweden, 2005.

23. Cortellino, F.; Sun, W.; Hyde, T.H. and Shingledecker, J. The Effects of Geometrical Inaccuracies of the Experimental Set-up on Small Punch Creep Test Results. *J Strain Anal Eng.* **2014***, 49,* 571-582.

Procedure of SPC data treatment for "uniaxial test correlation"

Y.Z. Li [1,*], P. Stevens [2], P. Dymáček [3,4], F. Dobeš [3]

1 retired from DNV-GL, Arnhem, the Netherlands; yingzhili1943@hotmail.com
2 DEKRA, Material Testing & Inspection, Utrecht, The Netherlands; paul.stevens@dekra.com
3 Institute of Physics of Materials, Academy of Sciences of the Czech Republic, Czech Republic; dobes@ipm.cz
4 CEITEC IPM, Institute of Physics of Materials, Academy of Sciences of the Czech Republic, Czech Republic; pdymacek@ipm.cz
* Correspondence: yingzhili1943@hotmail.com; Tel: +31-6-40917090

Abstract: In order to determine creep properties from small punch creep (SPC) tests, several theoretical models and analytic methods are applied, such as the Chakrabarty's membrane stretch model and reverse finite element method. However, because the problem is too complicated, differences are always found between the theoretical prediction and the uniaxial creep tests. In this paper, a concept of "Uniaxial test correlation" is proposed without any theoretical assumption and analytic calculation. By comparison of the rupture time in SPC with the uniaxial creep rupture data, the equivalent stress σ in SPC is determined. By using the obtained equivalent stress σ and the uniaxial creep strain rate data, the derived minimum strain rate in SPC can be found. A large experimental data pool is built up, containing 97 uniaxial creep tests and 159 SPC tests in total. From there, two empirical formulas are proposed to calculate the ratio of force F to stress σ, and the derived minimum strain rate $\dot{\varepsilon}_{min}$ in SPC. With these two important values known, the material creep properties can be determined accordingly.

Keywords: "Uniaxial test correlation"; small punch creep tests; creep properties; rupture time dependence; Norton creep law.

---

1. Background

In 1990s the SP test technique was introduced to Europe, and has been extended to the creep domain. In 1994, a Copernicus project entitled "Small Punch Test Method Assessment for the Determination of the Residual Creep Life of Service Exposure Components (Contract: ERB CIPA CT 94 0103)" has been set up and carried out in laboratories in different European countries [1-2]. From 2000 to 2003 a "Contribution In Kind" project was carried out within EPERC network, namely in the Technical Task Force 5 (TTF5, "Service Integrity during Operation"). The results of the Round Robin have been summarized in the EPERC Technical Reports [3].

Encouraged by the ASME standards F1248 and F2183 on small punch test for polyethylene pipe [4], further work for code acceptance for steels was organized by the European CEN workshop WS 21. Since 2006 the European Code of Practice (CoP) documents are available for both high and low temperature properties, which summarize documents in last 20 years and provide a guide line to perform small punch test for metallic materials [5]. At present, small punch testing is used for various applications to a broad range of materials [6-19]. Since 2015, a working group is engaged to upgrade the CoP to a European standard.

Let us re-call the progress of research on SPC in last 20 years. At beginning most of the work on the SPC test aimed to find the relation between SPC test load F and creep rupture time t_r [1-2]. Some of them introduced the Larson-Miller parameter for rupture time interpolation with stresses and temperatures [19]. Tettamanti and Crudeli put forward the equivalent stress concept: "What is the load value to use in the small punch test to obtain the same time to rupture as in a uni-axial test?" [20]. Chakrabarty's membrane stretch model [21] was introduced to calculate stress and strain in SPC by Yang and Wang [22]. Based on the Chakrabarty's model, CoP provides a formula for estimating the test load in SPC [5]. In order to derive creep properties from the SPC test, authors carried out a reverse algorithm to identify material parameters from the best match of the measured creep deflection curves [23-24]. Several reverse algorithm approaches were put forward by authors to determine the Norton creep law and rupture time dependence [25-26]. Abendroth introduced a neural network to identify the Norton creep properties automatically, and the optimization criterions were based on both the creep deflection curve and the rupture time. A neural network approach is useful to avoid the time-consuming finite element creep analysis [27]. Hyde and Sun pointed out that the stationary portion of the SPC curve is at the tertiary stage, rather than at the secondary stage, as the creep strain is already at a level of 10-15% in the stationary portion [28].

Interesting discussions have been taking place during the Nottingham and Petten symposia. David Allen questioned whether due to the excessive plastic deformation at initial loading, the creep behavior could be influenced. Authors pointed out that, due to large deformation, the stress and strains in SPC should be considered as true stress and true strain, in contrary to the uniaxial creep test, where these are engineering stress and engineering strain. Kristof Turba and Peter Hähner also pointed out that the effect of strain hardening should be also considered in creep analysis. Recently, experiments have been carried out to study an excessive plasticity during the initial loading and its influence on the creep behavior [29]. Actually, this phenomenon has been addressed in earlier literatures [30-31].

Although many efforts have been made to improve the interpreting approach for SPC and several conferences and symposia have been held to exchange ideas and experiences, up to now there is no generally accepted method to estimate uniaxial creep properties. This is because the complexity of the SPC consists in the inclusion of several non-linear problems: the geometrical non-linearity due to large deformation, the physical nonlinearity due to plasticity and creep and the contact nonlinearity due to the contact area between the punch and the specimen. Therefore, differences are always found between the theoretical prediction and the uniaxial creep tests, as some effects are still not taken into account in analysis.

2. Correlation using uniaxial creep test data

As the analytic approach is very complicated, let us turn on to an alternative approach. A concept of "Fracture-based correlation" was put forward by Dobeš and Dymáček [32, 33] in which, the equivalent stress is derived using the rupture time in SPC with the uniaxial rupture data. In this paper, the "Fracture-based correlation" is further improved, not only to estimate the rupture time, but also to estimate the minimum strain rate. This new methodology is called the "Uniaxial test correlation". This approach is fully based on experimental tests data, no model or assumption is adopted. Thus all the effects mentioned above are implicitly included. In addition, this approach delivers better prediction than the formula in CoP or the Chakrabarty model. Furthermore, it is very simple and user-friendly.

The basic idea of the correlation approach is to determine the relation between the uniaxial creep test and the small punch creep test. The uniaxial creep test is a one-dimensional test which has been historically the standard method for deriving creep material properties which are used in design- and remaining lifetime evaluation standards. Therefore, an analysis of a large number of experimental data to find the relation between the uniaxial tests and the small punch tests, is an effective way to solve the problem.

Purmenský and Matocha already applied a correlation approach to predict the yield strength and the ultimate tensile strength from small punch tests at constant deflection rate [34]. They build up a data pool that includes both small punch and uniaxial tensile tests data and found an optimal parameter to correlate between small punch test results and uniaxial tensile quantities.

A similar approach can be applied to SPC analysis. However, the SPC analysis is more complicated than the analysis of the constant deflection rate test. Because in SPC, both the creep rupture time and the minimum creep rate, or more specifically, its description in terms of Norton creep law should be dealt with.

The basic procedure of the "Uniaxial test correlation" is that, the equivalent stress σ in the SPC test can be estimated from the rupture time which is comparable with to the uniaxial rupture data, thus the ratio $\Psi = F/\sigma$ is obtained. Using the obtained equivalent stress σ, the minimum strain rate can be also derived from the uniaxial creep strain rate data. The resulting ratio Ψ and the minimum strain rate are summarized in a sufficiently large data pool, from which empirical formulas of the ratio Ψ and the minimum strain rate can be established with an optimal correlation parameter. The flowchart of the "Uniaxial test correlation" is shown in Fig. 1.
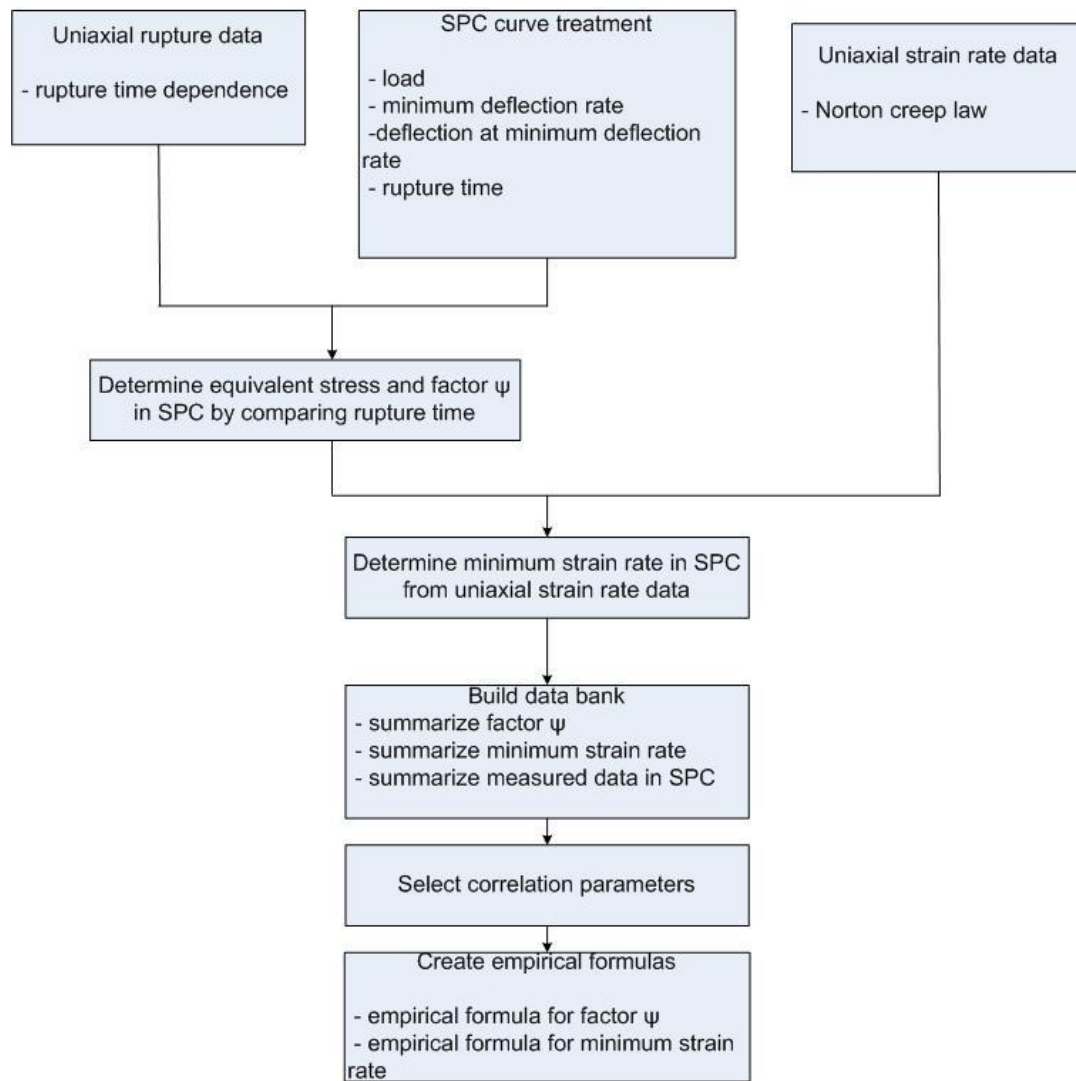
Figure 1. Flowchart of the "Uniaxial test correlation".

3. Build up the data pool

The test data pool contains 97 uniaxial creep tests and 159 SPC tests, covering temperatures from 550 ^{0}C -700 ^{0}C, loads from 300 N to 900 N. The current materials, both new and exposed, are mainly low alloy steels and 9Cr steels, such as 14MoV63, X20CrMoV121, P91, P92 and Eurofer 97. Single example of austenite steels, namely 316 L steel, is also included in the data pool. All material names, test temperatures and data sources in the data pool are listed in the references [37-39].

All the materials tested are "creep ductile" materials, and all the SP tests for these materials were carried out using the same type of specimen/punch/support/loading configurations etc. specified in the CoP [5]. For all test data, the specimen with diameter of 8 mm and with thickness of 0.5 mm; the diameter of support hole is 4 mm; the punch diameter is 2.5 mm, and that with punch radius of 2.0 mm is excluded. Therefore, the data used for fitting belong to "the same family", but under different temperatures.

4. Matlab code for data treatment

In order to deal with large data treatment for different materials with both uniaxial creep and SPC tests, a general Matlab code with name of Psi.m is compiled with Matlab version 2016a. As the data pool contains more than 20 materials, the material name is set as an input variable in the code Psi.m. The active command is Psi(*mat*). Here the *mat* is the material name in characters.

According to the input variable *mat*, the program Psi.m will identify the files "uniaxial_*mat*.txt" and "spt_*mat*.txt". These two files contain the list locations of the test curves for uniaxial creep and SPC tests.

The program Psi.m consists of three parts: 1) uniaxial creep curve treatment, 2) SPC curve treatment and 3) comparison of measured and predicted with respect to rupture time dependence and the Norton creep law. After the uniaxial creep and SPC curve treatments are finished, the obtained data are summarized using another Matlab code summary.m. Regressions are carried out to derive the constants of two empirical relations: rupture time dependence and Norton creep law. The summary results are input to Psi.m as prediction results for the comparison in part 3.

The uniaxial creep curve treatment output are written in the file history_uni.txt, including applied stress, minimum strain rate $\dot{\varepsilon}_{min}$ and rupture time tr. The SPC curve treatment output are written in the file history_spt.txt, including applied load F, equivalent stress σ, factor Ψ, derived minimum strain rate $\dot{\varepsilon}_{min}$, minimum deflection rate $\dot{u}_{min}$, deflection at minimum deflection rate u_{min} and rupture time t_r. The results derived from Chakrabarty's model are also included for comparison. The flow chart of the Matlab code Psi.m is shown in Fig. 2.
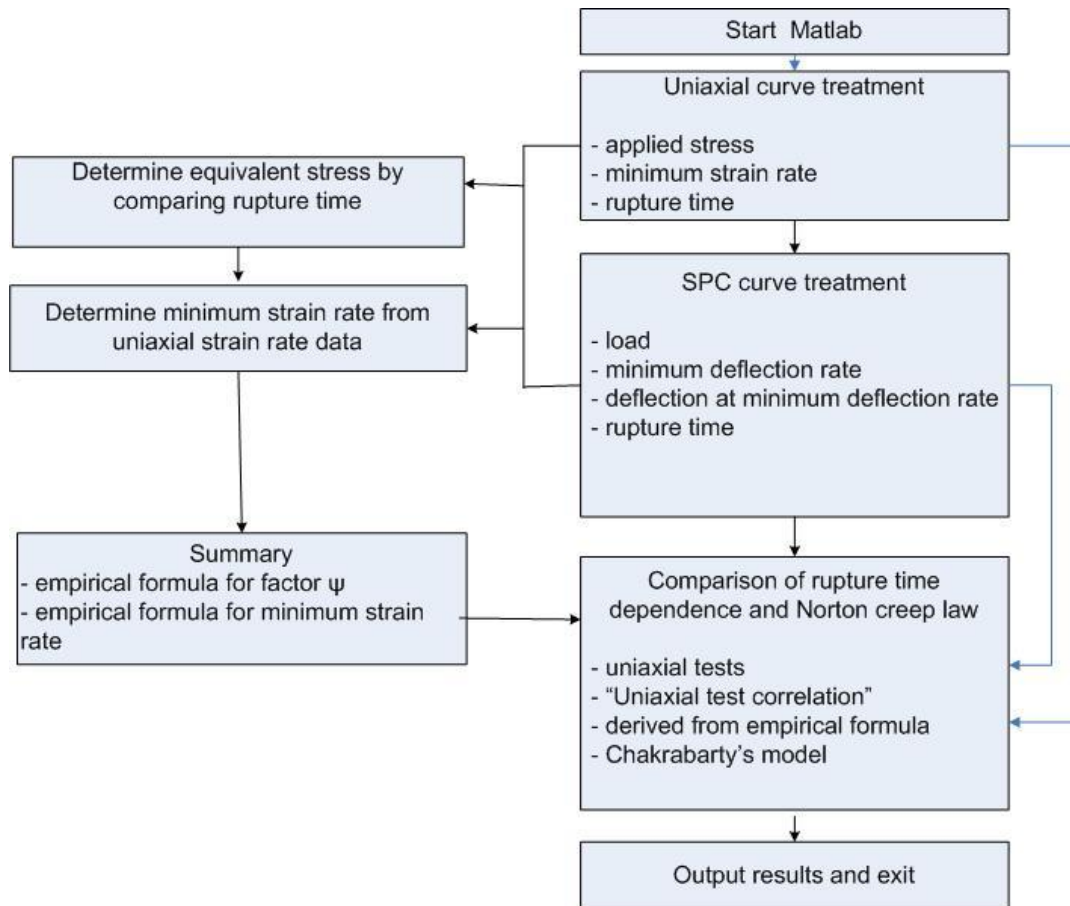
Figure 2. Flowchart of Matlab code Psi.m.

5. Parameters selection for factor Ψ and minimum strain rate

Actually, many factors could influence the value of factor Ψ, such as the temperature, the material, initial loading deflection and so on. All the factors will give influence on a deflection curve. In other words, the deflection curve reflects and represents all the influences. According to Chakrabarty's membrane stretch model, the factor $\Psi=F/\sigma$ depends on the deflection u only. Although this is for an extreme membrane stage, it could be suitable for a large deformation status like the SPC test. Therefore the deflection u could be a candidate parameter for factor Ψ.

The code summary.m outputs not only the factor Ψ, but also the following items: the equivalent stress σ, the minimum strain rate $\dot{\varepsilon}_{min}$, the minimum deflection rate $\dot{u}_{min}$, the deflection at minimum deflection rate u_{min}, the Monkman Grant constant MGC, the rupture time t_r and a few others. In order to find an optimal correlation parameter to calculate factor Ψ, several regressions for different candidates are carried out and the coefficient of determination, R^2, of the regression are compared. It turns out that the deflection at the minimum deflection rate, u_{min}, is the optimal parameter for the ratio Ψ. The deflection rates are calculated by derivative of deflection curve, and the deflection u_{min}, is corresponding to the minimum deflection rate.

The coefficient of determination, R^2, of regression for different parameters are summarized in table 1.

Table 1. The R^2 of regression for different parameters.

No.	Relation in logarithm	R^2
1	Deflection at minimum deflection rate, u_{min} vs. factor Ψ	0.5948
2	Average deflection at $1/3t_r$, $1/2t_r$, $2/3t_r$ vs. factor Ψ	0.5600
3	Rupture time t_r vs. factor Ψ	0.1332
4	Minimum strain rate $\dot{\varepsilon}_{min}$ vs. factor Ψ	0.2346
5	Minimum deflection rate $\dot{u}_{min}$ vs. factor Ψ	0.1436
6	Monkman-Grant constant MGC vs. factor Ψ	0.4290
7	Ratio of $\dot{\varepsilon}_{min}/\dot{u}_{min}$ vs. factor Ψ	0.3137

The acquired data pairs (F/σ, u_{min}) are then fitted to the following empirical formula (Fig. 3)

$$\Psi = \frac{F}{\sigma} = A.u_{min}^m \quad (N/MPa) \tag{1}$$

The best fit is found at $A = 1.9204$ and $m=0.6530$.
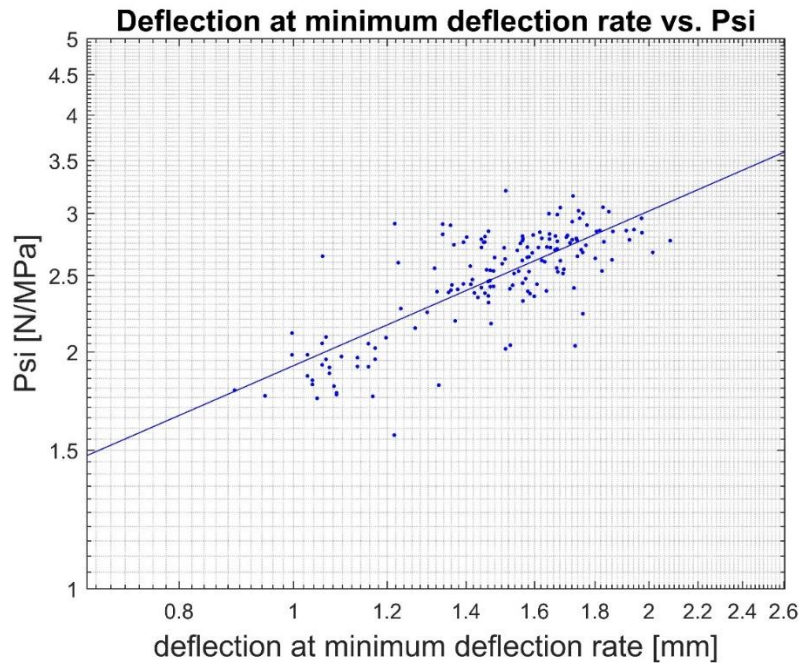
Figure 3. Relation between Ψ and the deflection at the minimum deflection rate, $u_{min.}$

The derived minimum strain rates are also output from summary.m. An empirical relation between the minimum deflection rate $\dot{u}_{min}$ and the minimum strain rate $\dot{\varepsilon}_{min}$ is established and expressed as follows (see Fig. 4).

$$\dot{\varepsilon}_{min} = 0.3922\dot{u}_{min}^{1.1907} \quad (1/h) \tag{2}$$
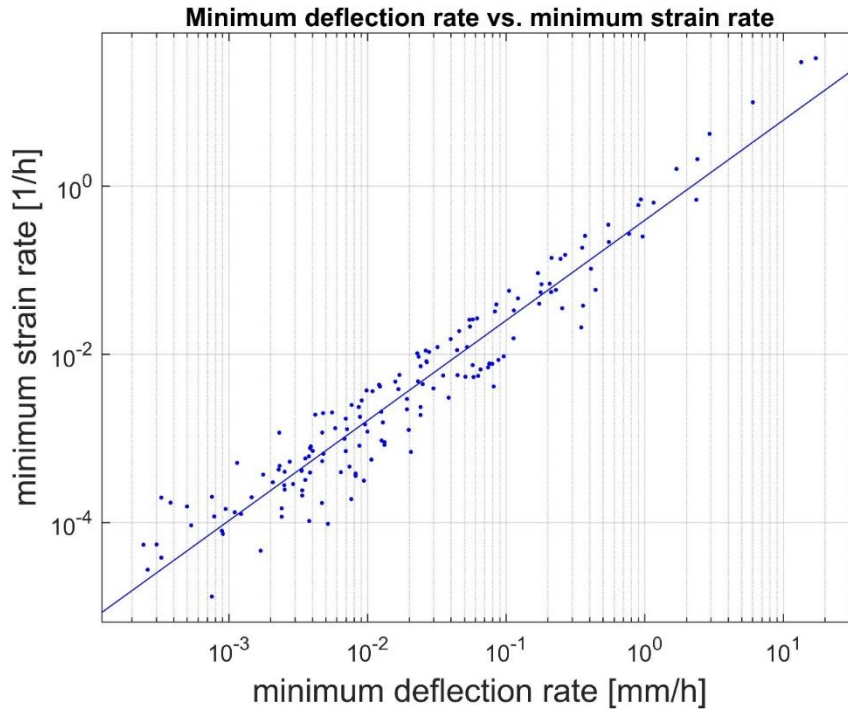
Figure 4. Relation between the minimum deflection rate $\dot{u}_{min}$ and the minimum strain rate $\dot{\varepsilon}_{min}$.

The correlation between the minimum deflection rate $\dot{u}_{min}$ and the minimum strain rate $\dot{\varepsilon}_{min}$ is quite good. The coefficient of determination, R^2, of the regression is equal to 0.9218. No other parameters reach this level of correlation.

6. Procedure for the application of "Uniaxial test correlation"

The procedure for application of the "Uniaxial test correlation" is described as follows:
1. Carry out multiple SPC tests at the equal temperature and follow the next steps for each test.
2. For a given load F, determine the rupture time t_r, the minimum deflection rate $\dot{u}_{min}$, and the deflection at the minimum deflection rate, u_{min}.
3. Using the deflection at the minimum deflection rate, u_{min}, determine the ratio $\Psi = F/\sigma$ from Eq. (1), and consequently the equivalent stress σ is also determined.
4. Using the minimum deflection rate $\dot{u}_{min}$, determine the minimum strain rate $\dot{\varepsilon}_{min}$ from Eq. (2).
5. With the equivalent stress σ, the rupture time t_r, and the minimum strain rate $\dot{\varepsilon}_{min}$ known, the rupture time dependence and the Norton creep law are determined by regression.

7. Verification

The best method for verification is to compare the prediction results directly with the uni-axial tests. The verification has been carried out for each test set during building up the data pool. Herewith some examples are shown below for predictions of the rupture time and the minimum strain rate. The prediction of the Chakrabarty model is also included. Obviously, the present approach gives better prediction than the Chakrabarty model.

In the following figures, the red points and the red lines are the uniaxial creep data. For the green points and green line, the equivalent stress σ is estimated using the rupture time in the SPC test to compare the uniaxial rupture data. Then using the obtained equivalent stress σ is used to calculate the minimum strain rate in SPC from the uniaxial creep strain rate data. Thus the red line and green line are always overlapping. The blue points and blue line are derived from the empirical formulae Eqs. (1) or (2) and represent the prediction by the "Uniaxial test correlation" approach. The black points and black line are derived from the prediction by the Chakrabarty model.
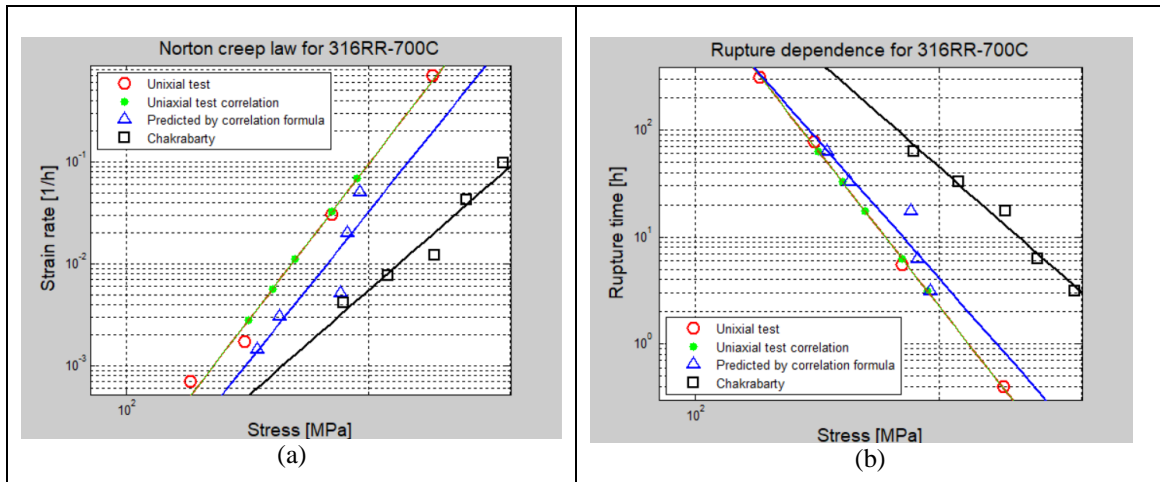
Figure 5. Comparison of uniaxial creep data with prediction methods for 316RR at 700 ^{0}C (a) Norton creep law, (b) Rupture time.
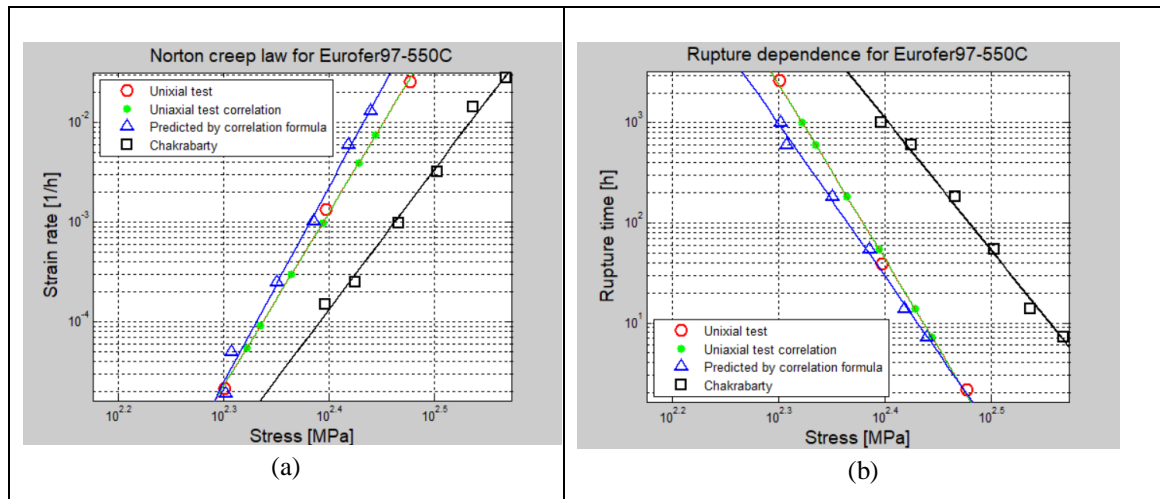

Figure 6. Comparison of uniaxial creep data with prediction methods for Eurofer97 at 550 ^{0}C (a) Norton creep law, (b) Rupture time.
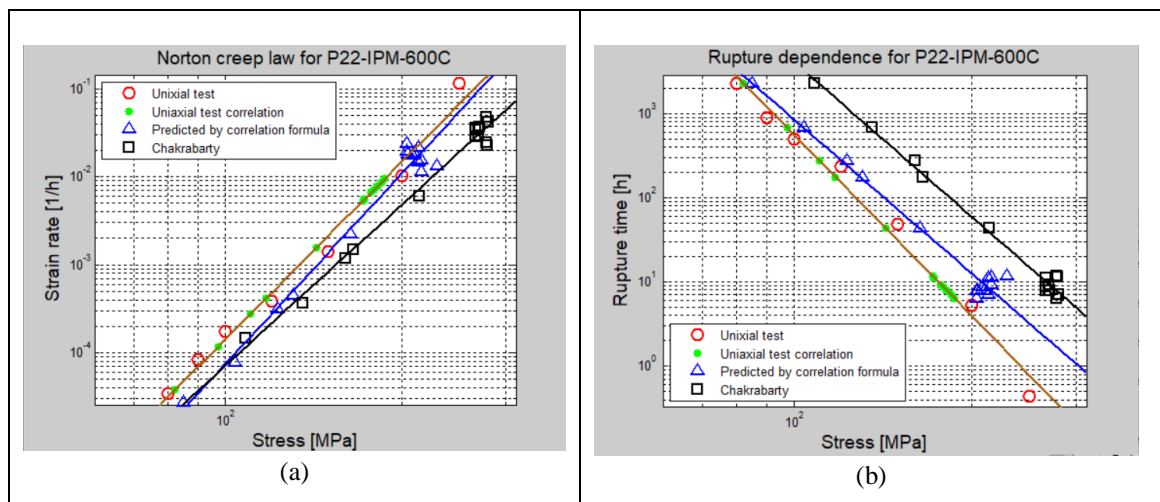

Figure 7. Comparison of uniaxial creep data with prediction methods for P22 at 600 ^{0}C (a) Norton creep law, (b) Rupture time.
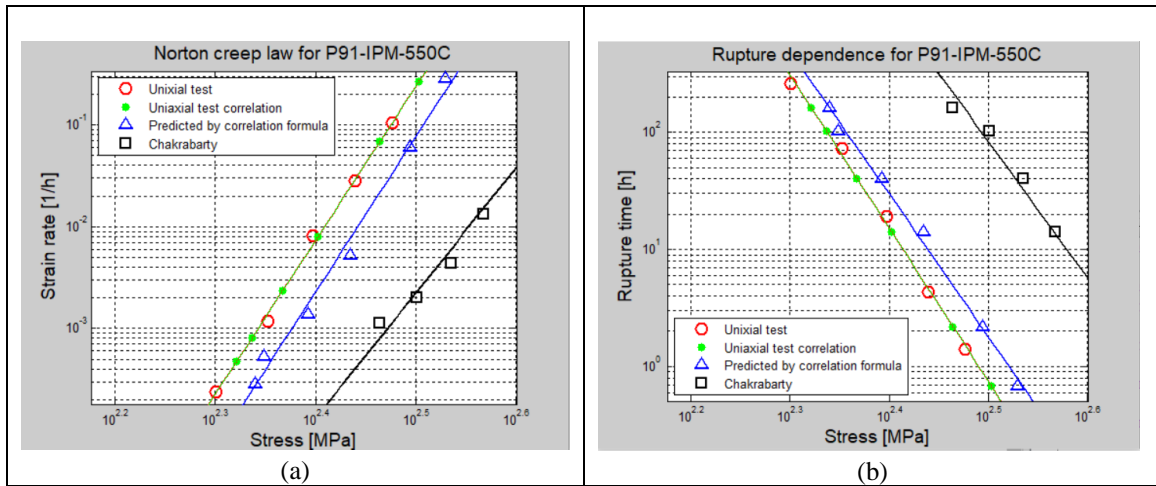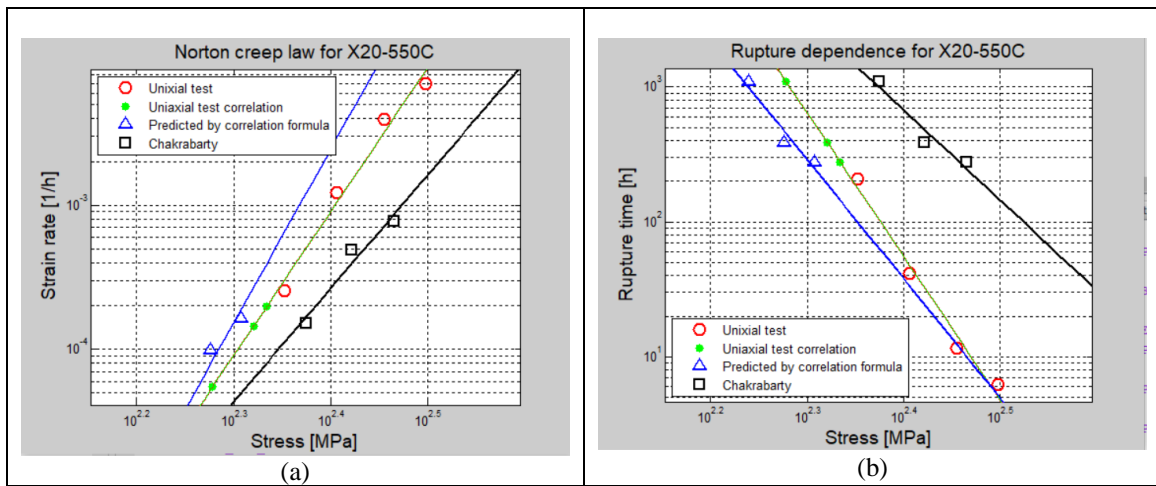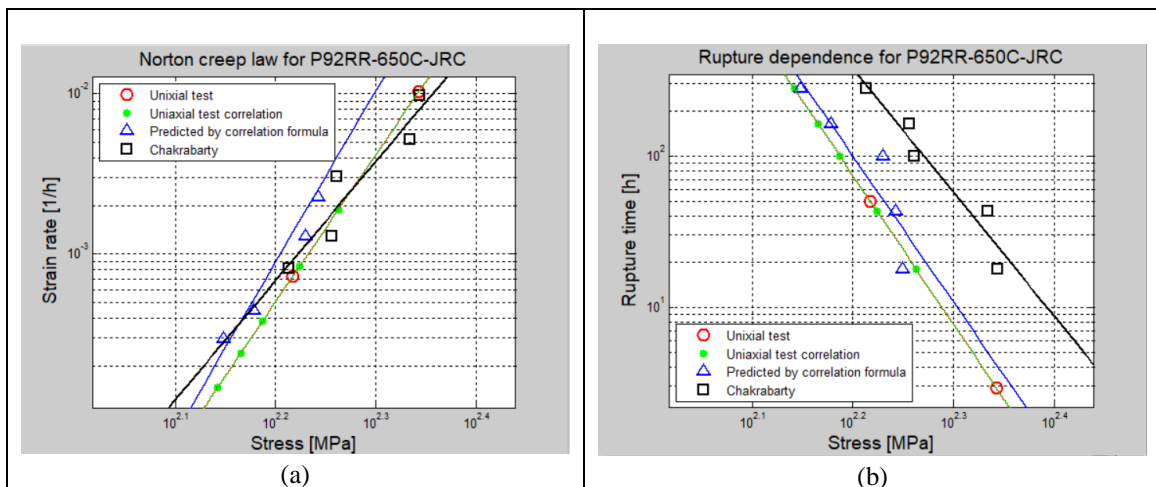
Figure 8. Comparison of uniaxial creep data with prediction methods for P91 at 550 ^{0}C (a) Norton creep law, (b) Rupture time.

Figure 9. Comparison of creep uniaxial data with prediction methods for X20 at 550 ^{0}C (a) Norton creep law, (b) Rupture time.

Figure 10. Comparison of uniaxial creep data with prediction methods for P92RR at 650 ^{0}C (a) Norton creep law, (b) Rupture time.

8. Discussion and conclusion

The Chakrabarty model [23] has been introduced in European CoP to estimate the creep load setting. However, it is not sufficient for the prediction of creep properties from SPC tests. This is because the complexity of the SPC problem, as too many non-linearities are involved. Efforts have been made by considering several effects; however none of them is commonly accepted yet.

This paper puts forward a new methodology based on direct use of experimental data. Because the experimental data implicitly contain all effects, a theoretical analysis with unavoidable assumptions is not needed.

Empirical formulas are given to estimate the equivalent stress σ and the minimum strain rate $\dot{\varepsilon}_{min}$, thus creep properties can be predicted using the measured SPC data.

Verification has been carried out and shows that, the predictions by the empirical formulas are in good agreement with the uniaxial creep data, and are much better than predicted by Chakrabarty model. From Figs. 5-10, one can notice that the fitting quality for rupture life is better than that for minimum strain rate. That is understandable, as the equivalent stress σ is derived from the comparison of the rupture time, while the minimum strain rate is derived from further comparison. Someone may feel a bit unexpected about the very high fitting quality in rupture life in Figs. 5-10(b). Due to the factor that the values of factor Ψ for these examples are close to the fitting line and far from the scattering points. In addition, the test data for these examples are provided by IPM, IMT and JRC with high quality.

The accuracy of the empirical formulas should be improved further, especially for the factor Ψ. At this moment, the coefficient of determination, R^2, of the regression is about 0.59, and this value is quite low. The consequence of using the fitting (straight) line in Fig. 3 for any random tests indicates that the stress error could be > 50% in the worst cases, which will lead to a huge difference in minimum strain rate (n is large) if used. Therefore a study should be carried out case by case for these scattering points to find the influence factors. It may be necessary to distinguish low-alloy steel from austenitic steel or consider the temperature difference. A neural network approach is under developing for this purpose.

References

1. Ule, B.; Sustar, T.; Dobes, F.; Milicka, K. (IPM, Czech); Bicego, V.; Tettamanti, S. (CISE, Italy); Maile, K.; Schwarzkopf, C. (MPA, Germany); Whelan, M.P. (JRC, Italy); Kozlowski, R.H.; Klaput, J. (IMMT, Poland). Small punch test method assessment for the determination of the residual creep life of service exposed components: outcomes from an inter-laboratory exercise, Proceedings of the SMiRT Post Conference Seminar **1997**, No. 13, Paris.

2. Ule, B.; Šustar, T.; Dobeš, F.; Milička, K.; Bicego, V.; Tettamanti, S.; Maile, K.; Schwarzkopf, C.; Whelan, M. P.; Kozlowski, R. H.; Klaput, J. Small punch test method assessment for the determination of the residual creep life of service exposed components: outcomes from an interlaboratory exercise. Nucl. Engng. Des. **1999**, 192, pp. 1–11.

3. Bicego, V.; Di Persio, F. (JRC); Rantala, J. H. (JRC); Hurst, R. C. (JRC). Small Punch Creep Test Method: Results from A round robin Carried out within EPERC TTF5, TTF5 technical report, 31 May 2003; or 8th EPERC Annual General Meeting, 23 Oct 2003, Gent (B).

4. ASTM. Standard test method for small punch testing of ultra-high molecular weight polyethene used in surgical implants, ASTM F2183-02, 2002.

5. CEN. Small Punch Test Method for Metallic materials, Part A: A Code of Practice for Small Punch Creep Testing. Part B: A Code of Practice for Small Punch Testing for Tensile and Fracture, CEN Workshop 21 document, 2005.

6. Ma, Y. W.; Shim, S.; Yoon, K. B. Assessment of power law creep constants of Gr91 steel using small punch creep tests. Fatigue & Fracture of Engineering Materials & Structures. **2009**, 32, 951–960, DOI: 10.1111/j.1460-2695.2009.01394.x.

7. Rouse, J. P.; Cortellino, F.; Sun, W.; Hyde, T. H.; Shingledecker, J. Small punch creep testing: review on modelling and data interpretation. Materials Science and Technology **2013**, 29, 1328-1345, DOI: 10.1179/1743284713Y.0000000278.

8. Cuesta, I. I.; Alegre, J. M.; Lorenzo, M. Influence of strain state in mechanical behaviour of aluminium alloys using the Small Punch Test. Mater. Des. **2014**, 54, pp. 291-294, DOI: 10.1016/j.matdes.2013.08.038.

9. Haroush, S.; Priel, E.; Moreno, D.; Busiba, A.; Gelbstein, Y. Evaluation of the mechanical properties of SS-316L thin foils by small punch testing and finite element analysis. Mater. Des. **2015**, 83, pp.75-84, DOI: 10.1016/j.matdes.2015.05.049.

10. Yang, S.; Ling, X.; Zheng, Y.; Ma, R. Creep life analysis by an energy model of small punch creep test. Mater. Des. **2016**, 91, pp. 98-103, DOI: 10.1016/j.matdes.2015.11.079.

11. Moreno, M. F.; Bertolino, G.; Yawny, A. The significance of specimen displacement definition on the mechanical properties derived from Small Punch Test. Mater. Des. **2016**, 95, pp. 623-631, DOI: 10.1016/j.matdes.2016.01.148.

12. Andrés, D.; Lacalle, R.; Álvarez, J. A. Creep property evaluation of light alloys by means of the Small Punch test: creep master curves. Mater. Des. **2016**, 96, pp. 122–130, DOI: 10.1016/j.matdes.2016.02.023.

13. Holmstrőm, S.; Auerkari, P.; Hurst, R.; Blagoeva, D. Using small punch test data to determine creep strain and strength reduction properties for heat affected zones. Materials Science and Technology **2014**, 30, pp. 63-66. DOI: 10.1179/1743284713Y.0000000311.

14. García, T. E.; Rodríguez, C.; Belzunce, F. J.; Suárez, C. Estimation of the mechanical properties of metallic materials by means of the small punch test. Journal of Alloys and Compounds **2014**, 582, pp. 708–717, DOI: 10.1016/j.jallcom.2013.08.009.

15. Geng, J. F.; Cai, H. S.; Ma, D. F.; Feng, X. S.; Guan, K. S. Identification of creep parameters of P91 by small punch test. Applied Mechanics and Materials **2014**, 529, pp. 439-443, DOI: 10.4028/www.scientific.net/AMM.529.439.

16. Naveena, S.; Komazaki, I. Evaluation of creep rupture strength of high nitrogen ferritic heat-resistant steels using small punch creep testing technique. Mater. Sci. Engng. A **2016**, 676, pp. 100-108, DOI: 10.1016/j.msea.2016.08.102.

17. Hurst, R. C.; Lancaster, R. J.; Jeffs, S. P.; Bache, M. R. The contribution of small punch testing towards the development of materials for aero-engine applications. Theoretical and Applied Fracture Mechanics **2016**, 86 (529), pp. 69-77, DOI: 10.1016/j.tafmec.2016.07.013.

18. Dyson, C. C.; Sun, W.; Hyde, C. J.; Brett, S. J.; Hyde, T. H. Use of small specimen creep data in component life management: a review. Materials Science and Technology **2016**, 32, pp. 1567-1581, DOI: 10.1080/02670836.2015.1132536.

19. Šturm, R.; Jenko, M.; Ule, B.; Šolar. Small Punch Testing of smart weld metals, Proceedings of 2nd International Conference "Integrity of High Temperature Welds", organized by IOM Communications Ltd., UK, 2003.

20. Tettamanti, S.; Crudeli, R. Small punch creep test: a promising methodology for high temperature plant components life evaluation. Baltica IV Plant Maintenance for Managing Life & Performance **1998**, Vol. 2, pp. 501-509.

21. Chakrabarty, J. A theory of stretch forming over hemispherical punch heads. Int. J. mech. Sci. **1970**, 12, pp. 315-325, DOI: 10.1016/0020-7403(70)90085-8.

22. Yang, Z.; Wang, Z. Relationship between strain and central deflection in small punch creep specimens. International Journal of Pressure Vessels and Piping **2003**, 80, pp. 397-404, DOI: 10.1016/S0308-0161(03)00069-3.

23. Li, Y. Z. An analytic approach for interpreting creep curves from small punch test, Proceedings of the 9th International Conference on Creep & Fracture of Engineering Materials & Structures, Edited by J.D. Parker, University of Wales Swansea, 2001, pp589-600. Or Proceedings of the 3rd Conference on Advances in Material Technology for Fossil Power Plants, Edited by R. Viswanathan, W.T. Bakker and J.D. Parker, University of Wales Swansea, 2001, pp473-488.

24. Li, Y. Z.; Sturm, R. Small punch test for weld heat affected zones, International Conference WELD 2005, GKSS Research Centre, Geesthacht, Germany.

25. Li, Y. Z.; Sturm, R. Determination of Norton creep law and rupture time dependence from small punch test, Proceedings of the 3rd International Conference on Integrity of High Temperature Welds, 24-26 April 2007; 1 Carlton House Terrace, London, UK.

26. Li, Y. Z.; Stevens, P.; Geng, J. F.; Ma, D. F.; Xu, L. Determination of creep properties from small punch test with reverse algorithm. Key Engineering Materials, April 2017; Trans Tech Publications. DOI: 10.4028/www.scientific.net/kem.734.212.

27. Abendroth, M. Identification of creep properties for P91 steels at high temperature using the small punch test, Metallurgical Journal **2010**, vol. LXIII, pp.39-43.

28. Hyde, T. H.; Sun, W. Interpretation of small punch creep test data for ductile materials, Metallurgical Journal **2010**, vol. LXIII, pp.25-33.

29. Cortellino, F.; Rouse, J. P.; Cacciapuoti, B.; Sun, W.; Hyde, T. H. Experimental and Numerical Analysis of Initial Plasticity in P91 Steel Small Punch Creep Samples. Experimental Mechanics **2017**, 57, pp. 1193-1212, DOI 10.1007/s11340-017-0296-9, DOI 10.1007/s11340-017-0296-9.

30. Milička, K.; Dobeš, F. Small punch testing of P91 steel. International Journal of Pressure Vessels and Piping **2006**, 83, 625–634, DOI: 10.1016/j.ijpvp.2006.07.009.

31. Ule, B.; Šuštar, T. The effect of initial hot plastic deformation on creep behaviour of 12 Cr steel specimens in small punch tests. Materials at High Temperatures **2001**, 18, pp. 163-170.

32. Dobeš, F.; Dymáček, P. Fracture-based correlation of uniaxial and small punch creep data. Theoretical and Applied Fracture Mechanics **2016**, 86, pp. 34-38, DOI: 10.1016/j.tafmec.2016.08.020.

33. Dymáček, P. Recent developments in small punch testing: Applications at elevated temperatures. Theoretical and Applied Fracture Mechanics, **2016**, 86, pp. 25-33, DOI: 10.1016/j.tafmec.2016.09.01.

34. Purmenský, J.; Matocha, K. Testing of small specimens in physical metallurgy. Proceedings of the 10th International Metalurgical Conference, METAL 2001, TANGER Ostrava, Czech Republic, Prnka, T. (Ed.), ISBN 80-85988-56-9, 2001; pp.70/1–70/13.

35. Dymáček, P.; Milička, K. Small punch testing and its numerical simulations under constant deflection force conditions. Strength Mater. **2008**, 40, pp. 24-27, DOI: 10.1007/s11223-008-0007-y.

36. Dobeš, F.; Milička, K.; Ule, B.; Šustar, T.; Bicego, V.; Tettamanti, S.; Kozlowski, R. H.; Klaput, J.; Whelan, M. P.; Maile, K.; Schwarzkopf, C. Miniaturized Disk-Bend Creep Test of Heat-Resistant Steels at Elevated Temperatures. Engineering Mechanics **1998**, 5, pp. 157-160.

37. Dymáček, P.; Dobeš, F.; Li, Y. Z.; Holmström, S.; Stevens P. Determination of creep properties from small punch test using experimental correlation. SSTT2018, Swansea, 2018 (submitted).

38. Dymáček, P.; Li, Y. Z.; Dobeš, F.; Stevens, P. New approach to determination of uniaxial creep properties from small punch creep curves, Materials at High Temperatures (under review).

39. Holmström, S.; Li, Y. Z.; Dymacek, P.; Vacchieri, E.; Jeffs, S.; Lancaster, R.; Omacht, D.; Zdenek, K.; Anelli, E.; Rantala, J.; Tonti, A.; Komazaki, S.; Narveena; Bruchhausen, M.; Hurst, R.; Hähner, P.; Richardson, M; Andres, D. Creep strength and minimum strain rate estimation from Small Punch Creep tests, Materials Science & Engineering A (under review).

Small ring testing of high temperature materials

C. J. Hyde [*]

Gas Turbine and Transmission Research Centre (G2TRC), University of Nottingham, UK, NG7 2RD
[*] Correspondence: christopher.hyde@nottingham.ac.uk; Tel.: +44-115-9513735

Abstract: In service components such as steam pipes, pipe branches, gas and steam turbine blades, etc. which operate in engineering applications such as power plant, aero-engines, chemical plant etc., can operate at temperatures which are high enough for creep to occur. Often, only nominal operating conditions (i.e. pressure, temperatures, system load, etc.) are known and hence precise life predictions for these components, which may be complex in terms of geometry or weld characteristics, are not possible. Within complex components it can also be the case that the proportion of the material creep life consumed may vary from position to position within the component. It is therefore important that non-destructive techniques are available for assisting in the making of decisions on whether to repair, continue operating or replace certain components. Small specimen creep testing is a technique which can allow such analyses to be performed. Small samples of material are removed from the component to make small creep test specimens. These specimens can then be tested to give information on the remaining creep life of the component. This paper presents the results of small ring specimens tested under creep conditions and shows the comparison to standard (full size) creep testing for materials used under high temperature in industry.

1. Introduction

In many cases it is desirable to achieve standard creep data (see Figure 1) from of pieces of material which are too small to manufacture conventional uniaxial specimens (see Figure 2). To remedy this, a few different small specimen creep test types have been developed over recent years. Such small specimen types are required for applications such as operating power-plant steam pipes, from which a small amount of material can be removed from the in-service component. Such small amounts of material are usually extracted via the 'scoop' method [1], as shown in Figure 3. These scoop samples can then be manufactured into small specimen form and tested.
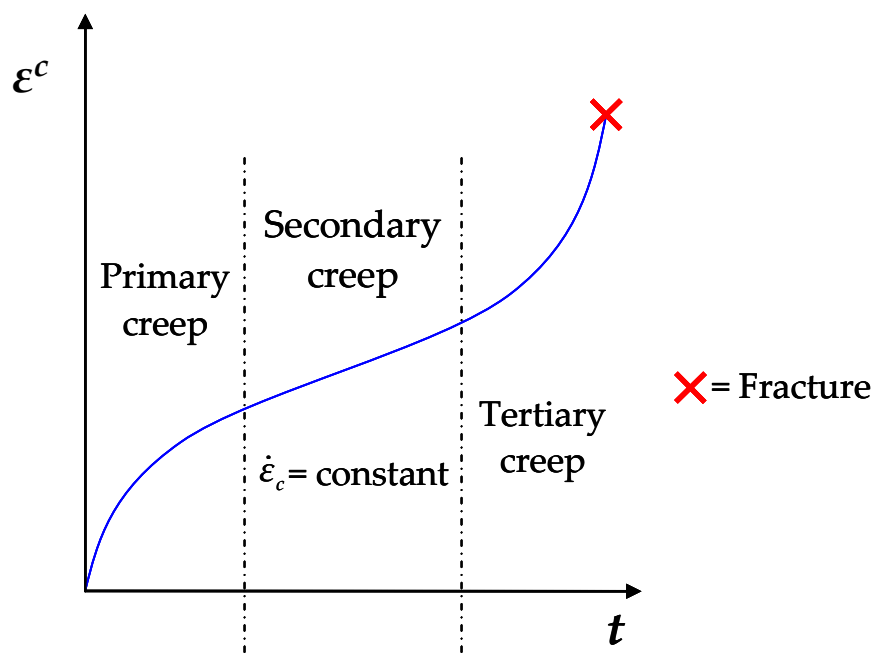

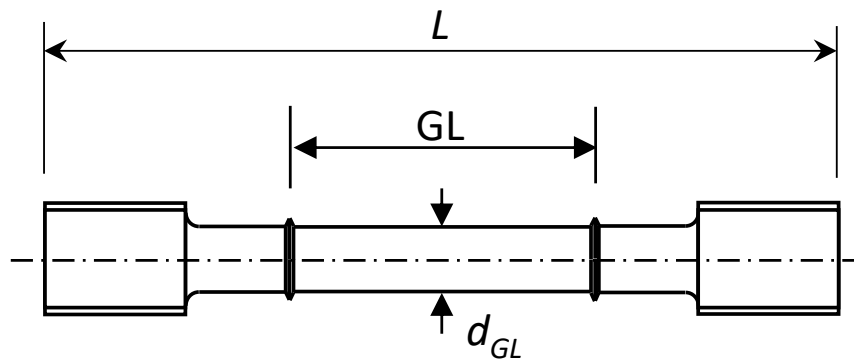**Figure 1**. Schematic representation of a conventional creep curve.

Figure 2. "Standard" uniaxial creep test specimen (GL ≈ 30 – 50mm; dGL ≈ 6 – 10mm; L ≈ 100 – 130mm).
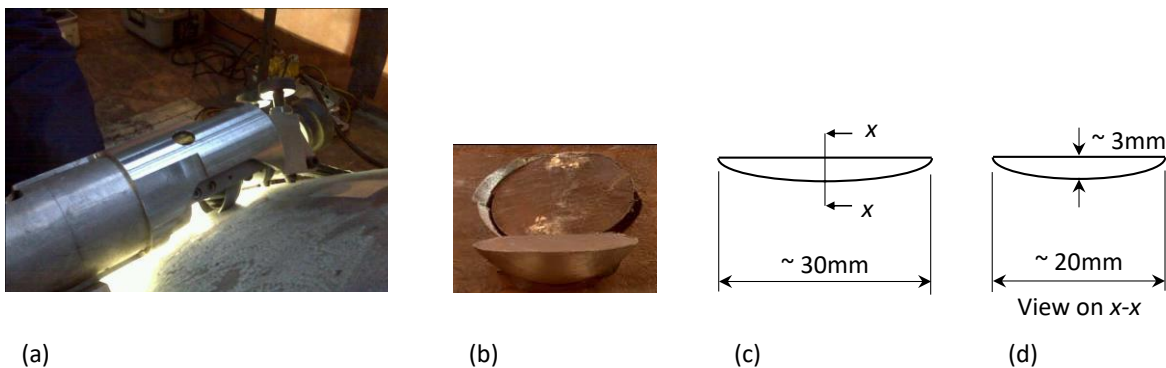

(a)　　　　　　　　　　(b)　　　　　　(c)　　　　　(d)

Figure 3. Scoop sample **(a)** Extraction of, **(b)** Close-up image, **(c)** Schematic representation of a typical scoop sample and **(d)** Schematic representation through x-x.

Another example application for small specimen creep testing is when creep information is required for the airfoil material of heavy-duty gas turbine components. The complex geometry of the internal cooling channels in turbine blades and vanes reduces the available material of what are sometimes already relatively small components. In such a case the component must be taken out of service and small specimen/s manufactured from the component, the results from which can assist decisions on similar/replacement components such as how much longer the component can safely stay in service and for ranking assessments [2].

There are several small specimen test types which can be used for obtaining creep properties from small amounts of material, namely sub-size conventional test specimens [3], impression creep (IC) specimen tests [4], small punch (SP) specimen tests [5] and small ring (SR) specimen tests [6], the performance of which is the subject of this paper. Each specimen type has its own unique advantages and disadvantages and in some cases it may not be obvious which one is the most appropriate test method to use. This paper shows the results SR testing of a Nickel-based superalloy (which is not possible with other small specimen types, as discussed in section 2.2) and gives a description of the major advantages of this specimen type.

2. Small Ring Creep Testing

SR creep testing (see Figure 4) has some unique advantages over other small specimen creep test types as discussed below. The test consists of diametrically loading of a (circular or elliptical) ring and measuring the load line deformation of the specimen.
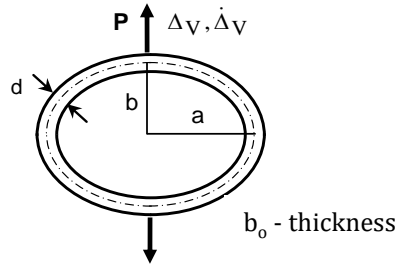
Figure 4. Schematic diagram of a SR specimen.

Typical geometrical values are as follows: a = b = 5mm, d = 1mm and bo = 2.5mm. For this test geometry, an analytical solution for the load line deformations has been obtained, based on the complementary strain energy approach [6]. A reference stress approach was used to establish the conversion relationships between the applied load and the equivalent uniaxial reference stress and between the experimentally measured load-line creep deformation rate, $(\Delta_V)^{\cdot}$, and the equivalent uniaxial creep strain rate, $\dot{\varepsilon}_c$, [6], these conversions are as follows:

$$\sigma_{ref} = \eta \frac{Pa}{b_o d^2} \tag{1}$$

$$\dot{\varepsilon}^c(\sigma_{ref}) = \frac{d}{4ab\beta} \dot{\Delta}_V \tag{2}$$

where η and β (conversion factors) are constants and vary with the specimen dimensions, as shown in Figure 5, a and b are the major and minor axis dimensions of the elliptical specimen, as shown in Figure 4, bo is the specimen depth and d is the specimen thickness as shown in Figure 4.
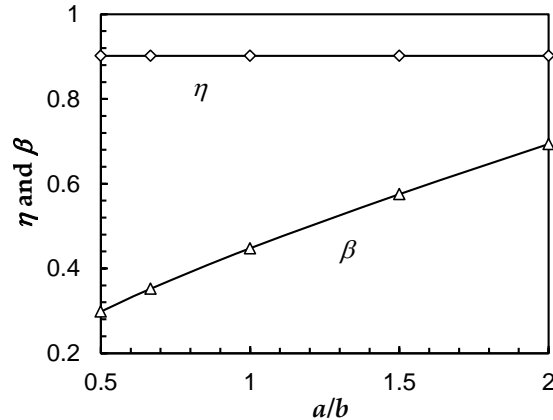
Figure 5. Variation of the η and β parameters with a/b.

2.1. Experimental procedure

Figure 6 shows a photograph of the experimental set-up shown in Figure 4 for the SR specimen test. The SR specimen is placed into the test machine and a load applied diametrically to the specimen via loading pins with large resulting deformations in comparison to that of the sub-size uniaxial and impression creep test types. This is due to the flexible nature of the SR specimen type which results in a large equivalent gauge length of the SR specimen type. These high levels of deformation allow for tests to be performed at lower equivalent stresses than the other specimen types and allows for low strains to be obtained from these relatively large deformations.

Figure 6. Experimental set-up for the SR test.

2.2. Advantages of the small ring testing technique

An analytical solution for the deformation of the specimen has been obtained by use of the complimentary strain energy approach and mechanics-based (reference stress) conversion relationships for load and deformation to the corresponding uniaxial stress and creep strain rate, which are relatively insensitive to the geometry changes which occur during deformation can be made.

Further advantages of the SR test include the fact that the specimens are very simple in geometry and therefore very easy to manufacture and test. Also, it is a highly sensitive test and hence the deformations measured during the test are large meaning that testing can be performed at low equivalent stresses. Hence low strains can be related to these larger deformations. The deformations from this test are large due to both the flexibility and the large equivalent gauge length (EGL) of the specimen. Due to the large deformations, the test is relatively insensitive to experimental noise.

In addition to above, a unique major advantage of the SR type of small specimen creep test type (and the main focus of this paper) is that, any material can be tested provided that the loading pins are similarly creep resistant to the specimen (could be made from the same material). For the other small specimen types, impression testing for example, the indenter must be significantly more creep resistant than the specimen. This makes testing materials such as Nickel-based superalloys extremely difficult for specimen types other than the small ring specimen.

3. Inconel 738 Material

Inconel 738 was selected for SR creep testing as Laborelec required the creep conditions of a service-aged turbine blade. It is one of the first nickel-based superalloys used for gas turbine hot gas path sections. Inconel 738 is considered as a standard reference material in literature and its creep properties have been widely studied. Mainly consisting of nickel (providing high strength at high temperature), Inconel 738 also contains alloying elements such as Chromium, Aluminium, Cobalt, Titanium, Tungsten and Tantalum in order to add further strength properties as well as corrosion and oxidation resistance. A scanning electron microscope equipped with an energy dispersive spectroscope provided a semi-quantitative analysis of the base material. The results of a semi-quantitative analysis using an energy dispersive spectroscope are provided in Table 1.

Table 1. Chemical composition of blade material compared with literature data, semi-quantitative analysis (wt.%).

	Ni	Al	Ti	Cr	Co	Mo	Ta	W	Nb
Blade material	60.39	3.13	3.46	17.20	8.58	1.94	1.88	2.52	0.83
IN738 [7]	bal	3.40	3.40	16.00	8.50	1.70	1.70	2.60	0.90

4. Specimen Manufacture

An ex-service Inconel 738 third stage blade from a heavy-duty gas turbine was selected for the testing program (see Figure 7a). The blade did not experience any refurbishment. The root of the blade was selected for creep assessment (see Figure 8). This area represents the material in its virgin condition, since it is not exposed to high stresses and temperatures. It is common practice to use the root of gas turbine blades as a reference of the as-cast and heat-treated material for metallurgical evaluation. Figure 9 shows how the small ring specimens were manufactured from a slice of the blade root.
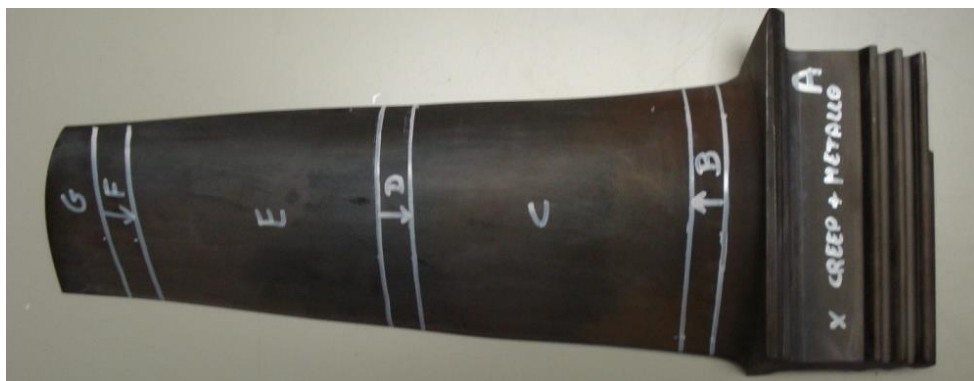
Figure 7. Third stage gas turbine blade from a heavy-duty gas turbine.

Figure 8. Piece of root extracted along the main direction of the blade.

Figure 9. Ring specimens and remains from EDM operations.

5. Small Ring Creep Testing Results for Inconel 738

Four SR creep tests have been performed using the Inconel 738 specimens described in section 4 and the result shown in Figure 10. It can be seen that the results exhibit primary and secondary creep strain regions.
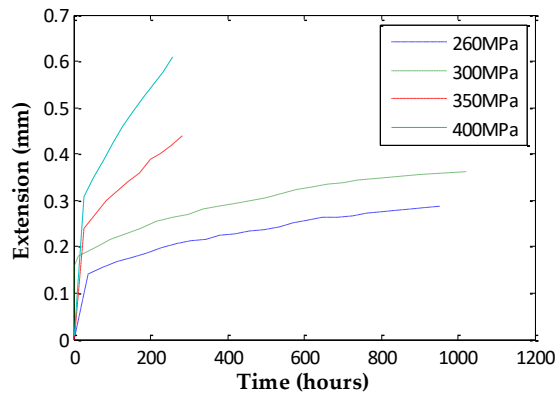

Figure 10. SR creep test data for Inconel 738 (nickel-based superalloy) at 800°C.

Due to the effect of the specimen deformation which occurs during the test, a small amount of continual curvature (decreasing deformation rate) is present within the 'secondary region' and a completely saturated (constant) strain rate is not quite achieved. It can be seen form equation (1) that the expression used to calculate the applied test load, P, which is assumed to remain constant throughout the test (calculated based in the initial specimen geometry) is based on a desired test reference stress, σ_{ref}. Whilst b_o and d are constant throughout the test and the variance of η with deformation as the test goes on is negligible (see Figure 5), the change in the ring major axis, a, should not be neglected and hence P should be updated based on the instantaneous specimen geometry. However, (as within this paper) if it is intended that the data is used to obtain the constants for a material model such as the Norton secondary creep model [8] as shown by equation (3), and for corresponding conventional plots of stress vs. minimum strain rate be made from the SR data, values for the secondary MSRs are required and can be obtained.

$$\dot{\varepsilon}^c_{min} = A\sigma^n \tag{3}$$

By considering the data within the secondary (small amount of curvature) creep region (see Figure 10), local values of extension and extension rate at regular time intervals can be used to calculate the values of σ_{ref} and $\dot{\varepsilon}^c$ at each interval position. The averages of the σ_{ref} values and the $\dot{\varepsilon}^c$ values from each time interval can then be taken in order to give the final values. These values can be used to produce a plot of stress vs. MSR on a log-log scale has been produced as shown in Figure 11 where these results are compared to equivalent conventional (full-size) uniaxial tests (see Figure 1) for the same material at the same temperature and shows that the SR data compares extremely well with this conventional creep test data.
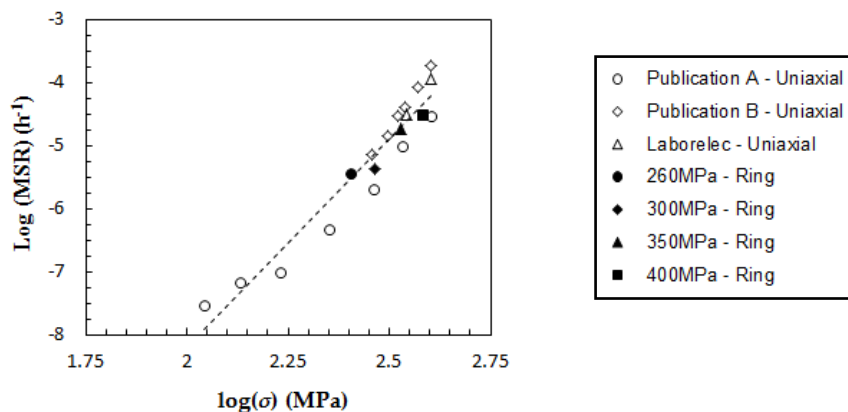

Figure 11. Data shown in Figure 10 plotted as stress vs. MSR (minimum creep strain rate) on a log-log scale and compared with equivalent uniaxial data (see Figure 1).

Work is currently being conducted to allow for adaptive load tests to be carried out for this SR creep test type in order that the σ_{ref} be constant throughout the test. This is expected to result in a clear secondary (constant strain rate) region being present in the resulting creep data (equivalent to Figure1 0). This will eliminate the need to interpret the data as described above and will allow for interpretation of the data to be identical to that of a conventional creep test in order to produce plots of the data in the form as shown in Figure 11.

6. Conclusions

This paper describes and demonstrates a recently been developed ring type small specimen creep test [6, 9, 10]. This specimen type displays many advantages compared to other small specimen creep test types. These advantages include the fact that any material, including highly creep resistant materials such as nickel-based superalloys, can be tested, as is the main topic of this paper. The current work, which shows the method applied to the root of an ex-service blade made of Inconel 738 material, is extremely encouraging when compared with conventional uniaxial data. In addition, an analytical method which relates the specimen load and dimensions to the load-line displacement has been obtained.

As mentioned in section 5, the reference stress will change, due to the changes in the dimensions of the specimen, which occur during a test, if a constant load is applied to the specimen throughout the test (see equation (1)). This results in a small amount of curvature (reducing strain rate) in the creep data in the secondary creep region. In order to rectify this, software is currently being developed at the University of Nottingham which will allow for the load to be adapted during the test according to equation (1) as the specimen deforms. It is believed that this will further improve the already extremely encouraging results presented in this paper in terms of both a more clear secondary creep region and the comparison of the small ring creep test data with the uniaxial equivalents.

The small ring creep test method has now been validated for steel materials [6, 9, 10], and a nickel-based superalloy material and further validation of the method, for highly creep resistant materials (e.g. other nickel-based superalloys), is in progress.

References

1. Hyde, T.H.; Sun, W.; Brett, S.J. "Some recommendations on standardisation of impression creep testing", European Creep Collaborative Committee on Creep and Fracture in high Temperature Components – Design and Life Assessment, 21st-23rd April 2009, Dubendorf, Switzerland.
2. Sun, W.; Hyde, T.H.; Brett, S.J. "Application of impression creep data in life assessment of power plant materials at high temperatures", Proceedings of the Institution of Mechanical Engineers, Part L , Journal of Materials: Design and Applications 222, 175-182.
3. Askins, M.C.; Marchant K.D. Estimating the remanent life of boiler pressure parts, EPRI Contract RP2253-1, Part 2, Miniature specimen creep testing in tension, CEGB Report., TPRD/3099/R86, CEGB, UK, 1987.
4. Hyde, T.H.; Sun, W.; Becker, A.A. Analysis of the impression creep test method using a rectangular indenter for determining the creep properties in welds, Int. J. Mech. Sci., 38, 1089-1102. 1996.
5. Parker, J.D.; James, J.D. Creep behaviour of miniature disc specimens of low alloy steel, ASME, PVP 279, Developments in a Progressing Technology, 167-172, 1994.
6. Hyde, T.H.; Sun, W. "A novel, high sensitivity, small specimen creep test", J. of Strain Analysis 44(3), 171-185.
7. Sims C.T.; Stoloff N.S. "Superalloys II: High Temperature Materials for Aerospace and Industrial Power", John Wiley & Sons, USA, 1987
8. Norton, F.H. "Creep of steel at high temperatures", McGraw-Hill Book Co., New York.
9. Hyde, T.H.; Sun, W. "Some considerations on specimen types for small sample creep tests", Int. Conf. WELDS 2009: Design, Testing, Assessment and Safety of High Temperature Welded Structures, 24th-26th June 2009, Fort Myers, Florida, USA.
10. Sun, W.; Hyde, T.H. "Determination of secondary creep properties using a small ring creep test technique", Metallurgical Journal, Vol. LXIII, 185-193, 2010.

Industrial applications of small punch test

P. Čížek [1,*], L. Kander [1], Š. Stejskalová [1]

[1] MATERIAL AND METALLURGICAL RESEARCH Ltd., Pohraniční 31/639, 703 00 Ostrava, Vítkovice, Czech Republic

[*] petr.cizek@mmvyzkum.cz; Tel.: +420-59595-3729

Abstract: Small punch test is an advantageous method for evaluation of mechanical properties of components especially in cases, where it is technically difficult or even impossible to obtain enough bulk material for standard tests. Therefore, the method is very well applicable in power industry, for example in residual lifetime assessment of critical parts of components and structures after long-term operation. The testing material is sampled by using special sampling device that ensures no component damage and the amount of material being sampled is so small that obviously no component repair is necessary after sampling. Small punch testing is exploited not only for evaluation of mechanical properties, but also microstructural and chemical analyses can be performed from the obtained sample and complex actual material characteristic of component can be assessed. Company MATERIAL AND METALLURGICAL RESEARCH, Ltd., has more than 20 years of experience with small punch testing in industrial applications and several examples of its application for analysis of material properties and residual lifetime assessment are presented in this paper.

Keywords: small punch testing, material properties, residual lifetime, sampling

1. Introduction

Small punch test (SPT) is a useful method for evaluation of actual material properties of components in power industry. A big advantage of this method is that material can be sampled from studied component directly on site without negative influence on its function. This method can be also used in cases when it is necessary to obtain test specimen from very narrow layers of material, for example from decarburized layers, segregations, coatings, etc. Another typical example of utilization of SPT method is evaluation of material characteristics of specific areas of weld joints or deposit layers.

Mechanical properties, especially yield stress or transition temperature (FATT), are degraded during long-term operation at elevated temperature. Microstructure of operated components can be degraded by appearance of cavities. An approach based on specimen sampling from critical parts of components in periodic intervals (including first sampling from virgin state of newly produced component) with complex material analysis allows to determine material degradation for each period and subsequently to assess the residual lifetime of a component. MATERIAL AND METALLURGICAL RESEARCH, Ltd., has been performing long-time monitoring of components in power industry for about 20 years. It is an owner and also a producer of special scoop sampling machine and offers long-term monitoring of operated components behaviour in Europe. This paper summarizes some key results, emphasizes an importance of SPT in this field and shows new results of small punch testing of materials used in ultra-super critical (USC) boilers.

2. Materials and Methods

Wide range of materials used for production of components in power industry has been monitored in last years. Most typical are materials of rotors, rotor cases, steam pipelines, valves, boiler drums, etc. Monitoring of degradation of material properties during operation is carried out by method of scoop sampling of material for testing without component damage. These samples are subsequently prepared for complex material analyses, namely chemical analysis, microstructure analysis and small punch tests. Test results and assessed degree of material degradation is then compared with results of previous analyses and residual lifetime of component is then estimated. This approach has been successfully used for many components and some of the most interesting cases are stated below.

3. Determination of actual material characteristic of boiler drums

Monitoring of material behaviour was performed on 4 boiler drums operating in a brown-coal fired power plant and produced in 1940s and 1950s. Material degradation has been assessed in 5 years interval [1]. No material certificates describing types and properties in the as-received state has been preserved. Boiler drum has been exposed to temperature 300°C and pressure 7.8 MPa for approximately 300,000 hours. An example of specimen sampling on an inner surface of boiler drum is shown in Figure 1.
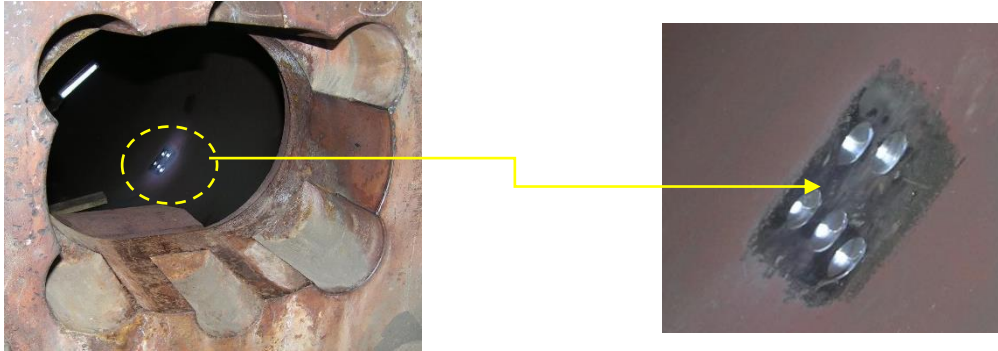
Figure 1. Specimen sampling on inner surface of boiler drum.

Results of chemical analyses performed on material of boiler drum No. 4 in 2009 and 2014 are stated in Table 1 and show the significant difference in concentration of some elements, especially high content of tramp elements (As, Sb, Sn) known for their embrittlement effect in the steel.

Table 1. Chemical analysis comparison of boiler No. 4 material (weight %).

Sampling Year	C	Mn	Si	As	Sb	Sn	Co
2009	0.34	0.75	0.019	0.010	0.016	0.003	0.009
2014	0.39	0.83	0.024	0.022	0.025	0.012	0.024

The results in Table 1 confirm low metallurgical quality of steel and also quite high scatter in concentration of some elements. This confirms the heterogeneity of material, because sampling locations were very close to each other. That fact is caused by small volume of sampling experimental material compared to the large size of analysed component.

Mechanical properties were tested using SPT [2]. Three specimens are usually used for tensile strength and yield stress determination at room temperature. A set of approximately 15-20 specimens is mostly used to test the transition temperature T_{SP} determined by SPT. Comparison of SPT records at room temperature performed in 2014 and 2009 is shown in Figure 2(a), calculation of T_{SP} is shown in Figure 2(b). Transition temperature FATT was subsequently calculated on the base of correlation.
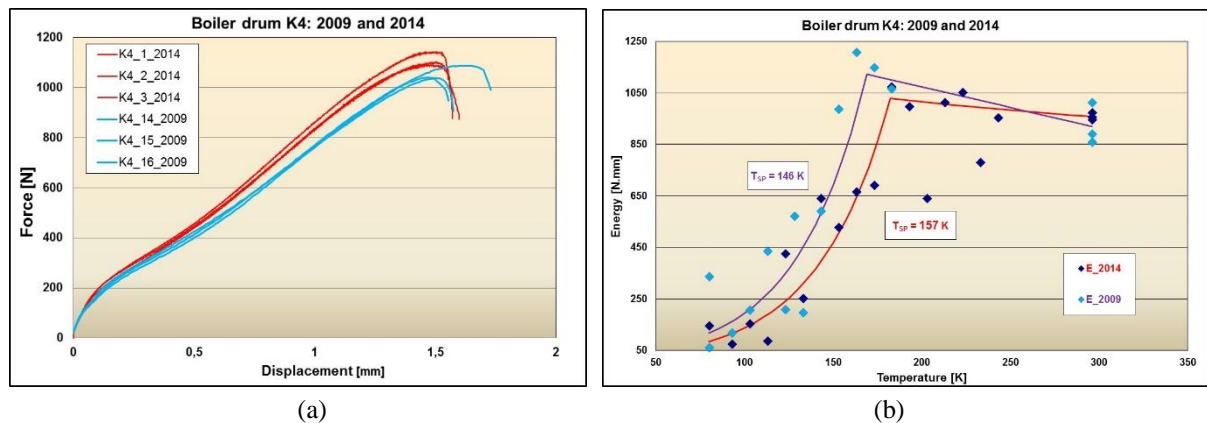

(a)	(b)

Figure 2. (a) Comparison of SPT records performed in 2009 and 2014, **(b)** Comparison of T_{SP} calculation using SPT performed in 2009 and 2014.

Figure 2(a) shows very small difference in force-displacement records between 2009 and 2014. Yield strength and tensile strength determined from these records are very well comparable. However, result of T_{SP} calculation increased by 11 K. T_{SP} value is used for determination of transition temperature (FATT) (see table 2). FATT increased by 26 °C between these two samples and it can be probably caused by locally increased concentration of tramp elements (Sn, As, Sb). But this change in FATT seems to be the only sign of material degradation after long-term operation at elevated temperature.

Table 2. Comparison of FATT values determined from SPT of boiler drum No. 4 in years 2009 and 2014.

Sampling year	T_{SP} [K]	FATT [K]	FATT [°C]
2009	146	340	66
2014	157	365	92

4. Determination of actual material characteristics of turbine case bodies at ethylene unit

Monitoring of material degradation of turbine casing using SPT was performed between years 2003 and 2014 [3]. Investigated components were approximately 37 years old in 2014. Several parts of turbine cases are exposed to the temperature about 500 °C and pressure 10.8 MPa (i.e. creep exposure), other parts are operated at maximum temperature 350°C and pressure 3.5 MPa. All these components were produced in Japan according to Japanese standards JIS. The main goal of performed analyses was to determine actual material properties in critical parts of components using chemical analysis, microstructure analysis and evaluation of mechanical properties, again by using SPT. Two parts of turbine case body GT201, made of the cast steel grade SCPH 21 (equivalent to GS 17CrMo 5-5 according to DIN 17 245) and working in the creep regime, were repeatedly analysed in 2003, 2008, 2012 and 2014, as can be seen in Figure 3, where are clearly visible sampling marks on the inner and outer parts of turbine case body GT201.
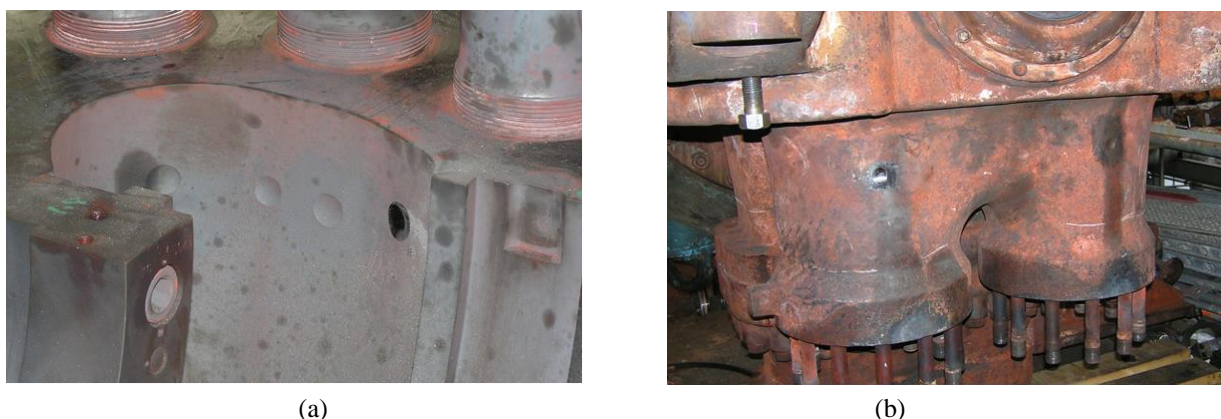

(a)   (b)

Figure 3. (a) Sampling marks on the inner surface of bottom part of turbine case body GT201, **(b)** Sampling marks on the outer surface of upper part of turbine case body GT201.

Comparison of mechanical properties of both part of the turbine case is stated in Table 3 and in Figure 4 and shows non-monotonic development of the both, proof stress and tensile strength. The both characteristics increased between the first two measurements, but then proof stress started to decrease, while tensile strength kept more or less the same values. An increase in tensile strength was in good accordance with the other analyses, namely metallographic analysis that confirmed higher concentration of carbides as well as the presence of annealing twins in microstructure in the respective sampling place.

Table 3. Change of mechanical properties of turbine case body GT201 determined by SPT.

Component	$R_{p0.2}$	R_m	$R_{p0.2}$	R_m	$R_{p0.2}$	R_m	$R_{p0.2}$	R_m
	[MPa]							
	2014		2012		2008		2003	
GT 201 bottom part of turbine case – inner surface	283	491	316	526	371	469	319	468
GT 201 upper part of turbine case – outer surface	261	445	358	520	410	473	351	465
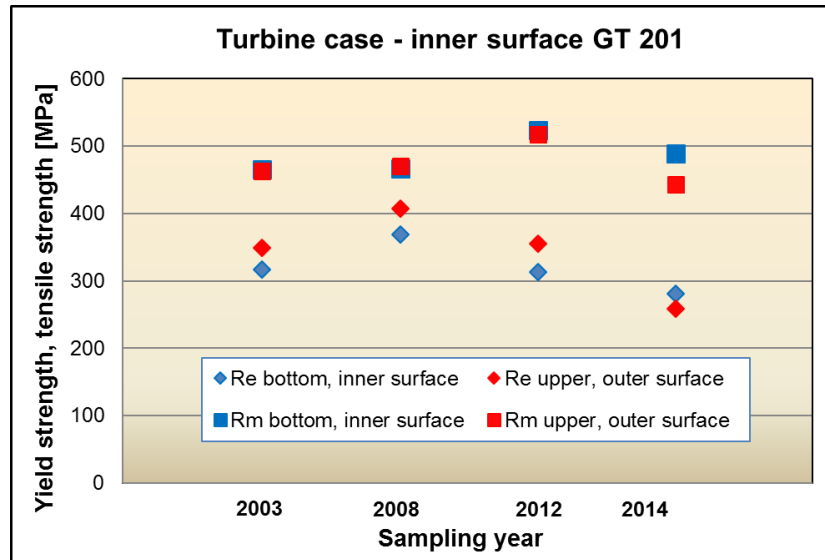
Figure 4. Trend of mechanical properties of GT201 turbine case between 2003 and 2014 determined by SPT.

5. Sigma phase precipitation and material properties of reheater tubes made of TP347HFG steel

Small punch testing of pressurised parts of USC boilers belongs to the last research activities focused on power industry. The development of the modern USC boiler is forced by demands on increasing the boiler efficiency altogether with the request for lowering CO_2 emissions. All these demands have to be accompanied by development of new steel grades with high creep strength and corrosion resistance. Due to relatively low price of iron-based materials in comparison with nickel-based superalloys the development was focused on new grades of austenitic heat resistant steels. Material properties and their testing by SPT tests were solved in the Czech Republic in the frame of a research project focused on three types of austenitic steels, namely Super 304H, HR3C and TP347HFG. Change of material properties due to necessary technological operations (bending, welding) and also the effect of long-term exposure at operating temperature were studied. Due to small dimensions of components (especially thin-walled tubes) SPT seems to be one of the best methods for evaluation of material properties. Small punch testing was also used to detect the effect of sigma phase on mechanical properties of TP347HFG steel after long-term operation.

The first research studies related to materials for USC applications were focused on the influence of sigma phase on material properties of TP347HFG [4] steel tubes used in an USC once-through Benson tower type boiler with double reheat in a Danish power plant.

Sigma phase is an intermetallic Fe-Cr phase that precipitates in stainless steel (especially ferritic and duplex) when the Cr content is above 20 wt.%. It precipitates also in austenitic stainless steels during long-term exposure at high temperatures and especially in steel grades with higher chromium content. The presence of sigma phase leads to embrittlement of the material at ambient temperature [5]. It is well-known that sigma phase represents a big problem in steels with higher Cr content and it was found that sigma phase developed in the AISI 316 steel within 1,000 hours at 700 °C and 50,000 hours at 650 °C [6]. However, its influence on toughness and plasticity of new

austenitic heat resistant steels has not been described in detail yet. The main goal of research work then was to quantify the influence of sigma phase on material properties including fracture behaviour using miniaturized test specimens and SPT.

Size and location of test specimens used for evaluation of effect of sigma phase on mechanical properties of TP347HFG steel are shown in Figure 5. Position 0° represents a tube orientation facing directly to the furnace (fire side) and thereby meeting the hottest flue gas, position 180° is an opposite side.
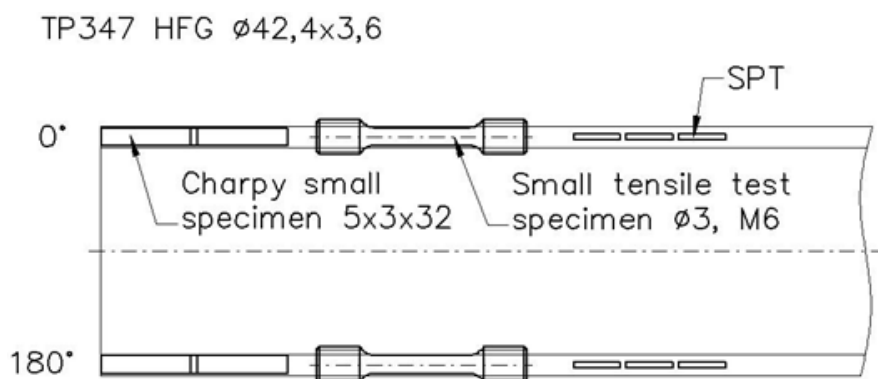
Figure 5. Size and location of test specimens machined from tube made of TP347HFG [4].

Microstructure of the steel and especially the presence and distribution of sigma phase particles was observed using LOM. Larger amount of sigma phase was observed in position 0° (fire side) than in position 180° (opposite side) and this fact can be clearly observed in Figure 6. The volume fraction of sigma phase at position 0° was 5.5 %, whereas at position 180° it was only 0.6 %.

| (a) | (b) |
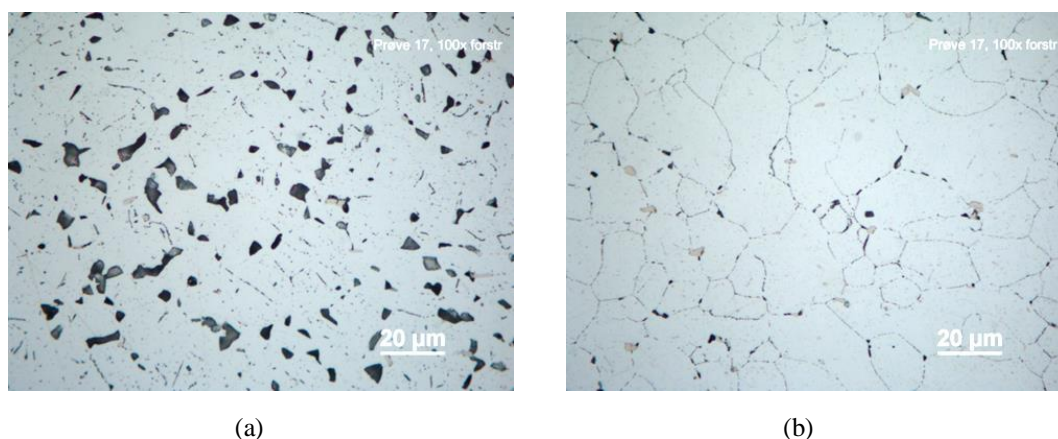
Figure 6. Microstructure analysis of TP347HFG with presence of sigma phase: (a) 5.5% in position 0°, (b) 0.6% in position 180° [4].

The both testing methods (miniaturized tensile test specimens and SPT) were subsequently used in order to compare the effect of sigma phase on mechanical properties. Tensile tests results performed on miniaturized specimens did not prove any significant difference in tensile strength on both sides of tube No. 17, whereas decrease of yield stress at the fire side of the tube was observed. Decreasing of plastic properties, elongation and reduction of area, also corresponded with increased sigma phase content.

Subsequently, five SPT specimens were cut from fire and opposite side of tubes in mid-thickness of the wall and testing was performed at room temperature. SPT is expected to reflect the changes in the microstructure more sensitively than tensile test. SPT records in the form force-elongation curves are compared in Figure 7 and clearly confirms the effect of sigma phase on mechanical properties. Fracture energy, calculated as an area under force–displacement curve, of specimens located in 0° position is 898 N·mm, which is significantly lower than fracture energy in 180° location (1408 N·mm).
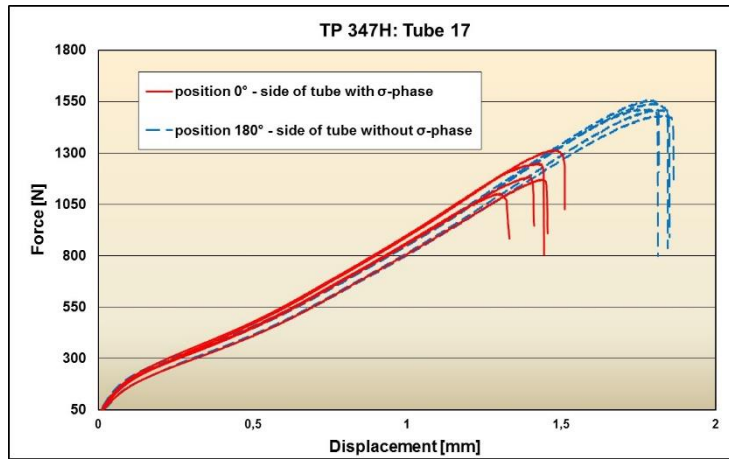
Figure 7. Comparison of small punch test results on fire and opposite sides of tube 17 with significant difference of sigma phase in the structure.

6. Material properties of welded joints of HR3C, TP347HFG and Super 304H steels

In this part of the research the attention was focused on material analysis of welded joints of HR3C, TP347HFG and Super 304H steels. Analyses were performed on circumferential welds of tubes with diameter 38 mm and wall thickness 6.3 mm. The main goal was to assess influence of one-year long exposure in the real operating environment of USC boiler on mechanical properties of welded joints. The samples had been exposed in the boiler without any loading at two working temperatures – one ranging from 635°C to 695°C and another ranging from 726°C to 775°C. Limited amount of material and low wall thickness are ideal conditions for using miniaturized test specimens or SPT. Altogether 21 combinations of base metals and welded joints of HR3C, TP347HFG, Super304H and P92 steels in as-welded state and after post-weld heat treatment were used for testing [7]. All material combinations were evaluated prior to exposure and subsequently after one-year exposure in the real USC boiler.

Evaluation of mechanical properties in as-received state was performed using miniaturized test specimens having 3 mm in diameter and 10 mm in length, absorbed energy was measured using miniaturized Charpy specimens and also SPT specimens were prepared. Location of test specimens inside the tubes is shown in Figure 8.
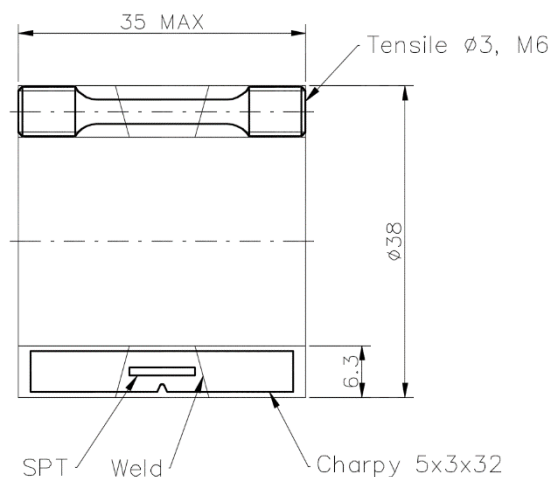
Figure 8. Location of test specimens in a welded joint.

Specimens for SPT were cut from welded joint and base material after exposure. Correlation established for these materials in 2011-2013 [8] was used for tensile strength and yield stress calculations of base materials. Charpy impact test was performed using specimens of welded joints in as-received state and after exposure.

Test results showed lack of sensitivity of tensile tests for assessment of material changes appearing in the locally restricted area of the studied welded joints. However, material degradation was very well detected and confirmed by using SPT method. Figure 9 shows significant influence of one-year exposure on material properties of TP347HFG-HR3C weld metal. Fracture energy was more than 50% lower compared to specimens after exposure.
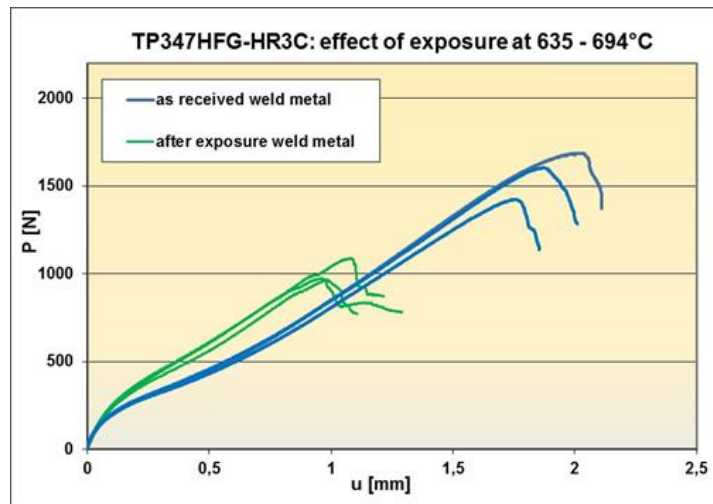
Figure 9. Influence of exposure on fracture energy of weld metal of TP347-HR3C weld joint.

Below is documented effect of PWHT and exposure at lower working temperature on fracture energy of the whole TP347HFG-HR3C weld joint (see Figure 10). It is evident that PWHT caused increasing of fracture energy of TP347HFG base material before high-temperature exposure (higher values of force and displacement in figures 10 (a) and (b)), but after high-temperature exposure values of fracture energy were nearly the same. On the contrary, HR3C material shows interesting behaviour. PWHT decreased its fracture energy moderately with bigger scatter of values in the as-received state. But fracture energy of HR3C base material after exposure shows drop to 50% of values in the as-received state independently of PWHT. Figure 10 shows that HR3C fracture energy after exposure corresponds to the level of weld metal.

a

b
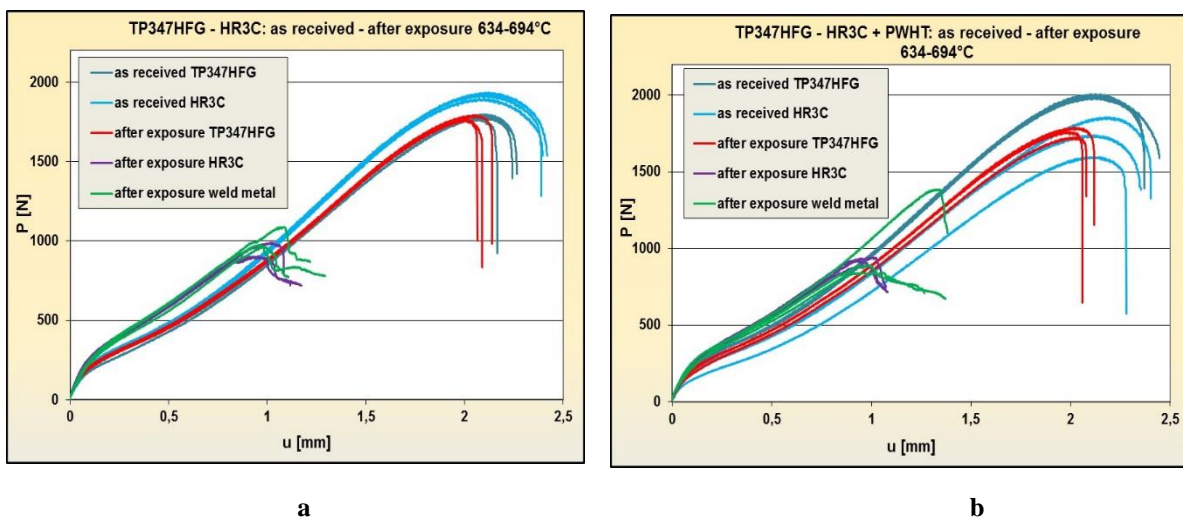
Figure 10. Comparison of SPT results of TP347HFG-HR3C welded joint in the as-received state and after exposure, **(a)** – as-welded state, **(b)** after PWHT.

The homogeneous welded joint was chosen as the other example of PWHT effect. The positive effect of PWHT especially on fracture energy of weld metal is evident in the Figure 11. In this case PWHT has a positive effect. Although fracture energy of TP347HFG base metal increased only moderately, increase of fracture energy of weld metal is evident.
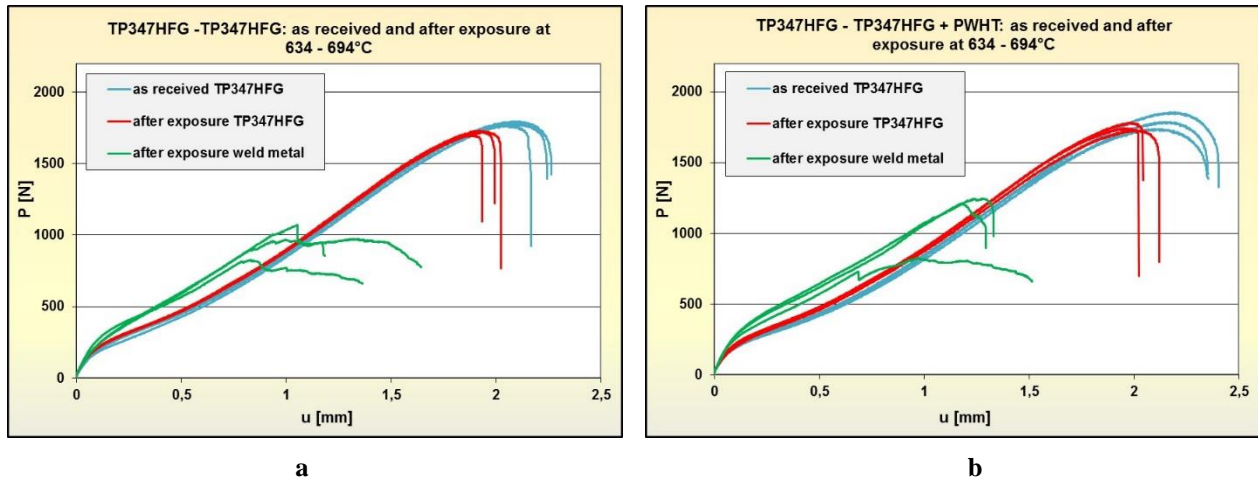
a   **b**

Figure 11. Comparison of SPT results of TP347HFG-TP347HFG in **(a)** as received state after exposure, **(b)** in as received state after heat treatment and exposure.

Degradation effects of high working temperature and corrosion environment of boiler was also demonstrated very well by Charpy test using miniaturized specimens. The absorbed energy of weld metal dropped down to 1/3 of the value in the as-received state (see Figure 12).
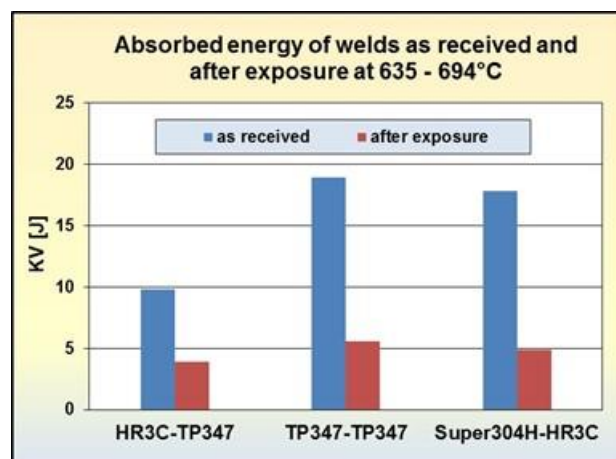

Figure 12. Effect of exposure on absorbed energy of chosen weld joints.

7. Mechanical properties of tube bends with different bend radii

In order to study the effect of plastic deformation on material properties of tubes, five tube bends of steel grades HR3C, TP347HFG and Super 304H with different bend radii were prepared by cold bending of tubes ø 38 x 6.3 mm [9]. R/D ratio as well as deformation of each bend was calculated for individual bend radii and is stated in Table 4. SPT specimens were also prepared in each bend from the area with corresponding deformation. In all tested bends were at disposal both results obtained by miniaturized tensile testing as well as by SPT, therefore it was possible put these data into correlation of force in SPT and stress in tensile tests. The correlation was further completed by the results of three tubes tested after long-term exposure (two tubes of grade TP347HFG exposed for 100,000 hours, one tube of grade Super 304H exposed for 13,000 hours). In Figure 13 is proved that data from SPT and tensile test, especially yield stress, can be very well correlated regardless deformation of material. The obtained results confirmed that all of the tested tubes and tube bends fitted the correlation line very well regardless of the bend radii (plastic deformation level) and/or the fact that they were tested in as-received condition or after long-term high temperature exposure.

Table 4. List of tested bends with calculated values of deformation.

Steel Grade/Radii	Deformation [%]				
	R50	**R60**	**R80**	**R100**	**R120**
▲ Super 304H	38	32	24	-	-
◆ HR3C	38	-	-	19	16
■ TP347HFG	38	32	-	19	16
R/D	1.32	1.47	2.10	2.63	3.16
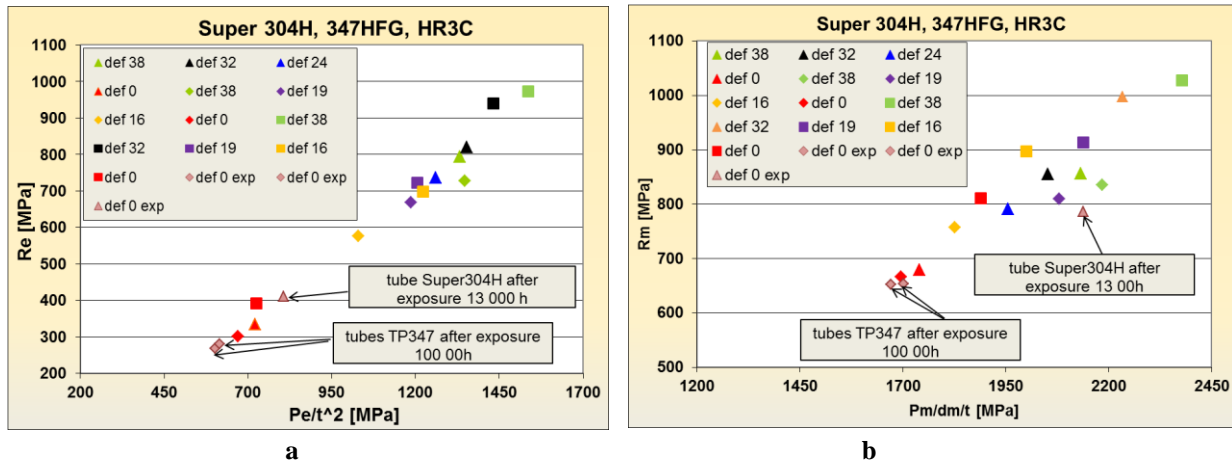
Figure 13. (a) SPT correlation of yield stress, **(b)** SPT correlation of tensile strength

8. Discussion

The presented paper summarized and reviewed the results of miniaturized tensile tests and small punch tests of various materials and components. It has proved the wide scale of use of SPT method, which seems to be a suitable method for evaluation materials not only in as-received state but also after long-term exposure at high temperature, e.g. after long-term degradation in power plant. It was demonstrated that the method is suitable for repeated assessment of material of boiler drums and it is capable of detecting little material changes manifested only by increasing of FATT, whereas yield stress and tensile strength stayed more or less constant. Differences in chemical composition of component correspond with heterogeneity of material and especially content of harmful tramp elements (Sb, Sn, Cu) influences fracture properties of material. Having in mind that the FATT is relatively high, it was recommended to pay attention to manipulation with this component during cold shutdown.

Another observation of material degradation was performed on turbine case bodies of ethylene unit. Periodically repeated analyses of mechanical properties confirmed decreasing tendency of the yield stress and also the yield stress/tensile strength ratio. Yield stress vs. tensile strength ratio is decreasing due to the process of grain boundary softening and decreasing of strain hardening and is one of the typical features of long-term high temperature exposure of metallic materials used in industrial components. On the other hand, perhaps all abrupt changes disturbing the trend of decreasing mechanical properties can be probably attributed either to the influence of material inhomogeneity of large castings or to a combination of other factors like decarburization on the surface of large castings accompanied by a change in strength. Therefore, it is also very important to machine small punch test specimens from the same distance from the outer surface of the tested component.

Big effort is devoted nowadays to the research of new materials for USC power plants. Small punch testing is capable to exactly analyse the material properties of thin-walled tubes as well as their welded joints and bends. The fracture behaviour of these tubes is significantly different in the fire-side and the opposite side of the tube due to precipitation of sigma phase in the microstructure. The embrittlement effect of sigma phase precipitating during long-term exposure at high temperatures is well-known [5], in the respective case the fracture energy determined using SPT was lowered by 50% in the fire- side tube.

Testing of welded joints of new austenitic heat resistant steels for USC application using SPT confirmed that weld metal was the weakest part of welded joints because its fracture energy was significantly lower compared to nearly all base materials except of steel HR3C after long-term exposure. The reason of this behaviour has not been reliably explained yet and could become a topic for further research focused on materials for USC application.

Within the study of change of mechanical properties of austenitic tube bends after technological operation the correlation between tensile test and SPT in as-received state was performed. The results of SP tests performed on tube bends with various plastic deformation (R/D ratio) fitted very well the correlation between conventional and SP tests for both yield stress and tensile strength, which means that the method can be used for the new austenitic heat resistant steel grades with wide range of strength, from solution annealed to deformation strengthened after cold plastic deformation. At the same time, the correlation can be used for materials analysed in as-received condition as well as after long-term exposure at high temperatures.

9. Conclusions

The paper presented some cases of exploiting small punch test method in analyses of mechanical properties, toughness and plasticity of materials used in the power industry and also evaluation of material degradation of power plant components after long-term exposure at high temperatures. Thanks to the minimized amount of sampled material the small punch test method is capable to perform repeated analyses in small area and to monitor changes of material properties and/or material degradation with prolonged time of exposure. Small punch testing programme performed on three newly developed austenitic heat resistant steel grades then confirmed that the method can be also used for evaluation of material properties and their changes due to both hardening caused by cold plastic deformation and degradation due to long-term exposure at high temperatures.

References

1. Stejskalová, Š. *Evaluation of Actual Material Properties of Boiler Drum K4,* Technical report No. T-51/2014, Materials and Metallurgical Research: Ostrava, 2014 [in Czech]
2. *Small Punch Test Method for Metallic Materials.* CEN WORKSHOP AGREEMENT CWA 15627, December 2007
3. Stejskalová, Š.; Kander, L. *Evaluation of Material Properties of Turbine Bodies GT 201, 601 and 651 of Ethylene Unit Using Small Punch Test Method*, Technical report No. T-82/2014, Materials and Metallurgical Research: Ostrava, 2014 [in Czech]
4. Korcakova, L.; Kander, L. Montgomery, M., Jensen, H. T., Stejskalová, Š.: *The Influence of Sigma Phase Precipitation on Mechanical Properties of TP347H Austenitic Steel after 100.000 h*, In: Determination of mechanical properties of materials by small punch and other miniature testing techniques (Eds. Matocha, K., Hurst, R., Sun, W.). Ostrava: Ocelot, 2014, pp. 119-132. ISBN 978-80-260-6722-1.
5. Kuboň, Z.; Stejskalová, Š.; Kander, L.: *Effect of Sigma Phase on Fracture Behaviour of Steels and Weld Joints of Components in Power Industry Working at Supercritical Conditions*. In: InTech: Austenitic Stainless Steels - New Aspects, Croatia 2017. doi.org/10.5772/intechopen.71569
6. Minami, Y.; Kimura H.; Ihara, Y. *Microstructural changes in austenitic stainless steels during long-term aging.* Mater. Sci. Technol.*,* vol. 2, 1986, pp. 795 – 806
7. Kander, L.; Stejskalová, Š. *Study of Material Properties and Structural Changes of Weld Joints of Tubes after Exposition in Corrosion Environment*, Technical report T-46/2014, Materials and Metallurgical Research: Ostrava, 2014, [in Czech]
8. Kander, L.; Stejskalová, Š. unpublished results, Materials and Metallurgical Research: Ostrava, 2015
9. Pomikálek, L.; Kander, L.; Hermanová, Š. *Evaluation of Material Properties of New Austenitic Steels and Welded Joints for Use in Boilers with Higher Steam Parameters using SPT and Miniaturized Test Specimens*, In: Determination of mechanical properties of materials by small punch and other miniature testing techniques (Eds. Matocha, K., Hurst, R., Sun, W.). Ostrava: Ocelot, 2014, pp. 204-211. ISBN 978-80-260-6722-1.

Considerations for the accreditation of small punch creep testing

A.J. Jones [1,*] and M.R. Bache [2]

[1] Swansea Materials Research and Testing Ltd, The Abbey, Singleton Park, Swansea, SA2 8PP;
andrew.jones@swansea.ac.uk

[2] Institute of Structural Materials, College of Engineering, Bay Campus, Swansea University, Swansea, SA1
8EN; m.r.bache@swansea.ac.uk

* Correspondence: andrew.jones@swansea.ac.uk; Tel.: +44-1792-602273

Abstract: Efforts to extend a pre-existing European Code of Practice (CoP) covering small punch creep and tensile testing into a full International standard procedure are progressing. Swansea Materials Research & Testing Ltd, in collaboration with the academic team based at Swansea University, have been proactive in anticipating some of the key recommendations from the ECISS TC 1010/WG 1 with a view to gaining accreditation for an extensive suite of small punch test equipment. Here, comparisons between the miniaturised form of small punch creep testing will be made to the expectations for calibration and measurement laid down by existing standards for creep testing of conventional scale specimens. In particular, the calibration requirements relating to load, displacement, alignment and temperature measurement will be addressed. With test reproducibility at the forefront of our attention, recent modifications to test rigs to control load application and validation exercises to define small punch temperature distribution will be described. Ultimately, the need to develop an uncertainty budget for small punch creep testing will be highlighted.

Keywords: Accreditation; Small punch creep; Equipment design; Procedures

1. Introduction

The suite of small punch test machines currently employed for creep evaluations at Swansea Materials Research & Testing Ltd (SMaRT) has been fashioned over the previous quarter century to address a wide range of assessment requirements. Originally designed to support investigations sponsored by the power generation sector in the 1990s, more recently these rigs have been modified and increased in number to also serve the aero-gas turbine industry. With the continual advancement in material capabilities, this has required increases in the maximum test temperature and applied load in particular.

Grounded on local best practice, Swansea based academics contributed to the establishment of the original European Code of Practice [1] in small punch testing. The fundamental requirements of creep testing were applied to the small punch technique, in particular the need for thermal and mechanical stability over long time periods, exceeding thousands of hours on test. Naturally, test procedures and International standards to describe conventional scale creep tests under axial tension were consulted. However, wider and more specific aspects of the small punch test design and procedures are now worthy of consideration. A rigorous assessment of typical small punch test equipment is required in anticipation of a new European test standard to be developed through the ECISS TC 1010/WG 1 committee, designated prEN 15627 [2]. Ultimately, it is hoped that by satisfying the current suggestions for small punch calibration and compliance to the European standard, multiple laboratories will be able to gain accreditation for small punch creep testing and thus offer a consistent market for such research and commercial testing.

2. Small Punch Mechanical Calibrations

The most obvious approach to small punch equipment calibration is to take a lead from established International standards describing the best practice to be adopted for conventional scale axial creep tests under tension. In the case of the ISO 17025 accreditation schedule for SMaRT [3], this incorporates guidelines from BS EN ISO 7500-2:2006 "Metallic materials – Verification of static uniaxial testing machines Part 2: Tension creep testing machines – Verification of the applied Force" [4] and BS EN ISO 9513:2012 "Metallic materials – Calibration of extensometer systems used in uniaxial testing" [5].

With reference to a typical small punch creep test frame, Figure 1, the majority of working laboratories continue to employ vertical dead pan loading to apply an axial load through an upper rod to the punch. Depending on the design and associated tolerances, potential losses due to friction could be experienced through the crosshead

bearing and between the flanks of the punch and walls of any concentric guiding clamp. To verify load application an annual verification between applied and actual load transferred through the disc should be considered. The range of load assessed should span the maximum envisaged loads during regular test campaigns with appropriate intermediate steps. This can be achieved by coupling an ISO 376 [6] certificated compression load cell device into the lower half of the load train, measuring load transferred between the load pan and the fixed base. An example of such verification performed on a single frame for a load range of 500N down to 100N is illustrated in Table 1. Acceptable tolerances for frictional losses must be agreed, but when comparing to BS EN ISO 7500-2:2006 errors equivalent or better than class 0.5 should be possible. In turn, individual weights used for calibration and subsequent testing should be formally verified to an accuracy of 0.1% on a five year cycle according to BS EN ISO 7500-2:2006. The requirement to perform regular applied load calibrations is even more pertinent to systems incorporating offset lever load application where errors are possible due to wear in rotary bearings and counterbalance settings.
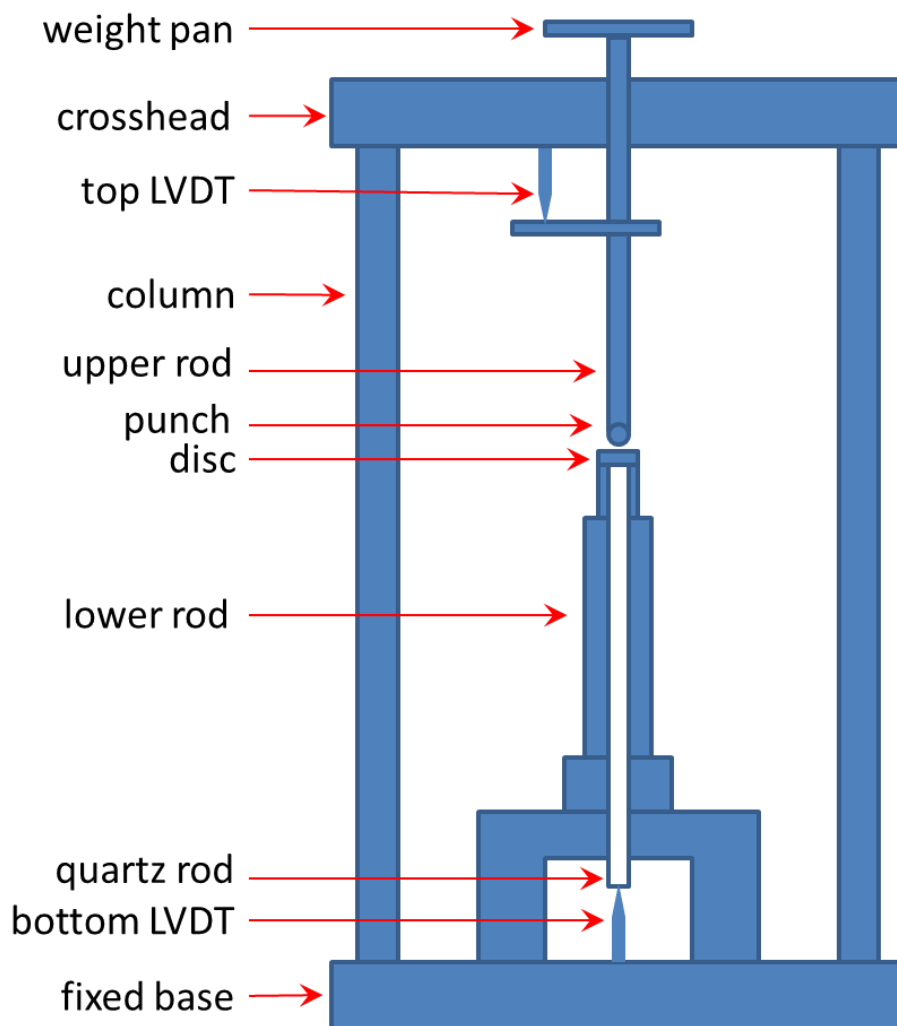
Figure 1. Principal components of a small punch creep rig.

The philosophy behind the practice to calibrate creep extensometry described in BS EN ISO 9513 is to define the performance of the complete extensometer assembly, i.e. in the case of tensile creep this is usually a complete drop leg cage instrument. This procedure recognizes the complex, multi-jointed nature of the assembly, subject to misalignment, bending displacemens and potential play between the clamping fixtures and the specimen. The cage is attached to a certified extensometer calibration rig remote from the test frame. Applied displacement is compared to the measured output, normally the electrical average of two linear variable displacement transducers (LVDTs). The entire electrical measurement system through to the eventual data logger must be incorporated into the calibration procedure.

Table 1. Load verification data for a single small punch creep rig.

Applied Force [N]	Mean true force [N]	Relative error [%]	Relative uncertainty of mean true force [%]
100	99.869	0.13	0.55
200	199.705	0.15	0.55
300	299.771	0.08	0.55
400	399.885	0.03	0.55
500	499.607	0.08	0.55

Displacement of a small punch disc should ideally be measured directly off the deforming specimen and preferably immediately below the contacting punch. This can be achieved through a lightly sprung, quartz rod running inside the internal bore of the lower rod, contacting the bottom LVDT fixed in space relative to the fixed base of the machine. Given the simple, direct transfer of displacement between the disc and the bottom LVDT, it is argued that the LVDT could be removed from its location for a simple remote calibration (based on BS EN ISO 9513:2012) against an extensometer calibration rig, Figure 2. Where laboratories also rely on a second top LVDT to measure the movement of the upper rod or load pan relative to the crosshead this should also be calibrated. Such LVDT devices should perform to class 0.5 or better.

In contrast to the effective self alignment of conventional creep load trains under tension, achieved for example through the employment of universal joints and validated through cold modulus checks, more rigorous attention to the alignment of small punch rigs will almost inevitably be expected into the future. Alignment checks of universal tension and low cycle fatigue machines usually employs a strain gauged specimen subjected to a range of tension and compression loads in accordance with ASTM E1012-14 or BS ISO 23788:2012 [7,8]. However, given the small scale of the small punch disc specimen and limited free access to the lower surface of the disc within the bore of the clamp (typically 4mm in diameter) it would be prohibitive to apply the same strain gauge techniques directly off a specimen under load. The upper and lower loading rods could be strain gauged around their external surfaces, however, to allow for checks against bending. The necessity for such detailed checks on alignment could be debatable. Good design and manufacturing practice can optimise the axiality of the upper and lower rods relative to each other and the machine columns. The employment of a deep throated linear bearing has been adopted at SMaRT to improve axial alignment of the top rod as it traverses the top crosshead. Finally, detailed checks between the opposite halves of the load train using clock gauges, precision edges and set squares are also performed on a regular basis, at least annually.

Figure 2. LVDT interfaced to a certificated calibration rig.

3. Operating Procedure

Again, the most rigorous aspects of the conventional creep standards have been adapted for our small punch creep testing procedure. Specifically, this refers to BS EN ISO 204:2009 "Metallic materials – Uniaxial creep testing in tension – Method of test" and BS EN 2002-005:2007 "Aerospace series – Test methods for metallic materials. Part 005: Uninterrupted creep and stress-rupture testing" [9,10].

The disc sample to be tested should be prepared carefully to the relevant dimensions and surface finish. After manufacture best practice would be to clean the disc in ethanol to remove remnants of polishing media and stored in a desiccator until ready for test. During insertion of the disc specimen into the supporting load train and clamping jig, the operator should wear nitrile gloves to avoid contamination by salts, particularly relevant to tests performed on titanium alloys. A standard clamping pressure between the disc and the support jig still requires agreement, but once defined the design of the clamping jig should allow for the application of measured torque via a calibrated wrench.

Despite the small height of the disc specimen, a two (minimum) or preferably three zone radiant furnace is recommended to perform testing (subjected to regular validation of temperature stability), given that specimen temperature is ultimately reliant on thermal conduction through the mass of the central clamping jig. Minimising the axial thermal gradient of the jig is advised through control of the separate heating zones. In respect of temperature measurement, to monitor tests below 1000°C pre-welded type N thermocouples are procured from an ISO 17025 accredited supplier, manufactured from certificated batches of wire. Otherwise, the laboratory is required to self calibrate thermocouples according to an appropriate standard procedure [11]. Throughout the course of a test the bead of a single thermocouple remains in contact with the upper surface of the disc via a vertical port machined into the wall of the die clamp. The thermocouple bead, therefore, makes contact within the constrained, clamped periphery of the disc. The specimen is brought up to test temperature in a controlled fashion to avoid over heating. It should be emphasized that during the heat up stage the upper rod and weight pan is mechanically supported such that the tip of the punch is suspended clear of the upper disc surface by a few millimetres. The central assembly sitting within the furnace is allowed to stabilize at the test temperature for a minimum of two hours.

This soak period has been established through thermal distribution checks of an instrumented disc. Thermocouples were spot welded to the top and bottom surfaces of a disc in the locations indicated in Figure 3, in addition to the usual monitoring thermocouple in contact within the clamped periphery (at position P). The distribution of temperature was measured over a range of typical test temperatures up to 800°C. Minimal variations (±1°C) were noted between the central locations on the top or bottom disc surface (T1 and B1). However, a difference of up to 10°C was measured between the disc periphery (P) and the centre (T1, B1), with the centre consistently the cooler position. Exposure of the central disc area to free space allowing radiated heat loss has been presumed to be the cause of this difference.
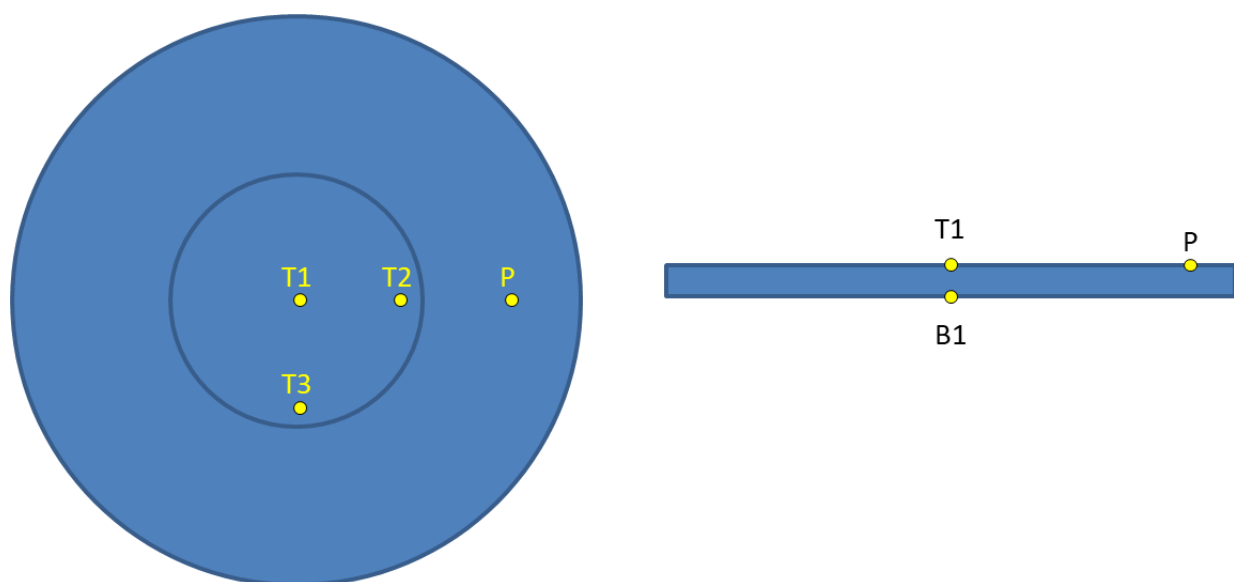

Figure 3. Thermocouple placement during temperature distribution measurements, plan and side views.

The original CoP recognized the probability of temperature variations across the specimen and recommended "validation measurements" to calculate acceptable off set control of test temperature. However, local practice is moving towards the best practice of any form of mechanical testing by ensuring the monitoring thermocouple is in contact with the specimen within the critically stressed volume. This is achieved using a thermocouple located within the hollow quartz rod used to measure displacement, with the thermocouple bead touching the lower face of the disc immediately below the point of punch contact on the upper face.

The proposed tolerances for variation in the specimen temperature during test currently envisaged in prEN 15627, Table 2, are actually more demanding than those employed under conventional creep testing, for example as defined within BS EN ISO 204. Working within these bounds is achieved during the course of long duration tests through adjustments to the furnace temperature control system as necessary. An appropriate laboratory environment is maintained and a PC based temperature logging system is employed and calibrated against a certificated thermocouple simulator on an annual basis.

The applied load is made up from a combination of selected, certificated weights plus the mass of the weight pan, upper rod and punch. The mass of the upper half of the load train is verified every twelve months and each individual set of rods recorded against specific machines. In the interests of health and safety, it is recognized that the applied mass required to perform tests on disc specimens of standard diameter and thickness (i.e. 8 to 9.5mm x 0.5mm respectively) in advanced engineering materials and nickel based supaeralloys in particular is becoming problematic [12]. A significant stack of weights is employed, usually balanced without circumferential constraint on the load pan. The issue can be addressed by deliberately increasing the mass of the upper rod and only requiring a few relatively small weights on the load pan to discriminate between the required load for individual tests. This can be achieved by employing a high density alloy for the rod or increasing the rod diameter. In turn this should lead to an improvement in rod stability and alignment within the load train.

Table 2. Permitted temperature deviations based on prEN 15627.

Test temperature, T [ºC]	Permitted deviation [ºC]
T ≤ 600	± 2
600 < T ≤ 800	± 3
800 < T ≤ 1000	± 4
1000 < T ≤ 1100	± 5
T > 1100	By agreement

The condition of the hemispherical punch tip is observed between each test, both for general condition, oxidation etc by eye and for form against a shadowgraph. This becomes more pertinent as advances in material creep strength demand ever increasing test temperatures and loads to be employed. During some campaigns it may be necessary to treat the punch as a consumable item to be replaced each test.

Given the sensitivity of some metallic systems to strain rate and the preference for a repeatable method of load application, it is recommended that the load pan be released in a single, smooth action. Historically, this has been achieved using a simple mechanical lever, however, more recently a fine threaded mechanical release has been incorporated to selected frames in a similar fashion to conventional creep frames, Figure 4.

4. Discussion

By comparing to the best practice employed for conventional scale creep testing under tension, the authors hope to initiate a debate relating to the requirements of research and commercial test laboratories alike in preparation for accreditation against the forthcoming European standard for small punch creep testing. We are confident that many of the issues discussed here are routinely addressed by most laboratories, however, more rigorous and test specific expectations from the various accreditation bodies must also be taken into account. Some of the suggestions made here relating to load calibration, alignment checks, temperature measurement and load application may be deemed demanding in terms of time, effort or cost, but they are typical of the issues raised by accreditation surveillance teams.

Ultimately, accreditation bodies will expect laboratories to develop uncertainty budgets to support small punch creep testing, similar to those derived for conventional creep tests [13]. It is recognized that this task is far from straight forward and detailed consideration should be directed at this requirement into the future.

Figure 4. Capstan style load release mechanism.

References

1. CEN, 2007. CEN Workshop Agreement - Small Punch Test Method for Metallic Materials CWA 15627.
2. prEN 15627 "Metallic materials - Small punch test method", working document, ECISS TC 1010/WG 1 committee.
3. ISO 17025 laboratory accreditation schedule, "Constant load creep testing", UKAS Laboratory 7772, 2018.
4. BS EN ISO 7500-2:2006 "Metallic materials – Verification of the static uniaxial testing machines Part 2: Tension creep testing machines – verification of applied force", British Standards Institution.
5. BS EN ISO 9513:2012 "Metallic materials – Calibration of extensometer systems used in uniaxial testing", British Standards Institution.
6. ISO 376:2011 "Metallic materials -- Calibration of force-proving instruments used for the verification of uniaxial testing machines", International Organization for Standardization.
7. ASTM E1012-14 "Standard practice for verification of testing frame and specimen alignment under tensile and compressive axial force application" ASTM International.
8. BS ISO 23788:2012 "Metallic materials – Verification of the alignment of fatigue testing machines", British Standards Institution.
9. BS EN ISO 204:2009 "Metallic materials – Uniaxial creep testing in tension – Method of test", British Standards Institution.
10. BS EN 2002-005:2007 "Aerospace series – Test methods for metallic materials. Part 005: Uninterrupted creep and stress-rupture testing", British Standards Institution.
11. ASTM E220 – 13 "Standard Test Method for Calibration of Thermocouples By Comparison Techniques.
12. Hurst, R.C.; Lancaster, R.J.; Jeffs, S.P. and Bache, M.R. "The contribution of small punch testing towards the development of materials for aero-engine applications", Theoretical and Applied Fracture Mechanics, vol. 86 pp. 69 – 77, 2016.
13. Foster, D.J. "Manual of Codes of Practice for the Determination of Uncertainties in Mechanical Tests on Metallic Materials, Code of Practice No. 10, The Determination of Uncertainties in Creep Testing to European Standard prEN 10291", Standards Measurement & Testing Project No. SMT4-CT97-2165, September 2000.

The role of punch eccentricity in small punch testing

F. Šebek [1,*], P. Dymáček [2], P. Kubík [1], J. Hůlka [3] and J. Petruška [1]

[1] Institute of Solid Mechanics, Mechatronics and Biomechanics, Faculty of Mechanical Engineering, Brno University of Technology, Technická 2896/2, 616 69 Brno, Czech Republic

[2] CEITEC IPM, Institute of Physics of Materials, Academy of Sciences of the Czech Republic, Žižkova 22, 616 62 Brno, Czech Republic

[3] Institute of Applied Mechanics, Resslova 972/3, 602 00 Brno, Czech Republic

* Correspondence: sebek@fme.vutbr.cz; Tel.: +420 54114 4925

Abstract: The small punch testing technique under quasi-static loading was examined in the view of punch eccentricity role. It might arise especially when the ball is used as the penetrating tool, instead of hemispherical-ended punch. The austenitic stainless steel AISI 316L was chosen to execute several various "large scale" tests in order to calibrate the multi-linear stress–strain relationship along with the ductile fracture criterion KHPS. All the calibration procedure was performed without using the small punch testing. Then, the model was applied to small punch tests to observe the prediction ability when compared to real small punch experiments. Consequently, a numerical study was conducted to see the role of eccentricity in the case of 2 and 2.5 mm ball diameters used as the penetrating tool. The magnitude of eccentricity up to 0.3 mm was numerically tested. The results showed negligible role of eccentricity for 2 mm ball diameter and minor role for 2.5 mm diameter and studied material.

Keywords: pressure vessel; piping steel grade; small sample technique; damage; elastic plastic; finite element method; associated flow rule; time independent plasticity; pressure and Lode dependent fracture criterion; nuclear industry

1. Introduction

The small sample techniques have been evolved since the second half of the twentieth century [1,2] along with the development of more accurate measuring systems, which are capable of assessment of such miniaturized testing. The penetration test has several embodiments: the Small Punch Test (SPT); shear punch test; and disc bend test [3–5]. These have been studied by scanning electron microscopy to reveal the changes in microstructure [6]. This can be advantageously used for examination of transition layers or weldments not only for quasi-static loadings but also for creep [7].

There is a shortage of material usable for testing in energy industry applications such as the turbine rotors or cases, pressure vessels and piping, or various components subjected to radiation in the primary circuit within the nuclear power plants [8]. Those facts open wide possibilities in miniaturized testing.

Analytical equations have been formulated in order to describe the states, which the specimen undergoes. Various approximations have been proposed to correlate the data to the standardized tensile test to obtain the basic mechanical properties, such as the yield stress and ultimate tensile strength [9]. It is crucial to interpret the experimental results correctly. This was reflected in using the numerical simulations to obtain more accurate results along with more assessment possibilities. One of them may be the flow curve of material estimated by the optimization task based on the comparison of experimentally and numerically obtained force–deflection curves [10]. Nevertheless, the computations are still complicated by means of numerous uncertainties represented by the presence of friction, unknown clamping forces [11] or eccentricity effect, which is studied within the present paper. The question of eccentricity may arise especially when using a ball as the penetrating tool instead of well centered punch with hemispherical penetrating end.

2. Materials and Methods

The austenitic stainless steel grade of ASI 316L was chosen because of its wide practical applicability in aggressive environments of petrochemical industry for storage tanks with various contents.

The punch eccentricity effect was numerically studied by means of the finite element method. Abaqus 2017 was employed together with Vectorized User MATerial (VUMAT) subroutine written in Fortran 77 imperative programming language. The VUMAT user subroutine was developed in order to implement the ductile fracture criterion, so the displacement at fracture can be tracked as well.

The stress–strain relationship was estimated on the basis of a standard tensile test. It was realized through the hybrid numerical–experimental approach until the satisfying match between the experimental and computational force–displacement curves was reached. Final multi-linear flow curve is depicted in Figure 1. Additionally, elastic properties were defined through the Young's modulus and Poisson's ratio of 160000 MPa and 0.3, respectively. Physical characteristic needed in explicit computations was the density of 7850 kg·m^{-3}.
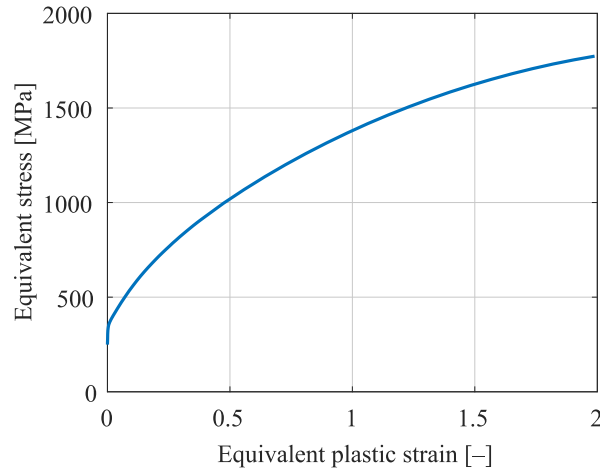
Figure 1. The flow curve in a multi-linear form for AISI 316L.

The ductile fracture was captured by a KHPS criterion with asymmetric weighting function of damage defined as [12]:

$$\bar{\epsilon}^f = \frac{P_5}{\langle \eta - \eta^c \rangle} \xi + \frac{P_4 - P_5}{\langle \eta - \eta^c \rangle} \frac{\xi + 1}{2},$$ (1)

where $\bar{\epsilon}^f$ is the fracture strain, P_4 and P_5 are the material constants, ξ is the normalized third invariant of deviatoric stress tensor, η is the stress triaxiality and η^c is the critical stress triaxiality, which is related to the cut-off region, where there is no damage accumulation because of infinite fracture strain:

$$\eta^c = \left(P_2 - \frac{P_1 - P_3}{2} - P_3 \right) \xi^2 - \frac{P_1 - P_3}{2} \xi - P_2,$$ (2)

where P_1, P_2 and P_3 are the material constants of this five parametric failure model.

The damage parameter was tracked through the equivalent plastic strain $\bar{\epsilon}^p$ as:

$$D = \int_0^{\bar{\epsilon}^D} \frac{d\bar{\epsilon}^p}{\bar{\epsilon}^f},$$ (3)

where $\bar{\epsilon}^D$ is the equivalent plastic strain at fracture for a given loading path at this linear damage accumulation law.
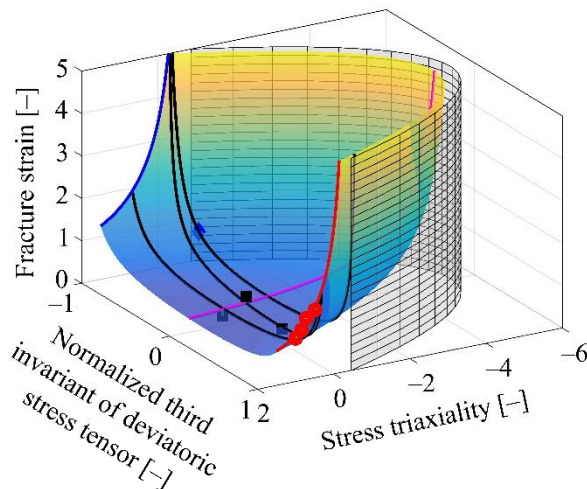
Figure 2. The KHPS criterion calibrated for AISI 316L.

Various fracture tests were used in order to calibrate the model. Those included the tensile tests of smooth and notched cylindrical specimens and notched tubular specimen; tensile–torsional test of notched tubular specimen; torsional test of notched tubular specimen; and compression of notched cylindrical specimen. These eight independent tests are represented by points in Figure 2 along with the calibrated fracture envelope. The state variables cannot be measured directly, so those were obtained from the numerical simulations. The calibration itself was realized through the averaged stress triaxiality and normalized third invariant of deviatoric stress tensor within MATLAB 2016b. All fracture-related material constants are given in Table 1.

Table 1. Material constants of a KHPS criterion for 316L.

P_1 [1]	P_2 [1]	P_3 [1]	P_4 [1]	P_5 [1]
0.471	5.416	0.873	1.583	2.980

3. Results

Real SPTs were performed using the hemispherical-ended punch of 2 mm in diameter. All these experiments should represent the case with no eccentricity. On the other hand, the device can work with a ball, too. The centering may not be ensured well if the ball is used, so the numerical analysis of three eccentricities of 0.1; 0.2; and 0.3 mm was conducted.

Numerical simulations with two widespread ball diameters of 2 mm and 2.5 mm were carried out. The first was directly compared to the experiments (Figure 3a) while the second one only served for observing the influence numerically (Figure 3b). The material behavior was only isotropic homogeneous with associated flow rule obeying von Mises plasticity, which is dependent on the second invariant of deviatoric stress tensor.
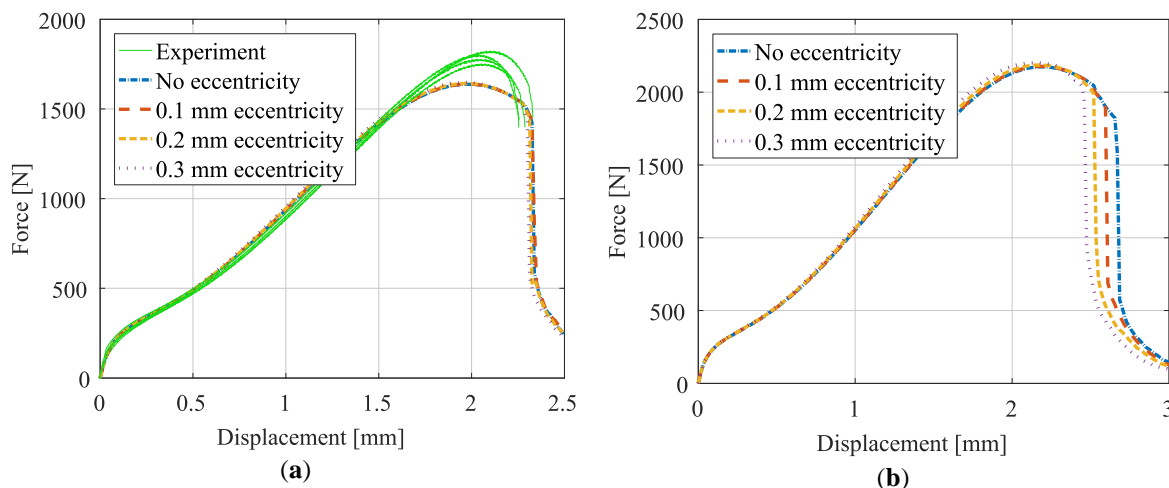
Figure 3. The SPT with punch of: (**a**) 2 mm in diameter within the experiments and numerical simulations; (**b**) 2.5 mm in diameter within the numerical simulations.

4. Discussion

The eccentricity had been assumed to play a negligible role in all previous studies. This was fully confirmed for the austenitic stainless steel and quasi-static SPT with 2 mm ball. For the 2.5 mm ball, the punching force is not influenced, whereas the displacement at fracture is. Both the eccentricity influence and the fit between the experimental and numerical curves of 2mm penetrator could be further improved. It could be interesting to incorporate the approach of continuum damage mechanics [13] because of the non-proportionality of the loading, which may play a role [14]. Another possibility is to use the plasticity model dependent on the normalized third invariant of deviatoric stress tensor [15], or to account for the material anisotropy. It would be useful to conduct a similar analysis for creep as well [16].

5. Conclusions

The small punch test was numerically studied in the view of punch eccentricity for AISI 316L steel grade. It was shown that the presumption of negligible influence of eccentricity is not always justified.

The computations revealed that there is almost no influence for ball of 2 mm in diameter, for which the experiments with some scatter was available. On the other hand, there is an apparent effect of eccentricity on the displacement at fracture for the case of ball of 2.5 mm in diameter. It needs a further study in accounting for more complex material description, which could apply to a broader range of metals.

References

1. Manahan, M.P.; Argon, A.S.; Harling, O.K. The development of a miniaturized disk bend test for the determination of postirradiation mechanical properties. *J. Nucl. Mater.* **1981**, *103–104*, 1545–1550, DOI: 10.1016/0022-3115(82)90820-0.

2. Lucas, G.E.; Okada, A.; Kiritani, M. Parametric analysis of the disc bend test. *J. Nucl. Mater.* **1986**, *141–143*, 532–535, DOI: 10.1016/S0022-3115(86)80096-4.

3. Kohse, G.; Ames, M.; Harling, O.K. Progress in developing DBTT determinations from miniature disk bend tests. *J. Nucl. Mater.* **1986**, *141–143*, 513–517, DOI: 10.1016/S0022-3115(86)80092-7.

4. Mao, X.; Takahashi, H. Development of a further-miniaturized specimen of 3 mm diameter for TEM disk (ø 3 mm) small punch tests. *J. Nucl. Mater.* **1987**, *150*, 42–52, DOI: 10.1016/0022-3115(87)90092-4.

5. Lucas, G.E. Review of small specimen test techniques for irradiation testing. *Metall. Trans. A* **1990**, *21*, 1105–1119, DOI: 10.1007/BF02698242.

6. Ma, Y.W.; Yoon, K.B. Assessment of tensile strength using small punch test for transversely isotropic aluminum 2024 alloy produced by equal channel angular pressing. *Mater. Sci. Eng. A* **2010**, *527*, 3630–3638, DOI: 10.1016/j.msea.2010.02.057.

7. Rouse, J.P.; Cortellino, F.; Sun, W.; Hyde, T.H.; Shingledecker, J. Small punch creep testing: review on modelling and data interpretation. *Mater. Sci. Technol.* **2013**, *29*, 1328–1345, DOI: 10.1179/1743284713Y.0000000278.

8. Halabuk, D.; Návrat, T. Thermomechanical assessment of fuel rod cladding made of zirconium alloy and silicon carbide material during reactivity-initiated accident. *Nucl. Sci. Eng.* **2018**, *189*, 69–81, DOI: 10.1080/00295639.2017.1373518.

9. Dobeš, F.; Dymáček, P.; Besterci, M. Estimation of the mechanical properties of aluminium and an aluminium composite after equal channel angular pressing by means of the small punch test. *Mater. Sci. Eng. A* **2015**, *626*, 313–321, DOI: 10.1016/j.msea.2014.12.054.

10. Abendroth, M.; Kuna, M. Determination of deformation and failure properties of ductile materials by means of the small punch test and neural networks. *Comput. Mater. Sci.* **2003**, *28*, 633–644, DOI: 10.1016/j.commatsci.2003.08.031.

11. Andrés, D.; Dymáček, P. Study of the upper die clamping conditions in the small punch test. *Theor. Appl. Fract. Mech.* **2016**, *86*, 117–123, DOI: 10.1016/j.tafmec.2016.07.012.

12. Kubík, P.; Šebek, F.; Hůlka, J.; Petruška, J. Calibration of ductile fracture criteria at negative stress triaxiality. *Int. J. Mech. Sci.* **2016**, *108–109*, 90–103, DOI: 10.1016/j.ijmecsci.2016.02.001.

13. Kubík, P.; Šebek, F.; Petruška, J. Ductile fracture criteria in prediction of slant fracture. In ECCOMAS Congress 2016, Proceedings of the 7th European Congress on Computational Methods in Applied Sciences and Engineering, Crete, Greece, 5–10 June 2016; Papadrakakis, M., Papadopoulos, V., Stefanou, G., Plevris, V., Eds.; Institute of Structural Analysis and Antiseismic Research School of Civil Engineering, National Technical University of Athens (NTUA): Athens, Greece; CS 212; 6699–6710.

14. Šebek, F.; Petruška, J.; Kubík, P. The role of loading path in ductile fracture. In Insights and Innovations in Structural Engineering, Mechanics and Computation, Proceedings of the 6th International Conference on Structural Engineering, Mechanics and Computation, Cape Town, South Africa, 5–7 September 2016; Zingoni, A., Ed.; Taylor & Francis Group: London, Great Britain; 090; 550–556.

15. Šebek, F.; Petruška, J.; Kubík, P. Behavior of Lode dependent plasticity at plane strain condition and its implication to ductile fracture. *Solid State Phenom.* **2017**, *258*, 213–216, DOI: 10.4028/www.scientific.net/SSP.258.213.

16. Dobeš, F.; Dymáček, P. Fracture-based correlation of uniaxial and small punch creep data. *Theor. Appl. Fract. Mech.* **2016**, *86*, 34–38, DOI: 10.1016/j.tafmec.2016.08.020.

Temperature measurement and calibration in small punch creep testing machines and equipment

D. Omacht [1,*], Z.Kubanek [2], R.Dolezal [3], Z.Kubon [4], P.Cizek [5]

[1]   daniel.omacht@mmvyzkum.cz
[2]   zdenek.kubanek@mmvyzkum.cz
[3]   roman.dolezal@mmvyzkum.cz
[4]   zdenek.kubon@mmvyzkum.cz
[5]   petr.cizek@mmvyzkum.cz
[*]   Material and Metallurgical Research Ltd., Pohranicni 693/31, Ostrava, 70300, Czech Republic
      daniel.omacht@mmvyzkum.cz, Tel.: +42-060-861-5303

Abstract: Serious lifetime estimation of machinery working in the power industry is conditioned by knowledge of an actual state of used construction materials. Determination of degradation degree by detection of mechanical properties of materials at machine parts used in operating conditions without the necessity of stopping operation of the apparatus and machine component disintegration in the past has led to the development of miniaturized test specimens associated with the emergence of special test procedures and methods. One of these methods is the small punch test (SPT) performed at room, low or elevated temperatures. Just testing temperature is one of the most important test parameters. The accuracy of measurement of this variable is a basic condition of repeatability, compatibility and comparability of the measured testing results. Very small specimen size, the way how it is stored in the heating system, the prescribed tolerance of measurement accuracy determines the way of measuring and controlling its temperature. One possible way of measuring specimen temperature is using a thermocouple directly touching its surface in the test process. However, this method is influenced by the unequal heat conduction between the specimen and the punch with the push pin in an upper direction and the cartridge sitting in the rod within the lower direction. How to determine the real specimen temperature in control systems of SPUTT500 testing machine is the subject of this paper.

Keywords: lifetime; temperature; calibration; thermocouple; small punch creep testing

1. Introduction

The constantly increasing need to determine the degree of degradation of machine parts operating under operating conditions without the necessity of machine shutdown and disintegration of the machine components led to the establishment of the ECISS / TC 101 technical committee at the end of 2016. The Commission was created within the French Standards Association AFNOR, a member of the International Standards Organization (ISO). ECISS / TC 101 consists of 40 members from 15 different European countries. Its purpose and the main objective were to elaborate and present a completely new proposal of the European Testing Standard (TC 101WI) dealing with the estimation of tensile, fracture and creep characteristics of materials from the results of Small Punch Testing. The Name of this proposal is 'Metallic materials-Small punch test method ' [2] and replaces the existing 'CEN Workshop Agreement' of 2007 (CWA 15627/2007) [1]. The proposal was submitted 12.12.2017. In 2018, the draft will be assessed and voted by representatives of each national standardization body. If the proposal is adopted, the new standard will be published by the end of 2019.

Small punch testing method is very simple at first glance. However, by upon closer examination we encounter a lot of issues arising from its use. In order to be able to compare the measured results in different laboratories and different devices, the prescribed test conditions must be strictly respected.

2. Specimen temperature measurement

One of the most important test parameters by small punch creep testing is undoubtedly the temperature. The method of its measurement, accuracy and tolerances are given in the draft standard [2]. How to ensure that these requirements are met under real test conditions? It should be noted that the test specimen is very small and that its properties in the test cannot be influenced in any way, for example by welding the specific end of the thermocouple onto its surface. The situation is also complicated by the fact that the sample is stored in a protective atmosphere of

argon and that SPT is a long-term continuous testing. Therefore, it is necessary to choose a method of measuring specimen temperature in the closest position and with the possibility of regular verification.

After many years of development and testing at the SPUTT500 (Fig.1), continuous specimen temperature measurement has been performed by a thermocouple that touches the lower surface of the sample and simultaneously transfers its deflection (Fig.2). The specially designed thermocouple (pos.5 -T3) is firmly integrated into the measuring system of the test machine. The basic question was whether the temperature measured by it is really the actual specimen temperature and how to verify it. In order to answer this, many tests were carried out. We had to modify the design of the cartridge, the argon chamber and machine control software too.

Figure 1. SPUTT 500 - Small punch creep testing machine.

1 – specimen

2 – upper die

3 – lower die

4 – punch (ball)

5 – deflection rod

T1 – calibration thermocouple measuring upper specimen surface

T2 – calibration thermocouple measuring lower specimen surface

T3 - measuring thermocouple
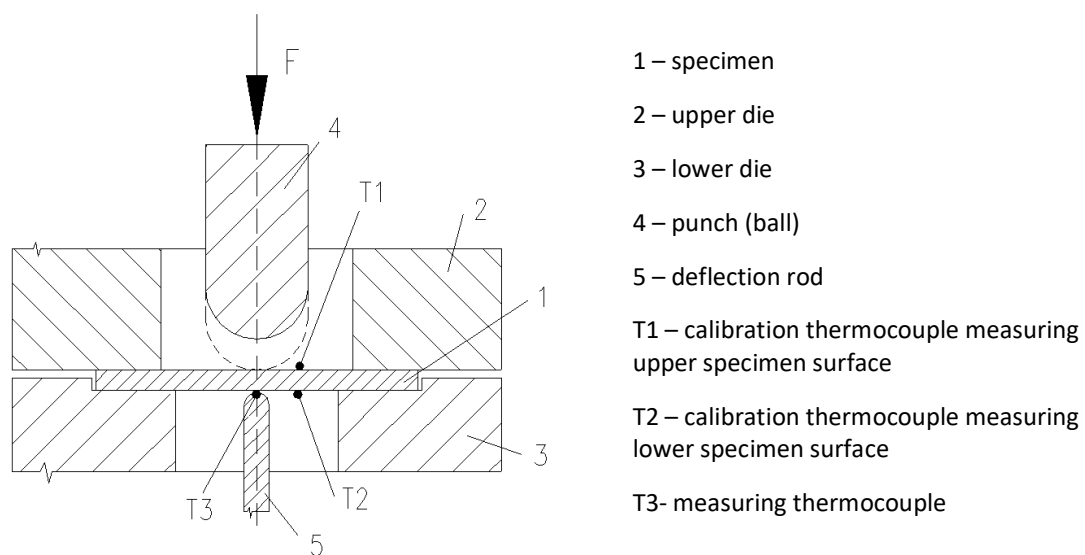
Figure 2. Comparative measurement scheme.

2.1. Comparative method

Performed tests were focused on the comparison of the temperature measured between the installed measuring thermocouple (T3) and the calibration thermocouple T1, T2 (Fig. 2).

2.2. Measuring thermocouple

The measuring thermocouple is a thermocouple type S (T3), which is the most suitable for performance long-term creep tests with highest accuracy and stability. The basic test prerequisite was the knowledge of the accuracy measurement of the used sensor. Therefore, it was removed from the machine system together with the data acquisition module and verified in an accredited metrological measuring center. The calibration protocol (Fig. 3, 4, 5) shows the observed deviations from the set nominal temperature.

Nominal Temperature [°C]	Thermocouple T1 [°C]	Deviation [°C]
404,8	404,7	-0,1
554,8	555,2	0,4
704,0	704,4	0,4
804,4	805,4	1,0

Figures 3, 4 and 5. Calibration certificate of the thermocouple.

2.3. 'Calibration' thermocouple

The actual temperature of the test sample was measured using a so-called 'calibration' thermocouple. It was carefully made and consists of two K-type thermocouples that were welded to the lower and upper surfaces of the specimen (Fig.6,7,8).

T1 – welded thermocouple measuring upper specimen temperature surface

T2 – welded thermocouple measuring lower specimen temperature surface
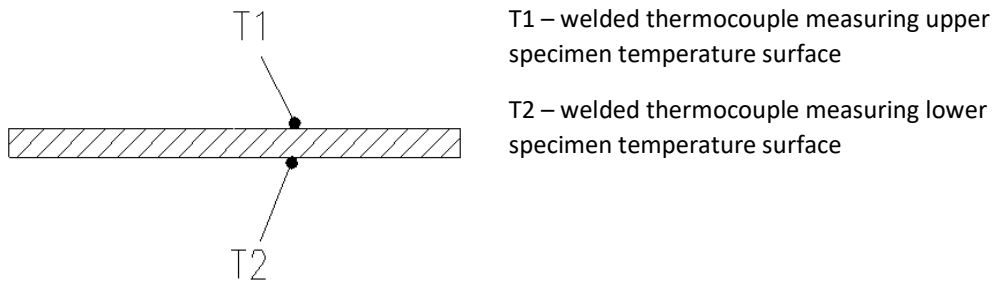
Figure 6. 'Calibration' thermocouple.
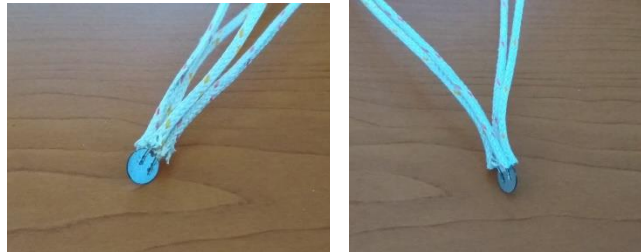
Figures 7 and 8. Location of measuring points in the 'calibration' thermocouple.

The 'calibration' thermocouple was subsequently verified in an accredited metrological measuring center with a data acquisition module (Fig. 9, Table 1, 2). As both sensors were made from the same footage, their variation from the set nominal temperature is almost identical (Table 1,2). The internal testing system of the machine has been modified so that thermocouple can be inserted into the test cartridge and the protective tube anytime (Fig. 10).

Figure 9. Calibration certificate of 'calibration' thermocouple.

Tables 1 and 2. Deviations of thermocouples T1, T2.

Nominal Temperature [°C]	Thermocouple T1 [°C]	Deviation [°C]
600,1	598,4	-1,7
650,4	648,6	-1,8
699,4	697,8	-1,6

Nominal Temperature [°C]	Thermocouple T2 [°C]	Deviation [°C]
600,1	598,3	-1,8
650,4	648,7	-1,7
699,4	697,8	-1,6

Figure 10. Mounting 'calibration' thermocouple into the machine.

2.4 Comparative testing

In accordance with the draft of the TC101WI test standard, the SP creep test can be performed either without preload or with little preload. For a higher repeatability of the measured results is required perfect heating of whole system before starting loading process. The condition is considered to be perfect warming where the dimension of the individual parts due to the influence of heating and thermal expansion remains stable or unchanging. It is possible to observe it at the deflection sensor, the value of which varies with changing specimen and inner system parts temperature.

Due to the asymmetric heat transfer in the cartridge where the test sample is stored, there is a certain redistribution of heat in the system after full load application. This may cause a rapid sample temperature change and also affects the measured specimen deflection.

For more uniform heating of the whole system and the higher repeatability of the measured results, it is advantageous to use a small preload - the pushing mandrel then contacts the upper surface of the punch which is in contact with the tested specimen. The whole system (specimen, cartridge, punch, lower and upper mandrel) is perfectly warm before full load application and this will not change even after application of the load.

To determine the actual specimen temperature, were performed five tests on the SPUTT 500 test machine with 12N preload. A calibration program (Fig. 11,12,13,14) was created with the possibility of setting five temperature levels in the range (400 ÷ 800) °C. The soaking time has been set to 90 minutes, which is sufficient time for a perfect and even heating of the whole system.
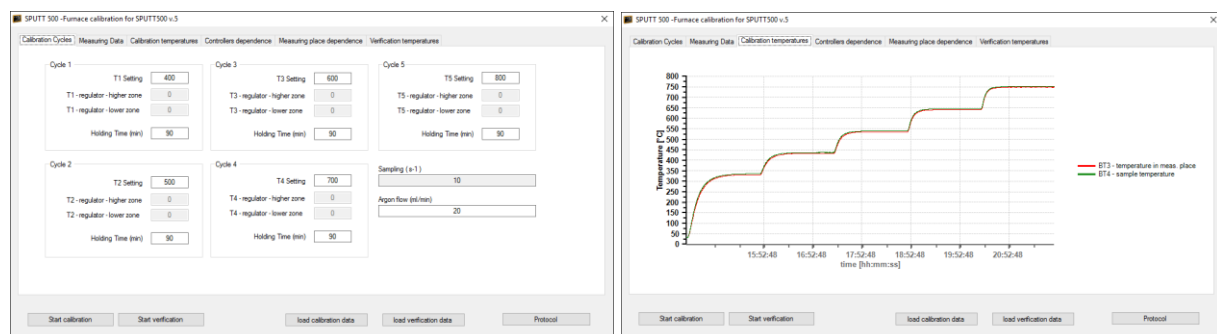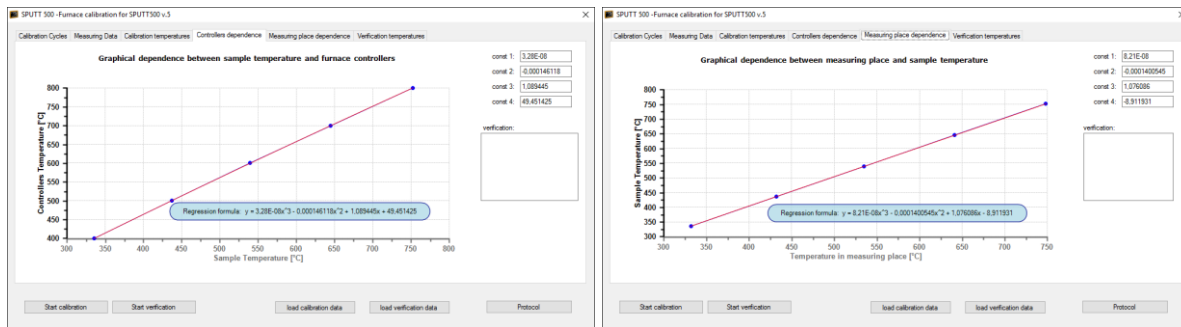
Figures 11, 12, 13 and 14. Screens of calibration software.

3. Test results and verification

The result of the comparison is the graphical dependence between the measured and the actual sample temperature (Fig.15), the measured values are given in Table 3.
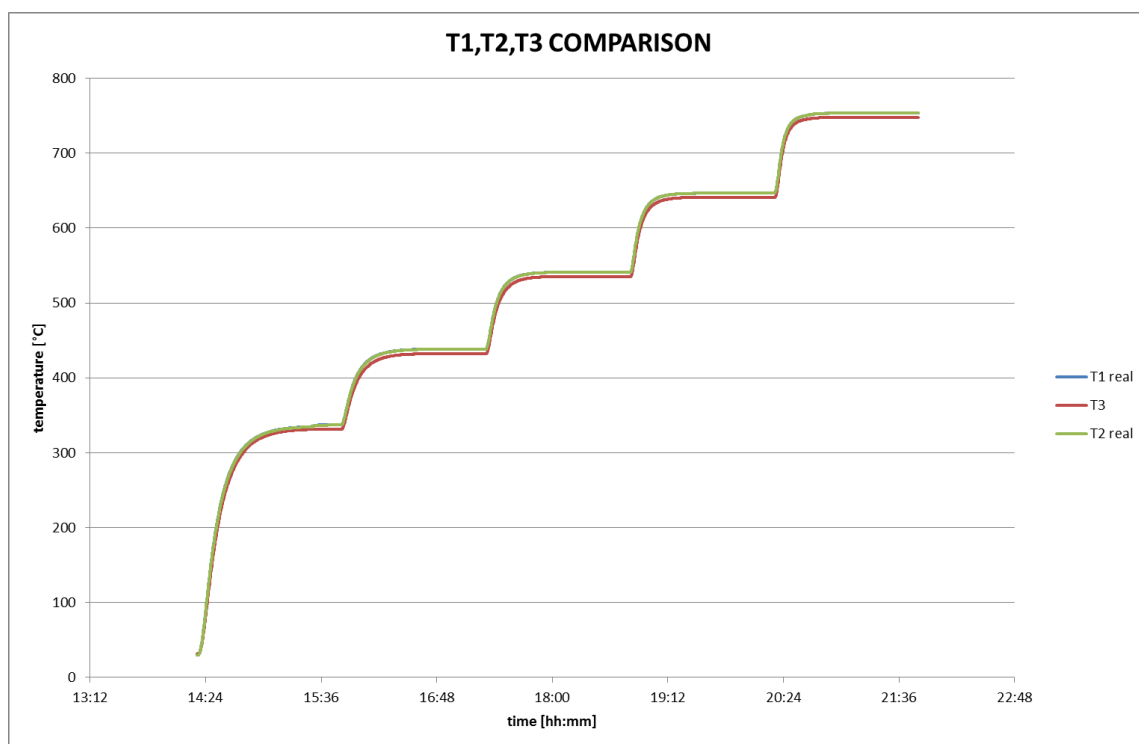

Figure 15. Temperature curves for measured points.

Table 3. Measured and calculated values obtained in comparative tests.

Test Nr.	Tcontroller [°C]	T 1 [°C]	T 2 [°C]	∅ (T1. T2) [°C]	T3 [°C]	Tdif [°C]	Tdif avg [°C]
I	400	337.4	337.1	337.25	331.8	5.45	6.19
	500	438.5	438.2	438.35	431.8	6.55	
	600	541.1	541.1	541.1	534.8	6.3	
	700	646.7	646.7	646.7	640.6	6.1	
	800	753.6	753.5	753.55	747	6.55	
II	400	336.9	337	336.95	331.6	5.35	6.16
	500	437.9	438.1	438	431.7	6.3	
	600	541.2	541.3	541.25	534.5	6.75	
	700	646.2	646.5	646.35	640.7	5.65	
	800	753.8	753.5	753.65	746.9	6.75	
III	400	337.1	337.2	337.15	331.9	5.25	6.1

	500	438.2	438.4	438.3	431.9	6.4	
	600	541.3	541.4	541.35	534.5	6.85	
	700	646.5	646.6	646.55	641	5.55	
	800	753.9	753.4	753.65	747.2	6.45	
IV	400	337.8	337.6	337.7	331.7	6	6.18
	500	438.7	438.8	438.75	432.1	6.65	
	600	541.5	541.7	541.6	535	6.6	
	700	646.7	646.3	646.5	641.1	5.4	
	800	753.4	753.1	753.25	747	6.25	
V	400	337.3	337.2	337.25	331.9	5.35	6.23
	500	438.4	438.4	438.4	431.9	6.5	
	600	541.5	541.4	541.45	534.7	6.75	
	700	646.8	646.9	646.85	640.7	6.15	

Table 4. Average result values.

Tcontroller [°C]	⌀ (T1, T2) [°C]	⌀ T3 [°C]	Tdif [°C]	Tdif avg [°C]
400	337,26	331,78	5,48	
500	438,36	431,88	6,48	
600	541,35	534,7	6,65	6,17
700	646,59	640,82	5,77	
800	753,52	747,04	6,48	

The relation between actual (T1,T2) and measured temperature value (T3) was obtained by mathematical interpolation (1).
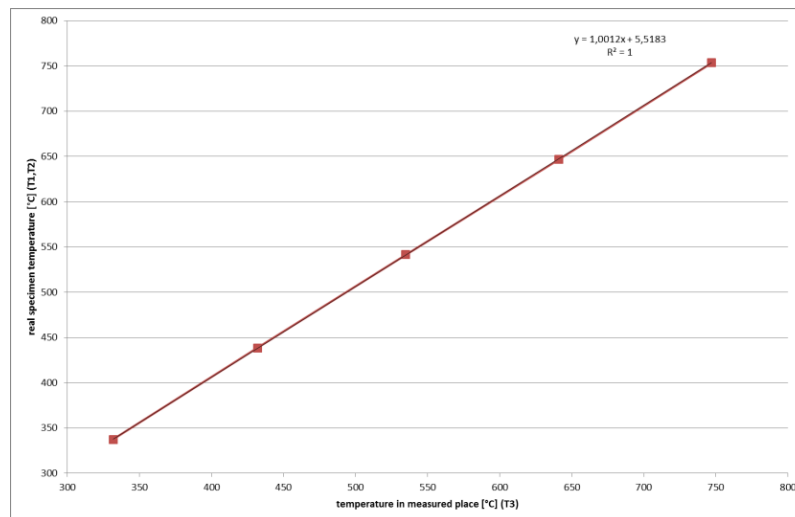
Figure 16. Graphical dependence of real specimen temperature (T1, T2) and measured one (T3).

$$y = 1.0012x + 5.5183 \qquad (1)$$

The constants of the above-mentioned dependence (1) of the actual specimen temperature on the measured one were entered into the calculation and subsequently verified by the test. The graphical temperature curve is shown in Fig. 17. In tab. 5 it is possible to see the temperature comparison at the set temperature levels.
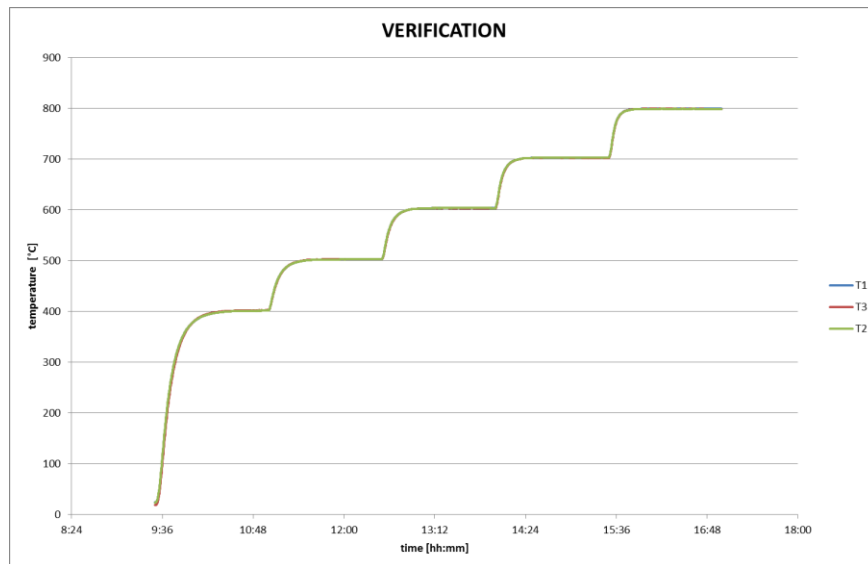
Figure 17. Temperature curves for measured points measured in verification process.

Table 5. Measured values found during verification.

Tnominal [°C]	Tcontroller [°C]	∅ (T1.T2) [°C]	T3 [°C]	Tdif [°C]	Tdif avg [°C]
400	461	399.3	399.8	-0.5	
500	558	500.2	500.3	-0.1	
600	653	600.3	599.9	0.4	0.1
700	748	700.1	699.8	0.3	
800	842	799.2	798.9	0.3	

4. Discussion

From the results obtained (Table 4) it is clear that the average difference between the actual and the measured temperature of the test sample is 6.17 °. The measured value is higher than allowed in the TC 101WI draft (Table 6).

Table 6. Permitted deviations between Ti and T.

Specified test temperature, T °C	Permitted deviation between Ti and T °C
T < 600	±2
600 <T ≤ 800	±3
800 <T ≤ 1 000	±4
1 000 <T ≤ 1 100	±5

Therefore, the measured temperature value needs to be corrected using mathematical interpolation. The kind of mathematical interpolation depends on the actual accuracy of the measuring thermocouple (type S), which is firmly embedded in the machine system and whose characteristics can be changed over time. In the control system of the SP creep machine SPUTT 500, it was therefore added the possibility of adjusting the dependence of the measured temperature transduction to the actual temperature, in addition to the linear interpolation, as well as the polynomial of the first and the second degree.

In all five tests, the difference between the temperature of the upper (T1) and the lower surface (T2) was less than 0.3 ° C, so the temperature of the upper and lower surface of the sample is almost the same. With regular verification, it is sufficient for the calibration thermocouple to have only one weld point.

Considering the consistency of the measured results, the temperature measurement system must be periodically calibrated not only at regular intervals, but also when the system configuration is changed, such as the change in the pressure of the measuring thermocouple, the change in the preload, the change of the die, punch material etc.

5. Conclusion

Performed tests clearly showed that it is not possible to carry out the small punch creep testing without proper calibration of the specimen temperature heating system. Furthermore, the proposed and approved method is fully functional and can be used regularly and repeatedly. The implemented system allows calibration and subsequent verification of the SPUTT 500 temperature measuring system with an accuracy of ± 1° C up to 800 °C.

References

1. CEN WORKSHOP AGREEMENT 'Small Punch Test method for Metallic Materials" CWA 15627:2007 D/E/F, December 2007
2. ECISS/TC 101 'Metallic Materials – Small punch test method", European Standard - Working Document, AFNOR, December 2017.

Small Punch Creep Testing for Structure Critical Design

Victoria Brown[1,2], Konrad Perzyński [3]
vbrown1@sheffield.ac.uk
Brad Wynne[1, 2], Amy Gandy[1], Mark Richardson[2]
1. University of Sheffield, Department of Materials Science & Engineering, Sheffield, UK , 2. Culham Centre for Fusion Energy, Abingdon, OX14 3DB, 3. AGH University of Science and Technology, aleja Adama Mickiewicza 30, 30-059 Kraków, Poland

Introduction

It is hoped that Small Punch Creep Testing, SPCT, will be able to measure the creep properties of new alloys while using as little material as possible.

However, the use of SPCT is still in its infancy and thus will require a lot of work and validation before it can be used confidently.

Background

- Samples are circular with a diameter of 8mm and thickness of 0.5mm±0.05mm
- The apparatus which consists of a punch, a receiving die, and an extensometer, all in temperature controlled furnace
- For a creep test deformation is controlled by constant load.
- Results of which can be plotted on an extension verses time graph
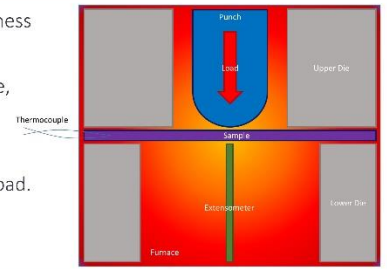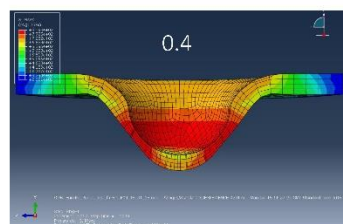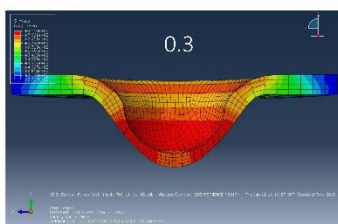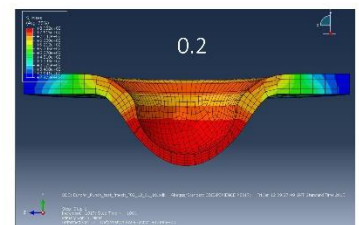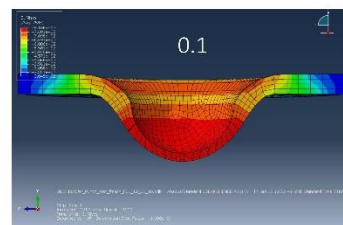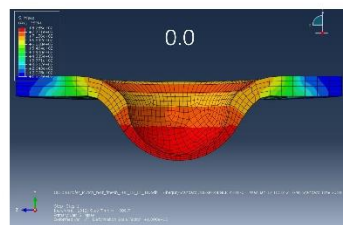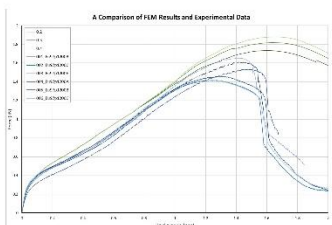

ASTM/CEN Standards

One of the recent advances in SPCT is the development of an ASTM and CEN standard. These standards outline several values which can be found by looking at the force and displacement data.
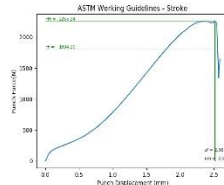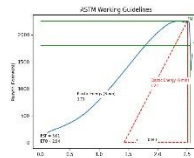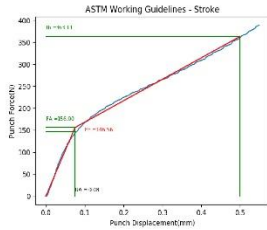
- Using Python 3, it is relatively simple to manipulate raw data sets to give meaningful information. The graphs to the left are the product of this Python 3 code.
- Data files produced from a SPCT experiment can be input and various points are selected by the user. The program then creates the graphs and also give the option to save all data as a text file.
- This allows multiple experimental runs to be analysed in the same way thus facilitating consistency.

Friction coefficient sensitivity analysis using Abaqus

- Abaqus was the chosen FEM software for this project. The model itself was built in collaboration with AGH University, Krakow.
- The initial run of tests was a friction sensitivity analysis. Friction coefficient was varied from 0.0 to 0.57 in increments of 0.1. This led to a significant change in deformed sample shape with increased friction. These images can then be compared with a cross section of a deformed sample to hopefully gain an estimate of the true friction coefficient.
- Force and displacement data was also recorded. They were then plotted alongside some SPT experimental data. The shape of the force displacement graphs are in good agreement with experimental data
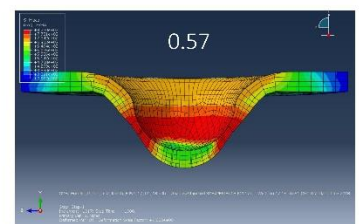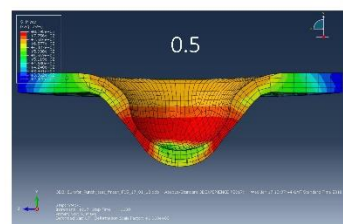
Conclusions and Future Work

- Python 3 was used to create a program that processes SPT experimental data and produces graphs and constants that comply with new ASTM and CEN standards.
- A friction sensitivity analysis was successfully carried out in Abaqus. Giving a promising starting point for a comprehensive model.
- Material damage and failure are to be added as the next step.
- This will lead in to validation of the model vial inverse analysis.

Institute of Structural Materials

Investigating the Consistency of a Laser Powder Bed Nickel Based Superalloy build using the Small Punch Test.

Swansea University Prifysgol Abertawe

Authors: B. Haigh[1], R.J. Lancaster[1], R. Johnston[1], M. White[2] and J. Minshull[2]
[1]Institute of Structural Materials, Swansea University, Fabian Way, Swansea, SA1 8EN
[2] GKN Additive, Golf Course Lane, Filton, Bristol, BS34 9AU

1. INTRODUCTION

The aerospace industry is constantly striving to establish new methods of producing components at a lower cost with faster production rates. Additive Manufacturing (AM) is a technique used to produce near net shape components from powdered material. This process limits the amount of starting material required and therefore reduces the amount of waste.

The Small Punch (SP) test is a miniaturised testing technique that can produce measurable mechanical properties to determine inconsistencies in build integrity. Small coupons of material from which SP specimens can be manufactured, can be added to the parts on the build plate, then broken off once the build is complete. The specimen can then be tested, leaving the original part with its desired dimensions.

2. PROJECT OBJECTIVES

The AM process is faced with many challenges, one being the consistency of the parts throughout the build plate. Laser powder bed was the AM technique employed to produce a build plate of 64 parts. The aim of this research is to compare the microstructure and mechanical properties of parts taken from five different locations on a build plate and to understand the consistency and varying population of any features that may result from the manufacturing process.

3. EXPERIMENTAL PROCEDURES

The initial cylindrical rods, with a 8mm diameter, were sliced into small punch discs, with an additional section used for microscopic analysis and to quantify any unwanted processing features.
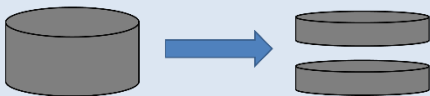

Figure 1. Representation of small punch coupons before and after sectioning.

The material used for SP testing was sliced to a thickness of 0.8mm, and then ground and polished to a thickness of 0.5mm ±0.005mm, in accordance with the directives detailed in the European Code of Practise for Small Punch Testing and the soon to be published EN Standard for Small Punch Testing of Metallic Materials

SP tests were performed on the five samples at room temperature. The samples were clamped between an upper and lower die, allowing a punch to pass through the upper die to impart a load on the top surface of the sample. The displacement rate was set to 0.5mm/min and a failure criteria of 20%Fmax was adopted throughout. All five tests were successfully completed and the results can be seen in the next section.
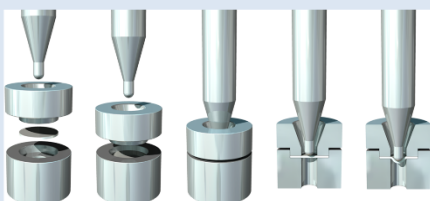

Figure 2. Small Punch tensile testing technique.

Optical microscopy was performed on the Smartzoom 5 microscope. For each sample, high magnification images across the cross sections were taken, then stitched together to produce an image of the whole sample at high magnification. Porosity calculations were then performed on these images to determine the integrity of the different build locations.

Figure 3. Smartzoom 5 setup.

4. RESULTS

The results generated from the small punch tensile tests were plotted on graphs of Standard Force (N) against Displacement (mm), where the displacement was measured by a transducer (LVDT1) sitting just below the sample in the setup. The five samples tested had the following Identification numbers: BR1-B1, BR3-B1, C3-B1, TR1-B1 and TR3-B1, with C3-B1 representing the central sample and the others being one from each corner. Figure 4 shows the results for all five samples.
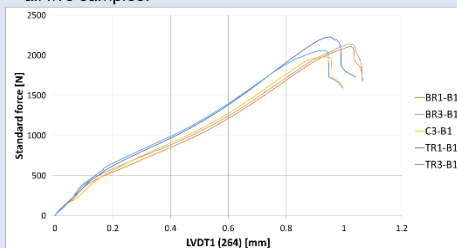

Figure 4. Small Punch tensile results.

All five locations showed a similar trend in the response to the test. The higher amount of displacement in both BR1-B1 and BR3-B1 shows a slightly more ductile response than the other three locations. The TR1-B1 and TR3-B1 curves sit above the rest, indicating these 2 samples have achieved a higher strength than the other samples. Table 1 shows the properties taken from the graph.

Specimen ID	F_{max}	d @ Fmax
	N	mm
BR1-B1	2109.86	1.02
BR3-B1	2143.33	1.02
TR1-B1	2230.63	0.95
TR3-B1	2062.35	0.92
C3-B1	1984.07	0.94

Table 1. Numerical data taken from the small punch tensile test, F_{max} = maximum force, d = displacement.

Optical images were taken of the surfaces of the five mounted samples. Figure 5 depicts an example of the stitched imaged that was produced. Small dark regions can be seen which indicate the presence of a pore. 'Imagej' was used to further analyse the pores and to calculate the volume fraction of such features, with the values displayed in Table 2.
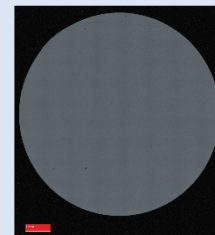

Figure 5. Stitched Smartzoom image of C3-B1.

Specimen ID	Average Size (µm²)	%Area (µm²)
BR1-B1	47.78	0.06
BR3-B1	36.50	0.03
TR1-B1	31.20	0.02
TR3-B1	56.65	0.03
C3-B1	23.84	0.02

Table 2. Porosity calculation results.

5. DISCUSSION

The overall aim of this research was to compare the microstructure and mechanical properties of the five locations to see if there is any consistency in the build.

From the SPT, for all locations up to 0.8mm displacement, the results are very similar, with just two of them slightly outperforming the others. Beyond this value of displacement, the results differ more, but still remain within a range that shows consistency throughout the build, with no outliers.

From the porosity calculations, the results generated show that both the average size and %area of the pores indicate a high level of consistency for all locations. There is a small deviation in results, but again, this variation is considered to be small enough to fall within expected scatter.

Overall, from the five locations tested, both the microstructure and property results have identified that the build is consistent and there are no specimens that act as anomalies that wouldn't be acceptable.

6. FUTURE RESEARCH

Currently, only five locations have been tested. However, in future work the project will evaluate other alternative build plate locations to be able to come to a final conclusion about total consistency across the build. In addition, the effect of alternative post processing will be assessed and compared with the results collected to date. Furthermore, testing the material at the in-service temperature would extend the understanding of the alloy's performance, whilst in their application. Taking coupons from different heights in the build will also reveal how the microstructure and properties evolve through the build.

ACKNOWLEDGEMENTS

EPSRC Engineering and Physical Sciences Research Council

SMaRT Swansea Materials Research & Testing Ltd

GKN

product**range**

tube**furnaces**

Our tube furnace range offers a high performance heat source allowing a furnace to be used in either vertical or horizontal orientation. Furnace hot zone diameters typically range from 38mm to 160mm. Furnaces are available in a variety of lengths to suit your application. Single or multi heated zone furnaces are also available as a standard option.
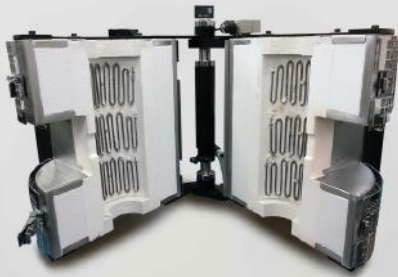
split**furnaces**

The split furnaces we design and manufacture are designed primarily for use with materials testing applications, where samples are being tested in tension and / or compression. This clamshell design is also well suited to other applications where ease of specimen access is required.

short**height** **split**furnaces

Specifically designed to enable samples to be gripped inside / outside of the "hot zone", therefore reducing the need for expensive high temperature tooling.

environmental **chambers**

We have a range of Environmental Chambers designed for general purpose, materials processing and materials testing applications. Temperature ranges from −180°C to +600°C. We are also able to provide bespoke solutions to suit your specific needs.

From a nuclear power generation background with considerable experience in materials testing and processing applications, STS are here to help you control your environment. Our knowledgeable engineering team have over 60 years of experience in the design and manufacture of a wide variety of advanced thermal systems within industry and academia. Quality, reliability, and innovative are all words used by our extensive list of customers when describing the products and services we provide. We pride ourselves in gaining customer satisfaction; this is only possible with our dedicated and highly skilled team. Our products and services speak for themselves.

Innovation in Thermal Systems

Version 4

temperature**control** systems

We design and manufacture a wide variety of standard and special temperature control systems to suit specific applications and furnace configurations. Whatever your requirements please discuss them with one of our experts to enable us to provide the most appropriate solution.

vacuum**furnaces**

MRF is a world leader in the design and manufacture of high temperature vacuum furnaces. Severn Thermal Solutions represent MRF in Europe through our sales & service organisation. Please discuss your requirements with us or visit the MRF website for additional information at www.MRF-Furnaces.com.

radiant**furnaces**

Our radiant furnace range has been specifically developed for semiconductor processing and rapid heating and cooling applications.
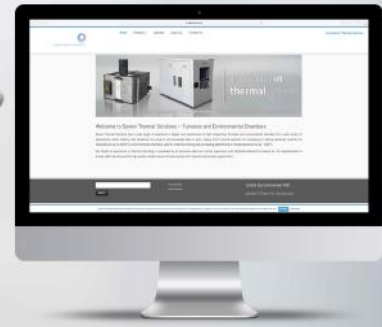
online

Visit our brand new, redesigned website where you can see our standard products and download/print technical datasheets. From here you can make product specific or general enquiries. Simply visit www.severnts.co.uk

service**repair**&**maintenance**

Whether you have a single furnace in need of repair or an entire high temperature laboratory requiring a maintenance contract, we can provide a quality service to meet your needs. With many years of experience and the facilities to repair not only our own systems but also other manufacturer's equipment, we offer the following services:
- Inspection & repairs
- Replacement or rework of products containing aging and potentially hazardous insulating materials
- Spares, such as elements, insulation, ceramic work tubes and thermocouples

Version 4